ISSN 0289-842X

# RIKEN Accelerator Progress Report

1991

vol. 25

理化学研究所
the Institute of Physical and Chemical Research

# RIKEN Accelerator Progress Report 1991
## January-December

理化学研究所
the Institute of Physical and Chemical Research
Wako-shi, Saitama, 351-01 JAPAN

# CONTENTS

Page



2. Atomic and Solid-State Physics

Page

Page



## 5. Instrumentation



## 6. Material Analysis

Page

# I. INTRODUCTION

M. Ishihara

This Annual Report covers the activities of the RIKEN Accelerator Research Facility for the year of 1991. The major facility available is an intermediate-energy heavy-ion accelerator complex consisting of a central booster accelerator, RIKEN Ring Cyclotron (RRC), and two injectors, a heavy-ion linear accelerator (RILAC) and an AVF cyclotron (AVF). Heavy ions to be accelerated up to 135 MeV/nucleon have been served for a variety of disciplines including nuclear physics, atomic physics, nuclear and radiation chemistry, condensed matter physics, and radiation biology. The RILAC has been also used in a stand-alone mode for atomic physics and other fields of application. On the other hand a separate use of the AVF is yet to start next year. In addition, a 1-MeV Tandetron is in operation.

Users of the facility have ranged over 11 among 50 laboratories in RIKEN. There has been also a large participation of outside users: About 240 researchers and 70 graduate students from domestic institutions have joined in the activities at the Facility. International collaborations with groups from more than 15 laboratories were also encouraged and promoted on the basis of institutional agreements or individual initiatives.

The Report also includes R & D works and construction status reports of two developing projects: One is the joint project between RIKEN and Japan Atomic Energy Research Institute (JAERI) to build an 8-GeV synchrotron radiation source (SPring-8) at the site of Harima Science Garden City, Hyogo Prefecture. The other is an international project between RIKEN and RAL (U.K.) on muon science. An intense pulsed muon beam is to be facilitated using the RAL synchrotron.

The accelerators have worked nicely through the year. The beam hours for experiments with RRC have nearly reached a level of 5000 hours per year. Installation of an ECR ion source (NEO-MAFIOS) at RILAC has significantly improved beam properties of heavier ions. Ions as heavy as $^{166}$Er have been used for an experiment. Meanwhile acceleration of protons has been tested successfully at different energies. In order to gain a broader prospect for hydrogen-beam experiments a polarized ion source is under construction at the AVF to be completed next spring.

There have been also steady developments with the experimental apparatus at RRC beam channels. In particular construction of a large-acceptance magnetic spectrometer has been completed. This is installed downstream of a projectile-fragment separator, RIPS, to serve for exclusive measurements of secondary reactions with radioactive beams. An on-line mass separator, GARIS-IGISOL, has improved in transmission efficiency significantly. Another spectrometer called SMART, a Tandem-type high-precision charged-particle analyzer, has started its operation for experiments.

Experimental studies on nuclear physics have been made primarily using beams from RRC, consuming about 70 % of the whole RRC beam hours. Emphasis has been placed on the studies on and with unstable nuclei. The fragment separator RIPS has continuously played the major role by supplying intense high-energy beams of radioactive isotopes. Nuclear density distribution and giant resonances of neutron-halo nuclei have been extensively studied through inclusive and exclusive measurements. A study of sub-barrier fusion reactions with extremely-neutron rich nuclei is under progress. Cross-sections of astrophysical interests were measured for several reactions involving unstable nuclei. In particular use of electro-magnetic dissociation process as an inverse radiative capture reaction was appreciated. A new method to produce spin-polarized unstable nuclei through projectile-fragmentation has been established: Measurements of g-factors of exotic nuclei were successfully started with such beams. Another unique approach to polarize unstable nuclei is under study, applying a laser optical pumping method to isotopes implanted in semi-conductors.

While RIPS cover relatively light isotopes heavy isotopes were studied using GARIS-IGISOL. A challenging program to search for super-heavy elements (SHE) has been continued. A possible new scheme based on a particular type of reaction process is under investigation to enhance the production and survival probabilities of SHE. The isotope separator was also used to study other heavy nuclei such as nonvolatile Hf isotopes and tin isotopes close to A = 100. An interesting attempt to produce beams of high-spin isomers has yielded a promising result. A fairly intense beam of $^{144}$Pm isomers with spin of about 30 ħ was obtained. With improved intensity this would serve to produce extremely-high-spin states at relatively low excitation energies via secondary compound reactions.

The first experiment with SMART was performed on (d,$^{2}$He) and (d, d* (S = 0, T = 1)) reactions by exploiting the wide momentum acceptance and easy access to neutron detection. Spin-isospin response is the issue of primary concern.

The activities on theoretical nuclear physics have been largely enhanced by a recently organized group consisting of three visiting professors and six post doctoral fellows. The subjects involve not only heavy-ion physics but also other aspects such as QCD nuclear phenomena and nuclei with strangeness.

Experiments on atomic physics were performed using RRC, RILAC and also the AVF ECR ion source by itself. Emission processes of $\delta$-rays in high energy atomic collisions were investigated with RRC. A detailed study of collision mechanism was performed at RILAC by observing impact parameter dependence of inner-shell ionization. Beam foil spectroscopy continued with RILAC Cr beams. Spectroscopy of doubly-excited states of He-like ions was performed with ECR. Micro cluster formation at energetic heavy-ion impact was studied with RILAC. Crystallization of Kr was studied using the Tandetron.

The major effort on muon research has shifted towards construction of the new beam channel at RAL. Meanwhile a production scheme of ultra-slow $\mu^-$ beam has been tested at RRC. Studies on muonic molecules are in progress in relation to muon catalyzed fusion.

Studies of nuclear and radiation chemistry have continued with various methodologies. Mössbauer and perturbed angular correlation techniques were used to study the properties of magnetic and high-$T_c$ superconducting materials. Rutherford scattering and PIXE techniques were applied to the impurity and composition analysis of high-purity industrial materials and environmental and geological samples. Positron annihilation analysis continued to probe dislocation in semi-conductors. A major effort was placed on development and application of a "multi-tracer" method in which a large variety of radioactive isotopes produced in high-energy heavy-ion reactions are used simultaneously as tracers. The new method has been proved to be an effective and useful means to study circulation of elements in vegetation and geographical environments.

Studies of radiation biology were performed in two aspects, space biology and radiotherapy. Effects of irradiation of high-energy heavy ions were studied on biological samples such as spores, beans, and shrimp eggs to simulate the effects of cosmic rays. Basic studies on heavy-ion cancer therapy were carried out by irradiating mice, mammal culture cells and so on at RRC.

Our scientific activities have involved a large number of seminars, workshops and symposia held at or organized by the Facility. In particular we were happy to promote the 4th international conference on Nucleus-Nucleus Collision on the basis of recent developments on heavy-ion nuclear physics at our facility. It was held successfully in June at Kanazawa with a large number of participants and lively reports and discussions.

RIKEN Accel. Prog. Rep. **25** (1991)

# II. OPERATION OF ACCELERATORS

## 1. RRC Operation

Y. Yano, A. Goto, M. Kase, T. Kageyama, T. Nakagawa, H. Isshiki,* R. Abe,* S. Otsuka,* H. Akagi,* T. Ishikawa,* R. Ichikawa,* and T. Maie*

Figure 1 summarizes the change in yearly operation hours of the RRC from 1987 to 1991 (as for 1991 see the figure caption). Since 1990 routine machine-time schedule for the year has almost been established, because there have been no interruptions due to construction works.

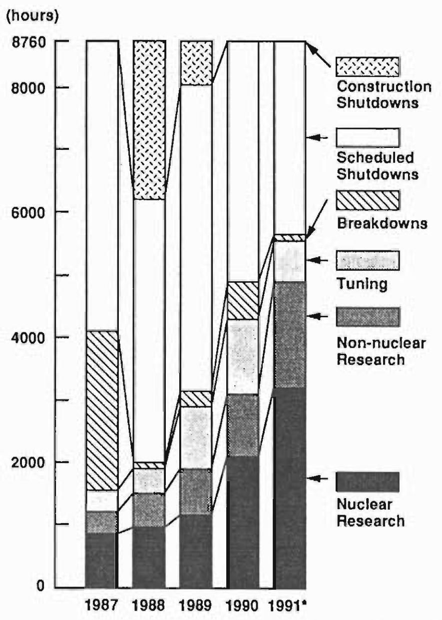


Fig. 1. Statistics of the RRC operation from 1987 to 1991. Operation hours of 1991* are the values predicted as of November 8, 1991, expecting no more breakdowns. Experiments of 710 hours as well as machine tunings of 130 hours remain scheduled.

In these two years extensive improvements have been made for the whole parts of the machine; this work was very effective in quick starting-up, stable operation, and easy maintenance. Thereby hours for tuning and breakdown have been cut back so that total effective hours for users are likely to reach nearly 5000 hours in 1991. These hours have been dovoted to carry out nuclear (70 % in portion) and non-nuclear (30 % in portion) experiments. The AVF-injected beam time has exceeded the RILAC-injected beam time in a ratio of 7 to 3. Regular long-term overhauls were carried out for 3 weeks in the winter and 6 weeks in the summer.

In Fig. 2 new beams from December 1990 through October 1991 are plotted in the available region of an energy-mass space together with the beams accelerated so far. Table 1 lists these new beams as well.

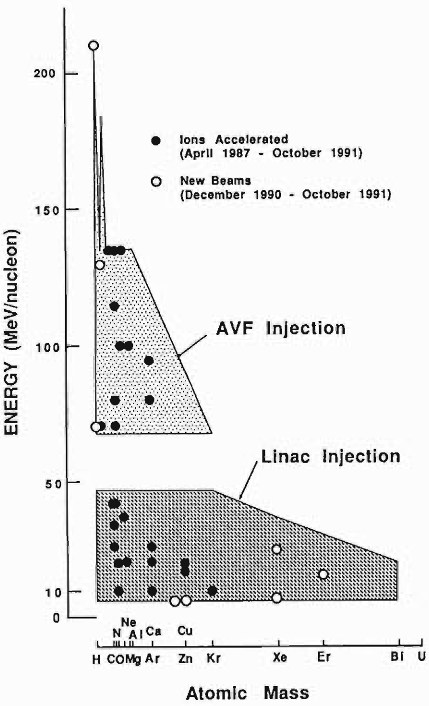


Fig. 2. RRC beams during April 1987-October 1991.

Table 1. New RRC beams in December 1990-October 1991.

| Particle | Charge | RF F (MHz) | h | Energy (MeV/nucleon) | Intensity (pnA) |
|---|---|---|---|---|---|
| p | 1 | 24.6 | 5 | 70 | 100 |
| | 1 | 38.7 | 5 | 210 | 30 |
| | 1 | 42.2 | 5 | 270 | - |
| d | 1 | 32.0 | 5 | 130 | 10 |
| $^{58}$Ni | 13 | 18 | 11 | 7 | 2 |
| | 8 | 18 | 11 | 7 | 18 |
| $^{65}$Cu | 8 | 18 | 11 | 7 | 3 |
| $^{136}$Xe | 23 | 18 | 10 | 8.5 | 4 |
| | 33 | 28 | 9 | 26 | 1.8 |
| $^{166}$Er | 32 | 22.3 | 9 | 16 | 2 |

* Sumijyu Accelerator Service, Ltd.

In late 1990 an ECR ion source, NEOMAFIOS, was installed on a high voltage terminal of the RILAC, being substituted for an old PIG ion source. Thanks to higher charge-states obtained, the RILAC acceleration performance has been roughly doubled for heavy ions, and consequently the RRC beam energies and intensities for heavy ions have been increased. In addition, when we accelerate ions of mass-to-charge ratio less than 8.1 up to the RRC minimum energy of 7 MeV/nucleon, no charge stripping is preferable owing to the high intensity for the high charge-states. Here the RRC has the K-value of 460 MeV for such a low velocity beam. We applied this acceleration mode to 7 MeV/nucleon $^{58}Ni^{8+}$ and $^{65}Cu^{8+}$ beams, and the intensities obtainable have been significantly increased by a factor of 5 as a result of no beam loss due to the stripping process.

We successfully accelerated 210 MeV and 70 MeV proton beams. In the latter, 70 MeV/nucleon $H_2^+$ ions were dissociated by a stripper foil placed at the object point of the RRC beam line.

Trim-coil power supplies have potentiality to create an isochronous field for a 270 MeV proton beam, while accoding to calculations a vertical betatron frequency crosses the dangerous resonace $v_z = 0.5$ at 210 MeV and decreases down to 0.2 at the final energy. In order to study the resonance-crossing phenomena, we tried to accelerate protons up to 270 MeV. In this trial, protons were successfully accelerated up to the final energy inside the RRC, but some part of the beam was lost near the resonance-crossing radius, where abrupt vertical shift of central particles was observed. These phenomena will be investigated in further detail.

In improvement works on the ECR ion source of the AVF cyclotron, it was found that applying a negative voltage to an electrode housed in a first-stage chamber as well as coating aluminum and magnesium oxide on a second-stage plasma chamber wall enhance the high-charge state performance. By these means 35 e$\mu$A of $^{40}Ar^{12+}$ and 6 e$\mu$A of $^{84}Kr^{20+}$ have been obtained, which allows the RRC to deliver approximately 2pnA of 110 MeV/nucleon $^{40}Ar$ and 70 MeV/nucleon $^{84}Kr$ beams, respectively.

A polarized proton/deuteron ion source of an atomic beam type is being assembled about 8 m directly above the AVF cyclotron center. Test of this ion source will be started in late 1991. R&D work on a polarized $^3He$ ion source is also pursued.

RIKEN Accel. Prog. Rep. **25** (1991)

# II-2. RILAC Operation

Y. Chiba, M. Hemmi, M. Yanokura, M. Kase, E. Ikezawa, T. Aihara,*
T. Ohki,* H. Hasebe,* T. Chiba, and Y. Miyazawa

The RILAC operation entered into a new era by replacing the PIG ion source used for many years with a new ECR ion source (Neomafios). Installation and test of the new ion source on the injector high voltage station was completed at the end of 1990. Beam service for users with the ECR source was started in Jan. 1991. Tables 1, 2, and 3, show the statistics of operation from Jan. through Dec. 1991. Highly charged ions available with the ECR source extended the usable energy range of RILAC as shown in Fig. 1. Difficulty in keeping a stable operation of the ECR source for several metal elements (e.g. Cu, Zn, and Bi) was got over in most cases by using oxide ceramics specimens. The details of the ECR source are reported in this issue also.[1] Hard machine troubles we met this year are as follows. A long bellows of NO. 3 resonator was mechanically damaged; the bellows was used for vacuum seal of the driving rod of the shorting

Table 1. Statistics of the operation for Jan. 1—Dec. 31, 1991.

| | Day | % |
|---|---|---|
| Beam time | 177 | 48.5 |
| Frequency change | 7 | 1.9 |
| Overhaul and improvement | 36 | 9.9 |
| Periodic inspection and repair | 29 | 7.9 |
| Machine trouble | 4 | 1.1 |
| Scheduled shut down | 112 | 30.7 |
| Total | 365 | 100 |

Table 2. Beam time for individual research groups.

| | Day | % |
|---|---|---|
| Atomic physics | 63 | 35.6 |
| Solid-state physics | 17 | 9.6 |
| Nuclear chemistry | 17 | 9.6 |
| Radiation chemistry | 9 | 5.1 |
| Accelerator research | 7 | 4.0 |
| Beam transportation to RRC | 64 | 36.2 |
| Total | 177 | 100 |

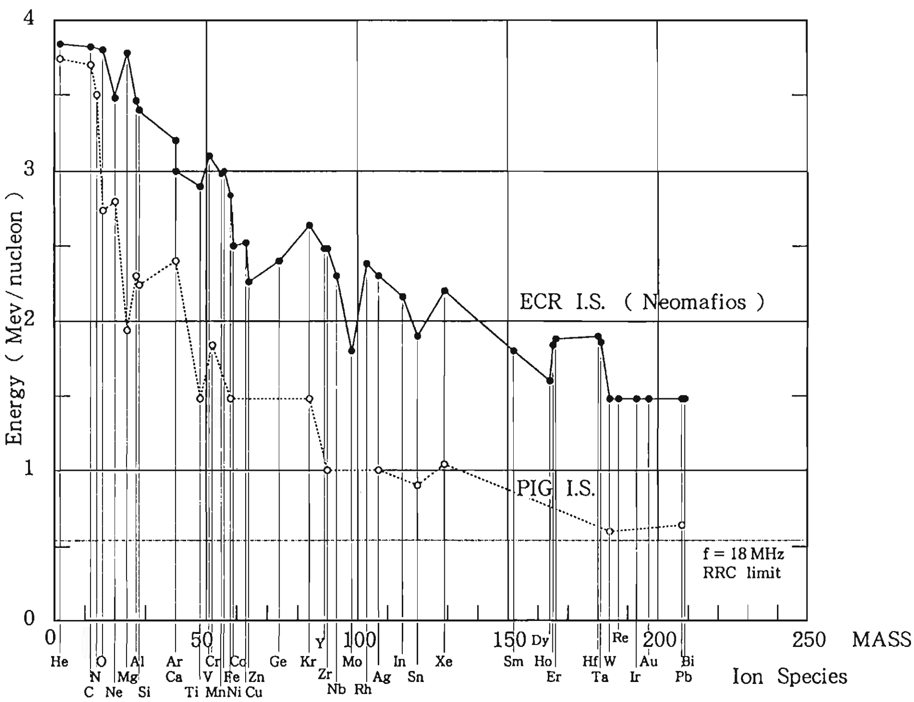


Fig. 1. Ion energies from RILAC with use of the ECR ion source compared with the previous PIG ion source.

* Sumijyu Accelerator Service, Ltd.

Table 3. List of ions used in this year.

| Ion | Mass | Charge state | Day |
|---|---|---|---|
| He | 4 | 1 | 7 |
| C | 12 | 4 | 1 |
| N | 14 | 2, 3 | 9 |
| N | 15 | 2, 3 | 3 |
| Ne | 20 | 4 | 2 |
| Si | 28 | 5 | 15 |
| Ar | 40 | 4, 6, 8 | 56 |
| Cr | 52 | 7 | 13 |
| Ni | 58 | 6, 8 | 16 |
| Cu | 65 | 8 | 5 |
| Kr | 84 | 9 | 7 |
| Sn | 120 | 13 | 1 |
| Xe | 129 | 13 | 1 |
| Xe | 136 | 9, 14 | 26 |
| Sm | 152 | 12 | 1 |
| Ho | 165 | 13 | 1 |
| Er | 166 | 13 | 8 |
| Hf | 180 | 14 | 1 |
| Bi | 209 | 10, 14 | 4 |

device. It took 3 days to repair it with a spare one. Troubles of rf contact silver sheets in the resonator, RILAC'S chronic trouble, took place again in NO. 6 resonator. In an electrostatic quadrupole lens installed at the beam exit of the ECR source, the surface insulation of electrode supports was deteriorated with sputtered metals; the shields from sputtering and the supports were improved. In the microwave source of the ECR ion source, the 8 GHz low level amplifier and the DC high voltage supply for the klystron had troubles.

References

1) E. Ikezawa *et al.*: This Report, p. 165.

RIKEN Accel. Prog. Rep. **25** (1991)

# II-3. AVF Cyclotron Operation

A. Goto, M. Kase, Y. Yano, T. Nakagawa, T. Kageyama, H. Isshiki,*
R. Abe,* S. Otsuka,* H. Akagi,* T. Ishikawa,* R. Ichikawa,* and T. Maie*

We have routinely offered AVF cyclotron beams to RIKEN Ring Cyclotron (RRC) for the last one year. Table 1 lists the characteristics of ion beams which were accelerated from December 1990 to October 1991. Among these, new ones are protons and $H_2^+$ ions. We succeeded in getting the designed maximum energies from RRC for protons (210 MeV) and deuterons (135 MeV/nucleon). We operated the AVF cyclotron for 98.5 days for beam services to users during this period.

In the summer-time overhaul, we found that there were no problems in the components of the cyclotron. The performance of the cyclotron was almost the same as in the previous year; the cyclotron has been operated with no serious troubles except that some beam losses occurred in the injection beam line and during extraction and that the beam transmission through the cyclotron was still around 10%.

Table 1. AVF beams accelerated in December 1990-October 1991.

| Ion | RF Frequency (MHz) | Energy + (MeV/nucleon) | Operation++ time (days) |
|---|---|---|---|
| $H_2^+$ | 12.3 | 4.0 ( 70) | 1 |
| p | 19.4 | 9.9 (210) | 3.5 |
| p | 21.1 | 11.8 (270) | 1 |
| d | 12.3 | 4.0 ( 70) | 3 |
| d | 16.3 | 7.0 (135) | 5 |
| d | 13.8 | 9.5 ( --- )† | 0.5 |
| $^{14}N^{5+}$ | 16.3 | 7.0 (135) | 13 |
| $^{16}O^{6+}$ | 16.3 | 7.0 (135) | 2.5 |
| $^{18}O^{5+}$ | 12.3 | 4.0 ( 70) | 4 |
| $^{18}O^{6+}$ | 14.5 | 5.5 (100) | 12.5 |
| $^{24}Mg^{7+}$ | 14.5 | 5.5 (100) | 4.5 |
| $^{40}Ar^{11+}$ | 14.05 | 5.2 ( 95) | 38 |
| | | Total | 98.5 |

\+ The values in the parentheses show the energies obtained by the coupled operation with RRC.

++ The time served to experiments.

† These ions were accelerated only with the AVF cyclotron.

* Sumijyu Accelerator Service, Ltd.

RIKEN Accel. Prog. Rep. **25** (1991)

# II-4. Tandetron Operation

T. Kobayashi, E. Yagi, T. Urai, H. Sakairi, and M. Iwaki

The Tandetron was operated for 152 days in the period from Oct. 1, 1990 to Oct. 31, 1991, during which $^{1}H$, $^{4}He$, and $^{11}B$ were accelerated.

The machine was shut down several times for replacement of a variable transformer of the electric power supply for an einzel lens, and a diffusin pump for a vacuum system of the RBS beam line, and for repairs of a high voltage power supply for a quadrupole doublet lens and an arc power supply in a duoplasmatron ion source. The acceleration tube was replaced with new one in September.

The Tandetron was used for the experimental studies on the following subjects.

(1) Rutherford backscattering spectroscopy (RBS)
  (a) Behavior of Kr atoms implanted into aluminum by the channeling method (Metal Physics Lab.)
  (b) Analysis of the Tb distribution and damage in a Tb-implanted $CaF_2$ (Semiconductor Lab. and Surface Characterization Center)

(2) Nuclear Reaction Analysis
  (a) Lattice location of hydrogen in niobium alloys by the channeling method (Metal Physics Lab.)

(3) Particle induced X-ray emission (PIXE)
  (a) Application of the PIXE to medical, environmental, archaeological,and material sciences (Inorganic Chemical Physics Lab.)

RIKEN Accel. Prog. Rep. **25** (1991)

# III. RESEARCH ACTIVITIES

## 1. Nuclear Physics

### 1. A Resonating-Group-Method Study of $^{16}O$ - $^{16}O$ Elastic Scattering

T. Wada

[ $^{16}O$-$^{16}O$ elastic scattering, resonating group method, equivalent local potential, deep potential. ]

Recently, Stiliaris *et al.*[1] reported that "nuclear rainbow" is found in the elastic scattering of the $^{16}O$-$^{16}O$ system at $E_{cm}=175$ MeV. This observation provides us with the first example of the nuclear rainbow in heavy-ion scattering. The rainbow structure can be reproduced by a deep real potential with a weak imaginary part, while the shallow potential failed to reproduce the data at large angles. This result seems to be contradictory to the fact that the molecular resonance phenomena observed in the light-heavy ion systems have been described almost exclusively using shallow potentials. It is now widely accepted that the $\alpha$-nucleus optical potential has been determined without ambiguities. We studied $\alpha$-$^{16}O$ and $\alpha$-$^{40}Ca$ elastic scattering by the resonating group method (RGM).[2] We found that the data fitting by the theory is very good in a wide energy range and that the equivalent local potential (ELP) constructed from the RGM non-local one is very similar to the real part of the unique optical potential which is deep. Thus, it is quite important to study the $^{16}O$-$^{16}O$ system by the RGM.

The oscillator parameter $\nu$ for the intrinsic wave function of $^{16}O$ is chosen to be 0.16 fm$^{-2}$. As for the effective nuclear force, we adopt the HNY interaction[3] which has a parameter in the $^{3}E$ strength of the medium-range attraction; $V_m(^3E) = -546 + \Delta$MeV. Figure 1 shows the elastic scattering angular distribution calculated with the RGM and the data[1] at $E_{cm}=175$ MeV. The value of $\Delta$ adopted here is 90.7 MeV. For the imaginary part of the $^{16}O$-$^{16}O$ potential, we adopt the Woods-Saxon form with the radius $R_i=5.5$ fm, the diffuseness $a_i=0.65$ fm, and the strength $W_0=29.7$ MeV. A surface-transparent imaginary potential is necessary to reproduce the rainbow structure. The fit to the data is very good. We also calculate the ELP from the non-local interaction of the RGM. Figure 2 shows the ELP ($L=50$) at the same energy together with the real part of the phenomenological optical potential by Kondo *et al.*[4] One of the quantities which characterize potentials is the volume integral per nucleon pair; $j_V = 4\pi \int V(r) r^2 dr / A_P A_T$, where $A_P$ and $A_T$ denote the mass number

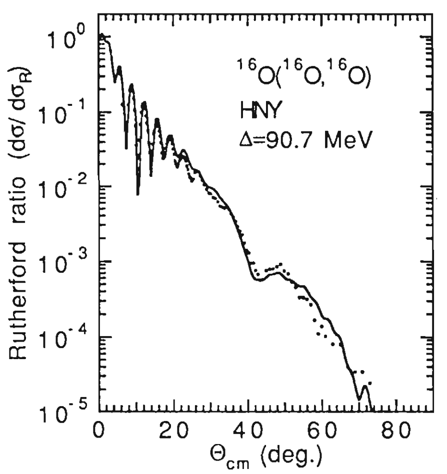


Fig. 1. Comparison of the $^{16}O$-$^{16}O$ elastic scattering angular distribution by the RGM at $E_{cm}=175$ MeV with the data of Ref. 1.

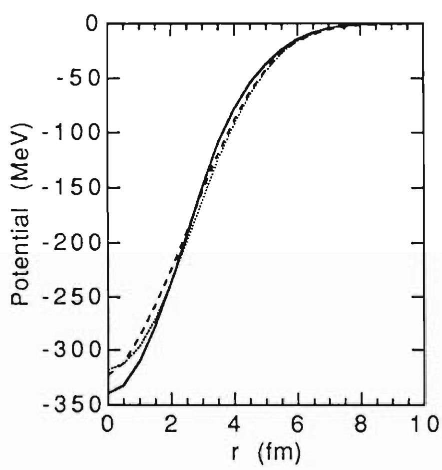


Fig. 2. Comparison of the equivalent local potential (solid line) at $E_{cm}=175$ MeV with the phenomenological potential of Ref. 4 (dashed line). Dotted line denotes the direct potential without antisymmetrization.

of the projectile and that of the target, respectively. The calculated value of $j_V$ for the ELP is 290 MeV$\cdot$fm$^3$, which agrees with that for the phenomenological potential of Ref. 4.

References


1) E. Stiliaris *et al*.: *Phys. Lett.,* **223B**, 291 (1989).
2) T. Wada and H. Horiuchi: *Phys. Rev. Lett.,* **58,** 2190 (1987); T. Wada and H. Horiuchi: *Phys. Rev.,* **C38,** 2063 (1988).
3) Y. Yamamoto: *Prog. Theor. Phys.,* **52,** 471 (1974).
4) Y. Kondo, F. Michel, and G. Reidemeister: *Phys. Lett.,* **242B,** 340 (1990).

RIKEN Accel. Prog. Rep. 25 (1991)

# III-1-2. Multi-Dimensional Langevin Approach to the Dissipative Dynamics of Nuclear Fission

T. Wada, N. Carjan,* and Y. Abe

(Fission, multi-dimensional Langevin equation, transient time, kinetic energy distribution.)

Nuclear fission is a multi-dimensional dissipative phenomenon. Various collective degrees of freedom which describe nuclear shapes such as elongation, necking, fragment deformation, and mass-asymmetry have to be taken into account for studying the dynamics of fission. The success of the transport theories in describing nuclear dissipation in deep inelastic heavy-ion collisions revived the old Kramers' picture[1] in studying induced fission; slowly varying collective degrees of freedom are viewed as a Brownian particle and fast nucleonic degrees of freedom as a heat bath. The Langevin approach[2] is more suitable for nuclear physics problems than the Fokker-Planck approach, because: (1) Langevin equation can be easily applied to multi-dimensional cases since it is an ordinary differential equation; (2) it can also be generalized to treat non-Markovian processes by introducing a retarded friction.

A characteristic aspect of the Brownian picture is that the fission rate is time dependent; there is a transient time before reaching the stationary limit. In fact, anomalously large number of pre-scission neutrons have been observed and are expected to be an evidence of the transient time.[3]

Nuclear viscosity which originates from the coupling between the collective degrees of freedom and the rest of the system is a crucial quantity for the macroscopic description of fission. For example, the fragment kinetic energy distribution is mainly governed by the dissipative dynamics during the descent from saddle to scission. On the other hand, the transient time which is needed for the system to establish stationary flow over the saddle is governed by the dissipative dynamics from the equilibrium shape to the saddle.

We have applied the multi-dimensional Langevin equation to the study of dissipative dynamics of fission. Using a liquid drop model potential and shape-dependent inertia and dissipation tensors, we have succeeded in solving the equation numerically. The potential is calculated as the sum of a Coulomb energy for a diffused charge distribution and a generalized surface energy with a Yukawa-plus-exponential folding function which takes into account the finite range of the nuclear force. The inertia tensor is calculated using the Werner-Wheeler approximation to incompressible irrotational nuclear flow. For the dissipation tensor we use two different models: the two-body hydrodynamical viscosity and the one-body wall-and-window dissipation, which have different strength and deformation dependence. Results concerning the time dependence of the fission rate and the distribution of the fragment kinetic energy have been compared with existing measurements for the symmetric fission of $^{213}$At.

Both the transient time and the time for the descent from saddle to scission increase as the dissipation becomes stronger. The fission delay time obtained with the one-body dissipation is consistent with that deduced from a recent measurement of pre-scission neutrons,[3] while the delay time with the two-body dissipation is shorter by an order of magnitude. The temperature dependence of the calculated mean value and of the variance of the total kinetic energy agrees with that of experimental data.[4] Multi-dimensional treatment is necessary to reproduce the observed variance of the fragment kinetic energy. Validity of the deterministic approach to the mean value of the pre-scission kinetic energy is also discussed.

By incorporating the coordinate dependence of the inertia and dissipation tensors as well as the potential, we have described the inner dynamics (from the equilibrium shape to saddle, *e.g.*, the transient time) and the outer dynamics (from saddle to scission, *e.g.*, the kinetic energy distribution) at the same time. This kind of approach is necessary for the elucidation of the nature and magnitude of the nuclear viscosity.

This report is a compressed version of Ref. 5.

* Centre d'Etudes Nucléaires de Bordeaux-Gradignan, 33175 Gradignan, France.

References

1) H.A. Kramers: *Physica,* **7,** 284 (1940).
2) Y. Abe, C. Grégoire, and H. Delagrange: *J. Physique,* **47,** C4-329 (1986).
3) D.J. Hinde, D. Hilscher, and H. Rossner: *Nucl. Phys.,* **A502,** 497c (1989).
4) F. Plasil, D.S. Burnett, H.C. Britt, and S.G. Thompson: *Phys. Rev.,* **142,** 696 (1966); E.N. Gruzintsev, M. G. Itkis *et al*.: *Sov. J. Nucl. Phys.,* **39,** 844 (1984).
5) T. Wada, N. Carjan, and Y. Abe: RIKEN preprint RIKEN-AF-NP-114 (1991).

RIKEN Accel. Prog. Rep. **25** (1991)

# III-1-3. Langevin Approach to the Pre-Scission Particle Evaporations

T. Wada, N. Carjan,* and Y. Abe

(Fission, Langevin equation, transient time, pre-scission particle evaporation.)

An experimental evidence for the slow fission time scale has come from measurements of the numbers of evaporated neutrons, charged particles, and giant dipole $\gamma$-rays emitted before scission, which are generally in excess of those predicted using static phase space arguments. Pre-scission particle multiplicities are influenced by the nuclear viscosity in three significant ways. The first is the Kramers' factor[1] which reduces the Bohr-Wheeler fission width in a pre-exponential factor. The second is the transient time needed for the system to establish the stationary flow over the saddle. The third is the time for the descent from saddle to scission, which is increased by dissipation. Phenomenologically, the excess neutrons have been interpreted in terms of the saddle-to-scission time and the pre-saddle delay which is related to the transient time.[2] Recently, the possibility of limiting the pre-saddle delay time using charged particle multiplicities was reported.[3] We have been studying the nuclear dissipative dynamics using the Langevin equation.[4] In Ref. 4, we showed the applicability of the multi-dimensional Langevin equation to the realistic study of fission and the importance of the simultaneous treatment of inner (equilibrium to saddle) and outer (saddle to scission) dynamics.

Here we report the preliminary results of our recent study of the dissipative dynamics of fission including particle evaporations using the Langevin equation. For the simplicity of the calculation, we adopted the one-dimensional model. The one-dimensional path is determined as the mean path of the two-dimensional Langevin trajectories. The potential is calculated as the sum of a Coulomb energy and a generalized surface energy with a Yukawa-plus-exponential folding function. The inertia tensor is obtained using the Werner-Wheeler approximation and the dissipation tensor is calculated with the wall-and-window formula. The shape dependence of the inertia and dissipation tensors is fully taken into account.

The formalism to study the competition between particle evaporations and fission decay is the same as that is adopted in Ref. 5. The difference is that the authors of Ref. 5 use the Fokker-Planck equation with the shape-independent mass and friction. In this formalism, the fission width in the quasi-stationary limit is time dependent because the excitation energy of the compound nucleus decreases owing to the particle evaporations. Figure 1 shows the calculated fission width at saddle and that at scission for

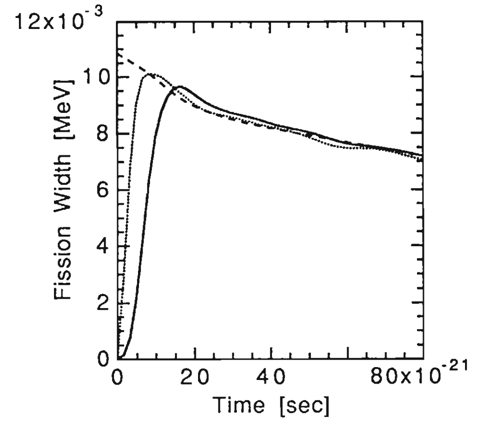


Fig. 1. Time dependence of the fission widths calculated at saddle (dotted line) and at scission (solid line). Dashed line denotes the quasi-stationary fission width.

the symmetric fission of $^{192}$Pb with the initial temperature $T=2$ MeV and $L=50$. The transient time is $6 \times 10^{-21}$s and the saddle-to-scission time is $8 \times 10^{-21}$s. The obtained multiplicities of the pre-scission particles for this spin are 2.30, 0.103, and 0.040 for neutron, proton, and alpha particle, respectively. While if we use the quasi-stationary fission width, they become 2.04, 0.092, and 0.036, respectively. Thus the effect of the transient time and the saddle-to-scission time is about 10 %. The reduction of the stationary fission width from the Bohr-Wheeler's one plays a more decisive role. Further studies are now in progress.

* Centre d'Etudes Nucléaires de Bordeaux-Gradignan, 33175 Gradignan, France.

References

1) H.A. Kramers: *Physica*, **7**, 284 (1940).
2) D.J. Hinde *et al.*: Proc. 4th Int. Conf. on Nucleus-

Nucleus Collisions, to be published in *Nucl. Phys.*, **A**.
3) J.P. Lestone *et al.*: *Phys. Rev. Lett.*, **67**, 1078 (1991).
4) T. Wada, N. Carjan, and Y. Abe: RIKEN preprint RIKEN-AF-NP-114 (1991).
5) H. Delagrange, C. Grégoire, F. Scheuter, and Y. Abe: *Z. Phys.*, **A323**, 437 (1986).

RIKEN Accel. Prog. Rep. **25** (1991)

# III-1-4. Stochastic and Deterministic Solutions of the 2-D Boltzmann Equation

M. Tohyama and E. Suraud*

(Nuclear reaction theories, Intermediate-energy heavy-ion collisions, Numerical simulations.)

Numerical simulations based on the nuclear Boltzmann equation (NBE) have extensively been done for intermediate-energy heavy-ion collisions.[1] Whatever numerical approaches are used to simulate NBE, it is desirable to know their validities and limitations. For this purpose we compare the results of the Boltzmann-Uehling-Uhlenbeck (BUU) simulation method of Ref. 1 and the weighted particle method (WPM) of Ref.2 with those of the "exact" numerical approach for the collision of two-dimensional nuclear matter; it is finite in the beam direction (the z direction) and infinite in the other direction (the x direction). NBE for the 2-D system becomes

$$\frac{\partial}{\partial t}f+\frac{Pz}{m}\frac{\partial}{\partial z}f-\frac{\partial}{\partial z}U\frac{\partial}{\partial p_z}f=I,$$

where the collision term I is written as

$$I=\frac{4}{(2\pi)^3}\int d^2p_2d^2p_3d^2p_4 \mid v(p-p_3) \mid^2 \times \delta^2(p+p_2-p_3-p_4)\,\delta(\varepsilon+\varepsilon_2-\varepsilon_3-\varepsilon_4) \times (\bar{f}\bar{f}_2f_3f_4-ff_2\bar{f}_3\bar{f}_4).$$

We obtain the numerical solutions of the above-mentioned three methods for the symmetric collision of a fragment with width of about 4fm at $E_{cm}/A=10$MeV and calculate the time evolution of distortion in momentum space defined by $<p_z^2>-<p_x^2>$ where $<\ \ >$ means an average value. In Fig.1 shown is the ratio of the distortion with to that without nucleon-nucleon (NN) collisions. The BUU result has rather large fluctuations which are not seen in the WPM result, though the number of test particles used for both BUU and WPM is similar. This is a consequence of the stochastic treatment of NN collisions in BUU: the momenta of two nucleons abruptly change after they suffer a collision. The smooth behavior of the WPM momentum distribution is due to a deterministic treatment of NN collisions[2] and demonstrates an advantage of WPM. The agreement of the BUU result with the "exact one" remains rather qualitative.

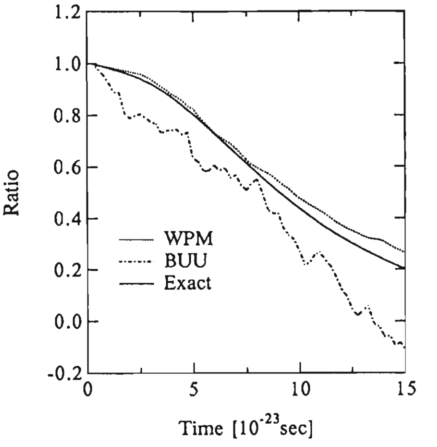


Fig. 1. The ratio of $<p_z^2>-<p_x^2>$ with to that without nucleon-nucleon collisions.

References

1) G.F. Bertsch and S. Das Gupta: *Phys. Rep.*, **160**, 189(1988).
2) M.Tohyama and E. Suraud: *Phys. Rev.*, **C43**, 1518(1991).

* GANIL, B.P. 5027, 14021 Cean-Cedex, France.

RIKEN Accel. Prog. Rep. **25** (1991)

# III-1-5. Distribution of Strength for Isoscalar Modes at Finite Temperature

S. Yamaji, H. Hofmann,* and A.S. Jensen**

[Large Scale Collective Motion, Linear Response Theory.]

We studied the collective response function as a function of the excitation energy for typical isoscalar modes.[1] We found that the strength function exhibits the usual low energy and giant resonance peaks at low temperatures whereas all the strength is concentrated in a low energy mode at temperatures higher than a temperature of around 1.5 MeV. Thus the vibrational inertia of slow motion turns into that of irrotational flow at high temperature.

In this report, we study the physical origins of the observed shift in the frequency. The effects found are related to the two features, which are specific to our approach.

Let us begin by looking at the influence of the residual interactions. They are taken into account through the imaginary part of particle and hole selfenergies. To some extent this effect can be simulated by a constant width $\Gamma$ being independent of both frequency and temperature. This allows us to check the importance of the temperature dependence of the selfenergies. In Fig. 1 we present by solid curves a calculation with $\Gamma = 0.25$ MeV for temperatures of 1 and 2 MeV in the case of the isoscalar quadrupole mode in $^{208}$Pb. One clearly observes a shift of strength towards low frequencies, which is very similar to the "true" case.[1]

Let us discuss the importance of the temperature-dependent coupling constant k of the separable two-body interaction.[2] The constant k changes sensitively with temperature in our model. To see the influence of the temperature-dependence, we show in Fig. 1 by dashed curves

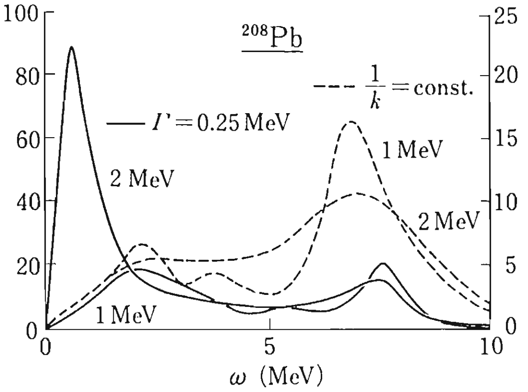


Fig. 1. The imaginary part of the response function (in arbitrary unit) as a function of frequency for temperatures 1 and 2 MeV. The solid curves (scale on the left vertical axis) show the results with constant $\Gamma = 0.25$ MeV. The dashed curves (scale on the right vertical axis) show the results with the constant coupling k.

a computation of the strength for different temperature T = 1 and 2 MeV, with the same selfenergy as in Ref. 1 but with the constant coupling calculated at T = 0 MeV. No shift of the strength is observed, but the peaks become somewhat broader with increasing temperature.

Thus we conclude that the shift of strength is mainly due to the temperature-dependence of the effective coupling constant k.

References


1) S. Yamaji, H. Hofmann, and A.S. Jensen: *RIKEN Accel. Prog. Rep.*, **24**, 28 (1990).
2) S. Yamaji, H. Hofmann, and R. Samhammer: *Nucl. Phys.*, **A475**, 487 (1988).



* Dep. Physics, Technical University of Munich, Germany.

** Institute of Physics, University of Aarhus, Denmark.

RIKEN Accel. Prog. Rep. **25** (1991)

# III-1-6. The "Finite $q_\perp$ Correction" for Coulomb Dissociation Cross Sections of $^{11}Li$

K. Soutome, S. Yamaji, and M. Sano

〔Coulomb dissociation cross section, neutron-rich nucleus, $^{11}$Li.〕

Interest in structure and reactions of neutron-rich radioactive nuclei, especially $^{11}$Li, has increased rapidly in the past few years. In Ref. 1, we pointed out the importance of the kinematical lower limit of momentum transfer $q_{min}$ in the Coulomb dissociation of $^{11}$Li. As shown there, the $q_{min}$ is given by $q_{min}=\max[\varepsilon/\gamma v, 2n\varepsilon/\gamma v]$, where $\varepsilon=0.25\pm0.10$ MeV is the two-neutron separation energy of $^{11}$Li, v is the relative velocity of $^{11}$Li and the target nucleus ( with charge $Z_T$ e ), $n\equiv 3\ Z_T e^2/v$ is the Sommerfeld parameter, and $\gamma\equiv(1-v^2)^{-1/2}$ ($\hbar=c=1$). The cutoff $2n\varepsilon/\gamma v$ emerges when we take account of the fact that the transverse component of momentum transfer $q_\perp$ must be non-vanishing in order that $^{11}$Li may be broken up ("finite $q_\perp$ correction").

With the use of this $q_{min}$, we can calculate Coulomb dissociation cross sections for the two-neutron removal process $^{11}Li+Target\rightarrow{}^9Li+X$ by

$$\sigma^{(C)}_{-2n}=\int_{q_{min}}^{\infty}dq\frac{8\pi n^2}{q^3}\times\left\{1-|S(q)|^2\right\}F^2_{^9Li}(q)F^2_T(q),\quad(1)$$

where $F_A(q)$ is the charge form factor of nucleus A. The S(q) is given in the "HO model" [1] by $S(q)=(1-Q^2/12)^2\exp(-Q^2/4)$, where $Q\equiv(\sqrt{2}/11)$ aq with a$\equiv$3.77 fm.

In Fig. 1, we plotted $\sigma^{(C)}_{-2n}$ for $^{208}$Pb target as a function of the incident laboratory energy by the solid line. In this case, $n\gg1$ and thus $q_{min}=2n\varepsilon/\gamma v$. To examine the "finite $q_\perp$ correction", we also evaluated $\sigma^{(C)}_{-2n}$ by using $q'_{min}\equiv\varepsilon/\gamma v$ as a lower limit of the integral in Eq. (1). The results are shown by the dotted line. By comparing the solid and dotted lines, we see that the cutoff $2n\varepsilon/\gamma v$ plays an important role in the Coulomb dissociation of $^{11}$Li.

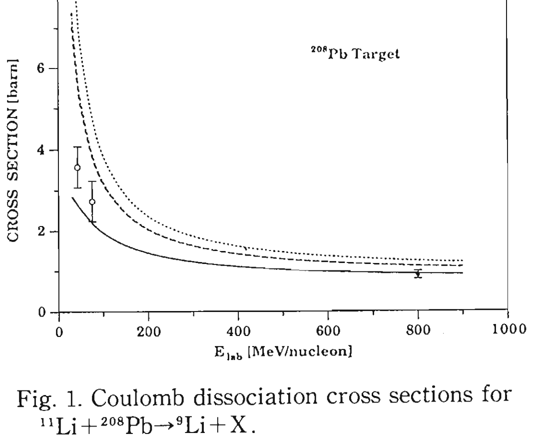


Fig. 1. Coulomb dissociation cross sections for $^{11}Li+{}^{208}Pb\rightarrow{}^9Li+X$.

Unfortunately, there is not enough data to compare. The solid square in Fig. 1 is from Ref. 2, which corresponds to the two-neutron removal process at $E_{lab}=800$ MeV/nucleon. The open circles are from the recent experiments by Inabe et al.[3] However, they measured cross sections for $^{11}Li+Target\rightarrow X(\neq{}^{11}Li)$ + Target′ at $E_{lab}=43$ and 75 MeV/nucleon. Since the cross section for this process contains the contribution from the dissociation of the $^9$Li core, the open circles should be regarded as the *upper limit* for $\sigma^{(C)}_{-2n}$.

To see effects of the usual "Rutherford bending correction", we calculated "E1 Coulomb dissociation cross sections" by using the virtual-photon formula of Bertulani and Baur.[4] The results are shown in Fig. 1 by the dot-dashed and dashed lines (though almost indistinguishable). These two lines differ in the definition of the "minimum impact parameter" $b_{min}$: the dot-dashed and dashed lines were calculated by setting $b_{min}$ equal to $b_0$ and $b_0+\pi n/2\mu v\gamma$, respectively, where $b_0$ is the sum of nuclear radii of $^{11}$Li and the target nucleus, and $\mu$ is their reduced mass. The dot-dashed line thus contains the Rutherford bending correction. However, this correction is small as seen from the figure, which indicates that this Rutherford bending correction is essentially different from the "finite $q_\perp$ correction".

References

1) K. Soutome, S. Yamaji, and M. Sano: Proc. 4th Int. Conf. on Nucleus-Nucleus Collisions, Kanazawa (1991); *RIKEN Accel. Prog. Rep.*, **24**, 29 (1990).
2) T. Kobayashi *et al.*: *Phys. Lett.*, **232B**, 51 (1989).
3) N. Inabe *et al.*: Contribution to 4th Int. Conf. on Nucleus-Nucleus Collisions, Kanazawa (1991).
4) C.A. Bertulani and G. Baur: *Nucl. Phys.*, **A480**, 615 (1988). Note that a factor 1/3 is missing in Eq. (4.3 b).

RIKEN Accel. Prog. Rep. 25 (1991)

# III-1-7. Coulomb Breakup of Loosely Bound System

N. Iwasa and T. Motobayashi

(dissociation of $^{8}$B, angular and virtual photon energy dependence, quantum and semiclassical calculation.)

Loosely bound nuclei are expected to have large Coulomb breakup cross sections. We calculate the cross section with both quantum mechanical and semiclassical methods, taking the reaction $^{8}B+^{208}Pb \to ^{7}Be+p+^{208}Pb$ at 50 MeV/u as an example. This reaction can be related to the $^{7}Be(p,\gamma)^{8}B$ reaction, one of the key reaction for the solar neutrino problem. The virtual photon number per unit solid angle $dn_{E1}/d\Omega$ is defined for the breakup reaction $c \to a+b$ as,

$$\frac{d^2\sigma}{dE_\gamma d\Omega}=\frac{1}{E_\gamma}\frac{dn_{E1}}{d\Omega}\sigma(c+\gamma\to a+b), \qquad (1)$$

where $d^2\sigma/dE_\gamma d\Omega$ is the double differential breakup cross section, $E_\gamma$ is the energy of a virtual photon absorbed by the projectile c, and $\sigma(c+\gamma\to a+b)$ is the photo disintegration cross section. The cross section of the radiative capture process $a+b\to c+\gamma$ is related to the disintegration cross section by the detailed balance theorem

$$\sigma(c+\gamma\to a+b)=\omega\sigma(a+b\to c+\gamma), \qquad (2)$$

where $\omega$ is the phase space factor. Figure 1 shows the results of a quantum mechanical calculation with the coupled channel code ECIS[1)] (solid line) and a semiclassical calculation[2,3)]. At a forward angle, a rapid decrease of photon number is observed especially for small $E_\gamma$. This decrease corresponds to the adiabatic limit expressed as $E_\gamma a/\hbar v=1$ (a is half the distance of the closet approach in a head on collision), where the virtual photon is not energetic enough to excite the projectile. The agreement of the above two calculations is good for small $E_\gamma$, but for large $E_\gamma$ the oscillating behavior is seen only in the quantal calculation. This may be due to the interference between the waves corresponding to two different trajectories, pure Coulomb trajectory of larger impact parameter and the one deflected by the nuclear attraction at smaller impact parameter, which is not taken into account in the semiclassical calculation. The difference at angles larger than 6 degree is due to the nuclear absorption which is accounted for only in the quantal calculation.

The total virtual photon number $n_{E1}$ is obtained by integrating eq. 1 over the angle. The results are shown in Fig. 2. In the case of the semiclassical calculation, a cut-off radius R has to be introduced to account for the absorption. The radius $R\approx1.5\ (A_P^{1/3}+A_T^{1/3})$ fm gives a good fit to the quantal calculation over a wide range of $E_\gamma$. Note that this cut-off radius is slightly larger than the strong interaction radius, $R\approx 1.3(A_P^{1/3}+A_T^{1/3})$ calculated from the total absorption cross section derived by the optical potential.

Finally we estimated the $^{8}$B Coulomb breakup cross section by putting the $(p,\gamma)$ cross section

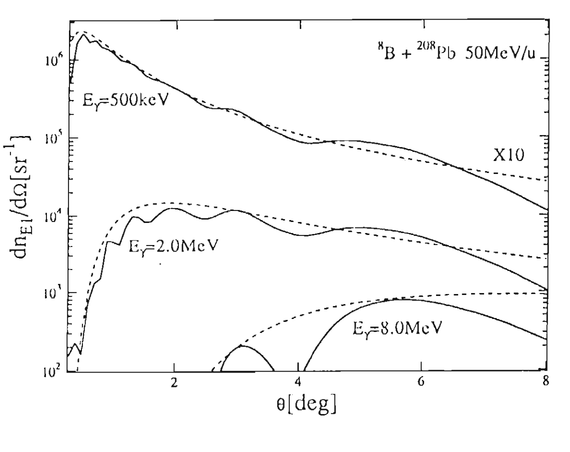


Fig. 1. Virtual photon number per unit solid angle $dn_{E1}/d\Omega$. Solid curves correspond to the quantum mechanical calculation, and dashed ones to the semiclassical one.

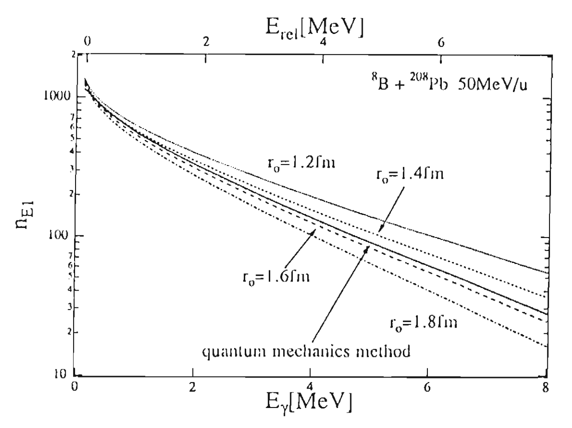


Fig. 2. Total virtual photon number spectrum. Solid line shows the result of the coupled channel calculation, and the others show the results of the semiclassical calculation with different cut-off radii.

by Filippone et al.[4] into eq. 1 with the help of the detailed balance theorem (eq. 2). The numerical results are shown in Table 1. The enormous enhancement of breakup cross section is due to the large virtual photon number and also to the big phase volume factor caused by a small $E_\gamma$ due to the small binding energy (137 keV) for $^8B \rightarrow {}^7Be + p$.

Table 1. $^8B$ Coulomb Breakup cross sections calculated from the $(p,\gamma)$ cross section by Filippone et al.[4]

| $E_{cm}$ | $E_\gamma$ | $(p,\gamma)$ cross section | phase space factor | $n_{E1}$ | breakup cross section |
|---|---|---|---|---|---|
| 100 keV | 237 keV | 1.3 nb | 2343 | 1068 | 13 mb/MeV |
| 200 keV | 337 keV | 22 nb | 2318 | 908 | 138 mb/MeV |

References

1) J. Raynal: *Phys. Rev.*, **C23**, 2571 (1981).
2) G. Baur, C.A. Bertulani, and H. Rebel: *Nucl. Phys.*, **A458**, 188 (1986).
3) C.F. Weizacker: *Z. Phys.*, **88**, 612 (1934); E.J. Williams: *Phys. Rev.*, **45**, 729 (1934).
4) B.W. Filippone, A.J. Elwyn, C.N. Davids, and D.D. Koetke: *ibid.*, **C28**, 2222 (1983).

RIKEN Accel. Prog. Rep. **25** (1991)

# III-1-8. Relativistic Many Body Theory of Nuclei Far from the Stability Line

H. Toki, D. Hirata, and I. Tanihata

〔Relativistic Mean Field Theory, Unstable Nuclei.〕

The recent experimental program in the use of radioactive nuclear beams has opened a new field to study the properties of nuclei far from the stability line. Many interesting phenomena are expected for nuclei with the neutron number largely different from the proton number. In order to predict such phenomena, we have started to study these unexplored nuclei theoretically. For this purpose, we chose the relativistic many body theory, the goodness of which has been demonstrated by the recent publications for stable nuclei.[1,2] We found that the relativistic mean field theory (RMF) with interaction strengths fixed by stable nuclei provided also very good account of known observables off the stability line.[3,4] We summarize here the interesting outcome of the theoretical calculations on nuclei up to the drip lines;

(1) The neutron radii are largely different from the proton ones for nuclei close to the neutron drip line. This finding should have a large influence on the neutron rapid process.

(2) The neutron drip line is sensitive to the rho meson coupling strength and the reasonable one provides the drip line be closer to the stable line as compared to the one of the mass formula.

(3) Near the proton drip line, the neutron and the proton radii are quite close and the proton drip line is insensitive to the isovector interaction.

We are now investigating the role of deformation on nuclear properties and also equations of state of neutron and nuclear matter at various temperatures and densities necessary for neutron star profiles.[5] We are planning to calculate all the existing nuclei and their properties between the proton and neutron drip lines within RMF. In addition, we are working on the relativistic Brueckner-Hartree-Fock (RBHF) theory for various nuclei. We have worked out density dependent Hartree approach, whose strengths are fixed by the RBHF calculations, for symmetric nuclei as $^{16}O$ and $^{40}Ca$ with great success.[2] The RBHF theory should provide the microscopic foundation of the RMF theory. In fact, we are working on the modification of the interaction strengths of RMF using the results of nuclear matter RBHF calculations. These informations will provide important constraints on the dynamics of supernova and neutron stars.

References

1) Y. K. Gambhir, P. Ring, and A. Thimet: *Annals. of Phys.*, **198**, 132 (1990).
2) H. Toki and R. Brockmann: TMU preprint (1991).
3) H. Toki, Y. Sugahara, D. Hirata, B.V. Carlson, and I. Tanihata: *Nucl. Phys.*, **A524**, 633 (1991).
4) D. Hirata, H. Toki, T. Watabe, I. Tanihata, and B.V. Carlson: *Phys. Rev.*, **C44**, 1467 (1991).
5) K. Sumiyoshi, H. Toki, and R. Brockmann: TMU preprint (1991).

RIKEN Accel. Prog. Rep. **25** (1991)

# III-1-9. Neutral Pion Condensation in Quark Matter Including Vacuum Fluctuation Effects

M. Katô,* W. Bentz,* and K. Tanaka

〔Vacuum instability, pion condensation, quark matter.〕

One problem in relativistic meson-quark or meson-nucleon field theories is the occurrence of unphysical tachyon poles (Landau ghost) in the meson propagators. Due to the Landau ghosts, the vacuum by itself exhibits an instability, i.e., the energy of the non-translational invariant vacuum in which the background meson fields have finite momenta can be made arbitrarily low relative to the translational invariant vacuum by increasing the momenta of the meson fields. Therefore, investigations including vacuum fluctuation effects based on a consistent treatment, like the loop expansion, have been hampered.

Recently, one possible method to eliminate the Landau ghost without introducing *ad-hoc* parameters has been developed[1] for finite density theories. In this paper[2] we show that the method of Ref. 1 is useful to remove the vacuum instability discussed above and allows a consistent description including vacuum fluctuation effects. We discuss the neutral pion condensation in quark matter as a typical example where the Landau ghost problem is unavoidable since the meson field configurations with non-zero momenta q should be taken into account.[3] We use the chiral $\sigma$-model[4] as a model for quark matter. An essential point in the application of the method of Ref. 1 to the chiral models is that chiral symmetry should be preserved through the elimination of the Landau ghost. For this purpose, we utilize the axial Ward-Takahashi identity[4] and guarantee chiral symmetry in the underlying dynamics.

In Fig. 1 the energy per quark in quark matter is shown as a function of the baryon density. There are two kinds of continuous phase transitions, one at a low density ($\rho_1$) from the normal phase to the pion condensed phase and another at a higher density ($\rho_2$) from the pion condensed phase to the Wigner phase. Both phase transitions emerge as a result of an interplay between the attractive Fermi sea contribution and the repulsive mesonic and Dirac sea contributions. Although the energy for the case where the ghost is included goes to minus infinity for large values of q, it is possible to find a local minimum for the density up to $\rho_3$. For higher densities, however, there does not exist even a local minimum. An important point to note is that, besides removing the instability for large momenta, the ghost elimination has the further important effect of rendering a chiral phase transition possible at some value of the baryon density.

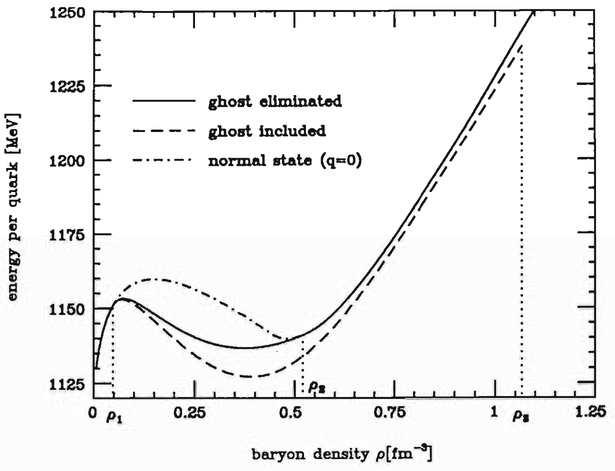


Fig. 1. Energy per quark in quark matter as a function of the baryon density in three cases. The full line is the ghost eliminated case, the dashed line is the ghost included one and the dashed-dotted line corresponds to the normal (no pion condensate) phase. For explanation of the three critical densities ($\rho_1$, $\rho_2$, $\rho_3$), see text.

References

1) K. Tanaka, W. Bentz, A. Arima, and F. Beck: *Nucl. Phys.*, **A528**, 676 (1991).
2) M. Kato, W. Bentz, and K. Tanaka: *Phys. Rev.*, **C**, submitted for publication.
3) W. Broniowski and M. Kutschera: *Phys. Lett.*, **B234**, 449 (1990).
4) B. W. Lee: "Chiral Dynamics", Gordon and Breach, New York (1972).

* Departmant of Physics, University of Tokyo.

RIKEN Accel. Prog. Rep. **25** (1991)

# III-1-10. 1/*N* Expansion and the Correlation Energy of Nuclear Matter in the Relativistic $\sigma$-$\omega$ Model

K. Tanaka and W. Bentz*

〔1/*N* expansion, correlation energy, $\sigma$-$\omega$ model.〕

Relativistic meson-nucleon field theories[1] have been successfully applied to the description of the nuclear matter and finite nuclei, mainly in the simple Hartree (mean-field) approximation. One of the simplest and the most popular models among those is the $\sigma$-$\omega$ model.[1] Recently, however, it was reported[2] that the description of nuclear matter in the $\sigma$-$\omega$ model required drastic changes of the overall physical picture if one included the higher order (2-loop) contribution beyond the Hartree approximation via the loop ($\hbar$-) expansion, and, therefore, the loop expansion scheme failed.

In this paper,[3] we propose a $1/N$ expansion method, where $N$ denotes the number of internal degrees of freedom of the nucleon and can be identified with 2 due to the isospin $SU(2)$, as an alternative systematic expansion scheme for the relativistic meson-nucleon many-body theory. We derive a general formula for the computation of the effective action in the $\sigma$-$\omega$ model based on the $1/N$ expansion, utilizing the functional integral method. In this scheme the leading contribution coincides with the familiar Hartree approximation. The elimination of unphysical tachyon poles (Landau ghost) from the meson propagators in the subgraphs, which appears to be essential for our formulation, is also established following the recently developed method[4] based on the Källēn-Lehmann representation.

We compute the energy density of nuclear matter beyond the Hartree approximation including the next-to-leading order contributions in the $1/N$ expansion. In this order one should include the ring energy contribution as a correlation energy in addition to the exchange energy (2-loop) contribution. We find that we can describe the nuclear matter saturation properties by a mechanism which is qualitatively the same as in the Hartree approximation, and, therefore, in conformity with the meson exchange picture of the nucleon-nucleon interaction. This is in contrast to the case of the loop expansion, and suggests that the $1/N$ expansion scheme is an appropriate expansion scheme.

For our successful description of the saturation property of nuclear matter, the correlation energy contribution plays an essential role. Figure 1 shows the binding energy per nucleon in nuclear matter as a function of the effective nucleon mass $M^*$ for the fixed baryon number density. The ground state of nuclear matter can be determined by minimizing the energy density with respect to $M^*$, and, therefore, the minimum of the solid curve represents the ground state. We see that the exchange energy (2-loop) contribution is "destabilizing" the ground state. This is the reason why the loop expansion failed. On the other hand, the ring energy is a large repulsive contribution, guaranteeing the formation of the stable ground state. This "stabilizing" behaviour is due to the vacuum polarization effects in the ring energy and is a general feature of our scheme, i.e., insensitive to the choice of the parameters in the lagrangian.

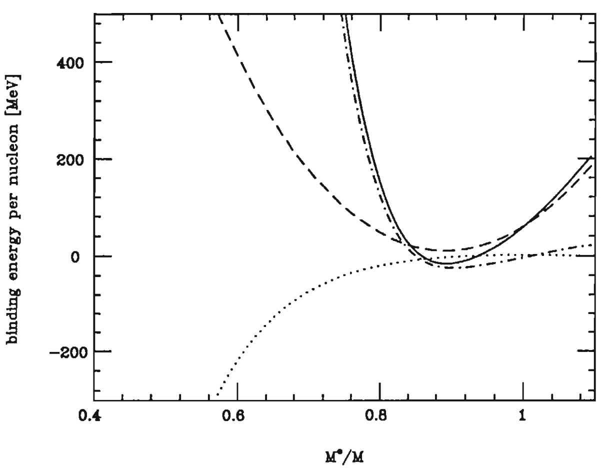


Fig. 1. The separate contributions to the binding energy per nucleon in nuclear matter in the $1/N$ expansion scheme as a function of $M^*/M$ for the fixed baryon number density ($k_F = 1.3\text{fm}^{-1}$), where $M^*$ and $M$ are the effective nucleon mass in nuclear matter and its free space value, respectively. The dashed line shows the Hartree contribution, the dotted line shows the exchange energy contribution, the dot-dashed line shows the ring energy contribution, and the solid line shows the total binding energy per nucleon.

* Department of Physics, University of Tokyo.

References

1) B. D. Serot and J. D. Walecka: "Advances in Nuclear Physics", eds., J. W. Negele and E. Vogt, Plenum, New York, **16**, 1 (1986).
2) R. J. Furnstahl, R. J. Perry, and B. D. Serot: *Phys. Rev.,* **C40**, 321 (1989).
3) K. Tanaka and W. Bentz: preprint (1991).
4) K. Tanaka, W. Bentz, A. Arima, and F. Beck: *Nucl. Phys.,* **A528**, 676 (1991).

RIKEN Accel. Prog. Rep. **25** (1991)

# III-1-11. $K^-$- Nucleus Optical Potential with a Non-Local Term

S. Hirenzaki, T. Harada, H. Toki, and M. Mizoguchi*

〔Kaonic atoms, non-local optical potential.〕

We have constructed a $K^-$-nucleus optical potential with a non-local term and compared the results with those of a local potential. It was found that the kaonic atom data were reproduced equally well in both cases, while the calculated wavefunctions were largely different.

It is very interesting to explore the $K^-$-nucleus optical potential since the potential, which was obtained by fitting the existing data, does not reproduce the data of kaonic atoms of p and He at all.[1] In addition, the $K^-$-nucleus potential is necessary to investigate the formation reactions of hypernuclei such as $^4$He(stopped $K^-$, $\pi$) theoretically.[2] In this paper, we have studied the non-local $K^-$-nucleus optical potential, which is written as

$$2\mu V_{\text{opt}}(r) = -4\pi(1+\mu/M)a\rho(r) + 4\pi(1+\mu/M)^{-1}b\nabla\rho(r)\nabla ,$$

where $\mu$ is the reduced mass of the K-A system, $M$ is the mass of the nucleon, $\rho(r)$ is the nuclear density distribution. '$a$' and '$b$' are complex numbers that determine the strength of the potential. The existence of the non-local (P-wave) term is indicated by P-wave resonances of $\Lambda$ and $\Sigma$. We treat '$a$' and '$b$' as parameters and consider the two sets, (1) $a=(0.34, 0.84)$, $b=(0, 0)$ and (2) $a=(-0.15, 0.68)$, $b=(1.1, 0.7)$ in fm unit. The set (1) is the generally used local potential.[3] The sign of the real part is opposite to the data of a scattering length. As for set (2), we fix '$a$' by the data of the scattering length[4] and get '$b$' by fitting the atomic data. The kaonic atom data are reproduced equally well in both cases. The results are also similar to the K-He case. On the other hand the behavior of the wave functions are largely different as seen in Fig. 1; this is because the sign of the real part in the local term is different in the two cases.

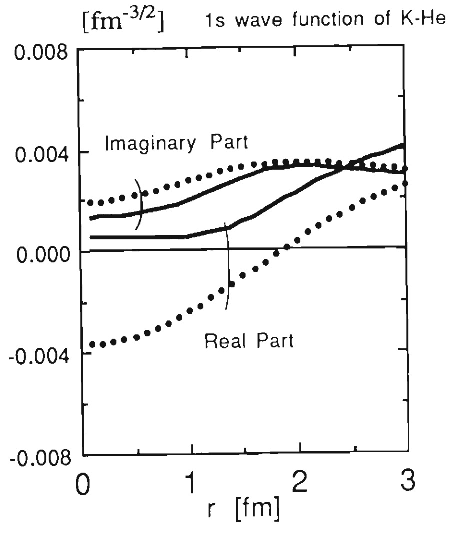


Fig. 1. The wave functions of the 1s state of the kaonic helium. The dotted line is the result with parameter set (1) and the solid line is the result with set (2).

This fact indicates that the formation cross sections of hypernuclei could be affected largely by the ambiguities of the $K^-$-nucleus optical potential. We are presently investigating the optical potential microscopically.

References

1) C.J. Batty: *Nucl. Phys.*, **A508**, 89c (1990).
2) T. Harada and Y. Akaishi: *Phys. Lett.*, **B262**, 205 (1991).
3) C.J. Batty: *Nucl. Phys.*, **A372**, 418 (1981).
4) A.D. Martin: *Phys. Lett.*, **B65**, 346 (1976).

* Department of Physics, Tokyo Metropolitan University.

RIKEN Accel. Prog. Rep. **25** (1991)

# III-1-12. (d, $^3$He) Reactions for the Formation of Deeply Bound Pionic Atoms

S. Hirenzaki, H. Toki, and T. Yamazaki*

[(d, $^3$He) reactions, deeply bound pionic atoms.]

We have investigated (d,$^3$He) reactions in detail for the formation of deeply bound pionic atoms, and found that the (d, $^3$He) reaction is much more favorable than the (n, p) reaction for the search. Deeply bound pionic atoms were investigated by Toki and Yamazaki[1] and were predicted to have narrow widths due to the repulsive pion-nucleus optical potential that pushes the pion wave function outwards.[2] These states cannot be observed in standard pionic-atom experiments that detect pionic X-rays. Hence, they proposed a use of pion-transfer reactions such as (n, p) and (d, $^2$He). Following their suggestions, deeply bound pionic states were searched for by using the (n, p) reaction at $T_n=$ 420 MeV at TRIUMF.[3] No positive evidence was observed in the experiment. To obtain better statistics with better resolution, another reaction(d, $^2$He) at $T_d=1000$ MeV at SATURNE[4] was measured and its analysis is in progress. It was pointed out that the charge-exchange pion-transfer reactions at large momentum transfer are sensitively affected by initial and final state interactions. It is found that the cross sections are about two orders of magnitudes smaller[3] than the PWBA predictions.[1,2] The same was also reported by Nieves and Oset.[5]

The formation of deeply bound pionic atoms by(n, d) reactions was also studied theoretically.[6] It was found that the distortion effects of (n, d) reactions are smaller than that of (n,p) reactions since the angular momentum matching condition is well satisfied in (n, d) reactions. It was concluded that (n, d) reactions are more suitable for pionic atom detection[6] and an experiment of this reaction at $T_n=400$ MeV is in progress at TRIUMF.[7] However, the weak neutron beam makes the experiment extremely difficult. We, therefore, have studied (d, $^3$He) reaction for deeply bound pionic-atom formation which uses a strong deuteron beam.

We have studied theoretically the possible use of the (d, $^3$He) reaction for the formation of deeply bound pionic states. The calculation was made at 600 MeV because the cross section is considered to be the largest due to the largest elementary cross section and small momentum transfer. We find the preferential population of quasi-substitutional states $[(nl)_\pi \cdot j_n^{-1}]J=0$ as in the case of (n, d) reaction. The pionic 2p state with neutron holes $3p_{1/2}$ and $3p_{3/2}$ are preferentially populated for a $^{208}$Pb target. We conclude that (d, $^3$He) reactions produce pionic atoms in a detectable manner.

References


1) H. Toki and T. Yamazaki: *Phys. Lett.,* **B213**, 129 (1988).
2) H. Toki, S. Hirenzaki, T. Yamazaki, and R.S. Hayano: *Nucl. Phys.,* **A501**, 653 (1989).
3) M. Iwasaki *et al.*: *Phys. Rev.,* **C43**, 1099 (1991).
4) T. Yamazaki *et al.*: SATURNE proposal, No. 214 (1988); R.S. Hayano and T. Miyamoto: private communication.
5) J. Nieves and E. Oset: *Nucl. Phys.,* **A518**, 617 (1990).
6) H. Toki, S. Hirenzaki, and T. Yamazaki: *ibid.,* **A530**, 679 (1991).
7) A. Trudel: private communication.


* Institute for Nuclear Study, University of Tokyo.

RIKEN Accel. Prog. Rep. **25** (1991)

# III-1-13. Production and Structure of Light Σ-Hypernuclei

T. Harada and Y. Akaishi

[Σ-Hypernuclei, Production, ($K^-$, $\pi^\mp$) Reaction, Bound State.]

In this note, we introduce a theoretical investigation of the structure of the Σ-hypernuclear (unstable) bound state ${}^4_\Sigma$He, and consider the production by ${}^4$He($K^-$, $\pi^\mp$) reactions in flight within the DWIA framework in order to establish the properties of the nucleus-Σ interaction. Hayano et al.[1] have reported the observation of the ${}^4_\Sigma$He by ${}^4$He(stopped $K^-$, $\pi^-$) reaction at KEK. The binding energy and width seem to be in agreement with a theoretical prediction by Harada et al.,[2] although the experimental results contain ambiguities how to subtract the background from the $\pi^-$ spectra.[3] The knowledge of the properties of the nucleus-Σ interaction gives us progress of Σ-hypernuclear studies.[4]

The nucleus-Σ potential derived from the microscopic four-body calculation[2] is a complex potential (SAP-1, 2), with considering the total spin $S=0$ case, as

$$\hat{U}(R)=U^0(R)+U^T(R)(\mathrm{T}_C\cdot \mathrm{t}_\Sigma), \qquad (1)$$

where $R$ is the relative distance between the core-nucleus (${}^3$H or ${}^3$He) and the Σ-hyperon; $\mathrm{T}_C$ and $\mathrm{t}_\Sigma$ are the respective isospin operators. The first term $U^0$ is repulsive near the nuclear center, which alone does not give any bound state. The second term $U^T$ called Lane's potential is sufficiently strong.

Let's consider the Σ-hypernuclear production by the ${}^4$He($K^-$, $\pi^\mp$) reaction in flight.[5] We calculate the double-differential cross section in the DWIA framework by using the Green function method.[6] Figure 1 (a) displays the inclusive spectra at $p_K=600$MeV/c, which were obtained in a recent BNL experiment. A peak appears below the $\Sigma^+$-emission threshold, which comes from the existence of the ${}^4_\Sigma$He bound state with isospin $T\simeq\frac{1}{2}$. The potential is attractive due to a combination of $U^0-U^T$. It is noticed that there appears a central repulsion in the real part. The Σ-density distribution is largely suppressed at the center and is pushed outside as a *strangeness halo*; the conversion width is reduced by 40% compared with the case of no repulsion.

On the other hand, we can learn the isospin dependence of Σ-hypernuclear states by comparing the $\pi^+$ spectra with $\pi^-$ ones, because the ${}^4$He($K^-$, $\pi^+$) reaction populates only $T=\frac{3}{2}$ states. The potential for $T=\frac{3}{2}$ which has a combination of $U^0+\frac{1}{2}U^T$, is strongly repulsive in the real part and very weak in the imaginary part. There exists no ${}^4_\Sigma$n bound state. Then the calculated spectrum as shown in Fig. 1(b) is very different from the $\pi^-$ spectra.

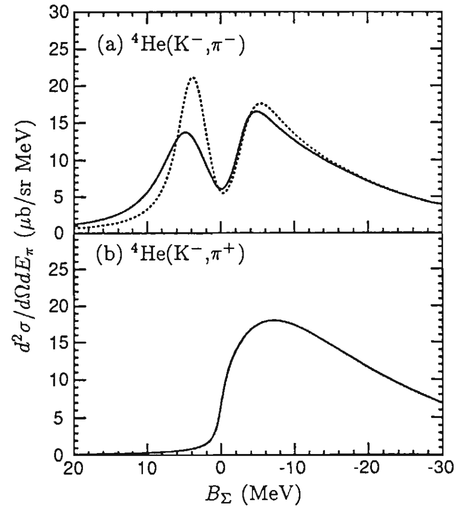


Fig. 1. (a) The inclusive spectra by ${}^4$He ($K^-$, $\pi^+$) in flight at $p_K=600$MeV/c; the solid and dashed curves are the spectra of SAP-1 and of SAP-2, respectively.[2] (b) The inclusive spectrum by ${}^4$He ($K^-$, $\pi^+$) in flight; the curve is the spectrum of SAP-1, which is almost the same as that of SAP-2.

In conclusion, the ${}^4$He($K^-$, $\pi^\mp$) reactions in flight can provide very valuable data for us to determine the nucleus-Σ potential and also to check the underlying ΣN interaction. There is a ${}^4_\Sigma$He bound state with $J^\pi=0^+$, $T\sim\frac{1}{2}$ (99%), where the nucleus-Σ potential has a strong Lane term and a repulsion near the nuclear center in its real part; the former makes the system bound and the latter suppresses the $\Sigma N\to\Lambda N$ conversion.

References

1) R.S. Hayano *et al.*: *Phys. Lett.*, **B231**, 355 (1989).
2) T. Harada *et al.*: *Nucl. Phys.*, **A507**, 715 (1990).
3) R.H. Dalitz, D.H. Davis, and A. Deloff: *Phys. Lett.*, **B236**, 76 (1990).
4) C.B. Dover, D.J. Millener, and A. Gal: *Phys. Rep.*, **184**, 1 (1989).
5) T. Harada and Y. Akaishi: *Phys. Lett.*, **B234**, 455 (1990); *Nucl. Phys.*, to be published.
6) O. Morimatsu and K. Yazaki: *Nucl. Phys.*, **A483**, 493 (1988).

RIKEN Accel. Prog. Rep. **25** (1991)

# III-1-14. Subthreshold $K^+$ and Hypernucleus Production in Nuclear Collisions

M. Sano and M. Wakai

〔hypernucleus, meson, strenge particle.〕

The experimental data for proton and $K^+$ meson producion in Ne+Ne collisions at 2.1 GeV/nucleon are well reproduced by a Glauber plus statistical phase-space model, which describes heavy-ion reaction as superposition of elementary processes in nucleon-nucleon collisions.

The primary production of $K^+$ mesons and $\Lambda$ particles at bombarding energies below the free nucleon-mucleon threshold is possible only by taking into account the internal Fermi motion in projectile and target nuclei. The production cross sections decrease abrutly in the far subthreshold region. On the other hand, the secondary yields of $K^+$ mesons and $\Lambda$ particles through $\pi+N\rightarrow\Lambda+K^+$ reactions become appreciable with a decrease in the bombarding energies and below 1 GeV/nucleon dominate the primary direct production. Calculated results well reproduce the experimental data[1] in proton-nucleus collisions as shown in Fig. 1. Our results are also consistent with a recent study[2] for proton-nucleus collisions made by using the VUU transport theory. The result for nucleus-nucleus collisions, however, is contrary to the VUU result,[3] which suggests a minor role of the secondary $K^+$ production.

Cross sections for the hypernucleus production via the secondary ($\pi$K) reaction in nuclear collisions are of several nb at 1 GeV/nucleon. The primary process[4-6] also gives cross sections of about a few nb.

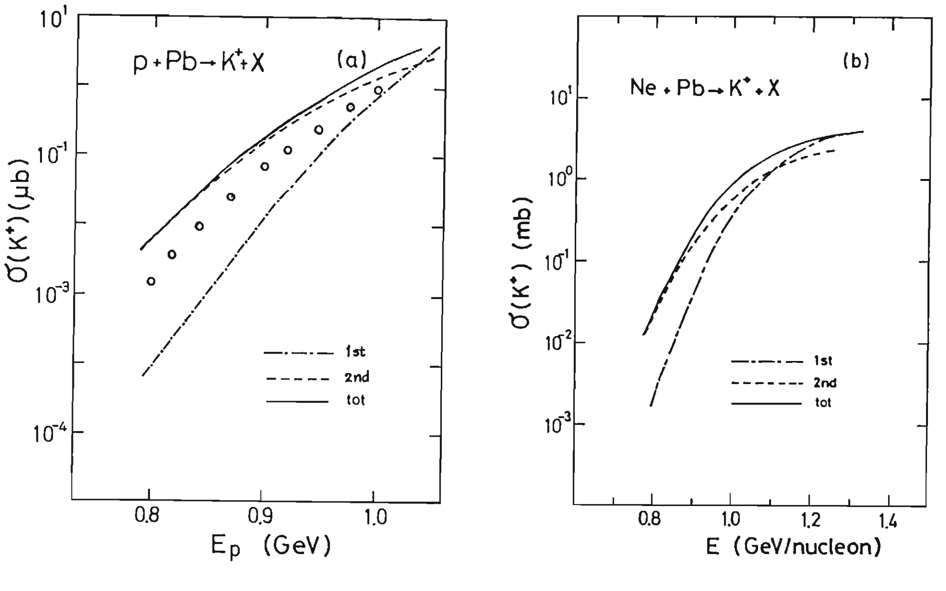


Fig. 1. The subthreshold $K^+$ production in p+Pb and Ne+Pb collisions.

References


1) V.P. Koptev *et al.*: *Sov. Phys. JETP,* **67**, 2177 (1988).
2) W. Cassing *et al.*: UGI-90-1.
3) G. Batko *et al.*: UGI-90-2.
4) H. Bando, M. Sano, J. Zofka, and M. Wakai: *Nucl. Phys.*, **A501**, 900 (1989).
5) F. Asai, H. Bando, and M. Sano: *Phys. Lett.*, **B145**, 19 (1984).
6) M. Wakai, H. Bando, and M. Sano: *Phys. Rev.*, **C38**, 748 (1988).

RIKEN Accel. Prog. Rep. **25** (1991)

# III-1-15. Formation and Fragmentation of Double-Λ Compound Nucleus

M. Sano, M. Wakai, and Y. Yamamoto*

〔hypernucleus, strange particle.〕

The existence of double-Λ hypernuclei is very interesting because it gives valuable information on ΛΛ interactions and is deeply related to other $S=-2$ systems such as Ξ hypernuclei and the H particle. Though our knowledge on double-Λ hypernuclei was originated from only two events in the nuclear emulsion for a long time,[1-3] recently new events have been observed at KEK (the E-176 experiment) with use of the emulsion-counter hybrid detector system.[4] These data are far more confident than the old ones, since $\Xi^-$ particls captured in emulsion were confirmed with high statistics. It is considered that those events follow the stopped $\Xi^-$ and subsequent formation of $\Xi^-$ atom. Another search for double-Λ hypernuclei near the ($K^-$, $K^+$) vertex points is also in progress.[5] In this case a quasi-free $\Xi^-$ is expected to produce a double-Λ hypernucleus. On the other hand, the formation of Ξ hypernuclei was reported in old articles,[6] though their realities are fairly doubtful. A Ξ hypernucleus will decay into a double-Λ one with some probability, if it is able to exist. Under these various situations it has not been investigated systematically how double-Λ hypernucleus is formed through ΞN-ΛΛ processes.

We propose a scenario of the formation of double-Λ hypernuclei. Our basic picture is as follows: In the first stage a double-Λ compound nucleus is formed as a result that two Λ particles produced after a Ξ capture stick to a uclear medium with some energy deposit, where the Ξ particle is captured from an atomic (nuclear) orbit or a quasi-free scattering state. In the second stage the double-Λ compound nucleus decays into various fragments and one of them is likely a double-Λ hypernucleus.

In Table 1 we demonstrate the calculated probilities of the formation of double-Λ fragments. The ones from C, N and O targets are averaged with the weight of the mol ratio in the mulsion.

Table 1. Production probabilities of various double-Λ fragments in emulsion.

| | | | | | | | |
|---|---|---|---|---|---|---|---|
| ${}^{4}_{\Lambda\Lambda}$H | 0.001 | ${}^{8}_{\Lambda\Lambda}$Li | 0.040 | ${}^{11}_{\Lambda\Lambda}$Be | 0.067 | ${}^{14}_{\Lambda\Lambda}$C | 0.066 |
| ${}^{5}_{\Lambda\Lambda}$H | 0.049 | ${}^{9}_{\Lambda\Lambda}$Li | 0.018 | ${}^{11}_{\Lambda\Lambda}$B | 0.013 | ${}^{15}_{\Lambda\Lambda}$C | 0.024 |
| ${}^{6}_{\Lambda\Lambda}$He | 0.093 | ${}^{9}_{\Lambda\Lambda}$Be | 0.002 | ${}^{12}_{\Lambda\Lambda}$B | 0.082 | ${}^{15}_{\Lambda\Lambda}$N | 0.006 |
| ${}^{7}_{\Lambda\Lambda}$He | 0.037 | ${}^{10}_{\Lambda\Lambda}$Li | 0.006 | ${}^{13}_{\Lambda\Lambda}$B | 0.070 | ${}^{16}_{\Lambda\Lambda}$N | 0.034 |
| ${}^{7}_{\Lambda\Lambda}$Li | 0.011 | ${}^{10}_{\Lambda\Lambda}$Be | 0.086 | ${}^{13}_{\Lambda\Lambda}$C | 0.004 | | |

Conclusions of this work are summarized as follows:

(1) A double-Λ compound nucleus is considered to be formed from the $\Xi^-$p-ΛΛ transition through the processes of the direct two Λ sticking and rescattering with nucleons. The former is caused only by a low momentum Ξ particle in the normal density region of a nuclear medium.

(2) In the case of $\Xi^-$ capture at rest, where a $\Xi^-$ particle of almost zero momentum is absorbed from atomic orbits, the calculated probability of direct double-Λ sticking is rather smaller than the experimental indication in the case of light nuclei. The rescattering contribution is very important. Our model predicts larger values of sticking probabilities in the case of heavy nuclei.

(3) The rescattering process plays an essential role in the case of $\Xi^-$ capture from a quasi-free scattering state, because a high momentum $\Xi^-$ particle produced by the ($K^-$, $K^+$) reaction passes through the nucleus. The contribution of direct double-L sticking is negligible in such case.

(4) A double-Λ compound nucleus breaks up into various fragments, which can be treated in a statistical way There are two identifications of ${}^{10}_{\Lambda\Lambda}$Be or ${}^{13}_{\Lambda\Lambda}$B for the double-Λ hypernucleus found in the KEK (E-176) experiment. Our calculation shows that the cases of ${}^{10}_{\Lambda\Lambda}$Be and ${}^{13}_{\Lambda\Lambda}$B are of relatively large and small probabilities, respectively.

* Physics Section, Tsuru University, Yamanashi.

References

1) M. Danysz *et al.*: *Nucl. Phys.,* **49**, 121 (1963).
2) D.J. Prowse: *Phys. Rev. Lett.,* **17**, 782 (1966).
3) R.H. Dalitz *et al.*: *Proc. Roy. Soc.,* **A426**, 1 (1989).
4) S. Aoki *et al.*: *Prog. Theor. Phys.,* **85**, 951; 1289 (1991); C.B. Dover *et al.*: preprint BNL-46383.
5) K. Imai *et al.*: KEK experiment E224.
6) C.B. Dover and A. Gal: *Ann. Phys.,* **146**, 309 (1983).

RIKEN Accel. Prog. Rep. **25** (1991)

# III-1-16. Energy Dependence of Hypernucleus Production in High-Energy Nuclear Collisions

M. Sano and M. Wakai

〔hypernucleus, nuclear collision.〕

The basic mechanism of hypernucleus production in nuclear collisions[1-4] involves (1) the coalescence of strange particles ($\Lambda$, $\Sigma$, $\Xi$) with a nuclear fragment produced in projectile nuclear fargmentation, (2) the coalescence of strange particles and nucleons both produced in the participant part, and (3) the secondary processes by $\pi$ and K mesons produced in the primary nuclear collisions. In high-energy nuclear colli sions the production of K- and especially of $\pi$-mesons becomes large. (The latter being more abundant by a factor of$\sim 10^3$). Thus the secondary yields of hypernuclei through ($K\pi$) and ($\pi K$) reactions becomes appreciable.

Figure 1 shows the energy dependence of ${}_{\Lambda}{}^{4}H$ hypernucleus production in the ${}^{4}He+{}^{12}C$ collision and experimental values of cross sections.[5-7] The $\Lambda$-particle production cross sections increase with increasing beam energy. However, a remarkable increase is not seen. On the contrary, the cross sections at 14.5 GeV/nucleon are about a few times smaller than at 3.7 GeV/nucleon, in spite of the increase of $\Lambda$-particle production with increasing beam energy. This comes from the fact that velocities of $\Lambda$ particles shift to the mid-rapidity region, resulting in a poor overlap between velocity distributions of a $\Lambda$ particle and a nuclear fragment. However, the secondary production of hypernuclei through ($\pi K$) reactions reaches values comparable with the primary direct process (1) in nuclear collisions at 14.5 GeV/nucleon.

The production cross section of ${}_{\Lambda}{}^{3}H$ by the mechanism (2) in ${}^{12}C+{}^{12}C$ collisions at 3.7 GeV/nucleon is 0.31 $\mu$b and is comparable to that from the mechanism (1), that is, 0.22 $\mu$b. For hypernuclei heavier than ${}_{\Lambda}{}^{3}H$, e.g. ${}_{\Lambda}{}^{4}H$, the production by the mechanism (2) at 3.7 GeV/nucleon yields a negligible contribution, compared to that from the mechanism (1). The hypernucleus production by mechanism (2) is effective only for ${}_{\Lambda}{}^{3}H$ and increases gradually with the increase of beam energy.

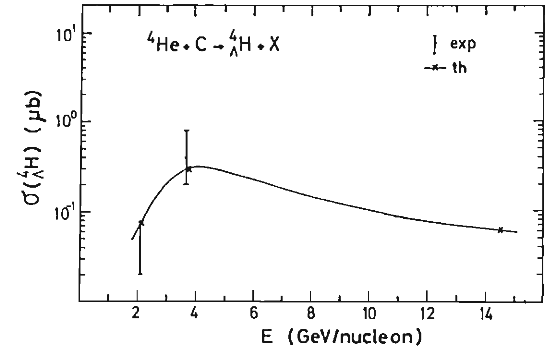


Fig. 1. Energy dependence of ${}_{\Lambda}{}^{4}H$ hypernucleus production cross section in ${}^{4}He+{}^{12}C$ collisions.

References


1) F. Asai, H. Bando, and M. Sano: *Phys. Lett.*, **B145**, 19 (1984).
2) M. Wakai, H. Bando, and M. Sano: *Phys. Rev.*, **C38**, 748 (1988).
3) H. Bando, M. Sano, J. Zofka, and M. Wakai: *Nucl. Phys.*, **A501**, 900 (1989).
4) J. Zofka, M. Wakai, M. Sano, and H. Bando: *Phys. Lett.*, **B235**, 25 (1990).
5) S. Avramenko *et al.*: *Sov. Phys. JETP.*, **48**, 477 (1988).
6) J. Lukstins: Proc. 23rd Yamada Conf. on Nucl. Weak Process and Nucl. Structure, Osaka (1989).
7) S. Khorozov: Proc. 10th Int. Seminar on High Energy Problem, Dubna (1990).

RIKEN Accel. Prog. Rep. **25** (1991)

# III-1-17. Hypernuclear Production in 14.5 GeV/nucleon Si+Au Collisions

M. Sano, M. Wakai, and S. Nagamiya*

〔hypermucleus, strange particle〕

The production of Λ hypernuclei in 14.5 GeV/nucleon Si+Au collisions is studied for four different mechamisms; (1) coalescence of a spectator nuclear fragment and Λ particles from a participant part,[1,2] (2) coalescence of Λ particles and nucleons both produced in the participant part,[3] (3) conversion of a $\Xi^-$ hypernucleus into single- and double-Λ hypernucleus,[3] and (4) the secondary process by $\pi$ and K mesons.[4]

Cross sections of particle productions in the collisions are calculated by a Glauber plus statisical phase-space model, which describes heavy-ion reactions as superpositon of elementary processes in nucleon-nucleon collisions, and are compared with the experimental data.

Tables 1 and 2 show a part of values of cross sections of Λ and Ξ hypernuclei produced by the mechanisms (1) and (2), respectively.

Table 1. Hypernucleus production cross sections in peripheral collisions.

| Nuclear Fragment F | $\sigma(_\Lambda F)$ [μb] | $\sigma(_{\Lambda\Lambda}F)$ [pb] | $\sigma(_\Xi F)$ [nb] |
|---|---|---|---|
| $^2H$ | 0.22 | 0.05 | 0.92 |
| $^3H$ | 0.15 | 0.11 | 0.58 |
| $^3He$ | 0.23 | 0.18 | 0.92 |
| $^4He$ | 2.11 | 1.41 | 8.13 |

Table 2. Hypernucleus production cross sections in central collisions.

| Nuclear Fragment F | $\sigma(_\Lambda F)$ [mb] | $\sigma(_{\Lambda\Lambda}F)$ [μb] | $\sigma(_\Xi F)$ [μb] |
|---|---|---|---|
| $^2H$ (pn) | 8.71 | 22.8 | 33.4 |
| $^3H$ ($pn^2$) | 0.34 | 1.01 | 1.26 |
| $^3He$ ($p^2n$) | 0.24 | 0.71 | 0.89 |
| $^4He$ ($p^2n^2$) | $1.1\times10^{-2}$ | 0.03 | 0.04 |

A $\Xi^-$ particle trapped in a nuclear fragment has a possibility to be converted to Λ particles via an elementary interaction process with protons in the fragment, $p+\Xi^-\rightarrow\Lambda_1+\Lambda_2$. If both $\Lambda_1$ and $\Lambda_2$ remain in the original nuclear fragment, the $\Xi^-$ hypernucleus $_\Xi F$ is converted to a double-Λ hypernucleus, $_{\Lambda\Lambda}F$. The conversion rates of a Ξ-hypernucleus into single- and double-Λ hypernuclei are about 30% and 10%, respectively.

References

1) F. Asai, H. Bando, and M. Sano: *Phys. Lett.*, **B145**, 19 (1984).
2) M. Wakai, H. Bando, and M. Sano: *Phys. Rev.*, **C38**, 748 (1988).
3) M. Sano and M. Wakai: RIKEN-AE-NP-94 (1990).
4) H. Bando, M. Sano, J. Zofka, and M. Wakai: *Nucl. Phys.*, **A501**, 900 (1989).

* Columbia University, Irvingtom, N.Y., U.S.A.

RIKEN Accel. Prog. Rep. **25** (1991)

# III-1-18. The Strangeness S=−2 Hypernuclei and the Predicted H-Particle

M. Sano

〔strangeness, hypernucleus, H particle.〕

Jaffe[1] predicted the existence of the H particle, which consists of six quarks (uuddss), with spin and isospin zero, and strangeness −2. The predicted binding energy of the H particle was about $B_H$ ($\Lambda\Lambda$) ($=2M_\Lambda - M_H$)$\approx$80 MeV below the energy of two lambda particles.

A search for the H particle was carried out in the reaction $p+p \rightarrow K^+ + K^+ + H$[2] and also recently in ($K^-$, $K^+$) reactions.[3] However, no evidence of the H - particle production was observed. Meanwhile, the problem of the existence of the H particle has been discussed by Kerbikov[4] and also Dalitz et al.[5] in connection with the data on double $\Lambda$ hypernuclei. According to their discussions, if the mass of the H particle is below the $\Lambda\Lambda$ threshold, the transition $\Lambda\Lambda N \rightarrow HN$ could occur in the presence of nucleon, as is the situation in double $\Lambda$ hypernuclei. Thus the disintegration of double hypernuclei following the above process would be possible. These processes are permitted through strong interactions. An explicit calculation of the transition rate was done by Kerbikov[4] for the decay process ${}_{\Lambda\Lambda}{}^{6}$He $\rightarrow {}^{4}$He+H, taking into account the coupling to hadronic channels $\Lambda\Lambda$, $N\Xi$ and $\Sigma\Sigma$. His calculation gives a transition rate of $10^{18}\sim10^{20}s^{-1}$ depending on the value of $B_H$ ($\Lambda\Lambda$). This shows to completely dominate the weak decay processes for hypernuclei which have rates of the order of $10^{10}$ $s^{-1}$. It was concluded, therefore, that the existence of the H particle contradicts the data on double hypernuclei.

The data on double strangeness (S=−2) hypernuclei are ones from emulsion measurements in the $\Xi^-$ capture at rest. There is no evidence that those data show double $\Lambda$ hypernuclei, except for the sequential weak decay. Rather than rejecting the existence of the H particle, we propose an alternative interpretation of the data.

Table 1 shows the observed binding energies of the strangeness −2 hypernuclei quoted in Refs., $B_{exp}$(S=−2), the binding energies of the H particle with core nucleus, $B_c{}^H$, and assumed values of the binding energy of the H particle, $B_H$($\Lambda\Lambda$). The minus sign of $B_c{}^H$ implies unbound for the H particle.

Table 1. Binding energies of H hypernuclei.

| | $B_{exp}$(S=-2) (MeV) | $B_c{}^H$ (MeV) | $B_H(\Lambda\Lambda)$ (MeV) | Refs. |
|---|---|---|---|---|
| ${}_H{}^6$He | 10.9 ± 0.5 | 0.9 | 10 | 6) |
| ${}_H{}^{10}$Be | 17.7 ± 0.4 | 7.7 | 10 | 5, 7) |
| | 8.5 ± 0.7 | -1.5 | 10 | 8) |
| ${}_H{}^{13}$B | 27.1 ± 0.7 | 17.5 | 10 | 9) |

A recent event seen by Aoki et al.[8] is assigned as either ${}_{\Lambda\Lambda}{}^{10}$Be or ${}_{\Lambda\Lambda}{}^{13}$B. If we take a possibility of ${}^{13}$B hypernucleus with S=−2 according to the arguments by Dover et al.[9] and take into account results of all identified S=−2 hypernuclei, the binding energy of the H particle satisfies the inequality

$$0 < B_H(\Lambda\Lambda) < 11 \text{ MeV}. \qquad (1)$$

This value is very small compared with the prediction by Jaffe.[1] However, the sequential weak decay which was directly observed is possible.

The problem is how to explain the H hypernucleus production. One of the possibilities is the formation of a compound hypernucleus with S=−2 in the $\Xi^-$ absorption. The compound hypernucleus decays into various fragments with and without strangeness. Calculated production rates of hypernuclei with S=−2 are consistent with the results of the KEK E-176 experiment.[8]


References

1) R.L. Jaffe: *Phys. Rev. Lett.*, **38**, 195 (1977).
2) A.S. Carrol *et al.*: *ibid.*, **41**, 777 (1978).
3) S. Aoki *et al.*: *ibid.*, **65**, 1729 (1990).
4) B.O. Kerbikov: *Sov. J. Nucl. Phys.*, **39**, 516 (1984).
5) R.H. Dalitz *et al.*: *Proc. Roy. Soc.*, **A426**, 1 (1989).
6) D.J. Prowse: *Phys. Rev. Lett.*, **17**, 782 (1966).
7) M. Danysz *et al.*: *Nucl. Phys.*, **49**, 121 (1963).
8) S. Aoki *et al.*: *Prog. Theor. Phys.*, **85**, 1287 (1991).
9) C.B. Dover *et al.*: BNL preprint (1991).

RIKEN Accel. Prog. Rep. 25 (1991)

# III-1-19. Particle Production in the Nuclear Fragmentation Region in Ultrarelativistic Heavy Ion Collisions

S. Daté

[multiple scattering model, event simulator, multiple production.]

The WA80 group at CERN have compared[1] the calculation of the Multi-Chain Fragmentation Model (MCFM)[2] with their results on pseudo rapidity distributions of charged pions and baryons, and the pT (transverse momentum) distribution of protons in the target fragmentation region. The comparison shows that the calculation overestimates the pion yield, underestimates the baryon yield and underestimates the proton's inverse pT slope parameter. Though this calculation involves inadequate estimates for the amount of secondary internuclear interactions, overestimation of the pion yield and underestimation of the proton's inverse slope parameter are common tendencies among event simulators. In an experiment at Brookhaven National Laboratory (BNL),[3] small pion yields and large values of proton's inverse pT slope parameter for central Si+Au collisions have been reported. It seems clear that the above mentioned common tendencies are also seen in the BNL.[4]

In my study using a new event simulator based on the multiple scattering picture, it has been suggested that the common tendencies in deviations of simulator calculations from experimental data can be understood in terms of the existence of the strong pion absorption. The mechanism of pion absorption by the two nucleon system is depicted in Fig. 1. We note that the intermediate $\Delta$ state may be highly off-mass-shell. We expect the following effects of the pion absorption on particle spectra in nuclear fragmentation regions: (1) the decrease in the pion yield, (2) the increase in the nucleon yield due to the additional momentum transfer to nucleons, (3) the increase of average pT of nucleons for the same reason as in (2), and (4) the increase of $K/\pi$ ratio due to the decrease of the denominator. The effects (1) and (3) account for the common tendencies, at least qualitatively.

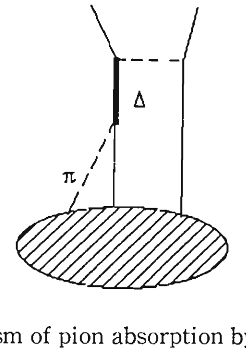


Fig. 1. Mechanism of pion absorption by the two nucleon system.

The experimentally observed $K/\pi$ ratio can be written as

$$\left(\frac{K}{\pi}\right)_{\exp}=\frac{K}{\pi(\text{no abs})}R_\pi,\ \text{where } R_\pi=\frac{\pi(\text{no abs})}{\pi(\text{abs})}.$$

The ratio $R_\pi$ of the pion yield in the absence of the absorption, $\pi$ (no abs), to that in the presence of the absorption, $\pi$ (abs), has a shape as depicted in Fig. 2. This shape is expected from the energy dependence of $\pi N$ and $\pi A$ cross sections.[5] These cross sections have peaks at pion momentum $P_\pi \approx 250$ MeV/c and the peaks end at $P_\pi \approx 500$ MeV/c. This momentum range of pions overlaps with that in $K/\pi$ measurements.

With a purpose of studying pion absorption

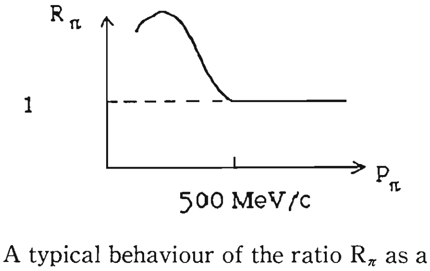


Fig. 2. A typical behaviour of the ratio $R_\pi$ as a function of pion's momentum $P_\pi$.

effects quantitatively, we are developing a new Monte Carlo simulator based on the nucleon level multichain model.[6] Coding of the simulator is already finished and it is under debugging. The existing code runs for about 5 min/O+Pb event on a 5 Mips machine. Preliminary results showed an excellent agreement with global data of CERN experiments and reasonable fitting to pion's pT distributions except for the region of pT <800 MeV/c.

References

1) R. Albrecht *et al.*: *Z. Phys.*, **C45,** 529 (1990).
2) J. Ranft: *Nucl. Phys.*, **A498,** 111c (1989).
3) T. Abbott *et al.*: *Phys. Rev. Lett.*, **66,** 1567 (1991).
4) S. Chapman and M. Gyulassy: Preprint No. LBL-30644 (1991).
5) H.J. Weyer: *Phys. Rep.*, **195,** 295 (1990).
6) A. Capella, U. Sukhatme, C. I. Tan, and J. Tranh Thanh Van: *Phys. Lett.*, **81B,** 68 (1979); S. Daté, M. Gyulassy, and H. Sumiyoshi: *Phys. Rev.*, **D32,** 619 (1985).

RIKEN Accel. Prog. Rep. **25** (1991)

# III-1-20. Toward Lattice QCD Simulation on Parallel Computer AP1000

S. Ohta

(Quantum chromodynamics, lattice field theory, parallel super computer.)

Quantum chromodynamics (QCD) is the fundamental theory of strong interactions. Hence it is at the basis of entire nuclear physics. Nuclei are many body systems made of nucleons and mesons which are in turn made of quarks and gluons. The QCD describes how quarks and gluons interact.

It is known that the QCD interaction at the nuclear energy scale is too strong to allow analysis by perturbation. We need a theoretical framework which is non-perturbative. Fortunately, a very powerful one is provided by the lattice field formulation of the theory, called the lattice QCD.

To obtan a quantitative prediction of the lattice QCD, we have to rely on the numerical importance sampling calculation of relevant path-integrals. This is where the need of supercomputing arises. Recent research papers in the field typically require $O(10^{17})$ floating point operations. At least one thousand times more computations would be necessary to obtain realistic predictions. Unfortunately the conventional supercomputers based on the socalled "vecter processor" technology cannot provide enough computational speed: their typical speed is at most a couple of GF's (GF: computational speed of one billion floating point operations per second) and is cleary inadequate. Fortunately, however, a new type on supercomputer based on "parallel computing" technology runs much faster[1]: Columbia University's 256-node parallel supercomputer easily sustains a speed of about eleven billion floating point operations per second for the lattice QCD. There are plans to build yet faster parallel supercomputers with 100 GF and 1TF (1000 GF) capabilities.[1]

AP1000 is Fujitsu Laboratory's experimental parallel supercomputer. It consists of a two dimensional rectilinear array of upto 32×32 microcomputer cells. Each cell consists of a reduced instruction set cpu, a floating point unit, local cache and main memories, and a set of custom designed communication chips. The cpu operates at 25 MHz clock. The fpu provides a peak speed of 8.3 MF (MF: computational speed of one million floating point operations per second). One of the machine's three communication networks allows, with the help of custom communication chips, data transfer between any pair of cells, not restricted to the nearest neighbors.

The author is developing a full QCD numerical simulation code for the machine.[2] Two important subprograms have been completed. One of them which does not require communications among the cells achieved a speed of about 3 MF per cell. The other one requires massive communication and yet achieved about 2 MF per cell. These numbers should translate into 3 GF and 2 GF speeds respectively for the full scale 32×32-cell machine, whose peak speed would be 8.3 GF.

The author would like to thank the Parallel Computing Research Facility of Fujitsu Laboratory for providing him AP1000 emulator and access to one of the 64-cell AP1000 machines.

References

1) N.H. Christ: in "Lattice 90", *Nucl. Phys. B* (Proc. Suppl.), **20**, 129 (1990), and references cited therein.
2) S. Ohta: in "Lattice 91", *ibid.*, to be published.

RIKEN Accel. Prog. Rep. **25** (1991)

# III-1-21. The $^8Li(\alpha,n)^{11}B$ Reaction Cross Section at Low Energy*

R.N. Boyd, X.X. Bai, D. Hirata, N. Inabe, K. Kimura, T. Kubo, S. Kubono, T. Nakagawa, S. Shimoura, T. Suzuki, and I. Tanihata

〔radioactive nuclear beam, nucleosynthesis.〕

The $^8Li(\alpha,n)^{11}B$ reaction, which is crucial to predictions of inhomogeneous model of primordial nucleosynthesis, has been measured using the radioactive beam facility at RIKEN.

Consideration of the quark-hadron phase transition, though to have occurred $10^{-5}$ s after the Big Bang, has led to the inhomogeneous models (IM) of primordial nucleosynthesis. In the IM, the predicted abundances of light nuclides are close to those observed, but that for $^7Li$ is apparently considerably higher. Unfortunately, the abundances which are fairly easily determined by astronomers, most notably that of $^7Li$, are difficult to interpret and to relate to predictions of primordial nucleosynthesis, so those of nuclides heavier than $^{12}C$ may become crucial in testing the IM. A critical reaction in predicting abundances of $^{11}B$ and heavier nuclides is $^8Li(\alpha,n)^{11}B$, as it apparently is the dominant one linking nuclides to those heavier than $^{12}C$. Thus we have studied this reaction. The ring cyclotron of RIKEN together with the Riken Projectile fragment Separator (RIPS) produced the $^8Li$ beam used. Because of the large energy spread of the beam, each ion was tagged and its energy was determined via a channel plate time-of-flight (TOF) system. The $^8Li$ ions then passed into the Multi Samplimg Ionization Chamber, a detector which maps out trajectories of ions passing through it and measures their energy losses in 5 cm increment. The detector gas used in the MUSIC was $^4He$; it thus served also as the target. $^8Li(\alpha,n)^{11}B$ event were identified by the change in $\Delta E/\Delta x$ which accompanied their change from $^8Li$ to $^{11}B$, and the energy at which each event occurred was determined by the point at which the change was observed.

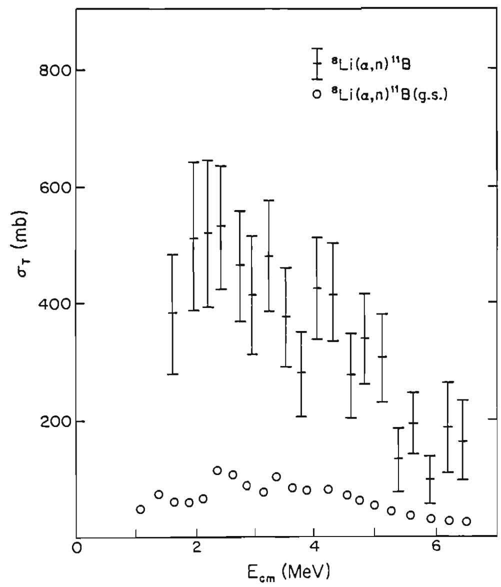


Fig. 1. Total cross section for the $^8Li(\alpha,n)^{11}B$ reaction (points with error bars) as a function of center of mass energy. The circles (E ) are for a representative sampling of the data for the cross section only to the $^{11}B$ ground state, as inferred from the inverse reaction data of Paradellis et al.[1]

The determined cross sections are shown in Fig.1. They are large (200∼500 mb) and thus the observable abundance of heavy elements is expected.

References

1) T. Paradellis *et al.*: *Zeitsch. Phys.*, **A337**, 211 (1990).

* Condensed from RIKEN-AF-NP-112.

RIKEN Accel. Prog. Rep. **25** (1991)

# III-1-22. Determination of the Astrophysical $^{13}N(p, \gamma)^{14}O$ Reaction Rate by the Coulomb Breakup of $^{14}O$ Nuclei in the Field of $^{208}Pb$

T. Motobayashi, T. Takei, S. Kox,* C. Perrin,* F. Merchez,*
D. Rebreyend,* K. Ieki, H. Murakami, Y. Ando, N. Iwasa, M. Kurokawa,
S. Shirato, J. Ruan (Gen), T. Ichihara, T. Kubo, N. Inabe, A. Goto,
S. Kubono, S. Shimoura, and M. Ishihara

NUCLEAR REACTIONS $^{208}Pb(^{14}O, ^{13}Np),^{208}Pb$, $E/A=87.5$ MeV, $^{208}Pb(^{13}N, ^{12}Cp)^{208}Pb$, $E/A=78.1$ MeV; measured coincidence $\sigma(\theta)$, Coupled channel analysis, deduced $\Gamma_\gamma$ of $^{14}O(1^-; E_{ex}=5.45$ MeV), $^{13}N(1/2^+; E_{ex}=2.37$ MeV).

The Coulomb breakup process in the field of a heavy nucleus can be used as a source of information on the radiative capture process of astrophysical interest.[1] We studied the breakup of $^{14}O$ nucleus,[2] which is related to the $^{13}N(p, \gamma)^{14}O$ reaction, a key reaction of the hot CNO cycle of hydrogen burning in stars. The experiment was performed at RIKEN Ring Cyclotron. The RIPS facility was used to obtain the radioactive $^{14}O$ beam. Since the secondary beam contained also $^{13}N$, the breakup reaction of $^{13}N \rightarrow {}^{12}C+p$ as well as $^{14}O \rightarrow {}^{13}N+p$ could be studied simultaneously. The beam energies of $^{14}O$ and $^{13}N$ were 87.5 A MeV and 78.1A MeV, respectively. The breakup products, proton and $^{12}C$ or $^{13}N$ were detected by a multi-detector system based on the EMRIC detector.[3]

Figure 1 shows the angular distributions for the reactions $^{208}Pb(^{14}O,^{13}Np)^{208}Pb$ and $^{208}Pb(^{13}N, ^{12}Cp)^{208}Pb$ exciting the $1^-$ state at $E_{ex} = 5.17$ MeV in $^{14}O$ and the $1/2^+$ at $E_{ex} = 2.37$ MeV in $^{13}N$, respectively. It is known that the stellar burning process of the hot CNO cycle is dominated by the E1 transition to the 0.547 MeV resonance, corresponding to the $^{14}O$ $1^-$ state. Therefore the quantity of astrophysical interest can be determined from the E1 transition strength or the radiative width $\Gamma_\gamma$ of this state. The data are compared with the result of the coupled channel calculation by a code ECIS79,[4] in which the Coulomb breakup mechanism is assumed. The Coulomb deformation parameter $\beta_C$ was adjusted so that the calculated angular distribution fits the data. The best fit was obtained with $\Gamma_\gamma = 3.1 \pm 0.6$ eV for $^{14}O$ and $\Gamma_\gamma = 0.59 \pm 0.18$ eV for $^{13}N$. The contribution from the nuclear breakup process was estimated to be very small. The present

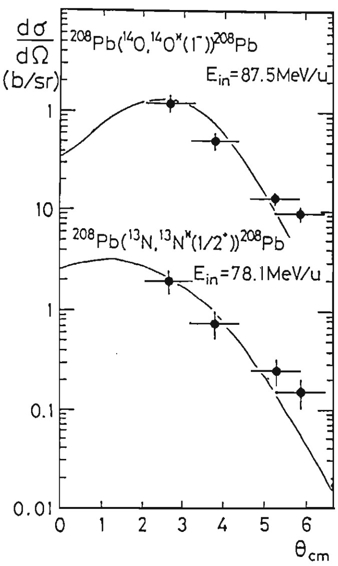


Fig. 1. Experimental and calculated angular distributions for the reactions $^{208}Pb(^{14}O,^{13}Np)^{208}Pb$ (upper part) and $^{208}Pb(^{13}N,^{12}Cp)^{208}Pb$ (lower part) exciting the $1^-$ state of $^{14}O$ and $1/2^+$ of $^{13}N$, respectively. The solid curves are obtained by the coherent sum of the nuclear and Coulomb excitation amplitudes assuming $\Gamma_\gamma = 3.1$ eV for $^{14}O(1^-)$ and $\Gamma_\gamma = 0.59$ eV for $^{13}N(1/2^+)$.

result for $^{13}N$, $0.59 \pm 0.18$ eV, agrees well with the value measured via the (p, $\gamma$) reaction, $0.50 \pm 0.04$ eV,[5] showing the validity of this Coulomb breakup method.

In Fig. 2, the present value of $\Gamma_\gamma$ for the $1^-$ state in $^{14}O$ is compared with values obtained by the other experimental and theoretical works. The recent direct capture measurement with radioactive $^{13}N$ beam at Louvain la Neuve gives $\Gamma_\gamma = 3.8 \pm 1.2$ eV,[6] which agrees with ours within the errors. The recent recommended value, 1.9 eV,[7] is smaller than the present result. Among the results from alternative measurements, our esti-

* Institut des Sciences Nucléaires, IN2P3-UJF, 38026 Grenoble Cedex, France.

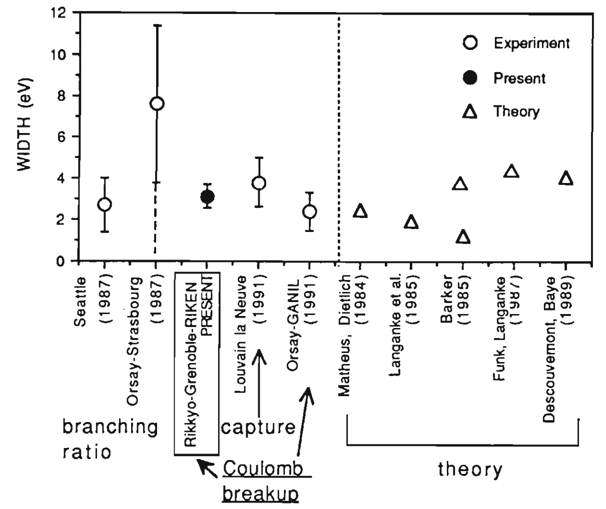


Fig. 2. The radiative width $\Gamma_\gamma$ for the $1^-$ state in $^{14}O$ obtained by experimental and theoretical studies.

mated errors are the smallest, which demonstrates the high experimental efficiency of the present experiment.

References

1) G. Baur, C.A. Bertulani, and H. Rebel: *Nucl. Phys.*, **A458**, 188 (1986).
2) T. Motobayashi *et al.*: *Phys. Lett.*, **B264**, 264 (1991); T. Motobayashi *et al.*: *RIKEN Accel. Prog. Rep.*, **24**, 12 (1990).
3) F. Merchez *et al.*: *Nucl. Instrum. Methods*, **A275**, 133 (1989).
4) J. Raynal: Coupled channel code ECIS79 (unpublished).
5) F. Ajzenberg-Selove: *Nucl. Phys.*, **A523**, 1 (1991).
6) P. Decrock *et al.*: *Phys. Rev. Lett.*, **67**, 808 (1991).
7) G.R. Caughlan and W.A. Fowler: Atomic Data and Nuclear Data Table, **40**, 283 (1988).

RIKEN Accel. Prog. Rep. **25** (1991)

# III-1-23. Proton Decay Measurement with RIPS for Astrophysical Interest

S. Kubono, Y. Funatsu, N. Ikeda, M.H. Tanaka, T. Nomura, H. Orihara, S. Kato, M. Ohura, T. Kubo, N. Inabe, T. Ichihara, M. Ishihara, I. Tanihata, H. Okuno, T. Nakamura, S. Shimoura, H. Toyokawa, C.C. Yun, H. Ohnuma, K. Asahi, A. Chakrabarti,* T. Mukhopadhyay,* and T. Kajino

[NUCLEAR STRUCTURE, $^{20}$Na, Radioactive beam of $^{20}$Mg, Explosive hydrogen burning process.]

An explosive hydrogen burning process, which is called rapid-proton (rp) - process,[1] will begin by breaking out of the hot-CNO cycle through the reaction sequence[1-5] ; $^{15}$O$(\alpha,\gamma)$$^{19}$Ne$(p,\gamma)$$^{20}$Na$(p,\gamma)$$^{21}$Mg. Among this sequence, the most crucial reaction is considered to be $^{19}$Ne$(p,\gamma)$$^{20}$Na. The first excited state above the threshold in $^{20}$Na was found[3] at 2.637 MeV with $J^{\pi}=1^{+}$; this suggests an enhancement of the reaction rate of $^{19}$Ne$(p,\gamma)$$^{20}$Na roughly by two orders of magnitude, and about 50 % reduction for the onset temperature of the breakout from the hot-CNO cycle.[3] However, the absolute onset temperature is not determined yet. For this problem, an experiment to study the decay property and the total width for the $1^{+}$ state was performed by measuring the decay particle and gamma rays with using the projectile fragment of $^{20}$Mg from the $^{24}$Mg beam at the RIKEN Ring Cyclotron Facility.

A 100-MeV/u $^{24}$Mg primary beam of about 10 - 20 nA was used to produce $^{20}$Mg particles at the rate of 10 - 20 particles of $^{20}$Mg per second with using RIPS. The secondary beam particles were identified by energy-loss and time-of-flight measurements, and stopped mostly in the third silicon detector of the five-silicon detector array, which was surrounded by a beta-ray spectrometer made of plastic scintillators. There were no specific gamma-ray observations related to the $^{20}$Na decay with two sets of Ge detectors. This could be due to the small beam intensity used for the experiment. The purity of the secondary beam was about 1 %.

There are four strong lines observed at 857, 1740, 2836, and 5892 keV in the energy spectrum with the silicon detector. The last two lines are found to be the delayed $\alpha$-particles via the 7.424- and 10.274- MeV states in $^{20}$Ne. The other low-energy peaks correspond to the proton decays of the $^{20}$Na states to $^{19}$Ne. The half-life measured by stopping the primary beam for 200 ms just after the $^{20}$Mg detection was about 110 ms, which is consistent with the known value of $^{20}$Mg.[6] The lowest energy peak of 857 keV (Ex=3.056 MeV in $^{20}$Na) is corresponding well to the previously known state, the 3.046 MeV $(1,2,3)^{+}$ state[3] in energy. This could be the second $1^{+}$ state above the proton threshold in $^{20}$Na. There was no clear peak observed at 438 keV for the 2.637 MeV $1^{+}$ state in the spectra. The upper limit of the branching ratio estimated for this state is about 1 %. The experimental branching ratios obtained are 86, < 1, 9, and 5 % for the the states at 1.057, 2.637, 3.056, and 3.939 MeV, respectively.

By comparing to the beta decay of the mirror nucleus $^{20}$O, the 3.045-MeV state is likely the analogue of the 3.488-MeV state in $^{20}$F, and the 2.637-MeV state is of the 3.175-MeV in $^{20}$F. The latter state was not fed in the beta decay of $^{20}$O,[7] and there is no $l=0$ strength for this state in the spectroscopic factor of the $^{19}$F(d,p)$^{20}$F reaction.[6] These data clearly suggest that the 2.637-MeV state has little component of $(sd)^{4}$ and the state could be an intruder $1^{+}$ state of $(p)^{-2}(sd)^{6}$.[8]

If one takes $\Gamma_{\gamma}=9.3$ meV for the 2.637-MeV $1^{+}$ state from the analogue, the 3.175-MeV state in $^{20}$F, the $^{19}$Ne$(p,\gamma)$$^{20}$Na reaction rate will be reduced roughly by a factor of two. Therefore, the main conclusion in the previous estimate[3] for the rate would not change if the assumption from the analogue state is correct.

* Bhabha Institute, Calcutta, India.

References

1) R. Wallace and S. E. Woosley: *Astrophys. J. Suppl.*, **45,** 389 (1981).
2) K. Langanke *et al.*: *Astrophys. J.*, **301,** 629 (1986).
3) S. Kubono *et al.*: *ibid.*, **344,** 460 (1989).

4) L. O. Lamm *et al*.: *Nucl. Phys.*, **A510,** 503 (1990).
5) S. Kubono *et al*.: *Z. Phys.*, **A334,** 512 (1989).
6) F. Ajezenberg-Selove: *Nucl. Phys.*, **A475,** 1 (1987).
7) D. E. Alburger *et al*.: *Phys. Rev.*, **C35,** 1479 (1987).
8) J. B. McGrory and B. M. Wildenthal: *ibid.*, **C7,** 974 (1973).

# III-1-24. g-Factor Measurements of $^{14}$B and $^{15}$B Ground States

H. Okuno, K. Asahi, M. Ishihara, T. Nakamura, M. Adachi, J. Kura, H. Ueno, H. Sato, N. Inabe, T. Kubo, A. Yoshida, T. Ichihara, Y. Ohkubo, T. Shimoda, H. Miyatake, N. Takahashi, D. Morrissey,* W.-D. Schmidt-Ott,** and D. Beaumel***

NUCLEAR REACTION $^{93}$Nb+$^{18}$O, E/A=69.5MeV/nucleon ; measured $\beta$-ray asymmetry of $^{12}$B,$^{14}$B and $^{15}$B ; deduced g-factors of $^{14}$B and $^{15}$B ground states.

Recent experiments[1,2] have revealed that ejectile nuclei in the fragmentation of intermediate-energy heavy-ion projectiles are largely spin-polarized. In this report we present the application of this phenomenon, resulting in the first measurements of the ground state nuclear moments of $^{14}$B ($T_{1/2}$=12.8 ms ) and $^{15}$B ($T_{1/2}$= 10.3 ms ). The experiments were carried out by using a radioactive beam line RIPS.[3] Short lived nuclei $^{12}$B, $^{14}$B and $^{15}$B were produced by fragmentation of $^{18}$O projectiles at 69.5 MeV/nucleon on a $^{93}$Nb target (200 $\mu$m in thickness). Those nuclei emitted at angles around 3 degrees were isotope-seperated and momentum-selected by the RIPS and implanted into a Pt stopper placed at the final focus of the RIPS (Fig. 1). The g-factors were deduced from the observation of NMR detected by the change of $\beta$-ray asymmetry. Examples of NMR spectra are shown in Fig. 2. The g-factors of $^{12}$B, which were already known to a good accuracy, were used for the calibration. From the peak position extracted from Lorentian fits, we obtained preliminarily the following values;

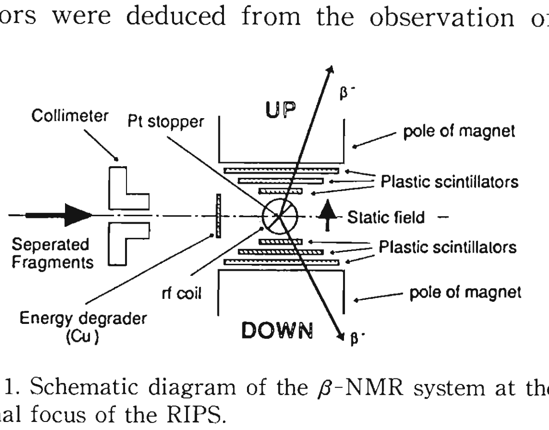


Fig. 1. Schematic diagram of the $\beta$-NMR system at the final focus of the RIPS.

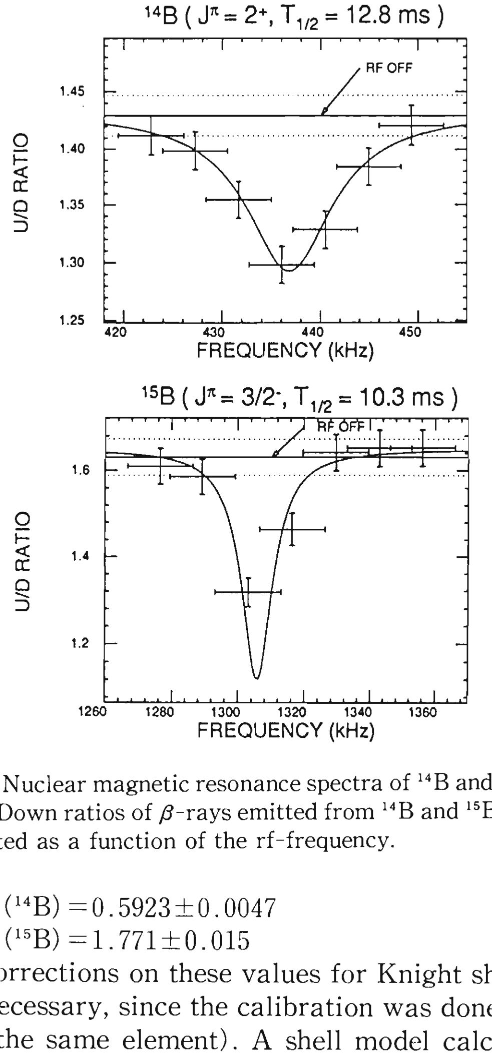


Fig. 2. Nuclear magnetic resonance spectra of $^{14}$B and $^{15}$B. Up/Down ratios of $\beta$-rays emitted from $^{14}$B and $^{15}$B are plotted as a function of the rf-frequency.

$$g(^{14}\mathrm{B}) = 0.5923 \pm 0.0047$$
$$g(^{15}\mathrm{B}) = 1.771 \pm 0.015$$

No corrections on these values for Knight shifts are necessary, since the calibration was done by $^{12}$B (the same element). A shell model calculation on $^{14}$B and $^{15}$B is now in progress.

* National Superconducting Cyclotron Laboratory, Michigan State University, U.S.A.
** II. Physikalisches Institut, Universitat Göttingen, F.R.G.
*** Institut de Physique Nucleaire, France.

References
1) K. Asahi *et al.*: *Phys. Lett.*, **B251**, 488 (1990).
2) H. Okuno *et al.*: *RIKEN Accel. Prog. Rep.*, **24**, 14 (1990).
3) T. Kubo *et al.*: Proc. 1st Int. Conf. on Radioactive Nuclear Beams, Berkeley, California, 1989, eds. W.D. Myers, J.M. Nitschke, and E.B. Norman, World Scientific, Singapore, p. 563 (1990).

RIKEN Accel. Prog. Rep. **25** (1991)

# III-1-25. Disappearance of the Giant Dipole Resonance in Hot Nuclei

K. Yoshida, J. Kasagi, H. Hama,* K. Furutaka, K. Ieki, W. Galster,** T. Kubo, M. Ishihara, and A. Galonsky***

NUCLEAR REACTION $^{nat}Ni$, $^{92}Mo$, $^{122}Sn+^{40}Ar$, $E(^{40}Ar)=$ 26 MeV/nucleon: measured GDR decay $\gamma$ rays in coincidence with fusion residues; deduced $dM_\gamma/dE_\gamma$/decay for $E_\gamma>5$ MeV.

The giant dipole resonance (GDR) $\gamma$-ray emission from highly excited nuclei has provided a unique tool to study the property of hot nuclei. It was shown that the GDR $\gamma$-ray decay is quenched above $E_x\sim350$ MeV for the $^{70}Ge+^{40}Ar$ fused system.[1] Our previous work,[2] performed with the $^{92}Mo+^{40}Ar$ reactions at $E/A=21$ and 26 MeV, suggested that the GDR disappears at $E_x\sim$ 200 MeV due to excessive broadening of the resonance. It is, thus, very interesting to obtain systematic information especially on the high temperature limit of the existence of the GDR.

For this purpose, the GDR decay $\gamma$-rays from other fused systems have been measured at the RIKEN Ring Cyclotron (RRC). High energy $\gamma$-rays were measured in coincidence with fusion-like residues in the $^{40}Ar+Ni$, $^{92}Mo$, $^{122}Sn$ reactions at $E/A=26$ MeV. The high energy $\gamma$-rays were detected with a $BaF_2$ $2\pi$ detector system consisting of 80 $BaF_2$ scintillators.

The emitted $\gamma$-rays from hot nuclei were calculated using the extended version of the code CASCADE. In order to obtain a limiting temperature for the existence of the GDR, two different analyses have been performed. The standard calculation with a fixed GDR width, used to analyze the data at low excitation energies, overestimates $\gamma$-ray yields in the region between 10 and 20 MeV. The only way to explain the saturation of the yield is to quench the $\gamma$-ray emission above a limiting excitation energy. Thus, in the analysis using the standard calculation, a limiting excitation energy can be defined as the excitation energy above which the nucleus does not emit $\gamma$-rays. The other method employed in Ref. 2 is to incorporate the energy dependence of the resonance width in the calculation. We applied the same excitation energy dependence of the width as employed for the $^{40}Ar+^{92}Mo$ system in Ref. 2. The width increases rapidly as the excitation energy increases, so that the strength of the energy windows of the GDR region ($12<E\gamma<20$ MeV) decreases without a reduction in the EWSR strength. The limiting excitation energy in this analysis was defined as the energy above which the width of the GDR becomes larger than 30 MeV.

The deduced limiting temperature for the existence of the GDR decreases as the mass number increases, described as $T_1\sim17A^{-1/3}$ MeV where $T_1$ is the limiting temperature and A the mass number. Since the resonance energy is approximated to be $80A^{-1/3}$ MeV, it can be said that the GDR disappears at the temperature of about a quarter of the resonance energy.

References

1) J.J. Gaardhoje *et al.*: *Phys. Rev. Lett.*, **59**, 1409 (1987).
2) K. Yoshida *et al.*: *Phys. Lett.*, **245B**, 7 (1990).

* Institute for Molecular Science.
** Université Catholique de Louvain.
*** Cyclotron Laboratory, Michigan State University.

RIKEN Accel. Prog. Rep. **25** (1991)

# III-1-26. Study of $^{33}$Si with Radiation-Detected Optical Pumping in Solids

K. Shimomura, T. Nakamura, H. Okuno, M. Koizumi, S. Hamada, N. Inabe, I. Ogawa, K. Suzuki, M. Wada, H. Sunaoshi, Y. Fukashiro, T. Murayama, T. Kohmoto, T. Shinozuka, T. Kubo, K. Asahi, T. Inamura, M. Ishihara, M. Fujioka, and S. Matsuki*

(NUCLEAR REACTION $^{40}Ar+{}^{9}Be$, $E(^{40}Ar)=94$MeV/nucleon; optical pumping in solids GaAs; measured $\beta$-ray asymmetry from $^{33}$Si; measured life time of $^{33}$Si; magnetic resonance of $^{33}$Si.)

Recently several experimental and theoretical investigations suggest that the neutron magic number may not be 20 in light neutron-rich region (Ne to Si), thereby some nuclei being deformed around N=20. To get more detailed nuclear-structure information on this region, we tried as a first step to measure the magnetic moment of $^{33}$Si with a newly developed method of $\beta$-RADOP in solids.[1]

The isotope $^{33}$Si was produced as a projectile fragment in the interaction of an Ar beam with a Be target at the incident energy of 94 MeV/nucleon. After mass separated with the mass separator RIPS at RIKEN, the $^{33}$Si isotopes were implanted into a GaAs crystal cooled by contact to a liquid He bath. The implantation rate of the isotopes was about 8000 $s^{-1}$. The GaAs crystal was irradiated with a circularly-polarized laser light from a Ti-sapphire laser under an external magnetic field (2.5kG). The spin polarization of electrons excited from the valence to the conduction bands was then transferred to the nuclear spin of $^{33}$Si via the hyperfine interaction.[2] The degree of nuclear polarization was measured by detecting the asymmetry of $\beta$-rays with a pair of scintillation-counter telescope.

Nuclear polarization was achieved only with the laser light in a narrow region of wavelength around 845nm. A preliminary data of magnetic resonance by applying a rf magnetic field together with the laser optical pumping is shown in Fig. 1. Neglecting a possible effect of the Knight shift, the measured magnetic resonance suggests that the g-factor of $^{33}$Si is $0.803\pm0.021$. We also obtained a more precise half-life of $^{33}$Si than previous data from a time spectrum of $\beta$-rays (Fig. 2); The deduced half-life is $6.332\pm0.029$ sec, which should be compared with previous adopted result of $6.18\pm0.18$ sec.[3]

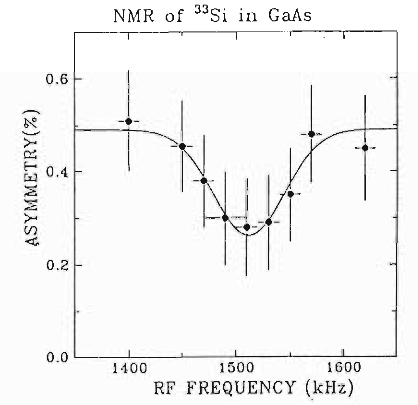


Fig. 1. Preliminary result of a $\beta$-ray radiation-detected magnetic resonance of $^{33}$Si as a function of the applied radio-frequency at 2.5 kGauss.

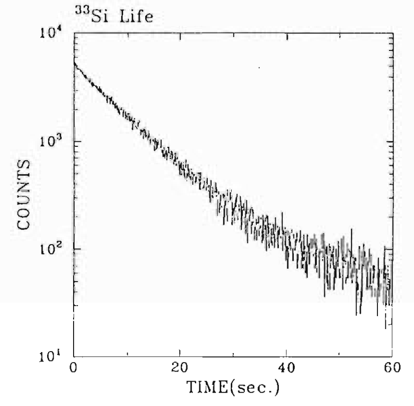


Fig. 2. A decay spectrum of $\beta$-rays from $^{33}$Si.

References

1) K. Shimomura, S. Uemura, T. Kohmoto, Y. Fukuda, S. Ito, K. Okano, T. Muramoto, T. Hashi, and S. Matsuki: *Phys. Rev.*, **C42**, R487(1989).
2) Optical Orientation (eds., F. Meier and B. Zakharchenya), North-Holland, Amsterdam (1984).
3) D.R. Goosman, C.N. Davids, and D.E. Alburger: *Phys. Rev.*, **C8**, 1324(1973).

* Institute for Chemical Research, Kyoto University.

RIKEN Accel. Prog. Rep. **25** (1991)

# III-1-27. Density Distribution and E1 Strength of $^{11}$Li

N. Inabe, S. Shimoura, T. Nakamura, H. Okuno, H. Okamura,
H. Sakai, T. Kubo, T. Nakagawa, H. Kumagai,
I. Tanihata, and M. Ishihara

(Interaction cross section, Density distribution, Neutron halo, Electromagnetic dissociation, El strength, Soft giant dipole resonance.)

The interaction cross sections($\sigma_I$) of $^{11}$Li on C, Al, Cu and Pb at 43 and 75 A MeV were measured by a transmission method using $^{11}$Li secondary beams provided by the radioactive beam facility RIPS [1] at RIKEN Ring Cyclotron.

To study a density distribution, we searched for the best t fit to the $\sigma_I$ on C at 43, 75, 400, 790 A MeV using a Glauber model [2] by changing parameters of a density profile. The density profile of $^{11}$Li is supposed to be composed of a Harmonic oscillator density and a Yukawa square tail. The best fit reproduces well the energy dependence of $\sigma_I$ as shown by the solid line in Fig. 1. The result shows that $^{11}$Li has the density distribution with a long tail, which is consistent with a picture that $^{11}$Li has a neutron halo.[3]

To study an El strength, we determined electromagnetic dissociation cross sections($\sigma_{EMD}$) on Pb by subtracting nuclear part($\sigma_{nuc}$) from $\sigma_I$. Here, we estimated $\sigma_{nuc}$ by the Glauber type calculation using the density distribution mentioned above. From the obtained $\sigma_{EMD}$'s, we searched an excitation energy and a reduced transition probability of $^{11}$Li using a virtual photon theory,[4] assuming that the only one excited state contributes to $\sigma_{EMD}$ mainly. The outer contour in Fig. 2 shows a limit in which the over all fitting is better than 1$\sigma$. The result shows that $^{11}$Li has a significantly large strength in a low excitation energy, which supports the existence of a soft giant dipole resonance.[5]

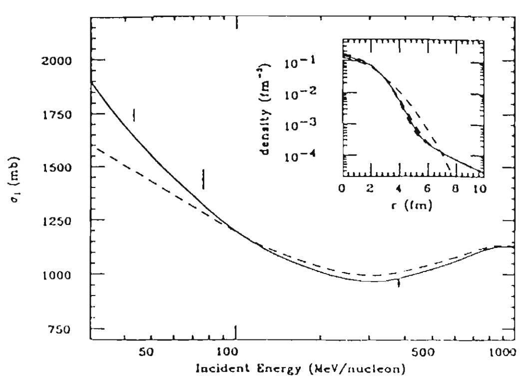


Fig. 1. Energy dependence of interaction cross sections of $^{11}$Li on carbon target and obtained density distribution (inset). Solid line shows the model calculation. Dashed line is the results without halo.

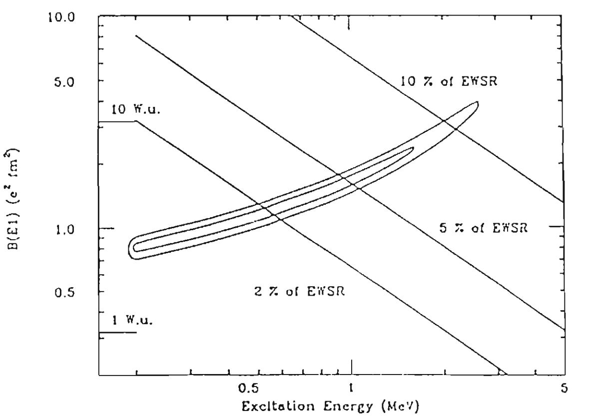


Fig. 2. Possible region in excitation energy vs. strength plane. The outer contour crresponds to 1 $\sigma$ error and inner, 0.5 $\sigma$. Three lines indicate the 2%, 5%, and 10% fraction of energy weighted sum rule(EWSR).

References

1) T.Kubo *et al.*: Proc. 1st. Conf. on Radioactive Nuclear Beams, p. 563 (1989).
2) P.J. Karol: *Phys. Rev.*, **C11**, 1203 (1975).
3) I. Tanihata *et al.*: *Phys. Lett.*, **206B**, 592 (1988).
4) C.A. Bertulani and G. Bauer : *Phys. Rep.*, **163**, 299 (1988).
5) K. Ikeda: INS report JHP-7 (1988).

RIKEN Accel. Prog. Rep. **25** (1991)

# III-1-28. Momentum Correlation of Halo Neutrons in $^{11}$Li
## Evidence of Di-Neutron Formation

T. Kobayashi, S. Shimoura, I. Tanihata, T. Suzuki, K. Yoshida, K. Matsuta,*
T. Minamisono,* K. Sugimoto,* O. Testard,** W. Müller,*** D. Olson,***
and H. Wieman***

(exotic nuclei, neutron halo, nuclear reaction, radioactive nuclear beam.)

The transverse momentum ($P_t$) distribution of $^{9}$Li fragment from 800A MeV $^{11}$Li on p, d, and C targets are measured with high statistics at the LBL Bevalac. Improvements of the intensity of primary $^{18}$O beam and the beam optics enabled us to use about 300 $^{11}$Li per pulse. The experimental system is essentially the same one as already reported in previous publications except the target system for liquid hydrogen and deuterium.[1,2] The thickness of the target was about 12 cm. Figure 1 shows thus determined $P_t$ distribution.

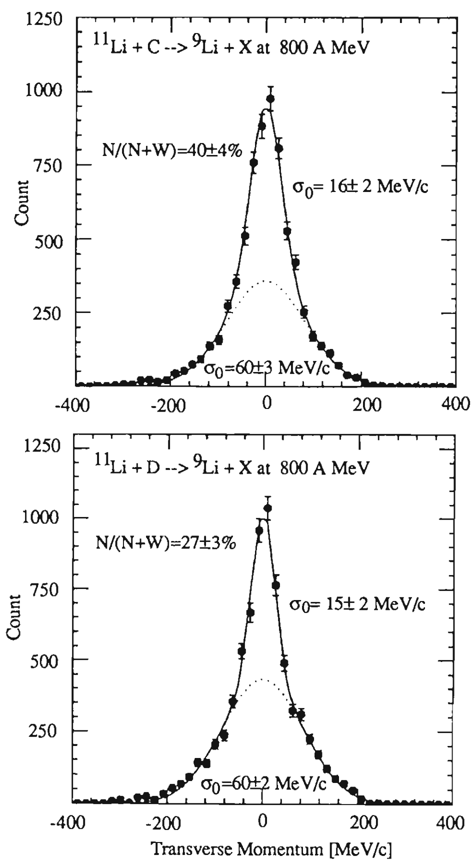


Fig. 1. Transverse momentum distribution of $^{9}$Li from $^{11}$Li reactions. Curves are the best fit by two Gaussian distributions.

The widths of $^{9}$Li and neutron fragment distribution were used to deduce the correlation term $<P_1 \cdot P_2>$ between two halo neutrons. It was found that the correlation term has a large positive value ($300 \pm 43$ (MeV/c)$^2$) and thus suggesting that these neutrons are moving to the same direction in average. It presents quite a contrast to normal nucleon correlations, in which the correlation has negative value. Therefore present data suggest a formation of a cluster of neutrons moving together "di-neutron". Present analysis, however, depends on the simple qualitative reaction model. Therefore we need a detailed realistic reaction model to confirm this correlation. Also we need high statistic data of the neutron distribution at high energies because they were measured only at a low energy (30 A MeV) where final state interactions may be important.

This work is supported by the US Department of Energy under the contract No. DE-AC03-76 SF0098, by the LBL-RIKEN collaboration program, and by the Japan-US Cooperative Program from the Japan Society for the Promotion of Science.

References

1) I. Tanihata, T. Kobayashi, O. Yamakawa, S. Shimoura, K. Ekuni, K. Sugimoto, N. Takahashi, T. Shimoda, and H. Sato: *Phys. Lett.,* **B206,** 593 (1988).
2) T. Kobayashi, O. Yamakawa, K. Omata, K. Sugimoto, T. Shimoda, N. Takahashi, and I. Tanihata: *Phys. Rev. Lett.,* **60**, 2599 (1988).

* Osaka University, Toyonaka, Osaka 560, Japan.
** Saclay, 91191 Gir Sur Yvette, France.
*** LBL, Berkeley, CA 94720, U.S.A.

RIKEN Accel. Prog. Rep. 25 (1991)

# III-1-29. Measurement of Angular Distributions for the $^{9,11}Li+p$ Elastic Scattering

C.-B. Moon,* K. Abe, M. Fujimaki, N. Inabe, K. Katori, J.C. Kim,** Y.K. Kim,** T. Kobayashi, H. Kumagai, T. Kubo, S. Shimoura, T. Suzuki, and I. Tanihata

NUCLEAR REACTIONS p($^{9,11}$Li,$^{9,11}$Li)p, E/A=62 MeV ($^{11}$Li), 60 MeV($^{9}$Li) : Measured $d\sigma(\theta)/d\Omega$.

The elastic scattering of 62 MeV/nucleon $^{11}$Li and 60 MeV/nucleon $^{9}$Li nuclei on a proton target as a reversed kinematics was measured for the first time at the RIKEN Ring Cyclotron facility. Secondary beams of $^{9,11}$Li were produced at the RIPS using 100 A MeV $^{18}$O primary beam on the $^{9}$Be target with the thickness of 7.5 mm. A disk of $CH_2$ with the thickness of 95 mg/cm$^2$ was used as a proton target. The experimental set-up and method are presented in the other pages in this progress report. Angular distributions obtained are given in Fig.1 in which $^{6,7}$Li isotopes data[1] are also shown for comparison. It is noted that angular distribution for the $^{9}$Li+p system may include some inelastic scattering due to the excited states in $^{9}$Li. On the other hand, $^{11}$Li data include only the elastic scattering because no particle stable excited states exists in $^{11}$Li.

One can clearly see two remarkable features in the $^{11}$Li+p cross section, one is the shift of the first minimum to forward angle, 44°, compared with those of the other isotopes and the other is the reduction of the cross sections compared with those of other isotopes. The general trends of the $^{9}$Li+p system, whereas, is in fair accordance with the systematics established for $^{6,7}$Li isotopes. The shift of the minimum position in the $^{11}$Li+p cross sections to forward angle is qualitatively understood as an influence of the greater matter extension due to the outer two neutrons.

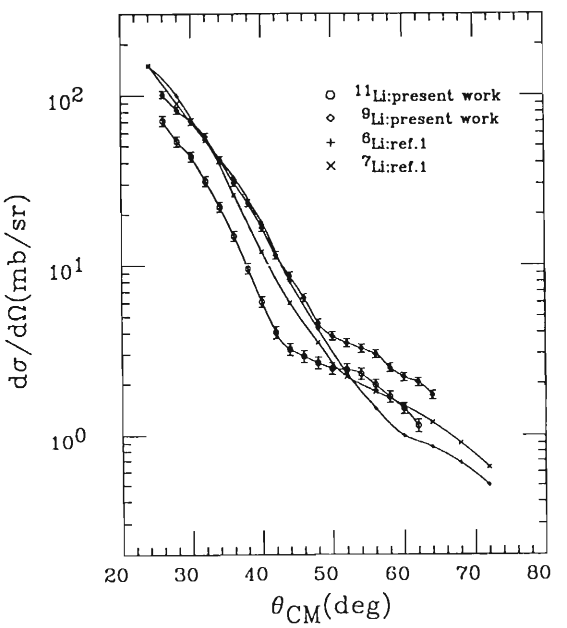


Fig. 1. Measured angular distributions for the $^{9,11}$Li+p system as obtained in the present work. For comparison, $^{6,7}$Li isotopes data are also shown. The solid lines from points to points are only for guiding eye.

On the other hand, a considerable reduction of cross sections in the $^{11}$Li+p system emphasizes the importance of two-neutron break-up in $^{11}$Li.

References

1) M. Tosaki: Ph.D. thesis, Osaka University (1989).

* Supported in part by the Korea Science and Engineering Foundation.
** Department of Physics, Seoul National University, Korea.

RIKEN Accel. Prog. Rep. **25** (1991)

# III-1-30. $E1$ Strength Distribution of $^{11}$Li through Invariant Mass Spectroscopy

S. Shimoura, K. Abe, N. Inabe, M. Ishihara, T. Kobayashi, T. Kubo, T. Nakamura, R.H. Siemssen,* I. Tanihata, and Y. Watanabe

NUCLEAR REACTIONS Heavy-ion collision, Radioactive beam, Coulomb dissociation, Pb ($^{11}$Li, $^{9}$Li+2n) X, $E1$ strength, Soft $E1$ mode.

One of the most interesting subjects of neutron halo nuclei is the $E1$ excitation. Large enhancements of interaction cross sections and two neutron removal cross sections of $^{11}$Li observed on high Z targets[1,2] suggest a notable $E1$ strength in a low excitation energy region of $^{11}$Li. In order to extract the $E1$ strength distribution of $^{11}$Li, we have performed a full exclusive measurement of $^{11}$Li→$^{9}$Li+2n process on a lead target.

Unstable $^{11}$Li beam provided by the RIPS facility at RIKEN irradiates a lead target at 43±3 A MeV. The energy and position at the target were measured by time-of-flight (TOF) of two plastic scintillators and a tracking of multiwire proportional chambers, respectively. Neutrons were measured by five layers of plastic scintillator hodoscopes at 3.5-5.5m distance from the secondary target, each of which consists of 16 scintillators of 6 cm square times 110 cm long. To identify a multi-hit by a cross talk caused by a scattering of a single neutron, the hodoscopes were separated each other by 55 cm.[3] Charged particles ($^{9}$Li) were measured by $\Delta E$ detectors (a Si SSD and a plastic scintillator) and the first layer of the neutron detector for $E$ and TOF. The $\Delta E$ detectors were set around the grazing angle (about 5 degree) away from beam direction in order not to be triggered by non-interacted $^{11}$Li beam.

The excitaion energy of $^{11}$Li is deduced by constructing an invariant mass of all the three particles ($^{9}$Li and 2n). The energy resolution for the excitation energy is less than 0.3 MeV, which is independent of the resolution of the beam. Figure 1 shows the relative energy spectra for $^{9}$Li and two neutrons. The excitation energy spectrum is obtained by shifting threshold energy of $^{11}$Li to $^{9}$Li+2n (300 keV). As shown in the figure, there is a peak around 600 keV corresponding to 0.9 MeV excitation, which is expected as a soft $E1$ mode. The excitation energy of the peak is slightly smaller than that observed in pion double charge exchange reaction $^{11}$B($\pi^-$, $\pi^+$)$^{11}$Li,[4] which may be due to the different reaction dynamics.

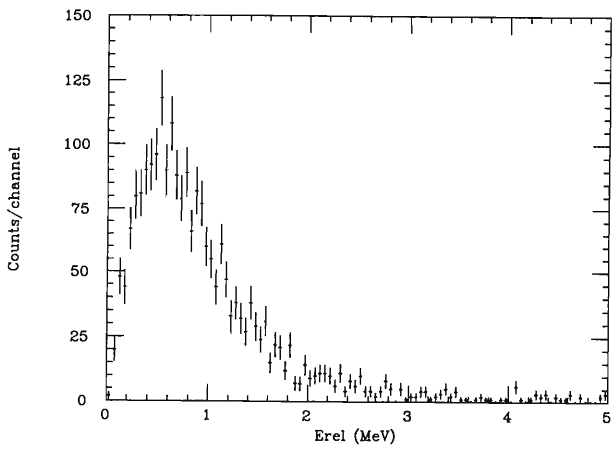


Fig. 1. Relative energy spectrum of $^{9}$Li and two neutrons. Excitation energy is obtained by adding the separation energy of two neutrons from $^{11}$Li (300 keV).

A Monte Calro calculation for the overall detection efficiency, including neutron detection efficiency, is now in progress to deduce the absolute magnitude of the cross section and strength. The correlation between detected neutrons will be investigated in a future analysis.

References

1) T. Kobayashi *et al.*: *Phys. Lett.*, **232B**, 51 (1989).
2) R. Anne *et al.*: *ibid.*, **250B**, 1219 (1990).
3) T. Nakamura *et al.*: *RIKEN Accel. Prog. Rep.*, **24**. 112 (1990).
4) T. Kobayashi *et al.*: LAMPF E1191.

* KVI, Groningen, the Netherland.

RIKEN Accel. Prog. Rep. **25** (1991)

# III-1-31. High Spin Isomers in $^{144}$Pm Observed in the $^{14}$N($^{136}$Xe, 6n) Reaction

T. Murakami, Y. Gono, A. Ferragut, Y. H. Zhang, M. Nakajima, H. Seki, M. Ogawa, B. J. Min, M. Oshima, T. Morikawa, H. Kusakari, K. Morita, A. Yoshida, and H. Kumagai

NUCLEAR REACTIONS $^{14}$N($^{136}$Xe, 6n)$^{144}$Pm, E/A=6.5 MeV; Gas Filled Recoil Ion Separator; Measured $E_\gamma$, $I_\gamma$, $\gamma$-$\gamma$ coin.

The search for high-spin isomers in $^{144}$Pm was carried out using a gas-filled recoil ion separator.[1] An 8.5 MeV/u $^{136}$Xe beam was delivered by RIKEN Ring Cyclotron. Nitrogen gas of 5 Torr, which also served as a target, filled the E1C beam course. The recoil products were separated from the beam and collected on a catcher surrounded by four BGOASC Ge detectors. Transitions originating from isomeric states were exclusively observed in the present setting.

Many new transitions were found above the known $9^+$ state at 841 keV. One of the $\gamma$-$\gamma$ coincidence spectra (gated by 538 keV) is shown in Fig. 1. The excitation function was measured[2] at the Tandem Accelerator Center, University of Tsukuba. The decay scheme shown in Fig. 2 was proposed based on the data, although it was a very preliminary one.

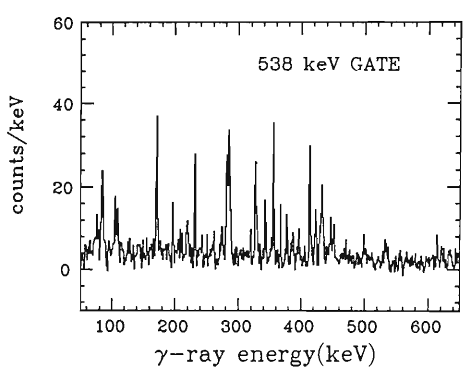


Fig. 1. Gamma-ray spectrum gated by 538 keV transition.

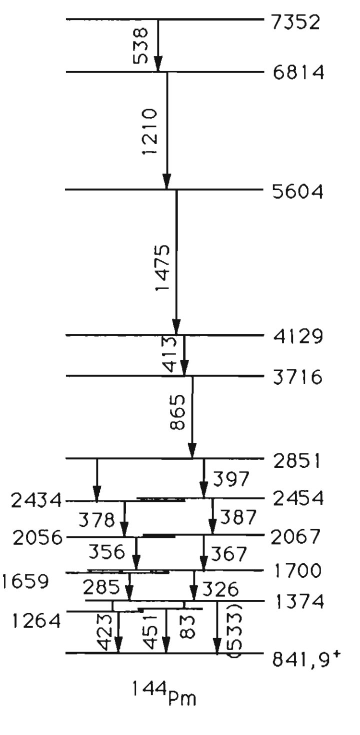


Fig. 2. Proposed decay scheme above the $9^+$ state at 841 keV of $^{144}$Pm.

References

1) Y. Gono *et al.*: *RIKEN Accel. Prog. Rep.*, **24**, 20 (1990).
2) Y. H. Zhang *et al.*: This Report, p. 49.

RIKEN Accel. Prog. Rep. **25** (1991)

# III-1-32. High-Spin States of $^{144}$Pm Studied by $^{138}$Ba($^{10}$B, 4n)$^{144}$Pm Reaction

Y.H. Zhang, T. Murakami, Y. Gono, A. Ferragut, K. Furuno,
T. Komatsubara,* and T. Hayakawa*

NUCLEAR REACTION $^{138}$Ba($^{10}$B, 4n)$^{144}$Pm, $\gamma$-ray excitation function, anisotropy.

In order to determine the location and its corresponding decay scheme of the new isomeric state in $^{144}$Pm,[1] we measured the $\gamma$-ray excitation functions and their anisotropies using $^{138}$Ba($^{10}$B, 4n)$^{144}$Pm reaction at the beam energies from 42.5 MeV to 55 MeV by 2.5 MeV step. The $^{10}$B beam was provided by the tandem accelerator of University of Tsukuba.

The $\gamma$ rays corresponding to the transitions both above and below the first isomeric state ($9^+$) at 841 keV, have been identified in the $\gamma$ energy spectrum and the excitation functions as shown in Fig. 1. The known transitions are indicated by the initial and final spins on the left of each curve.

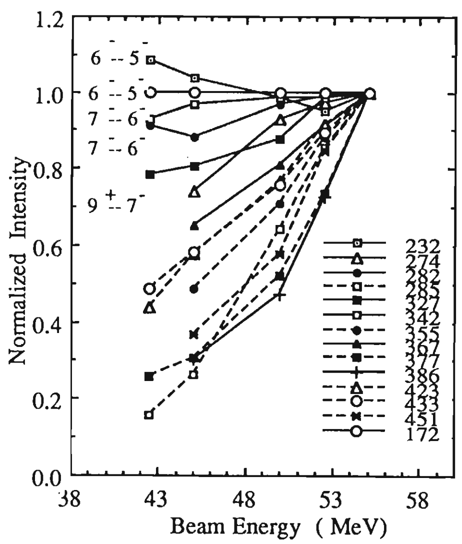


Fig. 1. $\gamma$-ray excitation functions. Intensities are normalized to that of 171.8 keV line.

Table 1. Measured $\gamma$-ray relative intensities and their anisotropies. Intensities are normalized to that of 171.8 keV line.

| E$\gamma$ (keV) | I$\gamma$ rel | W (90°) / W (0 °) |
|---|---|---|
| 232 | 0.95 | 1.18 ± 0.13 |
| 274 | 0.19 | 1.47 ± 0.16 |
| 282 | 0.94 | 1.17 ± 0.12 |
| 285 | 0.29 | 1.30 ± 0.14 |
| 327 | 0.89 | 0.97 ± 0.10 |
| 342 | 0.61 | 1.01 ± 0.15 |
| 355 | 0.36 | 1.31 ± 0.14 |
| 367 | 0.15 | 1.43 ± 0.15 |
| 377 | 0.34 | 0.99 ± 0.11 |
| 386 | 0.08 | 0.96 ± 0.10 |
| 423 | 0.22 | 0.78 ± 0.08 |
| 433 | 1.17 | 0.73 ± 0.08 |
| 451 | 1.15 | 1.27 ± 0.13 |

The relative intensities and anisotropies of these $\gamma$ rays measured with a 50 MeV beam energy are given in Table 1. The anisotropies of the new $\gamma$ rays suggest that they are prompt decays.

The peak at 538 keV, which is the strongest line among the $\gamma$ rays observed in the decay of the new isomeric state,[1] has not been observed in this experiment, that means this isomeric state was not populated in the $^{138}$Ba($^{10}$B, 4n)$^{144}$Pm reaction. The spin of the isomeric state may be understood as higher than 25 $\hbar$.

References

1) T. Murakami *et al.*: This Report, p. 48.

* Tandem Accelerator Laboratory, University of Tsukuba.

RIKEN Accel. Prog. Rep. **25** (1991)

# III-1-33. Coulomb Excitation of Unstable Nucleus Beam

A. Ferragut, T. Murakami, Y. Gono, M. Nakajima, H. Seki, M. Ogawa, B. J. Min, M. Oshima, T. Morikawa, H. Kusakari, K. Morita, A. Yoshida, H. Kumagai, and Y.H. Zhang

[ Coulomb excitation; Unstable nuclei; Gas Filled Recoil Ion Separator; Parallel Plate Avalanche Counter. ]

Coulomb excitation provides information on the nuclear structure through the matrix elements of the electromagnetic operator. These matrix elements can be deduced from the Coulomb excitation cross section measurement.[1]

A Coulomb excitation experiment of the unstable nucleus $^{152}$Dy was performed by using the gas filled recoil ion separator. The nucleus $^{152}$Dy was produced by the $^{24}$Mg($^{136}$Xe, 8n)$^{152}$Dy reaction. The average energy of the recoil nucleus $^{152}$Dy, at the position of the secondary target, was estimated to be 3.9 MeV/A, which is well below the Coulomb barrier between the $^{152}$Dy and the secondary target $^{208}$Pb.

Ions scattered by the lead target were detected by the position sensitive parallel plate avalanche counter (PPAC) to correct the Doppler shift of the $\gamma$-rays emitted in flight. The Doppler shift of the 614 keV $\gamma$-ray emitted by the $2^+ \longrightarrow 0^+$ transition in $^{152}$Dy and the width of the broadening were respectively about 30 keV and 50 keV, as indicated in the figure (the second spectrum from the top).

After a Doppler correction, the $\gamma$-ray peak appears (first spectrum from the top) at the energy of 613 keV which is very close to the energy of the $2^+ \longrightarrow 0^+$ transition of $^{152}$Dy (614 keV). The number of counts in the peak (50 counts) is also comparable to our estimation based on the known life-time of the $2^+$ state of $^{152}$Dy.

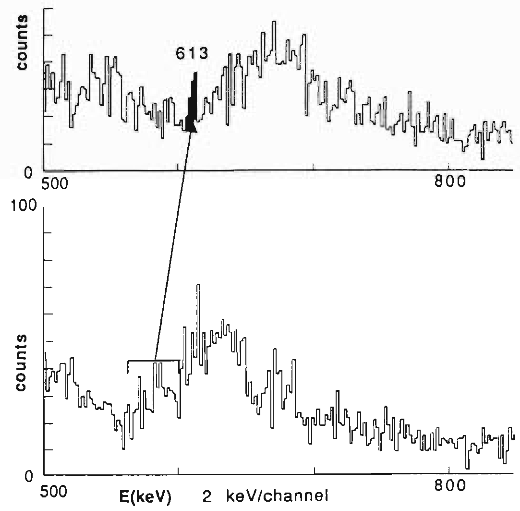


Fig. 1. Prompt gamma ray spectra with background subtraction. Bottom spectrum is the spectrum without correction. Top spectrum is corrected for Doppler shift, event by event.

This result shows that our set-up can be used for further studies of various unstable nuclei. The interesting quantity which can be extracted from this kind of experiment is the quadrupole moments of excited states by measuring the reorientation effect.

References

1) K. Alder and A. Winther: *Coulomb Excitation, Academic Press*, **1,** 82 (1966).

RIKEN Accel. Prog. Rep. **25** (1991)

# III-1-34. Spin Isospin Excitation in the Reaction (d, $^2$He)

Y. Tajima, K. Hatanaka, S. Hayakawa,* M. Hosaka, T. Ichihara, S. Ishida, M. Ishihara, S. Kato, T. Niizeki, H. Ohnuma, M. Ohura, H. Okamura, H. Orihara, H. Sakai, H. Shimizu, H. Toyokawa, Y. Yano, Y. Yashiro, H.Y. Yoshida, and M. Yosoi

〔NUCLEAR REACTION $^6$Li, $^{12}$C, $^{13}$C, $^{23}$Na(d, $^2$He) Ed=260 MeV.〕

Spin-isospin excitation modes of nuclei, Gamow-Teller (GT) transitions in particular, have been studied extensively by (p, n) reactions. The observed GT strengths are consistently below the sum rule limit. This so-called "quenching" of the GT strengths has been the subject of many theoretical and experimental studies. It is currently thought that there are two major origins of the quenching, RPA correlations in nuclei and subnucleon degrees of freedom of constituent nucleons. The GT strengths one measures in (p, n) reactions correspond to those for $\beta^+$ decays. It is necessary, however, to measure GT strengths in the $\beta^-$ counterparts to make a rigorous comparison with the sum rule. Intermediate energy (n, p) reactions are being studied at a few institutes in order to obtain the latter information. Such reactions are not easily done, however. Although spin-flip components are more strongly excited by intermediate energy (n, p) reactions than non-spin-flip components, spin-flip probability measurements are required, in principle, to distinguish the two components. Furthermore, neutron beam intensities are limited at present, and a long beam-time is needed even with thick neutron production targets at the sacrifice of resolution. On the other hand, there are several advantages of using intermediate energy (d, $^2$He) reactions instead. First, the detection of $^2$He, two protons in the relative singlet state, ensures automatically that the reaction goes through spin-flip components. Second, use of the primary beam from an accelerator makes the running time shorter with a possibility of higher-resolution measurement. A major disadvantage of (d, $^2$He) reactions may be the difficulty in measuring two protons emitted in the same direction in coincidence. This difficulty could be overcome by a new detection system SMART[1] at RIKEN ring cyclotron. Another disadvantage lies in the fact that the reaction mechanism of such reactions is not well understood. This could be circumvented if one could establish an empirical relation between the (d, $^2$He) cross sections (at small angles, preferably at 0°) and GT strengths.

We have studied the (d, $^2$He) reactions on $^6$Li, $^{12,13}$C, and $^{23}$Na at $E_d$=260 MeV to investigate the possibility of using (d, $^2$He) reactions as a probe to nuclear spin-isospin excitations. The $\beta$-decay log *ft* values are well known for the ground states of the residual nuclei in these reactions. The targets were 149 mg/cm$^2$ thick metallic $^6$Li, 180 mg/cm$^2$ thick $^{nat}$C, 166 mg/cm$^2$ thick $^{13}$C, and 133 mg/cm$^2$ thick metallic $^{23}$Na. Two sets of position counters, each consisting of four multiwire drift chambers,[2] and two scintillator hodoscopes were placed after the first dipole magnet of SMART, and used to detect two protons in coincidence.[3] Zero degree measurements are crucial in comparison with the $\beta^-$ decay strengths. This was realized by stopping the deuteron beam at an insulated carbon block inside the dipole magnet. The beam stopper was shielded by lead blocks to reduce background. Measurements were also made at 4°, 7°, and 12.5°.

Figure 1 shows a sample $^2$He energy spectrum at 0° for $^{12}$C. This is remarkably similar to those for the $^{12}$C(p, n) reactions. The strongest peak in the spectrum corresponds to the 1$^+$ ground state in $^{12}$N. The peaks around 4.3 MeV and 7 MeV observed in (p, n) reactions were interpreted as 2$^-$ and 1$^-$ spin dipole states. These two peaks become stronger at larger angles.

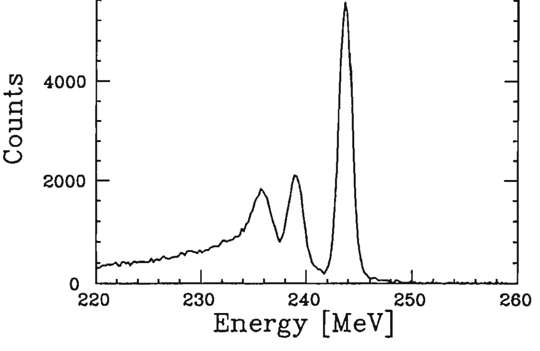


Fig. 1. Energy spectrum of $^2$He at 0° for the $^{12}$C(d, $^2$He) reaction at $E_d$=260 MeV.

* Asikaga Institute of Technology.

Zero-degree cross sections for the ground states of all the nuclei measured are compared

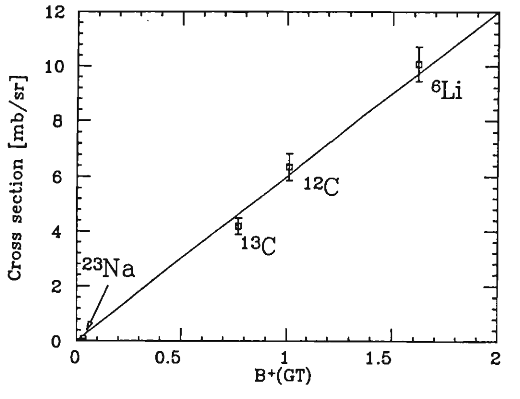


Fig. 2. A comparison between the (d, $^2$He) cross sections at 0° and B(GT). The straight line shows a least-squares fit to the data.

with the $\beta^-$ decay strengths B(GT) calculated from the known log *ft* values (Fig. 2). Cross sections were calculated using effective solid angles of the detection system estimated from Monte Carlo caluclations.[3] A proton relative-energy spectrum is discussed in detail in Ref. 3.

The present data demonstrate the usefulness of the large solid-angle spectrometer system SMART in $^2$He measurement and the applicability of (d, $^2$He) reactions to the study of spin-isospin excitation modes of nuclei.

References

1) H. Ohnuma *et al.*: *RIKEN Accel. Prog. Rep.*, **21**, 164 (1987); **22**, 148 (1988).
2) Y. Yashiro *et al.*: *ibid.*, **23**, 92 (1989).
3) H. Okamura *et al.*: This Report, p. 128.

RIKEN Accel. Prog. Rep. **25** (1991)

# III-1-35. The $^1$H(d,2p)n Reaction as an Analyzer for the Deuteron Tensor Polarimeter at Intermediate Energies

T. Motobayashi, S. Kox,[*1] C. Perrin,[*1] J. Arvieux,[*2] J.P. Bocquet,[*1] B. Bonin,[*3] A. Boudard,[*3] J. Carbonell,[*1] G. Gaillard,[*4] M. Garçon,[*3] L. Ghedira,[*1] G. Guillaume,[*5] J. Guillot,[*6] F. Merchez,[*1] Nguyen Van Sen,[*1] D. Rebreyend,[*1] C. Wilkin,[*7] and J. Yonnet[*2]

NUCLEAR REACTION $^1$H(d,2p)n, $E=200$, 350 MeV; measured $\sigma(\theta)$, $A_y(\theta)$, $A_{xx}(\theta)$, $A_{yy}(\theta)$, PWIA analysis, deduced figure of merit factor for deuteron tensor polarimeter.

A new analyzer reaction for the deuteron tensor polarimeter at intermediate energies should be found, because a polarimeter based on the $^3$He(d, p)$^4$He reaction is feasible only below $E_d \approx$ 40 MeV. The AHEAD polarimeter,[1] using the elastic deuteron-proton scattering, successfully measured tensor polarizations up to $E_d=200$ MeV. However this polarimeter quickly loses the efficiency at higher energies. The charge exchange reaction $^1$H(d, 2p)n is a candidate of the analyzer reaction at these higher deuteron energies, because an impulse approximation model predicts large tensor analyzing powers $T_{20}$, $T_{22}$ (or $A_{xx}$, $A_{yy}$) at the low excitation energy $E_x$ for the final two proton system.[2]

To confirm the above prediction and to check the feasibility of a tensor polarimeter based on the $^1$H(d, 2p)n reaction, the cross section and deuteron tensor analyzing powers $A_{xx}$, $A_{yy}$ have been measured at $E_d=200$[3] and 350MeV.[4] The experiment was performed with polarized deuteron beams delivered by the Laboratoire National Saturne synchrotron.

From the cross sections and tensor analyzing powers obtained, we deduced figures of merit for the polarimeter defined by integrating the square of the analyzing powers times the corresponding cross section,

Table 1. Figures of merit, in units of $10^{-2}$b$^{1/2}$, defined by eq. (1) and determined at $E_d=200$ and 350MeV.

| | | $0 \le E_x \le 1$ MeV | $0 \le E_x \le 4$ MeV | $0 \le E_x \le 8$ MeV |
|---|---|---|---|---|
| 200 MeV | $F_{20}$ | 1.0 | 1.4 | — |
| | $F_{22}$ | 0.7 | 0.9 | — |
| 350 MeV | $F_{20}$ | 0.6 | 0.9 | 1.0 |
| | $F_{22}$ | 0.7 | 1.1 | 1.2 |

$$(F_{\alpha\beta})^2=\int dq^2 dE_x (T_{\alpha\beta})^2 \frac{d^2\sigma}{dq^2 dE_x}. \quad (1)$$

Deduced values for 200 and 350 MeV incident energies are given in Table 1. These are a little smaller than the values $F_{20}=1.8\times10^{-2}$ b$^{1/2}$ and $F_{22}=1.6\times10^{-2}$ b$^{1/2}$ obtained for elastic d-p scattering at 170 MeV, which decreases rather quickly with energy.[1] These results demonstrate that the $^1$H(d, 2p)n reaction can be used to develop a new deuteron tensor polarimeter in the energy range 200-400 MeV. A new device for a real polarimeter is currently under construction.[5]

Another favourable aspect of the (d, 2p) reaction as an analyzer is that reliable interpolation to different energies is possible with the help of theory. The energy dependence of the tensor analyzing power for low $E_x$ at 0° is displayed in Fig. 1 in a wide energy range from $E_d=50$ MeV to 2 GeV. The data at 56 and 70 MeV are taken from Ref. 6 and the one at 2 GeV from Ref 7. Note that at 0°, $T_{22}=0$ and $A_{xx}=A_{yy}=-\sqrt{1/2}\,T_{20}$. The transverse spin transfer coefficients $K_y^y$ of the $^2$H(p, n)2p reaction[8] are converted to the $A_{yy}$ of the $^1$H(d, 2p)n reaction with the help of the relation,[2]

$$2A_{yy}+3K_y^y=-1 \quad (2)$$

As seen in the figure, the prediction of the

*1 Institut des Sciences Nucléaires, IN2P3-UJF, F-38026 Grenoble Cedex, France.
*2 Laboratoire National Saturne, F-91191 Gif-sur-Yvette, France.
*3 SEPN-Saclay, F-91191 Gif-sur-Yvette, France.
*4 DPNC, Université de Genève, CH-1211 Genève 4, Switzerland.
*5 Centre de Recherches Nucléaires, F-67037 Strasbourg, France.
*6 Institut de Physique Nucléaires, F-91406, Orsay Cedex. France.
*7 University College London, Gower St., London WC1E 6 BT, U.K.

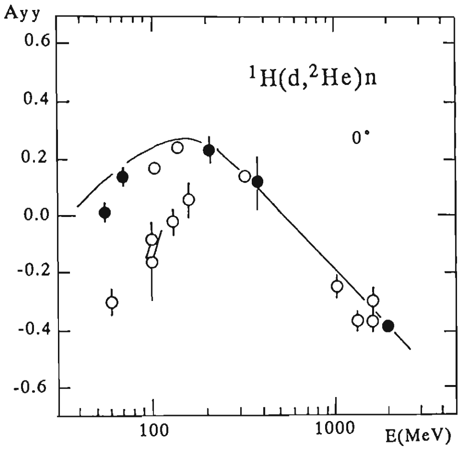


Fig. 1. Tensor analyzing power $A_{yy}$ at 0°. Open circles represent the results of the $^1$H(d, 2p)n reaction and closed ones the values converted from the $K_y^y$ values of the $^2$H(p, n)2p reaction (see in the text). Solid curve represents the prediction with the impulse approximation prediction.

impulse approximation model reproduces well the data for the entire energy range except for several low energy (p, n) reaction data. One possible explanation for this discrepancy is that these data were measured with poor energy resolution and hence with a possible admixture of the P-wave for the final two proton state, whereas the relation (2) is only valid for the singlet final state.

References

1) J.M. Cameron *et al.*: submitted to *Nucl. Instrum. Methods*.
2) D.V. Bugg and C. Wilkin: *Phys. Lett.*, **B152**, 37 (1985); D.V. Bugg and C. Wilkin: *Nucl. Phys.*, **A467**, 575 (1987).
3) T. Motobayashi *et al.*: *Phys. Lett.*, **B233**, 69 (1989); T. Motobayashi *et al.*: *RIKEN Accel. Prog. Rep.*, **24**, 13 (1990).
4) S. Kox *et al.*: *Phys. Lett.*, **B266**, 264 (1991).
5) S. Kox *et al.*: Mise au point d'un polarimètre tensoriel à deuytons dans le domaine d'énergie $E_d$=200 à 400 MeV, L.N.S. proposal 235 (1990), unpublished.
6) T. Motobayashi *et al.*: *Nucl. Phys.*, **A481**, 207 (1988).
7) C. Ellegaard *et al.*: *Phys. Rev. Lett.*, **59**, 974 (1987).
8) see references in Ref. 6.

RIKEN Accel. Prog. Rep. **25** (1991)

# III-1-36. Pion Absorption at 1 GeV/c

I. Nomura, I. Arai,*[1] T. Fukuda, H. Kitayama,*[1] P. Kitching,*[2]
T. Kobayashi, K. Maeda, H. Matsuyama,*[3] T. Nagae,*[4] Y. Nagasaka,*[1]
M.A. Prokhvatilov,*[5] V.I. Rasin,*[5] D. Rowntree,*[6] M. Sekimoto,*[4]
T. Suda, K. Tomizawa,*[1] S. Ueno,*[1] and K. Waki*[1]

NUCLEAR REACTION $^4$He, $^{12}$C($\pi^+$,pp), ($\pi^+$,pn), $P_\pi$ = 1 GeV/c, pion absorption.

The first experiments concerning the pion absorption in the GeV region have been performed. Both the ($\pi^+$, pp) and ($\pi^+$, pn) modes were measured at 1 GeV/c on $^4$He and $^{12}$C, and the isospin dependence of the two-nucleon absorption cross sections was obtained.

The experiments have been done with the 12 GeV Proton Synchrotron at National Laboratory for High Energy Physics (KEK). According to the kinematical condition of the two-body absorption, a magnetic spectrometer was set in the forward angles (5～40°) to detect the higher-momentum protons, and TOF walls were set in the backward angles (80～175°) to detect lower-momentum protons or neutrons. The forward protons were identified from the momentum and TOF in the spectrometer (Fig. 1), and two-nucleon absorption events which satisfy the kinematical condition were clearly observed (Fig. 2). Figure 3 shows preliminary results of the angular dependence of ($\pi^+$, pp) cross sections for $^4$He and $^{12}$C targets, with reference to the deuteron data.[1)] Tentative values of the angle-integrated cross sections for ($\pi^+$, pp) on $^4$He and $^{12}$C give $(6.8\pm1.2)\times10^2\,\mu$b and $(1.3\pm0.3)\times10^3\,\mu$b, respectively, while for deuteron it is 79 $\mu$b.

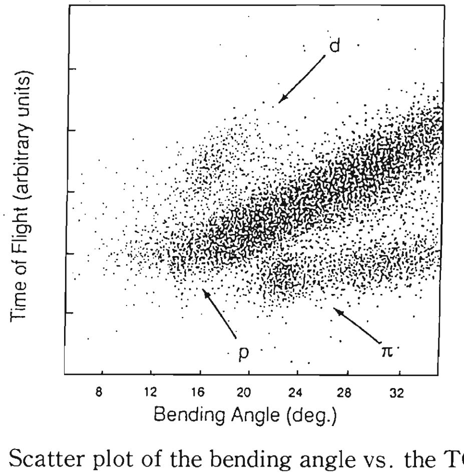


Fig. 1. Scatter plot of the bending angle vs. the TOF for forward-moving particles.

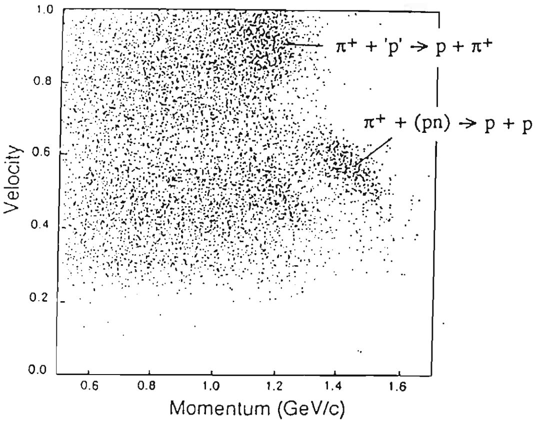


Fig. 2. Scatter plot of the momentum of forward protons vs. the velocity of backward particles. $\theta_{forward}$ = 15-18°.

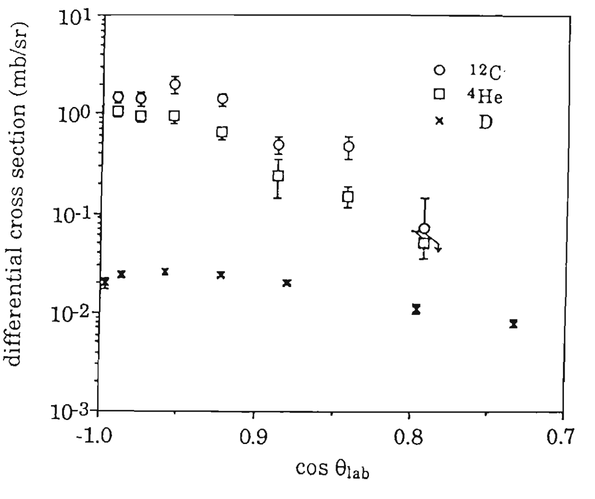


Fig. 3. Angular dependence of the ($\pi^+$, pp) events on $^4$He and $^{12}$C targets.

*[1] Institute of Physics, University of Tsukuba.
*[2] Nuclear Research Center, University of Alberta, TRIUMF and Institute for Nuclear Study, University of Tokyo (INS).
*[3] Laboratory of Nuclear Science, Tohoku University.
*[4] INS.
*[5] Institute for Nuclear Research, Academy of Science (INR) and INS.
*[6] Department of Physics and laboratory for Nuclear Science, Massachusetts Institute of Technology (MIT).

The yield of ($\pi^+$, pp) is presented with the absorption cross section on the pair with the initial isospin of T and Tz, as below,[2]

$$\sigma\ (\pi^+,\ \mathrm{pp}) = <1110 \mid 11>^2\ N_{1,0}\ \sigma_1 + <1100 \mid 11>^2\ N_{0,0}\ \sigma_0$$

where $N_{ij}$ and $\sigma_i$ denote the number of nucleon pair in nuclei with isospin T = i (i = 1,0) and $T_z$=j (j = −1,0), and the absorption cross section on that pair, respectively. Using this expression the ratio of the cross section for $^4$He to that for deuteron leads to the isospin ratio $\sigma_1$ to $\sigma_0$.

$$\sigma_1/\sigma_0 = 2R - 6 : R = \sigma(\,^4\mathrm{He}(\pi^+,\ \mathrm{pp}))/\sigma(\,\mathrm{D}(\pi^+,\ \mathrm{pp}\,))$$

A preliminary ratio $\sigma_1/\sigma_0$ is about 11. This result suggests a relatively large contribution of the T=1 pair absorption($\sigma_1$) to that of T=0 ($\sigma_0$) in the GeV region.

References

1) M. Akemoto *et al*.: *Phys. Lett.*, **149B**, 321 (1984).
2) D. Ashery and J.P. Schiffer: *Ann. Rev. Nucl. Sci.*, **36**, 207 (1986); H.J. Weyer: *Phys. Rep.*, **195**, 295 (1990).

RIKEN Accel. Prog. Rep. **25** (1991)

# III-1-37. Surface Muon Production in Reactions of $^{14}N$ at 135A MeV and of $^{40}Ar$ at 95A MeV with Various Target Nuclei

K. Ishida, T. Matsuzaki, R. Kadono, A. Matsushita, and K. Nagamine

NUCLEAR REACTION, Be,C,$CF_2$,Al,Ti,Cu,Ag,Ta,W ($^{14}N$, $\pi^+$),E($^{14}N$) =135A MeV, Be,C,Al,Ti,Cu,Mo,Ag,Ta,W ($^{40}Ar$, $\pi^+$),E($^{40}Ar$) =95A MeV, Measured Surface Muon Yield.

Surface muons are produced when pions produced in nuclear reactions are stopped near the surface skin of a production target. The probability that a produced pion is converted into a surface muon was calculated by a Monte-Carlo method and the result is shown in Fig. 1 as a function of the pion energy. It is shown that the surface muon yield is very sensitive to the low-energy part of the pion energy spectrum.

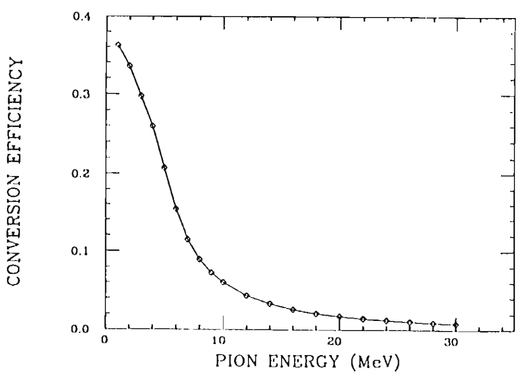


Fig. 1. Efficiency for the pions to be converted to surface muons as a function of the pion energy in a graphite target of 225 mg/cm$^2$ thickness. Pion emission angle was assumed to be isotropic.

We have already reported the measurement of the surface muon yields for $^{14}N$ at 135A MeV and with various target elements.[1] The result has indicated a strong suppression of low-energy pion yields for heavy target nuclei. The suppression was attributed either to the final pion energy shift by the Coulomb interaction or to the pion reabsorption. In that report, the Coulomb shift calculated was not strong enough to explain the observed suppression since only the hot spot of the fire-ball model was taken into acount as a Coulomb source. However, the Coulomb effect might become sufficiently large if all the reaction fragments are included in the calculation, since the fragments might not be so far away at the time of pion emission. These models might be selected if the size of the projectile nucleus is changed, for example, from N to Ar, since the hot spot size would be much larger for Ar projectiles, while the total charge is less dependent on the projectile size.

Thus we have carried out an experiment to measure the surface muon production rate for $^{40}Ar$ beams at 95A MeV from RRC. Preliminary analyzed data as well as the data for $^{14}N$ are shown in Fig. 2, which indicates that the target dependence of the low-energy pion yields is almost the same for the two incident nuclei and seems to favor the latter model. Detailed analysis is now in progress.

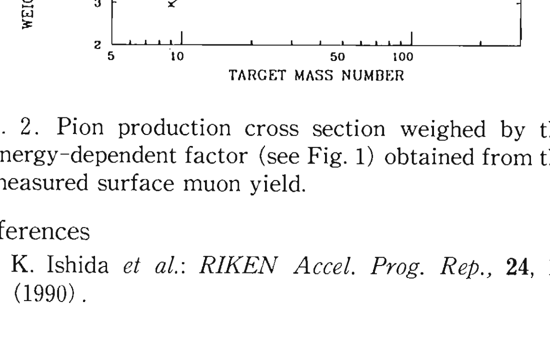


Fig. 2. Pion production cross section weighed by the energy-dependent factor (see Fig. 1) obtained from the measured surface muon yield.

References

1) K. Ishida *et al.*: *RIKEN Accel. Prog. Rep.*, **24**, 16 (1990).

RIKEN Accel. Prog. Rep. **25** (1991)

# III-2. Atomic and Solid-State Physics

## 1. Higher Differential Cross Sections for Ionization of Helium by Proton Impact

H. Fukuda, I. Shimamura, L. Végh,* and T. Watanabe**

The p-He collision is a prototype suitable for detailed studies of dynamics of ionization by comparing experiments with theories. Thus, this system is the subject of some recent papers on new aspects of differential ionization cross sections. We have applied to this system an eikonal distorted-wave approximation (EDWA) that accounts for the distortion of the proton motion from the plane wave due to the interaction with He; the eikonal approximation is used for the distorted waves in the distorted-wave Born approximation. The following summarizes the work published elsewhere.[1,2]

The deflection angle ($\theta_p$) of the protons (with a mass $m_p$) in high-energy ($E$) large-distance collisions is determined by the net effect of the perturbation interactions with the He nucleus and the electrons. The $\theta_p$ in intermediate-distance collisions is determined mainly by the binary collisions with the electrons (with a mass $m_e$). The largest possible angle of deflection of a proton by a stationary *free* electron is $m_e/m_p = 0.545$ mrad in the laboratory frame. At this angle the $\theta_p$ distributions measured for the p-He collisions show a shoulder at high $E$. This has been interpreted to be due to efficient binary collisions between the protons and the quasi-free electrons in He for $\theta_p < 0.545$ mrad, and to the absence of these collisions above 0.545 mrad.

The $\theta_p$ distributions, calculated in the EDWA for energies above 300 keV, agree well with experimental results; the agreement is substantially better than in the case of the plane-wave Born approximation (PWBA) especially for $\theta_p > 0.545$ mrad. After confirmation of this fact, higher differential cross sections with respect to both the scattered protons and the ejected electrons are calculated in detail. This clarifies, in particular, the momentum distributions of electrons contributing to the shoulder in the $\theta_p$ distributions. The momentum and angular distributions of the recoil $He^+$ ions at fixed values of $\theta_p$ are also compared with recent coincidence measurements. For extremely small $\theta_p$ for which the PWBA and the EDWA are known to be reliable and produce results in agreement with each other, these approximations lead to average momenta of $He^+$ significantly lower than the measured values. The reason is still unknown at this stage.

References

1) H. Fukuda, I. Shimamura, L. Végh, and T. Watanabe: *Phys. Rev.*, **A44**, 1565 (1991).
2) H. Fukuda, T. Watanabe, I. Shimamura, and L. Végh: *Nucl. Instrum. Methods,* **B53**, 410 (1991).

* ATOMKI, Debrecen, Hungary.
** Department of Physics, International Christian University.

RIKEN Accel. Prog. Rep. **25** (1991)

# III-2-2. Photoionization of Two Electrons in Helium

T. Ishihara,* K. Hino, and J. McGuire**

Photoionization of two electrons in helium is one of the simplest processes in atomic collisions in which the electron-electron interaction is reqiured. Without the electron-electron interaction the photon would have to interact with both target electrons for the double ionization to occur, and this is unlikely. When the photon energy, $E_\gamma$, is much larger than the target ionization potential, at least one of the outgoing electrons leaves the target region relatively fast. Thus the effects of the electron-electron interaction in the final state are expected to be weak. In this report,[1] we present the results of calculations for such a system by using the many-body perturbation theory (MBPT) in lowest-order. The details of the MBPT method employed are described elsewhere.[2] Furthermore, we compare the results with a recent measurement by Levin *et al.*[3] They have observed the ratio, $R_\gamma=\sigma^{++}/\sigma^{+}$, of the double to single ionization cross section at $E_\gamma=2.8$keV using the syncrotron radiation to obtain the result of $1.6\pm0.3\%$.

Amplitudes included in our calculation of the double ionization consist of the ground-state correlation (GSC), shake-off (SO), and two-step 1 (TS1) contributions. The TS1 amplitude corresponds to absorption of a photon by one electron which then hits the other electron on the way out of the target. Ratios of double to single ionization cross sections are shown in Fig .1 as functions of the photon energy. The destructive interefrence between the TS1 and GSC in our results is evident. Our results lie below the experimental data by Carlson,[4] Schmidt *et al.*,[5] and Hollard *et al.*[6] at lower photon energies because of the lack of higher-order correlations. At $E_\gamma=2.8$keV, our value is in agreement with the recent observation of $R_\gamma=1.6\pm0.3\%$ by Levin *et al.*[3]

To conclude, the effect of electron-electron interaction both before and after the photon absorption (*i.e.* GSC and TS1 amplitudes) is substaintial even in the high energy photon region. This fact suggests the essential roles of the electron-electron interaction in the double continuum state of helium as well as in the ground state. Furthermore, although $R_\gamma$ is approximately independent of $E_\gamma$ at a large photon energy in our MBPT calculations, no single mechanism dominates $R_\gamma$. Then the concept of simple SO, for example, is not valid. At least the three amplitudes contribute to the double ionization cross section.

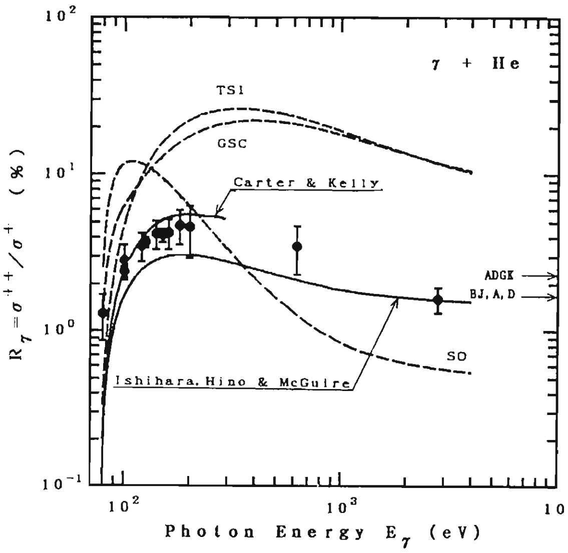


Fig. 1. Ratios, $R_\gamma$, of single to double ionization cross sections versus photon energy, $E_\gamma$. Results of other MBPT calculations of Carter and Kelly are taken from Reference 2. The arrows on the right side give the non -relativistic high energy dipole limits obtained by Byron and Joachain (BJ),[7] Åberg (A),[8] and Dalgarno *et al* (D),[9] who all omit the TS1 contribution; and Amusia *et al.* (ADGK).[10]

References

1) T. Ishihara, K. Hino, and J. McGuire: *Phys. Rev.*, **A44**, R6980 (1991).
2) S.L. Carter and H.P. Kelly: *ibid.*, **A24**, 170 (1981).
3) J.C. Levin, D.W. Lindle, N. Keller, R.D. Miller, Y. Azuma, N. Berrah Mansour, H.G. Berry, and I.A. Sellin: *Phys. Rev. Lett.*, **67**, 968 (1991).
4) T.A. Carlson: *Phys. Rev.*, **156**, 142 (1967).
5) V.A. Schmidt, N. Sander, H. Kuntzemuller, P. Dhez, F. Wuilleumier, and E. Kallne: *ibid.*, **A13**, 1748 (1976).
6) D.M.P. Hollard, K. Codling, J.B. West, and G.V. Marr: *J. Phys.*, **B12**, 2465 (1979).
7) F.W. Byron and C.J. Joachain: *Phys. Rev.*, **164**, 1 (1967).
8) T. Åberg: *ibid.*, **A2**, 1726 (1970).
9) A. Dalgarno and R.W. Ewart: *Proc. Phys. Soc.*, **80**, 616 (1962).
10) M. Ya Amusia, E.G. Drukarev, V.G. Gorshkov, and M. Kazachkov: *J. Phys.*, **B8**, 1248 (1975).

* Institute of Applied Physics, University of Tsukuba.
** Department of Physics, Tulane University, New Orleans, U.S.A.

RIKEN Accel. Prog. Rep. **25** (1991)

# III-2-3. Systematic Theoretical Study of the Thomas Double Scatterings

N. Toshima

The mechanism of the Thomas double-scattering process[1] has been one of the long-standing subjects in the physics of ion-atom collisions. Following the pioneering study of Drisko,[2] many theoretical methods based on the perturbation theory have been proposed and applied to the analysis of this process. Though a precise calculation of the second-order terms has become practically possible owing to the progress of high-speed computers, the success of the measurements of the Thomas peak for proton-helium[3] and for proton-hydrogen[4] collisions have urged the necessity of more elaborate theoretical investigations. Non-perturbative theoretical studies of the Thomas process have been realized recently by the coupled-channel method[5] and by the classical-trajectory Monte Carlo (CTMC) method.[6] In this report, we present brief results of advanced calculations of these two approaches and of exact calculations of the second Born approximation.

The coupled-channel method is a quantum mechanical approach in which all the electronic wave functions including very-high-lying continuum states are expanded by the Gauss-type orbitals. In the first report,[5] only $s$-orbitals ($l=0$) were used for the expansion. Though satisfactory agreement with experimental data was achieved, the contribution of higher-angular-momentum states as intermediate states has been still unsettled. In the present calculations, we have added $p$ ($l=1$) and $d$ ($l=2$) orbitals to the expansion. It is confirmed that the contribution of the higher partial waves is not significant though the agreement with the experiments is improved further.

In the classical treatment,[6] only two-dimensional collisions were studied. The probability of the Thomas process is extremely small and we need a huge number of trajectories for the statistical convergence. Even in this restricted case, only 82 events lead to the charge exchange out of total 109 million trajectories. While this calculation is useful for studying how the trajectories are deformed from the idealized picture of the Thomas process in close encounters, the two-dimensional treatment does not give any information concerning the interesting quantities such as differential cross sections. We have analyzed the trajectories that lead to the charge exchange from the two-dimensional calculations and learned that the charge exchange occurs under some restricted conditions when the projectile energy is high. Utilizing this knowledge we have succeeded in reducing the number of trajectories for solving equations of motion to make the calculations practically feasible . The obtained differential cross section for a proton-hydrogen collision at 5 MeV does not show a peak at the critical angle 0.47 mrad at variance with the experimental data and the quantal calculations. This unexpected result is caused by the peculiarity of classical bound states that have no minimum binding energy.

The other approach is the exact calculation of the second Born cross sections. Although there have been published a great deal of perturbative studies, most of them have recourse to further approximations for the evaluation of the matrix elements. These secondary approximations bring about errors that are difficult to assess. Occasionally an easy usage of a peaking approximation changes even the intrinsic character of the theory completely. We have evaluated the second Born amplitudes for the charge exchange rigorously for proton-hydrogen collisions at 1, 2.8 and 5 MeV and for proton-helium collisions at 2.82, 5.42, and 7.4 MeV for the first time.

Extensive comparison and detailed analysis of these calculations are now in progress.

References

1) L. H. Thomas: *Proc. Roy. Soc. London*, **114**, 561 (1927).
2) R. M. Drisko: thesis, Carnegie Institute of Technology (1955).
3) E. Horsdal-Pedersen, C.L. Cocke, and M. Stockli : *Phys. Rev. Lett.*, **50**, 1919 (1983).
4) H. Vogt, R. Schuch, E. Justiniano, M. Schultz, and W. Schwab: *ibid.*, **57**, 2256 (1986).
5) N. Toshima and J. Eichler: *ibid.*, **66**, 1050 (1991).
6) N. Toshima: *Phys. Rev.*, **A42**, 5739 (1990).

RIKEN Accel. Prog. Rep. **25** (1991)

# III-2-4. Muon Transfer Reaction $t+d\mu(1s)\rightarrow t\mu(1s)+d$

H. Fukuda and I. Shimamura

Introduction of muons into the $D_2/T_2$ mixture is the first step in the muon-catalyzed d-t fusion. After slowing down, the muons are captured by a deuteron d or a triton t and form $d\mu$ or $t\mu$ in excited states. These hydrogenlike atoms cascade down to lower levels, and eventually to the ground state. They penetrate through the electron cloud of $D_2$ or $T_2$ and collide with another d or t. Then the muon bound to d may be transferred to t. This process affects considerably the number ratio of the $d\mu$ atoms to the $t\mu$ atoms, and hence, the d-t fusion cycle catalyzed by muons.

Several different theoretical methods have been applied to the transfer of muons from the 1s state of $d\mu$ to the 1s state of $t\mu$, the latter state lying below the former by 48 eV. These methods yield results in fair agreement with each other.

Recently, possible importance of the muon transfer from d to t in excited states, because of its huge cross section, has been pointed out.[1] We intend to calculate these excited-state transfer processes. Since these processes are much harder to treat by fully quantum-mechanical methods than the 1s-state transfer processes, we have developed new methods that are accurate and convenient for applications. We have applied these methods to the easier 1s-state transfer processes to examine their validity.

Our first method is basically the two-state molecular-orbital (MO) expansion method in which the $1s\sigma_g$ and $2p\sigma_u$ MOs are coupled. In the ordinary MO expansion method, however, the MOs approach incorrect separated-atom limits. Our remedy is to reconstruct the basis by taking linear combinations of the two MOs with appropriate choices of the reduced masses for reproducing the correct separated-atom limits.

Although the asymptotic energies are corrected, this method has its own drawback. A method that is completely correct in the asymptotic region is to make an atomic-orbital (AO) expansion using the Jacobi coordinates. Since this expansion is inefficient at short distances, we switch from the AO method to the MO method at some point. This is referred to as the AO-MO switching method.

At a collision energy of 0.01 eV, the cross section for the vanishing total angular momentum is determined to be $1.24\times10^{-20}$ cm$^2$ by either method employed. For similar processes of p-to-d and p-to-t transfer, the cross sections are $2.43\times10^{-18}$ cm$^2$ and $1.19\times10^{-18}$ cm$^2$. These values are in good agreement with published data calculated by different theoretical methods.[2,3]

References

1) L.I. Menshikov and L. I. Ponomarev: *Z. Phys.*, **D2**, 1 (1986).
2) K. Kobayashi, T. Ishihara, and N. Toshima: *Muon Catalyzed Fusion,* **2**, 191 (1988).
3) M. Kamimura: *ibid.*, **3**, 335 (1988).

RIKEN Accel. Prog. Rep. **25** (1991)

# III-2-5. Energy Shift in the Molecule $[(dt\mu)^+\text{-}d^+]e^-e^-$ Due to the Finite Size of the Muonic Molecular Ion $(dt\mu)^+$

M.R. Harston, I. Shimamura, and M. Kamimura

A key step in the muon-catalyzed fusion in $D_2$/$T_2$ mixtures is the formation of the system $[(dt\mu)^+\text{-}d^+]e^-e^-$, which may be viewed as a $D_2$ molecule with one of the $d^+$ nuclei replaced by a small subsystem, i.e., a muonic molecule $(dt\mu)^+$. This subsystem is formed mostly in an excited state $(dt\mu)^+_{11}$ with a unit total angular momentum and a unit vibrational quantum. The calculated formation rate is sensitive to the molecular binding energy; an accuracy higher than 1 meV is needed. The nonrelativistic energy of the isolated $(dt\mu)^+_{11}$ was calculated accurately to be 660.2 meV.[1,2] It was corrected for relativistic, hyperfine, finite-nuclear-size, vacuum-polarization, and other effects.

Since $dt\mu$ is embedded in a $D_2$-like molecule, it is perturbed by two electrons and a deuteron. Recently the present[3] and other authors[4] have calculated the energy shift in $(dt\mu)^+_{11}$ due to $e^-$ in $[(dt\mu)^+_{11}]e^-$. It has been customary to estimate the shift in $[(dt\mu)^+_{11}\text{-}d^+]e^-e^-$ by scaling the result for $[(dt\mu)^+_{11}]e^-$ by the ratio of the electron density at $d^+$ in $D_2$ to that at $d^+$ in D. The result ranges from 0.3 to 0.6 meV. Here we report energy shifts in $[(dt\mu)^+_{11}\text{-}d^+]e^-e^-$ calculated to first order in the perturbation.[5] The aim of this work is to analyze the differences between the energy shifts in $[(dt\mu)^+_{11}\text{-}d^+]e^-e^-$ and $[(dt\mu)^+_{11}]e^-$, and thereby to examine the validity of the scaling procedure.

We choose a zeroth-order system that consists of the isolated $(dt\mu)^+$ and a $D_2$-like molecule with a nucleus whose mass is the sum of the masses of d, t, and $\mu$. The first-order perturbation energy $\Delta E$ has two parts, namely, one due to the interaction $V(2e\text{-}dt\mu)$ of the two electrons with the extended $dt\mu$ charge distribution, and the other due to the interaction $V(d\text{-}dt\mu)$ of the second d with this charge distribution. The monopole part of $V(2e\text{-}dt\mu)$ leads to $\Delta E$ of 25.79 meV, which is close to the monopole shift in $[(dt\mu)^+_{11}]e^-$ scaled by the electron-density ratio as in previous work.[3,4] The monopole part of $V(d\text{-}dt\mu)$ leads to $\Delta E$ of 0.016 meV and is negligible. The dipole parts contribute nothing due to the symmetry. The quadrupole parts, however, yield energy shifts of the order of meV. They partly cancel each other, but give a net value still as large as 1 to 2 meV, depending on the angular-momentum state. These quadrupole $\Delta E$ are absent in $[(dt\mu)^+_{11}]e^-$ and do not scale in proportion to the electron density in the region of $(dt\mu)^+_{11}$.

References

1) S.A. Alexander and H.J. Monkhorst: *Phys. Rev.*, **A38**, 26 (1988).
2) M. Kamimura: *ibid.*, p. 621.
3) M.R. Harston, I. Shimamura, and M. Kamimura: *Zeit. Phys.*, in press.
4) A. Scrinzi and K. Szalewicz: *Phys. Rev.*, **A39**, 4983 (1989).
5) M.R. Harston, I. Shimamura, and M. Kamimura: *ibid.*, in press.

RIKEN Accel. Prog. Rep. **25** (1991)

# III-2-6. Auger-Electron Due to the de-Excitation of $[(dt\mu)_{11}dee]$

S. Hara

When muons ($\mu$) are injected into a mixture of $T_2$ and $D_2$ molecules, the loosely bound $(dt\mu)_{11}$ molecular ion with the total angular momentum $J=1$ and vibrational quantum number $\nu=1$ is formed as a part of the $[(dt\mu)dee]$ molecule. The metastable state $[(dt\mu)_{11}dee]$ decays in several ways. The molecular ion $(dt\mu)_{11}$ may be de-excited by an Auger auto-ionization process where the excitation energy is partly carried away by an auto-ionized molecular electron. This brings about the change of the $(dt\mu)$ ion into the $(J, \nu)=(0, 1)$ and $(0, 0)$ states.

$$[(dt\mu)_{11}dee] \longrightarrow [(dt\mu)_{01}de]^{+}+e \qquad (1)$$

This process is important since the fusion of d and t in the $(dt\mu)$ ion occurs mainly in the $J=0$ states because there is no centrifugal potential between the two nuclei.

Several calculations[1-4] have been carried out on the transition rate of the process (1). The rate $\lambda$ can be written as follows;

$$\lambda=2\pi/\hbar\Sigma\,|\langle\Phi_{11}\,|\,V_{\mu}\,|\,\Phi_{01}\rangle|^2 \times |\langle\Psi_{i}\,|\,V_e\,|\,\Psi_f\rangle|^2 \qquad (2)$$

where $\Phi$ and $\Psi$ are the wave functions for $dt\mu$ and the molecule "$D_2$", respectively, and $V_\mu$ and $V_e$, the dipole-type operators for $dt\mu$ and molecular electrons, respectively. The above-mentioned calculations have been made by using various wave functions including very accurate one[3] to evaluate the transition matrix elements between the $(dt\mu)_{11}$ and $(dt\mu)_{01}$ states. Nevertheless, the initial molecular wave function $\Psi_i$ for "$D_2$" and the final molecular wave function $\Psi_f$ for "$D_2^{+}+e$" have been represented by fairly poor approximations, e.g., by the ground state hydrogen wave function for $\Psi_i$ and by the Coulomb wave function for $\Psi_f$.

Here, a calculation is performed to evaluate reliable value for the molecular matrix element $\langle\Psi_i\,|\,V_e\,|\,\Psi_f\rangle$, taking account of the molecular property of the whole system. That is, the CI wave function[5] of $D_2$ which includes 91% of correlation energy is adopted for the initial electronic state and the final electronic state is obtained by the two-centre static exchange approximation.[5] The rotational and vibrational structure of the whole system is properly taken into account in the frame of adiabatic nuclei approximation. The present results are compared with those of previous calculations in Table 1.

Table 1. Contributions to transition rate (in $10^{11}$/sec) from various symmetries of the system.

| | present | Ref. 1) | Ref. 2) | Ref. 3) | Ref. 4) |
|---|---|---|---|---|---|
| $\Sigma_u$ | 1.04 | | | | |
| $\Pi_u$ | 3.72 | | | | |
| $\Sigma_u+\Pi_u$ | 4.77 | 11.4 | 6.44 | | 6.00 |
| $\Sigma_g$ | 4.40 | | | | |
| $\Pi_g$ | 0.76 | | | | |
| Total | 9.93 | | | 10.20 | |

The author is grateful to Dr. E. Armour of Nottingham University for useful discussions.

References

1) L.N. Bogdanova *et al.*: *Sov. Phys. JETP*, **56**, 931 (1982).
2) A.K. Bhatia and R. J. Drachman: *Phys. Rev. A*, **38**, 3400 (1988).
3) A. Scrinzi and K. Szalewicz: *ibid.*, **39**, 2855 (1989).
4) E. G. Armour and D. M. Lewis: *J. Phys. B: Atom. Molec. Phys.*, **23**, L25 (1990).
5) S Hara *et al.*: *ibid.*, **19**, 1177 (1986).

RIKEN Accel. Prog. Rep. **25** (1991)

# III-2-7. Metastable States of Antiprotonic and Mesic Helium Atoms

I. Shimamura

When massive, negatively charged particles, such as antiprotons ($\bar{p}$), kaons ($K^-$), pions ($\pi^-$), and muons ($\mu^-$), impinge on matter, they slow down as they excite and ionize the atoms or molecules in the matter, and are eventually captured into bound states of exotic atoms. The negatively charged particles, say $X^-$, are generally considered to occupy, immediately after the capture, Rydberg orbitals having a high principal quantum number and spanning roughly the same spatial extent as the valence electrons.[1] The correlation between $X^-$ and the valence electrons must be strong, and therefore an atomic description of this exotic atom would require configuration mixing and would afford no simple independent-particle picture. If, however, it is regarded as a polar molecule with two nuclei, the vibrational motion, or the $X^-$ motion, is separable from the electronic motion in a good approximation. This idea has been applied to exotic helium in this work.

The exotic helium consists of $X^-$, an electron, and an alpha particle. The Born-Oppenheimer separation reduces the three-body problem to separate, solvable one-dimensional equations for the electronic and rotational-vibrational motions, from which unified, transparent physical pictures of these states for different particles $X^-$ are extracted. For example, an inspection of the molecular potential energy curves as functions of the alpha-$X^-$ distance gives an idea of the $X^-$ motion, and tells why the decay by the emission of an Auger electron has a low probability. The isotope effect may be discussed also on the basis of the potential energy curves. An estimation of the radiative transition intensity is provided by the inspection of the molecular dipole-moment function and the vibrational wave functions, just like the infrared absorption by the usual molecules; detailed calculations reveal that the radiative lifetimes are long, i.e., of the order of $\mu$sec for antiprotonic helium, for example. This is consistent with the recent experiments in which metastable antiprotonic helium has been observed in liquid- and gas-phase helium.[2]

References

1) G. Backenstoss: Progress in Atomic Spectroscopy, eds. W. Hanle and H. Kleinpoppen, Plenum, New York, Part B, p.1385 (1979).
2) M. Iwasaki *et al*.: *Phys. Rev. Lett.*, **67**, 1246 (1991); T. Yamazaki: Private communication.

# III-2-8. Rotational Excitation in Positron Scattering by the $H_2$ Molecule

I. Shimamura, E.A.G. Armour,* and M. Plummer*

The developments in the low-energy $e^+$ sources in these years and the consequential advances in the measurements on $e^+$-scattering processes have stimulated detailed calculations of the cross sections for $e^+$-atom and $e^+$-molecule collisions.[1] The integral cross sections for elastic scattering of $e^+$ by the $H_2$ molecules have recently been calculated by using the generalized Kohn method with trial functions involving the spheroidal coordinates.[2] The present work is an extension of this previous work to rotational excitation of $H_2$ and to differential cross sections.

The calculations have been carried out below the positronium formation threshold in the fixed-nuclei approximation. The symmetries $\Sigma_g^+$, $\Sigma_u^+$, $\Pi_u$, and $\Pi_g$ of the total scattering system have been included; the mixing of the two lowest spheroidal partial waves has been considered for the first three symmetries, but only the lowest spheroidal partial wave has been considered for the last symmetry. The trial functions include Hylleraas-type correlated functions containing the $e^+$-$e^-$ distances and functions appropriate for accounting for the long-range polarization of $H_2$, as well as separable correlation functions. Methods of calculations of rotational and differential cross sections from the asymptotic forms of the wave functions expressed in the spheroidal coordinates are well-documented in the literature.[3]

The calculated cross sections show a smooth behavior as a function of the $e^+$ energy. The rotational cross section for $e^+$-$H_2$ collisions is found to be smaller than that for $e^-$-$H_2$ collisions by more than an order of magnitude in most of the energy region covered in the present calculations. This trend is already seen in the total cross section for low energies, and may be ascribed crudely to the cancellation between the effects of the electrostatic and polarization interactions of $e^+$ with $H_2$; the former interaction changes the sign according to the sign of the charge of the incoming particle, and the latter interaction is independent of the sign of the charge at large distances.

References
1) E.A.G. Armour and J.W. Humberston: *Phys. Rept.*, **204**, 165 (1991).
2) E.A.G. Armour, D.J. Baker, and M. Plummer: *J. Phys.*, **B23**, 3057 (1990).
3) For example, S. Hara: *J. Phys. Soc. Jpn.*, **27**, 1592 (1969).

* Department of Mathematics, University of Nottingham, U.K.

RIKEN Accel. Prog. Rep. **25** (1991)

# III-2-9. Scaling of the Cross Sections for Vibrational Transitions

I. Shimamura

Collisional vibrational ($v \to v'$) and rotational ($J \to J'$) transitions of molecules are of crucial importance in such fields as radiation physics and chemistry and the physics of the earth's and planetary atmospheres and of gaseous discharges. Since the molecules often occupy many ($v,J$)-levels, a comprehensive set of cross sections for many pairs ($vJ, v'J'$) are necessary for a quantitative analysis of the moderation of charged particles.[1] Thus an accurate, independent determination of every necessary cross section seems almost impossible. In fact, a scaling law that relates any differential cross sections $q(J \to J')$ to $q(0 \to J'')$ greatly simplifies the analysis of the rotational transitions.[2,3] Sum rules for these transitions also exist.[3,4] The present work generalizes this previous work for vibrational transitions.

Regard a diatomic molecule as a harmonic oscillator. For a transition $v \to v'$ in a sudden collision, the adiabatic-vibration approximation is valid; the scattering amplitude is first defined with the internuclear distance $R$ fixed, and then it is averaged over the initial and final wave functions. Expand the fixed-nuclei amplitude in a Taylor series around the equilibrium $R$. Retain only the first four terms $f_n$ ($n=0-3$). Then $q(v \to v')$ take forms

$$q(v \to v) = |f_0 + (2v+1) f_2|^2,$$
$$q(v \to v \pm 1) = c v_> |f_1 + 3 v_> f_3|^2,$$
$$q(v \to v \pm 2) = c v_> (v_> - 1) \ |f_2|^2,$$
$$q(v \to v \pm 3) = c v_> (v_> - 1)(v_> - 2) \ |f_3|^2,$$

other transitions hardly occurring. Here, $c$ is the ratio of the final to initial channel wave number and $v_>$ is $\max(v, v')$. Among eight real quantities that determine the four unknowns $f_n$, *only the six quantities* $|f_n|$, $\mathrm{Re}(f_0{}^* f_2)$, and $\mathrm{Re}(f_1{}^* f_3)$, where $\mathrm{Re}(z)$ is the real part of $z$, are enough for obtaining all $q(v \to v')$.

Similar scaling laws hold for the integral cross sections. Sum rules are also proved for the cross sections summed over $v'$, with or without multiplication by the transition energies.

References

1) M. Inokuti: "Molecular Processes in Space", eds. T. Watanabe, I. Shimamura, M. Shimizu, and Y. Itikawa, Plenum, New York, p.65 (1990).
2) I. Shimamura: "Electron-Molecule Collisions", eds. I. Shimamura and K. Takayanagi, Plenum, New York, Chap.2 (1984).
3) I. Shimamura: *Phys. Rev.*, **A42**, 1318 (1990).
4) I. Shimamura: *ibid.*, **A23**, 3350 (1981).

RIKEN Accel. Prog. Rep. 25 (1991)

# III-2-10. Solid-Gas Effect in K-Vacancy Production in 41 MeV Ar-Ca and Ar-Cu Collisions

T. Kambara, R. Schuch,* Y. Awaya, T. Mizogawa, H. Kumagai, Y. Kanai, H. Shibata, and K. Shima

We have measured the impact parameter dependence of K-vacancy production probabilities and total cross section for 40.6 MeV Ar ions on Ca and Cu targets. We have also measured the target thickness dependence of the probability for the Ca target in order to study the effect of multiple collisions in solid targets on the K-vacancy processes.

An Ar beam from RILAC was collimated to a divergence of 0.02° and passed through a target of Ca or Cu. The thickness of Ca ranged from 2 to 30 $\mu g/cm^2$ and that of Cu was about 20 $\mu g/cm^2$. We measured K-vacancy probabilities as a function of the scattering angle between 0.13° and 1.4° by means of a K X-ray-particle coincidence. The scattering angle corresponds to an impact parameter between 510 and 5100 fm for the Ar-Ca and between 740 to 6700 fm for the Ar-Cu system. At the same time, the total cross section of K-vacancy production was obtained directly by normalizing the K X-ray yield with respect to the number of scattered ions at 25°.

A broad peak appears in the impact parameter dependence of K-vacancy probabilities of both the projectile and target in the Ar-Ca collisions. The present data and the results obtained with molecular and atomic gas targets[1] are compared in Fig. 1 using a scaling of 2p$\pi$-2p$\sigma$ rotational coupling[2] which gives a reduced impact parameter $b'$. The peak in the K-vacancy probability $P(b')$ for the thicker Ca targets is positioned at smaller b' than those obtained with the gas targets and the rotational coupling calculations, and it moves with decreasing target thickness towards those for the gas targets. Integration of the measured K-vacancy probability over the impact parameter gives a cross section which is significantly lower than the directly measured total cross section of K-vacancy production. From these observations a multiple collision L-vacancy process prior to 2p$\pi$-2p$\sigma$ rotational coupling is concluded.

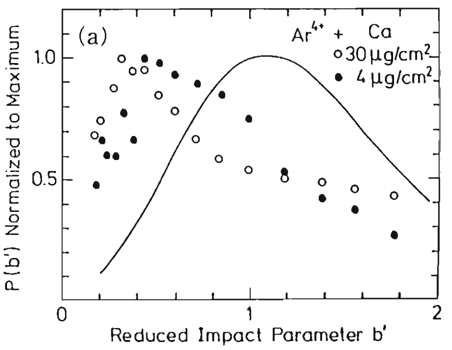


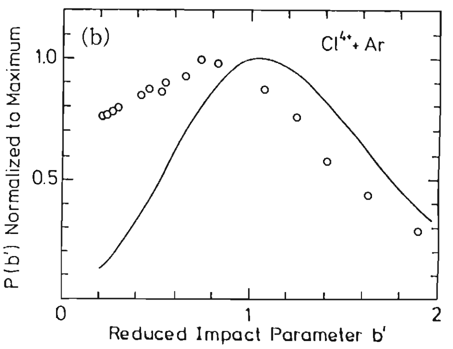


Fig. 1. Impact parameter dependence of the K-shell vacancy production probabilities in the scaling of a rotational-coupling model. The collision system is (a) Ar on Ca with open circles for the 30$\mu g/cm^2$ thick target and closed circles for the 4$\mu g/cm^2$ thick target, and (b) Cl on Ar. Solid lines show the results from the calculation. Each set of experimental and theoretical values is normalized with respect to its maximum.

In order to study the effect of the 1s$\sigma$-2p$\sigma$ radial coupling on the K-shell vacancy production process, the ratio of the K-vacancy probability of the target to that of the projectile is calculated from the data. Slight target thickness dependence is also seen in the ratio. Otherwise it is in good quantitative agreement with a simple model of K-vacancy sharing for both the Ca and Cu targets.

References

1) K. Taulbjerg, J. Briggs, and J. Vaaben: *J. Phys. B*, **9**, 1351 (1976).
2) R. Schuch, M. Schulz, E. Justiniano, R. Hoffmann, and J. Konrad: (unpublished results) (1982).

* Manne-Siegbahn Institute of Physics, Stockholm, Sweden.

RIKEN Accel. Prog. Rep. **25** (1991)

# III-2-11. Impact Parameter Dependence of K X-Ray Emission Probability and Charge State Distribution in 31 and 58 MeV $Si^{11+}$+Ar Collisions

T. Kambara, Y. Awaya, Y. Kanai, M. Ohura, J. Euler, M. Terasawa, and T. Sekioka

K-vacancy production processes in near-symmetric heavy ion-atom collisions have been studied systematically by measurements of the impact parameter dependence of K-X ray emission probability,[1] and they have been found to take place at only a small internuclear distance in a region of the K-shell radius. On the other hand, it is expected that outer-shell electron processes like single and multi-electron transfers are active over a much larger range of the internuclear distance. Not many experimental works have been reported about the impact parameter dependence of outer-shell electron processes.

We have investigated the K-vacancy production and electron transfer processes for a $Si^{11+}$-Ar collision system at collision energies of 31 and 58 MeV through the measurements of the impact parameter dependence of charge state distribution and K-X ray production probability. The experimental setup was described elsewhere.[2] A Li-like $Si^{11+}$ beam from RILAC passed through an Ar-gas target under a single-collision condition. The scattered Si-ions were charge-state selected by a dipole magnet and counted by a position sensitive counter. Thus the angular distribution of scattered ions was measured up to $4\times10^{-3}$ rad for each charge state from 7 to 13 at 31 MeV and from 8 to 14 at 58 MeV. From the measurements, the charge state distribution of the scattered ions was obtained as a function of the scattering angle which was converted to an impact parameter. At the same time, the K-X rays from the Si and Ar were measured with a Si(Li) detector in coinicdence with the scattered ions. The K-X ray emission probability was obtained from the measurements for each charge state of the scattered ions.

At impact parameters ($b$) larger than the K-shell radius, the fractions of $Si^{q+}$ with $q\leq11$, which correspond to the single and multi electron capture, have relatively flat $b$-dependence and the charge state distribution can be fitted by a binomial formula $\binom{t}{n}P_c{}^n(1-P_c)^{(t-n)}$ where $n$ is the number of captured electrons. At small $b$, the fraction of $Si^{7+}$ increases rapidly, which implies a new capture mechanism at a small internuclear distance. The fractions of $Si^{q+}$ with $q>11$, which correspond to the electron loss, decrease rapidly at $b$ larger than the K-shell radius.

The K-X ray emission probabilities have similar $b$-dependence in shape, independent of the charge state of the scattered ions. With these observations we conclude that in electron capture processes at a large internuclear distance region, the electrons are captured independently each other, and the electron capture processes are independent of the K-electron processes.

References

1) R. Schuch *et al.*: *J. Phys. A - Atoms and Nuclei*, **316**, 5 (1984).
2) T. Kambara, Y. Awaya, Y. Kanai, T. Mizogawa, M. Terasawa, H. Schmidt-Böcking, R. Dörner, and H. Vogt: *Nucl. Instrum. Methods,* **B53**, 426 (1991).

RIKEN Accel. Prog. Rep. **25** (1991)

# III-2-12. Target Element Dependence of the Intensity Ratio of K$\alpha$ Hypersatellites to Satellites for 50-95 MeV Ar Projectile

Y. Zou, T. Kambara, Y. Kanai, Y. Awaya, K. Ando,
M. Ohura, A. Hitachi, and S. Kravis

The K-shell vacancy production process of projectile Ar-ion was previously studied by measuring Ar K$\alpha$-X rays as a function of target atomic number $Z_2$ for the incident energy of 33 MeV (0.83 MeV/nucleon).[1] In that work the intensity ratio of the Ar K$\alpha$ hypersatellites to K$\alpha$ satellites, $I(K^h)/I(K)$, showed oscillatory dependence on $Z_2$. The obtained phase of oscillation was different from the results obtained for 64 MeV (2 MeV/nucleon) S ions[2] but similar to that obtained for 30 MeV (0.87 MeV/nucleon) Cl ions.[3] The vacancy production mechanism has been discussed by considering the incident energy, that is, in the case of faster collisions with S ions K-shell vacancies are mainly caused by the direct Coulomb interaction, whereas in the case of slower collisions with Cl and Ar ions the electron promotion process by rotational coupling plays an important role, and different process causes different oscillation of $I(K^h)/I(K)$ with $Z_2$.

In order to confirm this explanation and to systematically study the K-shell vacancy production process of Ar projectile when it collides with a solid target at different energies, the $I(K^h)/I(K)$ vs.$Z_2$ has been measured at incident energies of 52, 80.3, and 95 MeV (with $Z_2$=6-74).

This work was done at RILAC, and the experimental set-up was just as same as that in the previous work.[1] The results are shown in Fig. 1. As is seen in the figure, the target element dependence is different in the case of 52 MeV from that in the case of 80.3 and 95 MeV. At 80.3 and 95 MeV, $I(K^h)/I(K)$ vs. $Z_2$ curves show similar oscillations to that for 64 MeV S ions. It means that the direct Coulomb ionization is dominant in these two cases. Whereas at 52 MeV, the oscillation phase is more similar to that for 33 MeV Ar ions. It seems that, electron promotion process is still important for 52 MeV Ar ion colliding with target atoms. Further experiments will be done at projectile energies between 52 MeV and 80 MeV. More analysis and discussions are in progress.

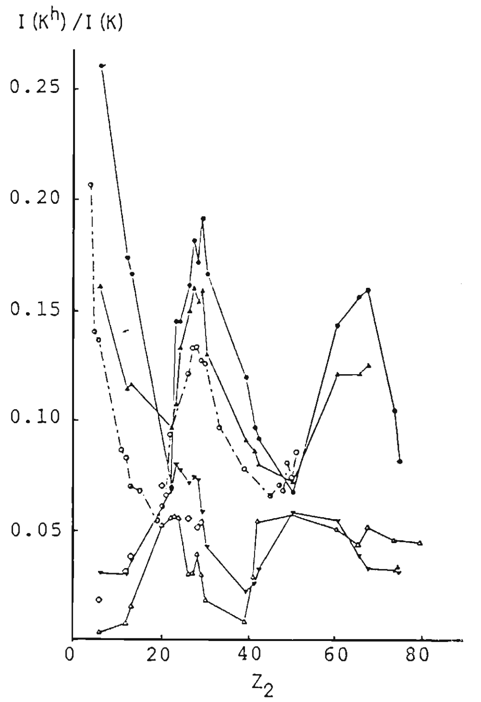


Fig. 1. The target element dependence of the intensity ratio of K$\alpha$ hypersatellites to satellites for ▼ 52 MeV, ▲ 80.3 MeV, and ● 95 MeV Ar ions (present work), and for △ 33 MeV Ar ions,[1] ◇ 30 MeV Cl ions,[3] and ○ 64 MeV S ions.[2] The curves are to guide the eye.

References

1) Y. Awaya, T. Kambara, M. Kase, H. Shibata, H. Kumagai, K. Fujima, J. Urakawa, T. Matsuo, and J. Takahashi: *Nucl. Instrum. Methods,* **B10**, 53 (1985).
2) R. L. Watson, J. R. White, A. Langenberg, R. A. Kenefick, and C.C. Bahr: *Phys. Rev.,* **A22**, 582 (1980).
3) W. Woods, F. Hopkins, R. L. Kauffman, D.O. Elliott, K.A. Jamison, and P. Richard: *Phys. Rev. Lett.,* **31**, 1 (1973).

# III-2-13. Low Energy K$\alpha$ Lines in Ar from Two-Electron Rearrangement Transitions

M. Ohura, T. Kambara, Y. Kanai, S.D. Kravis, Y. Zou, J. Pálinkás, and Y. Awaya

In heavy ion-atom collisions, the multiple inner-shell ionization process is enhanced, so that $KL^n$ satellite lines are observed in X-ray spectra, where $KL^n$ denotes a initial configuration with a single K vacancy and n L vacancies. Energies of these satellite lines are higher than $K\alpha_{1,2}$ X rays. On the other hand, some peaks with lower energies than $K\alpha_{1,2}$ line have been observed in the X-ray spectra from target atoms, and they have been attributed to the radiative Auger effect (RAE)[1] and the radiative electron rearrangement (RER).[2] These processes are schematically shown in Fig. 1. The studies of $KL^n$-RER satellites in ion-atom collisions have been made for various target atoms, but there have been no experiments to measure $KL^n$-RER satellites emitted from projectile ions.

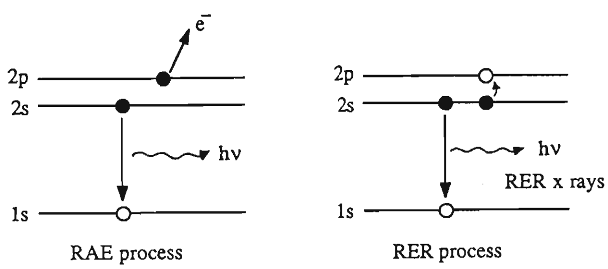


Fig. 1. Schematical diagram of the RAE and RER process. In the RAE process, the photon energy is not discrete. In the RER process, the photon energy is discrete and can be roughly estimated for a given $KL^n$ initial vacancy configuration as $E(KL^n\text{-RER}) \cong E(KL^n) - 2\Delta E_{2s-2p}$.

Thus we have measured X rays emitted from projectile ions passing through a thin foil target. In the experiment, 33 MeV $Ar^{8+}$ ions from RILAC impinged on a C or an Al-foil. Ar K X-rays were measured with a broad-range crystal spectrometer[3] with a flat Ge (111) crystal. The projectile Ar K X-ray energy spectrum obtained for an Al target is shown in Fig. 2. A small peak with a lower energy than Ar $K\alpha_{1,2}$ line (2.957 keV) is observed around 2.9 keV in Fig. 2. The $KL^n$-RER process has been well described by the configuration mixing of the atomic states, and

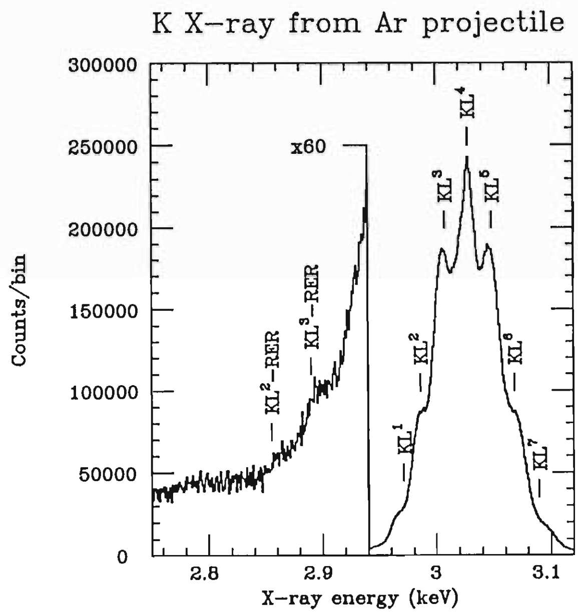


Fig. 2. X-ray energy spectrum emitted from $Ar^{8+}$ projectile ions. $KL^n$-RER energies were calculated by the MCHF method.

the branching ratios reflect the mixing coefficient.[2] Energies for $KL^2$-RER, $KL^3$-RER and $KL^4$-RER are estimated to be 2.855, 2.890 and 2.928 keV, respectively, by means of the multiconfiguration Hartree-Fock (MCHF) calculation.[4] By taking account of the Doppler effect, we conclude that the observed small peak around 2.9 keV is attributed to the $KL^3$-RER transition.

This is the first observation of RER satellites emitted from projectile ions. A rigorous analysis is in progress.

References

1) T. Åberg and J. Utriainen: *Phys. Rev. Lett.*, **22**, 1346 (1969); T. Åberg: *Phys. Rev.*, **A4**, 1735 (1971).
2) K.A. Jamison *et al.*: *ibid.*, **A14**, 937 (1976); T. Åberg *et al.*: *ibid.*, **A15**, 172 (1977).
3) A. Hitachi, H. Kumagai, and Y. Awaya: *Nucl. Instrum. Methods,* **195**, 631 (1982).
4) C. Froese Fischer: *Comput. Phys. Commun.*, **4**, 107 (1972).

RIKEN Accel. Prog. Rep. **25** (1991)

# III-2-14. Angular Distributions of United-Atomic Bremsstrahlung

K. Ishii, K. Maeda, Y. Sasa, M. Takami, M. Uda, and S. Morita*

We have previously reported[1] a scaling law on the cross sections of continuous X rays produced by 1.435 MeV / amu $Si^{3+}$-ion bombardments. This scaling law is expressed by

$$ds/d\hbar\omega = f[\omega a_0/\{v_p(Z_p+Z_T)\}],$$

where $\omega$ is the frequency of X rays, $a_0$ is the Bohr radius, $v_p$ is the projectile velocity and $Z_p(Z_T)$ is the atomic number of projectile(target). This formula just coincides with that of atomic bremsstralung(AB) except for the parameter of $(Z_p+Z_T)$.[2] We consider therefore that the continuous X rays are the atomic bremsstrahlung from the united-atom formed by projectile and target atom; we call this bremsstrahlung a united-atomic bremsstrahlung (UAB).

In symmetric collisions, the process of MO X-ray emission is predominant,[3] however the cross section of UAB should be almost zero because of a dipole transition process. Our previous results[4] of measurements of continuous X rays for the targets of $Z_T=6$-29, have confirmed this fact, that is, a maximum intensity of continuous X rays was obtained at symmetric collisions for the bombardment of 20 MeV $Si^{3+}$-ions ,while it was minimum for 40 MeV.

MO X rays are mainly produced by two-collision process in thick targets and the angular distributions are to be isotropic. On the other hand, the intensity of atomic bremsstrahlung depends on the X-ray emission angle with respect to the beam direction and it becomes maximum at 90°. We have measured the angular distributions of continuous X rays produced from the targets of C, Si, and Ti bombarded by $Si^{3+}$-ions of 14.9 MeV and 43.7 MeV from RILAC.

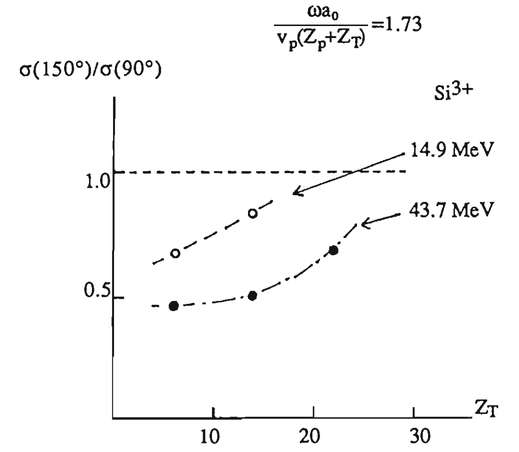


Fig. 1. Ratios of cross sections $\sigma(150°)/\sigma(90°)$ for $\omega a_0/\{v_p(Z_p+Z_T)\}=1.73$.

Figure 1 shows the ratios of X-ray intensity at 150° to that at 90°, for $\omega a_0/(v_p(Z_p+Z_T))=1.73$. In this figure, we can see anisotropies for the bombardments of 43.7 MeV ,but almost an isotropy for the case of Si target bombarded with 14.9 MeV $Si^{3+}$-ions.

This result on UAB and MO X rays is consistent with the previous one for energy dependence. The existence of UAB is now considered to be conclusive.

References


1) K. Ishii *et al.*: *RIKEN Accel. Prog. Rep.*, **23**, 47 (1989).
2) K. Ishii and S. Morita: *Nucl. Instrum. and Methods.*, **B22**, 68 (1987); M.C. Pacher and J.E. Miraglia: *Phys. Rev.*, **A41**, 2574 (1990).
3) R. Anholt: *Z. Phys. A*, **289**, 41(1978).
4) K. Ishii *et al.*: *RIKEN Accel. Prog. Rep.*, **24**, 49 (1990).


* Laboratory for Materials Science and Technology, Waseda University.

RIKEN Accel. Prog. Rep. **25** (1991)

# III-2-15. Multiple Ionization of He and Ne Atoms in Collision with Relativistic Heavy Ions

Y. Yamazaki, H. Watanabe, T. Azuma, K. Komaki, N. Kakutani, H. Tada, K. Kawatsura, Y. Kanai, T. Kambara, and Y. Awaya

The multiple ionizations of helium atoms ($He^{+}$, $He^{2+}$) and neon atoms ($Ne^{+}$, $Ne^{2+}$, $Ne^{3+}$) by 95 MeV/nucleon $Ar^{17+}$ ions have been investigated.

Some groups have intensively studied the double ionization of He atoms with relatively light charged particles[1] including antiprotons[2] and positrons,[3] where the interference between the shake-off and the two-step processes plays an essential role. In this case, multiple-electron transitions need theoretical treatments beyond the independent-electron model by taking into account the electron-electron correlation, which is a challenging subject in ion-atom collisions.

Here we present new data of the ratio of the double to the single ionization cross sections ($R=\sigma_{2+}/\sigma_{+}$) of He atoms bombarded by 95 MeV/nucleon $Ar^{17+}$ ions, the velocity of which is about one half of the light velocity. We measured the ratio at projectile charge $Z_P$ and velocity $V_P$ higher than other groups, where higher order corrections of $Z_P$ may be important.

The experiment was performed at RIKEN Ring Cyclotron with a recoil ion time-of-flight (TOF) spectrometer. A Ceratron (Murata Co.) was used as a recoil ion detector, because of its low sensitivity to high-energy contaminant particles and $\gamma$-rays. Projectiles were detected by a parallel-plate avalanche counter at about 5 m downstream from the target, and delivered start pulses to a time-to-amplitude converter (TAC).

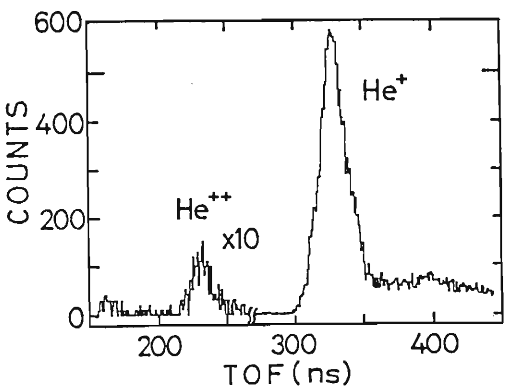


Fig. 1. TOF spectrum of recoil He ions by 95 MeV/nucleon $Ar^{17+}$ bombardment.

Figure 1 shows an example of the TAC spectrum. It is found that the ratio $R$ is about $1.07\times 10^{-2}$. As we are in a high-velocity regime, a scaling formula proposed by Knudsen et al.[1] may be applicable, i.e.,

$$R=2.20\times10^{-3}+4.55\times10^{-3}Z_P{}^2/[E_p\ln(13.12E_p{}^{1/2})],\quad(1)$$

where $E_p$ is the projectile energy in MeV/nucleon. This scaling formula is based on the general arguments on the double ionization; 1) a shake-off (proportional to $Z_p{}^2$) and 2) a two-step successive collision (proportional to $Z_p{}^4$). The observed ratio is larger than the prediction of this scaling formula by a factor of two, indicating that even higher order terms of $Z_p$, such as a two-step process with polarization (proportional to $Z_p{}^6$), may contribute to the ratio in the present experiment. However, if we employ another scaling formula by Andersen et al.,[2] the prediction agrees with our experimental findings.

The multiple ionization of Ne atoms has also been studied. It is found that $\sigma_{+}:\sigma_{2+}:\sigma_{3+}=1:0.24:0.04$. As $\sigma_{+}:\sigma_{2+}$ is $\sim 1:0.05$ for proton impacts[2] having the same $E_p/Z_p{}^2$, it is clear that the $Z_p{}^2$ scaling like Eq.(1) does not hold even qualitatively.

References
1) H. Knudsen *et al.*: *J. Phys. B: At. Mol. Phys.*, **17**, 3545 (1984).
2) L.H. Andersen *et al.*: *Phys. Rev.*, **A36**, 3612 (1987).
3) M. Charlton *et al.*: *J. Phys. B: At. Mol. Opt. Phys.*, **21**, L545 (1988).

RIKEN Accel. Prog. Rep. **25** (1991)

# III-2-16. Secondary Ions Produced in Frozen $H_2O$ Molecules under Energetic Heavy Ion Impact

T. Matsuo, T. Tonuma, H. Kumagai, H. Shibata, and H. Tawara

We have measured positive ions produced from frozen $H_2O$ as well as gas phase targets under impact of a few picoampere 1.25 MeV/nucleon $Ar^{q+}$($q=4,12,13$) ion beam provided from RILAC. The target gases are frozen (at the liq. $N_2$ temperature) on an Al foil which is thin enough to pass the projectiles. The foil is inclined 45° with respect to the incident ion beam, meanwhile the secondary ions are extracted normal to the foil surface and their mass/charge is analyzed through a double-focusing sector magnet.

A typical mass/charge spectrum of positive ions from the frozen $H_2O$ target is shown in Fig. 1(A) together with that from the gas target in Fig. 1(B). Significant differences in spectra in both target phases are clearly noticed. Multiply charged $O^{i+}$($i=1-6$) ions are clearly seen in the spectrum from the gas target. On the other hand, the production of multiply charged ions are strongly suppressed in the frozen target.

The heavy ion bombardment on frozen targets also produces cluster ions with formula

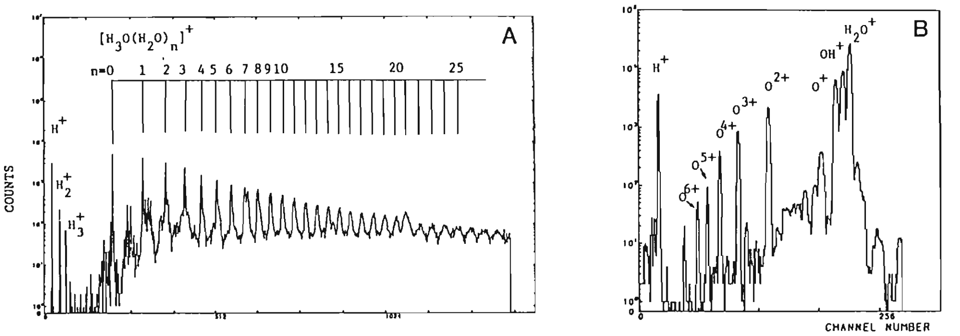


Fig. 1. Mass/charge spectra of positive ions from the frozen $H_2O$ target (A) and those from the gas target (B).

$[H_3O(H_2O)_n]^+$, n varying from 0 to more than 25, as well as $H_m^+$($m=1,2,3$) ions. The main cluster ions might have a structure with the core of $H_3O$ but not H because $H_3O^+$ ions are far more intense compared with $H_2O^+$ ions which are the dominant products in the gas phase targets. It should be noted that the cluster ions with the oxygen core are almost absent.

These features of cluster ion production in the frozen target are significantly different from those observed in the expanded nozzle beams,[1] the reason of which is probably related to the density of the target and the collisions followed in the target. To clarify the mechanisms of the secondary ion production, a series of experiments for various frozen targets are under way.

References

1) O. Echt, D. Kreisle, M. Knapp, and E. Recknagel: *Chem. Phys. Lett.*, **108**, 401 (1984).

RIKEN Accel. Prog. Rep. **25** (1991)

# III-2-17. Negatively Charged Cluster Ions Produced from Frozen $C_2H_2$ Molecules under the Energetic, Heavy Ion Impact

T. Tonuma, H. Kumagai, T. Matsuo, H. Shibata, and H. Tawara

Figure 1 shows a typical mass/charge spectrum of negatively charged atomic, molecular and cluster ions produced in collisions of 1.25 MeV/amu $Ar^{12+}$ projectile ions with frozen $C_2H_2$ targets. It can be seen from the figure that relative yields of $CH_m^-$(m=0 and 1) ions are much less than those of $C_2H_m^-$(m=0 and 1) ions. Relative yields of $[CH_m(C_2)_n]^-$ and $[C_2H_m(C_2)_n]^-$ (m=0 and 1) cluster ions seem to clearly reflect the production cross sections of $CH_m^-$ and $C_2H_m^-$ ions, respectively. The observed $O^-$ and $OH^-$ ions are understood to be due to the dissociative electron attachment of residual $H_2O$ molecules.

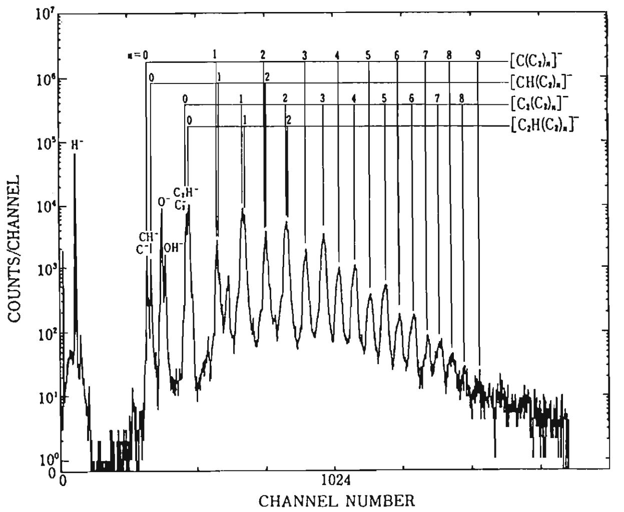

Fig. 1. Mass/charge spectrum of negative cluster ions from the frozen $C_2H_2$ target under 1.25 MeV/amu $Ar^{12+}$ ion impact.

As already discussed in a previous experiment of collisions between energetic heavy ions and frozen $CO_2$ targets,[1] it seems that the cluster ions, $[CH_m(C_2)_n]^-$ and $[C_2H_m(C_2)_n]^-$, observed in the present measurement are clearly based upon different atomic as well as molecular ion cores, namely, singly charged ions such as $CH_m^-$ and $C_2H_m^-$, which are formed in previous collisions under the energetic ion impact. These core ions produced under the energetic ion impact could have the initial kinetic energies due to the recoil or dissociation by Coulomb explosion[2] and, thus, reach the outer-most layers of the frozen surface where they collide with neutral molecules. The cluster ions formed through ion-molecule reactions finally leave the surface into vacuum. The main elementary unit of clustering particles in the present target seems to be $C_2$ molecules which are formed via the dissociation of the parent $C_2H_2$ molecules, but not the parent molecules $C_2H_2$ themselves.

Positively charged cluster ions such as $[CH_m(C_2)_n]^+$ and $[C_2H_m(C_2)_n]^+$ (m=0,1,2 and 3) have been also observed and seem to be based upon different atomic or molecular ion cores of $CH_m^+$ and $C_2H_m^+$ (m=0,1,2 and 3).

References

1) H. Tawara, T. Tonuma, H. Kumagai, T. Matsuo, and H. Shibata: *J. Chem. Phys.*, **94**, 2730 (1991).
2) H. Tawara, T. Tonuma, K. Baba, T. Matsuo, M. Kase, T. Kambara, H. Kumagai, and I. Kohno: *Nucl. Instrum. Methods in Phys. Res.*, **B23**, 203 (1987).

RIKEN Accel. Prog. Rep. **25** (1991)

# III-2-18. Measurements of Field Ionized Electrons from High Charge State Rydberg Ions

Y. Kanai, B. D. DePaola, P. Richard,* H. Schöne,* and J. Giese*

We started a study of high charge state Rydberg ions by using a Rydberg analyzer system. The beat structure in the spectra of field ionized electrons from high charge Rydberg ions was reported by some groups.[1,2] But, they have not measured the beat structure as a function of n (principal quantum number of the Rydberg electron) under the same collision conditions (the same collision system and the same collision energy). By using our system, we can measure the beat structure as a function of n. So we can get more information about the Rydberg states. Our analyzer system consists of three parts: (1) a set of deflector plates, (2) the Rydberg analyzer, and (3) the tandem electron spectrometer, as shown in Fig. 1.[3,4] The Rydberg ions are produced in a carbon target foil and pass through the perpendicular electric field between the deflector plates. Electrons produced before the deflector are deflected by the deflector and can not enter the Rydberg analyzer. Finally, the Rydberg electrons are ionized in the electric field of the Rydberg analyzer. These electrons are detected by the tandem electron spectrometer. Details of this system are in Refs. 3 and 4.

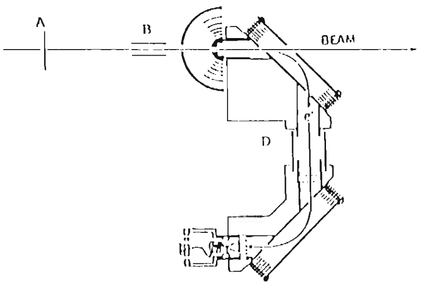


Fig. 1. Schematic diagram of the experimental set up. A: the target. B: a set of deflector plates. C: the Rydberg analyzer. D: the tandem electron spectrometer.

The experiments were performed at J. Mcdonald Laboratory of Kansas State University. A beam of 24- MeV $C^{4+}$ ions extracted from the tandem accelerator was analyzed by a bending magnet and focused into the scattering chamber. Targets were 10 and 20 $\mu g/cm^2$ carbon foils. At the last layer of the target, the Rydberg state was produced by collisions.[1] Considering the mean charge, +5.6, of the 24-MeV carbon ions after the carbon target,[5] we say that almost all Rydberg ions are H-like ions. We measured the intensity of the field ionized electron in the Rydberg analyzer as a function of the field strength ($E_p$) between the deflector plates. A typical result is shown in Fig. 2. In this case, the intensity of the electrons ionized from the H-like Rydberg ions (n=154) was measured as a function of $E_p$. Beat structure is clearly seen in it. This structure due to the population of the Rydberg state (n=154) ions was changed as a function of $E_p$. The period of this structure was changed with different n. A precise analysis is in progress.

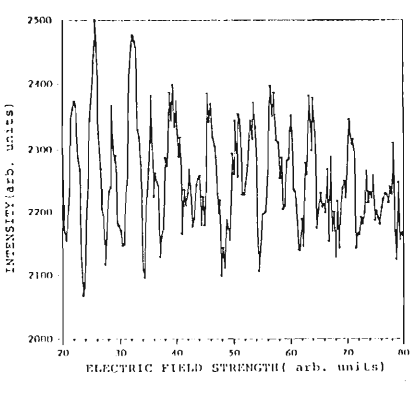


Fig. 2. Intensity of the field ionized electrons from the $C^{5+}$ (n=154) Rydberg ions as a function of the field strength ($E_p$).

References

1) D. Schneider, W. Zeitz, R. Kowallik, G. Schiwietz, T. Schneider, N. Stolterfoht, and U. Wille: *Phys. Rev.*, **A34**, 169 (1986).
2) P. Engar, M. Breing, R. DeSerio, C.E. Gonzalez-Lepera, and I.A. Sellin: *ibid.*, **A33**, 2096 (1986).
3) B.D. DePaola, W.J. Axmann, R. Parameswaran, D.H. Lee, T.J.M. Zouros, and P. Richard: *Nucl. Instrum. Methods*, **B40/41**, 187 (1989).
4) D.H. Lee, T.J.M. Zouros, J.M. Sanders, J.L. Shinpaugh, T.N. Tipping, S.L. Varghese, B.D. DePaola, and P. Richard: *ibid.*, p. 1229.
5) K. Shima, N. Kuno, M. Yamanouchi, and H. Tawara: NIFS-DATA-10 (1991).

* Department of Physics, Kansas State University, Manhattan, Kansas, U.S.A.

# III-2-19. $Z_2$-dependence of Energy Spectra of Electrons Excited by Grazing Angle Incident Fast Heavy Ions

H. Ishikawa,* A. Misu,* A. Koyama, T. Iitaka,** M. Uda, and Y. Ohtsuki**

Recently a new and prominent peak of electrons induced by fast multi-charged projectiles incident at a grazing angle on a target with nearly free valence electrons has been observed at energies higher than that of electrons isotachic to projectiles, $E_I$, and at emission angles lower than 10° or 15° with respect to the surface. This peak has been interpreted in terms of the convoy electron (CE) acceleration by a dynamic image potential (DIP) of a surface wake, which is due to projectileinduced polarization of target surface electrons.[1,2)]

In this report, energy spectra of electrons from Al, Si, Cu, Ag and Au have been measured at various emission angles for the impact of 1 MeV/amu $Ar^{12+}$ ions incident at an angle of 1° with respect to the target surface. Target meterials are in-situ evaporated on Si single crystal substrates of 10mm wide and 20mm long in a vacuum lower than $10^{-8}$ Torr.

Figure 1 shows the target dependence of electrons emitted at 10° with respect to the incident beam direction. The most probable energies, $E_m$, are higher than $E_I=530$ eV, and 625 eV for Al, 634 eV for Si, 624 eV for Cu, 652 eV for Ag, and 665 eV for Au. Therefore it is concluded that tha acceleration of a CE by a DIP occurs also for noble metals.

It is considered from the theory on nearly free electron metals that the acceleration of a CE is prominent for a large valence electron density, n, because a DIP is high for a large n. Actually, $E_m$ for Si is larger than that for Al, as seen in Fig. 1. On the other hand, for noble metals a DIP is not necessarily high for a material with a large n; n for Cu is the highest and $E_m$ for Cu is lower than those for Ag and Au. This point is open to further investigation.

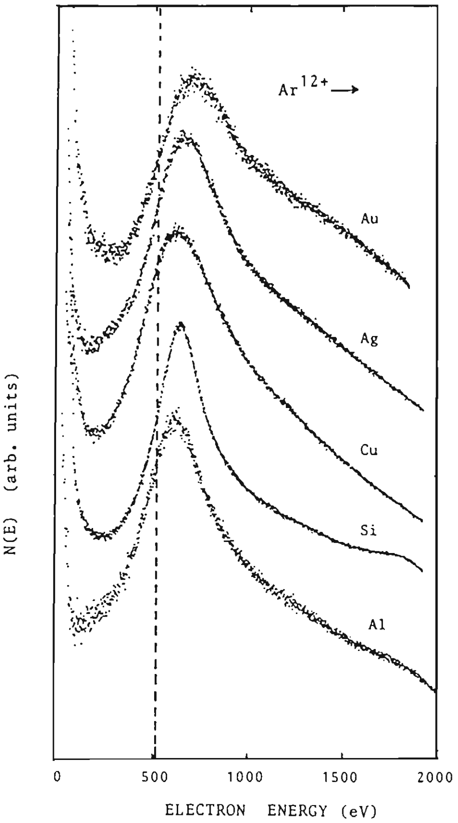


Fig. 1. Target dependence of accelerated convoy electrons induced by $Ar^{12+}$ions (1 MeV/amu) incident at an angle of 1° with respect to the surface. Detection angle is 10° with respect to the incident beam direction.

References

1) A. Koyama, Y. Sasa, H. Ishikawa, A. Misu, K. Ishii, T. Iitaka, Y.H. Ohtsuki, and M. Uda: *Phys. Rev. Lett.*, **65**, 3156 (1990).
2) T. Iitaka, Y.H. Ohtsuki, A. Koyama, and H. Ishikawa: *ibid.*, p. 3160.

* Science University of Tokyo.
** Waseda University.

RIKEN Accel. Prog. Rep. **25** (1991)

# III-2-20. Ejected Electron Spectra from $O^{4+}$ ($1s^23131'$) Produced by Double Electron Capture

T. Nabeshima, N. Nakamura, S. Ohtani, T. Takayanagi, K. Wakiya, H. Suzuki, A. Danjo, M. Yoshino, Y. Kanai, T. Kambara, and Y. Awaya

We carried out the high-resolution measurement of the electrons ejected by the following double electron transfer collisions at 60 keV;

$$O^{6+}(1s^2) + He(1s^2) \longrightarrow O^{4+}(1s^2nln'l') + He^{2+} \hookrightarrow O^{5+}(1s^2n''l'') + e \quad (1)$$

$$O^{6+}(1s^2) + O_2(2\pi_u{}^4 2\pi_g{}^2) \longrightarrow O^{4+}(1s^2nln'l') + O_2{}^{2+}(2\pi_u{}^4) \hookrightarrow O^{5+}(1s^2n''l'') + e. \quad (2)$$

60 keV $^{16}O^{6+}(1s^2)$ projectile ions were produced by the ECRIS (Electron Cyclotron Resonance Ion Source) constructed as an ion source for the RIKEN AVF cyclotron. Ejected electrons were measured by the zero-degree electron spectroscopy method.[1]

If the collision has not changed an electron spin,[2] only the singlet states of the doubly excited configurations can be produced by process (1). On the other hand, $O_2$ molecules have two electrons in its outer electron orbit$(2\pi_g)^n$ and their electron spins are of the same direction. We expected that the triplet states of the doubly excited configurations can be produced by process (2).

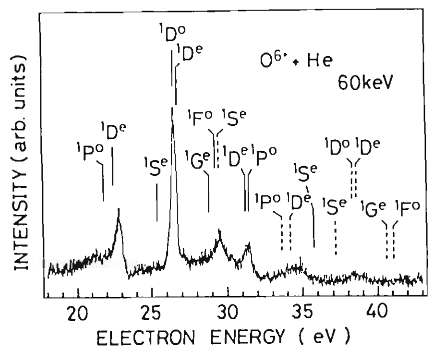


Fig. 1. High-resolution spectrum of ejected electron from the doubly excited $O^{4+}(1s^23131')$ ions produced in $O^{4+}$+He Collisions. Solid and broken vertical lines represent the theoretical energy for the transitions to the $O^{5+}(1s^22p)$ and $O^{5+}(1s^22s)$, respectively.

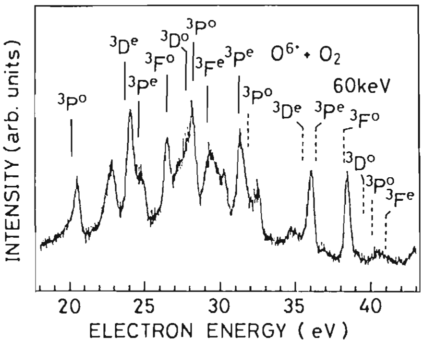


Fig. 2. High-resolution spectrum of ejected electron from the doubly excited $O^{4+}(1s^23131')$ ions produced in $O^{4+}+O_2$ collisions. Solid and broken vertical lines represent the theoretical energy for the transitions to the $O^{5+}(1s^22p)$ and $O^{5+}(1s^22s)$, respectively.

Ejected electron spectra from the doubly excited $O^{4+}$ ($1s^23131'$) ions are shown in Figs. 1 and 2. The vertical lines in the figures represent the theoretical values,[3] which include a post collision interaction (PCI) effect calculated from the lifetime.[4] Solid and broken lines correspond to the transitions to the $O^{5+}(1s^22p)$ and $O^{5+}(1s^22s)$, respectively. Only the peaks from the singlet state configurations are observed in Fig. 1. In Fig. 2, the peaks not only from the singlet state configurations but also from the triplet ones are observed. Precise analysis is in progress.

References

1) H.A. Sakaue, Y. Kanai, K. Ohta, M. Kushima, T. Inaba, S. Ohtani, K. Wakiya, H. Suzuki, T. Takayanagi, T. Kambara, A. Danjo, M. Yoshino, and Y. Awaya: *J. Phys.*, **B23**, L401 (1990).
2) M. Mack: *Nucl. Instrum. Methods*, **B23**, 74 (1987).
3) Z. Chen and C.D. Lin: *J. Phys.*, **B22**, 2875 (1989).
4) N. Veck and J.E. Hansen: *ibid.*, p. 3137.

RIKEN Accel. Prog. Rep. **25** (1991)

# III-2-21. High-Resolution L-Auger Spectroscopy of Mg-Like Scandium Produced in 89-MeV $Sc^{8+}$+He Collisions

M. Sataka,*1 K. Kawatsura, H. Naramoto,*1 Y. Nakai,*1 Y.Yamazaki, K. Komaki, K. Kuroki, Y. Kanai, T. Kambara, Y. Awaya, J.E. Hansen,*2 I. Kădăr,*3 and N. Stolterfoht*4

We measured scandium L-Auger electrons produced in 89-MeV $Sc^{8+}$+He collisions using the method of zero-degree Auger Spectroscopy. A light target atom He was used to ionize selectively the 2p electron of the scandium projectile. The experiments were performed at the tandem accelerator facility at the Japan Atomic Energy Research Institute of Tokai. A beam of 89-MeV $Sc^{8+}$extracted from the tandem accelerator was analyzed by a bending magnet and focused into the scattering chamber. After collimation of the beam to a diameter of about 2 mm, a current of about 100 nA was directed through the target gas cell and collected in a Faraday cup. The target gas pressure in the cell was a few mTorr and the target length was about 5 cm. During operation of the cell the pressure in the scattering chamber was about $10^{-5}$ Torr. The resulting target thickness was sufficiently thin to guarantee single collision conditions.

Figure 1 shows an example of the L-auger spectrum produced in 89-MeV $Sc^{8+}$+He collisions. The spectrum exhibits a pair of peaks at 143.5 eV and 147.8 eV which are attributed to the transitions from the $^2P_{3/2}-{}^2P_{1/2}$ doublet formed by the initial configuration $1s^22s^22p^53s^2$ in the $Sc^{10+}$ ion to the final state $1s^22s^22p^6$. The production of this doublet shows that in some collisions the 3p electron has been removed in addition to the ionization of the 2p electron. The intensity of the spectrum due to the $^2P_{3/2}-{}^2P_{1/2}$ doublet is only 7 % of the total intensity, which shows that, if the Auger decay is isotropic, there is a relatively small deviation from the assumption of selective 2p ionization.

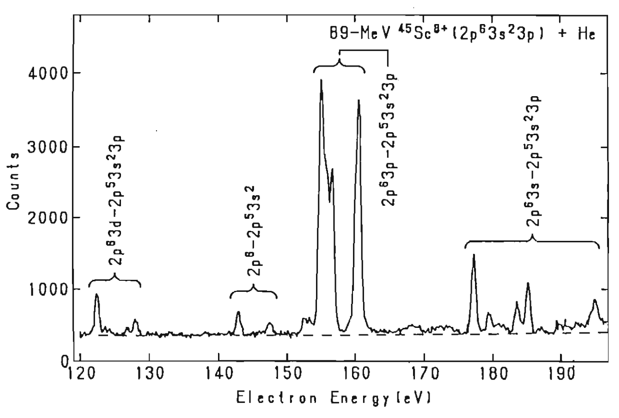


Fig. 1. Scandium L-Auger spectrum produced in collisions of 89-MeV $Sc^{8+}$ ions on He. The observation angle is 0°. The electron energy refers to the projectile frame.

The remainder of the spectral intensity is due to the initial configuration $1s^22s^22p^53s^23p$ Mg-like $Sc^{9+}$ which is produced by ionization of a single 2p electron in the ground state configuration $1s^22s^22p^63s^23p$ of $Sc^{8+}$. The three peak groups with centroid energies near 125 eV, 157 eV, and 181 eV are associated with transitions to the final state configurations $1s^22s^22p^63d$, $1s^22s^22p^63p$, and $1s^22s^22p^63s$, respectively. The structure in each feature is produced primarily by the level splitting in the initial state due to the interaction of the 2p hole with the 3p electron.

The transition to $1s^22s^22p^63d$ from $1s^22s^22p^53s^2$-3p involves three electrons. The branching ratios for that transition must be calculated with taking into account of the electron correlation. Calculated branching ratios are in good agreement with our observations.[1,2]

References

1) K. Kawatsura, M. Sataka, H. Naramoto, M. Imai, K. Komaki, Y. Yamazaki, K. Kuroki, Y. Kanai, T. Kambara, Y. Awaya, J.E. Hansen, I. Kadar, and N. Stolterfoht: *Nucl. Instrum. Methods,* **B53**, 421 (1991).
2) M. Sataka, K. Kawatsura, H. Naramoto, Y. Nakai, Y. Yamazaki, K. Kuroki, Y. Kanai, T. Kambara, Y. Awaya, J.E. Hansen, I. Kădăr, and N. Stolterfoht: *Phys. Rev. A*, in press.

*1 Japan Atomic Energy Research Institute, Tokai, Ibaraki.
*2 Zeeman Laboratorium, Universiteit van Amsterdam, Amsterdam, Netherlands.
*3 Institute of Nuclear Research, Debrecen, Hungary.
*4 Hahn-Meitner Institut, Berlin, F.R.G.

RIKEN Accel. Prog. Rep. **25** (1991)

# III-2-22. Lifetime Measurements of the $2p^5 3p$ and $2p^5 3d$ Levels in Cr XV

K. Ando, Y. Zou, T. Kambara, M. Ohura, Y. Awaya, T. Tonuma, and S. Tsurubuchi

Last year, we finished the measurements of lifetimes of neonlike Ti ion. Following Ti, we extended the isoelectronic sequence of lifetimes of neonlike ions to cromium. The experimental arrangement was the same as before.

Decay curves measured were analyzed by the multiexponential fitting using program DISCRETE.[1] For the decays of 3p $^1P_1$ and 3p $^3D_2$, cascading from upper states was corrected by means of the ANDC (Arbitrary Normalized Decay Curve) analysis using program CANDY.[1]

Though the experiment on cromium is not yet finished, the results of the ANDC analysis and the multiexponential fitting are displayed in Table 1 with the theoretical calculation.[2]

The decay curves of the 3d $^3D_2$ level include a short lived cascade of lifetime of 6.4 ps. The level of 3p $^3D_2$ is repopulated by long lived 3d cascades. The lifetimes of 3d levels obtained by the multiexponential fitting should be reliable, since all direct cascades to 3d levels are very fast.

Table 1. Lifetimes (ns) of levels in Cr XV.

| Upper level | Wave-length | Transition | Experiment | Theory |
|---|---|---|---|---|
| 3d $^3F_3$ | 308.895 | $^3D_2$-$^3F_3$ | 0.132±0.003 (0.972) [a] | 0.138 [c] |
| 3d $^3D_2$ | 318.439 | $^3P_1$-$^3D_2$ | 0.142±0.016 (0.635, 0.0064) [a] | 0.118 [c] |
| 3p $^3D_2$ | 416.59 | $(3/2, 1/2)_2$-$^3D_2$ | 0.218±0.065 [b]<br>[0.282±0.021 (1.17)] [a] | 0.255 [c] |
| 3p $^3P_1$ | 390.959 | $(1/2, 1/2)_0$-$^3P_1$ | 0.224±0.0022 [b]<br>[0.239±0.027 (0.119)] [a] | 0.187 [c] |

a) Results of the multiexponential fitting. In parentheses cascading lifetimes are given. The values inside a brackets are shown for comparing with the ANDC results.

b) Results of the ANDC analysis.

c) Results of Pokleba and Safronova.[2]

References

1) L. Engstrom: *Nucl. Instrum. Methods,* **202**, 369 (1982).

2) A. K. Pokleba and U. I. Safronova: *Opt. Spectrosc.,* U.S.S.R., **53**, 7(1982).

RIKEN Accel. Prog. Rep. **25** (1991)

# III-2-23. Direct Capture of Externally Produced Ions in an RF Ion Trap for Laser Spectroscopy of Atoms with Stable and Unstable Nuclei

Y. Matsuo, H. Maeda,* and M. Takami

Recent development of ion trap and laser cooling technique to reduce the kinetic energy of gaseous atoms well below ambient temperature has shown the feasibility of ultra-high resolution spectroscopy.[1] Laser spectroscopy in an ion trap will be one of the important techniques to determine the physical quantites of unstable nuclei by measuring their isotope shifts and hyperfine structures.

For the purpose of developing widely applicable spectroscopic scheme of atoms we have constructed a radio-frequency ion trap that directly captures the ions produced by laser ablation. The laser ablation method is expected to be suitable specifically for generating multiply charged ions and revaporizing implanted atoms containing unstable nuclei.

The ion trap system consists of trap electrodes (hyperbolic or cylindrical type), a vacuum chamber pumped with a turbo molecular pump, and a Nd:YAG laser that vaporizes and ionizes a sample metal placed near trap electrodes. The confinement of ions is confirmed with two methods. One is the detection of ions with a quadrupole mass spectrometer (QMS). Trapped ions are driven out of the trap by a pulsed voltage applied to one of the trap electrodes after a certain storage time and detected with a QMS. This allows mass-selective detection of any kinds of ions. The other is the observation of laser-induced-fluorescence (LIF) from trapped ions. A pulsed dye laser irradiates the central part of the trap. The emission from the trapped ions is focused on a photo-multiplier and the photo-electron signals are accumulated with a gated integrator synchronized with the dye laser pulse. This method is limited to the detection of those ions with optical transitions from the ground states, but has an advantage that it is non-destructive observation.

The QMS detection method has proven the successful confinement of $Ca^+$, $Ba^+$, $La^+$, $Nd^+$, $Tm^+$, $Lu^+$, $Hf^+$, and $Ta^+$ ions in both the hyperbolic and cylindrical traps for the time range of several minutes to 20 minutes in the presence of He buffer gas. Storage of $Ba^{2+}$ for several seconds has also been confirmed with the QMS method. LIF from trapped $Ba^+$ and $Lu^+$ (Fig. 1) is observed. Some ions such as $Lu^+$ are found to be highly reactive with background gaseous molecules.

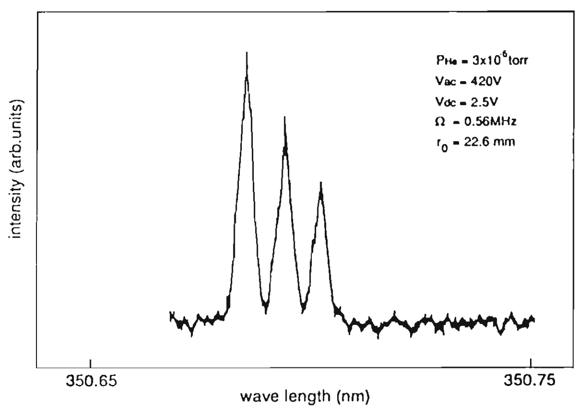


Fig. 1. LIF spectra from trapped $Lu^+$. $Lu^+$ ions are excited from the ground $^1S_0$ state to the $^3P_1$ state. The emission from $^3P_1$ to $^3D_{1,2}$ metastable states is observed. Triplet lines correspond to the nuclear quadrupole hyperfine splitting in $^3P_1$ level.

References

1) D.J. Wineland, W. M. Itano, and R. S. Van Dyck, Jr.: *Adv. At. Mol. Phys.*, **19**, 135 (1983).

* Department of Nuclear Engineering, Faculty of Engineering, University of Tokyo.

RIKEN Accel. Prog. Rep. 25 (1991)

# III-2-24. Ultra-Slow Monoenergetic $(^3He\mu^-)^+$ Beam and Novel Future Applications

K. Nagamine

So far, several proposals have been made for the possible slow $\mu^-$ sources. Recently, realization of slow $\mu^-$ beam has been pointed out by utilizing the $\mu^-$ liberation phenomena in muon catalyzed $(dt\mu^-)$ fusion,[1,2] where a successive (above 100 times) liberation of slow (around 10 keV) $\mu^-$ at the fusion reaction in $(dt\mu)$ molecule is used to produce slow $\mu^-$ from the surface of a thin $D_2/T_2$ layer.

In the recent experiments conducted by the UT-MSL and RIKEN group at UT-MSL/KEK, the following remarkable observations have been achieved for the $\mu^-$ transfer phenomena in liquid $D_2$ with $^3He$ and $^4He$ impurities;[3] (1) When the $\mu^-$ is injected into a high density (liquid or solid) $D_2$ with a low concentration (up to 500 ppm) He impurities, all the $\mu^-$ form muonic $(d\mu^-)$ and reach the ground state of $(d\mu^-)$; (2) Then, the transfer reaction of the $\mu^-$, $(d\mu^-)+He \rightarrow (He\mu)+d$, takes place through the formation of the $(dHe\mu)$ muon molecule at the level of $(dHe\mu)_{2p\sigma}$ state; (3) Thus formed $(dHe\mu)_{2p\sigma}$ has the following processes as a possible decay mode: (a) radiative transition to the unbound ground state, $(dHe\mu)_{2p\sigma} \rightarrow \gamma(6.8keV)+(He\mu)_{1s}+d$, (b) energetic emission of $(He\mu)_{1s}$ particles. It was found that the $(d^4He\mu)_{2p\sigma}$ decays mainly (more than 60%) through the radiative transition, while the $(d^3He\mu)_{2p\sigma}$ decays mainly (more than 80%) through the particle emission (process (b)).

As for the particle emission decay of $(d^3He\mu)$, it can be expected that the ionic particle of $(^3He\mu)^+$ is emitted at the unique energy of 3.2 keV. Once the $(d^3He\mu)$ molecule is formed, almost all the $\mu^-$ is emitted in the form of $(^3He\mu)^+$.

Thus, the following scheme can be considered as for the method of production of slow $(^3He\mu)^+$ particle beams. Suppose a solid layer of $H_2$ with 1,000 ppm $D_2$ is formed on the cold plate ($\sim$3K) with a thickness of 1 mm. Then, 1 $\mu$m thickness layer-coating of $^3He$ is formed on the surface of solid $H_2(D_2)$. The injected $\mu^-$ of MeV energy is almost fully stopped in the thick solid $H_2(D_2)$ layer. There, because of the celebrated Ramsauer resonance effect, the $(d\mu)$ of 3 eV is produced with a long diffusion length (up to 1 mm) without any scattering from H.[4,5] Thus, a half of $(d\mu)$ reaches the layer of $^3He$. Then, almost all the $(d\mu)$ form $(d^3He\mu)$ molecules and subsequently the 3.2 keV $(^3He\mu)$ is emitted (see Fig. 1).

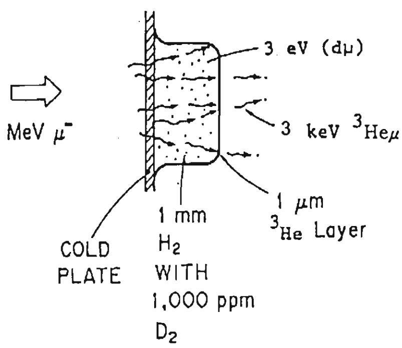


Fig. 1. Schematic picture for the target arrangement for slow $(^3He\mu^-)$ production from $^3He$ coated $H_2/D_2$ target.

The proposed method of slow beam production might be the easiest and the most efficient way for the $\mu^-$ associated particles, adjacent to pure $\mu^-$ and neutral muonic hydrogen.

The possible applications as well as future extensions of the slow monoenergetic $(^3He\mu)$ beam are listed in the followings. (1) $\mu^-$ transfer to heavier atoms on the surfaces and element analysis of material surfaces. (2) Studies of the high energy resonance states in $(d^3He)$ molecules and a possible application to the new muon catalyzed fusion phenomena. (3) Production of the highly polarized $(^3He\mu^-)$ state with polarized $^3He$ by the repolarization method and a possible application to the new $\mu$SR experiments. (4) Detachment of $\mu^-$ from $(^3He\mu^-)$ could be realized by an interaction of accelerated $(^3He\mu^-)$ upto 10 to 20 keV with e.g. a thin foil.

References

1) K. Nagamine: *Proc. Japan Academy*, **65**, 225 (1989).
2) K. Nagamine *et al.*: *Muon Catalyzed Fusion*, **5/6**, 371 (1991).
3) K. Nagamine *et al.*: preprint (1991); K. Nagamine: in Proc. 3rd Int. Conf. on Particle Nucl. Phys. Intersections (1991), in press.
4) G.M. Marshall *et al.*: *Hyperfine Interactions*, **65**, 1007 (1991).
5) M. Bubak *et al.*: JINR E4-87-464, Dubna (1987).

RIKEN Accel. Prog. Rep. **25** (1991)

# III-2-25. Search for Negatively Charged Isotopes Emitted from Solid Surfaces in Heavy Ion Reactions

R. Kadono, T. Matsuzaki, K. Ishida, A. Matsushita, and K. Nagamine

Unstable isotope beams with ultra-low emittance have potentially many applications to the investigation of solid surfaces. In particular, those isotopes which have shorter lifetime would provide an opportunity to study the dynamical property of the solid surface for which our current knowledge is still in a very preliminary stage. Unfortunately, so far conventional ISOL techniques are not successful to realize the low emittance beam ($<10^{-10}$ m·rad) for isotopes with short lifetime ($<10^{-4}$ s). Thus, we are motivated to search for the channels of isotope ion emission with thermal energy directly from the in-beam isotope production target: such a channel would reduce the time for the isotope extraction and post-ionization in the conventional system. Moreover, the investigation of such processes would certainly be helpful by itself to understand the dynamical property of the surface in which we are intrested.

It is established in the ion source techniques that negative ion sources have many advantages for the beam quality including the lower emittance over positive ion sources. For example, by using the metal surface where the transfer of electrons to atoms is greatly facilitated, one can obtain wide range of elements as negative ions. In order to examine the possibility to get a short-lived low emittance isotope beam in this negative ion channel we have investigated the thermal emission of the negatively charged isotopes produced near the surface of the in-beam metal target.

The present experiment was conducted at the SLOW beam channel in RIKEN Ring Cyclotron (RRC) facility. Direct emission of various stable and unstable isotope ions with thermal energy was investigated for the solid surfaces exposed to heavy ion (HI) beams provided by RRC (e. g. 135 MeV/u $^{14}N$ beam). These isotope ions were collected by an electrostatic lens and then separated on-line by the double-focusing mass spectrometer for the detection by using a multi channel plate (MCP). The specification of the SLOW beam channel is reported elsewhere.[1)]

It turned out that the vacuum level of the target chamber was deteriorated from $10^{-9}$ to $10^{-7}$ torr when the primary HI beam was present, which is probably due to the gas impurities dissociated from the inner walls of the system by the beam irradiation. Because of this problem the surface condition of the target was not in control for the present experiment, thereby the result should be regarded as very preliminary without any optimization of the target surface condition. We have searched Al, Be, and W targets at several temperatures (300～400 K for Al and Be, 900～1900K for W) with $^{14}N$ beam irradiation to find that there is no negative ion yield below the target mass with an upper limit of $5\times10^{-2}$ ions/s/nA ($N^{7+}$) as determined by the backgroud. We tentatively attribute this negative result to the contaminated target surface due to the deteriorated vacuum level, which might be improved by the further treatment (annealing) of the target chamber.

References

1) T. Matsuzaki, R. Kadono, K. Ishida, A. Matsushita, and K. Nagamine: Proc. 12th Int. Conf. on Electromagnetic Isotope Separators and Techniques Related to Their Applications, (EMIS-12, Sept. 2-6, 1991, Sendai, Japan), to be published.

RIKEN Accel. Prog. Rep. **25** (1991)

# III-2-26. $^{57}$Fe Mössbauer Studies of Single Crystal $YBa_2Cu_{3-x}Fe_xO_{7-y}$

T. Okada, K. Asai, Y. Kobayashi, R.N. Shelton,* and T. Matsumoto**

The effect of Fe substitution for Cu in $YBa_2Cu_{3-x}Fe_xO_{7-y}$ is interesting because the material is superconducting. In spite of a great number of $^{57}$Fe Mössbauer studies on the superconductors $YBa_2Cu_{3-x}Fe_xO_{7-y}$ using polycrystals,[1] the fundamental problems regarding the interpretation of the Mössbauer spectra, i.e., assignment of the site of Fe ions, still remain to be solved. In the present study, Mössbauer measurements using single crystals were made, which allows us to determine the directions of the principal axes and the asymmetry parameter $\eta$ of the electric field gradient (EFG) tensor in addition to its magnitude.

Single crystals of doped $YBa_2Cu_{3-x}{}^{57}Fe_xO_{7-y}$ were grown from nonstoichiometric melts of Y-Ba-Cu-Fe-O mixtures. The specimens with the concentrations of x=0.21 and 0.13 were subjected to $^{57}$Fe Mössbauer measurements at room temperature. The Mössbauer $\gamma$-rays were transmitted in the a-c plane with different angles $\theta\gamma$ from the c-axis. In this paper, the a-, b-, and c-axes refer to the crystalline axes with the c-axis perpendicular to the Cu plane, and the x-, y-, and z-axes denote the principal axes of the EFG following the usual definition; $|V_{zz}| \geq |V_{yy}| \geq |V_{xx}|$. The obtained Mössbauer spectra of the specimen with x=0.13 were almost the same as those with x=0.21.

The Mössbauer spectra of the single crystal with x=0.21 are shown in Fig. 1. The relative intensities of the absorption lines change systematically depending on the angle $\theta\gamma$. All the spectra can be well analyzed with four asymmetric doublets, named A, B, C, and D. Their quadrupole splittings are 2.0, 1.6, 1.3, and 0.5 mm/s, respectively. The intensity ratio of these four doublets is much different from that for polycrystalline samples, i.e., the intensity of A is markedly larger compared to the previous one in polycrystals.[1]

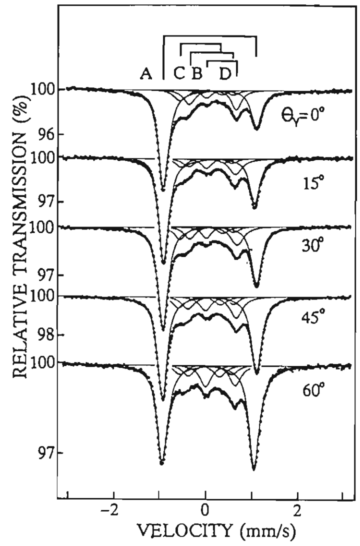


Fig. 1. $^{57}$Fe Mössbauer spectra for single crystalline $YBa_2Cu_{3-x}Fe_xO_{7-y}$ with x=0.21. The $\gamma$-rays are transmitted in the a-c plane with different angle $\theta\gamma$ from the c-axis.

The intensity ratios of the two resonance absorptions for the individual doublets are proportional to the function of $(3\cos_2\theta\gamma-1)/2$. Analysis of the observed angular dependences of the ratios for the doublets A, B, and C, showed that the principal axis with the largest field gradient is the c-axis ($V_{zz}<0$), and the values of $\eta$ are nearly 1, but the magnitude of the field gradient along the a-, or b-axis is comparable for three sites. On the other hand, for D the EFG is almost symmetric around the c-axis with the positive sign of $V_{zz}$.

The present results suggest that the majority of Fe ions occupy the Cu(1) sites in a $YBa_2Cu_{3-x}Fe_xO_{7-y}$ system.

References

1) T. Okada *et al.*: *Hyp. Int.*, **42**, 1231 (1988).

* Department of Physics, University of California-Davis, Davis, U.S.A.
** National Research Institute of Metals, Tokyo, Japan.

RIKEN Accel. Prog. Rep. **25** (1991)

# III-2-27. Epitaxial Regrowth of Kr-Bubbles in the Kr-Implanted and Annealed Aluminum

I. Hashimoto,* H. Yamaguchi,* E. Yagi, and M. Iwaki

Kr atoms were implanted at room temperature up to a dose of $1\times10^{16}$ $Kr^+$ ions/cm$^2$ at 50 keV into aluminum thin foils suitable for the transmission electron microscopy. It is known that at this dose a large portion of the Kr atoms precipitate into a solid phase. These precipitates are called solid Kr bubbles. With an electron microscope we examined, first, the diameter and the density of Kr-bubbles in the as-implanted specimens and also in the specimens which had been annealed at 673 K for 10 min after implantation. Furthermore, the temperature dependence of the lattice parameters of Al- and Kr-crystals in the as-implanted and the annealed specimens was investigated between 140 and 300 K by cooling them with a cooling stage equipped in the electron microscope.

The size distributions of Kr-bubbles are shown in Fig. 1. The distributions obtained from the bright field and the dark field images for the as-implanted specimens are nearly the same (Fig. 1(a)). This result indicates that in the as-implanted specimens almost all Kr atoms are in a solid phase at room temperature. In the annealed specimens (Fig. 1(b)), the bright field image gives a fairly wide range distribution of Kr-bubbles around 4.3 nm, while the dark field image gives a narrow one having approximately the same mean diameter of 2.7 nm as in the as-implanted specimens. This result indicates that a portion of the solid Kr-bubbles dissolve into a liquid phase on annealing.

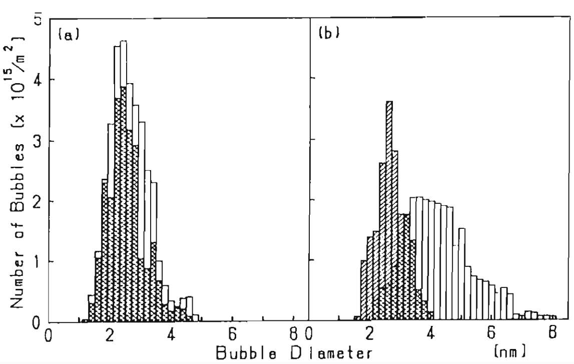


Fig. 1. Size distributions of Kr-bubbles. The bar graphs with the opened and the hatched areas represent the distributions obtained from the bright field and the dark field images, respectively, and the cross hatched area is the overlapping part in the distributions obtained from the both images. (a); in the as-implanted state, (b); after annealing at 673 K for 10 min.

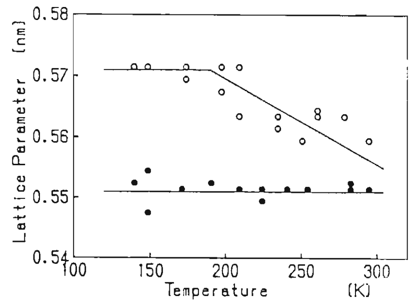


Fig. 2. A change in a lattice parameter of the Kr-crystals during cooling. Solid circles represent the parameter in the as-implanted specimens and open circles represent that in the annealed ones. The lines were drawn only to guide the eye.

A lattice parameter change during cooling is shown in Fig. 2. In the as-implanted specimen the lattice parameter is constant at 0.551 nm, while in the annealed one it changes from 0.560 to 0.571 nm during cooling from 300 to 190 K and becomes nearly constant below 190 K. From these results it can be said that in the as-implanted specimen almost all Kr-bubbles are in a solid phase, while in the annealed one the bubbles which dissolved into a liquid phase on annealing recrystallize epitaxially with decreasing temperature. More detailed experiments at temperatures lower than 140 K are now in progress.

* Faculty of Science, Science University of Tokyo.

RIKEN Accel. Prog. Rep. **25** (1991)

# III-2-28. Annealing Behavior of Kr Atoms Implanted into Aluminum

E. Yagi

It has been demonstrated that heavy inert gas atoms (Ar, Kr,and Xe) implanted into metals at ambient temperature precipitate into a solid phase (solid inert gas bubbles) at high implantation doses, and that they have an epitaxial face-centered cubic (fcc) structure in fcc matrices.[1-3] The growth of such bubbles has been extensively studied mainly by the transmission electron microscopy and by an X-ray diffraction method. Since these methods are sensitive to bubbles greater than a certain minimum size, they are more effective to the study on bubble growth rather than that on nucleation. On the other hand, a channeling method is useful to study phenomena such as nucleation, because it provides direct information on the lattice location of implanted atoms.

In previous studies on Kr-implanted aluminum we observed that at implantation doses lower than $2\times10^{15}$ Kr/cm$^2$ the Kr atoms are distributed over random (R), substitutional (S), tetrahedral (T) and octahedral (O) sites.[4-7] The R-site occupancy was ascribed to the Kr atoms in the Kr precipitates. The T- and O- site occupancies were interpreted to result from the fact that the Kr atoms were displaced to T- and O-sites by trapping 4 and 6 vacancies, respectively, and that these Kr-vacancy complexes acted as nucleation centers for the precipitation of Kr atoms.

In the present study, the annealing behavior of such complexes was investigated on the $1\times10^{15}$ Kr/cm$^2$-implanted specimen by the channeling method using a 1 MeV $He^+$ beam as in the previous experiments.[4-7]

Figure 1 shows the change of the fraction $f^{\langle hkl\rangle}$ for an ⟨hkl⟩ channel on annealing;

$$f^{\langle hkl\rangle}=\frac{1-\chi_0{}^{Kr\langle hkl\rangle}}{1-\chi_{min}{}^{Al\langle hkl\rangle}}, \qquad (1)$$

where $\chi_{min}{}^{Al\langle hkl\rangle}$ and $\chi_0{}^{Kr\langle hkl\rangle}$ represent the yields of $He^+$ ions backscattered by Al and Kr atoms, respectively, for the parallel incidence to the ⟨hkl⟩ channel. The value of $f^{\langle hkl\rangle}$ often used as the measure of the fraction of Kr atoms shadowed by the ⟨hkl⟩ Al atomic rows. From the channeling angular profiles the fractions of various site occupancies of Kr atoms after annealing at 371 K were estimated to be 62-63 % at R, 13-14 % at S, 3-4 % at T and 20-22 % at O-sites. If the Kr atoms are distributed over only R-, S-, T- and O-sites, $f^{\langle 111\rangle}$ should be greater than $f^{\langle 110\rangle}$. Upon annealing at temperatures higher than 423 K this relation reversed, indicating the change in configurations of Kr-vacancy complexes. After annealing at 593 K each of the ⟨100⟩, ⟨110⟩ and ⟨111⟩ Kr-profiles exhibited a simple dip with the same $f^{\langle hkl\rangle}$ value of 0.2. This result indicates that 80 % of Kr atoms are located at R- and 20 % at S-sites. This fraction of the S-site occupancy is larger than that in the 371 K-annealed specimen.

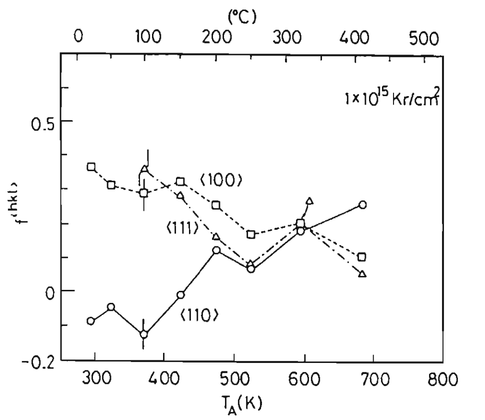


Fig. 1. The change of the fraction $f^{\langle hkl\rangle}$ (eq. (1)) with the annealing temperature.

From these results it is concluded that the T- and O-configurations become unstable at temperatures between 380 and 470 K to change to complexes of different configurations, and on annealing at 593 K they are decomposed completely to isolated Kr atoms (S-sites) and vacancies, the latter of which are annealed out.[8]

References

1) A. vom Felde, J. Fink, Th. Müller-Heinzerling, J. Plüger, B. Scheerer, G. Linker, and D. Kaletta: *Phys. Rev. Lett.*, **53**, 922 (1984).
2) C. Templier, C. Jaouen, J. -P. Rivière, J. Delafond, and J. Grilhé: *C. R. Acad. Sci. Paris*, **299**, 613 (1984).
3) J. H. Evans and D. J. Mazey: *J. Phys.*, **F15**, L1 (1985).
4) E. Yagi: *Phys. Stat. Solidi*, **A104**, K13 (1987).
5) E. Yagi, M. Iwaki, K. Tanaka, I. Hashimoto, and H. Yamaguchi: *Nucl. Instrum. Methods*, **B33**, 724 (1988).
6) E. Yagi: *ibid*., **B39**, 68 (1989).
7) E. Yagi, I. Hashimoto, and H. Yamaguchi: *J. Nucl. Mater.*, **169**, 158 (1989).
8) E. Yagi: Fundamental Aspects of Inert Gases in Solids, ed. S. E. Donnelly and J. H. Evans, Plenum Press, New York and London (1991) (in press).

RIKEN Accel. Prog. Rep. **25** (1991)

# III-2-29. Implantation-Temperature Dependence of the Lattice Disorder Produced by the $Tb^+$-Implantation in $CaF_2$

K. Aono, M. Iwaki, and Y. Aoyagi

We have carried out a study of irradiation and impurity doping effects on $CaF_2$ in the ion implantation for various kinds of impurities.[1] The striking feature of the Eu-implantation was that the high degree of substitutionality (~50%) of the Eu atoms was achieved even for a dose of $1 \times 10^{16}$ Eu/cm$^2$ during the implantation at room temperature, without any post-implantation annealing. The channeling experiments on the specimen which was kept at room temperature for one year or three years after implantation indicated that some of the implanted-atoms in the region deeper than the depth of the maximum concentration had moved from random sites to substitutional sites during keeping at room temperature. This result was considered to suggest the epitaxial regrowth of the damaged region from the interior towords the surface.[1]

In the present study, the behavior of the damaged layers created by the implantation of Tb ions, which belong to the same rare earth group as Eu, in $CaF_2$ was investigated by the Rutherford backscattering/channeling technique and by the measurements of luminessence during implantation.

The Tb-implantation was performed with a dose of $10^{16}$ ions/cm$^2$ at 100 keV in the random direction at a low (liq.$N_2$) or room temperature.[2] Channeling experiments were carried out at room temperature with a 1.5MeV $He^+$ beam.

Figure 1 shows random and ⟨111⟩ aligned spectra obtained with $CaF_2$ implanted at low (a) and room (b) temperatures. The random spectrum of $CaF_2$ obtaind from as-implanted specimen has almost the same shape as from unimplanted specimens. The $Tb^+$- implantation at a low temperature created a highly damaged layer at a dose of $1 \times 10^{16}$ Tb/cm$^2$ as shown in Fig. 1(a). In the case of the room temperature implantation, the spectrum shows recovery of the highly damaged layer as shown in Fig. 1(b).

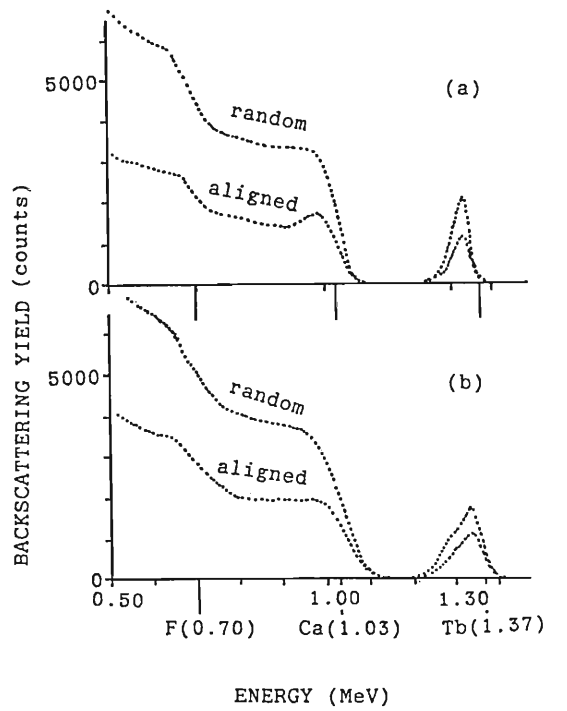


Fig. 1. Random and ⟨111⟩ aligned spectra obtained for $CaF_2$ implanted with $1 \times 10^{16}$ Tb ions/cm$^2$ at (a) low liq. $N_2$ and (b) room temperatures.

When the implantation temperature is higher, the Tb depth profile becomes broader and is shifted to a higher energy, i. e., towards the surface, as shown in Fig.1. These results suggest that the Tb atoms implanted in $CaF_2$ migrate to the surface, i. e., out-diffusion, during the ion-implantation at room temperature, and that the epitaxial growth from the interior towards the surface takes place.

References

1) K. Aono, M. Iwaki, and S. Namba: *Nucl. Instrum. Methods*, **B46**, 220(1990).
2) K. Aono, M. Iwaki, and S. Namba: *RIKEN Accel. Prog. Rep.*, **23**, 67(1989).

# III-2-30. Development of Nuclear Track Microfilters

N. Nakanishi and S. Nakajima

In order to develope nuclear track microfilters of polycarbonate and polyimid, the most suitable conditions for the beam irradiation and chemical etching have been investigated.[1] These polymer films of the thickness of less than 20 $\mu$m were irradiated with Ar, Kr and Xe beams of energies around 1 MeV/u . After irradiation, the films are etched chemically to make latent tracks visible with a scanning electron microscope. Pore size is very sensitive to the etching conditions such as etching time, temperature of etchants and chemical composition. We concentrate to establish the relation between the etching time and pore size and its reproducibility because it is difficult to keep the chemical composition and temperature constant precisely. The effect of supersonic wave in the etching process was also examined.

Figure 1 shows the relation between the pore size and etching time under a condition of a certain temperature and chemical composition of an etchant. A very simple relation was observed. This relation was reproducible. It may be easy to control the etching time in order to specify the pore size. However, the etching time required was too long for the pore diameter larger than 0.5$\mu$m, and was too short for that smaller than 0.1$\mu$m. It will be necessary, therefore, to establish different conditions for temperature and chemical composition in order to treat polymers in the moderate etching time irrespective of the pore size.

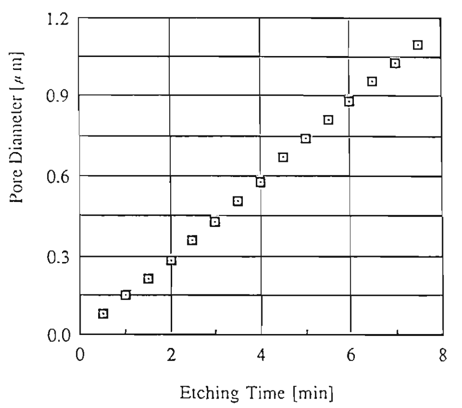


Fig. 1. Pore diameter vs. etching time. Polycabonate was etched in the absence of supersonic wave.

The effect of supersonic wave in the etching process was investigated on the pore size, which is shown in Fig. 2 as a function of the etching time. We can see from the figure that the pore size grows quadratically with the etching time.

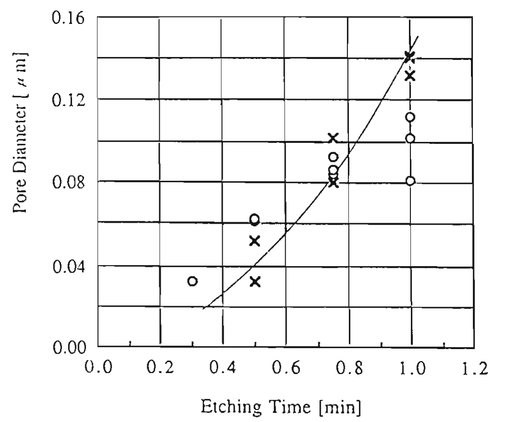


Fig. 2. Pore diameter vs. etching time. The effect of supersonic wave in the etching process is observed. × and ○ show measured points with and without supersonic wave, respectively. The solid line is a quadratic curve representing the case in the presence of supersonic wave.

References

1) N. Nakanishi *et al.*: *RIKEN Accel. Prog. Rep.*, **24**, 63(1990).

# III-3. Radiochemistry and Nuclear Chemistry

## 1. Time-Differential Perturbed Angular Correlation (TDPAC) and Emission Mössbauer (EM) Studies on $^{99}$Ru Arising from $^{99}$Rh in $Fe_3O_4$

Y. Ohkubo, Y. Kobayashi, K. Asai, T. Okada, and F. Ambe

In this period, we finished analyzing TDPAC and EM spectra of $^{99}$Ru in $Fe_3O_4$,[1] which is ferrimagnetic below $T_C = 858$ K. This oxide is an inverse spinel, in which one $Fe^{3+}$ ion in the chemical formula occupies the tetrahedral interstice (the A site) of cubically close packed oxygens, while remaining nominal $Fe^{3+}$ and $Fe^{2+}$ ions occupy the octahedral interstices (the B site).

In order to evaluate the mean value of the Lamor frequency, $\omega_L$, more precisely, we first determined the value of the quadrupole frequency, $\omega_Q$, by least-squares fitting the TDPAC $A_{22}G_{22}(t)$ data measured at 885 K, namely above the Curie temperature, with the expression: $A_{22}G_{22}(t) = A_{22}(1+4\cos 6\omega_Q t)/5$. The determined value of $\omega_Q$ at 885 K was $6.6\times10^5$ rad/s. Then, we analyzed the other $A_{22}G_{22}(t)$ data assuming that $\omega_Q$ is independent of temperature, $\omega_L$ has an apparent Gaussian distribution around $\omega_{L0}$ with a width of 5%, and the angle between the $H_{hf}$ and the principal axis of the electric field gradient is $\pi/2$. Figure 1 shows the temperature dependence of $H_{hf}$, calculated from the fitted parameter, $\omega_{L0}$, and the known magnetic moment of $^{99}$Ru(3/2+, $t_{1/2} = 20.5$ns), -0.284nm.[2] This temperature dependence is roughly characteristic of that of the magnetization.

The isomer shift obtained from the EM spectrum indicates that Ru exists either as $Ru^{2+}$ or $Ru^{3+}$. All the $Ru^{2+}$ and $Ru^{3+}$ compounds so far reported are of low-spin type.[3] Therefore, when Ru is divalent, it is considered to be diamagnetic. When Ru is trivalent, it has an unpaired electron. The magnetic moment of this unpaired d-electron produces the magnetic field at the nucleus, antiparallel to the magnetic moment, provided that this unpaired electron is localized. As described in Ref. 1, Ru is located at the B site and thus feels the $H_{STHF}$ due to the magnetic moments of $Fe^{3+}$ at the A sites. Figure 1 also shows the temperature dependence of the A site magnetization[4,5] (solid line) scaled to the measured $H_{hf}$ at 740 K. We assume that the temperature dependence of the $H_{STHF}$ due to the A-O-B supertransfer mechanism is the same as that of this A site magnetization. There is a clear difference between the measured $H_{hf}$ and the scaled A site magnetization. This difference (dashed line in Fig. 1) may be ascribed to the magnetic moment of $Ru^{3+}$ itself. If this speculation is correct, $Fe_3O_4$ ($^{99}$Ru) is the first example where $Ru^{3+}$ exhibits magnetism in its oxides.

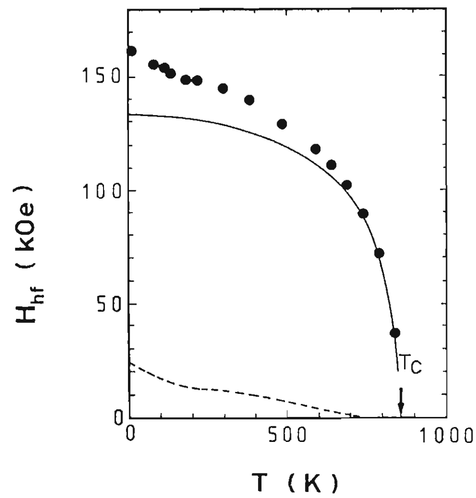


Fig. 1. Temperature dependence of $H_{hf}$. The solid points are the observed mean values of $H_{hf}$ at each temperature. The solid line is the scaled A site magnetization curve (Refs. 4 and 5) and the dashed line the difference between the observed $H_{hf}$ and the scaled A site magnetization.

References


1) Y. Ohkubo, Y. Kobayashi, K. Asai, T. Okada, and F. Ambe: *RIKEN Accel. Prog. Rep.*, **24**, 68 (1990).
2) E. Browne, J.M. Dairiki, R.E. Doebler, A.A. Shihab-Eldin, L.J. Jardine, J.K. Tuli, and A.B. Buyrn: Table of Isotopes, 7th ed., edited by C.M. Lederer and V.S. Shirley, Wiley, New York (1978).
3) F. A. Cotton and G. Wilkinson: Advanced Inorganic Chemistry, 3rd ed., Wiley, New York (1972).
4) T. Riste and L. Tenzer: *J. Phys. Chem. Solids*, **19**, 117 (1961).
5) T. Mizoguchi and M. Inoue: *J. Phys. Soc. Jpn.*, **21**, 1310 (1966).

RIKEN Accel. Prog. Rep. 25 (1991)

# III-3-2. Time-Differential $\gamma$-Ray Perturbed Angular Correlation (TDPAC) and Emission Mössbauer (EM) Studies on $^{99}Ru$ Arising from $^{99}Rh$ in $YBa_2Cu_3O_{7-x}$

Y. Ohkubo, Y. Kobayashi, K. Harasawa, S. Ambe, T. Okada, F. Ambe, S. Shibata, and K. Asai

This year we measured TDPAC and EM spectra for the $^{99}Ru$ 3/2+ level ($t_{1/2}$=20.5 ns) in an $YBa_2Cu_3O_{7-x}$ sample with $x \lesssim 0.2$ (YBCO7) and TDPAC spectra for one with $x \simeq 1$ (YBCO6), using $^{99}Rh$ ($t_{1/2}$=15 days) as the source nuclide. Since its ionic radius is close to that of $Cu^{2+}$, $^{99}Rh^{3+}$ is expected to occupy the Cu-1 or Cu-2 site of the matrices.

About 97% enriched $^{99}Ru$ was irradiated with 13-MeV protons available from the INS-SF cyclotron. A carrier-free solution containing $^{99}Rh^{3+}$ was obtained from the irradiated Ru target by radiochemical separation.[1] CuO powder was added to the solution in order to adsorb $^{99}Rh^{3+}$. Stoichiometric amounts of dried high-purity powders of $Y_2O_3$, $BaCO_3$, and CuO with $^{99}Rh$ were milled and heated in flowing oxygen to obtain YBCO7:$^{99}$Ru. A part of the prepared sample was heated in vacuum to obtain YBCO6:$^{99}$Rh. YBCO7 was superconducting at and below liquid nitrogen temperature, while YBCO6 was insulating. We used the same PAC spectrometer as described in a previous report.[2]

Measurements of TDPAC spectra were made in the temperature range from 10 to 1173 K for YBCO7:$^{99}$Ru and at 10 K, 80 K, and 293 K for YBCO6:$^{99}$Ru. An EM spectrum of YBCO7:$^{99}$Ru was taken at 5 K. The value of the isomer shift obtained from the EM spectrum indicates that $^{99}Ru$ exists as $Ru^{4+}$ in YBCO7. Figure 1 shows a part of the measured TDPAC (left) and their Fourier transformed (FT) spectra (right) of YBCO7:$^{99}$Ru, and Fig. 2 all of the measured TDPAC (left) and their FT spectra (right) of YBCO6:$^{99}$Ru. The temperature dependences of the frequency distributions show that the major hyperfine fields at $^{99}Ru$ are electric field gradients (EFGs). The TDPAC pattern of YBCO6:$^{99}$Ru at 10 K is rather smeared so that the frequency distribution is widespread. This is considered to be so because there is a hyperfine magnetic field at $^{99}Ru$ in addition to EFG. Alternatively, it is because of aftereffects of the EC decay, which are expected to be much more pronounced in the insulating YBCO6 than in the superconducting YBCO7. Figures 1 and 2 also

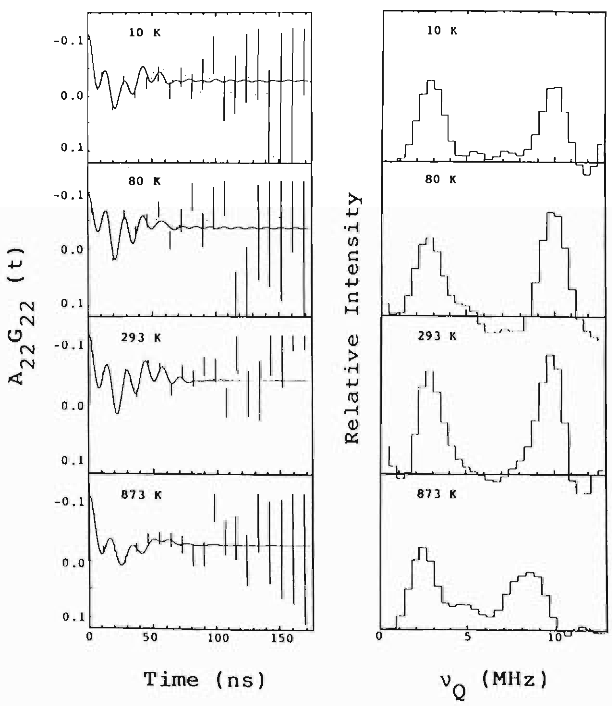


Fig. 1. TDPAC spectra of $^{99}Ru$ (3/2+) in $YBa_2Cu_3O_{7-x}$ ($x \lesssim 0.2$) measured at 10, 80, 293, and 873 K (left) and their frequency distributions (right).

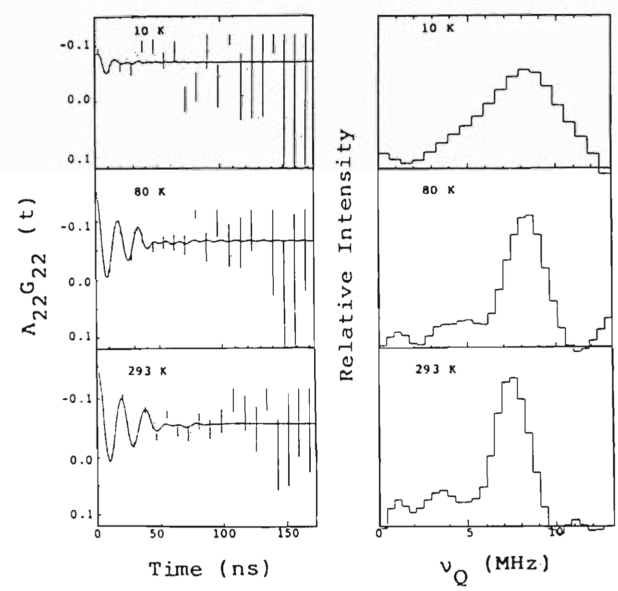


Fig. 2. TDPAC spectra of $^{99}Ru$ (3/2+) in $YBa_2Cu_3O_{7-x}$ ($x \simeq 1$) measured at 10, 80, and 293 K (left) and their frequency distributions (right).

show that there are two chemical states of Ru in YBCO7, but dominantly only one state of Ru in YBCO6.

References

1) D.F.C. Morris and M.A. Khan: *Radiochim. Acta*, **6**, 110 (1966).
2) Y. Ohkubo, Y. Kobayashi, K. Asai, Y. Yanagida, M. Iwamoto, and F. Ambe: *RIKEN Accel. Prog. Rep.*, **24**, 67 (1990).

RIKEN Accel. Prog. Rep. **25** (1991)

# III-3-3. $^{57}Fe$ Mössbauer Studies of $BiPbSr_2FeO_6$ Calcinated in $N_2$ Gas

Y. Kobayashi, T. Okada, F. Ambe, and K. Asai

Bi-based oxides, $Bi_2Sr_2Ca_{n-1}Cu_nO_y$ with n=1, 2, and 3 are well known high-Tc superconductors. Many studies on these compounds in which Cu ions are substituted by other transition metal ions have been performed in order to gain an insight into the mechanism of the superconductivity in the cuprates. The magnetic properties of these compounds are of great interest from the viewpoint of magnetic interactions in superconductivity. In a previous report,[1] $^{57}Fe$ Mössbauer and magnetic measurements of $BiPbSr_2FeO_6$ calcinated in air (sample I), being isostructural with the superconductor $Bi_2Sr_2CuO_6$, were made. It was found that the sample I was a weak-ferromagnet with $T_N$= 240 K. A large effect of the magnetic field cooling on the magnetization was observed. Fe ions were in the trivalent state and $^{57}Fe$ nuclei felt a hyperfine magnetic field of 50 T at low temperatures.

In this paper, the magnetic properties of $BiPbSr_2FeO_6$ calcinated at 815°C in $N_2$ gas (sample II) were studied with the $^{57}Fe$ Mössbauer spectroscopy and magnetization measurement. The X-ray powder analysis showed that the sample II was orthorhombic with the lattice parameters of 5.42, 5.51, and 23.20 Å The static magnetization of $BiPbSr_2FeO_6$ was measured between 4.2 and 325 K using a vibrating sample magnetometer and a SQUID susceptometer. The Mössbauer measurements of $^{57}Fe$ were carried out at various temperatures between 5 and 372 K.

The magnetization of the sample II increased monotonously with decreasing temperature. The Neel point was expected to be around 300 K from the results of the Mösbauer measurement, however no cusp in the magnetization could be observed at 300 K.

The Mössbauer spectra for the sample II at various temperatures are shown in Fig. 1. A large hyperfine magnetic filed ($H_{hf}$) is observed in addition to an electric field gradient at low temperatures. The values of IS (0.28 mm/s relative to an Fe foil) and $H_{hf}$ (50.0T) are typical for the $Fe^{3+}$ high-spin state. $H_{hf}$ decreases with increasing temperature, and disappears at about 300 K. It is shown that sample II is magnetically ordered below 300 K and is a weak-ferromagnet like the sample I. The magnetic property of the sample II has some distinct differences from that of the sample I on the following points:

1) The Neèl temperature is considerably higher ($T_N$=300 K).
2) No effect of magnetic field cooling appears.
3) The value of the magnetization was down to one-third of that of the sample I.

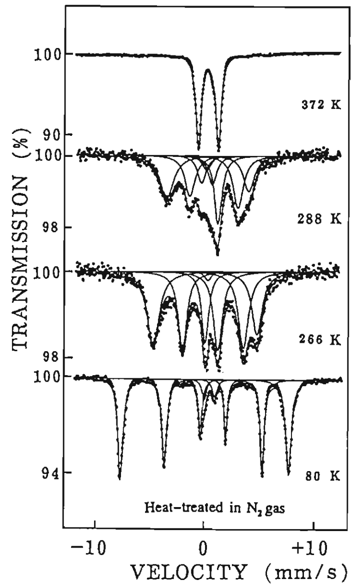


Fig. 1. $^{57}Fe$ Mösbauer spectra of $BiPbSr_2FeO_6$ calcinated in $N_2$ gas (sample II) at various temperatures.

References

1) T. Okada *et al.*: *RIKEN Accel. Prog. Rep.*, **24**, 60 (1990).

RIKEN Accel. Prog. Rep. 25 (1991)

# III-3-4. Angular-Momentum Effect in the Fusion Reaction of $^{141}Pr$ with $^{40}Ar$ Projectiles

H. Kusawake, K. Takesako, T. Saito, A. Yokoyama, M. Kiriu, N. Takahashi, H. Baba, Y. Ohkubo, and A. Shinohara

Heavy-ion-induced nuclear reactions are of much interest because of a large angular momentum brought in the reaction system. According to the Bass model,[1] cross sections for the fusion of heavy nuclei are predicted to be reciprocally proportional to the center-of-mass energy in the energy region higher than a specific value. This is interpreted as the appearance of a limiting angular momentum for the fusion. Fused medium-weight nuclei decay through either of the two competing channels, fission or evaporation-residue formation. Fission also follows non-fusion channels such as deep inelastic scattering and a few nucleon transfer. On the contrary, evaporation residues are definitely distinguishable from those formed in non-fusion reactions. It is thus expected that cross sections for the evaporation-residue formation will show the above relation with respect to energy more clearly than those for the fusion. This has not yet been established for reaction systems lighter than gold. In order to confirm the prediction, we measured the cross sections both for the evaporation-residue formation and fission by a nuclear-chemical method.

The reaction of a monoisotopic $^{141}Pr$ target with $^{40}Ar$ projectiles was studied at beam energies of 10, 25, and 95 MeV/nucleon. The target sandwiched by Al catchers was irradiated at the falling-ball irradiation facility[2] installed at the E3b course of the RIKEN Ring Cyclotron. An Al degrader with an appropriate thickness was inserted upstream of the target to adjust the projectile energy. Induced radioactivities were measured by non-destructive gamma-ray spectrometry with Ge detectors. Cross sections for the formation of gamma-emitting products were obtained, and mass-chain yields were then deduced on the basis of appropriate charge distributions. A reaction mechanism for the production of the nuclei concerned was considered from the recoil ranges measured with the aid of the catchers. Cross sections for the evaporation-residue formation and fission were obtained by integration of mass-chain yields with respect to the relevant mass region.

It was found that the reaction products obtained at low energies consisted of three components: evaporation residues, fission products, and non-fusion products. Although a similar feature was observed at medium energies, fusion and non-fusion components could not be clearly separated with each other. At the highest energy no evaporation residues were found and hence only an upper limit of the fusion cross section was obtained. The obtained cross sections for the fusion are plotted as a function of the reciprocal of center-of-mass energy together with those for the fission and evaporation-residue formation in Fig. 1. It is seen that the excitation function for the fusion has linear dependence on the reciprocal of energy as the Bass model predicts. The evaporation-residue formation shows the same dependence, which has already been found in the reaction of $^{197}Au$ with $^{12}C$ or $^{16}O$ ions.[4] We have further carried out an experiment at a 38-MeV/nucleon bombarding energy.

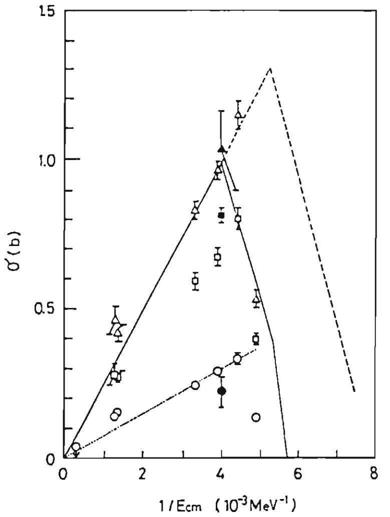


Fig. 1. Cross sections as a function of the reciprocal of center-of-mass energy. Triangles indicate those for the fusion, squares for the fission, and circles for the evaporation-residue formation. Solid marks are those obtained by Zank *et al.*[3] A solid curve shows that calculated by the Bass model. A dashed curve is calculated using a proximity potential.

References
1) R. Bass: Nuclear Reactions with Heavy Ions, Springer-Verlag, Berlin, p.283 (1980).
2) S. Ambe *et al.*: *Chem. Lett.*, **1991**, 149.
3) W.P. Zank *et al.*: *Phys. Rev. C*, **33**, 519 (1986).
4) S. Baba *et al.*: *Z. Phys.*, **A331**, 53 (1988).

RIKEN Accel. Prog. Rep. 25 (1991)

# III-3-5. Nuclear Reaction Products in the Interaction of Intermediate-Energy $^{14}N$, $^{15}N$, and $^{40}Ar$ Ions

M. Furukawa, A. Shinohara, E. Taniguchi, S. Kojima, T. Saito, K. Takesako, Y. Ohkubo, F. Ambe, and S. Shibata

The nuclear reactions induced by intermediate-energy heavy ions have been extensively studied. Further studies, however, are still required to elucidate the reaction mechanism in detail. Radiochemical technique is helpful to the studies of a wide variety of reaction systems. We have measured formation cross sections of radionuclides and mean recoil ranges in the interactions of V, Cu, Nb, and I with $^{40}Ar$ (59, 95 MeV/nucleon), $^{15}N$ (70 MeV/nucleon), and $^{14}N$ (135 MeV/nucleon) ions.

The targets were irradiated in the E3b course of RIKEN Ring Cyclotron. The targets were metal foils (10~30$\mu$m thick) and KI discs covered with catcher foils like mylar or aluminum to capture the recoil products. The irradiation conditions are shown in Table 1. $\gamma$-ray emitters in the targets were measured for three months after the bombardment. Mass distribution is obtained from the measured cross sections with the aid of a charge dispersion curve. The mean recoil ranges can be converted to the recoil energy by using the range-energy relationship.

Table 1. Irradiation conditions.

| Beam | $E_{lab}$ (Mev/nucleon) | Target | Duration (hour) | Charge (nC) |
|---|---|---|---|---|
| $^{40}Ar^{13+}$ | 95 | V | 0.936 | 31605 |
| | | Cu | 1.500 | 99640 |
| | | Nb | 1.439 | 79128 |
| $^{15}N^{7+}$ | 70 | V | 0.942 | 301459 |
| | | Cu | 1.008 | 416536 |
| | | Nb (S) | 0.113 | 54159 |
| | | Nb (L) | 1.624 | 97321 |
| | | I (S) | 0.169 | 144742 |
| | | I (L) | 1.554 | 94658 |
| $^{14}N^{7+}$ | 135 | V (S) | 0.137 | 61646 |
| | | V (L) | 1.536 | 161922 |
| | | Cu (S) | 0.078 | 40716 |
| | | Cu (L) | 1.731 | 239018 |
| | | Nb (S) | 0.049 | 21268 |
| | | Nb (L) | 1.664 | 173312 |
| | | I (S) | 0.107 | 20023 |
| | | I (L) | 2.580 | 150188 |
| $^{40}Ar^{13+}$ | 59 | V | 1.147 | 79208 |
| | | Cu | 1.680 | 110223 |
| | | Nb | 1.113 | 89984 |
| | | I (S) | 0.175 | 24254 |
| | | I (L) | 1.003 | 78519 |

(S) and (L) indicate the short and the long bombardments, respectively.

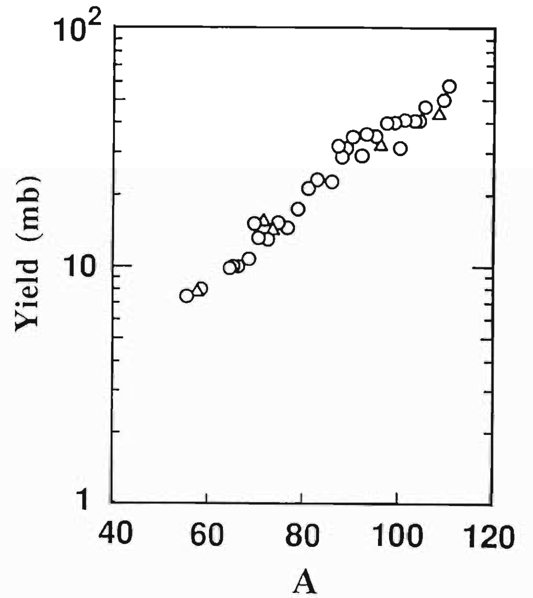


Fig. 1. Mass distribution in the interaction of $^{127}I$ with $^{14}N$ (135 MeV/nucleon). The data for the mass number less than 40 were rejected, because a KI disc was used as the target. The data for the mass number near the target are also excluded from the figure, since total yield of the given mass number cannot be determined accurately in that region. The different symbols indicate the fraction of measured yields. ($\triangle$, >40%; $\bigcirc$, $\leqq$ 40%)

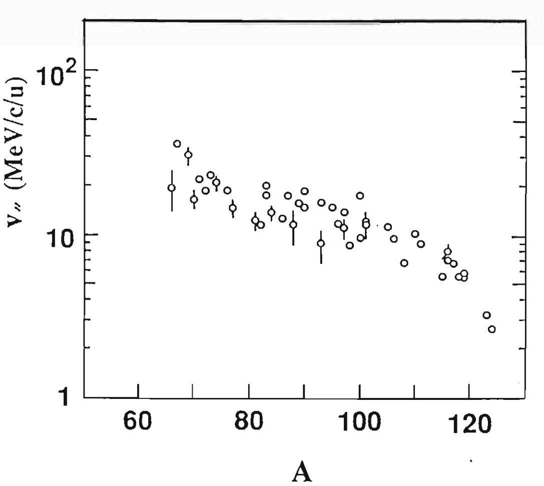


Fig. 2. The velocity distribution of the products in the interaction of $^{127}I$ with $^{14}N$ (135 MeV/nucleon).

As an example of the mass-yield curve, the result of $^{127}I + ^{14}N$ (135 MeV/nucleon) reaction is shown in Fig. 1, which can be compared with the results of high-energy proton or photon induced reactions. The velocity distribution of the products for the same reaction system obtained from the mean recoil ranges is shown in Fig. 2. Measurements of $^{10}Be$ and $^{26}Al$ in copper targets by the accelerator mass spectrometry (AMS) are in progress.

RIKEN Accel. Prog. Rep. 25 (1991)

# III-3-6. Preparation of Radioactive Multitracer Solutions from Ag Foils Irradiated with High-Energy Heavy Ions

S. Ambe, S.Y. Chen, Y. Ohkubo, Y. Kobayashi, M. Iwamoto, M. Yanokura, and F. Ambe

We have studied a convenient and reliable radiochemical procedure by which radioactive multitracer solutions free from both carriers and salts are prepared from Au, Ag, and Cu targets irradiated with a $^{12}C$, $^{14}N$, or $^{16}O$ beam. The preparative method of the multitracer solution from the Au target has been reported.[1-3] Here, we describe a separation procedure of a radioactive multitracer solution from the Ag target.[3]

Three foils (24 mm$\phi \times 100\ \mu$m) of Ag mounted in a 40 mm$\phi$ aluminum ball with a 20 mm$\phi$ piercing hole were irradiated with a 135 MeV/nucleon $^{12}C$ beam in the falling ball irradiation system installed in a beam course of RIKEN Ring Cyclotron. The beam intensity was about 100 nA and the irradiation time was several hours. The beam profile was roughly $10 \times 10$ mm.

The irradiated Ag foils (1.5g) were dissolved in 19 cm$^3$ of conc. $HNO_3$. After dilution with an equal volume of distilled water, 2 cm$^3$ of conc. HCl was added to the solution. After removal of AgCl by filtration, the filtrate was evaporated in a rotary vacuum evaporator. The residue was dissolved in dil. HCl to yield a multitracer solution. When AgCl formed again, it was filtered out.

The $\gamma$-ray spectra of the multitracer solution, precipitated AgCl, and solutions collected in traps of the evaporator were measured using pure Ge detectors. The spectra were analyzed with the BOB code[4] on a FACOM M780 computer at the Institute.

Figure 1 shows a $\gamma$-ray spectrum of the multitracer solution separated from the Ag target irradiated with $^{12}C$. The measurement was done 3 days after irradiation. The dominant peaks in the figure are ascribed to radioactive nuclides of the elements, Sc, Ga, As, Sr, Y, Zr, Nb, Mo, Tc, Ru, Rh, and Pd. No $\gamma$-rays due to the radioactive nuclides of the target element, Ag*, were detected in the solution. The $\gamma$-ray spectrum of the AgCl precipitate showed that it contains Br* along with Ag*. Minute fractions of Pd*, Zr*, and Rh* were also found in the AgCl precipitate, although most of them remained in the solution. A part of Tc* was found in the solution condensed in the trap of the evaporator. This is considered to show that a part of Tc* was distilled as $Tc_2O_7$ from the nitric acid solution.

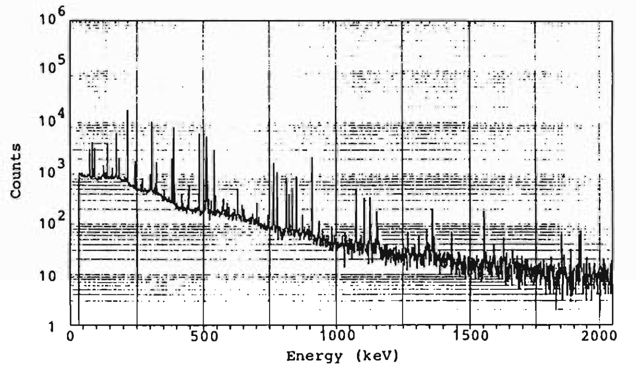


Fig. 1. The $\gamma$-ray spectrum of the multitracer solution measured 3 days after irradiation of the Ag target with a 135 MeV/nucleon $^{12}C$ beam.

In conclusion, the target element is selectively removed from the high-energy ion-irradiated Ag by precipitation as AgCl, yielding solutions containing a number of radioactive nuclides useful as multitracer solutions. It is to be noted that multitracer solutions containing neither carriers nor salts are obtained by the present radiochemical procedures. This is a great advantage in applying them to a variety of scientific studies.

References

1) S. Ambe, S. Y. Chen, Y. Ohkubo, Y. Kobayashi, M. Iwamoto, M. Yanokura, and F. Ambe: *RIKEN Accel. Prog. Rep.*, **24**, 73 (1990).
2) S. Ambe, S. Y. Chen, Y. Ohkubo, Y. Kobayashi, M. Iwamoto, M. Yanokura, and F. Ambe: *Chem. Lett.*, **1991**, 149.
3) S. Ambe, S. Y. Chen, Y. Ohkubo, Y. Kobayashi, M. Iwamoto, M. Yanokura, and F. Ambe: *Anal. Sci.*, (in press).
4) H. Baba, H. Okashita, S. Baba, T. Suzuki, H. Umezawa, and H. Natsume: *J. Nucl. Sci. Technol.*, **8**, 1227 (1972).

# III-3-7. Preparation of Radioactive Multitracer Solutions from Cu Foils Irradiated with High-Energy Heavy Ions

S. Ambe, S.Y. Chen, Y. Ohkubo, Y. Kobayashi, M. Iwamoto, M. Yanokura, and F. Ambe

The nuclear reactions of Cu with high-energy heavy ions result in production of useful radioactive nuclides lighter than those produced in Au and Ag targets. We report here a convenient and reliable radiochemical procedure by which radioactive multitracer solutions free from both carriers and salts are prepared by using Cu targets irradiated with a $^{14}N$ beam.[1)]

Three foils (24 mm$\phi$ $\times$100 $\mu$m) of Cu mounted in a 40 mm$\phi$ aluminum ball with a 20mm$\phi$ piercing hole were irradiated with a 135 MeV/nucleon $^{14}N$ beam in the falling ball irradiation system installed in a beam course of RIKEN Ring Cyclotron. The beam intensity was about 70 nA and the irradiation time was a few hours. The beam profile was roughly 10$\times$10 mm.

The irradiated Cu foils (1g) were dissolved in 15 cm$^3$ of conc. $HNO_3$. After neutralization with ammonia, $SO_2$ gas was introduced into the solution to reduce $Cu^{2+}$ to $Cu^+$. Subsequently, 1.9g of $NH_4SCN$ in 10 cm$^3$ of distilled water was added slowly to the solution. CuSCN precipitating immediately was filtered out. In order to remove $NH_4NO_3$ and $NH_4SCN$, the filtrate was heated in a rotary vacuum evaporator. After complete evaporation of water, $NH_4NO_3$ and $NH_4SCN$ were sublimated at about 300°C. The residue was dissolved in 6 mol dm$^{-3}$ HCl.

The $\gamma$-ray spectra of the multitracer solution and precipitated CuSCN were measured using pure Ge detectors. The spectra were analyzed with the BOB code[2)] on a FACOM M780 computer at the Institute.

Figure 1 shows a $\gamma$-ray spectrum of the multitracer solution separated from the Cu target irradiated with a $^{14}N$ beam. It was recorded 0.5 day after irradiation. The elements of radioactive nuclides found in the solution are Be, Mg, Na, Cl, K, Sc, Cr, Mn, Fe, Co, and Zn. No $\gamma$ rays due to the radionuclides of the target element, Cu*, were detected in the spectrum of the solution. This means that $Cu^{2+}$ ions were completely eliminated from the multitracer solution. No radioactive nuclides, other than Cu*, were found in the precipitate, suggesting that no metal ions coprecipitated with CuSCN.

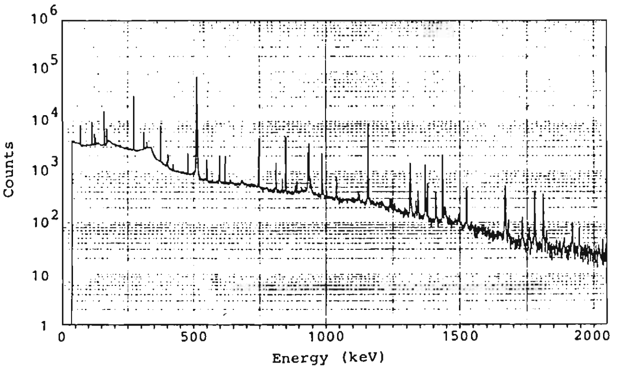


Fig. 1. The $\gamma$-ray spectrum of the multitracer solution measured 0.5 day after irradiation of the Cu target with a 135 MeV/nucleon 14N beam.

By the present procedure, the target element is selectively removed from high-energy ion-irradiated Cu by precipitation as CuSCN, yielding a solution containing a number of radioactive nuclides of the elements of low atomic number. The solutions separated from the Au,[1,3,4)] Ag,[1,5)] and Cu[1)] targets contain radioactive nuclides comprising over 50 elements.

References
1) S. Ambe, S. Y. Chen, Y. Ohkubo, Y. Kobayashi, M. Iwamoto, M. Yanokura, and F. Ambe: *Anal. Sci.*, (in press).
2) H. Baba, H. Okashita, S. Baba, T. Suzuki, H. Ume zawa, and H. Natsume: *J. Nucl. Sci. Tecnol.*, 8, 1227 (1972).
3) S. Ambe, S. Y. Chen, Y. Ohkubo, Y. Kobayashi, M. Iwamoto, M. Yanokura, and F. Ambe: *RIKEN Accel. Prog. Rep.*, **24**, 73 (1990).
4) S. Ambe, S. Y. Chen, Y. Ohkubo, Y. Kobayashi, M. Iwamoto, M. Yanokura, and F. Ambe: *Chem. Lett.*, **1991**, 149.
5) S. Ambe, S. Y. Chen, Y. Ohkubo, Y. Kobayashi, M. Iwamoto, M. Yanokura, and F. Ambe: This Report, p. 95.

RIKEN Accel. Prog. Rep. **25** (1991)

# III-3-8. Separation of Multitracers from Heavy-Ion Irradiated Targets by Heating under a Reduced Pressure

M. Iwamoto, Y. Kobayashi, S.Y. Chen, Y. Ohkubo, S. Ambe,
M. Yanokura, A.N. Garg, and F. Ambe

We continued in this period a series of experiments on the separation of multitracers from targets irradiated with heavy ions accelerated with RIKEN Ring Cyclotron by heating under a reduced pressure.[1,2] Target foils of Au, Ag and Cu were irradiated with 135 MeV/nucleon $^{12}C$, $^{14}N$, and $^{16}O$ ion beams by using the falling-ball irradiation system of RRC.[3,4] Thickness of the targets was 100 $\mu$m. The irradiation time was several hours and the beam intensity was 20-60 nA. The target foil was melted for 1 hour at a temperature slightly above the melting point; 1100 °C for Au and Cu, and 1000 °C for Ag, (m.p. of Au, 1064°C; Ag, 960°C; Cu, 1083°C), in a quartz tube equipped with a charcoal trap under a reduced pressure of about several Pa. After cooling, the cold finger and the inside wall of the tube were washed with hot water (70°C) and a dilute HCl solution successively to dissolve the radioactive nuclides evaporated from the foil and deposited. The $\gamma$-ray spectra of radioactive nuclides in the target before and after melting and those in the solutions were measured with a pure Ge-detector. The spectra were analyzed with the computer program BOB developed by Baba et al.[5] on the FACOM M780 computer of the institute. The results are summarized in Table 1.

Table 1. Elements for which radioactive nuclides were identifided in the Cu, Ag and Au targets and in the dilute HCl solutions of the deposits.

| Target | Before heating | Dil.HCl soln. of the deposit | Charcoal trap |
|---|---|---|---|
| Cu | Na,Mg,K,Sc,V,Cr, Mn,Co,Ni,Cu,Zn. | V,Mn,Co,Cu,Zn | - |
| Ag | Sc,V,Mn,Cu,Ga,As, Se,Br,Sr,Y,Zr,Tc,Ru, Rh,Pd,Ag | Sc,V,Mn,Cu,Ga,As, Se,Sr,Y,Zr,Tc,Ru. | Br |
| Au | Y,Zr,In,Te,Xe,Cs,Eu, Gd,Hf,Os,Ir,Pt,Au | Y,Cs,Eu,Gd,Hf,Pt | Xe |

References
1) M. Iwamoto, S. Ambe, S.Y. Chen, Y. Ohkubo, Y. Kobayashi, and F. Ambe: *RIKEN Accel. Prog. Rep.*, **24**, 72 (1990).
2) M. Iwamoto, Y. Kobayashi, S.Y. Chen, Y. Ohkubo, S. Ambe, M. Yanokura, A.N. Garg, and F. Ambe: *Anal. Sci.*, (in press).
3) M. Yanokura, Y. Ohkubo, S. Ambe, M. Iwamoto, and F. Ambe: *RIKEN Accel. Prog. Rep.*, **22**, 150 (1988).
4) S. Ambe, S.Y. Chen, Y. Ohkubo, Y. Kobayashi, M. Iwamoto, M. Yanokura, and F. Ambe: *Chem. Lett.*, **1991**, 149.
5) H. Baba, H. Okashita, S. Baba, T. Suzuki, H. Umezawa, and H. Natsume: *J. Nucl. Sci. Technol.*, 8, 1227 (1972).

RIKEN Accel. Prog. Rep. **25** (1991)

# III-3-9. Utilization of a Multitracer for Studies on the Ion Exchange Behavior of a Strongly Acidic Resin NAFION

J. Kawarada, T. Yaita, Y. Saito,* K. Kimura, S. Ambe, S.Y. Chen, Y. Ohkubo, M. Iwamoto, Y. Kobayashi, and F. Ambe

A radioactive multitracer solution,[1] in a carrier- and salt-free condition, prepared from a gold foil irradiated with 135 MeV / nucleon $^{14}N$ ions was used for the titled studies in a NAFION - HCl system. The NAFION-501 resin, manufactured by DuPont, is a perfluorinated polymer containing ~5 mmol $g^{-1}$ sulfonic acid group as shown below. Because of the strong acidity of the resin, a comparison of the exchange behavior with a common cation exchange resin attracts much attention.

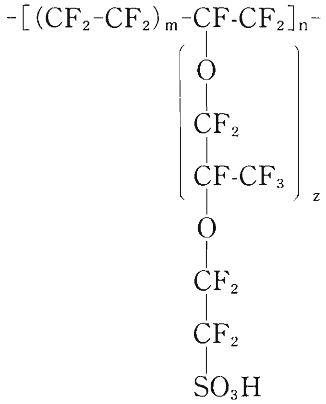


The resin, commercially available as a cylindrical shape of ca. 1mm$\phi$ × 1~3 mm L, was used as received. One milliliter of the multitracer solution and 3 g of the resin were taken into a small polyethylene bottle and the acidity of the system was adjusted to a certain molarity with hydrochloric acid by making the volume of the solution to 10ml. The contents of the bottle were shaken vigorously for 3 days at 25°C with an 8-shape mode shaker. Independent experiments for Co and Y showed that more than 90% of equilibrium was attained by the 3-days equilibration. After filtration, $\gamma$-ray spectrometry was carried out for both phases. The $\gamma$-ray spectra were analyzed on a FACOM M780 computer.

The distribution ratios (D) of Sc, V, Fe, Co, As, Rb, Y, Zr, Mo, Sb, Te, Ba, Eu, Gd, Tb, Tm, Yb, Lu, Hf, Ir, and Pt were so far obtaind in 0.02, 3, and 9M hydrochloric acid solutions. Log-log plottings of D versus the acidity show that the D values for alkaline earth and rare earth elements decrease smoothly with slopes of -2 and -3, respectively, with increasing acidity. Increase in D values at higher acidities, as commonly found for Dowex-50X4,[2] has not appeared up to a 9M hydrochloric acid solution.

References

1) S. Ambe, S.Y. Chen, Y. Ohkubo, Y. Kobayashi, M. Iwamoto, and F. Ambe: *RIKEN Accel. Prog. Rep.*, **24**, 73 (1990).
2) F. Nelson, T. Murase, and K.A. Kraus: *J. Chromatog.*, **13**, 503 (1964).

* Aoyama Gakuin University.

# III-3-10. Positron Annihilation Study on Defects in Undoped and Si-Doped LEC-GaAs Irradiated by Charged Particles

Y. Itoh, H. Murakami, T. Suzuki,* H. Yoshinaga, and R. Iwata**

To characterize the defects in a liquid encapsulated Czochralski (LEC)-GaAs, the defects were introduced into undoped and Si-doped crystals by the electron or proton irradiation. Their recovery by isochronal annealing from room temperature to 980 K was studied by the positron lifetime spectroscopy. Temperature dependence of the lifetime in these samples was also studied in a temperature range from 13 to 307 K.

An undoped (UD, carrier density at 300 K $C_d \doteqdot 2.03 \times 10^7 cm^{-3}$) or a Si-doped (SD, $Cd = 1.3 \times 10^{18} cm^{-3}$) n-type GaAs wafer of $20 \times 20 \times 0.6 mm^3$ was mounted on a water-cooled target-holder, and was irradiated with 3 MeV electrons up to a dose of $5 \times 10^{17} cm^{-2}$ in air (UDE- and SDE-samples) or with 15 MeV protons up to a dose of $10^{15}$ $cm^{-2}$ in helium gas (UDP- and SDP- samples). As a positron source, $^{48}V$ produced by the reaction of $^{48}Ti(p,n)^{48}V$ was used. The lifetimes were measured using a fast coincidence system with time resolution of 210 ps at the experimental positron window settings. As a total counts, $1 \times 10^6$ counts were accumulated in each time spectrum. The lifetime spectra were analyzed using the computer program POSITRONFIT.[1] In each spectrum, a component shorter than 100 ps, which is probably a result of the coincidence of two cascade gamma-rays from $^{48}V$, was eliminated. The standard deviation of fit was $\pm$ 1ps. Some samples were annealed isochronally in an argon atmosphere at temperatures from room temperature to 980 K at an interval of 50 K for 30 min. Positron annihilation measurements were performed at room temperature.

The lifetime $\tau$ in UD was independent of annealing temperature at $224 \pm 1$ ps as shown in Fig. 1. The lifetime in SD, 243 ps, which is longer than that in UD, also showed no variation with annealing temperature. The longer lifetime in SD probably means that there exist stable defects in SD, for example, Si and Ga-vacancy ($V_{Ga}$) pair $SiV_{Ga}$ as pointed out by Lee et al.[2] Figure 1 also shows the lifetime variations upon the isochronal annealing of the samples after proton irradiation. The lifetimes varied significantly between 224 and 255 ps. The lifetimes in UD and SD

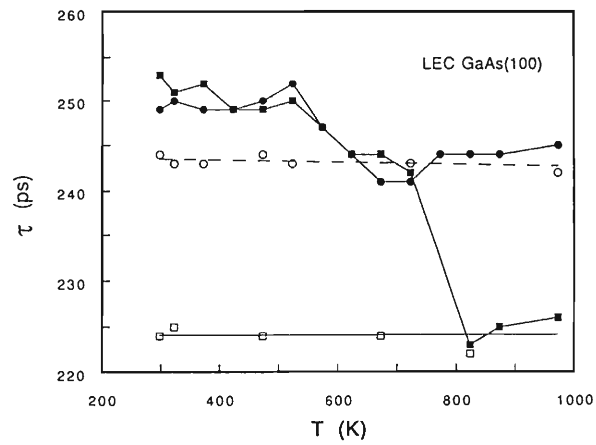


Fig. 1. Isochronal annealing of the positron lifetime in proton-irradiated GaAs; (■) undoped and (●) Si-doped samples. The results obtained before irradiation on undoped (□) and Si-doped (○) samples are also included.

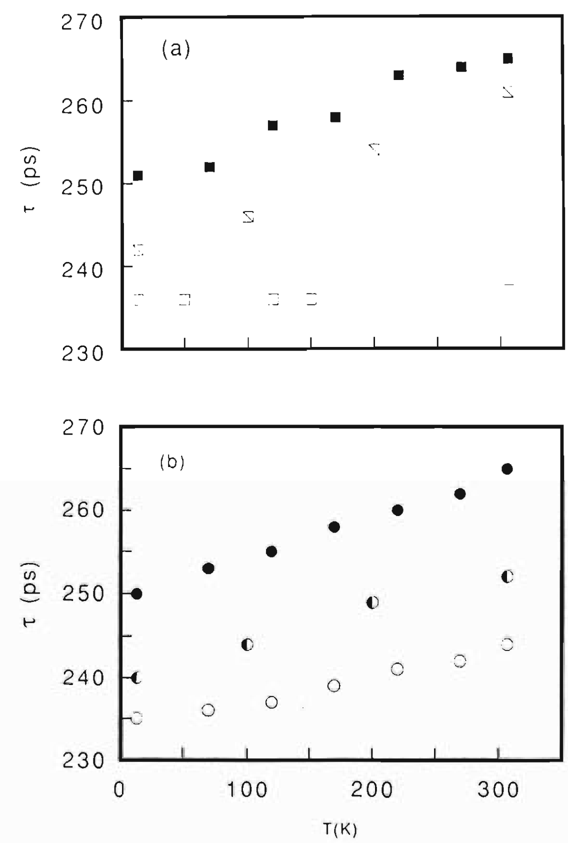


Fig. 2. Temperature dependence of positron lifetimes in undoped (a) and Si-doped (b) GaAs irradiated with protons(■,●) or electrons(◫,◐). The results obtained before irradiation on undoped (□) and Si-doped (○) samples are also included.

* National Laboratory for High Energy Physics.
** Tohoku University.

samples increased to 250-255 ps by the proton-irradiation (UDP and SDP) and decreased by 10 ps in the temperature range from 500K to 700 K. The lifetime in SDP recovered the value as obtained before irradiation, 243 ps, after annealing at 700 K, while the lifetime in UDP further decreased and also recovered the value in UD, 224 ps, on annealing above 800 K. The proton irradiation effects on both UD and SD were the same at least from the point of view of their annealing stage, and the defects introduced in both samples were annealed out at 800 K. Figures 2 (a) and (b) show the temperature dependence (13-307 K) of lifetime values in UD(□), UDE (⧅), and UDP(■) and in SD(○), SDE(◐), and SDP(●), respectively. Different samples were used in Figs. 1 and 2 but irradiation conditions were almost the same. The lifetimes in these samples, except UD, decreased with decreasing temperature. This temperature dependence of $\tau$ is in contrast to that of $\tau$ in silicon,[3] and may be explained by the lattice relaxation around vacancies as suggested by Dlubek et al.[4] The detailed configuration of the defects is under investigation.

References

1) P. Kirkegaard and M. Eldrup: *Computer Physics Communi.*, **7**, 401 (1974).
2) J. Lee, L. Wei, S. Tanigawa, and M. Kawabe: *J. Appl. Phys.*, **68**, 5571 (1990).
3) S. Makinen, H. Rajainmaki, and S. Linderoth: *Phys. Rev. B*, **42**, 166 (1990).
4) G. Dlubek, A. Dlubek, R. Krause, O. Brummer, K. Friedland, and R. Rentzsch: *Phys. Stat. Sol.*(*A*), **106**, 419 (1988).

RIKEN Accel. Prog. Rep. **25** (1991)

# III-3-11. Nitrided Carbon Foils as Long-Lived Charge Strippers

I. Sugai, M. Oyaizu,* M. Aratani, and M. Yanokura

We have developed various methods suited to prepare long-lived carbon stripper foils and improved them to give high reproducibility and creditability.[1-4] We reported last year[5] that the heavy ion beam sputtering (HIBS) could be used to prepare carbon stripper foils with long lifetimes. For this purpose, we used krypton and xenon ions. In that work the foil's lifetimes were strongly affected by preparation conditions, which also affected the amount of contaminants such as H, N and O in the foils.

The dependence of the foil lifetime upon the amount of contaminants introduced by the reactive ion beam sputtering of carbon using the gases $H_2$, $O_2$ or $N_2$, was investigated by comparing their lifetimes with those of foils made by the HIBS. With the use of ion beam sputtering of reactive nitrogen (IBSRN), an extraordinarily long lifetime was obtained.

The sputtering system is nearly identical to that described in Ref.1. The reactive gases were dried hydrogen, nitrogen or oxygen. In particular, when nitrogen was used, it was purified to 99.9999% with impurities less than 0.2ppm of oxygen and carbon monoxide, and less than 1 ppm carbon dioxide.

All foils used have surface densities of approximately $15\mu g/cm^2$, as measured by an electronic microbalance. The production method, however, is capable of producing foils in the range of $5\mu g/cm^2$ to $40\mu g/cm^2$.

The measurement of lifetimes of carbon foils was done by using the Van de Graaff accelerator at the Tokyo Institute of Technology. Typical beams consisted of singly charged 3.2MeV Ne at a flux of 3-4 $\mu$A, and had a diameter of 3.5mm. The pressure in the chamber was kept at about $1\times10^{-4}$Pa. The relative lifetime of a foil was taken as the total charge (integrated current) incident upon the foil that was neccessary to cause its rupture. Rupture was indicated by a sudden decrease in the current to a Faraday cup located downstreem from the foil.

In Fig. 1 are shown the results for foils produced by sputtering in pure gases and for commercially available carbon (CM) foils as a reference. Figure 1 shows clearly that the foils

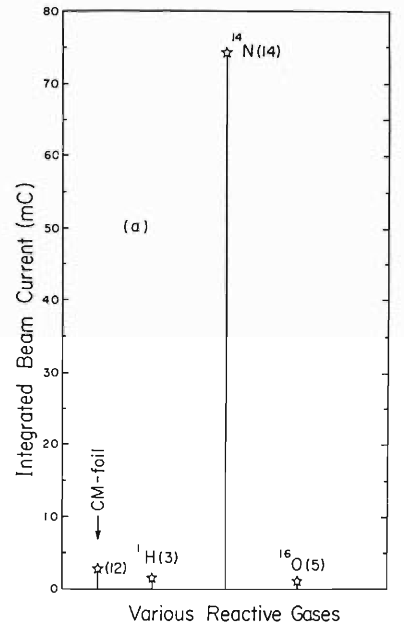


Fig. 1. Comparison of relative lifetimes of ion-sputtered foils when subjected to ion bombardment. Foil surface density was approximately 15$\mu$g/cm2;foils were made by sputtering carbon with pure gases (hydrogen, nitrogen, or oxygen). The average incident charge until rupture is plotted with the number of samples averaged given in parentheses beside each point.

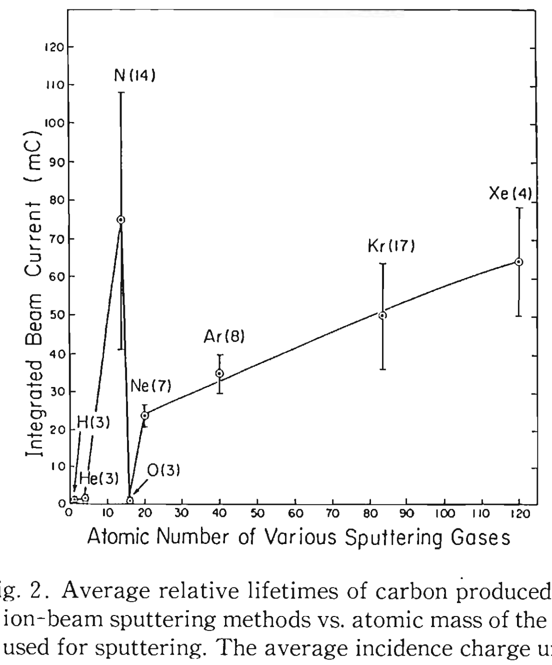


Fig. 2. Average relative lifetimes of carbon produced by ion-beam sputtering methods vs. atomic mass of the ion used for sputtering. The average incidence charge until rupture is plotted with the number of sample averaged given in parentheses beside each point.

* Institute for Nuclear Study, University of Tokyo.

made by the ion beam sputtering with reactive nitrogen(IBSRN) are superior to all of the other foils tested.

The lifetime of the best foil was 150mC which was about 60 times longer than that of the conventional carbon foils. Foils sputtered in the pure hydrogen or pure oxygen had shorter lifetimes than those of conventional carbon foils. It seems likely that admixtures of oxygen in carbon foils always cause reduction of the lifetime.

A comparison of the relative foil lifetimes obtained with the different sputtering ions is shown in Fig. 2, showing data for both reactive sputtering in this work (including the special case of IBSRN, sputtering with nitrogen) and the HIBS(the Krypton and Xenon data). Not only the lifetimes of the foils by the IBSRN are longer, but the manufacturing costs are less than the HIBS, since the expensive krypton and xenon gases are not used. Reliability and reproducibility of the IBSRN method appear to be greater than those of the CADAD[3] (Controlled Ac and DcArc Discharge) and HIBS methods.[4] In addition, the shrinkage rates of the IBSRN foils are the lowest among those examined.

References

1) I. Sugai and T. Hattori *et al.*: *Nucl. Instrum. Methods Phys. Res.*, **A265**, 376(1988).
2) I. Sugai and T. Hattori *et al.*: *ibid.*, **A236**, 576(1985).
3) I. Sugai and T. Hattori *et al.*: *ibid.*, **A282**, 164(1989).
4) I. Sugai and M. Aratani *et al.*: *ibid.*, to be submitted.
5) I. Sugai, M. Oyaizu, M. Aratani, and M. Yanokura: *RIKEN Accel. Prog. Rep.*, **24**, 80 (1990).

RIKEN Accel. Prog. Rep. 25 (1991)

# III-4. Radiation Chemistry and Radiation Biology

## 1. Irradiation Facility for Biological Experiments

T. Kanai, S. Minohara, M. Sudou, T. Kohno, E. Takada, F. Soga, K. Kawachi, and F. Yatagai

A new heavy ion irradiation course was designed and constructed for biological experiments at a Ring Cyclotron facility of RIKEN. Biological responses of culture cells, blood cells, mice or small animals for heavy ion irradiations are going to be examined by using this irradiation course. In these experiments, uniform irradiation fields over several cm in diameter are required. As shown in the Fig. 1, wobbler magnets and scatterer are used for the beam flattening. Uniform irradiation fields over 10cm in diameter was realized at the irradiation site in case of a Carbon 135MeV/nucleon beam. The range shifter in Fig. 1 is used for degrading the incident energy of the heavy ions so as to choose appropriate LET of the irradiation. The range modulator is used for spreading the sharp Bragg peak in the depth dose distribution to 2 or 3 cm width. A transmission parallel plate ionization chamber is used as the dose monitor.

Figure 2 shows a depth dose distribution in a Lucite absorber for a carbon 135 MeV/nucleon beam, which is measured by a small parallel plate ionization chamber. The absolute doses to the biological species are determined as follows. (1) The relative depth dose distribution is measured as in Fig. 2. (2) A particle fluence per monitor output is measured by a plastic scintillator for no absorber condition. (3) The heavy ion energy is estimated from the depth dose distribution. (4) Then the stopping power of the injected heavy ion is calculated from the estimated energy. (5) Then the dose per monitor output at the entrance position of the depth dose distribution is obtained by multiplying the stopping power by the measured number of the heavy ions.

Many biological experiments are now in progress with this irradiation course using Carbon 135MeV/nucleon or Ar 95MeV/nucleon beams.

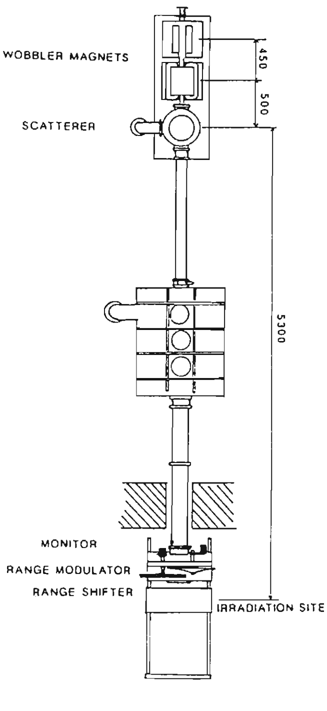


Fig. 1. Illustrative layout of the irradiation beam course for biological experiments.

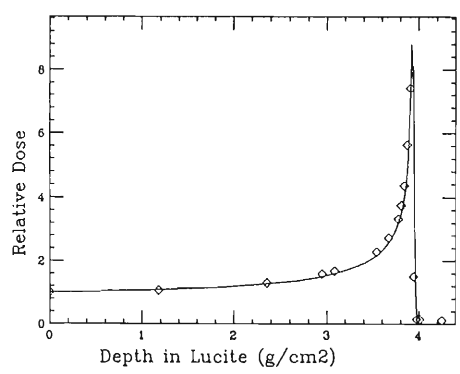


Fig. 2. Depth dose distribution of a 135 MeV/nucleon Carbon beam in a Lucite absorber.

# III-4-2. Heavy-Ion Irradiation of NaCl/DNA Films

K.F. Baverstock, S. McIntyre, M. Suzuki, K. Nakano, F. Yatagai, T. Kanai, I. Kaneko, and T. Takahashi

The influence of radiation quality on strand breakage in DNA that has been directly excited is an important issue in understanding the effects of ionizing radiation on living systems. Radiation quality can be characterized by a number of parameters but most commonly linear energy transfer (LET) is used. As far a strand breakage in DNA is concerned the current understanding is that as LET increases the probability of double strand breakage increases at the expense of that for single strand breakage. Early experiments using heavy ions in the range of up to 10 MeV per amu by Neary et al[1] seemed to indicate that this was not the case and that single and double strand breaks both increased with increasing LET keeping a constant ratio of about 20. The ratio observed at low LET is 10. The current program aims to extend the experiments performed by Neary to faster ions. Using Carbon, Nitrogen and Argon ions a range of LETs from about 20 keV per micron to more than 1000 keV per micron can be covered using the RRC.

In these experiments the DNA is irradiated in a dry salt (NaCl)/DNA target film formed on a glass substrate. The DNA is maintained in a state of almost full hydration by maintaining a relative humidity of 75 % during storage and irradiation. The DNA is in the form of a supercoiled plasmid and break yields are assessed using electrophoresis.

In the current reporting period two experiments (involving two machine sessions of two hours each) have been performed, one with Carbon ions, the other with Nitrogen ions. This was the first experience of using this beam and the results were disappointing. LET was varied using absorbers made of Lucite and three qualities were explored, namely 22, 50 and 100 keV per micron. Only the 50 keV/micron experiment gave reproducible results.

The second experiment with Nitrogen ion failed due to the lack of solubility of the samples after irradiation. This was the second experiment with this ion which has failed in a similar manner. The reasons for this are not clear.

Heavy ions present particular technical problems with the salt/DNA target used for these experiments. Before useful and reliable results can be obtained a number of technical problems must be resolved. The salt/DNA target has proved particularly valuable in other applications. For low LET radiations strand break yields in DNA in this target form are closely similar to those measured in DNA in a cellular environment, indicating that the DNA strand breakage in cells is probably due to the direct excitation.[2] More recently experiments using I-125 incorporated into the salt phase of the target have demonstrated the existence of an energy delocalization process, probably multiplasmon formation. This phenomenon may well be responsible for the observations of Neary et al.[1]

References

1) G.J. Neary, V.J. Horgan, D.A. Bance, and A. Stretch: *Int. J. Radiat. Biol.*, **22**, 525(1972).
2) K.F. Baverstock and S. Will: *ibid.*, **55**, 563(1989).

RIKEN Accel. Prog. Rep. **25** (1991)

# III-4-3. Induction of Chromosome Aberrations by Randomly Directed Accelerated Heavy Ions

T. Takatsuji, Y. Okumura,* T. Takahashi, F. Yatagai,
K. Nakano, M.S. Sasaki,** K. Komatsu,* and M. Yoshida*

An exchange type chromosome aberration is a main source of radiation cell killing and mutation. Therefore, the mechanism of aberration is a main question in radiation biology. One unknown and important point in this question is whether the aberration arises from the interaction of two radiation damages (interaction model) or from only one radiation damage.

Kellerer and Rossi developed the idea of the interaction model. They succeeded in explaining the dose-effect relationship of cell killing and chromosome aberration, and the LET dependence of these effects.[1,2] But Goodhead supported the idea that one radiation damage is sufficient to make lethal damages or mutation with an experimental result that very short range low energy photoelectrons of ultrasoft X-rays had relatively high efficieny.[3] But Zaider and Brenner clarified that the experimental result did not contradict the theory of Kellerer and Rossi.[4] The two models are very different, but both have no fatal contradiction to experimental results.

If the chromosome aberration induction depends on the spatial distribution of radiation damages, the interaction mechanism operates between the radiation damages to make chromosome aberrations. The distribution of the radiation damages when cells were exposed to randomly directed heavy ions (random irradiation) is very different from the one when exposed to uniformly directed ions (parallel irradiation).

We have prepared a sample holder that can rotate sample dishes of 30 mm diameter with an axis tilted against the beam axis. Living cells in a dish fixed on the rotated sample holder can be irradiated from random directions. We irradiated human peripheral blood lymphocytes with 135 MeV/nucleon $^{12}C$ ion beams using this sample holder at RIKEN Ring Cyclotron. Rotated samles show higher frequency of dicentric chromosomes than stationary samples (Fig. 1). The result shows that the interaction mechaism operates between radiation damages to induce dicentric chromosomes.

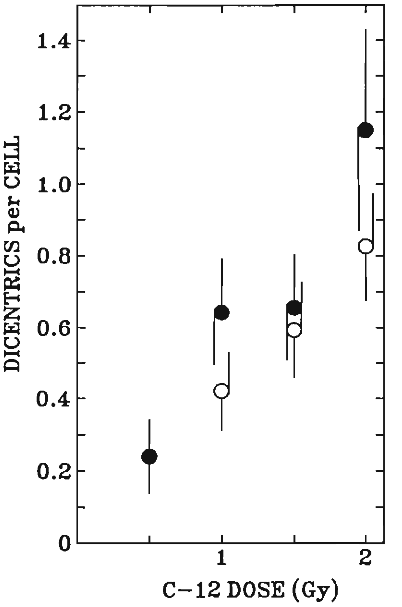


Fig. 1. Frequency of Dicentrics plotted against dose. Bar indicates the standard error of the mean. Closed circles:rotated samples. Open circles:stationary samples.

References

1) A.M. Kellerer and H.H. Rossi: *Current Topics in Radiat. Res. Quarterly,* 8, 85 (1972).
2) A.M. Kellerer and H.H. Rossi: *Radiat. Res.*, **75**, 471 (1978).
3) D.T. Godhead: *Int. J. Radiat. Biol.*, **32**, 43 (1977).
4) M. Zaider and D.J. Brenner: *Radiat. Res.,* **100**, 213 (1984).

* Atomic Disease Research Institute, Nagasaki University.
** Radiation Biology Center, Kyoto University.

RIKEN Accel. Prog. Rep. **25** (1991)

# III-4-4. Heavy-Ion-Induced Chromosome Fragmentation Studied by Premature Chromosome Condensation (PCC) in Syrian Golden Hamster Embryo Cells

M. Watanabe, M. Suzuki,* K. Suzuki,*
K. Nakano, and F. Yatagai

The technique of premature chromosome condensation (PCC) is very useful in detecting both radiation- and chemical-induced damages since the cell cycle delay after irradiation needs not to be considered. It may be a powerful method to compare effects of high and low linear energy transfer (LET) radiations which may produce difference in the cell cycle progression after irradiation. X-ray-induced damages have been investigated using the PCC technique by several investigators and their data suggested that the PCC technique is a very sensitive method for detecting chromatin damages in interphase cells. Limited reports, however, have been published concerning chromatin damages induced by high LET radiations. Bedford an Goodhead[1] reported the dose-response relationship of the chromatin break formation induced by alpha particles. They showed that the chromatin breaks increased linearly with absorbed dose in the case of both alpha particles and X-rays . However, the relative biological effectiveness (RBE), compared to $^{60}Co$ gamma ray, for alpha particles was 2.3 times larger than that for X-rays. Goodwin et al.[2] studied biological effects of Ne ions (LET= 182 keV/$\mu$m) and X-rays, and found that the amount of chromatin breaks by Ne ions was 1.5 times more than that by X-rays. In addition, although 90 % of the chromatin breaks induced by X-rays were rejoined within 8 hours after irradiation, only 50% of the chromatin breaks induced by Ne ions were rejoined. These data suggest that high LET radiations are more biologically effective in producing chromatin damages than low LET radiation. We previously reported that $^{14}N$ and $^{4}He$ ions were more effective in both cell killing and neoplastic cell transformation than gamma ray in SHE cells.[3]

In this study, we detected chromosome aberrations as chromatin breaks in $G_1/G_0$ interphase cells using the PCC technique. We assessed the RBE of the induction of chromatin breaks induced by heavy ions and examined the repair kinetics to qualitatively determine the difference in radiation damages between high and low LET radiation. SHE cells were irradiated with $^{14}N$ ions (95MeV) and $^{4}He$ ions (22MeV) generated by the cyclotron at the Institute of Physical and Chemical Research in Japan. Irradiated SHE cells were fused with mitotic Chinese hamster ovary cells by the polyethylene glycol mediated cell fusion to induce PCC.

The incidence of chromatin breaks was highest in cells irradiated with $^{14}N$ ions when it was compared at the same absorbed dose level. The RBE, compared to $^{137}Cs$ gamma ray, was 2.4 for $^{14}N$ ions (LET=530 keV/$\mu$m), 1.8 for $^{4}He$ ions with a 100$\mu$m Al absorber (LET=77keV/$\mu$m), and 1.4 for $^{4}He$ ions without the absorber (LET=36keV/$\mu$m), respectively. The PCC fragments induced by gamma ray were rejoined within 8 hours of the post-irradiation incubation. In the case of heavy ions, however, only 35 - 45% of the fragments were rejoined. These results suggest that there is a qualitative difference in the chromatin damage caused by high LET radiations and low LET radiations.

References

1) J.S. Bedford and D.T. Goodhead: *Int. J. Radait. Biol.*, **55**, 211 (1989).
2) E. Goodwin, E. Blakely, G. Ivery, and C. Tobias: *Adv. Space Res.*, **9**, 83, (1989).
3) M. Suzuki, M. Watanabe, K. Suzuki, K. Nakano, and I. Kaneko: *Radiat. Res.*, **120**, 468 (1989).

* Division of Radiation Biology, School of Medicine, Yokohama City University.

# III-4-5. Lethal Effects of Carbon Beams of RIKEN Ring Cyclotron on Cultured Mammalian Cells

H. Ohara, T. Kanai, K. Ando, K. Kasai, and K. Kawachi

In this study, we aimed to clarify the characteristics of the carbon beams available in RIKEN Ring Cyclotron for physics and biology. A main question is apparently concerned with the correlation between LET (linear energy transfer) as radiation quality and RBE (relative biological effectiveness) as its dependent biological effects for survivals of cultured mammaliancells. At RIKEN Ring Cyclotron, a carbon beam (135 MeV/n), of which range in water was 40 mm, has become available for the irradiation of biological materials with a uniform field of 10cm$\phi$. Different values of dose average LET were produced by changing the thickness of absorbers in the beam path. This range shifting system was able to provide 64 different LET values between 20 and 300 keV/$\mu$m. In this study we have tested several dose responses of Chinese hamster V-79 cells against the carbon beams with following LET values, namely 22.6, 74.2, 106.7, 125.5, 177.0, and 304 keV/$\mu$m, and in addition at the tail portion of unmodulated beams. The V-79 cells were cultured in an F10 medium with 10 % of fetal calf serum and antibiotics. Experimental cells were irradiated in flasks and assayed for cellular survivals in order to establish each survival curve for the estimation of RBE. For reference we have used helium ion beams of the NIRS cyclotron with LET of 18.6 keV/$\mu$m, of which biological effect was identified as the same as that of X-rays.

The experimental results indicated that the LET dependent change of survival curves was apparently pronounced as the LET of carbon beams was increased. The experimental curves showed the presence of a broader shoulder with a dull slope in a low LET (22.6 keV/$\mu$m) and tail regions, but they showed no shoulder with steep slopes in a high LET region. The minimums of slopes and shoulders were found in the LET of 125 keV/$\mu$m, while the curves for higher LET values (177 and 304 keV/$\mu$m) showed a restoration of decreased slope but no restoration of shoulder. Such a change of the survival response may suggest a local existence of a maximum peak of biological effect vs. linearly increasing LET. Existence of a local peak of the cellular lethality has been known by other studies in LBL.[1] Present results are generally in agreement with those of previous reports. One of the features of the present study was the variety of cell survival responses vs. carbon beams. The cellular RBE was varied from 1.3 - 4.0 depending upon different LET.

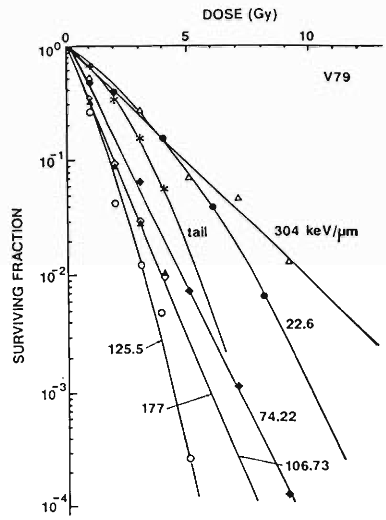


Fig. 1. The survival curves of Chinese hamster V-79 cultured cells irradiated by carbon beams (135 MeV/n) with different LET.

References
1) E. A. Blakely, F. Q. Ngo, S. T. Curtis, and C. A. Tobias: *Adv. Rad. Biol.,* **11**, 295 (1984).

# III-4-6. Effect of Carbon Iron Irradiaiton on the Cell Survival

H. Ito, S. Yamashita, S. Hashimoto, F. Yatagai, and T. Kanai

The effect of the heavy particle irradiation on the cell survival is different from that of the X-ray irradiation. In Japan, heavy particles will be applied to cancer patients in the near future. This study was performed to determine the effect of the carbon particle irradiation on cells in vitro.

A RUMG cell line which was established from a human serous ovarian cancer, was irradiated either with carbon particles from the RIKEN Ring Cyclotron or with 200KVp X-rays. The cells were maintained in an F10 medium with 10% fetal bovine serum in a 5% $CO_2$ incubator. The cells in a proliferative phase were irradiated with carbon particles of various linear energy transfers (LET). The irradiated cells were trypsinized and survival curves were etermined by the colony assay. The recovery between two equal split doses (6 hour interval) was also determined.

Figure 1 shows the survival curves at various LETs of carbon particles. The survival curve for the 200KVp X-ray irradiation was also shown. The Do values were increased and a shoulder appeared on the survival curve with the reduction of LETs. The relative biological effectiveness (RBE) at a 0.01 survivals were 1.7 at 20 keV/$\mu$m, 2.3 at 40 keV/$\mu$m and 2.8 at 80 keV/$\mu$m. When two eqaul doses were irradiated at a 6 hour interval with 200KVp -rays, recovery (recovery rate at 0.01 survivals: 1.8) was observed. In the case of the split irradiation using 40 keV/$\mu$m carbon particles, however, there was no recovery (Fig. 2). This result suggests that radiation damages made by 40keV/$\mu$m carbon particles are different from those by 200KVp X-rays and cannot be repaired.

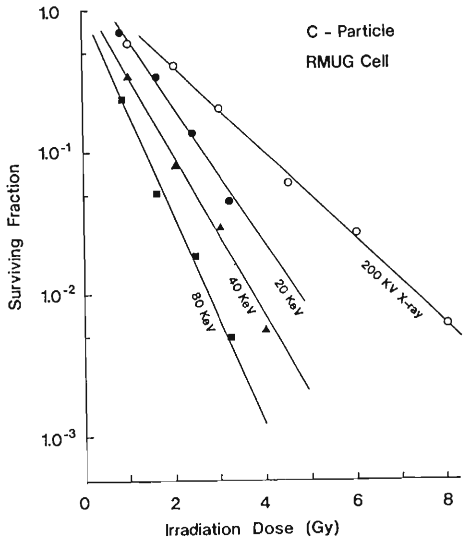


Fig. 1. Dose response curves of RMUG cells.

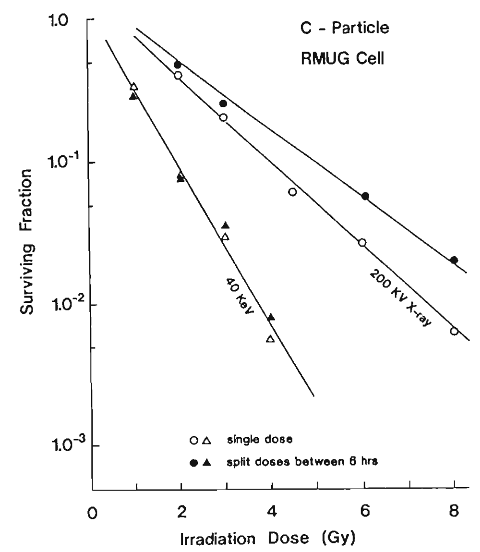


Fig. 2. Recovery at the 6 hour interval of two equal doses.

RIKEN Accel. Prog. Rep. **25** (1991)

# III-4-7. Sensitivity of XP Cells to Heavy Ions

F. Yatagai, K. Nakano, T. Takahashi, T. Kanai, and F. Hanaoka

Recent studies have revealed that Xeroderma pigmentosum (XP) cells are deficient in the repair processes of UV damages, probably nucleotide-excision pathway. Our interest in this research project is to make clear the possibility that DNA damages, reparable by the same process as that for UV lesions, are also produced by the heavy-ion irradiation. The XP cells involved in two different complementary groups, C and D, were selected for this study. The cells were exposed to carbon ions accelerated by the cyclotron to compare their sensitivity with that of normal human fibloblast cells (NB-1). Linear energy transfer (LET) of carbon ions was fixed to be 22.5 keV/$\mu$m at the position of cells attached on the inside surface of flask. As an average over two separate determinations (Fig. 1), XP-C showed a little higher sensitivity compared with the NB-1 case. In contrast, XP-D didn't show any significant difference from NB-1. Here, we have already confirmed no difference in the sensitivity for $\gamma$-rays among these cell lines (Fig. 2).

We plan further experiments to examine whether the observed difference is statistically significant or not.

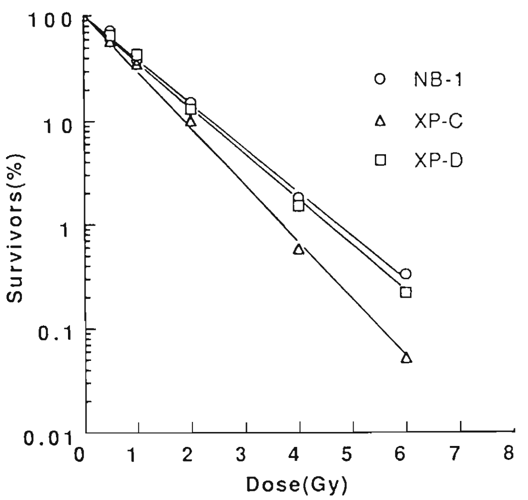


Fig. 1. Sensitivity for carbon ions (LET=22.5 keV/$\mu$m).

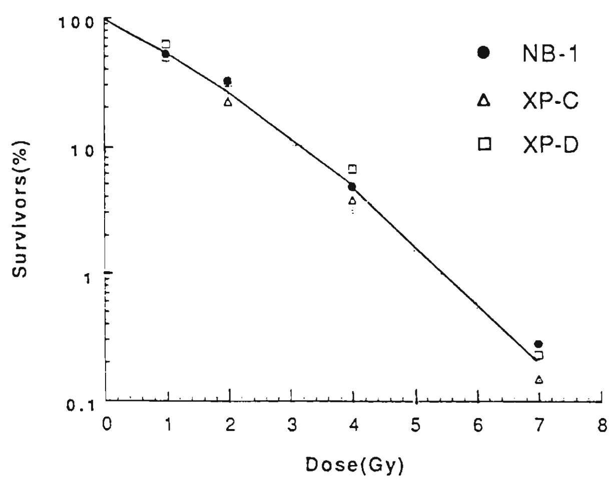


Fig. 2. Sensitivity for Cobalt-60 $\gamma$-rays.

# III-4-8. Studies on Induced Mutations by Ion Beam in Plants

H. Nakai, H. Watanabe, A. Tanaka, T. Asai,* and S. Kitayama

Knowledge about the Relative Biological Effectiveness (RBE) of various radiations is helpful for analyzing radiobiological effects in plants. The RBE of ion beams ($^{14}N^+$) for $M_1$ (the first generation after mutagen treatment) damages in the root length and seedling height relative to $\gamma$-rays was compared with that of thermal neutrons in this experiments using rice.

Dry seeds of rice, *Oryza sativa* L., a variety of Koshihikari, were exposed to an ion beam of $^{14}N$ (135 MeV/n) from the Ring Cyclotron with a dose of 0-300 Gy and were exposed to thermal neutrons for 0,1,2,3,4 and 6 hr in the heavy water facility of the Kyoto University Reactor operating at 5000KW. The flux of thermal neutrons was about $2.5 \times 10^9$ Nth/cm$^2$/sec. For comparison, the seeds were irradiated by $^{60}Co$ $\gamma$ rays with doses of 0,2,5,10,15,20,30,40,50 and 60 krad. Irradiated seeds were sown to be germinated in petri-dishes at room temperature. Two weeks later, the root length and seedling height were measured; the results were presented in Fig. 1. The RBE of thermal neutrons and ion beam for the root length and seedling height were calculated by the formula, $D_{50}$ of relevant radiation/ $D_{50}$ of $\gamma$ rays, where the $D_{50}$ means a dose which reduces the root length or seedling height to 50% of control. As shown in the figure, the RBE of thermal neutrons was 11.5 and 10.7, respectively, for the root length and seedling height.This result supports the data previously obtained.[1,2] The RBE of $^{14}N^+$ was found to be 2.2 and 1.8, respectively, for the root length and seedling height. It is noted that the RBE of ion beam ($^{14}N^+$) was significantly lower than that of thermal neutrons for the both traits. Analysis of mutations on the $M_2$ (second generation after mutagen treatment) will be conducted next year.

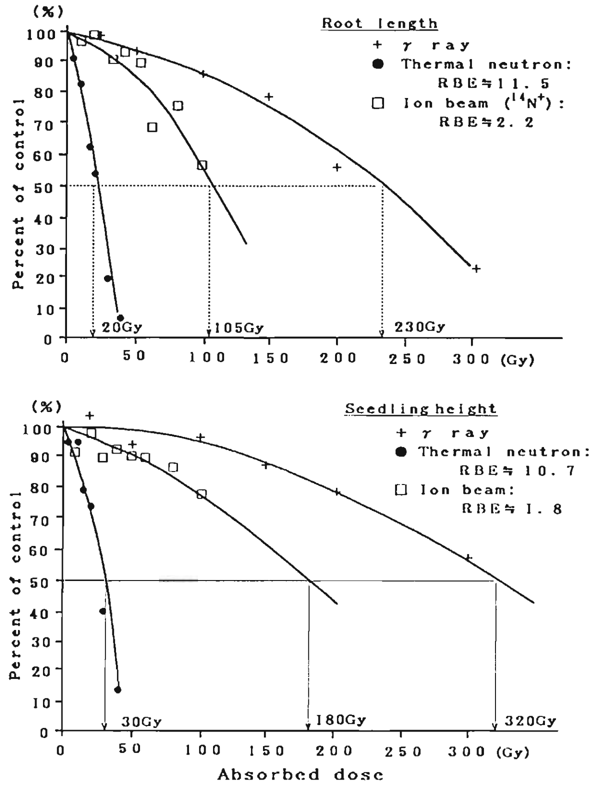


Fig. 1. RBE(Relative Biological Effectiveness) of ion bean($^{14}N^+$) and thermal neutrons for the M1 root length and seedling height in rice.

References

1) H. Nakai, M. Saito, and H. Yamagata: *Environmental and Experimental Bot.*, **20**, 191 (1980).
2) H. Nakai and M. Saito: *ibid.*, **25**, 385 (1985).

* Faculty of Agriculture, Shizuoka University.

RIKEN Accel. Prog. Rep. **25** (1991)

# III-4-9. Genetic Effects of Heavy Ion Irradiation in Maize and Soybean

O. Yatou, E. Amano,* and T. Takahashi

Genetic effects of the heavy ion irradiation were investigated with maize and soybean strains. This experiment was carried out as a preliminary experiment 1) to examine the potential of the heavy ion irradiation as mutagen, and 2) to evaluate the genetic effects of the exposure of organs to heavy ions in a space ship outside the earth.

In maize seeds heterozygous at *Yg2* locus (*Yg2/yg2*) and soybean seeds heterozygous at *Y11* locus (*Y11/y11*), mutagenic treatments induce visible mutant sectors on their leaves. The number of these sectors reflects the genetic effects of the treatments.

Maize seeds were irradiated with N (160MeV/n), Fe (555 or 825MeV/n) and U (919MeV/n) ions by the accelerator of Lawrence Berkeley Laboratory, Univ. of California. Dose response of the mutation frequencies in the Fe ion irradiation was detected at the dosage of higher than $10^3$ ions/cm$^2$ (Fig. 1). The lowest dosage to detect genetic effects of the ion irradiation is supposed to be $10^2$ to $10^3$ ions/cm$^2$. Both the irradiation with Fe and U ions had an identical effect. The irradiation dosage of N ions was too low in this experiment for analysis.

Soybean seeds were irradiated with N (133 MeV/n) ion by RIKEN Ring Cyclotron. The dosage was monitored by the reading of PPAC. The irradiation of $2.2\times10^7$ ions/cm$^2$ corresponeds to 1 Gy. Linear dosage responce in mutation frequencies was obtained (Fig. 2). The genetic effect of the irradiation was detected at the dosage as low as $10^5$ ions/cm$^2$.

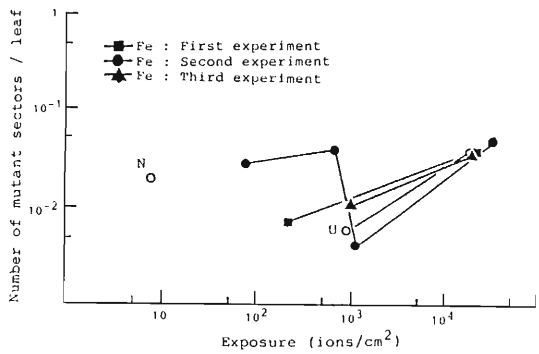


Fig. 1. Frequencies of mutant sectors on third leaves induced by the heavy ion irradiation in maize seeds (*Yg2/yg2*).

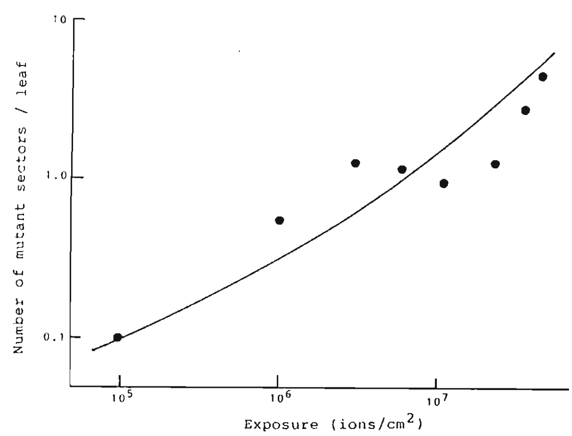


Fig. 2. Frequencies of mutant sectors on simple leaves induced by the N ion irradiation in soybean seeds (*Y11/y11*).

* FAO/IAEA, Vienna, Austria.

# III-4-10. Effects of Heavy Ions on the Development of Fish Embryos

K. Ijiri, K. Tao, K. Nakano, M. Suzuki,
and T. Takahashi

As one of the Space Shuttle experiments on the second mission of International Microgravity Laboratory (IML-2) scheduled in 1994, a project using the fish 'medaka' has been selected. The project aims to study whether the fish, medaka (*Oryzias latipes*), can carry out the mating behavior and lay eggs in space. When eggs are laid, we further intend to see the early development, i.e., all the processes from fertilization to hatching can take place normally or not under the microgravity. In such space biology experiments, radiation is probably one of the major environmental factors we have to always be aware of, in order to evaluate the microgravity effects justly.[1) ] Since cosmic radiations characteristically contain high-energy heavy ions (HZE), their effects should correctly be assessed. The present experiment was carried out to see the effects of heavy ions on the fish development.

The materials used in this study were embryos of the teleost fish, medaka. Fertilized eggs were collected after natural spawning between the 1-year-old adult fish, and were incubated at 25 °C for further development. Matui's normal table[2)] of this species was employed for the identification of the stages of their development.

Embryos were irradiated with the beams from RIKEN Ring Cyclotron. So far, N ions (135 MeV/nucleon) and Ar ions (about 88 MeV/nucleon) were employed. The beam dosimetry was carried out using an ionizing chamber. Then, the flux of the beam was calculated using the ratio of the count of a parallel-plate avalanche counter (PPAC) to that of the ionizing chamber. Twenty to forty embryos, each embryo with a diameter of about 1 mm, were put together in a small plastic dish filled with 3 mm depth of water along the beam axis. After irradiation, they were placed in glass vessels with stored tap water to develop at 25 °C.

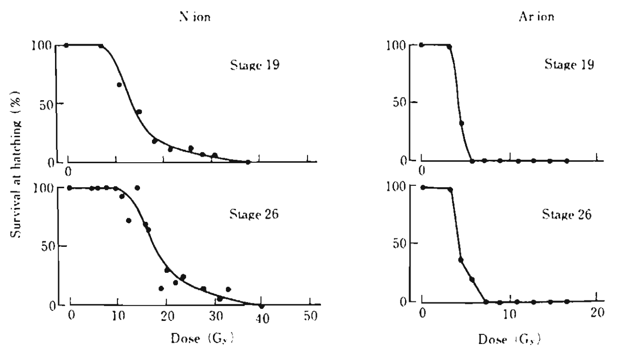


Fig. 1. Hatching rates of medaka (*Oryzias latipes*) embryos as a function of the dose of N ions (left panels) and Ar ions (right panels). The developmental stage of embryos at the time of irradiation is given in each panel.

Figure 1 shows the hatching rate of embryos as a function of the doses of N and Ar ions. The embryos were irradiated at stage 19 (optic bud formation) and stage 26 (start of pigmentation of eyes). When these preliminary data were compared with the hatching rate after the $\gamma$-ray irradiation, the relative biological effectiveness (RBE) relative to 137Cs $\gamma$ rays was obtained to be about 2 for N ions (LET=28,5 keV/$\mu$m), and 5 to 6 for Ar ions (LET=250 keV/$\mu$m).

References
1) K. Ijiri: Proc. 1st NASA-Japan Space Biology Workshop, p. 107 (1987).
2) T. Yamamoto: "Medaka (Killifish), Biology and Strains", Keigaku, Tokyo, p. 30 (1975).

# III-4-11. Therapeutic Effectiveness of Carbon Ions Against Experimental Tumors

K. Ando, S. Koike, T. Kanai, M. Kimoto, K. Kawachi, H. Ohara, and F. Yatagai

Accelerated carbons could penetrate human body and produce a Bragg-Peak at a given depth. For clinical use, the peak should be broadened to achieve the homogeneous distribution of dose within sizable tumors. Here we investigated and reported the therapeutic effectiveness of carbon-12 against a radioresistant fibrosarcoma growing in syngeneic mice. [Materials and Methods] Animals used here were C3 H/He male mice of 12 week-old. NFSa fibrosarcoma was transplanted into hind legs. Tumor was sized $7.5 \pm 0.5$ mm in diameter at the time of irradiation. Carbon-12 ions with kinetic energy of 135 MeV/nuclean were accelerated and provided by RIKEN Cyclotron. The maximum depth of beam penetration was approximately 4 cm in water. The Bragg-Peak was spread out by a ridge filter (Fig. 1). The design of the filter was based on biological data such as survivals of in vitro cultured V79 cells. Tumor-bearing mice received pentobarbital anesthesia and immobilized on an acrylic plate by a masking tape. Legs with tumors were placed in a doughnut-shaped radiation field of a 2.5 cm width. Five mice were used for each radiation dose and a total of 165 mice served in experiments including the radiation of Cs-137 $\gamma$ rays. Tumor sizes were measured by calipers every other day for up to 2 months. Calculated tumor volumes were plotted on a logarithmic scale, which provided the growth delay time. In some experiments, tumor control probabilities were employed as another endpoint where 10 mice were used for each radiation dose. Tumor recurrence was checked by palpation once a week for up to 120 days after irradiation. A tumor control rate for each dose was obtained and used to calculate the 50% tumor control radiation dose, i.e., $TCD_{50}$. [Results] Tumors were positioned at either 3 different places of the same spread-out carbon beams or unmodulated plateau. The tumor growth delay time at each position was plotted as a function of the absorbed dose. The relative biological effectiveness of carbon-beams (i.e., RBE) was calculated by comparing doubling doses between carbon beams and $\gamma$ rays. RBE of the unmodulated plateau was 1.4 and similar to that of RBE of the entrance position (ep), i.e., 1.5. The Spread-Out-Bragg-Peak showed larger RBEs than other positions; 1.8 for the proximal peak (pp) and 2.5 for the middle peak (mp). When tumor control probabilities were measured instead of the growth delay, both proximal and middle peaks showed identical RBEs, i.e., 2.2 (Fig. 2).

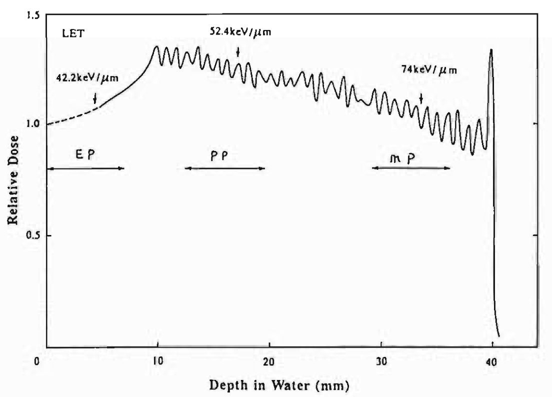


Fig. 1. Positions of tumors within the Spread-Out-Bragg-Peak. Leg-tumors in C3H mice were positioned at the entrance plateau (ep), proximal peak (pp) and middle peak (mp). A representative LET for each position was shown by an arrow.

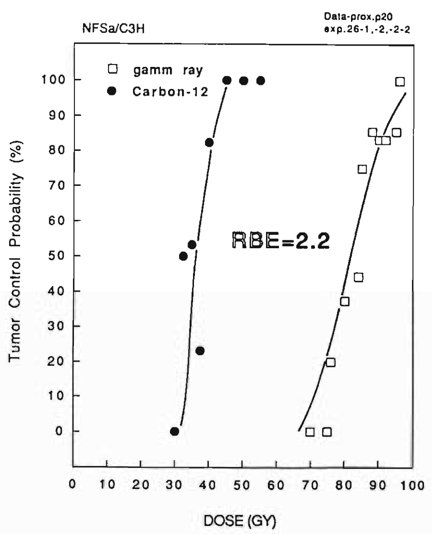


Fig. 2. Tumor control probabilities after the Carbon-12 and $\gamma$ ray irradiation. The NFSa fibrosarcomas growing in the right hind legs were irradiated by single doses of Carbon-12 (135MeV/amu, proximal peak in the Spread-Out-Bragg-Peak) and Cs-137 $\gamma$ rays. Tumor control probabilities were determined 120 days after irradiation. Each dose point consists of 10 mice. RBE was obtained by comparing 50% tumor control doses, i.e., $TCD_{50}$, between Carbon-12 and $\gamma$ rays.

RIKEN Accel. Prog. Rep. **25** (1991)

# III-4-12. High-Density Excitation Effect by the Heavy-Ion Irradiation: Track-Depth Resolved Dynamics of He Excimers in N-Ion Impinged Near-Liquid He

K. Kimura

A track scope which is composed of an imaging fiber-bundle, a cryostat, and a position sensitive photon-counter was developed to measure the depth-resolved luminescence spectra and its dynamics along the path of ion tracks.[1-3] Results inform us dynamical behavior of excited states, namely, the information of the primary processes induced by ions with regard to various parameters such as the track-depth, ionic energy, velocity, stopping power, excitation density, and so on. These measurements may be regarded as the measurements of detailed dynamical Bragg - curves for condensed matter and heavy ions.

Previously, we reported some new findings for a system of helium sample and $\alpha$ and N-ions: the second Bragg peak in the luminescence efficiency being ascribable to the charge exchange and direct forbidden transition; limiting of the excimer luminescences observed; enhancement of luminescence efficiency at the track termination.[1-3] At present, we report the dynamics for the formation and quenching of helium excimers in the environment of an extremely high-density excitation. Figure 1 implies that the formation process should be ascribed to only one process. Based on previous results, this process can be ascribed to reaction (1) which produces radiative excimers by reactions of nonradiative triplet excimers, **a**.

$$\mathbf{a}+\mathbf{a}+\mathrm{He} \longrightarrow \mathbf{d},\ \mathrm{D},\ \mathrm{J},\ \mathrm{H},\ \mathrm{A}+3\mathrm{He} \qquad (1)$$

$$\mathbf{d}, \longrightarrow \mathbf{b}+\text{photon} \quad \text{(an origin of luminescence)} \qquad (2)$$

Depth-resolved specific luminescence, dL/dx, has a peak dependent on helium density but the peak position is fixed at a given excitation density (See Fig. 2). The increasing part in dL/dx with increasing excitation density could be explained by reaction (1). To explain the decreasing part, a following incomplete three-body reaction caused by an extremely high density excitation was proposed based on the kinetics.

$$\mathbf{a}+\mathbf{a}+\mathbf{a} \longrightarrow \text{dissociative} \qquad (3)$$

Quenching of **d** by any reactions with **a** or other intermediates, which one may consider at first, was ruled out by kinetics.[4]

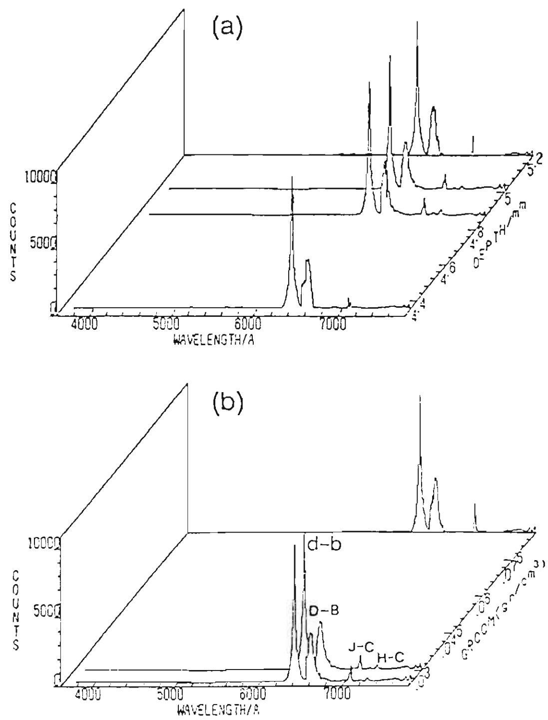


Fig. 1. Track-depth and density dependent luminescence spectra of N-ion irradiated helium illustrated in equal heights for d -b. a: at helium density of 0.02552 g/cm$^3$; b, track depths from 0.8 to 5.3mm. Intensities at wavelengths larger than 6500A are 10times enlarged. GRCCM stands for the helium density.

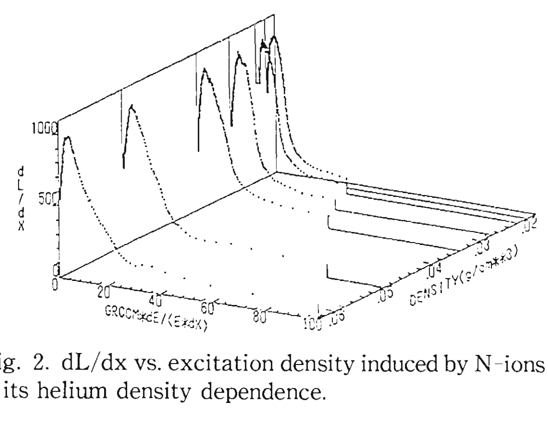


Fig. 2. dL/dx vs. excitation density induced by N-ions and its helium density dependence.

References

1) K. Kimura: *J. Chem. Phys.*, **84**, 2002 (1986).
2) K. Kimura: *ibid.*, p. 2010.
3) K. Kimura: *Nucl. Instrum. Methods*, **B53**, 301 (1991).
4) K. Kimura: *J. Chem. Phys.* (to be published).

RIKEN Accel. Prog. Rep. **25** (1991)

# III-4-13. A Technique of Emission Decay Measurement of 100 ps Resolution on Heavy-Ion Excitation: Effects of High-Density Excitation on the Auger-Luminescence of $BaF_2$

K. Kimura and H. Kumagai

A principal radiation effect of the heavy-ion irradiation is the high-density excitation. In order to study the dynamics of excited states formed in the track, we have developed a technique for fast luminescence measurements, and a single-ion hitting and single-photon counting technique( SIPC). Since ion-pulses of ps widths are too difficult to be realized at present, a single-ion hitting is very powerful in a view of its negligibly short pulse-width. Figure 1 shows FASD (a fast secondary electron detector) which is a part of an equipment and can give a fast timing pulse of the ion penetration. An ensemble of the equipment composed of FASD, MCP-photomultiplier, CFD, TAC, ADC, and a computer is essentially the same as previously reported.[1] A resolution was about 100ps at present, without a deconvolution.

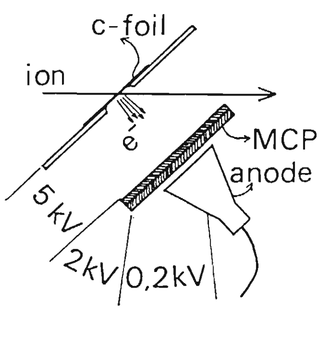


Fig. 1. FASD ( a fast secondary electron detector).

Recently, photo- or electron irradiated $BaF_2$ has been found to show two luminescence peaks at 2200A and 3100A and the former peak was assigned to the Auger-free luminescence due to the transition from a 2P electron of F to an inner shell vacancy of Ba, 5P, which was reviewed in Ref. 2. Decay measurements on the Auger-free luminescence with various ion irradiations were reported by us[1]. In this report, we show one of the recent results obtained by the decay analysis.

The decay curve of the Auger-free luminescence can be decomposed into double exponents, as shown in the following Table 1.

This shows that decay times are shortened with increasing LET, although the shortening is settled down with ions heavier than N-ions. The decay times reported with the electron irradiation were from 600 to 800 ps, but these values are between those of photon and $\alpha$-particle. Also, luminescence yields for the ion irradiation were much lower than that for photon. We propose the following model, tentatively. The exponential decay indicates that the decay cannot be explained by second order decay processes such as recombinations of the 5P vacancy with excited or ionic states. Since the high-density excitation produces free (or quasi-free ) electrons at high density around the Ba 5P vacancy, the Aurger-free luminescence should compete with transitions from the free electrons. This model is expressed by following equations.

Table 1. Decay times of Auger-free luminescences.

| | photon[3] | $\alpha$ | N-, Ar-, and Xe-ions |
|---|---|---|---|
| fast | 800ps | 450ps | 250ps |
| slow | — | 1100 | 820 |

All the ionic energies were 1.4MeV/amu.

$$\mathrm{Ba(5P)^5} + e_F \xrightarrow{k_1} \mathrm{Ba(5P)^6} + \text{photon} \qquad (1)$$

$$\mathrm{Ba(5P)^5} + e_{cb} \xrightarrow{k_2} \mathrm{Ba(5P)^6} \cdots\cdots\cdots \text{nonradiat.} \qquad (2)$$

where $e_F$ and $e_{cb}$ stand for electrons in F-2P orbitals and in conduction bands( perhaps high Rydberg states), respectively. The time-dependent luminescence can be expressed as,

$$I(t) = k_1[(5P)^5]\exp\{-(k_1+k_2[e_{cb}])t\} / (k_1+k_2[e_{cb}])$$

At an early stage where $[e_{cb}]$ is high, the luminescence decays exponentially with a rate constant of $(k_1+k_2\ [e_{cb}])$. After annihilation of a large number of $e_{cb}$ through recombinations with F atoms of a high concentration, the rate constant turns to be $k_1$ which is that of the Auger-free luminescence.

References

1) K. Kimura, T. Matsuyama, and H. Kumagai: *Radiat. Phys. Chem.*, **34**, 575 (1989).
2) M. Itoh, S. Kubata, J. Ruan, and S. Hashimoto: *Rev. Solid State Sci.*, **4**, 337 (1990).
3) M. Itoh, S. Hashimoto, S. Sakuragi, and S. Kubota: *Nucl. Instrum. Methods*, **A289**, 253 (1990).

RIKEN Accel. Prog. Rep. **25** (1991)

# III-5. Instrumentation

## 1. A New Gas-Target Technique for Isomer-Search with Use of a Gas-Filled Recoil Isotope Separator

K. Morita, Y. Gono, T. Murakami, A. Yoshida, A. Ferragut, and Y. Zhang

A new gas-target technique has been succesfully applied to the search for new isomers with use of a gas-filled recoil isotope separator.

A gas-filled type recoil separator, in general, has been used to collect isotopes, which are produced by nuclear reactions, with large efficiency and with short separation time for the spectroscopic study of unstable nuclei. Taking an advantage of the short separation time of the separator (typically a few 100 ns) we constructed a gas-filled recoil isotope separator at E1 experimental hall of the RIKEN Ring Cyclotron Facility, and performed delayed $\gamma$ ray measurements at the focal point of the separator to search for new isomers[1] using inverse-kinematic fusion reactions.

In the experiment searching for isomers with a solid target ($^{24}$Mg) and beam ($^{136}$Xe) combination we found as a byproduct that a buffer gas of the separator, nitrogen gas, works as a target for the nuclear reaction. A reasonable amount of $^{144}$Pm-isomer, which was produced by the reaction $^{136}$Xe($^{14}$N,6n)$^{144}$Pm, was collected at the focal plane of the separator simultaneously with the $^{152}$Dy-isomer produced by the reaction $^{136}$Xe($^{24}$Mg, 8n)$^{152}$Dy. Figure 1 shows an example of delayed $\gamma$ ray energy spectra obtained at the focal point of the separator for the $^{136}$Xe(Ei=7MeV/u) induced reaction with a $^{24}$Mg target and with nitrogen buffer gas. Marked peaks in the figure are those from $^{144}$Pm-isomer and the others are mainly from $^{152}$Dy-isomers.

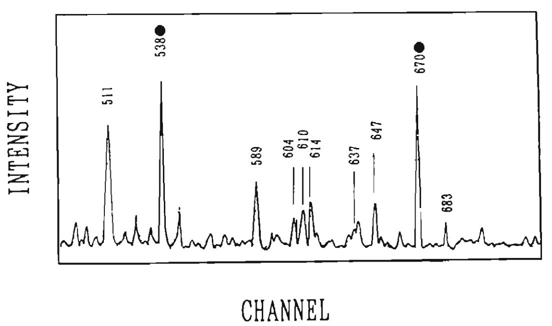


Fig. 1. Energy Spectrum of the delayed $\gamma$ rays measured at the focal point of the gas-filled recoil isotope separator. Marked peaks correspond to decays of the isomers produced through a $^{136}$Xe($^{14}$N,6n)$^{144}$Pm reaction. Energies are also indicated in the figure in keV.

In the gas-target case, the target region is ranging widely and is not well defined as in the case of a solid target. The flight time distributes widely depending on the place where the isomers are produced. However a foil is placed at 1 m upstream of a catcher foil to limit the gas region so that only $\gamma$-ray from isomers can be detected at the catcher position. Therefore, this method is applicable to the search for isomers of shorter lifetimes (less than 50 ns) with large efficiency comparing with the solid target's case.

This new gas-target thechnique enables us to use unique and a variety of beam-target combinations which are difficult to realize by using solid targets. For example, it is not easy to find a proper solid-target and stable beam combination to form a compound nucleus $^{176}$Hf, while it is easy to find a $^{40}$Ar+$^{136}$Xe reaction if a gas-target is available.

References

1) T. Murakami, Y. Gono, M. Oshima, H. Kusakari, K. Morita, A. Yoshida, and H. Kumagai: *J. Phys. Soc. Jpn.*, **60**, 1424 (1990).

# III-5-2. Refractory Element Production with GARIS/IGISOL

M. Koizumi, T. Horiguchi, A. Iivonen, T. Inamura,
T. Ishizuka, H. Katsuragawa, S. Matsuki, K. Morita,
T. Murayama, I. Nakamura, M. Nakaoka, K. Shimomura,
T. Shinozuka, I. Sugai, M. Takami, Y. Tagishi, K. Valli,
M. Wakasugi, and A. Yoshida

We have constructed a fast atomic-beam collinear laser spectroscopy system coupled with an on-line isotope separator GARIS/IGISOL at RIKEN to study nuclear properties of radioactive refractory elements.[1] Hf isotopes, which are of a typical refractory element, were chosen for the first on-line experiment with this system. To produce radioactive Hf isotopes, use was made of an inverse kinematics of fusion reaction, $^{9}Be(^{166}Er,xn)^{175-x}Hf$, and $^{169}$Hf was successfully extracted from the GARIS/IGISOL.

In a previous paper,[2] it was pointed out that the transmission efficiency of GARIS depends strongly on the angular distribution of the recoil products. For recoil products having lower momentum, the efficiency of GARIS is further reduced by an energy loss and straggling caused by the multiple scattering with gas in the GARIS. Therefore, the inverse kinematics of a fusion reaction is useful to produce radioactive isotopes because the recoil products have narrower angular distribution, larger momentum, and narrower momentum spread.

An incident energy of the $^{166}$Er beam was 16.3 MeV/nucleon and the beam current was a few pnA. A $^{9}$Be target of 50-$\mu$m thickness was placed at the target position. The GARIS was filled with a nitrogen gas of 10 mbar. The produced Hf isotopes were transported to and focused at the ion-guide chamber that was filled with a helium gas of 600 mbar. Singly-charged ions extracted from the ion-guide chamber were accelerated to 30 keV. The accelerated ion beams of the Hf isotopes were stopped with an aluminum foil and accumulated on its surface. After about 10-minutes accumulation, $\gamma$ rays from the decay of Hf isotopes were measured, and the 492.9-keV $\gamma$ rays from the decay of $^{169}$Hf ($\tau_{1/2}$=3.26 m) were clearly identified. The observed yield of $^{169}$Hf was about 100 p/s for an $^{169}$Er beam current of 1 pnA.

Table 1. An expected yield of radioactive Hf isotopes for the on-line experiment with GARIS/IGISOL.

| Reaction | $^{9}Be(^{166}Er,xn)^{175-x}Hf$ |
|---|---|
| Beam current | 1 pna |
| Cross section | 1 b ($x = 4 \sim 9$) |
| Effective target thickness | 3 $mg/cm^2$ |
| GARIS efficiency | $\sim$ 100 % |
| IGISOL window | 40 % [2] |
| IGISOL efficiency | 1 % [2] |
| Yield of Hf isotopes | 5 x $10^3$ |

An expected yield of radioactive Hf isotopes with the GARIS/IGISOL is presented in Table 1. The observed yield was considerably smaller than the estimated one. There are several reasons for that: mainly, (1) the He-gas pressure (600 mbar) in the gas cell was too low to stop the whole $^{169}$Hf ions; and (2) the optimization of the GARIS/IGISOL was not made completely. We expect that the yield will be, at least, several times more by increasing the He-gas pressure. And the problems on the optimization will be solved in due course.

References
1) M. Koizumi *et al.*: 3rd Workshop on Ion Guide Based Isotope Separation, Blankenberg, Belgium (1990).
2) K. Morita *et al.*: Proc. 1st Specialist Research Meeting on the Electromagnetic Isotope Separators and Their Applications, Res. Reactor Inst., Kyoto Univ., Kumatori, p. 32 (1991).

RIKEN Accel. Prog. Rep. **25** (1991)

# III-5-3. Collinear Fast Atomic Beam Laser Spectroscopy of Hf

M. Wakasugi, M. Koizumi, M. Nakaoka, T. Inamura, I. Nakamura, T. Ishizuka, M. Takami, T. Murayama, K. Morita, and Y. Tagishi

We constructed a collinear laser spectroscopy system connected with an on-line isotope separator GARIS/IGISOL to study nuclear properties of refractory elements. An extracted ion beam from the IGISOL is accelerated to 30 keV, mass-separated with an analysing magnet and transported to the laser spectroscopy system. The ion beam is neutralized with a charge exchange cell. The neutralized fast atomic beam crosses collinearly with a laser beam and is detected by means of the resonance fluorescence method. With this system, we carried out collinear laser spectroscopy of stable Hf isotopes. Laser ablation technique with a high power Nd:YAG laser was used to produce the Hf ion.

First, the neutralization efficiency of the charge exchange cell was measured. The central region of the charge exchange cell which contains high purity metallic sodium was heated with a tangsten filament and the both ends of the cell were cooled by circulating water to prevent the escape of sodium vapor. The incident Hf ion beam was neutralized by collision with sodium atoms. The neutralized Hf atoms were detected by means of a laser-induced fluorescence method using a transition from the ground state $5d^2 6s^2 (^3F_2)$ to the $5d^2 6s6p (^3D_2)$ state. The relative yield of the produced Hf atoms was measured as a function of the temperature of the cell. The result is shown in Fig. 1. The relative yield of neutral Hf atoms gradually increased from 250°C and saturated above 380°C. A similar measurement for an Ar-ion beam was done using a transition from the $3d'(^2G_{7/2})$ state to the $4p'(^2F_{7/2})$ state in $Ar^+$. The relative yield of the remaining Ar ions was measured and the result was consistent with that for Hf. It has been confirmed that our charge exchange cell is working well for the collinear laser spectroscopy.

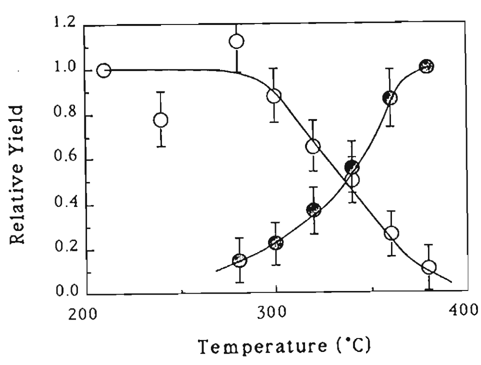


Fig. 1. The temperature dependence of relative yields of Hf (closed circles) and $Ar^+$ (open circles). These values are normalized at 380 °C for Hf and at 200°C for $Ar^+$.

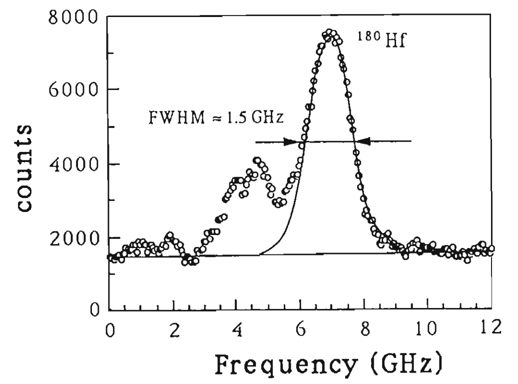


Fig. 2. The laser induced fluorescence spectrum of Hf.

Figure 2 shows a laser-induced fluorescence spectrum of $^{180}Hf$ where the temperature of the cell was 380°C. A small peak at the lower frequency side consists of fluorescence peaks of unseparated $^{179}Hf$ and $^{178}Hf$ isotopes. The full width at the half maximum (FWHM) of the peak is 1.5 GHz, which is too large to resolve the hyperfine structure or isotope shift. A momentum transfer in the charge exchange reaction with sodium atoms is negligibly small.[1] It seems that mainly the momentum spread of the ion beam due to the laser ablation has broadened the FWHM. The momentum spread could be reduced by placing a laser ablation ion source in a gas cell of the IGISOL.

In this experiment, collinear fast atomic beam laser spectroscopy for stable Hf isotopes was successfully done and we have confirmed that this system will have good performance for the laser spectroscopy of refractory elements. Improvement to achieve high resolution is under way.

References

1) R. Neugart: *Hyperfine Interact.*, **24**, 159 (1985).

# III-5-4. $2\pi$-PPAC for the Coulomb Excitation Study

H. Kumagai and Y. Gono

A $2\pi$- parallel plate avalanche counter ( PPAC ) was constructed for the Coulomb excitation experiment of the unstable nucleus beam. This PPAC has a pyramid shape covering $2\pi$ solid angle for the scattered particles. The other type of PPAC which was used for the Coulomb excitation experiment of the stable nuclei was reported previously.[1]

A photo of the PPACs is shown in Fig. 1. This detector consists of four independent two dimensional position sensitive PPAC. The sensitive area of each plane is an equilateral triangle with a 173mm base and a 122mm height. The electrodes were composed from two cathodes determining the position of x- and y-direction and an anode. They were placed 3 mm apart from one another in sequence of the y-cathode, the anode and the x-cathode from the inside to the outside. The y-cathode was made of a 2.5$\mu$m polyester foil on which 33 gold stripes were deposited to 80 $\mu g/cm^2$ in thickness. The anode was a 2.5$\mu$m thick polyester foil, on both sides of which 40$\mu g/cm^2$ gold was deposited . The x-cathode was made of a printed circuit which had 25 gold stripes. The width of stripes was 4.5mm with a 0.5mm inter-stripe spacing. All the contiguous stripes in the cathodes were connected each other with 1k$\Omega$ chip resistors. The position detection was accomplished by the charge division technique for the charges induced on the cathode stripes by avalanche. Isobutane of about 7 Torr was used as a counter gas. The applied anode voltage was about 500 V.

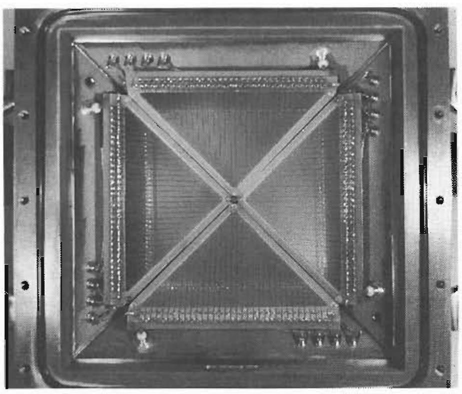

Fig. 1. Photograph of the $2\pi$-PPAC.

The window of the PPAC was placed in the beam line to minimize the dead space of the sensitive area. The secondary target for the Coulomb excitation was set in the PPAC.

Timing signals from four anodes were obtained through fast amplifiers (gain of about 300) and constant fraction discriminators. Sixteen position signals from eight cathodes were obtained through charge sensitive pre-amplifiers and shaping amplifiers with a time constant of 2 $\mu$s. These signals were analysed by CAMAC ADCs to construct the position spectra in the computer.

A position spectrum of the y-direction is shown in Fig.2. This spectrum was taken without a collimator by placing an $\alpha$ source of $^{241}$Am at the secondary target position. The 33 peaks corresponding to the 33 stripes of the y-cathode were well separated. Though FWHM of peaks were 0.8mm, the upper limit of the position resolution is 5mm as the stripes of cathodes were placed every 5mm with 4.5mm width.

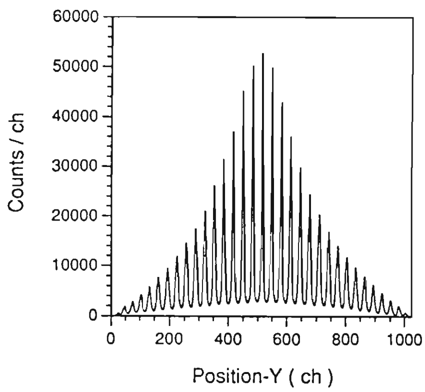


Fig. 2. Position spectrum of the y-direction of the PPAC. The peak indicates exact locations of the center of strips.

This PPAC was successfully used in the Coulomb excitation experiment of the unstable nucleus beam at RIKEN Ring Cyclotron.[2]

References

1) H. Kumagai, M. Fuse, E. Gotoh, M. Ohsima, A. Hasizume, and T. Inamura : *RIKEN Accel. Prog. Rep.*, **20**, 126 (1986).
2) A. Ferragut *et al.*: This Report, p.50.

# III-5-5. The Effect of Heavy-Ion Irradiation on a 12-Strip Position-Sensitive Silicon Detector

M. Kurokawa, T. Motobayashi, T. Nomura, K. Morita, and A. Yoshida

Radiation damage of a silicon position-sensitive detector (PSD) was studied for the purpose to estimate the practical life time of the PSD in advance to the experiment. The characteristics of the PSD are shown in Table 1. The PSD is separated into 12 strips and is designed to detect the $\alpha$ particle from a superheavy nucleus. The surface p-type layer has resistivity and both ends of each strip are connected to pins for signal outputs. The charge generated by the deposition of an ion is separated into two ends through the resisitive surface layer. The output charge is proprtional to the inverse of the distance between a deposited point and an end of the strip. Thus the information on position along the length of one strip is determined by the ratio of the two charge signals, therefore the whole detector with 12 strips can be used as the two-dementional PSD. The energy is given by the sum of these two signals.

Table 1. Characteristics of the position-sensitive detector.

| | |
|---|---|
| Effective area | 60×60 mm$^2$ |
| Thickness of wafer | 400 μm |
| Dark current | 0.1 μA ($V_r$=70 V) |
| Reverse voltage (totally depleted) | 70 V |
| Thickness of dead layer | 0.7 μm |
| Resisitivity of p-type lyer | 3 kΩ |

A 370MeV $^{58}$Ni beam provided by RIKEN Ring Cyclotron bombarded a $^{58}$Ni-target. The PSD was irradiated by elastically scattered $^{58}$Ni and fusion fragment $^{110}$Xe. The total flux injected into one strip depends on the strip due to the spacial destribution of the incident ions. After the irradiation, the reverse current and the energy resolution were measured for each strip .

Figure 1 shows the relation between the reverse current per unit volume of the detector and the fluence of irradiation. The open circles represent our data, and the closed ones the data obtained by 65MeV protons.[1] The reverse current increases with the fluence, showing clearly the effect of radiation damage. As seen in figure, the effect is determined linealy by the fluence (in a unit of Gy). The reverse current is greater for heavy ions than for protons when compared at the same dose.

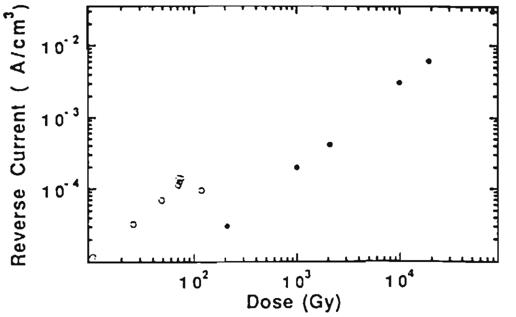


Fig. 1. Relation between the reverse current and the dose for each strip (open circles) and PIN photodiodes (closed circle).[1] The PSD and PIN photodiodes were irradiated by heavy-ions and protons respectively.

In Fig. 2 the energy resolution for 5.5MeV $\alpha$ particles is plotted versus the reverse current. A linear relation is obtained when the current is plotted by its square root. This relation gives a practical estimate of the effect of the damage during an experiment.

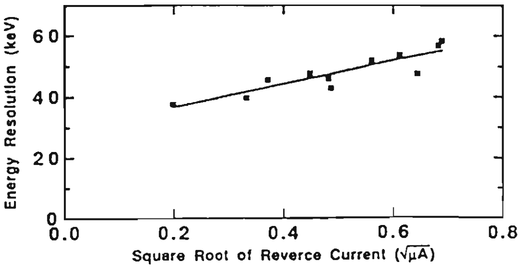


Fig. 2. The energy resolution plotted versus the square root of the reverse current.

References

1) T. Ohsugi *et al.*: Preprint, Hiroshima Univ., HUPD-9017 (1990).

RIKEN Accel. Prog. Rep. **25** (1991)

# III-5-6. Development of a Phoswich Detector for Identification of Charged Particles and $\gamma$ Ray

Y. Futami, Y. Honjo, T. Mizota, Y.H. Pu, S. Tomita, K. Yuasa-Nakagawa, H. Toyokawa, K. Furutaka, A. Yajima, T. Murakami, J. Kasagi, T. Nakagawa, and S.M. Lee

We have developed a phoswich detector[1] which applies to the $4\pi$ detector system to study the property of hot nuclei. Here we report the detector response for charged particles that are expected to play an important role in such heavy ion collisions of intermediate energies.

Particle identification in a $BaF_2$ scintillator can be achieved by the pulse shape discrimination technique[2] since a signal from the $BaF_2$ scintillator has two components: a fast component superimposed on a slow one. In our phoswich detector,[1] a fast plastic scintillator (NE102A) is attached in front of the $BaF_2$ crystal to measure the energy-loss of a charged particle passing through it. The data of the response of the phoswich detector for charged particles were obtained at UTTAC ( University of Tsukuba, Tandem Accelerator Center ). Charged particles of $^{1}H$ (22.0MeV), $^{2}D$ (22.0 MeV), $^{11}B$ (31.7, 39.5, 54.5, 65.3MeV), $^{12}C$ (34.7, 39.7, 54.6, 65.5, 76.4, 80MeV), $^{16}O$ (39.6, 53.5, 62.4, 69.3, 98MeV), $^{28}Si$ (71.3, 79.6, 88.5, 118.9 MeV) and $^{35}Cl$ (97, 106.7, 117.3, 122.2MeV) were used. These ions were obtained from the elastic scattering on a gold target. The data of the response of the $BaF_2$ stand alone detector for heavy charged particles were also taken and compared with those of the response of the phoswich detector.

In Fig. 1 we plot the relations between the fast component, $L_{fast}$, and the total output (=fast component +slow one ), $L_{total}$, of a signals for the elastically scattered ions[3], where the letters represent the position of the elastic peak. It is seen that the heavy ions cannot be separated by the $BaF_2$ detector stand alone. The phoswich detector, however, clearly identifies heavy charged particles. This improvement is considered to be due to an additional contribution to the $L_{fast}$ by the plastic scintillator. We identified the atomic number of charged particles ($Z$) up to 8 using the phoswich detector which consists of the plastic scintillator (50$\mu$m) and $BaF_2$.

Figure 2 shows the relations between $L_{fast}$ and $L_{total}$ for light charged particles. In the case of 100$\mu$m, $^{1}H$ and $^{2}D$ lines overlap the $\gamma$-ray area. In the case of 200$\mu$m and 500$\mu$m, we could distinguish between $\gamma$ray and light charged particles.

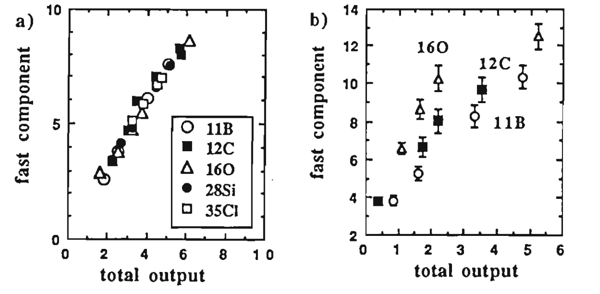


Fig. 1. Relations between the fast component ($L_{fast}$) and the total output ($L_{total}$) of elastic peak positions in the two dimensional plots : a) $BaF_2$ detector and b) phoswich detector with a 50$\mu$m plastic scintillator. Relative gains of the two light outputs are arbitrary. Error bars on $L_{fast}$ of the phoswich detector represent the full width at the half-maximum in the elastic peak distribution.

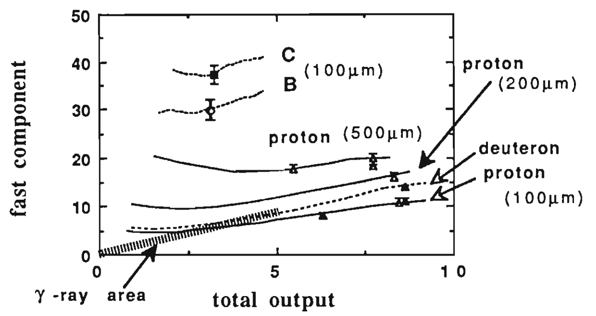


Fig. 2. Similar plots to those in Fig. 1 for various types of phoswich detectors. Values in parentheses represent the thickness of plastic scintillators.

References
1) Y.Futami *et al*.: *RIKEN Accel. Prog. Rep*., **24**, 120 (1990).
2) T.Murakami *et al*.: *Nucl. Instrum. Methods,* **A253**, 163 (1986).
3) Y.Futami *et al*.: *UTTAC Annual Report,* **57**, 8 (1990).

RIKEN Accel. Prog. Rep. 25 (1991)

# III-5-7. A Magnetic Spectrometer for Studies of Unstable Nuclei through Secondary Reactions

T. Nakamura, S. Shimoura, T. Kobayashi, T. Kubo, N. Inabe, Y. Watanabe, K. Abe, I. Tanihata, and M. Ishihara

We have constructed and completed a magnetic spectrometer which is installed downstream of the radioactive beam line RIPS.[1,2] The cross sectional view of the magnet is schematically shown in Fig. 1. The magnet forms one of the components of the spectrometer and detector system,[3] as shown in Fig. 2, which aims at studies of structures of unstable nuclei through secondary reactions such as electromagnetic dissociation (EMD), $p$(HI, HI') $n$ reactions and $d$ (HI, HI') $p$ reactions. For example, the soft giant dipole mode of $^{11}$Li can be studied by reconstructing the invariant mass of $^{11}$Li which is excited and is broken into $^{9}$Li and two neutrons by END process. The magnet with a tracking counter gives us the momentum of $^{9}$Li and the neutron-TOF counters which are the other main components of the system gives us the momentum of two neutrons, so that we can get the invariant mass of the excited states. The roles of the magnet are not only to analyze the charged reaction products, but also to sweep beams off from the neutron-TOF counters and to separate emitted charged particles from beams.

To get enough resolutions and separation for the experiments mentioned above, we determined the designed value of bending power B•L for the magnet to be 1.3 T•m, which enables 80-A-MeV $^{9}$Li (magnetic rigidity of 3.94 T•m) to bend 20 degrees. The simulation tells us that we can get the resolution of invariant mass to be less than 200 KeV FWHM for the 80-A-MeV $^{10}$Li with the relative energy of 1 MeV decaying into $^{9}$Li and a neutron. Here, to make the simulation easier, we used the 2-body dacay ($^{10}\mathrm{Li} \rightarrow {}^{9}\mathrm{Li} + n$) instead of the 3-body decay ($^{11}\mathrm{Li} \rightarrow {}^{9}\mathrm{Li} + n + n$) and neglected the effect of the multiple scattering and the energy loss in the target. As for the separation of charged reaction products, we estimated that the bending angle of 20 degrees is necessary.

The maximum field of the magnet was determined to be 1.5 Tesla and the size of the pole

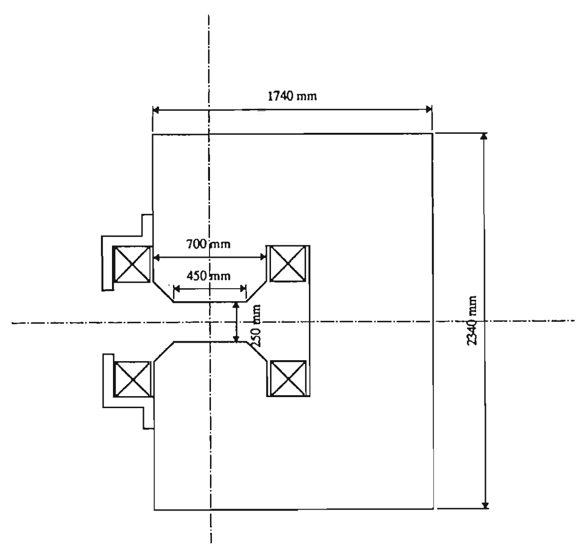


Fig. 1. Cross sectional view of the analyzing magnet in the vertical direction.

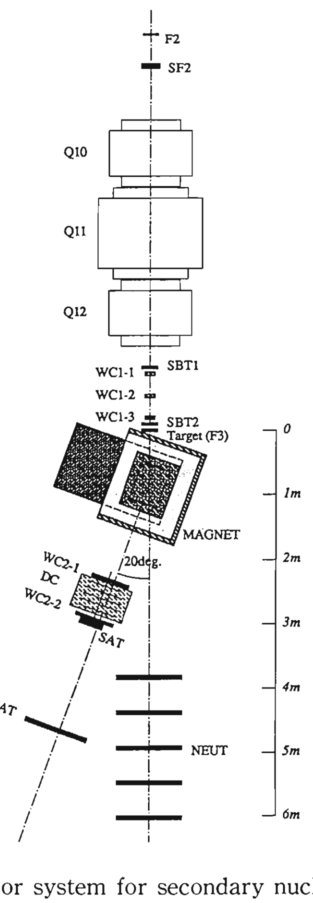


Fig. 2. Detector system for secondary nuclear reaction experiments. SF2, Scintillator at F2; SBT1 and SBT2, Scintillators before a target; WC1, MWPC's before a target; WC2, MWPC's after a target; SAT, Scintillator after a target; DC, a drift chamber; HAT, hodoscopes for charged particles; Neut, hodoscopes for neutrons.

was determined to be 85cm in length and 70cm in width to satisfy the required bending power. To accept forward emitted neutrons sufficiently, the shape of the magnet was determined to be of a C-type and the gap height to be 25cm. The size of the gap allows us to get the vertical acceptance of 200 mrad which is larger than the acceptance of 190 mrad limited by the neutron counters when they are positiond 5 meters downstream from the target. For emitted charged particles, the acceptance is limited by the size of the drift chamber to 140 mrad which is also less than the above value.

The measurement of magnetic fields is now in progress. The maximum field was measured to be 1.59 T by the NMR probe, which satisfies the designed value.

References

1) T. Kubo and M. Ishihara: Proc. 2nd IN2P3-RIKEN Symp. on Heavy-Ion Collisions, World Scientific, Singapore, p. 40 (1990).
2) T. Kubo *et al.*: *RIKEN Accel. Prog. Rep.,* **24**, 96 (1990).
3) T. Nakamura *et al.*: *ibid*., p. 112.

# III-5-8. Experimental Set-Up for Measuring the Proton Scattering by Secondary Radioactive Beams

C.-B. Moon,* M. Fujimaki, J. C. Kim,** Y. K. Kim,** T. Kobayashi, H. Kumagai, T. Suzuki, and I. Tanihata

High intensity secondary beams in the RIPS provides a possibility of spectroscopic study of unstable nuclear reactions. Here we present a method for scattering measurement of a reaction between a radioactive nucleus and proton with a reversed kinematics.

Figure 1 illustrates the detector arrangement.

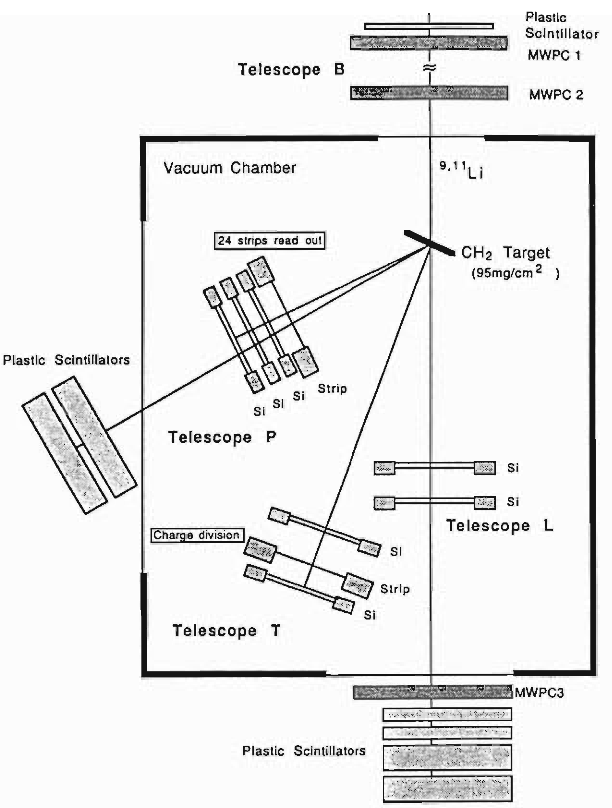


Fig. 1. Schematic representation of the experimental set-up for measuring scattering cross sections of the $^{9,11}$Li+p system.

The telescope B located upstream of the target provided information about beam profiles and it was composed of one plastic scintillator and two MWPCs. Both X and Y coordinates in two MWPCs provided not only the position of a beam particle at the target, but also provided the incident angle of the particle. The telescope L consisted of two fully depleted silicon detectors with active area of 45×45 mm and thickness of 3 mm, one MWPC, two plastic scintillators with 100×100 mm area and 10 mm thick, and also two plastic scintillators with the same area but 25.4 mm in thickness. Incident $^{11}$Li and $^{9}$Li beams are stopped in the third and the second scintillators, respectively. The MWPC in this telescope measured the angles of scattered particles arising from the nuclear reactions as well as incident beam. The telescope P, which was for detecting recoil protons on the elastic scattering kinematics, consisted of a silicon strip detector, three Si detectors, and two plastic scintillators. The silicon strip detector was to measure the scattering angle of recoil protons. Although it was 48 strips of 1mm interval, two adjacent strips were connected for read out. The position resolution was therefore 2mm. The recoil angles between 55° and 80° were covered by this telescope. Figure 2 shows angular distribution spectrum corresponding to each strip detecting recoil protons by $^{11}$Li nucleus. Kinematics for the $^{9,11}$Li+p system in which the projectile is heavier

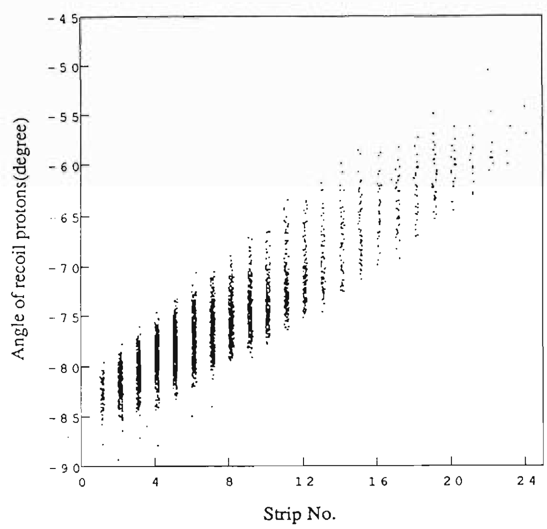


Fig. 2. Angular distribution spectrum for the $^{11}$Li+p system detected by the separate read out of 24 strips. A wide range of angle in each strip is attributed to spreading out of incident beam. Density of dots corresponds to the angular cross section.

* Supported in part by the Korea Science and Engineering Foundation.

** Department of Physics, Seoul National University, Korea.

than the target shows that the energy of recoil protons varies significantly with recoil angles. Protons stop by turn in the telescope P detector stacks according to their recoil energy. Futher information on other reaction channels, such as those of break-up and transfer, was acquired by the telescope T, which was composed of one strip and two silicon detectors. The telescope T covered the scattering angles between 15° and 25°. The read-out of this strip detector, contrary to that in telescope P, was a resistive charge division.

RIKEN Accel. Prog. Rep. 25 (1991)

# III-5-9. Performance of Low-Energy Radioactive Beams in RIPS

A. Yoshida, T. Fukuda, T. Kubo, T. Nakamura, H. Okuno, S. Shimoura, T. Shinozuka, K. Kimura, K. Asahi, J. Kura, H.J. Kim, H. Kumagai, I. Nomura, T. Nomura, S. Kubono, and M. Ishihara

We are planning to measure the sub-barrier fusion cross section for the unstable neutron-rich Al isotopes (A=27~33) plus $^{197}$Au system.[1] We pay special attention to a role of excess neutrons, which may be dynamically polarized against core nucleus in the collision, be transferred easily to the target nucleus, play a role as glue between colliding nuclei and then facilitate a fusion. This experiment will be done by using the RIPS facility in Nov. '91. Al isotopes are produced by bombarding ~95 MeV/u Ar beams on a Be production target, mass separated and introduced to the second focus point (F2). Their energy is, however, about 50 MeV/u which is too high for a sub-barrier fusion reaction. So we need to make their energy about ten times smaller. In that case, the effects of energy straggling and multiple scattering will become large, so that we had to know the emmittance of the low-energy Al secondary beam at the experimental target position (F3) beforehand.

This time, we measured the purity and the emmitance of $^{33}$Al beam which is the severest case of neutron-rich Al isotopes. The primary beam $^{40}$Ar + $^{17}$(E(Ar) = 94 MeV/u) was bombarded to the production target Be, 3mm in thickness, and $^{33}$Al were produced, separated and introduced to the F2 position. The center value of its energy was 53 MeV/u. And its yield was 280 cps/pnA with F1 momentum slit $\Delta p/p$ = 1.1%, F2 slit = ±10mm. We installed two energy degraders just after the F2 position. One was a rotatable Al plate whose effective thickness is 1.8 mm. And the other was a plastic scintillator whose thickness is 1mm, and this was used as a start counter for the TOF measurement between F2 and F3 to determine precisely the decelerated Al isotope energy. In the experimental target region F3, two position sensitive PPAC (parallel plate avalanche counter) were installed in order to measure the emittance of the beam. About the mixing of the other isotopes, 73.5% was $^{33}$Al, 23.9% was $^{36}$P and the remainder was $^{34}$Si. But these isotopes were easily separated by using the TOF measurement between the cyclotron RF and F2 plastic transit signal. The transport efficiency from F2 to F3 was 45%. The energy distribution of $^{33}$Al was 5.4±1.2 MeV/u (fwhm) which is shown in Fig. 1. The energy dependence of the beam spot size and the angular

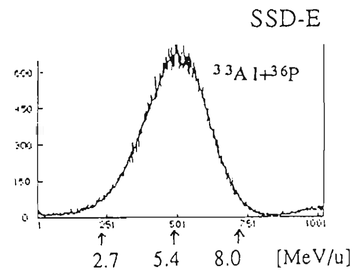


Fig. 1. The energy distribution of the decelerated $^{33}$Al beams at F3. There was a little mixing of isotope $^{36}$P.

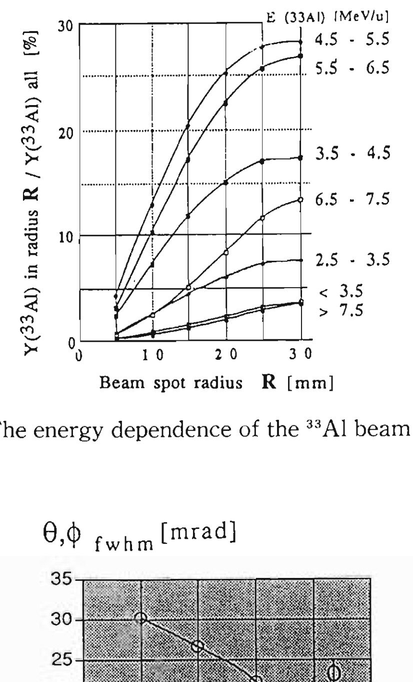


Fig. 2. The energy dependence of the $^{33}$Al beam spot size at F3.

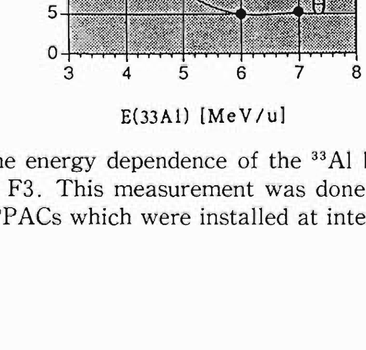


Fig. 3. The energy dependence of the $^{33}$Al beam divergence at F3. This measurement was done by using a pair of PPACs which were installed at intervals of 460 cm.

distribution at F3 is shown in Figs. 2 and 3. Concerning the $5 \pm 0.5$ MeV/u energy region, which corresponds to the sub-barrier fusion excitation energy region of the Al+Au system, the beam spot size was X=20mm, Y=16mm and the angular distribution was $\theta = 8$ mrad, $\phi = 26$ mrad (fwhm values).

In the main experiment, we are expecting to use a stack of Au thin multi targets (25 foils) whose thickness is 150 ug/cm$^2$ with Mylor 50 ug/cm$^2$ backing of $22 \times 28$ mm in size. From this result, about 10% of Al isotopes which is passed through the F2 slit will be used on the first Au target.

References

1) T. Fukuda and A. Yoshida: Post Conference of the 4th Int. Conf. on Nucleus-Nucleus Collisions, Niigata, Jun. (1991).

RIKEN Accel. Prog. Rep. **25** (1991)

# III-5-10. First Focal Plane of SMART and Its Detector System

H. Okamura, K. Hatanaka, T. Ichihara, S. Ishida, S. Kato, T. Niizeki, H. Ohnuma, H. Sakai, H. Shimizu, Y. Tajima, H. Toyokawa, and M. Yosoi

The first focal plane (FP-1) of the SMART spectrograph[1] has a characteristic of large angular and momentum acceptance ($\Delta\Omega$=20msr and $\Delta p/p=\pm17\%$) with a medium energy resolution ($p/\delta p$=3000). The detector system for the FP-1 is required to be able to reconstruct trajectories with a high precision since the focal plane is inclined by 70° with respect to the central orbit while the arrangement of detectors is restricted by the size of a detector box. The present system consists of two sets of multi-wire drift chambers (MWDC) and a plastic-scintillator hodoscope. Each MWDC has a structure of $X$-$X'$-$Y$-$Y'$ to resolve left-right ambiguities. The hodoscope is segmented by 14 in horizontal direction and by 7 (later increased to 14 for the $^2$He measurement) in vertical direction. All detectors have a sensitive area of $84^H\times42^V cm^2$ and thus the momentum acceptance is currently limited to $\pm12\%$.

A diagnostic study has been made by using elastically scattered deuterons from a gold target at $E_d$=140MeV. Some empirical properties of the FP-1 were obtained and were compared with calculations based on the magnetic field data.[2] It was found that the angular acceptance was slightly reduced for high momentum particles. Little information was obtained on vertical angles due to poor resolution. In the present setup, the multiple scattering by the entrance window of the detector box and by the air restricts the energy and angular resolution dominantly.

A problem of the detector system was the unstable operating condition of MWDCs. It was greatly improved by changing the preamplifier and discriminator from the KEK-VENUS system to LeCroy 2735DC. But the weak electric field caused by the large drift space (13mm) still deteriorated the detection efficiency and the position resolution. By changing the thickness of anode wires from 20$\mu$m to 30$\mu$m, by optimizing the operating gas mixture and by applying negative high voltages to the field shaping wires, the drift-time-to-distance relation and, consequently, the position resolution were remarkably improved. The efficiency, however, was kept at an unsatisfactory level.

A major subject using the FP-1 is the measurement of the ($d$,$^2$He) reaction.[3] The large angular and momentum acceptance, combined with the medium energy deuteron beam provided by the RIKEN Ring Cyclotron, greatly enhances the detection efficiency of the $^2$He, two protons coupled to the $^1S_0$ states. The detector system, however, causes some inefficiency in resolving trajectories of two protons. The efficiency has been estimated by the newly developed Monte Carlo code, which can fully take account of the properties of the FP-1 and the detector system, various types of reaction dynamics and the three-body relativistic kinematics. The code also provides other information valuable for diagnostic studies, as well as continuum spectra arising from quasifree knockout reactions or from accidental coincidences by the inclusive breakup. Figure 1 shows an experimental $p$-$p$ relative energy spectrum as an example compared with the Monte Carlo calculation based on the Migdal-Watson formalism.

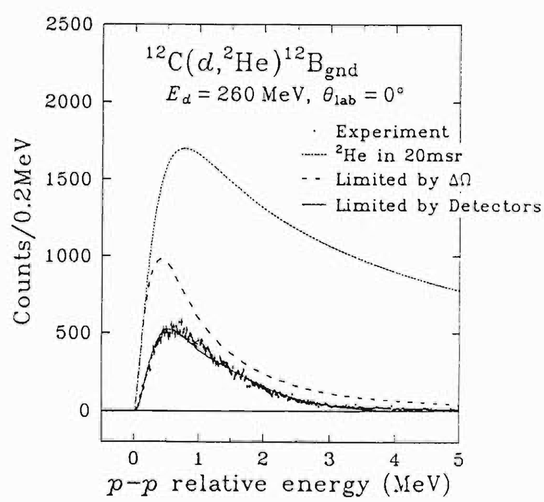


Fig. 1. A $p$-$p$ relative energy spectrum for the $^{12}C(d,{}^2He)^{12}B_{gnd}$ reaction at $\theta$= 0° with $E_d$=260 MeV.

References


1) H. Ohnuma *et al.*: *RIKEN Accel. Prog. Rep.*, **24**, 108 (1990) and references therein.
2) Y. Tajima *et al.*: *ibid.*, **24**, 109 (1990).
3) Y. Tajima *et al.*: This Report, p.51.

RIKEN Accel. Prog. Rep. **25** (1991)

# III-5-11. Development of Detectors for the Second Focal Plane of SMART

Y. Fuchi, M.H. Tanaka, S. Kubono, H. Kawashima, K. Takaku, T. Ichihara, and SMART Construction Group

Focal-plane detectors are being developed which are to be used for the LRsecond focal plane of SMART. Requirements for the detectors are as follows. RNThe detection region is 50 cm in the x direction (the momentum dispersion NQdirection) and 10 cm in the y direction (the angle direction). The position QNresolutions should be better than 0.5mm FWHM in both x and y directions. The counting rate should be 10 k cps, and the particle identification should be made up to Ne.

The detector system consists of two drift counters and two plastic scintillators. They are all arranged perpendicularly to the beam. The two sets of gas detectors are placed with a distance of 55 cm. Between the two proportional counters there is the second focal plane which is inclined by an angle of 70 degrees with respect to the beam-axis. The two plastic scintillators, put together, are placed a little behind the second counter. Two plastic scintillators are needed to reduce the back grounds.

The position information in the x direction was obtained by the two IGways discussed later with the proportional counters. The position GOinformation in the y direction is given by the drift time measurement with O=the proportional counters and the plastic scintillators.

The two kinds of drift counters were developed to meet experimental KLdemands on the second focal plane of SMART. One is a single wire drift counter (SWDC), and the other is a cathode read-out single wire drift KOcounter (CRDC). The x position resolution with the 50 cm SWDC is expected to be about 0.5 mm FWHM, and the one with the CRDC to be about 0.3 mm FWHM. R Since the SWDC has been used extensively,[1] the SWDC was fabricated first and used for testing the large drift distance.

Figure 1 shows a cross-sectional view of the SWDC for the second focal plane of SMART. It has a hybrid structure of two proportional counters and a common drift space. The proportional counters consist of a resistive wire to read out position information in the x direction, and a tungsten wire to read out ΔE information. The resistive wire made of 15 KΩ nichrome is 17.5 $\mu$m in diameter and 55 cm in length. The gold gilded tungsten wire is 12.5 $\mu$m diameter and 55 cm in length. The field wires are placed at intervals of 1 cm on both sides of drift space. A uniform parallel electric field in the drift space is formed by providing certain voltages to each field wire.

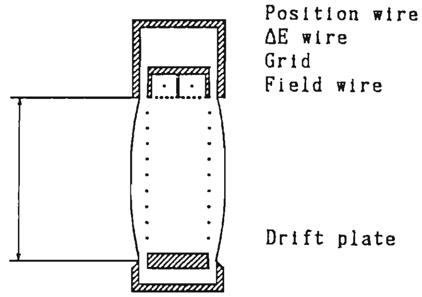


Fig. 1. Cross section of the SWDC.

The position information in the x direction is obtained by using a HNcharge division technique. The position information in the y direction is given by measuring the drift time of electrons from the incident point to the ΔE wire. Start and stop signals are obtained with the plastic scintillators and the ΔE wire, respectively.

The voltages applied to the nichrome wire, the tungsten wire, the drift-plate and the grid are 1900 V, 1700 V, −3000 V, and 0 V, respectively. The counter gas is a mixture of 70% Ar and 30% $CH_4$ at atmospheric pressure. The electric field is 300 V/cm. Under this condition, the drift velocity is relatively constant as a function of voltage.

The test of the y position resolution was performed with the SWDC. The SWDC was set on the focal plane of the QDD magnetic spectrograph and tested PNwith a faint proton beam of 30 MeV from the SF-cyclotron at the Institute for Nuclear Study(INS), University of Tokyo. The two identical slit plates were prepared to get a small beam width. Each plate has slits of 0.2 mm and 0.5 mm width with a distance of 5 mm. The two slit plates were placed just before and behind the detector. The obtained y-position resolutions were 0.4mm FWHM. It is good enough to use for the second focal plane of SMART.

The SWDCs have been extensively used on the second focal plane of SMART for tuning the spectrograph and also testing the study of heavy-ion induced charge exchange reactions.

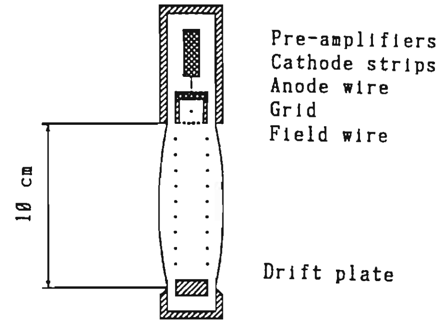


Fig. 2. Cross section of the CRDD.

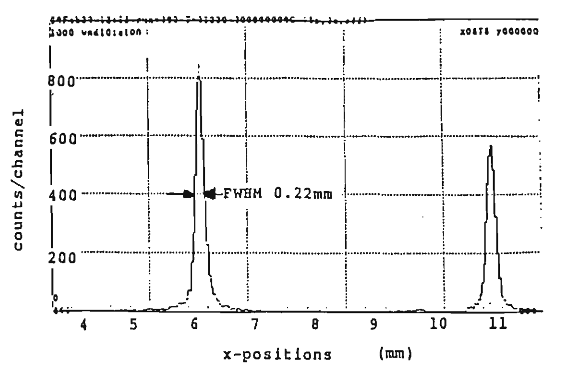


Fig. 3. A x-position spectrum of protons obtains with the CRDC. The two peaks a separated by a distance of 5.7 mm.

All the spectra on the second focal plane of the SMART were obtained with these detectors so far.

The second detector, a CRDC has been developed so as to provide a higher position resolution in the x direction and a higher counting rate capability, and to detect possibly multi-particle events. Figure 2 shows a cross sectional view of the detector. It has also a hybrid structure of a drift space and a proportional counter. The wire of the proportional counter, which is a gold gilded tungsten wire, is 12.5 mm in diameter and 55 cm in length. The detector has 60 cathode strips with the area of $20 \times 7.5 mm^2$ along the proportional-wire in the proportional counter. The distance between the strips is 0.5 mm. Each strip is followed by an independent charge-sensitive pre-amplifier, which is enclosed in the detector box to reduce the noise level.

The wire in the proportional counter provides not only $\Delta E$ information but also x-position information by inducing charges to the cathode strips. The position in the x direction is obtained by determining the center of gravity of charges induced on each strip. The method of determining y-position is the same as that of SWDC.

The beam test was performed with a faint proton beam of 30 MeV from the SF-cyclotron at INS, since the beam spot on the second focal plane of SMART is not small enough to test the position resolution of the CRDC. The CRDC was placed on the focal plane of the QDD spectrograph, where a smaller size CRDC was used to fit in the focal plane of the QDD spectrograph. The counter gas used is a mixture of Ar 70% and $CH_4$ 30% at atmospheric pressure. The drift-plate voltage is $-3000$ V, the same as the SWDC, and the voltage for the anode wire is 1980 V. The obtained x-position resolution was 0.22mm FWHM, which is shown in Fig. 3.

The deterioration in x-resolution is not tested as a function of drift distance and also of counting rate. These tests are under way.

References

1) M. H. Tanaka, S. Kubono, and S. Kato: *Nucl. Instrum. Methods*, **195,** 509 (1982).

RIKEN Accel. Prog. Rep. **25** (1991)

# III-5-12. Performance Test of SMART Neutron Detectors

H. Orihara, K. Hatanaka, M. Hosaka, T. Ichihara, M. Ishihara, S. Kato, T. Niizeki, H. Ohnuma, M. Ohura, H. Okamura, H. Sakai, H. Shimizu, Y.Tajima, H. Toyokawa, Y. Yano, H.Y. Yoshida, and M. Yosoi

The SMART system[1] is equipped with neutron detectors for neutron time-of-flight measurements. These detectors, 20cm in diameter and 5 cm in thickness, have been tested with a 210MeV proton beam in the course of performance tests of the SMART system during the fall run in 1991.

Figure 1 shows an energy spectrum of monochoromatic neutrons emitted from the $^{7}Li(p,n)^{7}Be$ reaction at 0 degree over a flight path of 10 m. Energy per bin was 1MeV. The neutron threshold is estimated to be 25 MeVee. The overall time resolution was 500ps.

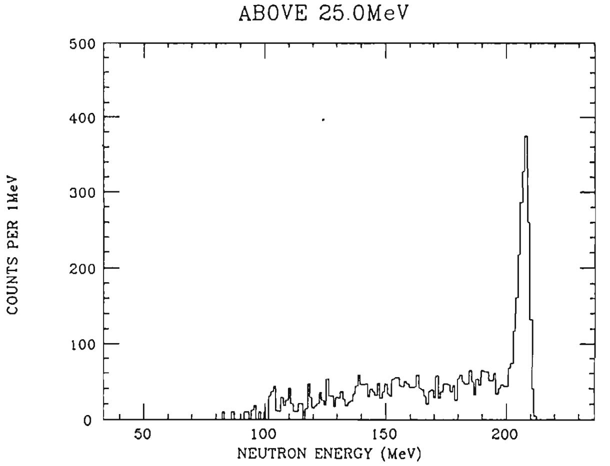


Fig. 1. Neutron energy spectrum for the $^{7}Li(p,n)^{7}Be$ reaction at $E_p$=210MeV measured at 0 degrees over a flight path of 10m. The peak corresponds to neutron groups leading to the ground state and the 0.429MeV excited state in $^{7}Be$.

The thickness of the NE213 liquid scintillator is much smaller than the range of recoil protons produced in the detector. Thus, it is important to measure the response functions of the detector to neutrons in the energy region of interest. White neutrons were produced for this purpose by bombarding a thick aluminum block by 210MeV protons. Energy spectrum for neutrons emitted from the $^{27}Al(p,xn)$ reaction is presented in Fig. 2. The response functions for monochromatic neutrons were obtained by applying the TOF gates on light-output spectrum. Representative response functions thus obtained are illustrated in Fig. 3 for neutrons in the energy ranges $E_n$= 60−70MeV and 170−180MeV. The thickness of the present detector did not affect reliable detections of energetic neutrons.

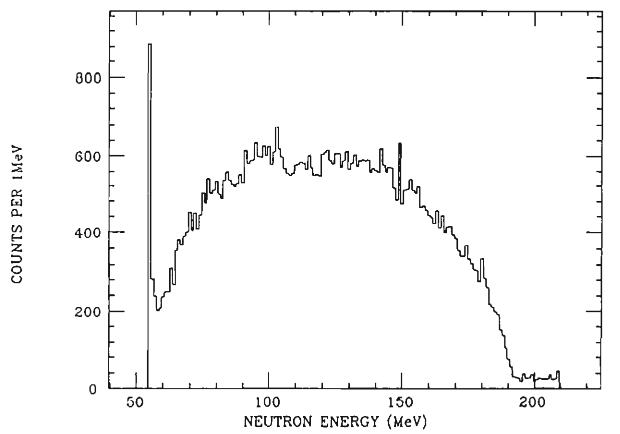


Fig. 2. Neutron spectrum obtained by a thick aluminum target.

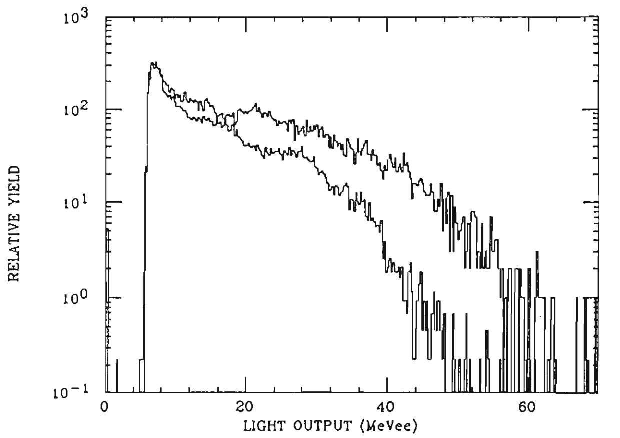


Fig. 3. Sample response functions of the neutron detector for monochromatic neutrons with $E_n=65\pm5$ and $175\pm$ 5MeV obtained by selecting appropriate regions of the continuous neutron spectrum of Fig. 2.

References

1) H. Ohnuma *et al.*: *RIKEN Accel. Prog. Rep.*, **21**, 164 (1987); **22**, 148 (1988).

RIKEN Accel. Prog. Rep. **25** (1991)

# III-5-13. Energy Deposition and Straggling of High Energy Heavy Ions in Silicon Detectors

K. Nagata, T. Doke, N. Hasebe, N. Itsumi,* T. Kashiwagi, J. Kikuchi, T. Kohno, H. Moriya,** H. Murakami, A. Nakamoto, T. Shino,* and T. Yanagimachi

Deposition energy and its straggling of heavy-ions in Si detectors of 50, 100, 200, 500, 1000, 2000, and 3000 $\mu$m in thickness are measured by using ion beams of 95MeV/u $^{40}Ar$, 135 MeV/u $^{12}C$, 135 MeV/u $^{14}N$, and 100MeV/u $^{18}O$ from the RIKEN Ring Cyclotron. The experimental results are compared with the theoretical energy losses and the theoretical Bohr's widths.

An example of a silicon detector stack used to measure the energy loss straggling of heavy ions is shown in Fig. 1. The stack consists of several silicon detectors. Experimental results of the energies deposited in Si detectors and their fluctuations are summarized in Table 1. Only data obtained from the first detector in each stack are shown in the table in comparison with theoretical values, since preceding materials might produce some effects on the energy deposition in the following detectors. The values of the energy deposition in the Si detectors are in good agreement with theoretical ones[1)] within the uncertainty of about 10%. On the other hand, the agreement between the distribution widths and the theoretical ones is not so good. To make the correction of thickness nonuniformity in detec-

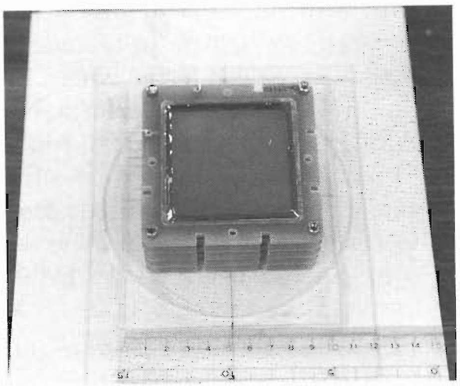

Fig. 1. Photograph of a stack of four Si(Li) detectors. Each detector has a sensitive area of 62×62mm×mm, and 2mm in thickness.

Table 1. Comparison of the theoretical and experimental energy losses and FWHMs for $^{40}Ar$, $^{6}C$, $^{14}N$, and $^{18}O$ ions in silicon detectors.

| Particle and Energy | Thick. ($\mu$m) | Incident Angle | Vavilov $\varkappa$ | Energy Loss (MeV) Exp. | Theor. | Exp. /Theor. | FWHM (MeV) Exp. | Theor. | Exp. /Theor. |
|---|---|---|---|---|---|---|---|---|---|
| $^{40}Ar$ | 51.5 | 0° | 6.8 | 22.37 | 22.73 | 0.984 | 1.64 | 1.28 | 1.28 |
| 95MeV/u | 101.8 | 0° | 13.5 | 47.33 | 45.55 | 1.039 | 1.85 | 1.81 | 1.09 |
| | 100.7 | 0° | 13.5 | 46.40 | 45.55 | 1.019 | 1.98 | 1.81 | 1.02 |
| | 201.3 | 0° | 27.0 | 89.19 | 91.50 | 0.975 | 3.05 | 2.55 | 1.20 |
| | 202.9 | 0° | 27.0 | 89.37 | 91.50 | 0.977 | 2.92 | 2.55 | 1.15 |
| $^{12}C$ | 958. | 0° | 8.6 | 37.58 | 39.83 | 0.944 | 2.08 | 1.90 | 1.09 |
| 135MeV/u | 2068. | 0° | 17.1 | 79.55 | 80.38 | 0.990 | 3.54 | 2.69 | 1.32 |
| | 2016. | 0° | 17.1 | 77.03 | 80.38 | 0.958 | 3.58 | 2.69 | 1.33 |
| $^{14}N$ | 498.9 | 5° | 5.8 | 24.08 | 27.12 | 0.888 | 1.61 | 1.57 | 1.03 |
| 135MeV/u | 498.9 | 0° | 5.8 | 24.11 | 27.01 | 0.893 | 1.84 | 1.57 | 1.17 |
| | 3089. | 5° | 35.0 | 155.5 | 167.0 | 0.931 | 4.13 | 3.85 | 1.07 |
| $^{18}O$ | 3130. | 0° | 71.6 | 271.5 | 276.2 | 0.983 | 5.51 | 4.39 | 1.25 |
| 100MeV/u | | | | | | | | | |

* Waseda University.
** Ehime University.

tor, the spatial distribution of thickness in each detector was measured by the aide of a 2-dimensional position sensitive detector. The result shows that the thickness variation for a 50$\mu$m or 100$\mu$m thick detector is $\pm 1\mu$m and for a 3000$\mu$m thick detector $\pm 5 \sim 10\mu$m. Even if the correction for such a thickness variation is made, the ratios of the distribution widths experimentally obtained for the 0° incidence to the theoretical one are ranging from 1.0 to 1.33. This is caused by the fact that ions incident at small angles ( < 0.2°) to the crystal axis or plane of a Si crystal exhibit an anomalous energy loss rate and energy loss width, and for ions incident to the peripheral region ($0.2° < \theta < 1.5°$) only the energy loss width is deteriorated. If the incident angle of ions is different from such axis and planes, the distribution width should not show the variation as in the case of the normal incidence. As expected, the distribution widths measured by the ion beams with an incident angle of 5° showed a good agreement with the Bohr's theoretical values within an error of 7%. Therefore, it is necessary to select the data free from a channeling effect of ions in a Si crystal, when we compare the observed values of the energy loss straggling with those redicted by the theory.[2)]

References

1) H. Bichsel: AIP Handbook, 3rd ed., p. 8 (1972); W. H. Barkas and M.J. Berger: NSS Report, No.39, p. 103 (1964).
2) K. Nagata *et al.*: *RIKEN Accel. Prog. Rep.*, **24**, 115 (1990).

RIKEN Accel. Prog. Rep. **25** (1991)

# III-5-14. Mass Resolution Measurement of a Cosmic-Ray Heavy Ion Telescope

T. Kohno, C. Kato, T. Imai, A. Yoneda, and K. Munakata

A cosmic-ray heavy ion telescope having a very large geometric factor is going to be put into a geosynchronous orbit on board the Engineering Test Satellite (ETS-VI) in 1993.[1] The observation of elemental and isotopic abundance of galactic cosmic rays (GCR) and solar energetic particles (SEP) from Li to Fe nuclides is our final purpose. We use a $\Delta E \times E$ method for the particle identification.

We already have repeated many tests of individual detectors such as energy detectors and two-dimensional position sensitive detectors using heavy ion beams from RIKEN Ring Cyclotron so far.[2-5] The flight model of the telescope is already manufactured and in test phase now.

In addition to obtain the chracteristics of each detector, it is also very important to check the basic ability of the overall telescope itself. Therefore we tried to measure the mass resolution of the flight model telescope using the Ring Cyclotron.

The cross sectional view of the telescope is shown in Fig. 1. The total thickness of Si for the vertical incidence amounts to 28.2 mm except the last veto detector. The beam used was $^{16}O$ with an energy of 135 MeV/nucleon whose range in Si is about 17 mm. Therefore the beam stopped in the fourth Si(Li) detector. We set a thin (200$\mu$) mylar film at the end of the vacuum tube and guided the beam from vacuum to the atmosphere through the film. The block diagram of the telescope system is shown in the reference.[5] The data acquisition system of the real observation in space allows only one particle input per 4 seconds because the counting rate in space is very low except the case of huge solar flare events. Hence we added a special circuit to process quickly the digital data coming from the ADC independent of the clock of the satellite telemeter system. The digital data after the ADC were transmitted through an optical fiber of 50m length wired from the beam site to the measurement room.

We analyzed thus obtained list mode data by the method based on a $\Delta E \times E$ method (see Ref. 6 for detail). In Fig. 2 we show one example of the mass resolution for $^{16}O$ with energy of 135 MeV/nucleon. This histogram was obtained by using the detectors from the first PIN to the second Si(Li) for the $\Delta E$ detection and those detectors from the third to the fourth Si(Li) for the residual $E$ detection. The resultant mass resolution for this measurement was 0.6 amu in FWHM. This value is about 20% larger than the value obtained by the numerical simulation. The main reason of this broadening is due to the larger energy straggling in the detector than that expected from the Bohr's equation used in the

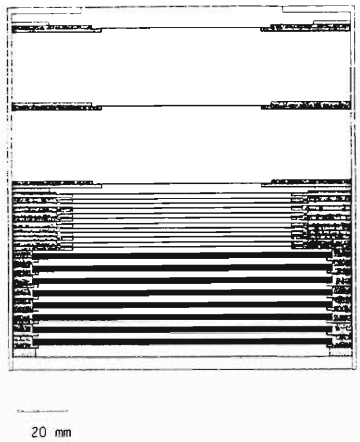


Fig. 1. Cross sectional view of the cosmic-ray heavy ion telescope. An aluminum window of 0.2 mm in thickness is used for a light shield. Three PSDs can decide the particle incident angle. The following twelve thin detectors are ion-implanted PIN-type detectors with 85 mm $\varphi$ effective area and 0.5 mm in thickness. The last group of eight thick detectors are lithium-drifted type (Si(Li)) with effective area of 110 mm $\varphi$ and thickness of 3 mm.

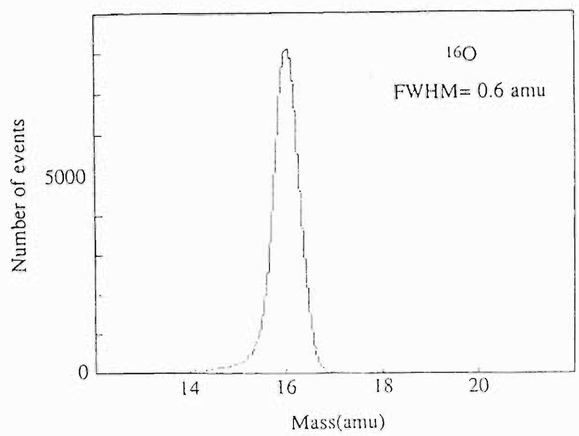


Fig. 2. One example of obtained results of mass resolution for $^{16}O$ with an energy of 135 MeV/nucleon.

simulation.[7] The value of 0.6 amu, however, is tolerable for our current purpose in the space observation.

References


1) T. Kohno: *Space Sci. Rev.*, **51**, 185 (1989).
2) T. Kohno *et al.*: *RIKEN Accel. Prog. Rep.*, **21**, 152 (1987).
3) K. Munakata *et al.*: *ibid.*, **22**, 168 (1988).
4) T. Imai *et al.*: *ibid.*, **23**, 91 (1989).
5) C. Kato *et al.*: *ibid.*, **24**, 116 (1990).
6) K. Munakata *et al.*: *Nucl. Instrum. Methods*, **A276**, 306 (1989).
7) T. Kohno *et al.*: *J. Phys. Soc. Jpn.*, **60**, 3967 (1991).

RIKEN Accel. Prog. Rep. 25 (1991)

# III-5-15. A Transputer Add-In Board for PC-9801

J. Fujita

It is frequently encountered in the experiment and control of the accelerator that events are needed to be processed concurrently. A transputer is a microprocessor which was developed as a parallel-processor by INMOS, and executes programs written in a parallel process language or OCCAM. The transputers T414 and T425 have a 32 bits multiplexed data and address bus, 2 to 4 Kbytes on-chip static RAM for the high speed processsing, a configurable memory interface to allow the use of a variety of external memory types, and four pairs of serial communication links. T800 has a 64 bits floating point unit in addition to the above-mentioned functions and is pin-compatible with T414 and T425.

A block diagram of the transputer board is shown in Fig. 1. There is no ROM for monitoring the board, but a 4 MB RAM(4×1MB dynamic RAM module THM81000AS) for downloading a system program from a host computer PC-9801. Since a refresh circuit for the dynamic RAM is built in the transputer, 20 bits addesses are separated into the row and column addresses and selected with each appropriate timing. Address bit-2 to 10 and bit-20 are selected by the high level of MS2(Memory Strobe signal 2) and latched as 10 bits row address of the dynamic RAM with the falling edge of MS1. Address bit-11 to 19 and bit-21 are latched with the falling edge of MS0 and passed to the RAM as 10 bits column address during the low level of MS2. MWB0 to 3(four byte-addressing write strobes) write each byte of the single data word (32 bits) into the four dynamic RAM modules.

The four bi-directional serial links provide synchronized communication between processors and with the outside circuits. Each link comprises an input channel and output channel. The link 0 of the transputer is connected to the channel of a link adapter C012 which converts bi-directional serial link data into parallel data bus. The transputer is not directly addressed by the PC-9801. The lower data byte D0-D7 on the external bus of the PC-9801 is fed to the bus of the link adapter through a transceiver 74LS245.

5MHz clock is supplied on the ClockIn inputs of the transputer and the link adapter by a quartz oscillator SG531. Both chips operate at the high frequency internal clock 20MHz derived from this ClockIn.

The circuit test is performed by running TDS2(Transputer Development System II) which was developed by INMOS. The TDS2 comprises an integrated editor,file manager,compiler and debugging system which enables transputer to be programmed in OCCAM or in another industry standard language such as a language C. The transputer can be bootstrapped either from a link or from external ROM. As the BootFromRom input of the transputer is con-

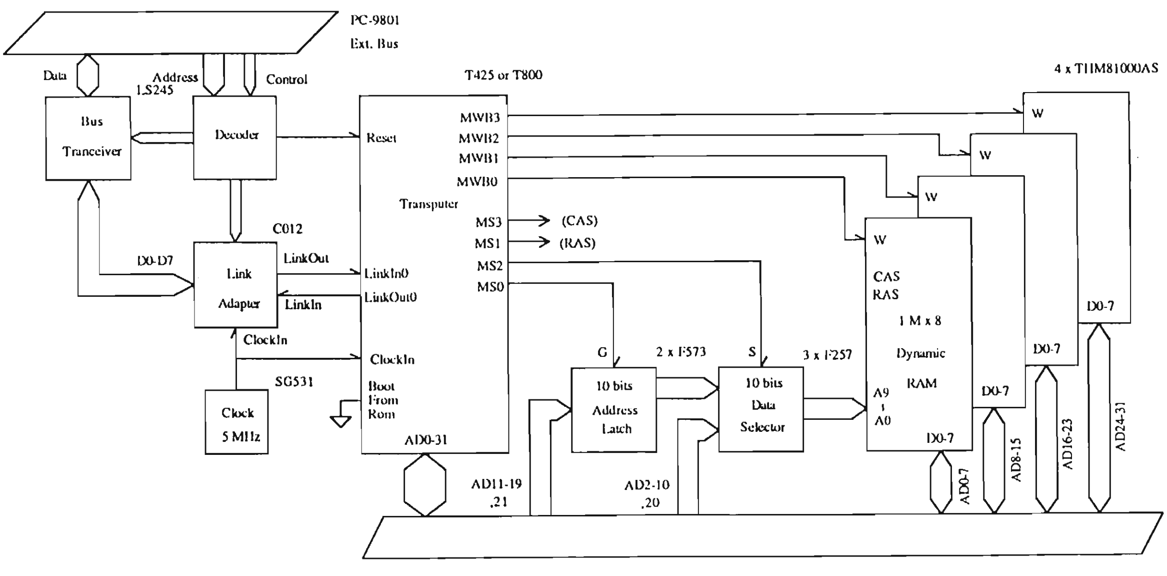


Fig. 1. Block diagram of a transputer board.

nected low, the transputer is booted from the channels of the link 0 after Reset is taken low, and TDS2 is loaded on the RAM of the transputer board. When TDS2 runs on the board, the transputer becomes a master, and the PC-9801 a slave. The basic I/O operations of the transputer are performed by a server program running on the PC-9801. It is found that the transputer on the board works well as a single transputer.

Since TDS2 supports a transputer network, a multiple transputer system can be constructed by addition of new modules of a small size which consists of only a transputer, static RAM and some logic ICs. Ability of the transputer will be found in view of parallel processor by this system.

RIKEN Accel. Prog. Rep. **25** (1991)

# III-5-16. Low Energy Unstable Nuclear Beam Channel "SLOW" at RIKEN Ring Cyclotron

T. Matsuzaki, R. Kadono, K. Ishida, A. Matsushita, and K. Nagamine

A low-energy radioactive isotope (RI) beam channel "SLOW" has been constructed at RIKEN Ring Cyclotron Facility (RRC), intended not only to study the emission mechanisms of various stable and unstable isotope ions with low-energy from a characterized surface of the primary target, but also to generate useful secondary RI beams for surface physics.[1]

The layout of the new beam channel is illustrated in Fig. 1. The thermal energy ions directly emitted from the target are extracted by an electrostatic lens and then separated on-line by a double-focussing mass spectrometer consisting of an electrostatic toroidal bender and a magnetic dipole bender. The whole electrostatic components are contained in ultra-high vacuum vessels to control the surface condition of the primary target.

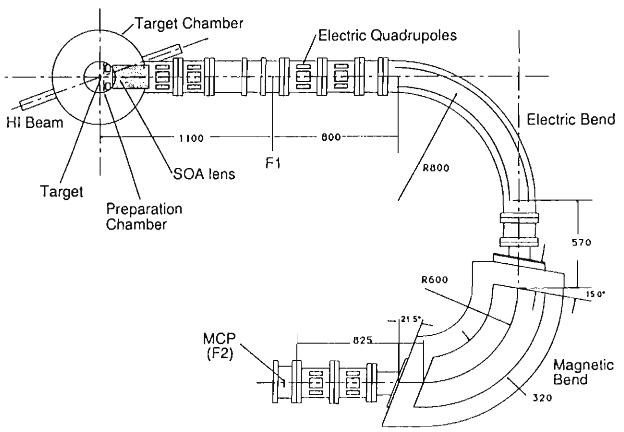


Fig. 1. Layout of the SLOW beam channel.

In the commissioning experiment the mass spectrum of the emitted ions from a hot tungsten target was observed both during and after the irradiation of the target by $^{40}$Ar beam of 95MeV/A from RRC. The magnetic field was scanned at a rate of 16min per whole mass range. Typical mass spectra are shown in Fig. 2, where the target temperature was 2040K and the acceleration voltage for the ion extraction was 1kV. The spectrum taken in the beam-on period (Fig. 2a) shows several broad peaks possibly corresponding to alkaline ions (Na, K, Rb), alkali-earth ions (Mg, Ca), rare-earth ions (Sm, Eu, Tm) and

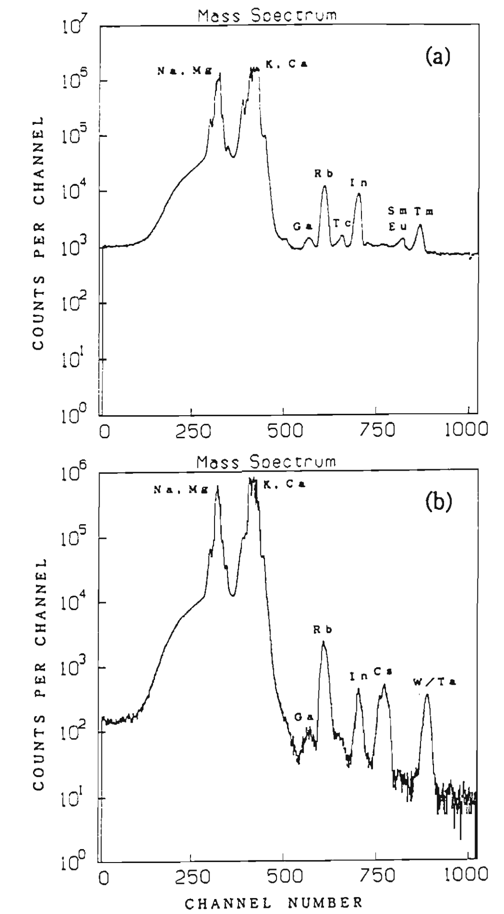


Fig. 2. Typical mass spectra of the emitted ions from the hot tungsten target during (a) the beam irradiation period (8 scans; 2hr) and (b) the beam-off period (3 scans; 50min).

other metal ions (Ga, In, Tc). Some additional peaks (Cs, Ba, Ta/W) are present in the spectrum (Fig. 2b) taken just after the termination of the primary beam. Note that the observed peaks may include those corresponding to the long-lived isotopes slowly accumulated in the target to diffuse out of the surface. The background spectrum (without primary beam) was measured at 1,920K and only two peaks were observed near the mass numbers of 23 and 39. The detailed analysis is still in progress.

References

1) T. Matsuzaki, K. Ishida, and K. Nagamine: *RIKEN Accel. Prog. Rep.*, **23**, 90 (1989).

# III-5-17. High Resolution Soft X-Ray Spectrometer for Chemical State Analysis by PIXE

K. Maeda, Y. Sasa, and M. Uda

Soft X-ray emission spectroscopy is one of the powerful tools to investigate chemical bonding states of matters. Chemical effects are greatly enhanced on structures of X-ray satellites arising from multiply ionized states when high energy heavy ions are used for excitation. We have developed a high-resolution soft X-ray spectrometer suitable for the particle (ion) induced X-ray emission (PIXE) method. We report here on the design and evaluation of a prototype of this spectrometer.[1]

Target materials were bombarded with $He^{+}$ or $N^{2+}$ ions produced by RILAC. X-rays emitted from the target were diffracted with a plane single crystal and detected by a windowless position-sensitive detector. Figure 1 shows a schematic construction of the detector. The photodiode array was a row of 1024 silicon photodiode sensor elements. Center-to-center spacing and height of the elements were 25$\mu$m and 2.5mm, respectively. To reduce dark signals caused from thermal noise, the array was cooled with a Peltier thermoelectric device which was in thermal contact with a cold finger. Dark signals, which were around 700 cps/channel at 24°C, were reduced to 3.5 cps/channel at −18°C.

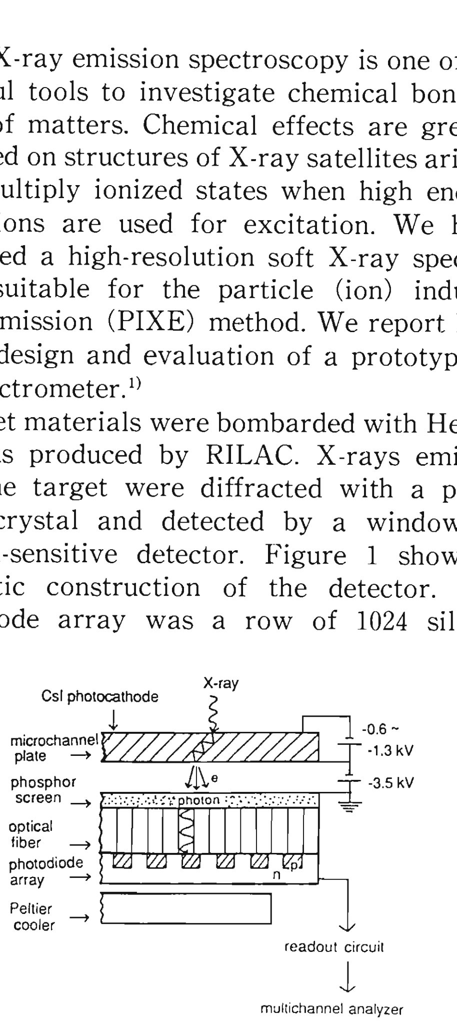


Fig. 1. Schematic construction of the detector.

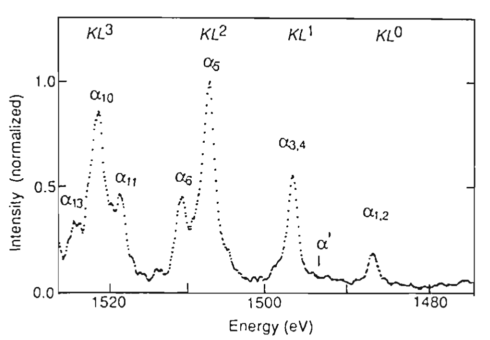


Fig. 2. Al K$\alpha$ spectrum for an Al metal induced by 15MeV $N^{2+}$ ions. The spectrum was accumulated for 1000 sec with a beam current of 100 nA.

Figure 2 shows an Al K$\alpha$ spectrum, for a 0.3 mm thick Al metal, induced by the 15MeV $N^{2+}$ impact and analyzed with an ADP crystal after subtraction of the background dark signals. The diagram line of K$\alpha$ and its satellites emitted from multiply ionized states were well resolved. Moreover, fine structures in the satellites, e.g. $\alpha_5$ and $\alpha_6$, were easily distinguished. FWHM (full width at half maximum) for the Al K$\alpha_{1,2}$ peak at 1487 eV estimated from this spectrum was 1.5 eV; a reasonable value considering geometrical factors such as X-ray source width and spatial resolution of the detector. Reproducibility of the measurement was assured to be less than 0.1 eV for peak energies, and less than 6% for peak intensities relative to the strongest peak.

By using an RAP analyzing crystal, the spectrometer was also tested for X-rays of energies less than 1 keV by measuring Fe L X-ray spectra induced by the 5 MeV $He^{+}$ and 15 MeV $N^{2+}$ impacts. FWHM of FeL$\alpha_{1,2}$ for metallic Fe was 4.2 eV for both $He^{+}$ and $N^{2+}$ induced spectra. The observed intensity ratio of Fe L$\beta$/FeL$\alpha_{1,2}$ was much higher for $Fe_2O_3$ than for metallic Fe. The satellites arising from multiply ionized states appeared prominently when heavy ions, i.e. N ions in the present study, were served for excitation. Intensities of the satellites were greatly enhanced in the spectrum for $Fe_2O_3$ compared to metallic Fe. This type of spectrometer is potentially useful for the chemical state analysis by PIXE.

References

1) K. Maeda, Y. Sasa, and M. Uda: *Int. J. PIXE*, in press.

RIKEN Accel. Prog. Rep. 25 (1991)

# III-5-18. Detection of Liquid Xe Scintillation from Heavy Ions Using Si Photodiodes and Photomultipliers

T. Doke, E. Aprile, A. Hitachi, M. Ichige, N. Ishida, M. Kase, T. Kashiwagi, J. Kikuchi, K. Kuwahara, K. Masuda, T. Matsuda, Y. Qu, K. Sumorok,* M. Suzuki, and T. Takahashi

Liquid xenon (LXe) is a good scintillator for the radiation detection and will be possibly used in nuclear and particle physics in near future. The critical factors for detection of LXe scintillation photons are the reflection of the scintillation light (170nm) on walls and the light attenuation in the liquid. To investigate these factors, we have measured the light intensity as a function of the distance between the incident position of heavy ions and the photodiode (PD) as a photon detector. Also the decay times of the scintillation from the LXe excited by heavy ions have been preliminarily measured with a single photon counting method.

The apparatus is a double vacuum chamber shown in Fig. 1, the inner is a container of LXe and the outer is for thermal insulation. The effective length of the chamber is 65cm. The chamber has seven beam windows which are separated by 10cm from the neighbors along its length. Four trapezoidal flat mirrors for vacuum ultraviolet photons are installed in the inner chamber and form a tapered reflector cell. The areas of the cross section are $3.7\times3.7\text{cm}^2$ and $2.4\times2.4\text{cm}^2$ at the respective end. Two PDs are placed at the both ends of the cell. The incident ions entered and stopped in LXe after passing through a Mylar or Ti window of the beam line, about 10cm air, and then the chamber windows (a 40microns Havar foil and a 200microns SUS foil). A thin (100microns) plastic scintillator was sometimes used to obtain a beam trigger. The ions used were 135MeV/n C and N, 100MeV/n O and Mg, and 95MeV/n Ar from RIKEN Ring Cyclotron.

Xe gas was purified by passing through an Oxisorb purifier and molecular sieves (4A) with a flow rate of 5 l/min and then liquefied in the chamber. The LXe temperature was kept at −75°C with dry ice. Surface-barrier type Si PDs made at Waseda University were used as photon detectors. A mesh-type gold electrode is used to ensure a good transparency of the surface for 170 nm photons. Charge signals from the PD were processed with preamplifiers, shaping amplifiers (peaking time of 1 microsec), and ADCs. The decay time measurement was carried out by a single photon counting method[1] with photomultiplier using a mall test chamber.

From the dependence of the light intensity on the distance between the incident position of heavy ions and the PD, the effective attenuation length of about 10cm was obtained for the scintillation in LXe. This value includes the geometric factor (solid angle), the reflectivity of the mirrors, the light attenuation length of the LXe

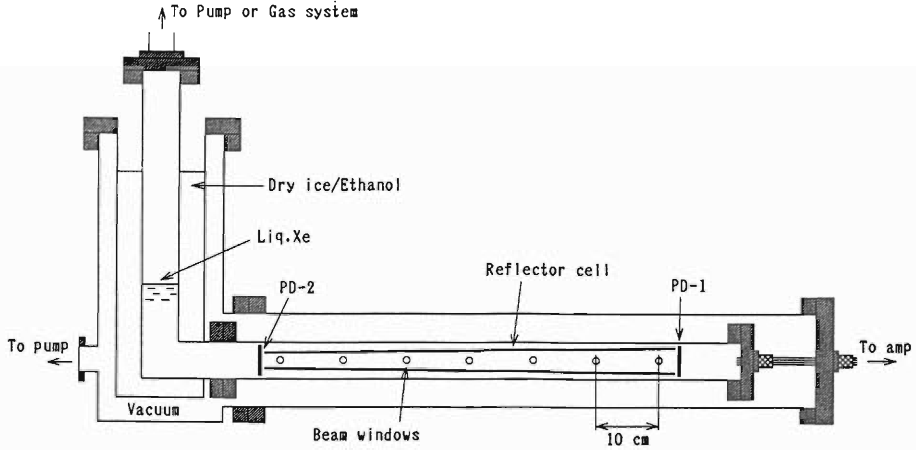


Fig. 1. Liquid Xe scintillation chamber for heavy ions.

* Massachusetts Institute of Technology.

itself. The mirrors used were essentially designed for vacuum ultraviolet photons in vacuum. However, the refractive index of LXe is much larger than unity (about 1.7) and the optics is considerably different from that in vacuum. Therefore, the obtained small effective attenuation length may be due to the low reflectivity of the mirrors.

The decay time was measured for 100 MeV/n O ions. From the preliminary analysis, two decay components were found, the decay times of which are 17nsec and 95nsec. The former decay time may correspond to the triplet state of excited Xe molecules and the latter to the slow recombination of ions and electrons produced by incident heavy ions.

References

1) A. Hitachi *et al.*: *Phys. Rev.*, **B27**, 5279 (1983).

# III-5-19. Data Acquisition System of the RIKEN Ring Cyclotron

T. Ichihara, A. Yoshida, Y. Watanabe, T. Inamura, and M. Ishihara

A general description of the data acquisition system at the RIKEN Ring Cyclotron is given elsewhere.[1,2] In this report, we will describe the recent modification of the system. Figure 1 shows the overview.

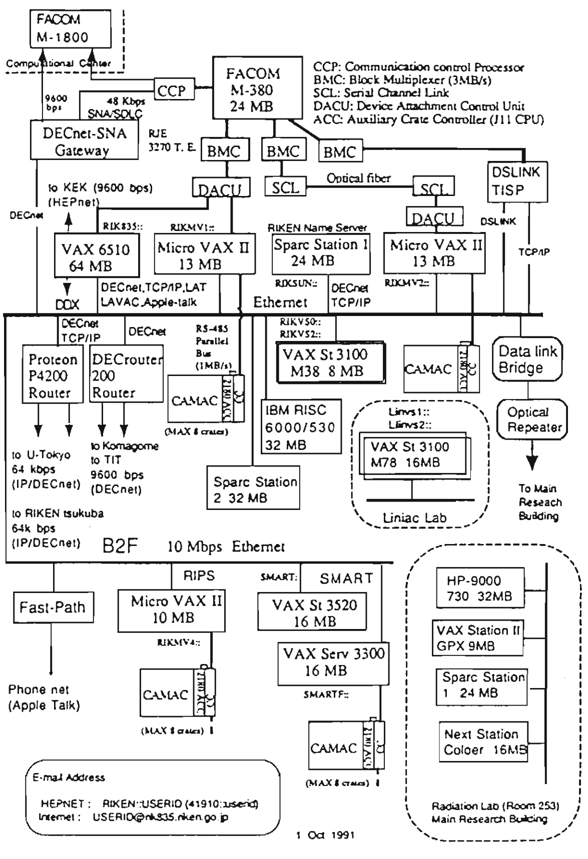


Fig. 1. Overview of the data acquisition system at the RIKEN Ring Cyclotron.

(1) On-line data acquisition system

Currently, seven Micro VAX's are used for the on-line experiments of the Ring Cyclotron. The node names and locations are :

RIKMV1: Micro VAX II (1F)
RIKMV2: Micro VAX II (1F)
RIKMV3: Micro VAX II (Linac)
RIKMV4: Micro VAX II (B2F RIPS)
SMART: VAX Station 3520 (B2F SMART)
SMARTF: VAX Server 3300 (B2F SMART)
TKYVS8: VAX Station 3200 (B2F RIPS)

We can perform independent measurements and counter tests without interference. The current version of the data-taking program supports the multi-crate parallel-readout using multi-J11's (Starbursts). The throughput of the data taking is increased by using these parallel readout features. The problem in the DMA transfer of VAX Station 3520,resulting from the incompleteness of Q22 bus of the VAX-Stations 3520, has been fixed by installing the VAX Server 3300 as a front-end VAX.

(2) Off-line data processing system-1 (VAX/VMS)

The following VAX's are available for the off-line data analysis and for general purposes.

RIKEN: (virtual node name of the cluster)
RIKVAX: VAX-6510 ( LAVC Server)
RIKVS0: VAX STATION 3100/M38
RIK835: VAX Station II/GPX
RIKVS2: VAX Station 3100/M38
RIKLV1: VAX Station 3100/M78 (Linac)
RIKLV2: VAX Station 3100/M78 (Linac)
RIKSNA: DECnet/SNA Gateway

Theses computers are connected by LAVC (Local Area VAX Clusters) using Ethernet. They are also connected to HEPNET(DECnet) and TISN(DECnet/IP) Internet and reachable from all over the word. (see Session 6 for detail)

Since the recent load of the VAX-8350 (RIK835:) was too heavy, we have replaced the VAX-8350 by a VAX-6510. The new VAX was installed in the end of November 1991. By this replacement, the overall performance has been increased to about a factor of five (from 2.3 VUPS to 13 VUPS). We have also a plan to upgrade the VAX-6510 (13 VUPS) to a VAX-6610 (32 VUPS) early in 1992.

(3) Off-line data processing system-2 (FACOM MSP)

Following FACOM MSP Main Frames are available at the RIKEN AcceleratorFacility.

FACOM M-380 (RIKEN Accelerator Research Facility)

FACOM M-780/20(RIKEN Computational Center)

These two FACOM's are connected by the NJE and DSLINK via the Ethernet. These two FACOM's are also connected to the DECnet/SNA Gateway, and therefore 3270 full-screen terminal emulations and file transfer using RJE (Remote Job Entry) are available from the VAX. The FACOM M-780/20 is scheduled to be replaced by a FACOM M-1800in December, 1991.

(4) RISC-based work stations

Some recent RISC-based Unix workstations (HP 9000/730 [21MFLOPS, 76MIPS], Sparc Station, Next Station) have been installed for the development of the UNIX based data processing system. The performance of the numerical calculation of HP 9000/730 is almost equal to that of the Main Frame Computer FACOM M-780. We are now planning to use these recent RISC workstations to process the experimental data.

(5) Wide area network

The RIKEN Accelerator facility is connected to the world-wide network of HEPNET (High Energy Physics NETwork)/SPAN (Space Physics Analysis Network) as Area 40, which is a part of the DECnet Internet, and the TISN internet (Todai International Science Network) which is a part of "The Internet" (NSFnet, ESnet, NSI, DDN etc.).

In order to support these wide area network connections, we are now supporting following 6 leased lines at the accelerator facility.

64 kbps (DECnet/IP) to the University of Tokyo, Faculty of Science

19.2 kbps (DECnet) to RIKEN Komagome site (SOR group)

9.6 kbps (DECnet) to KEK (National High Energy Physics Laboratory )

9.6 kbps (DECnet/IP) to RIKEN Life Science Tsukuba Center

9.6 kbps (DECnet) to Tokyo Institute of Technology, Faculty of Science

9.6 kbps (DDX-80) to NTT DDX. (Dial in from the telephone).

The leased line between RIKEN-Wako and RIKEN-Tsukuba will be upgraded from 9.6kbps to 64kbps in February 1992. Also the leased line between RIKEN-Wako and University of Tokyo will be replaced from 64kbps to 512kbps in June 1992.

The address of the electric mail of the general users of the RIKEN Ring Cyclotron VAX is as follows.

(HEPnet/SPAN)
RIKVAX:USERID(or 41316:USERID)
(Internet/BITnet)
USERID@RIKVAX.RIKEN.GO.JP

References

1) T. Ichihara: This Report, p.144.
2) T. Ichihara *et al.*: *IEEE Trans. Nucl. Sci.*, **36**, 1628 (1989).

RIKEN Accel. Prog. Rep. **25** (1991)

# III-5-20. Data Acquisition System for the Spectrograph SMART

T. Ichihara

A new data acquisition system of the spectrograph SMART has been developed.[1)]

Figure 1 shows a block diagram of the system. This system consists of two VAXes, VAX Server 3300 and VAX Station 3520. These two VAXes are configured as a Local Aria VAX Cluster (LAVC). The boot node is VAX Station 3520 and the Satellite node is VAX server 3300. Data acquisition is carried out on the VAX Server 3300 with a CAMAC crate and the data are recorded on a standard 2400 feet 6250 BPS Magnetic Tape or 2GB Digital Audio Tape (DAT). VAX Station 3520 is mainly used to display the spectrum during the experiment and also for the man-machine interface.

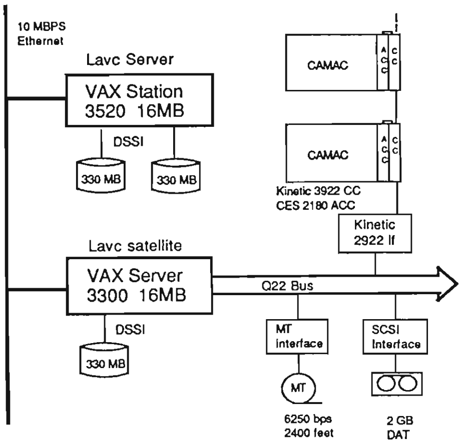


Fig. 1. Data acquisition system for the spectrograph SMART.

We have installed a Starburst auxiliary crate controller (CES 2180 ACC) on the CAMAC crate. For each event, a J11 micro processor in the Starburst ACC is interrupted by the trigger signal and reads the data form the CAMAC modules. The peak rate of CAMAC access from the Starburst ACC is 800kB/s (2.5$\mu$ sec./16bit mode) for a block read operation. The average rate including the overhead is about 100-200kB/s. Data are doubly buffered and when the current buffer is filled, Starburst changes the buffer immediately and generates a LAM signal to the host computer to start a DMA. The data transfer rate in the DMA depends on the length of the cable between the CAMAC crate controller and the interface in the VAX. The transfer rate is about 1MB/s for a short cable (5m) and about

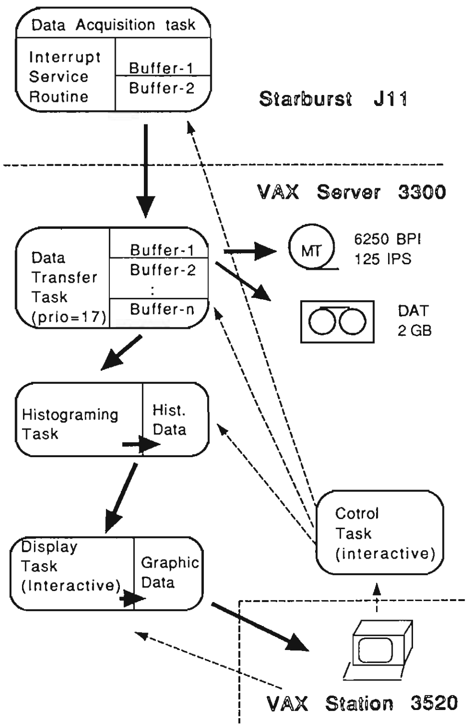


Fig. 2. Task and data flow of the data acquisition system.

310kB/s for a long cable (90m). The data acquisition of event by event and DMA transfer can be carried out simultaneously. The priority of the CAMAC bus access between the CC and ACC is determined by the cable connection of the request-grant chain. Usually ACC has the higher priority.

Figure 2 shows the tasks and the data flow of this data acquisition system. On-line monitor programs are running in the VAX-Server 3300 to fetch the new data buffer, analyze the data, and increment the histogram of spectra. The user can create any kind of the spectra by a simple fortran language. If the data rate is low, all the data are analyzed on line. But if the data rate is very high, only a portion of the data are analyzed on line. For the typical experiment of the spectrograph SMART, we can create a momentum spectrum of a particle gated by the particle identifications on line.

In 1989, we installed the VAX Station 3520 for the data acquisition system of the spectrograph SMART. But we encountered a serious problem in the VAX Station 3520. The Q22 bus features of VAX Station 3520 were not complete and it did not support the burst mode DMA which is necessary to operate the Kinetic 2922 Crate Controller Interface. To fix this problem, we have installed a VAX Server 3300 as a front-end VAX. The kinetic 3922 Crete controller interface and the Victor Magnetic tape (2400 feet) controller have been migrated from the VAX Station 3520 to the VAX Server 3300. The Q22 Bus of the VAX Server 3300 satisfies the complete Q22 standard and the problem of the burst mode DMA of the Kinetic 2922 Crate controller interfaces has been solved.

We have also installed the Digital Audio Tape (DAT) to record raw data. We can record about 2GB per one cartridge of the DAT. The error rate of the DAT is extremely low ($10^{-15}$) and reliability is better than an 8mm tape. This DAT will be the standard media to record raw data in the facility.

References

1) T. Ichihara *et al.*: *IEEE Trans. Nucl. Sci.*, **36**, 1628 (1989).

RIKEN Accel. Prog. Rep. **25** (1991)

# III-5-21. New Computer System for Data Analysis

Y. Watanabe, T. Ichihara, and A. Yoshida

We report here about three new workstations that were introduced in our laboratory. These workstations have a common ability that distinguishes them from the computer we have used. It is a UNIX operating system that is recently spreading in many fields from computer science to business application.

For contemporary physics, computer is one of the important apparatus. Particularly in our field, recent research is going more precise and requiring a larger quantity of data. So, we have been using the mainframe (FACOM M380) for theoretical calculations and data analysis, because of the computing power.

Recently, computer technology expands drastically, especially some workstations based on the RISC* technology (so called RISC-workstation) get comparable power as the mainframe (Table 1). Since they are much cheeper than the mainframes, we can get much computing power with a small expense. In fact, these workstations are spreading quickly in many fields. We may replace the mainframe by such workstations. However there are some problems that must be overcome. UNIX that is only available operating system on such RISC-workstations does not have all functions we need, such as realtime capability and flexible handler for magnetic tape devices.

In such situation, we introduced three new workstaions in our laboratory to investigate the possibility of the RISC-workstation and UNIX operating system for our purpose. The main component is HP9000/730 that was selected for the high computing power. It has also a DAT tapedrive (2GB/tape) and a Magnet-Optical disk (660MB/disk) that must be needed to store our experimental raw data (Typical data size is several GB in one experiment).

We connected closely this HP with SUN and NeXT in our laboratory (Fig. 1). Multi vender connectability is also important because no single system gives us all of the feature we want. These three workstations have peculiar characteristics each other. HP has high computing power as we mentioned above. SUN (SPARCstation 1) is the most popular workstation in the world. The population is very important for software availability. NeXT that takes newest software technologies, has most elegant environment for the software development. We hope these machines work in complementary and give us powerful and elegant computer environment.

We have already succeeded to introduce in our HP the CERNLIB that is developed for data analysis and ported to many computers by CERN. The performance investigation is in progress.

Table 1. Relative performance of some computers.

| | C1 | C2 | C3 | C4 | Avr |
|---|---|---|---|---|---|
| (RISC UNIX) | | | | | |
| HP9000/730 | 92 | 101 | 621 | 202 | 185 |
| PowerStation530 | 101 | 135 | 149 | 66 | 122 |
| SparcStation 1 | 9 | 6 | 41 | 18 | 15 |
| (VAX/VMS) | | | | | |
| VAX6510 | 25 | 20 | 69 | 45 | 35 |
| MicroVAX II | 1 | 1 | 4 | 3 | 2 |
| (MainFrame) | | | | | |
| FACOM M380 | 100 | 100 | 100 | 100 | 100 |

C1-C4 are floating point calculations that are prepared by T. Ichihara for a benchmark test.
C1,2: simple calc. with single and double precision
C3: matrix
C4: many nestings and conditional branches

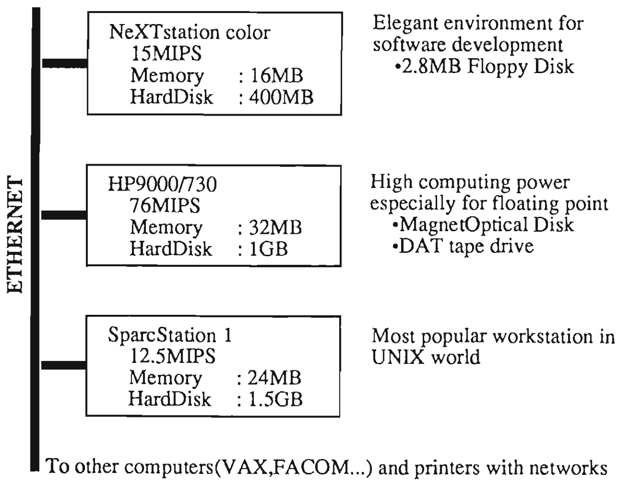


Fig. 1. Diagram of workstaions in Radiation Laboratory.

* Reduced Instraction Set Computer.

RIKEN Accel. Prog. Rep. **25** (1991)

# III-6. Material Analysis

## 1. Theory of *L*-*V* X-Ray Emission Spectra of Copper Compounds

J. Kawai and K. Maeda

It is believed that the copper $L\alpha$ ($L_3$-$M_{4,5}$ or $L_3$-$V$) X-ray fluorescence spectra (XRF) are related to the local (Cu atom) and partial (3*d*) densities of states (DOS) of the compounds. Figure 1 compares the measured $L_3$-$V$ X-ray emission spectrum[1] of a copper oxide with that calculated by the local and partial DOS.[2] Since the DOS calculation by Redinger *et al.*[2] is quite reliable, the disagreement between the theory and the experiment in Fig.1 is mostly due to the fact that the $L_3$-$V$ X-ray emission is not directly related to the local and partial DOS. Therefore we have proposed a theory[3] to interpret the Cu $L_3$-$V$ line shape of various copper compounds based on the theory of X-ray photoelectron spectra (XPS) of van der Laan *et al.*[4] as follows.

The Cu $2p_{3/2}$ X-ray photoelectron spectra (XPS) of divalent copper compounds (nominally $3d^9$ electron configuration) have generally one main peak (at 933.6eV) and one higher binding energy satellite (at 943eV, so-called 'shake-up' satellite, since this satellite was believed to originate from electron shake-up). After the study of van der Laan *et al.*,[4] it has been revealed that the main peak is, in fact, a charge-transfer satellite. That is to say, an electron is transferred from one of the ligands to the central $Cu^{2+}$ ion at the moment ($<10^{-14}$sec) of the 2*p* electron photoionization. On the other hand, the so-called 'shake-up satellite' is, in fact, the main line, *i.e.*, one of the 2*p* electrons is photoionized and the rest of the electrons in the vicinity of the photoionized Cu ion remains still. The final states of the $2p_{3/2}$ XPS are the initial states of the $L_3$-$V$ X-ray emission, thus we must include this charge-transfer effect in the line shape analysis of Cu $L_3$-$V$ spectra. The relation between the 2*p* XPS and $L_3$-$V$ XRF we have proposed in the previous paper[3] is that the $L_3$-$V$ main line (930eV) of XRF corresponds to the main line of $2p_{3/2}$ XPS and that the high energy shoulder (932-935eV) of XRF corresponds to the so-called 'shake-up' satellite of $2p_{3/2}$ XPS.

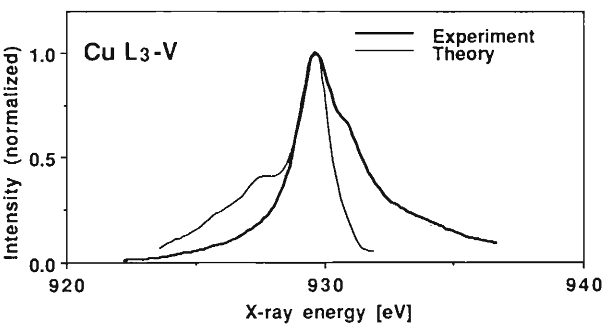


Fig. 1. Comparison of the experimental $L_3$-$V$ line shape of $La_2CuO_4$ (Barnole *et al.*[1]) with the theoretical one which has been calculated from the local and partial DOS (Redinger *et al.*[2]).

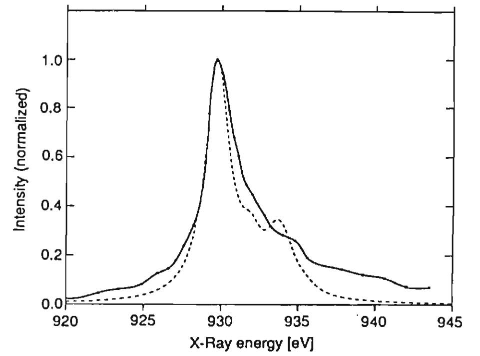


Fig. 2. Comparison of the spectrum measured by Bonnelle[5] (solid line with dotted points) with that calculated by the present theory (dashed line).

To check the above theory, we have calculated the $L_3$-$V$ spectrum of CuO, as shown in Fig. 2. The transition energy was calculated from Slater-Condon parameters determined by the atomic Hartree-Fock-Slater calculations. The relative intensities of the components of the X-ray lines were determined by the *LS* coupling. Comparing the calculated spectrum with the measured spectrum by Bonnelle,[5] it is concluded that the agreement between our theory and the experiment is satisfactory.

References

1) V. Barnole, J.-M. Mariot, C. F. Hague, C. Michel, and B. Raveau: *Phys. Rev.*, **B41**, 4262 (1990).
2) J. Redinger, J. Yu, A. J. Freeman, and P. Weinberger: *Phys. Lett.*, **A124**, 463 (1987).
3) J. Kawai and K. Maeda: *Spectrochim. Acta,* **46B**, 1243 (1991).
4) G. van der Laan, C. Westra, C. Haas, and G.A. Sawatzky: *Phys. Rev.*, **B23**, 4369 (1981).
5) C. Bonnelle: *Ann. Phys.*, **1**, 439 (1966); *J. de Phys. (Paris)*: *Colloq.*, **28**, C3-65 (1967).

# III-6-2. Nickel *L-V* PIXE Spectra of Alloys

J. Kawai, K. Maeda, Y. Sasa, M. Takami, T. Urai,
T. Hanada, and M. Uda

The $L_{2,3}$-$V$ or $L_{2,3}$-$M_{4,5}$ (Siegbahn notation $L\beta$, $\alpha$) X-ray emission spectra measured by an electron probe X-ray microanalyzer (EPMA) or X-ray fluorescence (XRF) spectrometer have been used to characterize the transition-metal compounds such as oxide superconductors. This is mainly because the $L$-$V$ X-ray transition involves the valence orbital ($V$) of the analyte.[1] Therefore the $L$-$V$ spectra contain information on the partial and local densities of states (DOS) of the analyte. However a group of satellite lines are usually observed on the high energy shoulder of the $L$-$V$ main lines. These satellite lines are believed to be emitted either by multiple ionized states or by poorly screened states. However the contribution from these two origins are not well clarified till now. Therefore it is required to clarify the contribution from the two origins to use the profile changes of EPMA spectra for the characterization of transition-metal compounds. A comparison between electron and ion (particle) induced X-ray emission (PIXE) spectra with high energy resolution measurements clarifies the degree of contribution from the above two origins.

We have measured the $L$-$V$ X-ray spectra of nickel metal and alloys ($\mu$-metal and nickel-cromium alloy) by 2.6 keV electron beam and 1.5 MeV/nucleon (21.03 MeV) $N^{2+}$ heavy ion beam at RILAC. The analyzing crystal was RAP (100) ($2d$=26.12 Å). The sample (target) current was 20 $\mu$A for the electron excitation and ~100 nA for the $N^{2+}$ ion excitation. The spectra were stored till the integrated ion current became more than 2 mC. A position sensitive detector composed of a microchannel plate and a photodiode array was used for the X-ray detection. A Perkin-Elmer Φ04-015 grazing-incidence electron gun, which was set on the same PIXE chamber as shown in Fig.1 to use the same X-ray optics for comparison of the difference in the two excitation methods, was used for the electron excitation. The pressure of the sample chamber was kept lower than $10^{-5}$ Torr during the measurements.

The measured spectra of a nickel metal are shown in Fig.2. Though the spectra excited by electrons are significantly different from those excited by $N^{2+}$ ions, no significant difference was detected among the measured metal and alloys if the excitation method was the same. Two strong satellites were found in the $N^{2+}$ excited X-ray spectra of nickel metal and alloys (denoted by S1 and S2 in Fig. 2).

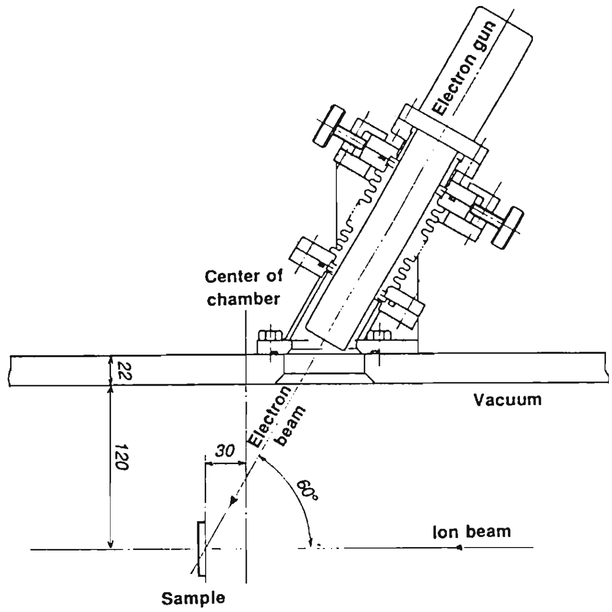


Fig. 1. Setup of the electron gun.

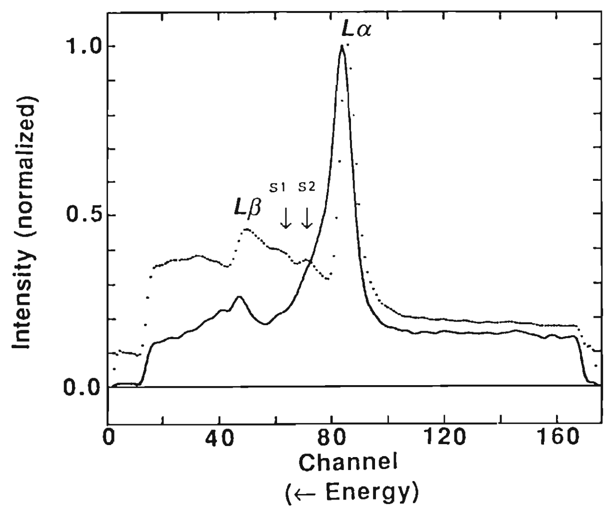


Fig. 2. Measured Ni $L$-$V$ X-ray spectra of a nickel metal excited by 2.6 keV electron (solid line) and by 21.03 MeV $N^{2+}$ ion (dotted). S1 and S2 indicate the multiple ionized satellites.

Though theoretical calculations are required to assign the X-ray transitions of the two satellites, it is concluded that the comparison between the PIXE and electron excitation X-ray emission spectra reveals the presence of multiple ionized satellites which are usually hidden in the spectra of EPMA and fluorescent X-ray spectra. It has also been clarified that the contribution from the multiple ionization is negligible compared with that from a poorly screened state as the origin of the high energy shoulder of $L$-$V$ X-ray lines measured by EPMA or XRF spectrometers.

References

1) J. Kawai: "Advances in X-Ray Analysis", Edited by C. S. Barrett, J. V. Gilfrich, I. C. Noyan, T. C. Huang, and P. K. Predecki, Plenum Press, New York , **34**, 91 (1991).

RIKEN Accel. Prog. Rep. **25** (1991)

# III-6-3. Particle Induced Optical Luminescence of Lanthanoid Metals

J. Kawai, K. Ando, T. Kambara, and K. Maeda

Though the detection of electron or X-ray induced optical luminescence of lanthanoid metals in insulators is one of the most powerful methods of trace elemental analysis,[1,2] it is not widely used in analytical chemistry. This is mainly because the intensity of X-ray induced optical luminescence depends on the sample preparation method as well as the concentration in the sample. It is not detected for either metallic samples nor insulators of perfect crystals. Therefore it is interesting to study whether such metallic samples which are not luminescent by the X-irradiation emit optical luminescence when they are bombarded by high energy heavy ions.

We measured the optical luminescence of several rare earth compounds at RIKEN Linear Accelerator (RILAC). The samples measured were a Sm metal deposited on an Al foil (2 $\mu$m) and $EuF_3$ (49.5 $\mu g/cm^2$) on Mylar (2.5 $\mu$m) for the 4.03-MeV $He^+$ excitation, and Sm metal, $Eu_2O_3$, $Nd_2O_3$ on Al foils (2 $\mu$m) for the 52.0-MeV $Ar^{8+}$ ion beam. The sample was irradiated by the ion beam in vacuum ($<10^{-6}$ Torr). The emitted optical signal going through a quartz view port of the vacuum chamber was then analyzed by a Nikon G-250 Czerny-Turner type grating spectrometer and detected by a quartz window photomultiplier. Typical measured spectra are shown in Figs. 1 and 2.

Whereas the emission lines from argon ions were observed (488, 435, and 410 nm peaks in Fig. 2) in the $Ar^{8+}$-induced spectra for all the samples measured in the present study, the $He^+$-induced spectra (Fig. 1) were significantly different each other and also were different from those excited by the $Ar^{8+}$ ion. Since the basic research in this area has not well been performed, the profile changes of the measured spectra have not been interpreted. However it is concluded that the optical signal can be detected for very low amounts of samples, thus this method has a potential to be a powerful tool of trace elemental analysis.

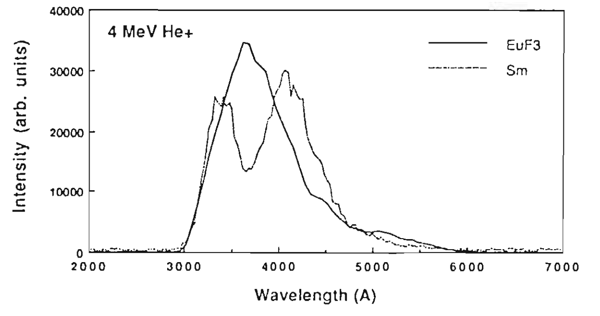


Fig. 1. $He^+$-induced optical emission spectra of $EuF_3$ and Sm.

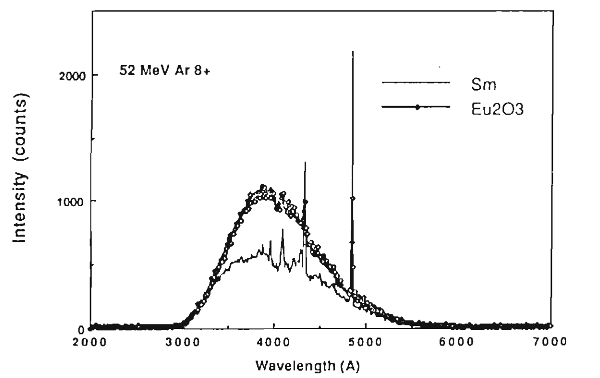


Fig. 2. $Ar^{8+}$-induced optical emission spectra of Sm and $Eu_2O_3$.

References

1) A. P. D'Silva, E. L. DeKalb, and V. A. Fassel: *Anal. Chem.*, **42**, 1846 (1970).
2) E. L. DeKalb and V. A. Fassel: *ibid.*, **47**, 2354 (1975).

# III-6-4. Analysis of an Accident during Ozone Experiments by Means of the Heavy-Ion Rutherford Scattering

M. Aratani and M. Yanokura

An accident happened during ozone distillation in an inorganic synthesis experiment at a certain National Institute in the Capital Region. A spiral stainless steel pipe used as the ozone distillator exploded into fragments, which flew over and sticked to human body near by. Observation on the exploded pipe showed that the explosion site of the pipe was situated at the bottom of the distillator and at the end point of the spiral part, from which the pipe went up vertically to the next part of the apparatus. Two substances loomed up as possible suspects through discussions; carbonaceous contaminant gas and ozone gas itself. The very gaseous substances for sampling, however, had been lost in the explosion. Thus, the heavy-ion Rutherford scattering was suggested for the inside surface characterization of the fragments so as to make clear the cause of the accident.

Three kinds of samples were provided; one was a fragment from the explosion site, another was a portion of the pipe at a distance of 30 cm from the explosion site, and the other was an unused stainless steel pipe of the same kind. The samples were cut into 19 mm in length, opened and made flat, and the inside surfaces of the samples were examined by use of a 50 MeV $^{40}Ar$ ion beam. The details of the HIRS method was previously reported in RIKEN Accel. Progr. Rep. and elsewhere.[1]

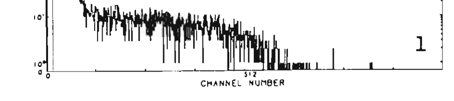


Fig. 1. Comparison of the three spectra shows that a thick oxide film but not a carbon film was formed on the inside surface of the pipe at the exploded site.
1 : Spectrum of the exploded site.
2 : Spectrum of $SiO_2$ as the oxygen standard sample.
3 : Spectrum of a diamond-like carbon (DLC) film as the carbon standard sample.

Simultaneous measurements for light and heavy elements were performed with the samples. Some of the spectra were shown in Fig.1. A large quantity of oxygen atoms were found for the sample from the explosion site. For the sample 30 cm distant from there, oxygen atoms also observed but in a much less quantity. Oxygen atoms were scarcely found for the unused-pipe sample. Carbon atoms were not observed for any samples. The presence of a small quantity of tungsten atoms was suggested for the samples from the explosion site. A series of measurements led us to the conclusion that ozone was responsible for the explosion due to decomposition into oxygen to make a thick oxide layer on the inside surface.

According to our suggestion of the presence of tungsten atoms by HIRS, a destructive chemical analysis was performed at their Institute. Origin of the tungsten atoms was also examined by the destructive chemical analysis of all the materials used in the apparatus. The results showed the electrodes of an ozone generator prior to the ozone distillator were made of tungsten. It may be supposed that fine particles of tungsten oxide which were formed by the discharge in the ozone generator, transported to the bottom of the ozone distillator by ozone stream and accumulated there, would have played a role in the explosive decomposition of ozone.

References

1) H. Nagai, S. Hayasi, M. Aratani, T. Nozaki, M. Yanokura, I. Kohno, O. Kuboi, and Y. Yatsurugi: *Nucl. Instrum. Methods*, **B28**, 59 (1987).

RIKEN Accel. Prog. Rep. 25 (1991)

# III-6-5. Light-Element Impurities in a TiN Film Studied by Heavy-Ion Rutherford Scattering

H. Akiyama, K. Onoe,* M. Yanokura, and M. Aratani

A thin film of titanium nitride (TiN) is employed for coating cutting tools because of its hardness and for coloring decorative art works because of its beautiful color. Contamination by impurities has so much influence on various properties of the thin film that their characterization is indispensable for manufacturing high-purity thin films. So, we have examined light-element impurities in a thin TiN film prepared on a Si substrate by the sputtering technique. The thickness of the TiN film was 350 Å. The heavy-ion Rutherford scattering (HIRS) method has been used in combination with the TOF measurement. The incident beam was argon of 1.3 MeV/nucleon in energy.

The samples were cut into pieces of a size of 19 mm × 9 mm. In a one meter scattering chamber in A-1 course of RILAC, we set a target holder with nine pieces of samples at an angle of 10° ($\theta_1$) and surface-barrier semiconductor detectors (SSD) at angles of 37° and 47° ($\theta_2$) to the incident beam. The SSD at angles of 37° detected forward-scattered argon ions and forward-recoiled ions. The SSD at angles of 47° was used for monitoring the incident argon beam. The samples were bombarded with a 52.46 MeV Ar beam under a vacuum ($6.7\times10^{-4}$Pa). The spot size of the incident ion beam was 1.5 mm × 1.5 mm on the specimen. The beam current and irradiation doses during measurements were 7 to 8 nanoamperes and 8 to 10 microcoulombs, respectively which are thought to be within the dose range to produce no serious irradiation effect in this experiment.

Energy spectrum for recoiled silicon and oxygen from a $SiO_2$ standard is shown in Fig. 1(a), and that for recoiled ions and forward scattered ions from the thin TiN film are shown in Fig. 1(b). The thick arrow in Fig. 1(b) indicates the position of the energy of recoiled light-impurity atoms which were contained in the thin TiN film. The light element has been identified to be oxygen, because the energy of the peak marked with the thick arrow agrees with the energy of oxygen atoms from the $SiO_2$ standard. Total content of the oxygen in the TiN film is calculated to be 6.0 at% which corresponds to 3.1 wt%. The origin of impurity oxygen atoms may be attributed to those absorbed into the film from residual gas in the processes of preparation of the TiN film.

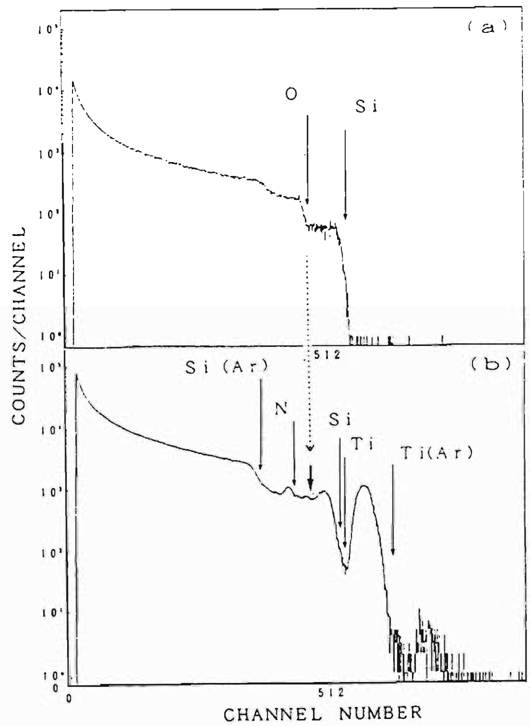


Fig. 1. Energy spectra of recoiled ions and forward scattered Ar ions from (a) $SiO_2$ and (b) a thin TiN film. Si(Ar) and Ti(Ar) represent Ar ions forward-scattered by Si and Ti atoms, respectively. Target angle, $\theta_1=10°$; Detector angle, $\theta_2=37°$

As stated above, the nondestructive nitrogen-oxygen separation and the simultaneous quantitative analysis of light elements have been successfully performed by the HIRS with argon. The nitrogen-oxygen separation also has been confirmed by the TOF measurement.

The present TiN film can be used as a standard material of $1.05\times10^{17}$ atoms/cm$^2$ nitrogen.

* Institute for Super Materials, ULVAC JAPAN, Ltd.

RIKEN Accel. Prog. Rep. **25** (1991)

# III-6-6. Non-Destructive Analysis of Hydrogen Isotopes in the Volcanic Glass by Linear Accelerator

A. Okada, M. Aratani, M. Yanokura, and H. Akiyama

Obsidian, a natural glass of volcanic origin, contains 0.3-8.0wt.% $H_2O$.[1] It is geochemically interesting to investigate the source of water in the volcanic eruptives from volcanoes which distribute in the active areas on the earth. In addition, obsidian is an archaeologically important material, with which the antiquity made implements in the stone age of ancient Japan. It is also significant to investigate where and how the ancients got obsidian for the production of stone implements. For these purposes, we measured the $^1H$ and D abundance of obsidian samples.

Recently the scattering analysis using a linear accelerator has been applied to the determination of hydrogen in solid materials. Further, the high-sensitive analysis of deuterium in solid samples using nuclear reaction of $^{15}N$ with deuterium, i.e., $D(^{15}N, p\gamma)^{16}N \rightarrow {}^{16}O$ and $D(^{15}N, n\gamma)^{16}O$, has been recently developed.[2]

The intense 6.13 MeV $\gamma$-ray emitted by the decay of excited $^{16}O$ is measured with a BGO, bismuth germanate ($Bi_4Ge_3O_{12}$), scintillator. This method is highly sensitive to deuterium in solids.

In this work, we examined the possibility of the simultaneous and non-destructive analysis of both $^1H$ and D contents of obsidian, combining both the scattering reaction and nuclear reaction by a $^{15}N^{2+}$ beam of RIKEN linear accelerator. Figure 1 shows the schematic arrangement of the sample-detector system in the scattering chamber. Polished obsidian samples from Tokachi-dake, Hokkaido, Japan, and from Arizona, U.S.A., were set at 15° to the incident $^{15}N^{2+}$ beam (15 MeV and 20 nA). The recoiled hydrogen atoms from the sample were measured by the solid state detector set at an angle of 30° to the incident beam. A BGO scintillator was set close by the target to detect $\gamma$-ray emissions. Figure 2 shows the $\gamma$-ray spectrum detected by the BGO scintillator. The result showed that the simultaneous analysis of $^1H$ and D of the geological sample by using a linear accelerator is promising. But in this experiment, the energy resolution of the BGO scintillator was not so enough for the calculation of the hydrogen isotope abundance. At present, improvements in the resolution of the BGO detector are being done.

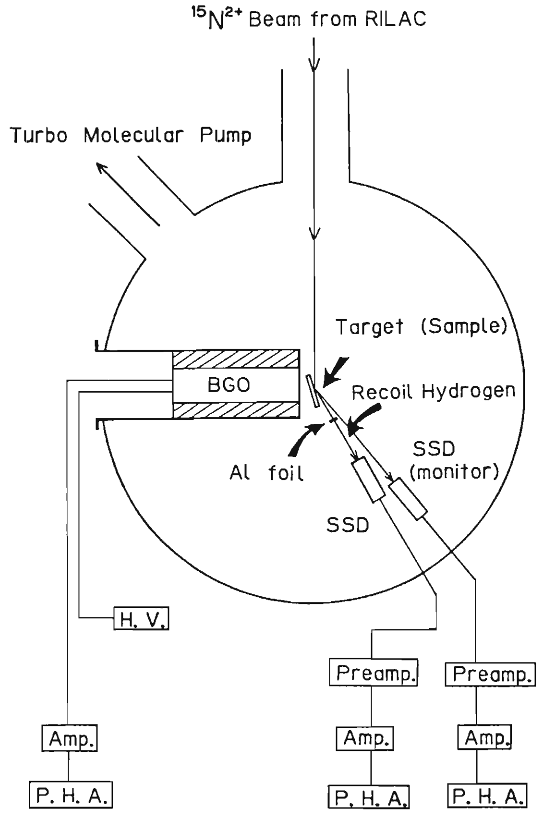


Fig. 1. Schematic arrangement of the sample-detector system in the scattering chamber (1000 mm in dia.).

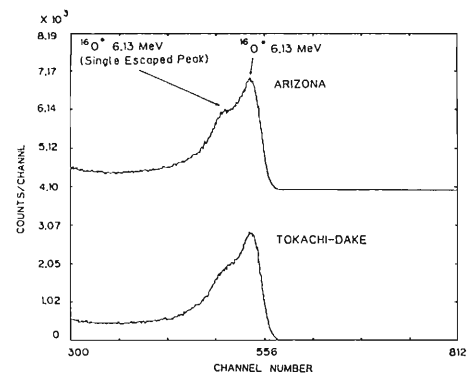


Fig. 2. $\gamma$-ray spectrum of $^{16}O$ produced by $^{15}N$-induced nuclear reaction with deuterium in obsidian.

References

1) K. Shibata (ed.): Nihon Ganseki-shi, Asakura Shoten, III, p. 384 (1968).
2) S. Hayashi, H. Nagai, M. Aratani, T. Nozaki, M. Yanokura, I. Kohno, O. Kuboi, and Y. Yatsurugi: *Nucl. Instrum. Methods*, **B16**, 377 (1986).

RIKEN Accel. Prog. Rep. **25** (1991)

# IV. NUCLEAR DATA

## 1. Status Report of the Nuclear Data Group

Y. Tendow, A. Yoshida, Y. Ohkubo, A. Hashizume, and K. Kitao

The Nuclear Data Group has suffered a change in the staff this year. Hashizume, the group leader, has retired from RIKEN. He has been making efforts for years to establish and expand the activities of our group and he is supposed to continue the nuclear data compilation works as a part-time staff of the group. The decrease of experienced compilers is a general trend seen in the fields of nuclear data activities. It is an urgent matter to train new hands in order to keep up good maintenance and constant supply of nuclear data in the future. We have been continuing the following data activities since previous years.[1]

(1) Nuclear reaction cross-section data (EXFOR)

Compilation of nuclear reaction cross-sections induced by charged particles in the EXFOR format has been continued. We had restricted our scope of compilation to the production cross-sections for 20 radioisotopes commonly used in biomedical applications: $^{11}C$, $^{13}N$, $^{15}O$, $^{18}F$, $^{28}Mg$, $^{52}Fe$, $^{67}Ga$, $^{68}Ge$, $^{68}Ga$, $^{74}As$, $^{77}Br$, $^{82}Br$, $^{77}Kr$, $^{81}Rb$, $^{82m}Rb$, $^{111}In$, $^{123}Xe$, $^{123}Cs$, $^{127}Xe$, $^{123}I$, $^{124}I$, and $^{125}I$. Although the most of the cross-section data have already been compiled into the EXFOR file, a considerable number of important works still remain untouched. We tried to pick up and compile these works as well as recent data. It is essential to cover these missing works for the completeness of the EXFOR data base.

An effort was made to complete the collection of the cross-sections for the production of $^{74}As$ nuclides.[2] As is one of the important elements in the biomedical and environmental studies.

The evaluation of excitation functions for the monitor reactions $^{12}C(p, pn)^{11}C$, $^{27}Al(p, 3pn)^{24}Na$, $^{63}Cu(p, 2n)^{62}Zn$, and $^{65}Cu(p, n)^{65}Zn$ is continued.

We sent a transmission tape #R006 to the IAEA Nuclear Data Section (NDS) which contained a new EXFOR file of 4 entries (works) consisted of a total of 41 subentries. (Each subentry corresponds to an excitation curve.)

(2) Evaluated nuclear structure data file (ENSDF)

As a member of the Sigma Committee of JAERI, we have been participating in the ENSDF compilation network coordinated by the Brookhaven National Nuclear Data Center (NNDC). We have continued evaluation and compilation of the A=177 mass chain. We have set about a new evaluation of the A=129 mass chain and in the first place references were surveyed and collected. The re-evaluation of A=120 is also planned.

The complete ENSDF with mass A=1 through 266 is provided from NNDC periodically. The complete file is now stored in the FACOM mainframe computer as a partitioned data set of 6 members and occupies about 1990 tracks in the disk memories. The file is planned to be installed into the VAX networks in the accelerator facility area.

(3) Nuclear structure references file (NSR)

We are engaged in collection and compilation of secondary references (annual reports, conference proceedings etc.) published in Japan into Nuclear Structure References (NSR) file and sending it to NNDC. The NSR file is offered for on-line retrieval service by NNDC and also published as RECENT REFERENCES periodically. We have completed the compilation for 1988 and 1989 references and set about compiling 1990 ones. Secondary sources surveyed are RIKEN (Accel. Prog. Rep.), JAERI-TLV (JAERI), INS (Univ. Tokyo), UTTAC (Univ. Tsukuba), RCNP (Osaka Univ.) and CYRIC (Tohoku Univ.).

The 11th IAEA Consultants' Meeting of the Nuclear Reaction Data Centers was held on October 7 - 11 at the Nuclear Data Center in the Institute of Physics and Power Engineering in Obninsk, USSR. Participants were the delegates from 9 data centers which are engaged in CINDA and EXFOR compilation networks in the world. Each center reported the status of activities and discussed relevant issues of CINDA and EXFOR.

References

1) A. Hashizume, Y. Tendow, Y. Ohkubo, K. Kitao, and K. Sueki: *RIKEN Accel. Prog. Rep.*, **24**, 128 (1990).
2) Y. Tendow, A. Hashizume, Y. Ohkubo, and K. Kitao: This Report, p. 155.

RIKEN Accel. Prog. Rep. **25** (1991)

# IV-2. Cross Section Data for $^{74}As$ Production

Y. Tendow, A. Hashizume, Y. Ohkubo, and K. Kitao

Arsenic is one of the important elements menacing the environment with its growing distribution through modern industrial activities. Radioarsenic is used as a tracer in biology and in the study of water and soil pollution to set environmental health criteria for As. Among radioarsenic nuclides available, $^{74}As$ is especially convenient for biomedical studies because of the positron emission and its moderate half-life of 17.78 d.

Table 1. Cross Sections for $^{74}As$ Production.

| Reaction | Energy (MeV) | $\sigma_{max}$ (mb at MeV) | Reference |
|---|---|---|---|
| $^{74}Ge$ (p, n) | 3.43 - 5.83 | 167 (at 5.83) | 1) |
| $^{74}Ge$ (p, n) + | 19 - 64 | 85.1 (at 31.6) | 2) |
| $^{76}Ge$ (p, 3n) | 6.5 - 41 | 30* (at 10) | 3) |
| $^{75}As$ (p, pn) | 21.5 | 350 | 4) |
| $^{75}As$ (p, spall) | 2900 | 47 | 5) |
| | 540 | 60.5 | 6) |
| Br (p, spall) | 593 | 18.8 | 6) |
| Rb (p, spall) | 593 | 12.8 | 6) |
| $^{89}Y$ (p, spall) | 540 | 6.9 | 6) |
| | 240 | 0.77 | 7) |
| $^{90}Zr$ (p, spall) | 1000 | 4.2 | 8) |
| $^{91}Zr$ (p, spall) | 1000 | 4.7 | 8) |
| $^{94}Zr$ (p, spall) | 1000 | 7.3 | 8) |
| $^{96}Zr$ (p, spall) | 1800 | 5.1 | 9) |
| $^{96}Mo$ (p, spall) | 1800 | 3.3 | 9) |
| $^{96}Ru$ (p, spall) | 1800 | 1.1 | 9) |
| Ag (p, spall) | 3000 | 3.01 | 10) |
| | 29000 | 2.43 | 10) |
| In (p, spall) | 2900 | 2.7 | 11) |
| Au (p, spall) | 2900 | 1.8 | 11) |
| U (p, spall) | 2900 | 5.1 | 11) |
| $^{71}Ga$ ($^3He$, $\gamma$) | 1.3 - 30.2 | 34.4μb (at 13.7) | 12) |

* μCi/μAhMeV

$^{74}As$ is produced through $^{74}Ge$(p, n) and/or $^{76}Ge$(p, 3n) reactions on natural Ge targets.[2,3] Excitation functions are shown in Fig. 1. The curve from Basile et al.[3] has two peaks at around 10 MeV and 30 MeV corresponding to $^{74}Ge$(p, n) and $^{76}Ge$(p, 3n) reactions respectively and that from Horiguchi et al.[2] is for the $^{76}Ge$(p, 3n) reaction. Basile et al.[3] reported also the excitation functions for the $^{71,72,76}As$ production. Only a few works on excitation functions are found in literature until now.

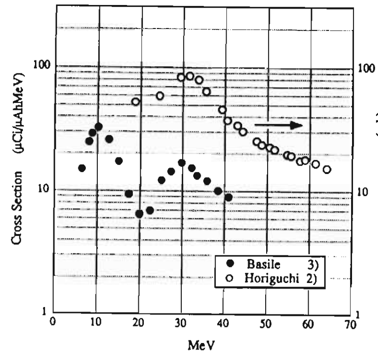


Fig. 1. Excitaion functions for the $^{nat}Ge$(p, xn)$^{74}As$ reaction.

A number of cross-sections for spallation reactions reported so far, together with the excitation function data, are summarized in Table 1.

Utilization of radioarsenic will be increasing in the studies of biomedical and environmental fields in the future. More precise and overall measurements are expected to be advantageous.

References

1) C. H. Johnson, A. Galonsky, and C. N. Inskeep: ORNL-2910, p. 25 (1960).
2) T. Horiguchi, H. Kumahora, H. Inoue, and Y. Yoshizawa: *Int. J. Appl. Radiat. Isot.*, **34**, 1531 (1983).
3) D. Basile, C. Birattari, M. Bonardi, L. Goetz, E. Sabbioni, and A. Salomone: *ibid.*, **32**, 403 (1981).
4) B. L. Cohen and E. Newman: *Phys. Rev.*, **99**, 718 (1955).
5) S. Kaufman: *ibid.*, **126**, 1189 (1962).
6) A. Grütter: *Int. J. Appl. Radiat. Isot.*, **33**, 725 (1982).
7) A. A. Caretto, Jr. and E. O. Wiig: *Phys. Rev.*, **103**, 236 (1956).
8) B. N. Belyaev, V. D. Domkin, Y. S. Egorov, Y. G. Korobulin, and L. M. Krijansky: *Izv. Akad. Nauk USSR, Ser. Fiz.*, **42**, 2392 (1978).
9) N. T. Porile and L. B. Church: *Phys. Rev.*, **B133**, 310 (1964).
10) S. Katcoff, H. R. Fickel, and A. Wyttenbach: *ibid.*, **166**, 1147 (1968).
11) S. Kaufman: *ibid.*, **129**, 1866 (1963).
12) R. V. Carlson and P. J. Daly: *Nucl. Phys.*, **A102**, 161 (1967).

RIKEN Accel. Prog. Rep. 25 (1991)

# V. DEVELOPMENT OF ACCELERATOR FACILITIES

## 1. Ion Accelerator Development

### 1. Beam Phase Meter for RIKEN Ring Cyclotron

M. Kase and I. Yokoyama

In cyclotron tunings, to build an isochronous magnetic fields is one of the most important processes. Main and trim coil currents in the sector magnet are initially set according either to the estimation using the field mapping data or to the data of the previous operation in the same conditions. These initial settings are not good enough for making an accurate isochronous field. The beam phase measurement is always necessary for the further tuning. Inside a cyclotron, in one of valley between two sector magnets, a set of phase probes is installed.[1] Twenty pairs of capacitive phase probes consisting of parallel plate electrodes are aligned radially and cover almost all orbital region of beam. The magnetic currents are finally tuned so that these phase probes will feel the beam simultaneously. As the result a good isochronism can be achieved.

So far these measurements have been done by observing signals from these phase probes on an oscilloscope display. A position of the beam signal on time axis is read for each phase probe step by step. In order to make these measurements more efficiently, a phase meter has been developed to convert timing information of these signals into dc voltage ones which can be easily read by a computer.

A block diagram of the phase meter is shown in Fig. 1. The circuit has been designed to handle the second harmonic component selectively on basis of the heterodyne scheme. A frequency of 455 kHz has been selected as its intermediate frequency, $f_i$. The phase meter needs two kinds of signals with frequencies, $2f_0$ and $2f_0-f_i$, where $f_0$ is the fundermental frequency of the radio frequency (rf) system. These signals are made with a frequency doubler and a local oscillator. A phase probe signal, after amplified, is mixed with a $2f_0-f_i$ signal in a double balanced mixer (DBM). A narrow band pass filter (455kHz) selects only 455 kHz signal which has a phase information of $2f_0$-component of phase probe signal. A reference signal is also converted into

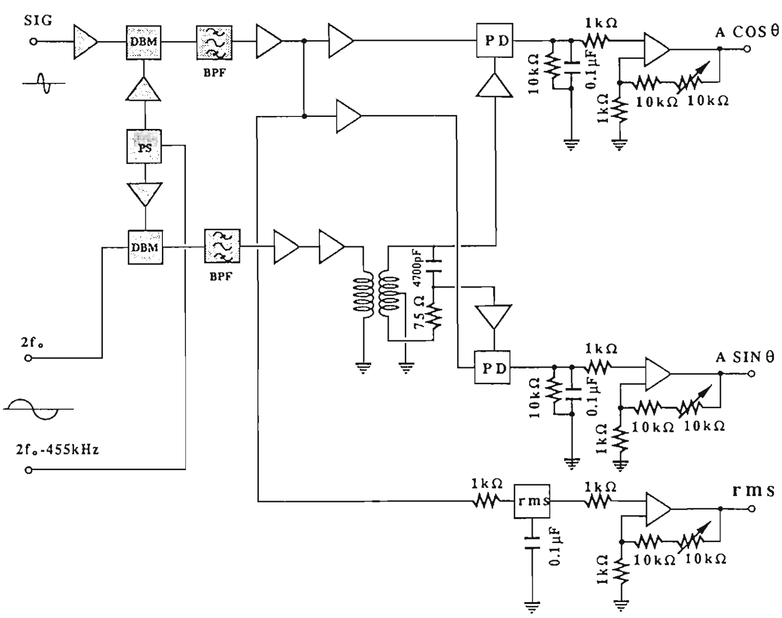


Fig. 1. Block diagram of the phase meter. Shadow triangles show wide band amplifiers of 1 - 400MHz. DBM is the double balanced mixer, PD the phase detector, PS the power splitter, rms the route mean square converter, and BPF the narrow band pass filter, $f_B = 455 \pm 1$kHz.

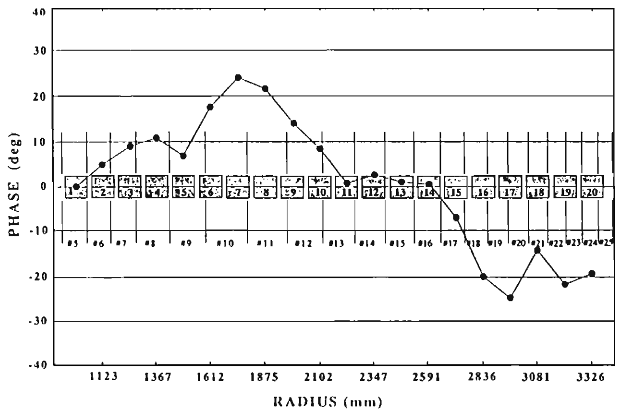


Fig. 2. Typical result of beam phase measurement for twenty pairs of phase probes inside RRC. Horizontal axis is the radius of beam orbits and vertical one is the beam phase in deg. Plots in the positive phase region mean that beam is late relative to that at the first inside probe location. Squares aligned along 0 deg line show the location of phase probes and figures with # the location of trim coils. Beam is 95MeV Ar in $f_0$=28.1 MHz. Beam intensity is 100 enA.

455kHz signals keeping its phase unchanged in the same way. With two phase detectors, PD, two components of $A\cos\theta$ and $A\sin\theta$ are obtained, where $A$ is the amplitude and $\theta$ the phase of $2f_0$-component of phase probe signal. $A$ should be proportional to a beam intensity and is monitored directly with a rms converter.

These three dc signals are fed into an analog input of interface board, DIM (Devise Interface Module) of control system,[2] where they are converted into 12-bit digital signals every 1 ms and stored into an 8 kbite memory inside. After the memory is full, data are transferred to a host computer, and then averaged values of $X=\overline{A\cos\theta}$ and $Y=\overline{A\sin\theta}$ are calculated. To eliminate the noise effect, these measurements are done in two ways, that is, with beam ($X_s$ and $Y_s$) and without beam ($X_n$ and $Y_n$). Beam can be stopped easily and rapidly by an electric beam switcher just after the ion source. The duration of cutting beam is 0.5 s for one phase probe. Beam phase is obtained by subtracting the noise effect, that is, using $\theta_s=\arctan(Y_s-Y_n)/(X_s-X_n)$. Beam phase values, which are relative to the phase probe no. 1, are obtained for the all phase probes by switching the probes. These are done automatically by a computer control.

Typical result of the measurement is shown in Fig. 2 for twenty pairs of phase probes in the RIKEN Ring Cyclotron (RRC), which shows that the magnetic field is lower than isochronous one for a radius around 1800mm and higher than it for a radius around 3000mm. The data obtained in this way are consistent with those obtained by observing an oscilloscope. This circuit is also applicable to pahase probes in the AVF cyclotron and beamline.

References

1) M. Kase, I. Yokoyama, I. Takeshita, Y. Oikawa, M. Saito, and Y. Yano: Proc. 11th Int. Conf. on Cyclotrons and Their Applications,Tokyo, p. 443 (1987).
2) T. Wada, J. Fujita, I. Yokoyama, T. Kambara, and H. Kamitsubo: *Sci. Papers I.P.C.R.*, **79**, 28 (1985).

RIKEN Accel. Prog. Rep. **25** (1991)

# V-1-2. Recent Improvement of Micro-Program in a Control Interface for a Magnet Power Supply

M. Nagase, I. Yokoyama, M. Kase, and Y. Yano

The CIM (Communication Interface Module) and the DIM (Device Interface Module) were completed in 1984,[1] and a computer control system using them was completed in 1985,[2] one year before the completion of the RRC (RIKEN Ring Cyclotron). Since then, they have been used for the control of RRC as a remote end I/O interface of a main control computer M-60 (Melcom 350-60). Among them, the DIM is a programmable and active device consisting of a CPU (8-bit micro processor), ROM (read only memory), RAM (randum access memory), I/O ports, etc. The DIM executes a function according to its micro-program, which is stored in the ROM and written in a special 8-bit assembler language. The computer control of a magnet power supply is carried out by the main-program of M-60 calling a function of DIM.

Table 1 shows the access commands and their functions for the DIM. The MCST (Multi Current Setting Task for a magnet power supply),[3] which is one of the automatic processing functions programmed on the DIM, could successfully decrease the initial setting time of large number of magnet power supplies and also decrease the task load of M-60.

Recently, it became necessary for the DIM to have an automatic trouble check function for the magnet power supply, because of the occasional trouble of magnet power supply due to the damage of electric parts, the failure in the water cooling system, etc. The CCT (Current Check Task) and the SCT (Status Check Task) were newly added to the function of DIM, and two

Table 1. Command Code Reference for CIM and DIM in 1991.

| F. CODE | COMMAND CODE (Z6) | FUNCTION | NOTE |
|---|---|---|---|
| 22 | 000000 | CIM INITIALIZE | |
| 22 | 010000 | ENABLE CIM LAM (Look At Me signal for CAMAC) | |
| 22 | 020000 | DISABLE CIM LAM (Look At Me signal for CAMAC) | |
| 22 | 100000 | DIM INITIALIZE | |
| 22 | 200000 | DIM MODE GET | |
| 22 | 21mmmm | DIM MODE SET | *1 |
| 22 | 300000 | DIM TASK CYCLE TIME GET | |
| 22 | 31tttt | DIM TASK CYCLE TIME SET | *2 |
| 22 | 4pttdd | DIM PULSE OUTPUT (OR 1 BYTE OUTPUT) | *3, *4, *5 |
| 22 | 5pdddd | DIM 2 BYTE OUTPUT | *3, *6 |
| 22 | 70aadd | DIM MEMORY WRITE | *7, *5 |
| 22 | 8p0000 | DIM DIGITAL PORT READ (1 BYTE) | *3 |
| 22 | 9p0000 | DIM DIGITAL PORT READ (2 BYTE) | *3 |
| 22 | Ap0000 | DIM ANALOG PORT READ | *3 |
| 22 | Bp00hh | DIM DIGITAL RECORD READ (SINGLE PORT) | *3, *8 |
| 22 | Bp10hh | DIM DIGITAL RECORD READ (ALL PORT) | *3, *8 |
| 22 | Cp00hh | DIM ANALOG RECORD READ (SINGLE PORT) | *3, *8 |
| 22 | Cp10hh | DIM ANALOG RECORD READ (ALL PORT) | *3, *8 |
| 22 | Dxxxxx | NO OPERATION | *9 |
| 22 | E00000 | DIM TASK STATUS READ (READ AND RESTART) | *10 |
| 22 | E10000 | DIM TASK STATUS READ (READ ONLY) | |
| 22 | F0aaaa | DIM MEMORY READ | |
| 22 | 600001 | DIM MEMORY CLEAR (ALL REGION) | |
| 22 | 610001 | DIM MEMORY CLEAR (RECORD REGION) | |
| 22 | 600002 | NO OPERATION | |
| 22 | 600003 | NO OPERATION | |
| 22 | 600004 | NO OPERATION | |
| 22 | 600005 | START MPS. MULTI CURR. SET & CURR. CHECK TASK | *11 |
| 22 | 600006 | START PORT RECORD TASK (ENDLESS) | |
| 22 | 610006 | START PORT RECORD TASK (48 CYCLE ONLY) | |
| 22 | 600007 | START RFI. RECORD TASK (ENDLESS) | *12 |
| 22 | 610007 | START RFI. RECORD TASK (48 CYCLE ONLY) | *12 |
| 22 | 600008 | START RFS. RECORD TASK (ENDLESS) | *13 |
| 22 | 610008 | START RFS. RECORD TASK (48 CYCLE ONLY) | *13 |
| 22 | 600009 | START VAC. RECORD TASK (ENDLESS) | *14 |
| 22 | 610009 | START VAC. RECORD TASK (48 CYCLE ONLY) | *14 |
| 22 | 60000A | NO PPERATION | |
| 22 | 60000C | START MPS. CURR. CHECK TASK | *11 |
| 22 | 60000D | START HIGH SPEED ANALOG RECORD TASK | |
| 22 | 600010 | STOP TASK | |
| 22 | 600020 | RESTART RESTING TASK | |
| 22 | 600035 | MPS. CURR. CLEAR | |

NOTE
*1 "mmmm" is a mode code.
*2 "tttt" is a hex. time (ms.).
*3 "p" is a port address.
*4 "tt" is a high order hex. time (ms.).
*5 "dd" is a 1 byte data.
*6 "dddd" is a 2 byte data.
*7 "aa" is a high order memory address.
*8 "hh" is a record history depth.
*9 "xxxxx" is not care.
*10 "aaaa" is a absolute memory address.
*11 "MPS" stands for Magnet Power Supply.
*12 "RFI" stands for Radio Frequency system Interlock status.
*13 "RFS" stands for Radio Frequency system operation status.
*14 "VAC" stands for Vacuume system interlock status.

Table 2. DIM. Task Mode Holder (Read/Write Possible).

| Bits | Field | Description |
|---|---|---|
| b15 | TRM | On/Off of Error Transition Record Mode |
| b14 | PCT | On/Off of Input Port Check Task (Status Check Task) |
| b13 | ESI | Enable/Disable Software Interruption by a task |
| b12 | EHI | Enable/Disable Hardware Interruption at checking port varied |
| b11 b10 b9 b8 b7 | CHECKING PORT ADDRESS | Analog or Digital Input Port Address to be checked |
| b6 b5 b4 | RECORD DEPTH | Transition Record Depth after Error |
| b3 b2 b1 b0 | ANALOG ERR LIMIT | Analog Deviation Error Limit |

Table 3. DIM. Task Status Holder (Read Only).

| Bits | Field | Description |
|---|---|---|
| b15 | TRUN | Indecate Run/Stop state of Task Excitable Timer |
| b14 | TRST | Indecate Runing/Resting state of Back Ground Task |
| b13 | TERR | Indecate Error Detection by a Task |
| b12 | PVAR | Indecate Checking Port Varied |
| b11 b10 b9 b8 | TASK NUMBER | Running or Resting Task Number |
| b7 b6 b5 b4 | ERR ADDRESS | Error Subaddress or Error Port Address |
| b3 b2 b1 b0 | ERR GRADE | Error Grade or Error Bit |

memory locations defined as the TMH (Task Mode Holder) and the TSH (Task Status Holder) were provided for these tasks. Their operations and characteristics are documented as follows.

1) CCT: This is automatically started after the end of MCST. It takes actual current data of magnet power supply, and calculates the deviation between the actual data and their reference data, which were previousely set on the RAM as the result of MCST. This task is cyclically repeated in a certain time interval if no error occurs. An error code is set into the TSH when the deviation is over a limit, and an interruption code is sent to the M-60. After that, the task rests, keeping the error status on the TSH until the M-60 reads out its contents.

2) SCT: This can be executed in parallel with other tasks, and is operated similarly to CCT. Difference is that the check target is not the actual current but a status bit pattern of magnet power supply. So that, an error code is set into the TSH when a status bit varies, and also an iterruption code is sent to the M-60.

3) TMH: Contents of TMH are shown in Table 2. They can be read or written by M-60, and referred by a task. It keeps a check mode such as whether an interruption is enable or disable, whether the STC runs or stops, an input port address to be checked, a limit data of current deviation, etc.

4) TSH: Contents of TSH are shown in Table 3. They are written by the CCT and SCT, and read by M-60. It keeps status information such as whether an error happened or not, running task number, error source address, error grade, etc.

Thus, M-60 can find a trouble of the magnet power supply easily and immediately by only reading out the two-byte status in TSH. Performance of CCT and SCT was tested and confirmed using an Analog I/O Interface, which had been made in 1987 as an I/O simulator of the real magnet power supply.

Replacement of the micro-program in the all DIM was completed. Development of a practical application program of the M-60 including the new interruption processing, is in progress now, and will be established in near future. They will be useful not only for the rapid trouble discovery of magnet power supplies but also for the reduction of M-60's task load.

References


1) K. Simizu: *Nucl. Instrum. Methods Phys. Res. A,* **236**, 109 (1985).
2) T. Wada, J. Fujita, K. Shimizu, I. Yokoyama, T. Kambara, and H.Kamitsubo: *RIKEN Accel. Prog. Rep.,* **19**, 186 (1985).
3) M. Nagase, H. Takebe, T. Wada, and K. Shimizu: Proc. 11th. Conf. on Cyclotron and Their Applications, Tokyo, p. 410 (1987).

# V-1-3. Effect of Coating the Plasma Chamber Wall in RIKEN Electron Cyclotron Resonance Ion Source (ECRIS) on the Beam Intensity of the Highly Charged Ions

T. Nakagawa

Recently, several authors reported that the condition of a chamber wall of the ECRIS is important to produce the highly charged ions and the enhancement of the beam intensity is observed after coating the chamber wall with thorium[1] or $SiO_2$.[2] We also observed the enhancement of performance of highly charged ions after coating the chamber wall of the RIKEN ECRIS with $Al_2O_3$ and MgO.

The beam intensity was measured before and after producing Al and Mg ions with the ECR ion source. In order to produce Al ions, an $Al_2O_3$ ceramic rod was directly inserted into the plasma in the second stage and heated to obtain the sufficiently high vapor pressure. The support gas was oxygen. The diameter and length of the rod were 4 and 200 mm, respectively. The consumption rate was 0.1 mm/10 min.. The evaporated aluminium oxide was ionized in the plasma and extracted from the ECR ion source. Part of the ions were attached to the chamber wall.

In order to minimize other effects on the beam intensity, other parameters ( gas pressure, RF power, axial and radial magnetic fields) were not changed before or after producing Al ions. RF powers of the first and second stages were 50 and 800 W, respectively. The extraction voltage was 10 kV for all elements.

In Fig. 1 (a) and (b), open and closed circles are the beam intensity for each charge state before and after producing Al ions, respectively. It is clear that the intensity of highly charged ions was strongly enhanced after producing Al ions. This effect continued for several months. Then, the beam intensity decreased with the same parameter set of the ECR ion source.

We have observed the same effect after producing Mg ions. Mg ions were produced by inserting a MgO ceramic rod into the plasma in the second stage. The diameter and length were 4 and 200 mm, respectively. The consumption rate was 0.1 mm/15 min.. The performance of the higher-charge-state of argon, nitrogen, and carbon ions after producing Mg ions was the same as those after producing Al ions.

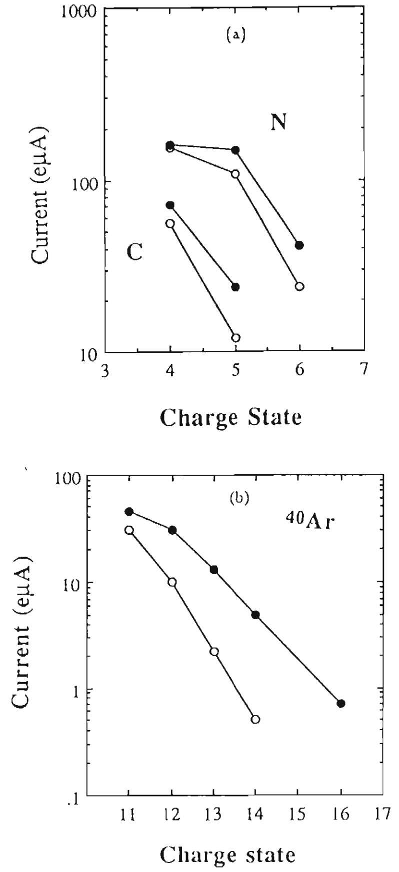


Fig. 1. (a) Beam intensity of carbon and nitrogen ions as a function of the charge state Open and closed circles are the beam intensities before and after producing Al ions. (b) Beam intensity of argon ions as a function of the charge state. Open and closed circles are the beam intensities before and after producing Al ions.

References
1) C. M. Leyneis : Proc. Int. Conf. ECR Ion Source and their Applications, East Lansing, 1987 (Michigan State Univ.), p. 42 (1987).
2) R. Geller : *Annu. Rev. Nucl. Part. Sci.*, **40**, 15 (1990).
3) K. Hatanaka and H. Nonaka: Proc. Int. Conf. the Physics of Multiply Charged Ions and Int. Workshop of ECR Ion Sources, Grenoble, 1988, J. de Physique C-1, p. 821 (1989).

RIKEN Accel. Prog. Rep. **25** (1991)

# V-1-4. The Effect of Electrode in RIKEN Electron Cyclotron Resonance Ion Source (ECRIS) on the Beam Intensity of Highly Charged Ions

T. Nakagawa and T. Kageyama

Many laboratories make an effort to increase the intensity of highly charged ions from the ECRIS. The probability of producing highly charged ions by the single electron impact falls off rapidly with increasing ion charge. Therefore the only efficient way to obtain highly charged ions is the successive ionization. We are then led to increase the exposure time of ions to the cloud of electrons or to increase the electron density in the plasma. In order to increase the electron density in the plasma, a Grenoble group has put the electrode near the gas injection of the MINIMAFIOS which has an operating frequency of 18 GHz and then supply the electrode with a negative voltage to push out electrons from the first to the second stage.[1] We also put the electrode in the first stage of the RIKEN ECRIS and supplied a bias voltage to the electrode to push out the electrons from the first to the second stage.

Figure 1 shows the beam intensity of $^{40}Ar^{11+}$ as a function of the bias voltage of the electrode. The beam intensity increased with decreasing the bias voltage to $-250$ V and then became rather constant. Open triangles are the beam intensity when we used the electrode. Open squares are the beam currents when we used the electrode after coating the chamber wall with the $Al_2O_3$. As described in Refs. 2 and 3, the condition of chamber wall is very important to increase the intensity of highly charged ions. Figure 2 shows the beam intensity of argon ions as a function of the charge state. Open circles are the "best result" before setting the electrode. Open triangles are the beam currents when we used the electrode ( bias voltage is $-250$ V). Open squares are the beam currents when we used the electrode after coating the chamber wall with $Al_2O_3$.

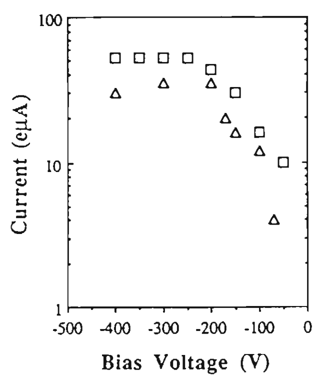


Fig. 1. The Beam intensity of $^{40}Ar^{11+}$ as a function of the bias voltage of the electrode. Open triangles are beam currents when the electrode was used. Open squares are beam currents when the electrode was used after coating the chamber wall with $Al_2O_3$ by inserting an $Al_2O_3$ ceramic rod into the second stage plasma for 30 min.

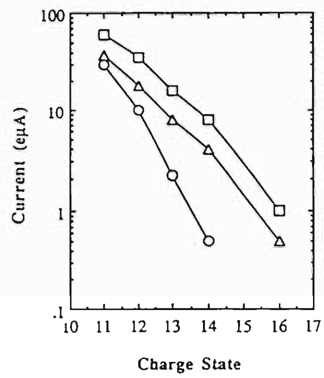


Fig. 2. The Beam intensity of argon ions as a function of the charge state Open circles are the best result before setting the electrode in the first stage. Open triangles are the beam intensity when the electrode was used. Open squares are the beam intensity when the electrode was used after coating the chamber wall with $Al_2O_3$ by inserting an $Al_2O_3$ ceramic rod into the second stage plasma. Lines are drawn to guide the eye through the data points.

Usually the RF power of the first stage is 50–100 W. The beam intensity becomes unstable with increasing the RF power of the first stage. An advantage of the RIKEN ECRIS compared with the MINIMAFIOS is that the two separated RF power supplies can be controlled independently. So we can control the RF power of the first stage itself. We should stress that we need only a few ten watts of RF power of the first stage to obtain these results and the beam intensity becomes more stable compared with that before setting the electrode.

References

1) G. Melin *et al.*: Proc. 10th Int. Workshop on ECR Ion Sources, Oak Ridge National Laboratory Knoxville, 1990, p. 1 (1991).
2) T. Nakagawa: *Jpn. J. Appl. Phys.*, **30**, L930 (1991).
3) R. Geller : *Annu. Rev. Nucl. Part. Sci.*, **40**, 15(1990).

# V-1-5. High Intensity Polarized Ion Source

H. Sakai, H. Okamura, N. Sakamoto, K. Hatanaka, Y. Yano,
T. Kubo, N. Inabe, M. Saito J. Fujita, and T. Kageyama

The RIKEN Ring Cyclotron can accelerate a proton ($p$) and a deuteron ($d$) upto 210 MeV and 270 MeV, respectively. Use of a polarized beam provides unique opportunity to study the spin dependent phenomena in nuclear physics.

A new atomic beam source of positive polarized p and d ions is being constructed. The new ion source is essentially a copy of the one built by T.B. Clegg and associates at Triangle Universities Nuclear Laboratory (TUNL) which produces in excess of 100 $\mu$A polarized beams.[1] Indiana University Cyclotron Facility (IUCF) is also constructing the ion source which is also a copy of TUNL with some modifications.[2] We obtained a lot of information both from TUNL and IUCF and also mechanical drawings from IUCF, which allows us rapid copying.

Figure 1 shows the schematic side view of the polarized ion source which is consisted of a dissociator with a cooled nozzle ($\sim$30 K), a pair of sextupole magnets, a pair of weak and strong radio-frequency transition units to form the polarized atomic beam and an electron cyclotron resonance (ECR) ionizer.

We have started assembling the source. At the time of writing this report, a vacuum test with most of components in place is in progress. We are expecting an on-line beam test in the winter of 1992.

Polarized beams will be accelerated by the injector AVF cyclotron and the main Ring cyclotron. A low energy vector and tensor beam-polarimeter will be installed between two cyclotrons. We have studied the possibility of the $^{12}C$ (d, p)$^{13}C$ reaction at $E_d = 14$ MeV as a low energy polarimeter by using the polarized beam at Kyushu University tandem accelerator laboratory. The data analysis is in progress.

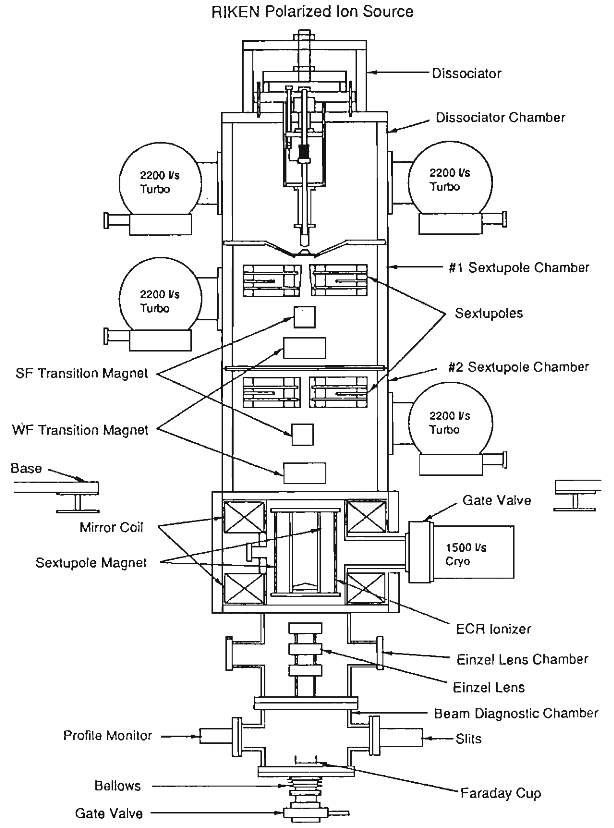


Fig. 1. Side view of the polarized ion source.

We greatly acknowledge the help and assistance of Prof. T. Clegg of TUNL and of Dr. M. Wedekind of IUCF in providing us mechanical drawings.

References

1) T.B. Clegg: *AIP Conf. Proc.*, **187**, 1227 (1989).
2) M. Wedekind *et al.*: *IUCF Annual Reports*, p. 1525 (1990); *ibid*, p. 192 (1991).

RIKEN Accel. Prog. Rep. **25** (1991)

# V-1-6. Development of an LNA Laser for Polarized $^3$He Ion Source of the Injector AVF Cyclotron (II)

A. Minoh and T. Fujisawa

The lanthanum neodymium hexa-aluminate (LNA) laser for the polarized $^3$He ion source must deliver the output power more than 100mW at the wavelength of 1083nm and the spectral width must nearly equal the doppler width (2GHz) of the 2S →2P transition of $^3$He atoms.[1)]

In our previous experiment,[1)] the output power of 75mW was obtained at the Ar laser pumping power of 1.6W and the output power increases in proportion to the pumping power. The spectral width of about 30GHz was obtained by inserting a 0.1mm air-gap etalon in the cavity. In order to reduce the width to 2GHz, we plan to add the other etalon (Etalon II) as shown in Fig.1. Etalon

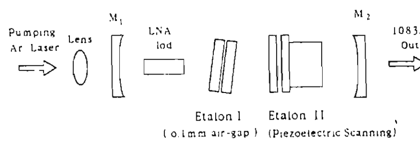


Fig. 1. LNA laser cavity to study the laser oscillation spectrum.

II controlled with a piezoelectric-transducer, is also used to tune automatically the laser frequency in the hiperfine frequency of $^3$He. Now we are precisely studying the structure of the laser oscillation spectrum with a Fabry-Perot spectrum analyzer (New Port Co. SR-250) in order to design the Etalon II.

It is necessary to develop a system for measuring the nuclear polarization of $^3$He, in order to design the polarized ion source. Figure 2 shows the energy level of a $^3$He atom and Fig. 3 shows

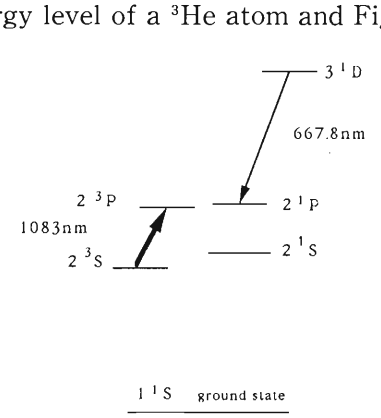


Fig. 2. Energy level of a $^3$He atom concerning the measurement of the nuclear polarization of $^3$He.

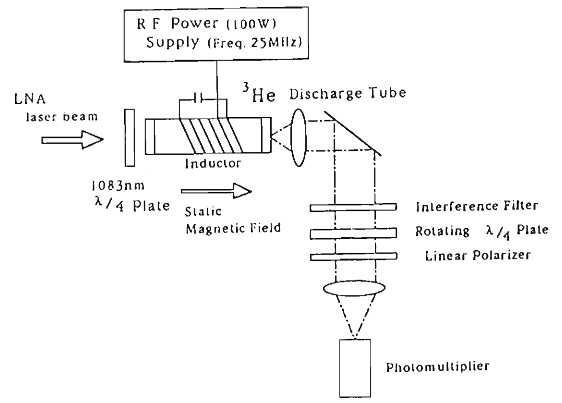


Fig. 3. Detection system of the nuclear polarization of $^3$He in the discharge tube.

the experimental set up to measure the nuclear polarization. The $^3$He atoms (gas, about 0.5 Torr) are excited to the $2^3$S metastable state by the RF electro-magnetic field in the static weak magnetic field, and excited to the $2^3$P state by the circular polarized light from an LNA laser parallel to the static magnetic field. Through the hiperfine interaction the nuclear spin of metastable $2^3$S state is polarized and is transferred to the ground state by the spin exchange collision. Then nuclei of the other states are polarized. The circular polarization of the light from the excited atoms depend on the nuclear polarization.

Pinard et al.[2)] give the relationship between the nuclear polarization of $^3$He and the circular polarization of light emitted from the excited $^3$He atom as follows.

$$P=\frac{P_0}{2}\;\frac{J+1}{(\Gamma^2/a^2)+(J+(1/2))^2}$$

where P is the degree of circular polarization of a light, $P_0$ is a nuclear polarization of $^3$He, G is the decay rate of the state and a is hiperfine coupling constant.

We plan to measure the circular polarization of 3D→2P (667.8nm). The light of 3D→2P transition in the RF discharge is selected by an interference filter, and the circular polarization is measured with the rotating $\lambda/4$ plate and a linear polarizer. Now the systems is almost set up.

We will also study the condition of the $^3$He discharge to give the highest nuclear polarization.

References

1) T. Fujisawa, A. Minoh, Y. Taniguchi, and K. Hatanaka: Proc. Int. Workshop on Polarized Ion Source and Polarized Gas Jet., KEK, Tsukuba, p. 302 (1990); A. Minoh, T. Fujisawa, and Y. Taniguchi : *RIKEN Accel. Prog. Rep.,* **24**, 136 (1990).
2) M. Pinard and J. Van Der Linde: *Can. J. Phys.,* **52**, 1615 (1974).

# V-1-7. Status of ECR Ion Source (Neomafios) for RILAC

E. Ikezawa, Y. Miyazawa, M. Hemmi, Y. Chiba, T. Chiba,
M. Kase, T. Aihara,* T. Ohki,* and H. Hasebe*

In the last year, the performance test of an ECR ion source (Neomafios)[1] on its test bench[2] was finished and it has been reconstructed on the high voltage terminal of RILAC injector. Figure 1 shows a schematic plan view of the ion source

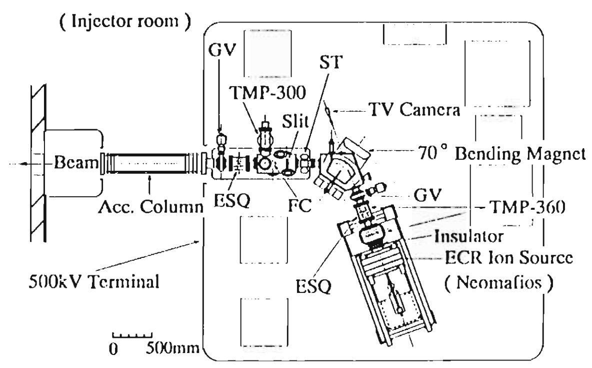


Fig. 1. Schematic plan view of the ECR ion source and the charge analyzing system reconstructed on the high voltage terminal of RILAC injector. ESQ, Electrostatic quadruple doublet; ST, Steering magnet; FC, Faraday cup; GV, Gate valve; TMP, Turbo-molecular pump.

and the charge analyzing system. The beams extracted from the Neomafios are analyzed according to the charge to mass ratios of ion beams by a 70° magnet with a radius of curvature of 350mm. Opening of the slit is 5 mm wide and 28 mm high. The two electrostatic quadruple doublets are used for the beam focussing. Two turbo-molecular pumps (360 ℓ/sec) are installed between the ion source and the analyzing magnet. Another pump (300 ℓ/sec) is equipped with a slit box. The operating pressure is usually around $6\times10^{-7}$ Torr at the extraction stage. The RF power (8 GHz) of around 100 W is usually applied to the Neomafios.

The Neomafios source has been producing various kinds of ion beams and also supplying them to RILAC. So far we have produced up to 42 different ion species with this source. Table 1 gives ion currents obtained by the Neomafios and the inverted number represents the ions accelerated at RILAC. All measurements were done with an 10 mm extraction aperture at 10 kV. The Neomafios displayed quite stable operation in production of gaseous ion beams. The rate of gas flow was $1\times10^{-5}-1.5\times10^{-4}$ Torr ℓ/sec when a gaseous ion was produced. For production of $^{136}Xe^{14+}$, an isotopically enriched xenon gas (80%) was supplied to the source at the rate of gas flow of $2.1\times10^{-5}$ Torr ℓ/sec with the mixing gas of oxygen. Ions of solid elements, Y, Rh, Sm, Dy, Ho, Er, Hf, Re, and Ir were newly produced by the Neomafios source in this year. We have produced the highly charged ions of solid elements with use of a metal or an oxide rod having a high melting point and obtained very stable ion beams over long periods of time. The flow rate of a support gas to keep an ECR plasma is $2\times10^{-4}-3\times10^{-4}$ Torr ℓ/sec. The consumption rate of solid materials was around 10 mg/hr. For example, when $^{166}Er^{13+}$ was continuously produced for 162 hours, the consumption rate of the erbium rod was 2.1 mg/hr. To obtain the stable metallic ion beams, we use the helium and oxygen as support gas at the rate of flow of around $2\times10^{-4}$ Torr ℓ/sec for each gas at the same time. Figure 2 shows a typical charge-state spectrum obtained with bismuth. We also tested

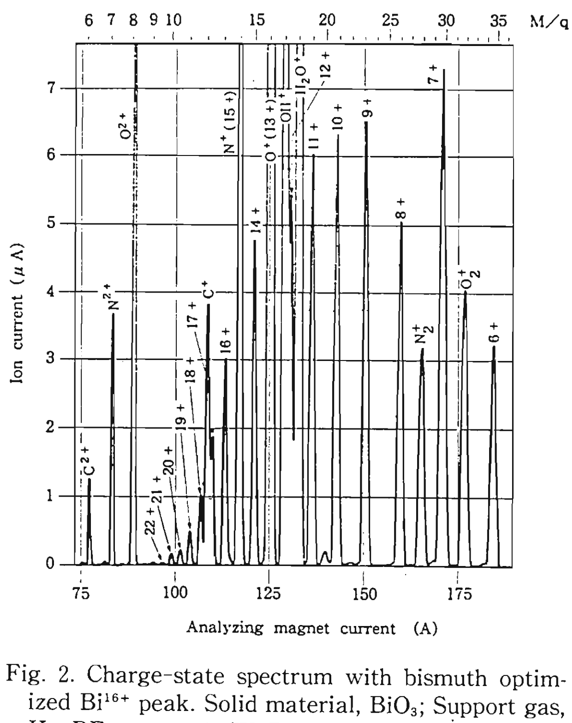


Fig. 2. Charge-state spectrum with bismuth optimized $Bi^{16+}$ peak. Solid material, $BiO_3$; Support gas, He; RF power, 100 W; Beam extraction voltage, 10 kV.

* Sumijyu Accelerator Service, Ltd.

Table 1. Ion currents from the ECR ion source ($\mu$A). Inverted number represents the ions accelerated at RILAC.

| Isotope | Gas | Charge State 1+ | 2+ | 3+ | 4+ | 5+ | 6+ | 7+ | 8+ | 9+ | 10+ | 11+ | 12+ | 13+ | 14+ | 15+ | 16+ | 17+ | 18+ | 19+ | 20+ | 21+ | 22+ | Remarks |
|---|---|---|---|---|---|---|---|---|---|---|---|---|---|---|---|---|---|---|---|---|---|---|---|---|
| $^{4}$He | He | **500** | 210 | | | | | | | | | | | | | | | | | | | | | |
| $^{12}$C | $CO_2$,He | 75 | 57 | | **18** | 2.3 | | | | | | | | | | | | | | | | | | |
| $^{14}$N | $N_2$,He | 90 | **95** | **63** | 50 | 30 | 2.8 | | | | | | | | | | | | | | | | | |
| $^{16}$O | $O_2$ | 93 | 85 | 65 | | 15 | 6 | 0.25 | | | | | | | | | | | | | | | | |
| $^{20}$Ne | Ne,He | 215 | 96 | 82 | **65** | | 6.5 | 1.7 | | | | | | | | | | | | | | | | |
| $^{40}$Ar | Ar,$O_2$ | | 75 | 55 | 50 | | **30** | 24 | **26** | 10 | | 0.7 | 0.1 | | | | | | | | | | | |
| $^{84}$Kr | Kr,$O_2$ | | | | 17.5 | 16 | | | 17 | **11.5** | 9 | 6.8 | | 3.7 | | 1.2 | | 1 | | 0.5 | | | | |
| $^{129}$Xe | Xe,$O_2$ | | | | | 11 | 11 | 13.5 | | **10** | 6.6 | | 3.8 | **3.1** | 2.5 | 2.2 | | 1.3 | 1.1 | | 0.4 | | | |
| $^{24}$Mg | He | 45 | | | | 30 | | 7.5 | | | | | | | | | | | | | | | | MgO, $\phi$ 4, rod |
| $^{27}$Al | $O_2$ | | 22 | 34 | 33 | | **15** | **6** | 2 | | | | | | | | | | | | | | | $Al_2O_3$, $\phi$ 4, rod |
| $^{28}$Si | He | | | 15 | | **33** | | | | 1 | | | | | | | | | | | | | | $SiO_2$, $\phi$ 3, rod |
| $^{40}$Ca | $O_2$ | | 72 | 70 | 55 | | 36 | 27 | 26.5 | 25.5 | | 5.5 | 1 | | | | | | | | | | | CaO, $\phi$ 5.7, rod |
| $^{48}$Ti | $O_2$ | | 5.2 | | | 15 | | 14 | | | 6.5 | 4.4 | | 0.3 | | | | | | | | | | Ti, $\phi$ 2, rod |
| $^{51}$V | $O_2$ | | 2.5 | | 7.5 | 12 | 12 | 12 | 10 | 7.5 | **4.8** | 2.4 | 1 | | | | | | | | | | | V, $\phi$ 1, 2 rods |
| $^{52}$Cr | $O_2$ | | 9 | | 27 | 30 | 32.8 | **25.5** | 15 | 8.3 | 5.8 | 3.6 | 2 | | 0.3 | | | | | | | | | Cr, $\phi$ 2, rod \| $Cr_2O_3$ |
| $^{55}$Mn | $O_2$ | | | | 51 | 68 | 60 | 42 | 19 | 9 | 4 | 2.6 | 0.8 | | | | | | | | | | | $\phi$ 4, Ta crucible \| $Mn_3O_4$ |
| $^{56}$Fe | He,$O_2$ | | | | | 15 | 15 | | | 11.3 | 8.2 | **4.8** | 3 | 1 | | | | | | | | | | Fe, $\phi$ 1, 2 rods |
| $^{58}$Ni | He,$O_2$ | | 4 | 4.8 | **5.2** | 8 | **12** | 13.5 | 14 | 11 | 8 | | 1.7 | 0.75 | 0.25 | | | | | | | | | Ni, $\phi$ 1, 2 rods \| NiO |
| $^{59}$Co | He | | 3.6 | 7 | 15.6 | 26 | 25.6 | 19 | 11 | 6 | 2.2 | | 2 | 0.7 | 0.2 | | | | | | | | | Co, $\phi$ 1, 2 rods |
| $^{63}$Cu | $O_2$ | | | **9** | | **17** | 19 | 17 | **15** | | 6.5 | 4 | | | | | | | | | | | | $\phi$ 4, Ta crucible \| $Cu_2O$ |
| $^{64}$Zn | He | | | 32 | | 35 | 34 | 26 | | 8.3 | 3.3 | 1.1 | | | | | | | | | | | | $\phi$ 4, Ta crucible \| ZnO |
| $^{74}$Ge | $O_2$ | | 1.8 | 3 | | 4.3 | 5.5 | 6.3 | 6 | 4.6 | 2.6 | 1.3 | 0.5 | 0.27 | | | | | | | | | | $\phi$ 4, Ta crucible \| $GeO_2$ |
| $^{89}$Y | He | | | 5.4 | 3.1 | | 2.6 | 3 | 4.5 | 6.6 | 7.5 | | 5.6 | | 1.1 | | | | | | | | | $Y_2O_3$, 4 × 4, rod |
| $^{90}$Zr | $O_2$ | | | | 1 | | 1.7 | 1.9 | 2.6 | 4.2 | 4.5 | 5 | 6.5 | | 2.6 | | 0.8 | | | | | | | Zr, $\phi$ 2, rod |
| $^{93}$Nb | $O_2$ | | | 11 | 19 | 23 | 13 | 9.5 | 7 | 7 | 7 | 5 | 3 | 1.7 | 0.6 | | | | | | | | | Nb, $\phi$ 3, rod |
| $^{98}$Mo | $O_2$ | | | | 3.8 | 5 | | | | 3.5 | 3.5 | 3 | | 0.65 | | | | | | | | | | Mo, $\phi$ 2, rod |
| $^{103}$Rh | $O_2$ | | | 0.5 | 1.2 | 2.3 | | 4.1 | 5.2 | 8.1 | 8.9 | 9.2 | 8.9 | | 5.7 | | 2.1 | | 0.7 | | | | | Rh, $\phi$ 1, rod |
| $^{107}$Ag | He | | | 1.2 | 2.6 | 5.2 | | 8.4 | 8.7 | 9 | 7.3 | 6.5 | 4.9 | 2.5 | 1.6 | 1.2 | 0.9 | 0.4 | | | | | | Ag, $\phi$ 3, rod |
| $^{115}$In | $O_2$ | | | 10 | 21 | 31 | 24 | 22 | 16 | 13.5 | 10.5 | 7.5 | 5.3 | 4.5 | 3 | 2 | 1.2 | 0.6 | 0.2 | | | | | $\phi$ 4, Ta crucible \| $In_2O_3$ |
| $^{120}$Sn | He,$O_2$ | | | | 3 | 5.2 | 5.7 | | 10 | 7 | | 4.2 | 2.7 | 1.8 | 1 | | 0.2 | | | | | | | $\phi$ 4, Ta crucible \| $SnO_2$ |
| $^{152}$Sm | $O_2$ | | | | 0.4 | | 0.8 | 1.3 | 1.8 | | 4.7 | 5.1 | **6** | 5.8 | 5.3 | 4.9 | 3.6 | 2.4 | | | | | | Sm, $\phi$ 4, rod |
| $^{164}$Dy | He,$O_2$ | | | | | | 4 | 5.1 | 5.9 | | | 6.7 | 4.9 | 2.9 | 2 | 1.8 | 1.5 | 1.1 | 0.7 | 0.3 | | | | Dy, $\phi$ 6.3, rod |
| $^{165}$Ho | $O_2$ | | | | | | | 0.7 | 1.2 | | 2.5 | 5.3 | | **6.4** | | 6 | 5 | 3.9 | 2.6 | 1.6 | 0.6 | | 0.15 | Ho, $\phi$ 1, rod |
| $^{166}$Er | He,$O_2$ | | | | | | | 2 | 3 | 4.3 | | 11 | | **13.2** | | 9.5 | 7.7 | 5.7 | 4.1 | 1.9 | | | | Er, $\phi$ 4, rod |
| $^{180}$Hf | $O_2$ | | | | | | | 2 | 2.5 | 3.7 | | | 7.6 | | **6.6** | | 4.3 | 3 | | 1.3 | 1 | 0.5 | | Hf, $\phi$ 2, rod |
| $^{181}$Ta | $O_2$ | | | | | 8.5 | | 18 | 19 | 19 | | 14 | 12 | | **8.2** | | 5.5 | 5 | 4.3 | 3 | 2 | 1.1 | 0.6 | Ta, $\phi$ 1, rod |
| $^{184}$W | $O_2$ | | | | | 0.9 | 1 | 1.4 | 1.7 | 2.4 | | | 4 | | 3 | | 1.5 | 0.9 | 0.5 | 0.2 | | | | W, $\phi$ 1, rod |
| $^{187}$Re | $O_2$ | | | | | 4.8 | 7 | 10.6 | 12 | 10.5 | 8.3 | | 4.1 | 4.3 | 3.6 | 2.3 | 1.8 | 1 | 0.6 | 0.3 | | | | Re, $\phi$ 1, rod |
| $^{193}$Ir | $O_2$ | | | | | | | 2.9 | 9.2 | 10.5 | 8.5 | 6.5 | | 5.4 | 4.8 | 3.5 | | 1.7 | 0.9 | 0.5 | 0.2 | 0.1 | | Ir, 1 × 1, rod |
| $^{197}$Au | $O_2$ | | | | | | 13.7 | | 19.2 | 16.5 | 13.7 | | 10 | 6 | | 4.3 | 4.0 | 2.6 | 1.5 | 0.8 | 0.4 | 0.3 | | $\phi$ 4, Ta crucible |
| $^{208}$Pb | $O_2$ | | | | | | 7.7 | | 13.8 | 13.3 | 10.8 | 8.3 | | | **5.2** | | **3.5** | | 1.7 | 1 | 0.5 | 0.3 | 0.1 | $\phi$ 4, Ta crucible \| PbO |
| $^{209}$Bi | He | | | | | | 3.3 | | 8.3 | 10 | **8.7** | 7.6 | 5.6 | | 5.6 | | 3.6 | 2.3 | 1.4 | 0.87 | 0.45 | 0.32 | 0.1 | $\phi$ 4, Ta crucible \| $BiO_3$ |

oxide rods such as $Mn_3O_4$, $Cu_2O$, ZnO, $GeO_2$, $In_2O_3$, $SnO_2$, PbO, and $BiO_3$ to obtain metallic ions. Ion currents with use of those oxide rods except the case of Ge and Pb were very stable compared with those obtained in a crucible method.

References


1) G. Melin *et al.*: Proc. Int. Conf. on Physics of Multiply Charged Ions and Int. Workshop on E.C.R. Ion Sources, Grenoble, France, p. 673 (1988).

2) E. Ikezawa *et al.*: *RIKEN Accel. Prog. Rep.*, **24**, 133 (1990).

RIKEN Accel. Prog. Rep. 25 (1991)

# V-1-8. Design of a Second-Harmonic Buncher for RILAC

S. Kohara, M. Kase, and A. Goto

A second-harmonic buncher for RILAC is planned to be installed between RILAC and a Cockcroft. More efficient bunching of DC beam at the injection point of RILAC is expected to be obtained by adding the second-harmonic buncher to the existing buncher of a fundamental frequency. Detail of the designed buncher system is reported elsewhere.[1)]

Characteristics of the second-harmonic buncher are given in Table 1. The buncher needs an operational frequency range from 34 to 90 MHz because that of RILAC is from 17 to 45 MHz. The calculation showed that the total peak voltage required in the second-harmonic buncher is 3 kV

Table 1. Characteristics of the second-harmonic buncher.

| | |
|---|---|
| Frequency range | 34-90 MHz |
| Harmonics | 2 |
| Number of gaps | 2 |
| Maximum peak voltage per gap | 1.5 kV |
| Voltage stability | $\pm 1\times10^{-3}$ |
| Phase stability | ±0.5 ° |
| Width of each gap | 10 mm |
| Separation of gaps | 27.5 mm |
| Aperture of beam transmission | 30 mm |

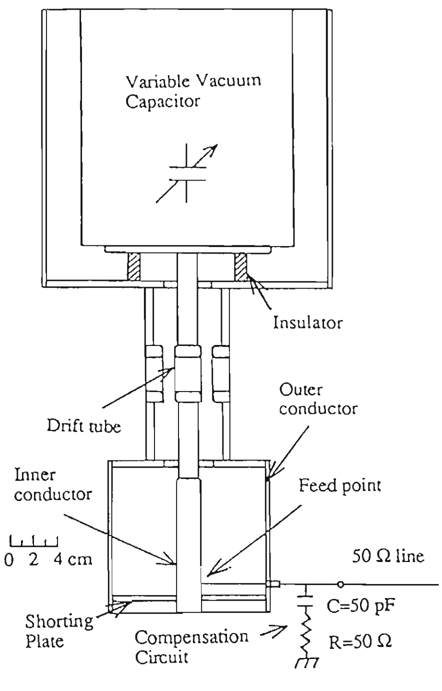


Fig. 1. Cross sectional view of the second-harmonic buncher and a coupling circuit.

at the maximum. A cross sectional view of the resonator is shown in Fig. 1. The resonator of the buncher is of a coaxial quarter-wave-length type with its shorting plate fixed. It has two gaps and is of a $\pi$-mode. The separation of gaps is 27.5 mm. The resonant frequency is tuned only by a variable vacuum capacitor installed at the open end of the resonator.

Resonant frequencies, shunt impedances, power losses, and Q-values calculated with the transmission-line approximation are shown in Fig. 2. The capacitance of the variable vacuum capacitor has to be varied from 15 to 225 pF to cover the frequency range. The maximum current of the capacitor is 120 A (peak) at 34 MHz. The shunt impedances calculated at the drift tube gap are varied from 20 kΩ at 34 MHz to 80 kΩ at 90 MHz. The maximum power loss is about 70 W at 34 MHz when the peak gap volt-

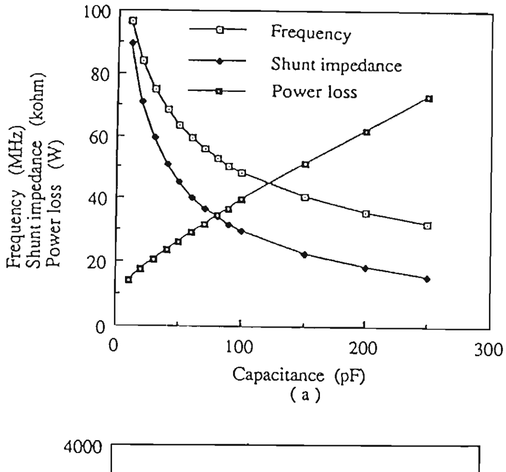


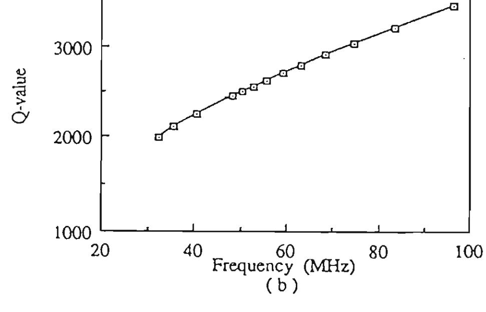


Fig. 2. (a) Resonant frequencies, shunt impedances, and power losses calculated as a function of capacitance of the tuning capacitor. Power losses are calculated for the peak gap voltage of 1.5 kV. (b) Q-values calculated as a function of frequency.

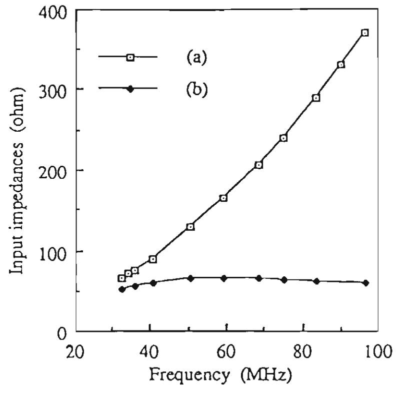


Fig. 3. Input impedances of the resonator at the feed point calculated as a function of frequency. Curve (a) : without compensation and curve (b) : with compensation.

age is 1.5 kV. Q-values are from 2000 to 3300. The maximum current density at the shorting plate is 20 A(peak)/cm.

A simple power feed circuit shown in Fig. 1 provides a good voltage standing wave ratio (VSWR) without adjustment ; a compensation circuit improves VSWR within 1.3 by absorbing surplus rf power in the high frequency region. (see Fig. 3)

The buncher will be manufactured in the near future.

References

1) S. Kohara, M. Kase, and A. Goto : Proc. 8th Symp. on Accel. Sci. and Tech., p. 133 (1991).

RIKEN Accel. Prog. Rep. **25** (1991)

# V-1-9. Measurement of Surface Resistance of High-Tc Superconductor $(Bi,Pb)_2Sr_2Ca_2Cu_3O_x$ at 10.5 GHz

K. Ikegami, Y. Chiba, Y. Kawamura, M. Hemmi, Y. Taniguchi,* and T. Fujisawa*

In order to study feasibility of an accelerator cavity with high critical temperature (high-Tc) superconductor, we measured the surface resistance by measuring quality factors of the TM010 cavity (10 mm in height × 11 mm in radius), which has a resonance frequency of 10.5 GHz and is made of a bulk superconductor $(Bi,Pb)_2Sr_2Ca_2Cu_3O_x$ of a density of 80∼85%.

Figure 1 shows cross-sectional views of the cavity and the copper housing. The cavity** is composed of a flat end plate and a hollow body machined with bulk ceramic blocks. Then they are joined by the heat treatment using a high-Tc superconductor paste on their contact surfaces. The cavity is set on a cooling head in a vacuum chamber and is cooled down to about 20K with a refrigerator. Figure 2 shows a block diagram of the experimental setup. The cavity is connected to a waveguide system with a 40 cm low thermal conductance waveguide made of silver plated cupro-nickel. An rf signal is fed into the cavity through a small coupling hole and a reflected signal is detected with a directional coupler. A coupling adjustor adjoining the cavity makes impedance matching by minimizing a reflected signal at the center of resonance. A resonant absorption curve is measured in the best impedance matching and absolute values of the reflection coefficient (Γ) around the resonant frequency are deduced from the curve.

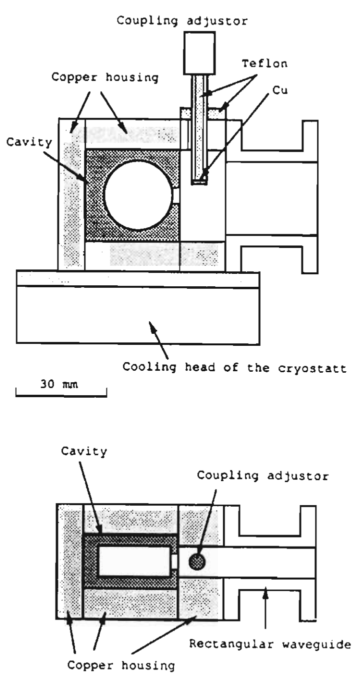


Fig. 1. Cross-sectional views of the cavity and the copper housing.

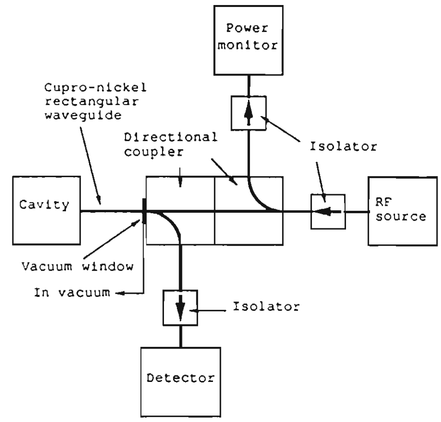


Fig. 2. Block diagram of the experimental setup.

Figure 3 shows a typical resonant absorption curve. The ordinate is voltage amplitude of the reflected signal in a linear scale. At the resonant frequency, the input power is absorbed completely by the cavity. In this case the unloaded quality factor ($Q_u$) is given by the following equation: $Q_u = f_o/\Delta f$, where $f_o$ is a resonant frequency and $\Delta f$ is a frequency width of a resonance curve at $\Gamma = 0.447$.

A surface resistance (Rs) of the cavity is deduced from $Q_u$ by the following equation: Rs=

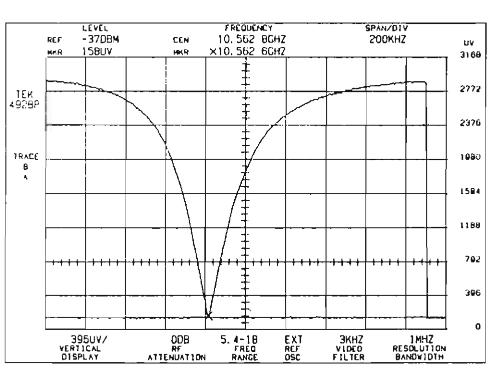


Fig. 3. Typical resonant absorption curve. Frequency: 10.5626 GHz, Temperature: 50.5 K, Maximum surface current: 3 A/m.

* DENKI-kogyo Co. Ltd.
** The cavity was made by DOWA kogyo Co. Ltd.

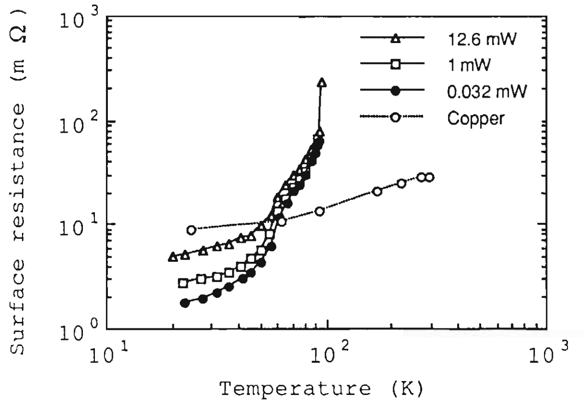


Fig. 4. Temperature dependence of the surface resistance.

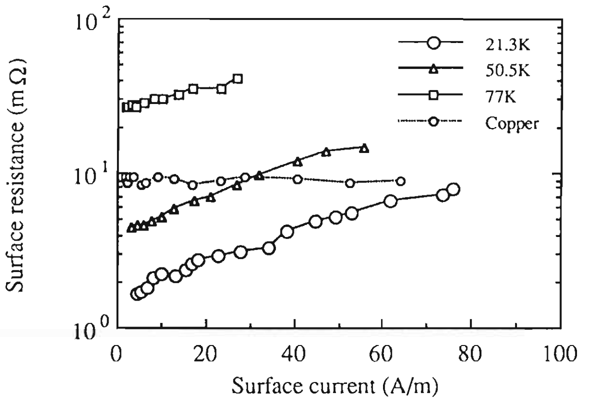


Fig. 5. Surface current dependence of the surface resistance.

$\pi f_0 \mu / (Q_u (1/a+1/h))$, where $\mu$ is the permeability of vacuum, a and h are the radius and the height of a cavity, respectively.

Temperature dependence of the surface resistance in three input power levels are shown in Fig. 4, together with a result of the copper cavity which has the same geometry as the high-Tc superconducting cavity. The obtained Rs of copper is consistent with calculation within 5 %. The Rs of this high-Tc superconductor has strong temperature dependence below the Tc as that of YBaCuO.[1] The values of Rs are about one tenth of those obtained by Delayen.[2] Figure 5 shows the surface current dependence of Rs at temperatures of 21.3K, 50.5K, and 77K. The abscissa is the maximum surface current density which is observed at a radius of 0.765a on a circular base of a cavity. The surface resistance increases from 1.8 mΩ to 80 mΩ at 22 K with increasing surface current from 4 A(peak)/m to 70 A/m, as well as with increasing temperature, and reaches 200 mΩ at 90 K for the surface current of 45 A/m.

This work is supported by the Multi-Core Project of Science and Technology Agency.

References

1) H. Itozaki and K. Higaki: MWE' 91 Microwave Workshop, p. 157 (1991).
2) J. R. Delayen, C. L. Bohn, and C. T. Roche: *Journal of Superconductivity*, **3**, 243 (1990).

RIKEN Accel. Prog. Rep. 25 (1991)

# V-1-10. Possibility of Simultaneous Acceleration of $H^-$ and $D^-$ with a Cyclotron

N. Nakanishi

Compact cyclotrons have been used extensively in the isotope production, micro-analysis, nondestructive test and so on. Specially, they play an important role in producing such positron emitters as $^{11}C$, $^{13}N$, $^{15}O$, and $^{18}F$ for the positron emission tomography which is one of the promising imaging techniques for in-vivo studies. Recently, negative ion cyclotrons are coming in fashion because of some merits in view of the beam extraction, energy variability, and beam intensity.[1,2]

An accelerated beam in a negative ion cyclotron is extracted by using a thin stripping foil of carbon or aluminum. The technique makes the 100% extraction efficiency possible, and moreover, makes it easy to vary the extraction energy of beams. The simultaneous acceleration of $H^-$ and $D^-$ beams is possible by installing two internal ion sources at two opposite dees, and by extracting p and d toward opposite directions with two stripping foils at a nearly equal radial position. Interest focuses on the final energies of these particle beams.

It will be considered that the maximum energies of the two particles depend not only on the radial distribution of the magnetic field strength and radio-frequency but also on the rf voltage and harmonic numbers related to the dee angle. It is easily found out that the higher the accelerating voltage is, the higher the maximum energy is. The voltage, however, is desirable to be as low as possible to reduce the electrical power consumption and to prevent the discharge phenomenon. Here, the voltage is taken to be 60 kV tentatively. The central magnetic field strength after a bump field deduction is set to be 1.2 T so that the first turn of each accelerated particle does not interfere with both of the partner and its own ion sources. We can make various radial distributions of the magnetic field. As one of the examples, an adopted system is the isochronous field for $H^-$ beams to be accelerated to Ep at the radius of 48 cm. Therefore, the relative radial distribution is specified by the $H^-$ energy Ep which the particle achieves at the radius of 48 cm. Incidently, results of calculation do not depend on these parameters. These influence the accuracy of formation of magnetic field and radio-frequency. Figure 1 shows the achievable maximum energy in the case of 90° dees. Harmonic numbers of $H^-$ and $D^-$ are 1 and 2, respectively. Points in the figure mean calculated values. The figure also shows three different regions of Ep<4 MeV, 4 MeV<Ep<16 MeV and 16 MeV<Ep which are favorable for $D^-$, $D^-$and $H^-$, and $H^-$, respectively. It seems that an objective magnetic field distribution exists in the region of 6 MeV<Ep<12 MeV. Frequency dependence of the maximum energy of both particles is shown in Fig. 2 together with a half $H^-$ energy and twice $D^-$ energy for the distribution of Ep= 8 MeV. The crossing point of the curves for the $H^-$ energy Ep and twice $D^-$

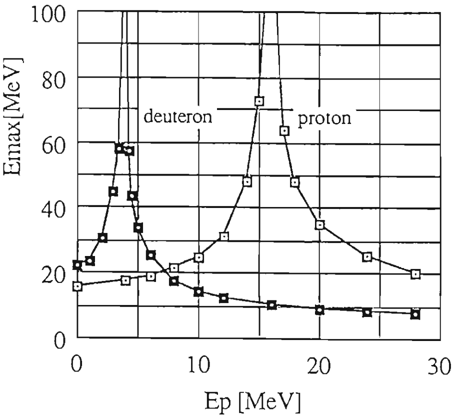


Fig. 1. Maximum energies of $H^-$and $D^-$particles vs. Ep. See the text for the meaning of Ep. Dee angle is 90°.

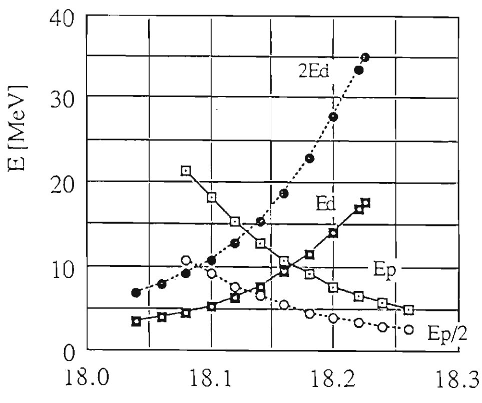


Fig. 2. Radio-frequency dependence of maximum energies at the magnetic field Ep = 8 MeV. Ep, Ed, Ep/2, and 2Ed in the figure mean maximum energies of $H^-$and $D^-$, a half $H^-$ energy, and twice $D^-$ energy, respectively.

energy 2Ed and that of the curves for the $D^-$ energy Ed and a half $H^-$ energy Ep/2 represent the achievable maximum energies of $H^-$ and $D^-$ particles, respectively.

It can be seen from Fig. 2 that the maximum energies of $H^-$ and $D^-$ particles are found to be 14 and 7 MeV, respectively. It is expected that such a cyclotron with energy constant K=14 MeV will be useful for the isotope production. Hereafter, conditions for the simultaneous extraction must be investivated.

References

1) M. Abs, J.L. Bol, A. Chvalier *et al.*: Proc. 12th Int. Conf. on Cyclotrons and Their Applications, Berlin, p. 164 (1990).
2) B.F. Milton, G. Dutto, R. Helmer *et al.*: Proc. 2nd European Particle Accelerator Conf., Nice, p. 1812 (1990).

RIKEN Accel. Prog. Rep. **25** (1991)

# V-2. Synchrotron Radiation Source Development

## 1. Status of the SPring-8 Project

H. Kamitsubo and M. Hara

SPring-8 Project is being carried out by RIKEN and Japan Atomic Energy Research Institute (JAERI). The facility is designed by the joint team of these institutes and JAERI is responsible for the injectors while RIKEN is for the storage ring. The project was started in FY1990. In FY1991, design of the injector building and the construction of the storage ring building were started.

The injector system was reviewed from the cost reduction point. The final design is as follows: The preinjector is composed of a high current linac (250 MeV, 10 A), an electron positron convertor and a main linac (0.9 GeV). Total length is reduced to 140 m. Electron beams with 1.15 GeV and/or positron beams with 0.9 GeV will be obtained. Transport line from the linac to the synchrotron was also shortened and the layout of the linac was changed (Fig. 1). A part of the linac was ordered to manufacturers in March 1991. Synchrotron was also modified by increasing the length of the straight section and simplifying RF, but keeping circumference.

The design of the storage ring has almost completed, and the detailed design of some accelerator components is still in progress. Design reports of the SPring-8 Project were issued in 1991. Major parameters of the storage ring are listed in Table 1. Dimensional tolerances of the magnets are investigated and alignment of the accelerator components is being studied. The final design of dipole, quadrupole, and sextupole magnets has been fixed and the first production magnet of each type is in manufacturing. Power supplies for these main magnets have also been designed. Design of pulse magnets for injection (bump and septum) is underway.

A klystron test stand was installed in the end of 1990, and has been operated for a year. There were initial troubles in the 1 MW operation,

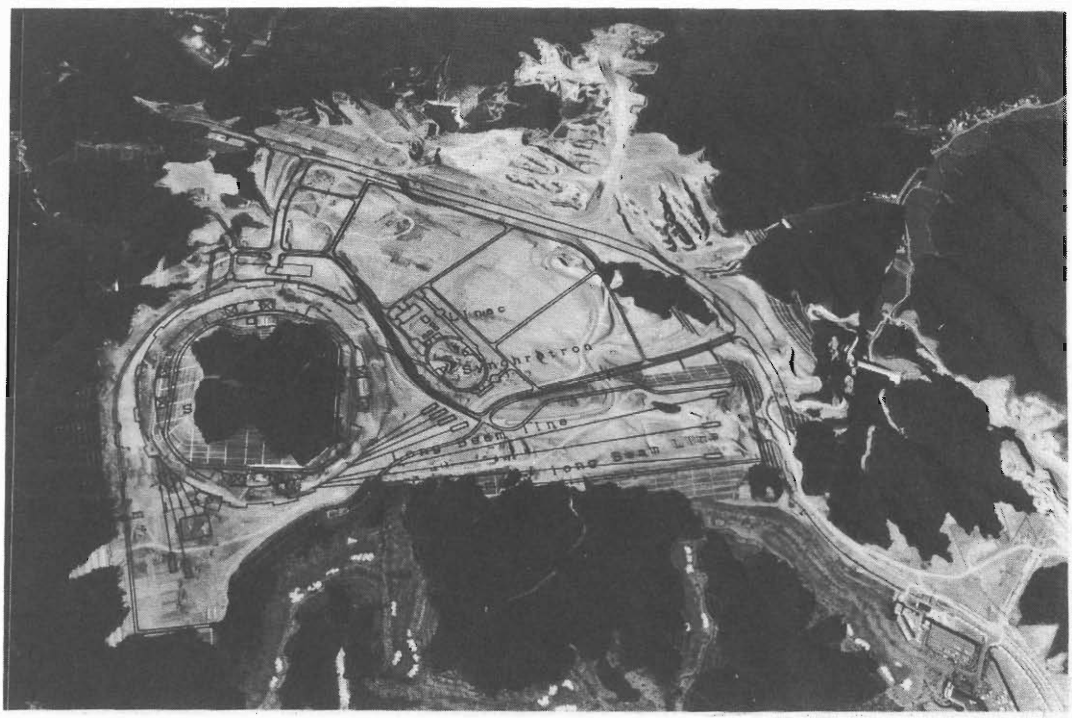

Photo : Sept. 5 . 1991.

Fig. 1. An overview of the construction site for the SPring-8 in Harima Science Garden City. This photo was taken in September 1991. Layout of the facility is shown on this picture. The direction of the injector linac was changed.

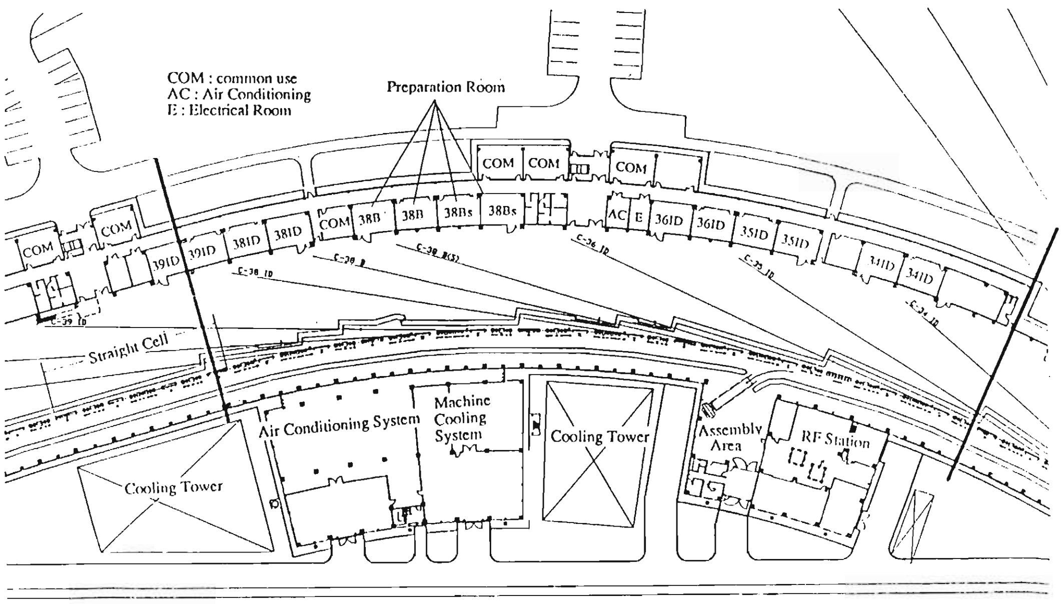


Fig. 2. Layout of the beamlines in a part of the storage ring (D area).
The first construction area is between the two bold lines.

Table 1. Main parameters of storage ring in SPring-8.

| | | |
|---|---|---|
| Electron energy | E [GeV] | 8 |
| Current (multi-bunch) | I [mA] | 100 |
| Current (single-bunch) | I [mA] | 5 |
| Circumference | C [m] | 1435.95 |
| Dipole magnetic field | B [T] | 0.679 |
| Bending radius | $\rho$ [m] | 39.2718 |
| Type of lattice | Chasman-Green | |
| Number of cells | Normal cell | 44 |
| | Straight cell | 4 |
| Length of straight section | | |
| normal | L [m] | 6.65 |
| long | L [m] | 30.0 |
| Natural emittance | $\varepsilon_n$ [m·rad.] | $6.99 \times 10^{-9}$ |
| Critical photon energy | $\varepsilon_c$ [keV] | 28.9 |
| Tune | $\nu_x$ | 51.22 |
| | $\nu_y$ | 16.16 |
| Synchrotron tune | $\nu_s$ | 0.0101 |
| Momentum compaction | $\alpha$ | $1.46 \times 10^{-4}$ |
| Natural chromaticity | $\zeta_x$ | -115.66 |
| | $\zeta_z$ | -40.00 |
| Energy loss in the arcs | $U_0$ [MeV/rev] | 9.23 |
| Energy spread | $\sigma_e/E$ | 0.001094 |
| Damping time | $\tau_x$ [msec] | 8.30 |
| | $\tau_z$ [msec] | 8.31 |
| | $\tau_e$ [msec] | 4.15 |
| Harmonic number | h | 2436 |
| R.F. voltage | $V_{rf}$ [MV] | 17 |
| R.F. frequency | $f_{rf}$ [MHz] | 508.58 |

which were however overcome on the advice of the KEK RF group. A power test for a five-cell prototype cavity was carried out in this stand. Two single-cell prototype cavities, two couplers, and two tuners which have different design or different fabrication method have been already manufactured and installed in the test stand. Power tests for these components are in progress. There are four RF stations in the storage ring and design of the RF system has almost been fixed based on these operation experiences. An RF system of one RF station is scheduled to be ordered to manufacturers within this year. Specification of the vacuum components has almost been fixed and some of the vacuum components are also scheduled to be ordered to manufacturers within this year.

This facility is sited in Harima Science Garden City in Hyogo Prefecture. Land preparation started in February 1990 and will be finished in March 1992. At present, the land preparation has almost finished as shown in Fig. 1. The storage ring buildings are to be constructed in four phases. The construction of the first phase building started in November 1991 and the ground-breaking ceremony was held on the site. A top view of the first construction part was shown in Fig. 2.

RIKEN Accel. Prog. Rep. 25 (1991)

# V-2-2. Behavior of Lattice Parameters in the Vicinity of the Operation Point of SPring-8 Storage Ring

H. Tanaka and N. Kumagai

Behavior of the lattice parameters was investigated in the vicinity of the standard operation point ($\nu_x = 51.22$ and $\nu_y = 16.16$) to find the effective operation range. We concentrated here on variations of following critical parameters; emittance, chromaticities, dynamic aperture, and strength of magnets against tunes. To avoid negative effects due to a strong structure resonance, $1 \times \nu_x = 48$, the investigation is restricted in the range, where the horizontal tune is larger than 50. From the following results, we have set $51 \leq \nu_x \leq 54$ and $16 \leq \nu_y \leq 20$ as the operation range.

(1) The dynamic aperture decreases according to the increase of horizontal and vertical tunes. This reduction is caused by the strength-increase of sextupoles for the chromaticity correction. Linear optics, of which dynamic aperture is larger than 30 mm, can be designed under the condition that $\nu_x$ and $\nu_y$ are smaller than 54 and 21 (Fig. 1).

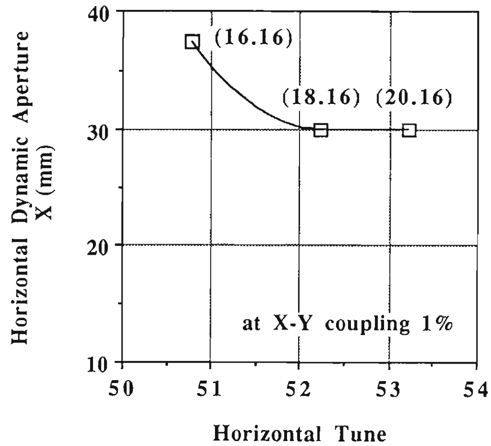


Fig. 1. Dynamic aperture versus horizontal tune. Values inside the round brackets represent vertical tunes.

(2) The emittance varies linearly with the horizontal tune. It is adjustable from 7.5 to 5.5 nm·rad in the horizontal tune range, $50 \leq \nu_x \leq 54$ (Fig. 2). Therefore, the emittance can be reduced to about 80 % of a present design value (7.0 nm·rad).

(3) The horizontal chromaticity varies linearly with the horizontal tune, but the vertical one does not markedly depend on the vertical tune

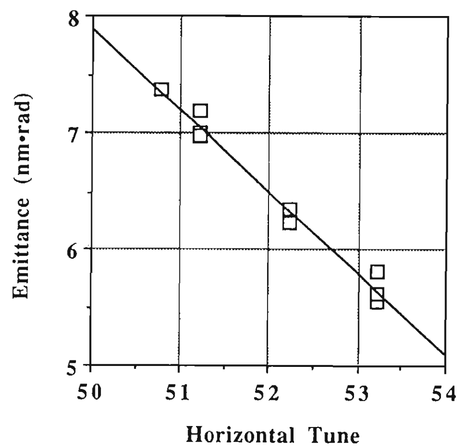


Fig. 2. Emittance versus horizontal tune.

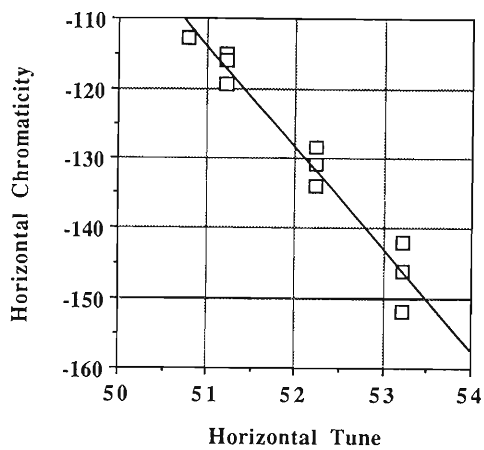


Fig. 3. Horizontal chromaticity versus horizontal tune.

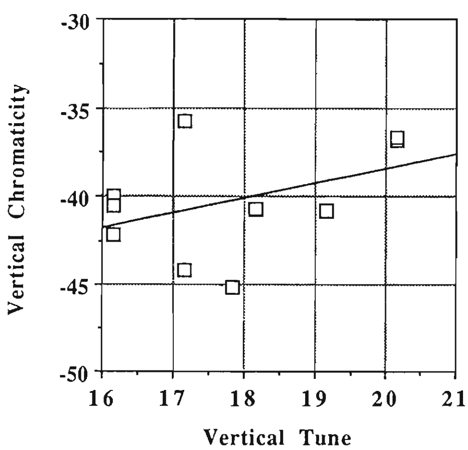


Fig. 4. Vertical chromaticity versus vertical tune.

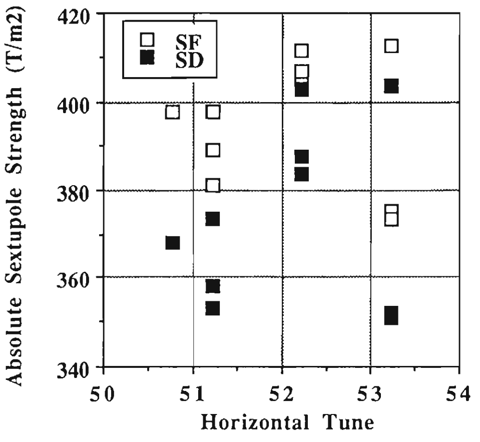


Fig. 5. Absolute strength of sextupoles versus horizontal tune.

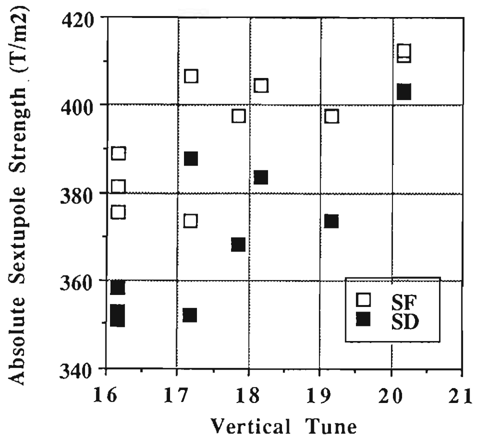


Fig. 6. Absolute strength of sextupoles versus vertical tune.

(Figs. 3 and 4). On the other hand, the absolute strength of sextupoles is almost proportional to the tunes and kept lower than 420 T/m2 in the operation range, $50 \leq \nu_x \leq 54$ and $16 \leq \nu_y \leq 21$ (Figs. 5 and 6). The absolute strength of harmonic sextupoles for the dynamic aperture enlargement can be lower than 420 T/m$^2$ in the three cases shown in Fig. 1. The absolute strength of each quadrupole can be also kept lower than 18 T/m$^2$ in this operation range.[1)]

References

1) H. Tanaka and M. Hara: *RIKEN Accel. Prog. Rep.*, **24**, 141 (1990).

RIKEN Accel. Prog. Rep. **25** (1991)

# V-2-3. Analysis of the Sensitivity Reduction Against the Magnet Misalignment in Low Emittance Synchrotron Radiation Sources by Unifying Magnets in Each Straight Section[1)]

H. Tanaka, N. Kumagai, and K. Tsumaki*

We investigated the effects of a two-stage magnet alignment method, in which a couple of focusing and defocusing magnetic elements such as quadrupoles and sextupoles are treated as a unit like a composite lense, on the sensitivity reduction against the magnet misalignment in low emittance synchrotron radiation sources.

The sensitivity reduction is closely related to the lattice characteristics and linear optics of the radiation sources. The feature of this method is that the object of highly precise alignment can be restricted to the inside of each unit, which is straight and shorter than several meters.

The formulae for the expected values of horizontal and vertical orbit distortions were derived in consideration of the unit alignment. By using these formulae and computer simulations, the effects of the method on the sensitivity reduction against the quadrupole misalignment were investigated in detail for the storage ring of SPring-8 as an example. The effects on the correction of the closed-orbit distortion (COD) and the dynamic aperture were also investigated by means of computer simulations.

The results of this study are:

(1) The two-stage magnet alignment method reduces the amplitudes of the orbit distortions induced by the quadrupole misalignment. The sensitivity reduction against the quadrupole misalignment depends on how precisely the quadrupoles are aligned within the units, but it hardly depends on how the units are aligned.

(2) The sensitivity reduction against the quadrupole misalignment requires the magnet alignment within the units which is at least 20% more precise than the unit alignment performed by the conventional triangular method. Theoretically, the sensitivity against the horizontal misalignment of the quadrupoles can be reduced by 50～60 % and that against the vertical one by 80～95 % at the condition that the magnet misalignment within the units is zero.

(3) The sensitivity reduction against the vertical quadrupole misalignment is always larger than that against the horizontal one. This is desirable for the ring-commissioning, because the vacuum chamber aperture is generally narrow in height. On the other hand, the high precision is required for the angular-alignment of the bending magnets to reduce the amplitude of the vertical orbit distortion.

(4) The two-stage magnet alignment method reduces the maximum strength of the horizontal and vertical correctors and orbit displacements at the sextupoles. This reduction is caused by the precise sextupole alignment within the units. Owing to the orbit displacement reduction, the dynamic aperture after the COD correction is enlarged. Since the magnitude of the orbit displacements is proportional to the standard deviation of the sextupole misalignment, the sensitivity against the sextupole misalignment is also reduced by this magnet alignment method.

References

1) H. Tanaka *et al.*: This is a summery of paper, which has been accepted in Nuclear Instruments and Methods in Physics Research, Section A (Reg. no. 24-151).

* Hitachi Works, Hitachi, Ltd.

RIKEN Accel. Prog. Rep. **25** (1991)

# V-2-4. Calculation of the Resonance Band-Width Induced by Multipole Fields

Y. Ishii*

Since a magnetic pole is finite for a three-dimensional space, higher harmonics, i.e. magnetic multipole errors, are induced in a magnetic field. The ideal magnetic field (and multipole field) gives linear force to beam and multipole field gives nonlinear force to beam, respectively. The linear force is used to make beams stable. The nonlinear force is not generally considered, since it is weak. However, to install number of strong magnets in the storage ring of SPring-8, nonlinear forces which are generated from these magnets can not be ignored. The nonlinear force induces the third order and higher order resonance in addition to the first and second order resonance which are induced by the linear force. The second order resonance of the linear force and all the resonance of the nonlinear force cause the band-width of oscillation frequency. The band-width becomes wider for the strong multipole error and makes the beam amplitude larger. Therefore the beam emittance blows up when the oscillation frequency (tune) goes though the band-width and the dynamic aperture is reduced. In this report, the band-widths for the multipole errors from octapole to 14-pole fields were formulated and calculated.

In an accelerator, the beam dynamics is described by Hamilton's equation. The formulation of band-width is made from the Hamiltonian. For the linear force, the Hamiltonian of a single particle is described by the Hamiltonian-like harmonic oscillation. As one example, formula of band-width for the decapole field was given by the following, and those for the other multipole errors were also derived. First, the decapole field are added to the Hamiltonian, and a new Hamiltonian is made.

$$H=\frac{1}{2}(X^2+Y^2+P_x^2+P_y^2)+\delta_p A_{10}(X^5-X^3Y^2+XY^4) \qquad (1)$$

where X, Y are coordinates, $P_{x,y}$ are the momentum, $\delta_p$ is the periodic delta function, and $A_{10}$ is the magnetic strength. Secondly, the new Hamiltonian is expanded into harmonics and is approximately represented by the single-resonance, and the Hamiltonian which truncates the higher harmonics is obtained for the single resonance.

$$H=\nu_x J_x+\nu_y J_y+\sum_{k,m}\frac{4A_{10(k)}\sqrt{2}}{5\pi}\beta_{x(k)}^{\frac{3}{2}}\beta_{y(k)}^{\frac{2}{2}}J_x^{\frac{3}{2}}J_y^{\frac{2}{2}}$$
$$\times\Big[\Big(\exp\big[\{3\psi_{x(k)}+2\psi_{y(k)}+(m-3\nu_x-2\nu_y)\theta_{(k)}\}i\big]\Big)\Big(\exp\big[(3\phi_x+2\phi_y-m\theta_{(k)})i\big]\Big)$$
$$+\Big(\exp\big[-\{3\psi_{x(k)}+2\psi_{y(k)}+(m-3\nu_x-2\nu_y)\theta_{(k)}\}i\big]\Big)\Big(\exp\big[-(3\phi_x+2\phi_y-m\theta_{(k)})i\big]\Big)\Big], \qquad (2)$$

where

$$\Psi_{x,y}(s_{(k)})=\int_0^{s_{(k)}}\frac{ds'}{\beta_{x,y}(s')}$$

with

$$s_{(k)}=\frac{\theta_{(k)}}{2\pi}C$$

and $\nu_{x,y}$ are tunes, $\beta_{x,y}$ are betatron functions, $\phi_{x,y}$ and $J_{x,y}$ are action-angles, m is the harmonic number, k is the data number of one period, i is a unit of imaginary number, and C is the circumference of the ring. Thirdly, the band-width is formulated from the Hamiltonian by considering a stable fixed point and unstable fixed point on the phase space. The band-width ($\Delta$) is given by the following.[1)]

$$\Delta=\pm|f|\,(10K_x^{\frac{2}{3}}+3K_x^{\frac{1}{2}}K_y), \qquad (3)$$

with

$$f=\sum_k\frac{3A_{10(k)}}{125\pi}\sqrt{\frac{6}{5}}\beta_{x(k)}^{\frac{3}{2}}\beta_{y(k)}e^{\{3\phi_{x(k)}+2\phi_{y(k)}+(m-3\nu_x-2\nu_y\}i} \qquad (4)$$

$$K_x=\frac{5}{3}J_x, \quad K_y=J_y-\frac{2}{3}J_x. \qquad (5)$$

Adequacy of the the formula for band-width was confirmed by the following. For a simplified model ring, the band-width of the fifth order coupling resonance ($3\nu_x+2\nu_y$=integer) was calculated for the following two cases. The band-width was calculated by using the result of tracking shown in Fig. 1, and the theoretical band-width was calculated from eq. (3). The two band-widths became nearly equal, so that adequacy of the formula could be confirmed. Adequacy of the formula for the other multipole field was similarly confirmed.

These formulae were applied to the storage

* Research Laboratory for Nuclear Reactor, Tokyo Institute of Technology.

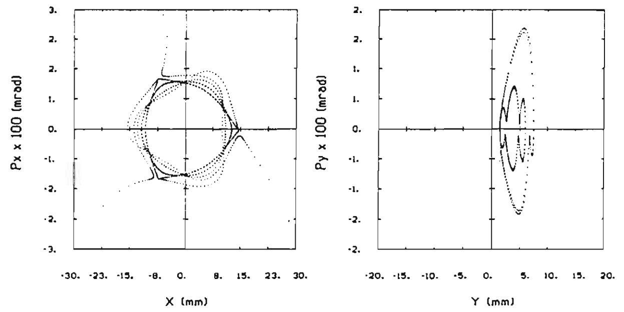


Fig. 1. Phase space for the resonance condition of a simplified model ring. Tracking conditions: In the ring. One decapole field is installed. Injection points are $(x, x') = (1.4\times10^{-2}, 0.0)$, $(y, y') = (1.4\times10^{-4}, 0.0)$. A beam is diffused at 951 turns.

ring of SPring-8. Presently the operation point of the ring is $(\nu_x, \nu_y) = (51.22, 16.16)$. The fifth ($\nu_x = 51.2$) and sixth ($\nu_x = 51.333$) order resonance lines are close to the operation point. Table 1 shows

Table 1. Band width for the resonance which is close to the operation point. Amplitudes of x and y directions are 10 mm and 0.1 mm, respectively.

| |
|---|
| Fifth order resonance ($\nu_x = 51.20$) |
| $\Delta = 5.19\text{x}10^{-9}$ |
| Sixth order resonance ($\nu_x = 51.333$) |
| $\Delta = 6.64\text{x}10^{-5}$ |

the band-widths for these resonance lines. It is found out that the two band-widths are very small and have weak effects on beams.

References

1) R. D. Ruth: *IEEE Trans. Nucl. Sci.,* **NS-30,** 2669 (1980).

RIKEN Accel. Prog. Rep. **25** (1991)

# V-2-5. Effects of Multipole Errors on the Dynamic Aperture of SPring-8 Storage Ring (I)

Y. Ishii,* H. Tanaka, and N. Kumagai

In the SPring-8 storage ring, numbers of strong quadrupole and sextupole magnets are installed to achieve the emittance of nm•radian-order. Field and alignment errors of the magnets markedly distort the closed-orbit and reduce the dynamic aperture. Among those errors, effects of systematic multipole errors on beam dynamics have been investigated to determine multipole error tolerances. We here describe their effects on the dynamic aperture.

Truncation of a magnetic potential induces higher harmonics in the magnetic field, for example, sextupole field, decapole field, and so on for a dipole magnet. These fields are localized at the both edges where beams go through. The strength of them is determined by the shape and the strength of a magnet. We simulated the

Table 1. Coefficients of power series of dipole and quadrupole magnetic fields based on the measurement data of model magnets. The strength of multipole fields except for a decapole one represents the measurement value for model magnets. The strength of a decapole field is decided in order that it gives a beam the same horizontal kick as a sextupole one at the amplitude of 35 mm.

| Multipole Component | 2-pole $a_0$ | 4-pole $a_1$ | 6-pole $a_2$ | 8-pole $a_3$ | 10-pole $a_4$ | 12-pole $a_5$ |
|---|---|---|---|---|---|---|
| Dipole Magnet | 0.0718 | | -0.0236 | | -19.290 | |
| Quadrupole Magnet | | 0.3422 | | -0.0263 | | -318.75 |

$$\frac{BL}{B\rho} = a_0 + a_1 x + a_2 x^2 + a_3 x^3 + \cdots$$

$$a_n = [m^{-n}]$$

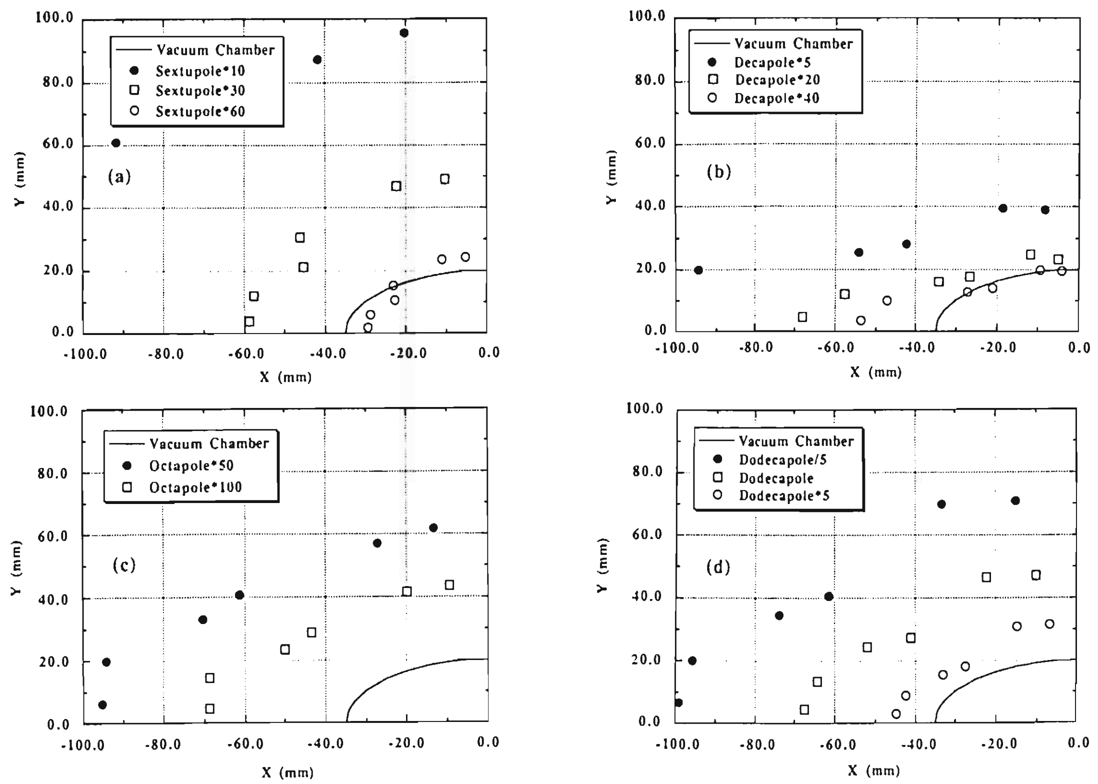


Fig. 1. Dynamic aperture reduction due to systematic errors of one kind of multipole components. Tracking conditions: Revolution period is 500. Tracking initial phase is 180 degree. The observation point is at the center of a high $\beta$ straight section. Symbols, ' * ' and '/' represent multiplication and division, respectively. For example, 'sextupole * 10' means that the strength of the sextupole field used in the simulation is ten times larger than that in Table 1.

* Research Laboratory for Nuclear Reactor, Tokyo Institute of Technology.

dynamic aperture in the presence of these systematic multipole errors by using the particle tracking code RACETRACK.[1] The following model was used in this simulation:

(1) In the case of a dipole magnet, the multipole errors are treated as nonlinear kicks at the both edges, and in the case of a quadrupole magnet, they are treated as a single nonlinear kick at a magnet-center by considering the short length of the magnet.

(2) Sextuple and decapole components only are considered as the multipole errors of a dipole magnet, and octapole and dodecapole components as those of a quadrupole one.

To clarify effects of each component on the reduction of dynamic aperture, particle tracking was performed in the presence of the systematic errors of one kind of multipole components, using the strength of the component as a parameter. The expected strength of each component is shown in Table 1. This was determined on the basis of measurement data of model magnets.[2] Sextupole magnets were turned off in the calculation to avoid the situation that the dynamic aperture is limited by them.[3]

We show in Fig. 1 the results of the calculation. Figures 1-(a) and (b) show the effects of sextupole and decapole errors of dipole magnets on the dynamic aperture. The dynamic aperture is larger than the vacuum chamber, 35 mm in half width and 20 mm in half height, unless sextupole and decapole fields exceed thirty times and five times larger than the values listed in Table 1, respectively. Figures 1-(c) and (d) show the effects of octapole and dodecapole errors of quadrupole magnets on the dynamic aperture.

Table 2. Strength of each multipole field which keeps the dynamic aperture larger than the vacuum chamber.

| Dipole Magnet | | |
|---|---|---|
| 6-pole | -0.71 | $(1/m^2)$ |
| 10-pole | -96 | $(1/m^4)$ |
| **Quadrupole Magnet** | | |
| 8-pole | -1.3 | $(1/m^3)$ |
| 12-pole | -1600 | $(1/m^5)$ |

The dynamic aperture is also larger than the vacuum chamber unless octapole and dodecapole errors exceed one hundred times and five times larger than the values listed in Table 1, respectively. We summarize in Table 2 the strength of each multipole error which keeps the dynamic aperture larger than the vacuum chamber. These results show: (1) The dynamic aperture is kept large enough by the multipole errors which are expected from the data of model magnets. (2) On the basis of the data of model magnets, the dynamic aperture is mainly limited in the horizontal direction by the dodecapole fields of quadrupole magnets and in the vertical direction by both the decapole fields of dipole magnets and dodecapole fields of quadrupole ones.

References

1) A. Wrulich: *DESY Rep.*, p. 84 (1984).
2) J. Ohnishi *et al.*: to be published in Proc. Int. Conf. on Magnet Tech. (1991).
3) H. Tanaka and M. Hara: *RIKEN Accel. Prog. Rep.*, **24**, 147(1990).

RIKEN Accel. Prog. Rep. **25** (1991)

# V-2-6. Effects of Multipole Errors on the Dynamic Aperture of SPring-8 Storage Ring (II)

Y. Ishii,* H. Tanaka, and N. Kumagai

Systematic field errors of dipole and quadrupole magnets were divided into multipole components and effects of each component on the dynamic aperture were studied.[1] In this report, we investigate the combined effects of the systematic multipole errors on the dynamic aperture. Furthermore, we investigate the effects of random ones on the dynamic aperture, which are caused by the dispersion of magnet-manufacturing.

Dynamic aperture is calculated in the presence of the systematic multipole errors, each of which keeps the aperture larger than the vacuum chamber,[1] to investigate combined effects of multipole components. The result is shown with filled circles in Fig. 1. We find that the combined effects mainly reduce the dynamic aperture at low X-Y coupling, which is the ratio of vertical emittance to horizontal one at the initial condition.

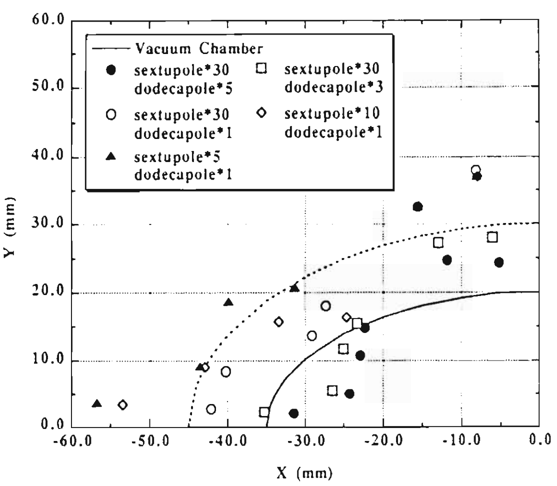


Fig. 1. Dynamic aperture in the presence of systematic multipole errors; sextupole, octapole, decapole, and dodecapole fields. Octapole and decapole errors are fixed to be 50 times and 5 times as large as those of model magnets, respectively. Sextupole and dodecapole errors are used as parameters in the simulation. Symbols, ' * ', 'sextupole', and 'dodecapole' represent multiplication, sextupole and dodecapole errors of model magnets, respectively. For example, 'dodecapole * 3' means that the strength of the dodecapole error used in the simulation is three times larger than that of the model magnet shown in Table 1. Tracking conditions: Revolution period is 500 and tracking initial phase is 180 degree. The observation point is at the center of a high $\beta$ straight section.

Upper limits of the multipole errors are investigated to make the dynamic aperture larger than the vacuum chamber in the presence of all kinds of systematic multipole components. Since the dodecapole and the sextupole components mainly limit the dynamic aperture at the low X-Y coupling under this condition,[1] the dynamic aperture is calculated using the strength of those components as parameters. The results are shown in Fig. 1. We find that the dynamic aperture is larger than the elliptical cross section, about 45 mm in half width and 30 mm in half height, under the condition listed in Table 1, where the strength of sextupole and dodecapole errors is made to be five times and one times as large as that of the model magnets, respectively.

Table 1. Upper limits of systematic multipole errors to keep the dynamic aperture larger than the vacuum chamber. Curly brackets represent systematic multipole errors of the model magnets.

| | | | |
|---|---|---|---|
| Dipole Magnet | | | |
| 6-pole | -0.12 | {-0.024} | ($1/m^2$) |
| 10-pole | -96 | {-19.3} | ($1/m^4$) |
| Quadrupole Magnet | | | |
| 8-pole | -1.3 | {-0.026} | ($1/m^3$) |
| 12-pole | -320 | {-320} | ($1/m^5$) |

To investigate the effects of the random multipole errors on the dynamic aperture, we use the dodecapole fields of quadrupole magnets as an indicator, because they dominate the reduction of the dynamic aperture in both the horizontal and vertical planes.[1] In this calculation, the systematic multipole errors are set as listed in Table 1 on the basis of the results described above. The dynamic aperture is calculated only at 1 % X-Y coupling under the condition that a root mean square (rms) value for the random dodecapole errors is varied from 5 to 100 % of the value for the systematic ones in Table 1. The results are shown in Table 2. We can predict that the rms value for each kind of random multipole

* Research Laboratory for Nuclear Reactors, Tokyo Institute of Technology.

errors is less than about 25 % of the value for that in Table 1, to keep the dynamic aperture

Table 2. Dynamic aperture at 1% X-Y coupling in the presence of all systematic errors shown in Table 1 and random dodecapole errors. Calculation is performed for 5 rings, each of which has a different set of random dodecapole errors. Tracking conditions are the same as those of Fig. 1.

| | Random Dodecapole Error (rms value) (T/m$^5$) | Dynamic Aperture (mm) |
|---|---|---|
| Case 1 | 0.0 (0%) | -67.4 |
| Case 2 | 318.73 (100%) | -32.3 ~ -39.4 |
| Case 3 | 159.37 (50%) | -35.1 ~ -41.4 |
| Case 4 | 79.68 (25%) | -41.2 ~ -44.0 |
| Case 5 | 31.87 (10%) | -47.1 ~ -53.9 |
| Case 6 | 15.94 (5%) | -49.9 ~ -59.4 |

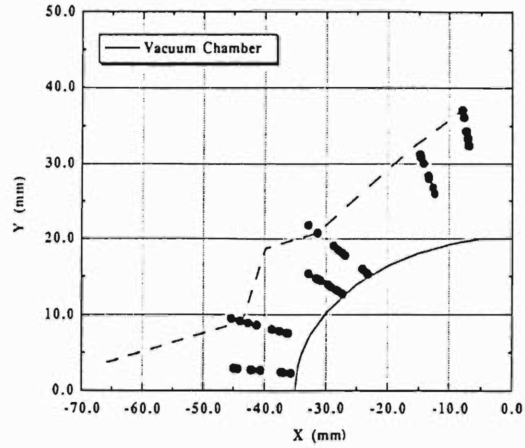


Fig. 2. Dynamic aperture with all systematic and random multipole errors shown in Table 3 for 10 rings, each of which has a different set of random multipole errors. The broken line represents the dynamic aperture with only systematic multipole errors. Tracking conditions are the same as those of Fig. 1.

larger than the vacuum chamber in the presence of all systematic and random multipole errors. We show in Fig. 2 the dynamic aperture calculated for 10 rings, each with a different set of random multipole errors. The systematic and random multipole errors are set to the values in Table 3, in which 10 % of the values in Table 1 are adopted as the rms values of random multipole errors by considering combined effects on the reduction of the dynamic aperture. The broken line in the figure represents the dynamic aperture in the presence of only systematic multipole errors. We find that the dynamic aperture is kept larger than the vacuum chamber at any X-Y coupling and random multipole errors markedly reduce the dynamic aperture at low X-Y coupling.

Table 3. Upper limits of systematic and random multipole errors to keep the dynamic aperture larger than the vacuum chamber.

Dipole Magnet

| Random Error (rms value) | | | Systematic Error | |
|---|---|---|---|---|
| 6-pole | 0.012 | (1/m$^2$) | -0.12 | (1/m$^2$) |
| 10-pole | 9.6 | (1/m$^4$) | -96 | (1/m$^4$) |

Quadrupole Magnet

| Random Error (rms value) | | | Systematic Error | |
|---|---|---|---|---|
| 8-pole | 0.13 | (1/m$^3$) | -1.3 | (1/m$^3$) |
| 12-pole | 32 | (1/m$^5$) | -320 | (1/m$^5$) |

References

1) Y. Ishii, H. Tanaka, and N. Kumagai: This Report, p.180.

RIKEN Accel. Prog. Rep. **25** (1991)

# V-2-7. Optimization of the Lattice with 4 Long Magnet-Free Straight Sections for SPring-8 Storage Ring (I)

H. Tanaka, M. Hara, and T. Nakamura

Four long magnet-free straight sections are constructed in the storage ring through two steps at the final stage.[1] We have made an effort to optimize the lattice with the long magnet-free straight sections. Here, we show preliminary lattice parameters and optics designed under following conditions: (1) The length of each long magnet-free straight section is larger than 30 m. (2) Highly periodic optics, high $\beta$ optics, is used in normal Chasman-Green (CG) cells to keep the dynamic aperture large. (3) Betatron functions at the long magnet-free straight sections are set to be 20~30m for the installation of FEL devices. (4) Betatron functions are kept lower than ~50m along the whole ring to suppress chromaticities.

The designed lattice and optics[2] are shown in Fig. 1. In this case, the magnet-free straight section is 30.1 m long and the maximum horizontal betatron function is about 50 m. Five families of quadrupole magnets are used at the both ends of the magnet-free straight sections. These might be reduced to four families and the length of the magnet-free straight section might be adjustable from 30 to 35 m by further optimization. Four families of sextupole magnets are used and the strength of each magnet is much smaller than that in the standard (24-fold symmetrical) hybrid optics.[3] In Table 1, major parameters of the lattice are listed for the 8 and 4 GeV operation without damping wigglers.

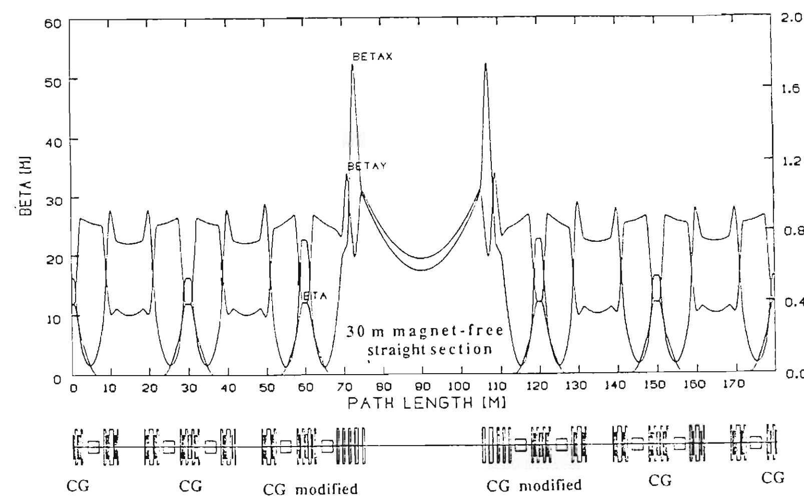


Fig. 1. Lattice and linear optics for 1/8 of the ring.

Momentum dependent tune shifts are shown in Fig.2. Horizontal and vertical tune shifts are 0.03 and 0.02, respectively within a momentum deviation of ±2 %. These are smaller compared with the tune shifts of the standard hybrid optics[3] and almost the same as that of the high $\beta$ optics. These results show that the chromatic characteristics are scarcely affected by introduction of the magnet-free straight sections into the ring.

Table 1. Major parameters of the lattice with 4 long magnet-free straight sections.

| | | |
|---|---|---|
| Energy (GeV) | 8 | 4 |
| Current (multi-bunch) (mA) | 100 | --- |
| Current (single-bunch) (mA) | 5 | --- |
| Circumference (m) | 1435.948 | 1435.948 |
| Dipole magnetic field (T) | 0.679 | 0.3395 |
| Bending radius (m) | 39.2718 | 39.2718 |
| Type of lattice | Chasman-Green | Chasman-Green |
| Number of cells Normal/Straight | 44/4 | 44/4 |
| Length of straight section Normal/Long (m) | 6.65/~30 | 6.65/~30 |
| Natural emittance (nm·rad.) | 9.00 | 2.25 |
| Critical photon energy (keV) | 28.90 | 3.61 |
| Tune $\nu_x/\nu_y$ | 38.2/14.16 | 38.2/14.16 |
| Synchrotron tune $\nu_s$ | 0.01005036 | 0.01005036 |
| Momentum compaction $\alpha$ | $1.4597\times10^{-4}$ | $1.4597\times10^{-4}$ |
| Natural chromaticity $\zeta_x/\xi_y$ | -70.44/-33.20 | -70.44/-33.20 |
| Energy loss in the arcs (MeV/rev) | 9.2263 | 0.577 |
| Energy spread $\sigma_e/E$ | 0.0010936 | 0.0021872 |
| Damping time $\tau_x/\tau_y/\tau_e$(msec) | 8.30/8.31/4.15 | 66.4/66.5/33.2 |
| Harmonic number | 2436 | 2436 |
| R.F. voltage (MV) | 17 | 5 |
| R.F. frequency (MHz) | 508.58 | 508.58 |
| Bunch Length $\sigma_s$ (mm) | 3.63 | 1.18 |

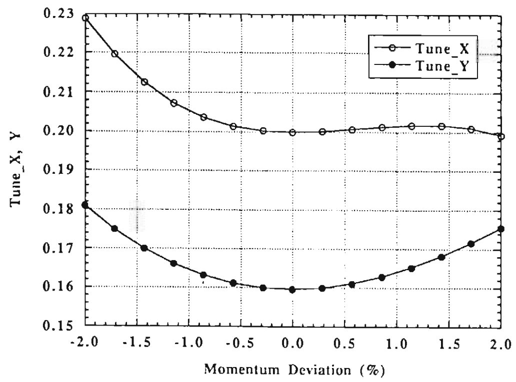


Fig. 2. Momentum dependent tune shifts.

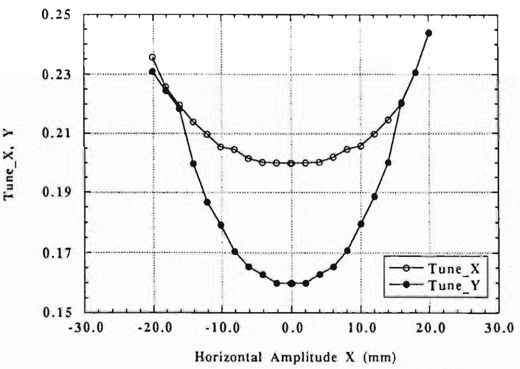


Fig. 3. Amplitude dependent tune shifts.

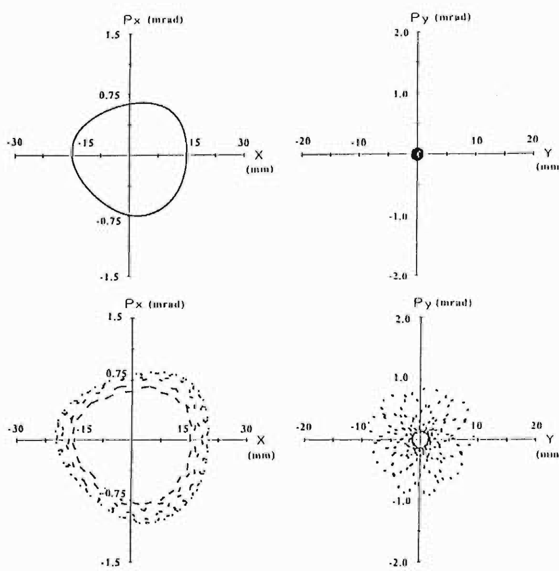


Fig. 4. Transverse phase space at the center of a high $\beta$ dispersion-free straight section. A coupling ratio between the horizontal and vertical emittance is 1 % and the revolution period is adjusted to 1000. Upper figures show the phase space for a particle with the initial horizontal amplitude of 15 mm and lower ones with that of 20 mm.

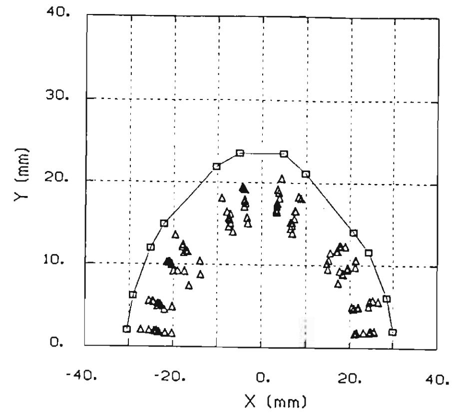


Fig. 5. Dynamic aperture at the beam-injection point. Empty squares show the aperture calculated under the condition with no magnetic error and filled triangles with magnetic error tolerances. A revolution period is adjusted to 500.

Amplitude dependent tune shifts are shown in Fig. 3. These are also the same as those of the high $\beta$ optics. We can expect from this figure that horizontal and vertical oscillations are decoupled in the region where the amplitude is smaller than 10 mm. Since the both tunes behave in a similar way in the region where the amplitude is larger than 15 mm, horizontal and vertical oscillations begin to couple in this region. In Fig. 4 transverse phase space plots are shown. At the amplitude of 20 mm, the horizontal and vertical oscillations are fully coupled, whereas they are almost decoupled at the amplitude of 15 mm.

The dynamic aperture calculated under the condition with and without magnetic errors is shown in Fig. 5. The aperture of 20 mm can be assured at the horizontal plane of the beam injection side under the condition with magnetic error tolerances.[4] This is large enough for the stable beam-injection.

References

1) H. Kamitsubo: *Nucl. Instrum. Methods*, **A303**, 421 (1991).
2) M. Hara, T. Nakamura, T. Takada, and H. Tanaka: Proc. SRI Conf., Chester, U.K. (1991).
3) H. Tanaka and M. Hara: *RIKEN Accel. Prog. Rep.*, **24**, 141 (1990).
4) SPring-8 Project Design Report Part I Facility Design [REVISED], Aug. (1991).

RIKEN Accel. Prog. Rep. **25** (1991)

# V-2-8. Study on a Free Electron Laser at a SPring-8 Long Straight Section

T. Nakamura

The performance of a free electron laser (FEL) at a 30m-long straight section of the SPring-8 storage ring was studied. The wave length of the FEL was set to be 4nm in this study.

The storage ring has two lattice parameters, normal and detuned, which are for usual operation and commissioning, respectively, and have very different emittances and momentum-compaction factors.

The peak current of the storage ring is limited by the bunch-lengthening instabilities which accompany the energy spread of the beam and cause the serious degradation of the FEL performance.[1)]

The beam performance and threshold currents of the bunch-lengthening are shown in Table 1. The latter values are calculated with the formula

$$I_{th,BL} = \frac{2\pi\alpha(E/e)}{|Z_{\parallel}/n|_{eff}}\left(\frac{\sigma\gamma}{\gamma}\right)^2 \tag{1}$$

where $\alpha$ is the momentum-compaction factor. In our case, the effective impedance $|Z_{\parallel}/n|_{eff}$ is limited to be $26m\Omega$ by the free space impedance $|Z_{\parallel}/n|_{eff} = 300b/R$ where b and R are the vacuum chamber radius and the bending radius, respectively.

The FEL performances with the FEL wiggler of parameters shown in Table 2 were analyzed with the three-dimensional simulation code ELFIN, which is developed by the author. One of the results is shown in Fig. 1.

Table 1. The storage ring parameters and the threshold current of Bunch Lengthening.

| Lattice | Normal | Detuned |
|---|---|---|
| Damping Wiggers | ON | |
| Energy | 3 GeV | |
| Energy Spread($\sigma_\gamma/\gamma$) | 0.00065 | 0.00065 |
| Momentum-Compaction Factor | 0.000146 | 0.00112 |
| Emittance(x,y)[nm rad] | 0.1 | 1.3 |
| $I_{th,BL}$(natural $\sigma_\gamma$) | 50 A | 330 A |
| $I_{th,BL}$(1.5 natural $\sigma_\gamma$) | 112 A | 742 A |

Table 2. FEL wiggler.

| | | |
|---|---|---|
| Period | 3 cm | 3.5 cm |
| Kw | 4.0 | 3.7 |
| Matched $\beta_{x,y}$ | 14.2 m | 17.7 m |
| Length | 30.0 m | |
| | x,y equal focusing | |

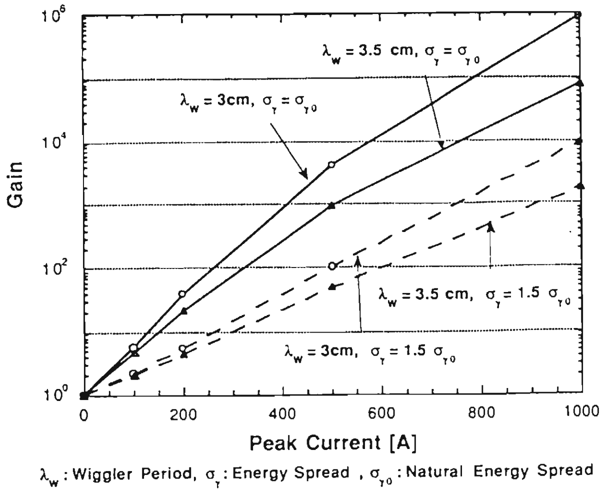


Fig. 1. Gain vs peak current (in a normal lattice with damping wigglers).

This result shows that the higher peak current was obtained with the higher energy spread. However high energy spread causes degradation of the FEL performance. From another result, not shown here, the higher peak current was obtained with the detuned lattice of higher momentum-compaction factor. But this lattice has also higher emittance and the high emittance also causes degradation of the FEL performance. Hence the gain is not so different in both cases.

References

1) A.S. Fisher *et al.*: "A 40 Å FEL on the PEP Storage Ring", SSRL ACD, Note 87 (1990).

# V-2-9. The Relation between an Undulator Radiation in SPring-8 and a Diffraction Limit Radiation on Spectral Brightness at the X-Ray Wavelength

T. Takada and M. Hara

SPring-8 is one of the third generation storage rings, which is designed to be operated with the electron energy of 8 GeV and the beam current of 100 mA (multi-bunch), has a low natural emittance (electron beam emittance) of 6.99 nm• rad, and is optimized for many 4 meter undulator straight sections. One of the directions toward the next generation synchrotron radiation light sources is to provide even higher spectral brightness, coherence and the diffraction limit radiation on brightness at the X-ray wavelength. In this report, the conditions[1] for the diffraction limit radiation from a planar undulator is described. Then the relation between a typical undulator radiation in SPring-8 and the diffraction limit radiation on brightness at the X-ray wavelength is investigated.

When we observe the photon beam at a large distance from the sources (the Fraunhofer zone), the photon beam emittance has its intrinsic value[2] which depends only on the radiation wavelength, $\lambda$:

$$\varepsilon_p = \sigma_p \sigma_{p'} = \lambda / 4\pi, \tag{1}$$

where $\sigma_p$ is the RMS photon beam size and $\sigma_{p'}$ is the RMS angular divergence. This situation is called "diffraction limited" because $\sigma_{p'}$ is limited by the constraint of eq. (1) when $\sigma_p$ is given.

Fundamental wavelength, $\lambda_{1st}$, and the peak spectral flux at the fundamental wavelength, $F_{1st}$, radiated from a planar undulator are given by

$$\lambda_{1st}[\text{Å}] = 1.31 \times 10^3 \frac{\lambda u[\mathrm{m}]}{Ee^2[\mathrm{GeV}]}(1 + Ky^2/2), \tag{2}$$

$$F_{1st}[\text{photons/sec/0.1\%b.w.}] = 1.43 \times 10^{14} \times Nu \frac{Ky^2}{(1 + Ky^2/2)} \left\{ J_0\left[\frac{Ky^2}{4(1 + Ky^2/2)}\right] - J_1\left[\frac{Ky^2}{4(1 + Ky^2/2)}\right]\right\}^2 I[\mathrm{A}] \tag{3}$$

where Ee is the electron energy, I is the beam current, Nu is the number of magnetic periods, Jn (x) is the n-th-order Bessel function of the variable, x, and Ky is called the deflection parameter which is proportional to the product of the magnetic period length, $\lambda u$, and the peak of periodic sinusoidal magnetic field, $By_p$, as:

$$Ky\ [\text{non-dimension}] = 93.4\ By_p[\mathrm{T}]\lambda u[\mathrm{m}]. \tag{4}$$

The peak on-axis spectral angular flux density, $D_{1st}^{on-axis}$, in photons/sec/0.1%b.w./mrad² and the peak on-axis spectral brightness, $B_{1st}^{on-axis}$, in photons/sec/0.1%b.w./mrad²/mm² at the fundamental wavelength are given as follows[1] by taking into account the effect of electron beam emittance:

$$D_{1st}^{on-axis} = \frac{F_{1st}}{2\pi\Sigma_{x'}\Sigma_{y'}},\ B_{1st}^{on-axis} = \frac{F_{1st}}{(2\pi)^2\Sigma_x\Sigma_y\Sigma_{x'}\Sigma_{y'}}, \tag{5}$$

where $\Sigma_x$, $\Sigma_y$, $\Sigma_{x'}$ and $\Sigma_{y'}$ are given by

$$\Sigma_{x,y} = \sqrt{\sigma_{x,y}^2 + \sigma_p^2},\ \Sigma_{x',y'} = \sqrt{\sigma_{x',y'}^2 + \sigma_{p'}^2}. \tag{6}$$

Here, $\sigma_x$ ($\sigma_y$) is horizontal (vertical) RMS electron beam size and $\sigma_{x'}$ ($\sigma_{y'}$) is RMS angular divergence. They are given at a dispersion free straight section by:

$$\sigma_{x,y} = \sqrt{\varepsilon_{x,y}\beta_{x,y}},\ \sigma_{x',y'} = \sqrt{\varepsilon_{x,y}/\beta_{x,y}}, \tag{7}$$

where $\beta$x ($\beta$y) is horizontal (vertical) betatron function value, and $\varepsilon_x$ ($\varepsilon_y$) is horizontal (vertical) electron beam emittance. The relationship between $\varepsilon_x (= \sigma_x \cdot \sigma_{x'})$, $\varepsilon_y = (= \sigma_y \cdot \sigma_{y'})$ and the natural emittance, $\varepsilon_n$, are given as:

$$\varepsilon_x = \frac{\varepsilon_n}{1 + \kappa},\qquad \varepsilon_y = \frac{\kappa\varepsilon_n}{1 + \kappa} = \kappa\varepsilon_x, \tag{8}$$

where $\kappa$ is the coupling coefficient which stands for the ratio between the horizontal and vertical emittance. When the angular divergence of the planar undulator radiation at the fundamental wavelength is approximated to a Gaussian distribution, $\sigma_{p'}$ is first identified with

$$\sigma_{p'} = \sqrt{\lambda_{1st}/Lu} = \sqrt{\frac{(1 + Ky^2/2)}{2Nu}}\frac{1}{\gamma}, \tag{9}$$

where Lu is the length of undulator, $\gamma$ is the ratio of the total electron energy to the rest mass. Then, the diffraction limited beam size, $\sigma_p$, is obtained by using eqs. (1) and (9) as:

$$\sigma_p = \sqrt{\lambda_{1st}Lu}/4\pi. \tag{10}$$

In order to fully utilize the high brightness of undulator radiation, the natural emittance has to be made smaller, e.g., by installing the damping wigglers in the storage ring. There are 3 phases about the behavior of the peak brightness at the fundamental wavelength in progress of decreasing the natural emittance, as given by[1]:

<u>Phase. 1</u> $\sigma_x,\ \sigma_y \gg \sigma_p$ and $\sigma_{x'},\ \sigma_{y'} \gg \sigma_{p'}$ (11)

$$B_{1st}^{on-axis} = \frac{F_{1st}}{2} \propto \varepsilon_n^{-2},\ Nu, \tag{12}$$

<u>Phase. 2</u> $\sigma_x,\ \sigma_y \gg \sigma_p$ and $\sigma_{x'},\ \sigma_{y'} \ll \sigma_{p'}$ (13)

$$B_{1st}^{on-axis} = \frac{F_{1st}}{(2\pi)^2 \sigma_x \sigma_y \sigma_{p'}^2} \propto \varepsilon_n^{-1},\ Nu^2, \quad (14)$$

<u>Phase. 3</u> $\sigma_x,\ \sigma_y \ll \sigma_p$ and $\sigma_{x'},\ \sigma_{y'} \ll \sigma_{p'}$ (15)

(Diffraction Limited)

$$B_{1st}^{on-axis} = \frac{F_{1st}}{(2\pi)^2 \sigma_{p'}^2 \sigma_p^2} = \frac{F_{1st}}{(2\pi)^2 \varepsilon_p^2} = \frac{F_{1st}}{(\lambda_{1st}/2)^2} \propto Nu \quad (16)$$

Equation (16) gives the maximum peak brightness available at the fundamental wavelength from the planar undulator, which is independent of the natural emittance.

A typical undulator in SPring-8, whose $\lambda$u is 3 cm and Ky is 0.75 (Table 1), provides the fundamental wavelength on-axis of 0.78 Å in the hard X-ray region, when installed in the 8 GeV storage ring. Figure 1 shows the spectral brightness radiated from the typical undulator installed in a high-$\beta$ straight section (large beam size and small angular divergence) in SPring-8, whose parameters are listed in Table 2. The peak brightness of $1.95\times10^{18}$ photons/sec/0.1%b.w./mrad$^2$/mm$^2$ is obtained at the fundamental wavelength with 100 mA operation. When we compare the natural emittance of 6.99 nm•rad designed for SPring-8 and the photon beam emittance at the wavelength of 0.78 Å using eq. (17) in practical unit:

$$\varepsilon_p[\mathrm{nm \cdot rad}] = \frac{\lambda_{1st}[\text{Å}]}{4\pi} \times 10^{-1} = \frac{1}{Ep_{1st}[\mathrm{keV}]} \times 10^{-1}, \quad (17)$$

the natural emittance is much larger than the photon beam emittance (Table 3), which corresponds to the phase 1 described above. If one want to obtain a diffraction limits radiation at 0.78 Å, the storage ring has to be operated with the natural emittance which is much smaller than $6.21\times10^{-3}$ nm•rad. It is impossible to operate the storage ring with such a small natural emittance in SPring-8 because the natural emittance can be decreased to only about 5.5 nm•rad with damping wigglers of 100 m in total length in the storage ring[3]. In order to estimate how far the typical undulator radiates from the diffraction limit, the following are calculated[4] under the assumption that design values of $\beta$x, $\beta$y and $\kappa$ in Table 2 are held to be constant even if the natural eimttance is varied. (Actually, $\beta$x and $\beta$y are varied when the natural emittance is decreased.) In Fig. 2, the sets of ($\sigma_x$, $\sigma_y$, $\sigma_{x'}$, $\sigma_{y'}$) and ($\Sigma_x$, $\Sigma_y$, $\Sigma_{x'}$, $\Sigma_{y'}$) are shown as a function of the natural emittance. In Fig. 3, the peak flux, the peak flux density and the peak brightness are shown at the

Table 1. Parameters of the typical planar undulator in SPring-8.

| | | |
|---|---|---|
| Technology | Pure Permanent Magnet : Halbach design | |
| Magnet block material | Nd-Fe-B alloy | |
| Remnant field | Br [T] | 1.25 |
| Magnetic period length | $\lambda$u [m] | 0.03 |
| Height of magnet | h [m] = $\lambda$u [m] / 2 | 0.015 |
| Number of periods | Nu | 133 |
| Total length | Lu [m] = $\lambda$u [m] • Nu | 3.99 |
| Peak magnetic field on-axis a) | By$_p$ [T] | 0.265 |
| Deflection parameter a) | Ky = 93.4 By$_p$ [T] • $\lambda$u [m] | 0.75 |
| Fundamental wavelength on-axis a) | $\lambda_{1st}$ [Å] | 0.78 |
| Fundamental photon energy on-axis a) | Ep$_{1st}$ [keV] | 15.8 |

a) at magnetic gap width, g, of 20 mm.

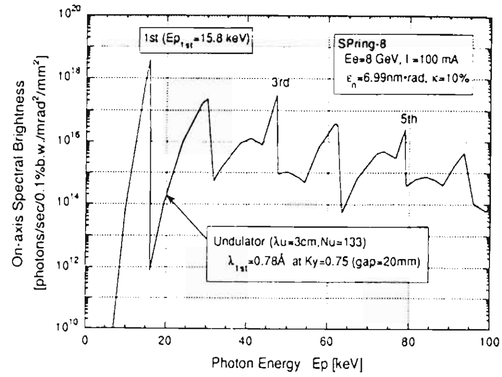


Fig. 1. Spectral brightness radiated from a typical undulator in the SPring-8 storage ring operated at the electron energy of 8 GeV, the beam current of 100 mA and the natural emittance of 6.99 nm•rad. The couping coefficient is assumed to be 10 %.

Table 2. Parameters at the center of the high-$\beta$ straight section in SPring-8.

| | | |
|---|---|---|
| Electron energy | E [GeV] | 8 |
| Natural emittance | $\varepsilon_n$ [nm•rad] | 6.99 |
| Coupling coefficient | $\kappa$ [%] | 10 |
| Horizontal emittance | $\varepsilon_x$ [nm•rad] | 6.35 |
| Vertical emittance | $\varepsilon_y$ [nm•rad] | 0.635 |
| Horizontal betatron function value | $\beta_x$ [m] | 23.346 |
| Vertical betatron function value | $\beta_y$ [m] | 10.283 |
| Horizontal RMS beam size | $\sigma_x$ [$\mu$m] | 385.2 |
| Vertical RMS beam size | $\sigma_y$ [$\mu$m] | 80.8 |
| Horizontal RMS angular divergence | $\sigma_{x'}$ [$\mu$rad] | 16.5 |
| Vertical RMS angular divergence | $\sigma_{y'}$ [$\mu$rad] | 7.9 |

Table 3. RMS photon beam size and angular divergence at the fundamental wavelength of the typical planar undulator in SPring-8.

| | | |
|---|---|---|
| Fundamental wavelength on-axis | $\lambda_{1st}$ [Å] | 0.78 |
| Total length of undulator | Lu [m] | 3.99 |
| Photon emittance | $\varepsilon_p$ [nm•rad] | $6.21 \times 10^{-3}$ |
| RMS photon beam size | $\sigma_p$ [$\mu$m] | 1.4 |
| RMS photon angular divergence | $\sigma_{p'}$ [$\mu$rad] | 4.4 |

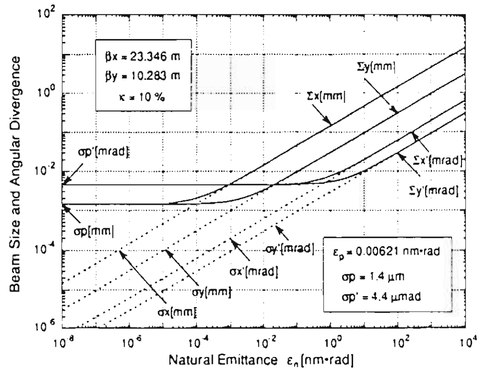


Fig. 2. Horizontal and vertical RMS beam sizes and angular divergences of electron beam only, ($\sigma_x$, $\sigma_y$, $\sigma_{x'}$, $\sigma_{y'}$), and the convolution of electron beam and photon beam, ($\Sigma_x$, $\Sigma_y$, $\Sigma_{x'}$, $\Sigma_{y'}$, as a function of natural emittance.

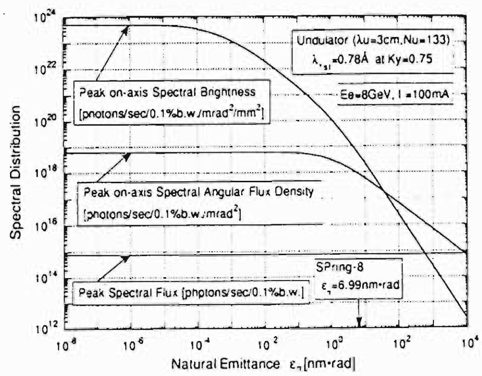


Fig. 3. Peak spectral flux, peak spectral angular flux density and peak spectral brightness at the fundamental wavelength radiated from a typical undulator, whose parameters are listed in Table 1, as a function of natural emittance.

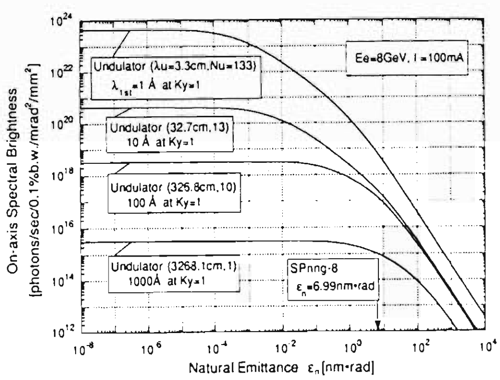


Fig. 4. Peak spectral brightness at fundamental wavelengths of 1, 10, 100 and 1000 Å radiated from four typical planar undulators in the 8 GeV storage ring, whose parameters are listed in Table 4, as a function of natural emittance.

Table 4. Four typical planar undulators with fundamental wavelengths of 1, 10, 100 and 1000 Å in the 8 GeV storage ring.

| | U1 | U2 | U3 | U4 |
|---|---|---|---|---|
| $\lambda u$ [cm] | 3.3 | 32.7 | 326.8 | 3268.1 |
| Nu | 133 | 13 | 10 | 1 |
| Lu [m] | 4.389 | 4.251 | 32.68 | 32.681 |
| Ky | 1.0 | 1.0 | 1.0 | 1.0 |
| $\lambda_{1st}$ [Å] | 1 | 10 | 100 | 1000 |

fundamental wavelength radiated from the typical undulator as a function of the natural emittance.

On the other hand, it is possible to obtain a diffraction limit radiation in a wavelength longer than about 900 Å against the natural emittance of 6.99 nm•rad designed for SPring-8. Such a fundamental wavelength is realized by the undulator in the 8 GeV ring whose period length is longer than about 30 m and Ky is 1. Although this undulator can be installed in a long straight section of 30 m in length prepared in SPring-8, it is meaningless to discuss the diffraction limit radiation because the number of periods is only 1 and the coherent radiation is not available. The peak brightness at the fundamental wavelengths of 1, 10, 100 and 1000 Å is shown in Fig. 4 as a function of the natural emittance under the same assumption as mentioned above. Those wavelengths can be obtained from four typical undulators, U1, U2, U3 and U4, in the 8 GeV storage ring, whose parameters are listed in Table 4.

References

1) K.-J. Kim: "Characteristics of Synchrotron radiation", Proc. AIP Conf. on the US Particle Accelerator School, p. 565 (1989).
2) D. Attwood, K. Halbach, and K.- J. Kim: *Science*, **228**, 1265 (1985).
3) M. Hara, T. Nakamura, T. Takada, and H.Tanaka : *Rev. Sci. Instrum.*, **63**, 1 (1992). to be published (Contributed to the 4th SRI Conf., Chester, U.K., on July 15-19, 1990).
4) M. Hara : 4th Ann. Meeting Hoshakou, Nagoya, April, p. 20 (1991).

RIKEN Accel. Prog. Rep. **25** (1991)

# V-2-10. Angular Distribution of the Radiation Power from a Bending Magnet in SPring-8

T. Takada and M. Hara

Extremely high radiation power is expected from a bending magnet (BM) in SPring-8 compared to that in the facilities under operation. In this report, the total power and angular power densities of the BM radiation in SPring-8 are calculated to estimate the heat load.

*Parameters of BM* : The SPring-8 storage ring has 88 BMs to make the orbit closed. Twenty three of them can be equipped with a beam line (BL) to bring out a radiation having a broad and smooth spectrum. Parameters and characteristics of the BMs in SPring-8 are shown in Table. 1. Critical photon energy and bending radius are given by eqs. (1) and (2), respectively, in practical unit:

$$\mathrm{Ep_c[keV]} = 0.665\mathrm{Ee^2[GeV]B[T]}$$
$$= 28.9\mathrm{[keV]} \text{ for SPring-8 BM.} \qquad (1)$$
$$\rho\mathrm{[m]} = 3.336\frac{\mathrm{Ee[GeV]}}{\mathrm{B[T]}}$$
$$= 39.30\mathrm{[m]} \text{ for SPring-8 BM.} \qquad (2)$$

where Ee is the electron energy and B is the magnetic field strength.

The coordinate system for the orbit of an electron and the BM radiation are shown in Fig. 1. An electron moves with time, t, and velocity,

Table 1. Characteristics of the BM in SPring-8.

| | | |
|---|---|---|
| Electron energy | Ee [GeV] | 8 |
| Field strength | B [T] | 0.679 |
| Bending radius | ρ [m] | 39.30 |
| Critical photon energy | Epc [keV] | 28.9 |
| Critical wavelength | λc [Å] | 0.429 |

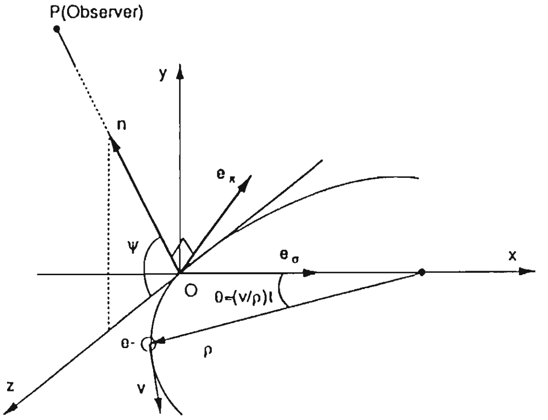


Fig. 1. The coordinate system for the orbit of an electron and the BM radiation.

V, heading to the tangential direction of trajectory, and lies in the x-z plane with an instantaneous radius of curvature, $\rho$, making an angle (the latitude), $\theta$, with x-axis. A vector **n** is a unit vector heading from the electron to the observer, P, and $\psi$ is the observation angle between **n** and the orbit plane. $\mathbf{e}_\sigma$ is a unit vector in the x-axis corresponding to polarization on the orbit plane; $\mathbf{e}_\pi$ $(=\mathbf{n}\times\mathbf{e}_\sigma)$ is a unit vector corresponding approximately to polarization that is perpendicular to the obit plane if $\psi$ is very small.

*Total Power*[1] : The total power of BM in the arc of L $(=\rho[\mathrm{m}]\theta[\mathrm{rad}])$ is given by integrating the spectral angular power density over all angular frequencies, $\omega$, all vertical angles, $\psi$, and horizontal angles, $\theta$, in the interval of $[0, L/\rho]$ as:

$$\mathrm{P_T[kW]} = \int_0^\infty d\omega \int_0^{L/\rho} d\theta \int_{-\pi/2}^{\pi/2} d\psi \frac{d^3P_T}{d\omega d\theta d\psi}$$
$$= 1.27\mathrm{Ee^2[GeV]B^2[T]I[A]L[m]}$$
$$= 1.27\mathrm{Ee^2[GeV]B^2[T]I[A]}\rho\mathrm{[m]}\theta\mathrm{[rad]}$$
$$= 146.8\theta\mathrm{[rad]} \text{ at 100mA for SPring-8 BM.} \qquad (3)$$

where I is the beam current. The energy loss per 1 turn in all BMs is given by

$$\mathrm{P_{1turn}[kW/turn]}$$
$$= 1.27\mathrm{Ee^2[GeV]B^2[T]I[A]}\rho\mathrm{[m]}2\pi\mathrm{[rad]}$$
$$= 922.0\mathrm{[kW/turn]} \text{ at 100mA for SPring-8 BM.} \qquad (4)$$

*Angular Power Density*[1] : The linear angular power density, which is defined as the power per a unit horizontal angle, is derived by integrating the spectral angular power density over all angular frequencies and all vertical angles as:

$$\frac{dP_T}{d\theta}\mathrm{[kW/mrad(horiz.)]} = \int_0^\infty d\omega \int_{-\pi/2}^{\pi/2} d\psi \frac{d^3P_T}{d\omega d\theta d\psi}$$
$$= 1.27\times10^{-3}\mathrm{Ee^2[GeV]B^2[T]I[A]}\rho\mathrm{[m]}$$
$$= 0.147\mathrm{[kW/mrad(horiz.)]} \text{ at 100mA for SPring-8 BM.} \qquad (5)$$

The linear angular power density, $dP_T/d\theta$, is independent of $\theta$.

The angular power density is defined as a power per unit horizontal and vertical angles obtained by integrating the spectral angular power density over all angular frequencies. It is given by

$$\frac{d^2P_T}{d\theta d\psi}(\gamma\psi) = \int_0^\infty d\omega \frac{d^3P_T}{d\omega d\theta d\psi}$$
$$= \frac{d^2P_\sigma}{d\theta d\psi}(\gamma\psi) + \frac{d^2P_\pi}{d\theta d\psi}(\gamma\psi), \qquad (6)$$

where

$$\begin{bmatrix} \frac{d^2P_\sigma}{d\theta d\psi}(\gamma\psi) \\ \frac{d^2P_\pi}{d\theta d\psi}(\gamma\psi)\end{bmatrix} = \left(\frac{d^2P_T}{d\theta d\psi}(\gamma\psi)\Big|_{\Psi=0}\right) \cdot \frac{1}{(1+\gamma^2\psi^2)^{5/2}} \begin{bmatrix} 1 \\ \frac{5}{7}\frac{\gamma^2\psi^2}{1+\gamma^2\psi^2}\end{bmatrix}, \tag{7}$$

and where $\gamma$ is called the 'relativistic energy factor' that is the ratio of the total electron energy to the rest mass of 511 keV. As $\gamma$ is 15656 in SPring-8, the vertical FWHM radiation cone at the critical photon energy is 63.9 $\mu$rad ($=1/\gamma$). Here, the angular power density on the orbit plane ($\psi=0$), $d^2P_T/d\theta d\psi\mid_{\Psi=0}$, is given by

$$\begin{aligned} &\frac{d^2P_T}{d\theta d\psi}(\gamma\psi)\Big|_{\Psi=0}[\mathrm{kw/mrad^2}] \\ &=\int_0^\infty d\omega \frac{d^3P_T}{d\omega d\theta d\psi}\Big|_{\Psi=0} \\ &=5.42\times10^{-3}B[T]Ee^4[GeV]I[A] \\ &=1.51[\mathrm{kW/mrad^2}] \text{ at 100mA for SPring-8 BM.} \end{aligned} \tag{8}$$

Total power and angular power densities (linear angular power density and angular power density on the orbit plane) are shown in Table 2 for a BM in SPring-8 with 100 mA operation. The angular distribution is shown in Fig.2 against the vertical observation angle of the angular power density for a BM.

The quantities so far described were obtained with the assumption that the electron beam has no angular divergence, that is, zero emittance limit. The electron emittance, in particular, the vertical RMS angular divergence of the electron, $\sigma_{y'}$, gives an effect on the angular distribution against the vertical direction of angular power density which depends on vertical angle, $\psi$. At finite emittance, the angular power density on the orbit plane is 1.48 kW/mrad² which is only about 2% smaller than that at zero emittance, and the shape of angular distribution is almost the same as that at zero emittance because the vertical RMS angular divergence of electron of 5.2 $\mu$rad in SPring-8 is small compared to that of the radiation power of about 30 $\mu$rad at zero emittance.

Table 2. Total power and angular power densities of the BM in SPring-8.

( I = 100 mA )

| | | |
|---|---|---|
| Total power per turn | $P_{1turn}$ [kW/turn] | 922.0 |
| Linear angular power density | $\frac{dP_T}{d\theta}$ [kW/mrad(horiz.)] | 0.147 |
| Angular power density on the orbit plane | $\frac{d^2P_T}{d\theta d\psi}(\gamma\psi)\Big\vert_{\psi=0}$ [kW/mrad²] | 1.51 |

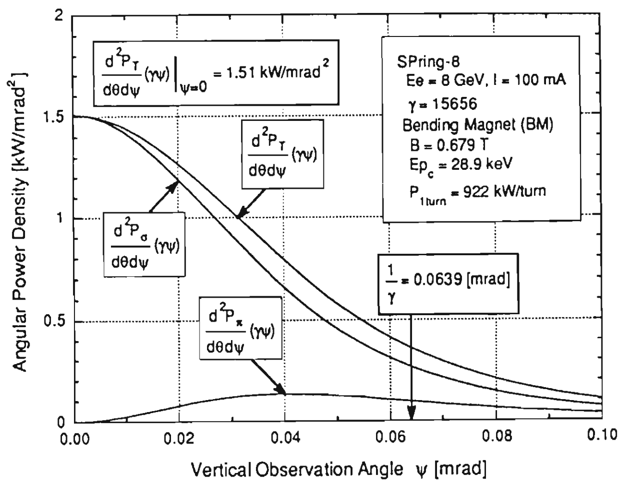


Fig. 2. Angular distribution against vertical angle of angular power density for the BM in SPring-8.

References


1) K.-J. Kim : Proc. US Particle Accelerator School 1987-1988 (AIP Conf. Proc. 184), p. 565 (1989).

RIKEN Accel. Prog. Rep. 25 (1991)

# V-2-11. Angular Distribution of the Undulator Radiation Power in SPring-8

T. Takada and M. Hara

Extremely high radiation power from light sources (bending magnets and insertion devices such as wigglers or undulators) in SPring-8 is expected compared to that in the facilities under operation. Heat load is a problem to be overcome in the design of accelerator components (such as, vacuum chamber, crotch and absorber, etc.) and photon beam line components (cooling system for optics, etc.). In this report, the total power and angular power densities radiated from a typical undulator in SPring-8 are calculated to estimate the heat load.

*Undulator Parameters* : Parameters of a typical planar undulator in SPring-8 are shown in Table 1. We assume a typical undulator to be a pure magnet type configuration which has a periodic sinusoidal magnetic field of vertical direction, period length of 3 cm, and a gap width range from 35 mm to 20 mm. The n-th harmonic photon energy of on-axis undulator radiation is given by

$$\mathrm{Ep(n)[keV]} = 9.5\times10^{-3}\mathrm{n}\frac{\mathrm{Ee^2[GeV]}}{\lambda\mathrm{u[m]}(1+\mathrm{Ky}^2/2)}, \quad (1)$$

where Ee is the electron energy, $\lambda$u is the period length and Ky is a dimensionless parameter called the "deflection parameter" expressed as in practical unit:

$$\mathrm{Ky[non\text{-}dimension]} = 93.4\mathrm{By_p[T]}\lambda\mathrm{u[m]}, \quad (2)$$

where $\mathrm{By_p}$ is the peak of periodic sinusoidal magnetic field. Photon energy will be scanned by means of changing the Ky parameter (that is, magnetic gap width) for this type of device. This undulator, when installed in the 8 GeV storage ring, provides the photon energy from 15.8 keV to 20.0 keV at fundamental harmonic radiation on-axis, which corresponds to a gap width from 20 mm to 35 mm.

Table 1. Parameters of a typical planar undulator in SPring-8.

| | | |
|---|---|---|
| Configuration | Pure permanent magnet : Halbach design Planar type | |
| Magnet block material | Nd-Fe-B alloy | |
| Remnant field | Br [T] | 1.25 |
| Magnetic period length | λu [m] | 0.03 |
| Height of magnet block | h [m]=λu [m]/2 | 0.015 |
| Number of periods | Nu | 133 |
| Total length | Lu [m]=λu [m] · Nu | 3.99 |
| Magnetic gap width range | g [mm] | 35 – 20 |
| Peak magnetic field on-axis range | $\mathrm{By_p}$ [T] | 0.055 – 0.265 |
| Deflection parameter range | Ky = 93.4 $\mathrm{By_p}$ [T] · λu [m] | 0.15 – 0.75 |
| Fundamental photon energy on-axis range | Ep(1) [keV] | 20.0 – 15.8 |

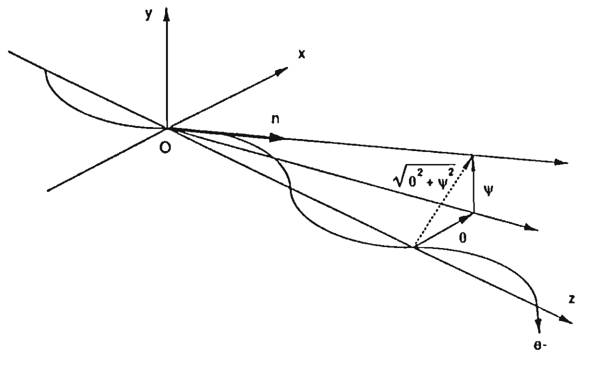


Fig. 1. The orbit and the coordinate system for a planar undulator radiation. The orbit of an electron lies on the z-x plane with sinusoidal motion. The vector **n** is a unit vector heading from the electron to the observer, $\theta$ and $\psi$ are horizontal and vertical observation angles, respectively.

*Total Power*[1] : When electrons move along on an ideal sinusoidal trajectory in a horizontal plane guided by a vertical periodic sinusoidal magnetic field of an undulator as shown in Fig. 1, the total radiation power is given by eq. (3) in practical unit by integrating the spectral angular power density over all angular frequencies, $\omega$, and all square solid angles, $\theta$ and $\psi$:

$$\mathrm{P_T[kW]} = \int_0^\infty d\omega\int_{-\pi}^{\pi} d\theta\int_{-\pi}^{\pi} d\psi\,\frac{d^3\mathrm{P_T}}{d\omega d\theta d\psi}$$
$$= 0.633\mathrm{Ee^2[GeV]By_p{}^2[T]Lu[m]I[A]}$$
$$= 1.16\mathrm{[kW]}\ \text{for the typical undulator with gap of 20 mm at 100 mA operation.} \quad (3)$$

where I is the beam current. As the total power is proportional $\mathrm{By_p}^2$, the maximum total power is radiated at the minimum gap width. This undulator at a gap width of 20 mm radiates total power of 1.16 kW in the 8 GeV storage ring with 100 mA operation.

*Angular Distribution of Power*[1] : The angular power density is given by eq. (4) in practical unit by integrating the spectral angular power density over all angular frequencies:

$$\frac{d^2\mathrm{P_T}}{d\theta d\psi}(\gamma\theta,\gamma\psi)\mathrm{[kW/mrad^2]} = \int_0^\infty d\omega\frac{d^3\mathrm{P_T}}{d\omega d\theta d\psi}$$
$$= 1.60\mathrm{P_T[kW]Ee^2[GeV]}\frac{\mathrm{G(Ky)}}{\mathrm{Ky}}\,\mathrm{f}(\gamma\theta\mathrm{[mrad]},\ \gamma\psi\mathrm{[mrad]},\ \mathrm{Ky})$$
$$= 1.084\times10^{-2}\mathrm{Ee^4[GeV]By_p[T]I[A]}\ \mathrm{Nu\ G(Ky)f}(\gamma\theta\mathrm{[mrad]},\ \gamma\psi\mathrm{[mrad]},\ \mathrm{Ky})$$

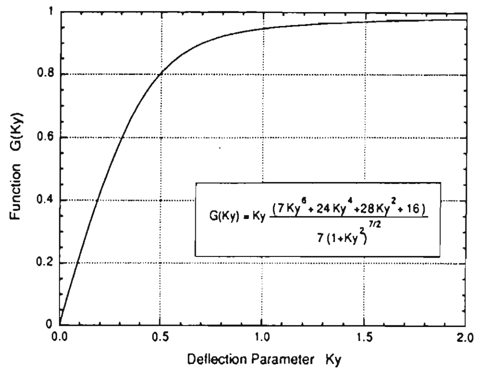


Fig. 2. The behavior of the function G(Ky).

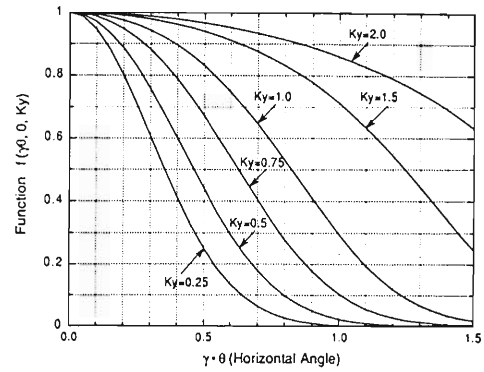


Fig. 3. The behavior of the function $f(\gamma\theta, 0, Ky)$ for the values of Ky ranging between 0.25 and 2.0.

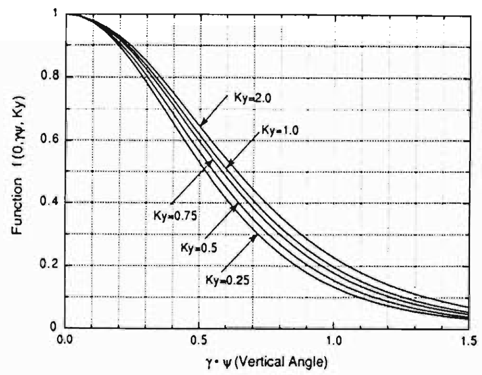


Fig. 4. The behavior of the function $f(0, \gamma\psi, Ky)$ for the values of Ky ranging between 0.25 and 2.0.

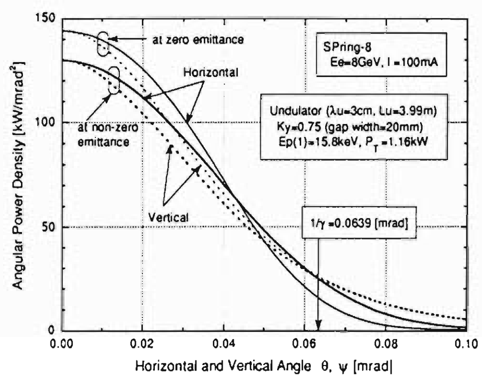


Fig. 5. Angular distribution of the angular power density radiated from a typical undulator in SPring-8 at zero emittance and finite emittance.

$= 144.2[\mathrm{kW/mrad^2}]G(Ky)f(\gamma\theta[\mathrm{mrad}], \gamma\psi[\mathrm{mrad}], Ky)$
for the typical undulator with a gap of 20 mm at 100 mA operation. (4)

where G(Ky) is given by eq. (5), which is a normalized factor ranging from 0 to 1 as a function of Ky. The function, G(Ky), is plotted in Fig. 2 for the values of Ky ranging from 0 to 2. The behavior of G(Ky) is a monotonically-increasing function; if Ky is larger than about 1 (wiggler mode), then G(Ky) is saturated to be 1.

$$G(Ky) = Ky\frac{(7Ky^6 + 24Ky^4 + 28Ky^2 + 16)}{7(1+Ky^7)^{7/2}} \tag{5}$$

$$\approx (16/7)Ky \quad \approx 2Ky \quad (0 < Ky \lesssim 0.25) \tag{6}$$

$$\rightarrow 1 \qquad (1 \lesssim Ky) \tag{7}$$

$f(\gamma\theta, \gamma\psi, Ky)$ is given as follows:

$$f(\gamma\theta, \gamma\psi, Ky) = \frac{16Ky}{7\pi G(Ky)} \int_{-\pi}^{\pi} \left(\frac{1}{D^3} - \frac{4(\gamma\theta - Ky\cos\alpha)^2}{D^5}\right)\sin^2\alpha\, d\alpha, \tag{8}$$

where

$$D = 1 + (\gamma\psi)^2 + (\gamma\theta - Ky\cos\alpha)^2. \tag{9}$$

It is a normalized factor with $f(0,0,Ky)=1$, which gives the angular dependence including Ky parameter. The function $f(\gamma\theta, 0, Ky)$ and $f(0, \gamma\psi, Ky)$ are plotted in Fig. 3 and Fig. 4 for the values of Ky ranging between 0.25 and 2.0 covering the Ky range of the typical undulator. The horizontal and vertical HWHM angular divergences of a planar undulator radiation with Ky ranging between 0.25 and 2.0 can be roughly identified as follows:

$$\theta_{HWHM} \approx 0.8Ky/\gamma \approx Ky/\gamma, \tag{10}$$

$$\psi_{HWHM} \approx 1/2\gamma. \tag{11}$$

Here, $\gamma$ is called the 'relativistic energy factor' that is the ratio of the total electron energy to the rest mass of 511 keV. It can also be expressed as in practical unit:

$$\gamma = 1957Ee[\mathrm{GeV}]. \tag{12}$$

As $\gamma$ is 15656 in SPring-8, the vertical FWHM radiation cone is 63.9 $\mu$rad ($=1/\gamma$).

The total power and on-axis angular power densities of a typical undulator power in SPring-8 are summarized in Table 2, and the angular distributions are shown in Fig. 5 against horizontal and vertical directions of the angular power density radiated from a typical undulator in SPring-8. The quantities so far described were obtained with the assumption that the electron beam has no angular divergence, that is, zero emittance limit. It is necessary to consider the effect of electron emittance on the angular distri-

Table 2. Total power and on-axis angular power densities radiated from a typical undulator in SPring-8.

| | | |
|---|---|---|
| Total power | $P_T$ [kW] | 1.16 |
| On-axis angular power density | $\frac{d^2P_T}{d\theta d\psi}(\gamma\theta,\gamma\psi)\Big\vert_{\theta=0 \text{ and } \psi=0}$ [kW/mrad$^2$] | |
| | | 144.2 (at zero emittance) |
| | | 130.0 (at finite emittance) |

bution of angular power density because an undulator will be usually installed in a high-$\beta$ (large electron beam size and small angular divergence) section in a finite electron emittance storage ring. The parameters of the high-$\beta$ section in SPring-8 are listed in Table 3. The angular distribution of the angular power density at finite electron emittance is calculated using a computer code called 'URGENT'[2,3]. The calculated results are included in Table 2 and Fig. 5. The on-axis angular power density at finite electron emittance is about 10 % lower than that at zero emittance.

Table 3. Electron beam size and angular divergence at the center of a high-$\beta$ straight section in SPring-8.

| | | |
|---|---|---|
| Natural emittance | $\varepsilon_n$ [m·rad] | $6.99 \times 10^{-9}$ |
| Coupling coefficient | $\kappa$ [%] | 10 |
| Horizontal emittance | $\varepsilon_x$ [m·rad] | $6.35 \times 10^{-9}$ |
| Vertical emittance | $\varepsilon_y$ [m·rad] | $6.35 \times 10^{-10}$ |
| Horizontal betatron function value | $\beta_x$ [m] | 23.346 |
| Vertical betatron function value | $\beta_y$ [m] | 10.283 |
| Horizontal RMS electron beam size | $\sigma_x$ [μm] | 385.2 |
| Vertical RMS electron beam size | $\sigma_y$ [μm] | 80.8 |
| Horizontal RMS angular divergence | $\sigma_{x'}$ [μrad] | 16.5 |
| Vertical RMS angular divergence | $\sigma_{y'}$ [μrad] | 7.9 |

References

1) K.-J. Kim: *Nucl. Instrum. Methods,* **A246**, 67 (1986).
2) R.P. Walker: *Rev. Sci. Instrum.*, **60**, 1816 (1989).
3) R.P. Walker and B.Diviacco: to be published to *Rev. Sci. Instrum.*, **63**, No.1 (1992). (Contributed to the 4th SRI Conf., Chester, U.K., on July 15-19, 1990.)

RIKEN Accel. Prog. Rep. **25** (1991)

# V-2-12. Effect of Energy Spread on the Multi-Pole Wiggler Radiation Spectrum

T. Takada and M. Hara

SPring-8 is a third generation ring, which is to be operated with the electron energy of 8 GeV and the beam current of 100 mA, and optimized for insertion devices (IDs). Thirty four straight sections of 6.65 m in length (19 high-$\beta$ and 15 low-$\beta$ ones) are prepared for insertion devices (IDs) in SPring-8. Multi-pole wigglers (MPWs) will be usually installed in the low-$\beta$ straight section (small electron beam size and large angular divergence as shown in Table 1). The spectrum radiated from a typical MPW in SPring-8, whose parameters are shown in Table 2, was calculated by two different methods, and the results will be described in this report.

*Method 1*[1]: The MPW, that has a vertical periodic sinusoidal magnetic field, can be regarded as a sequence of bending magnets (BMs) with alternate polarities. Thus, the spectrum of a MPW is broad and smooth similar to that of a BM, but has 2 Nw intensity enhancements of the BM radiation, where Nw is the number of magnetic periods. On-axis spectral brightness in the unit of photons / sec / 0.1%b.w./ mrad²/ mm² from MPW is expressed in practical unit as follows:

$$B(Ep)=\frac{1.33\times10^{13}Ee^2[GeV]I[A](Ep/Ep_c)^2K_{2/3}^2(Ep/Ep_c)}{2\pi\sigma_x\sigma_y}2N_w , \qquad (1)$$

where Ee is the electron energy, I is the beam current, Ep is the photon energy, and Kn(u) is the n-th modified Bessel function, and $Ep_c$ is the critical photon energy given by

$$Ep_c[keV]=0.665Ee^2[GeV]By_p[T]. \qquad (2)$$

Here, $By_p$ is the the peak of periodic sinusoidal magnetic field on-axis. When the effect of electron beam emittance is taken into account, the intensity of on-axis spectral brightness is reduced by multiplying the factor A, expressed as follows:

$$A=\frac{1}{\sqrt{1+[\sigma_{x'}/(Ky/\gamma)]^2}\sqrt{1+[\sigma_{y'}/\sigma_{SR}(Ep/Ep_c)]^2}} , \qquad (3)$$

where Ky is the deflection parameter expressed as in practical unit:

$$Ky\ [\text{non-dimension}]=93.4By_p[T]\lambda w[m], \qquad (4)$$

and $\gamma$ is called the "relativistic energy factor" expressed as in practical unit:

$$\gamma=1957\ Ee\ [GeV]. \qquad (5)$$

As $\gamma$ is 15656 in SPring-8, the vertical FWHM radiation cone is 63.9 $\mu$rad ($=1/\gamma$) at the critical photon energy. $\sigma_{SR}$ (u) is the vertical RMS angular divergence for synchrotron radiation by an electron as a function of photon energy, which is given by

$$\sigma_{SR}(Ep/Ep_c)=\frac{1}{\sqrt{2\pi}}\left[\frac{2\pi}{\sqrt{3}}(Ep/Ep_c)^{-1}\frac{\int_{Ep/Ep_c}^{\infty}K_{5/3}(y)dy}{K_{2/3}^2(Ep/Ep_c)}\right]\frac{1}{\gamma} , \qquad (6)$$

when the angular spread against the vertical direction of the radiation is identified to a Gaussian distribution.

The on-axis spectral brightness from a typical MPW in SPring-8 with the effect of electron emittance is sown in Fig. 1; the result of a calculation in which the MPW is regarded as a sequence of BMs. The on-axis spectral brightness from a BM in SPring-8 with the effect of electron emittance is also shown in the same figure.

*Method 2*: In the second method, the MPW is regarded as a large Ky limit of an undulator. The on-axis spectral brightness from undulator with electron beam emittance effect was calculated by using the code of 'URGENT'.[2,3] In this case, the spectrum appears as a series of a very large number of harmonics, and has a periodic structure. However, the effect of electron energy spread is not included in URGENT. The energy spread was included as described in the following.

The energy spread of electrons in a storage ring has a Gaussian distribution, and can be

Table 1. Electron beam size and angular divergence at the center of a low-$\beta$ straight section.

| | | |
|---|---|---|
| Natural emittance | $\varepsilon_n$ [nm·rad] | 6.99 |
| Coupling coefficient | $\kappa$ [%] | 10 |
| Horizontal betatron function value | $\beta_x$ [m] | 1.116 |
| Vertical betatron function value | $\beta_y$ [m] | 8.715 |
| Horizontal RMS beam size | $\sigma_x$ [$\mu$m] | 84.2 |
| Vertical RMS beam size | $\sigma_y$ [$\mu$m] | 72.1 |
| Horizontal RMS angular divergence | $\sigma_{x'}$ [$\mu$rad] | 75.5 |
| Vertical RMS angular divergence | $\sigma_{y'}$ [$\mu$rad] | 8.8 |

Table 2. Parameters of a typical MPW in SPring-8.

| | | |
|---|---|---|
| Magnetic period length | $\lambda w$ [m] | 0.18 |
| Number of periods | Nw | 22 |
| Total length | Lw [m] = $\lambda w$ [m] · Nw | 3.96 |
| Peak magnetic field on-axis | $By_p$ [T] | 0.952 |
| Critical photon energy | $Ep_c$ [keV] | 40.5 |
| Critical wavelength | $\lambda c$ [Å] | 0.31 |
| Deflection parameter | Ky = 93.4 $By_p$ [T] · $\lambda w$ [m] | 16 |
| Fundamental photon energy on-axis | Ep(1) [eV] | 26.2 |

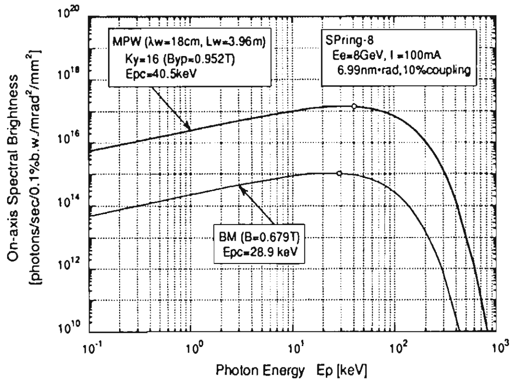


Fig. 1. On-axis spectral brightness with the effect of electron emittance from a typical MPW when the MPW is regarded as a sequence of BMs. The on-axis spectral brightness with the effect of electron emittance from a BM in SPring-8 is also shown. Critical photon energies for the BM and the typical MPW in SPring-8 are represented by open circles.

Table 3. Parameters of the SPring-8 storage ring.

| | | |
|---|---|---|
| Electron energy | <Ee> [GeV] | 8 |
| Beam current | I [A] | 0.1 |
| Energy spread | $\sigma_{Ee}$/<Ee> [%] | 0.10936 |

expressed as

$$p_{Ee}(Ee)=\frac{1}{\sqrt{2\pi}\,\sigma_{Ee}}\exp[(Ee-\langle Ee\rangle)^2/2\sigma^2_{Ee}], \quad (7)$$

where $\langle Ee\rangle$ is the nominal energy of the storage ring and $\sigma_{Ee}$ is the standard deviation. Here, $\langle Ee\rangle$ is 8 GeV and $\sigma_{Ee}/\langle Ee\rangle$ is designed to be 0.10936 % in SPring-8 as shown in Table 3.

The photon energy at the peak of the nth-harmonics on-axis spectral brightness of MPW radiation is given by in practical unit:

$$Ep(n)\,[keV]=9.5\times10^{-3}nEe^2[GeV]/(1+Ky^2/2)/\lambda_W[m]. \quad (8)$$

Since the photon energy is proportional to the square of the electron energy as shown by eq. (8), the relative energy spread of photon energy is 2 times as large as that of electron energy.

$$\frac{\Delta Ep}{Ep}=2\frac{\Delta Ee}{Ee}. \quad (9)$$

In order to include the electron energy dependence in the MPW radiation spectrum, B(Ep;Ee) is defined as the on-axis spectral brightness from the electron energy of Ee. Then, the spectrum with the effect of electron energy spread is given by the following integration:

$$\overline{B(Ep)}=\int_{-3\sigma_{Ee}}^{3\sigma_{Ee}}B(Ep;\langle Ee\rangle+\Delta Ee)\,p_{Ee}(\langle Ee\rangle+\Delta Ee)d\Delta Ee. \quad (10)$$

Practically, it is sufficient to integrate only in the region of $[-3\sigma_{Ee},3\sigma_{Ee}]$. However, this integration is a very time consuming calculation, because many $B(Ep;\langle Ee\rangle+\Delta Ee)$ have to be calculated for different ΔEe. Therefore, an assumption expressed by eq. (11) is introduced:

$$B(Ep;\langle Ee\rangle+\Delta Ee)\approx B(Ep-\Delta Ep;\langle Ee\rangle). \quad (11)$$

Equation (11) means that the effect of electron energy shift, ΔEe, is approximated by the same amount of the photon energy shift, ΔEp, given by eq. (9) with opposite sign. This assumption would be sufficient to estimate the energy spread effect in the region of $[-3\sigma_{Ee}, 3\sigma_{Ee}]$. Then, eq. (10) is rewritten as

$$\overline{B(Ep)}=\int_{-3\sigma_{Ee}}^{3\sigma_{Ee}}B(Ep-\Delta Ep;\langle Ee\rangle)\,p_{Ep}(\Delta Ep)d\Delta Ep, \quad (12)$$

where $p_{Ep}(Ep)$ is a Gaussian distribution of photon energy:

$$p_{Ep}(\Delta Ep)=\frac{1}{\sqrt{2\pi}\,\sigma_{Ep}}\exp[\Delta Ep^2/2\sigma^2_{Ep}], \quad (13)$$

using variable transformation expressed by eq. (14), with the constraint of eq. (15),

$$p_{Ee}(\langle Ee\rangle+\Delta Ee)d\Delta Ee=p_{Ep}(\Delta Ep)d\Delta Ep, \quad (14)$$

$$\frac{\sigma_{Ep}}{Ep}=2\frac{\sigma_{Ee}}{\langle Ee\rangle}. \quad (15)$$

The on-axis spectral brightness from the typical MPW was calculated using the code of URGENT including only the effect of electron emittance, and the modification mentioned above was adopted to obtain the spectrum with the effect of energy spread. The spectra with and without inclusion of the effect of energy spread around the photon energy of 1 keV and 10 keV are shown in Figs. 2 and 3, respectively. As a result, the spectrum around 1 keV oscillates in a range of about 2 figures when the energy spread

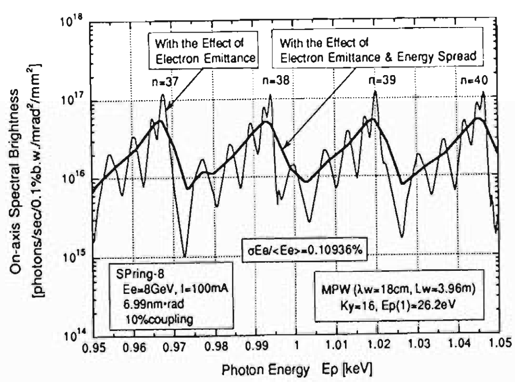


Fig. 2. On-axis spectral brightness around the photon energy of 1 keV including the effect of electron emittance with and without the effect of electron energy spread from the typical MPW SPring-8. Solid line represents the spectrum with the effect of electron emittance only, bold line the spectrum with the effect of both electron emittance and energy spread.

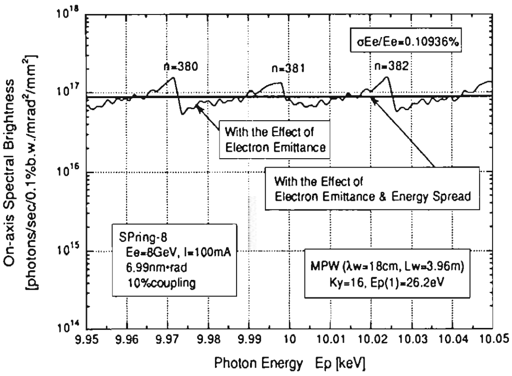


Fig. 3. On-axis spectral brightness around the photon energy of 10 keV including the effect of electron emittance with and without the effect of electron energy spread from the typical MPW SPring-8. Solid line represents the spectrum with the effect of electron emittance only, bold line the spectrum with the effect of both electron emittance and energy spread.

is not included. The inclusion of the effect of energy spread reduces the oscillation so that the ratio of the spectral maximum value to the minimum is about 8. In the vicinity of 10 keV, the oscillation is totally smoothed out by the effect of energy spread. This smoothing spectrum is obtained if the conditions $3\sigma_{Ep} > Ep(1)$ and $Ep \ll Ep_c$ are satisfied. Both spectra using method 2 are consistent with the spectrum shown in Fig. 1 using method 1 when the average value is taken only for the spectrum of 1 keV region.

References

1) K.-J.Kim : Proc. US Particle Accelerator School 1987-1988 (AIP Conf. Proc. 184), p. 565 (1989).
2) R. P. Walker: *Rev. Sci. Instrum.*, **60**, 1816(1989).
3) R. P. Walker and B. Diviacco: to be published to *Rev. Sci. Instrum.*, **63**, No. 1 (1992). (Contributed to the 4th SRI Conf., Chester, U.K., July, 1990.)

# V-2-13. Progress in the Magnet System for SPring-8 Storage Ring

J. Ohnishi, N. Kumagai, S. Motonaga, H. Takebe, S. Matsui,
K. Kumagai, and T. Ouchi

SPring-8 storage ring has 88 dipole, 480 quadrupole, and 336 sextupole magnets.[1)] We have finished manufacturing and test of their prototypes.[2)] Presently, design of real magnets has been almost completed and their production has started. Each first magnet of the three types will be completed in March, 1992. All magnets will be delivered by March, 1995.

Figure 1 shows the magnet arrangement in a unit cell of the storage ring. Two synchrotron radiation beam lines are extracted from an insertion device and a dipole magnet in the unit cell. Quadrupole and sextupole magnets have two sizes of magnet yokes in order to make the radiation beam line pass through. Detailed drawings of dipoles, quadrupoles, and sextupoles are shown in another report.[1)] Table 1 shows parameters of these magnets.

Completed magnets will start to be delivered from the beginning of 1993 in Nishi-Harima site where the storage ring will be constructed. All the magnets will be subjected to field measurements to verify their field performances. After the field measurements, ten quadrupoles and seven sextupoles in each unit cell will be aligned precisely on three straight girders and will be transferred to the storage ring building. Finally, 144 girders and 88 dipole magnets will be aligned along the ideal orbit of the storage ring.

Followings are also in progress in order to perform a construction program for the magnet system; design of power supplies,[3)] design of steering magnets[4)] and pulsed magnets for beam injection,[1)] design of water cooling system for magnets, design of the girders, preparation and improvement of field measurement devices, and

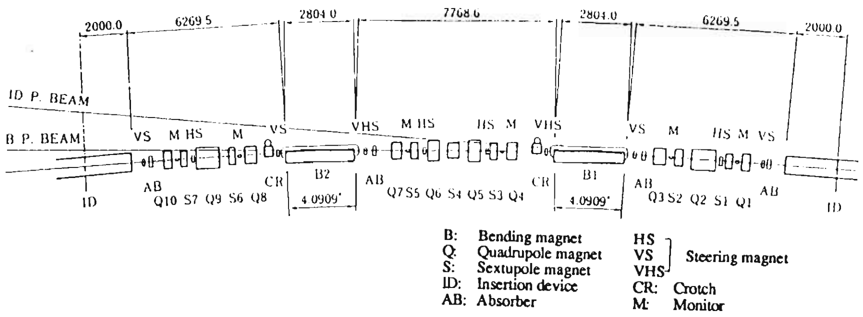


Fig. 1. Magnet arrangement in a unit cell of the storage ring. Two synchroton radiation beams are extracted from an insertion device and a dipole magnet. Quadrupoles indicated as Q5, Q9 and sextupoles as S2, S3, S5,S6 have large size yokes.

Table 1. Parameters of the storage ring magnets.

| Family | | dipole | Q1,Q10 | Q2,Q9 | quadrupole<br>Q3, Q8 | Q4,Q7 | Q5,Q6 | S1,S7 | sextupole<br>S2,S3<br>S5,S6 | S4 |
|---|---|---|---|---|---|---|---|---|---|---|
| Number of magnets | | 88 | 96 | 96 | 96 | 96 | 96 | 96 | 192 | 48 |
| Gap height/Bore diameter | (mm) | 63.8 | 85 | 85 | 85 | 85 | 85 | 92 | 92 | 92 |
| Effective field length | (m) | 2.804 | 0.35 | 0.97 | 0.51 | 0.41 | 0.51 | 0.30 | 0.29 | 0.50 |
| Magnet length | (m) | 3.09 | 0.48 | 1.10 | 0.64 | 0.54 | 0.64 | 0.41 | 0.37 | 0.61 |
| Magnet weight | (Kg) | 4950 | 970 | 2520/3090 | 1390 | 1130 | 1690/1390 | 635 | 800 | 1060 |
| Field strength, max | (T, T/m, T/m$^2$) | 0.679 | 17 | 17.6 | 17.4 | 16.2 | 17.1 | 420 | 420 | 420 |
| Turn numbers per pole | | 14 | 24 | 24 | 24 | 24 | 24 | 19 | 19 | 19 |
| Conductor size | (mm) | 26 x 18.5 | 10 x 16 | 10x 16 | 10 x 16 | 10 x 16 | 10 x 16 | 9.5 x 8 | 9.5 x 8 | 9.5 x 8 |
| Hollow size | (mm) | ø10.5 | ø5 | 5 x 9 | ø5 | ø5 | ø5 | ø5 | ø5 | ø3.2 |
| Current, max | (A) | 1270 | 536 | 552 | 544 | 504 | 533 | 300 | 300 | 300 |
| Current density | (A/mm$^2$) | 3.22 | 3.81 | 4.80 | 3.88 | 3.59 | 3.80 | 5.45 | 5.45 | 5.45 |
| Conductor resistance | (mΩ) | 8.64 | 16.6 | 39.7 | 20.9 | 18.2 | 20.9 | 36.0 | 34.7 | 42.1 |
| Voltage drop, max | (V) | 11.0 | 8.90 | 21.9 | 11.4 | 9.17 | 11.1 | 10.8 | 10.4 | 12.7 |
| Power dissipation | (KW) | 13.9 | 4.77 | 12.1 | 6.28 | 4.62 | 5.94 | 3.24 | 3.12 | 3.79 |
| Cooling circuits | | 2 | 4 | 4 | 4 | 4 | 4 | 2 | 2 | 6 |
| Water flow | (l/min) | 22.1 | 11.0 | 15.8 | 9.6 | 10.4 | 9.6 | 4.0 | 4.0 | 5.4 |
| Pressure drop | (Kg/cm$^2$) | 5 | 5 | 5 | 5 | 5 | 5 | 5 | 5 | 5 |
| Temperature rise | (°C) | 9.0 | 6.2 | 11.0 | 9.4 | 6.4 | 8.9 | 11.6 | 11.2 | 10.0 |

investigation of precise alignment of magnets.

References

1) SPring-8 Project Team: SPring-8 Project, Part I, Facility Design [Revised], (1991).
2) J. Ohnishi, H. Takebe, K. Kumagai, and S. Motonaga: Proc. 12th Int. Conf. on Magnet Technology, to be published.
3) H. Takebe *et al.*: This Report, p. 153.
4) K. Kumagai *et al.*: *ibid.*, p. 150.

RIKEN Accel. Prog. Rep. **25** (1991)

# V-2-14. A Preliminary Test for Precise Alignment of SPring-8 Sextupole Magnets

J. Ohnishi and S. Motonaga

336 sextupole magnets will be installed in the SPring-8 storage ring for chromaticity correction.[1] Their alignment accurracy is required to be less than about 0.1 mm from calculation so that the stop band width of a certain resonance of the beam may be kept smaller than the allowance value. In achievement of such a precise alignment, it becomes important that the magnetic field center of the sextupole magnet is measured and marked acccurately.

As a preliminary test for the precise alignment, we tried to analyze the position of the field center and the strength of a dipole field from the field measurement of a prototype magnet.[2] The magnetic field was mapped with a hall probe on vertical planes of $\pm 15$ mm square. Mapping interval was 1 mm and measured data were obtained at 961 points a plane. Using these data, following parameters were fit by the least square method;

expression $B_{meas} = -B_x \sin\theta + B_y \cos\theta + B_o$

$Bx = 6a(x - x_o)(y - y_o)$

$By = 3a\ \{(x - x_o)^2 - (y - y_o)^2\}$

parameters a: the strength of a sextupole field

$x_o$, $y_o$: position of the field center

$B_o$: the strength of a dipole field

$\theta$: tilt of the hall probe

Figure 1 shows displacement of the field center with the strength of an exciting current. The displacement of about 10 $\mu$m is small enough to affect the beam. Figure 2 shows the change of a dipole field with excitation levels. The strength of the dipole field produces COD smaller than an expected alignment error of quadrupole magnets. However, even a dipole field of several gausses shifts zero field lines by about a handred micron meters and leads diffculty in finding the field center.

We need to measure the positional difference between the magnetic and the geometric center

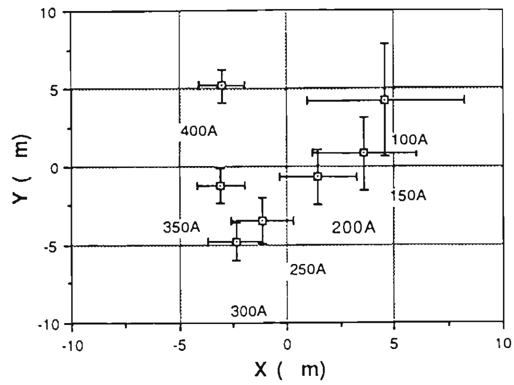


Fig. 1. Movement of the field center of the sextupole magnet with excitation currents.

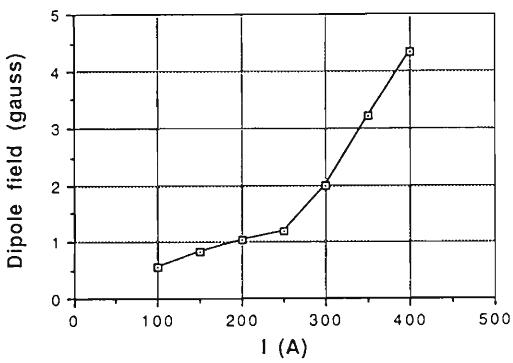


Fig. 2. Dipole error field of the sextupole magnet with excitation currents.

for precise alignment of sextupole magnets. We start to develop an equipment for measuring and marking the field center of the sextupole magnets in consideration of the above results.

References


1) SPring-8 Project Team: SPring-8 Project, Part I, Facility Design (1991). [Revised]
2) J. Ohnishi, H. Takebe, K. Kumagai, and S. Motonaga: Proc. 12th Int. Conf. on Magnet Technology, to be published.

RIKEN Accel. Prog. Rep. **25** (1991)

# V-2-15. Design of Steering Magnet System for the SPring-8 Storage Ring

K. Kumagai, H. Takebe, J. Ohnishi, and S. Motonaga

Twelve steering magnets are installed in the unit cell for COD collection as shown in Fig.1. Six magnets are prepared for the horizontal steering, the rest of magnets for the vertical steering, and a total of 576 steering magnets are placed along the ring.

Maximum field strength of 0.0267 T m for the horizontal and 0.0133 T m for the vertical correction are required. The design parameters for these magnets are summarized in Table 1. In order to make use of commercial power supplies, the peak current and voltage are set a ceiling to 5A - 50V. In the first step of operation of the storage ring, about 160 power supplies will be prepared and assigned by the matrix switch to the magnets which are most effective for the COD correction. All magnets are cooled by air.

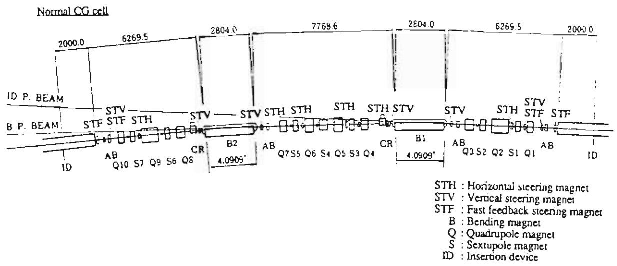


Fig. 1. Arrangement of the steering magnets, lattice magnets and other elements in the unit cell of the 8 GeV storage ring.

Table 1. Design parameters of the steering magnets.

| Family | | STH 1-6 (H) | STV 1,2,4,6 (V) | STV 3,5 (V) | STF (H) | STF (V) | STF (H) |
|---|---|---|---|---|---|---|---|
| Number of magnets | | 288 | 192 | 96 | 12 | | 12 |
| Magnet type | | C | C | - | WF | WF | - |
| Kick angle | (mrad) | 1.0 | 0.5 | 0.5 | 0.094 | 0.047 | 0.071 |
| Gap width | (mm) | 70 | 105 | 130 | 94 | 140 | - |
| Core length | (m) | 0.14 | 0.13 | 0.19 | 0.07 | | - |
| Effective field length | (m) | 0.19 | 0.20 | 0.27 | 0.12 | 0.14 | 0.20 |
| Magnet length | (m) | 0.22 | 0.23 | 0.19 | 0.12 | | 0.23 |
| Magnet weight | (Kg) | 64 | 60 | 68 | 22 | | 6 |
| Field strength,max | (T) | 0.14 | 0.08 | 0.05 | 0.028 | 0.012 | 0.023 |
| Magnetomotive force | ($\times 10^3$AT) | 7.80 | 6.68 | 5.32 | 1.40 | 1.49 | |
| Turn numbers per pole | | 780 | 674 | 1064 | 440 | 440 | 300 |
| Conductor diameter | (mm) | 2.2 | 2.3 | 2.5 | 1.9 | 1.9 | 1.6 |
| Current,max | (A) | 5 | 5 | 5 | 5 | 3.2 | 5 |
| Current density | (A/mm$^2$) | 0.93 | 0.84 | 0.68 | 1.22 | 0.78 | 1.58 |
| Voltage drop,max | (V) | 24 | 21 | 22 | 11 | 7 | 19 |
| Power dissipation | (W) | 120 | 105 | 110 | 52 | 22 | 94 |
| Cooling | | air | air | air | air | air | air |
| Power Supply | | 5A-50V | 5A-50V | 5A-50V | 5A-20V | 5A-20V | 5A-30V |
| Temperature rise | (°C) | 25 | 27 | 26 | 27 | 12 | 50 |

One type of the horizontal steering magnets (STH) and two types of the vertical steering magnets (STV) have been designed. Fig.2 shows the field distributions calculated by a 2-D code, LINDA. The region where the field deviation is less than 1% is calculated to be over the horizontal and vertical ranges of 40 mm. The magnets

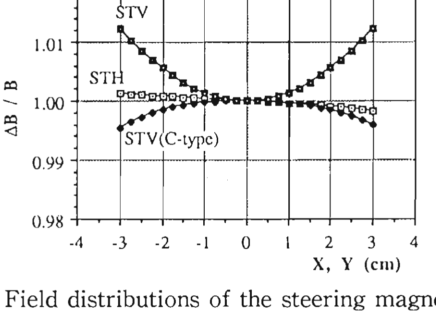


Fig. 2. Field distributions of the steering magnets calculated with a 2-D code LINDA. Each distribution is normalized at x, y=0.

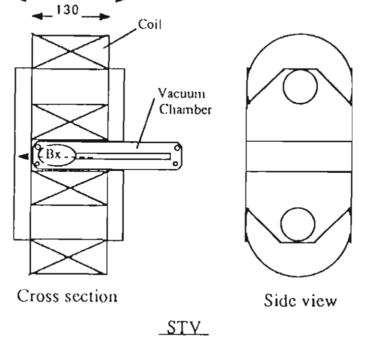


Fig. 3. One type of the vertical steering magnets (STV).

are ordinary C-magnets except one of the vertical steering magnets which is shown in Fig. 3. A prototype of this magnet was constructed so as to measure the fields to verify the design.

Two pairs of fast feedback steering magnets (STF) which are used to collect the slight vibration of optical axis are installed on both sides of the insertion devices. The STF magnets produce vertical and horizontal fields. The magnets can be controlled in several tenths Hz. The vacuum chamber in the gap of a magnet is made of stainless steel in order to avoid the growth of eddy currents on the chamber. Two of the fast feedback steering magnets are incorporated to the vertical steering magnets (STV), and the remaining two magnets are window flame-magnets. Details of these magnets' design is now in progress.

# V-2-16. Magnetic Properties of a Pulsed Septum Magnet

K. Kumagai, S. Matsui, and H. Miyade

The injection system of the storage ring of SPring-8 is composed of four septum magnets and four bump magnets.[1] The last septum magnet located most downstream of the injection line is a passive type shielding magnet excited with a pulsed current. The magnetic fields on the reference orbit and the bump orbit of the storage ring (It is called 'stray fields') are shielded by eddy currents in the septum (wall).[2] Actually, the thickness of the septum wall at the exit from injection section is required to be about 1.5 mm to acquire high injection efficiency. In the respect of beam dynamics, the strength of stray fields should be smaller than 30 G m on the bump orbit, while smaller than 1 G m on the reference orbit is required.

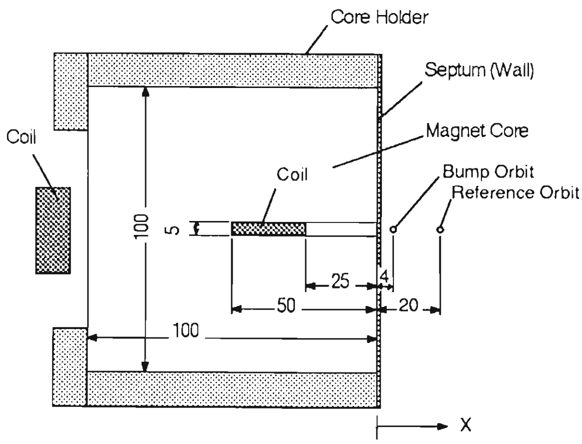


Fig. 1. Cross sectional view of the septum magnet.

We have made experiments using a septum magnet in order to estimate the strength of the stray field, pulse width of an exciting current, and thickness and structure of septum.

A cross sectional view of the septum magnet is shown in Fig. 1. The magnet length is 1 m and the core is made of 0.35 mm thick laminated silicon steel plates coated with electrical insulator and glued with epoxy. The septum magnet is operated with a half-sine pulse of 40-$\mu$sec or 100-$\mu$sec width produced by the discharge of capacitors. Magnetic fields were measured by a cylindrical search coil.

Figure 2(a) shows the time dependence of the stray field against the magnet gap field (source field) in case of the copper septum of 0.8 mm thick and a pulse width of 100 $\mu$sec. The strength of the stray field has a maximum just after when an exciting current finishes. The stray field is given by the subtraction of the field induced by eddy currents on the septum (wall) from the source field. Figure 2(b), (c) shows the stray field under the condition that a no-oriented silicon steel plate of 0.15-mm thickness is added to the outside of the copper septum (wall). Figure 2(c) shows the strength of the stray field at the current strength that the silicon steel plate is just saturated magnetically. Figure 2(b) is the stray field under the condition that the silicon steel plate is saturated enough and the stray field

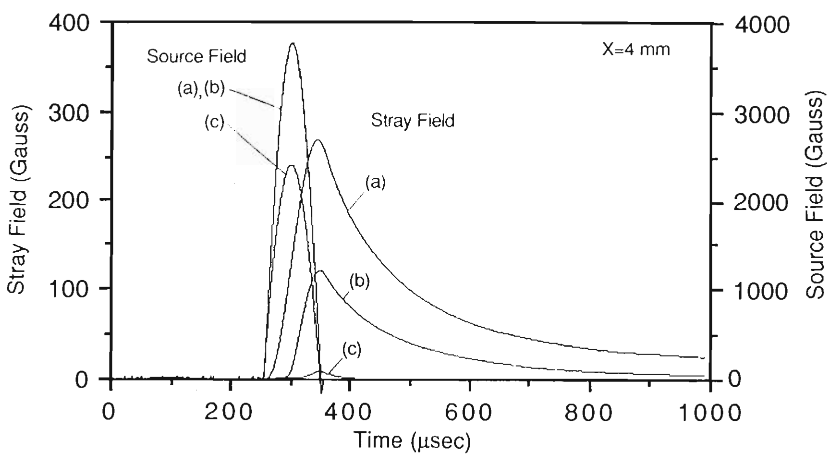


Fig. 2. Time dependence of the magnetic stray fields against the source fields. Pulse width is 100 $\mu$sec. (a), in case the septum (wall) is a copper plate of 0.8-mm thickness; (b) and (c), in case the silicon steel plate of 0.15-mm thickness is combined with copper septum.

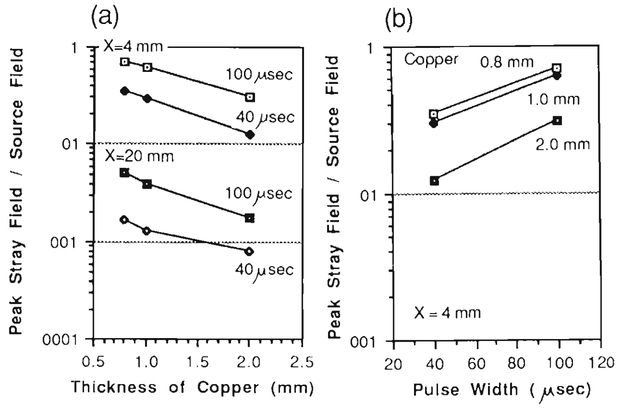


Fig. 3. Peak strength ratio of the stray fields to the source field. (a), against the thickness of copper septum; (b), against the pulse width of an exciting current.

appears. From these results, it is clear that the stray fields are reduced to be small enough for the tolerances unless the silicon steel plate is saturated magnetically.

Figure 3(a) shows the peak strength ratio of the stray field to the source field as a function of the thickness of copper septum(wall). It decreases exponentially with the thickness. Figure 3(b) shows the peak strength ratio of the stray field to the source field as a function of the pulse width of an exciting current. It also decreases as the pulse width reduces. A design of the septum magnet in case that a field strength is about 5000 G in a gap is suggested by using Figs. 2 and 3. Following conditions are required in order not to make the silicon steel plate saturated: Pulse width is 40 μsec (required for flatness at the peak current), thickness of the copper plate and the silicon steel plate are 0.85 mm and 0.15 mm, respectively.

On the basis of the experimental results we could find a design plan for the actual magnet for SPring-8 storage ring.

References

1) JAERI-RIKEN SPring-8 Project Team: SPring-8 Project Part I, Facility Design (1991). [Revise]
2) N. Marks and M.W. Poole: IEEE Trans. on Mag., **MAG-17**, No.5, p.1579 (1981).

RIKEN Accel. Prog. Rep. 25 (1991)

# V-2-17. Calculation of Magnetic Field Attenuation by Metallic Coating and Core Material for Pulsed Magnet

S. Matsui, K. Kumagai, H. Miyade, N. Kumagai, and H. Takebe

(1) Calculation of magnetic field attenuation by metallic coating

A ceramic chamber whose inside surface is covered with thin metallic coating is used to avoid the eddy current field induced by the magnetic field with fast time dependence. A precise calculation is required for holding a longer flat top in a short pulse width. It is not easy to calculate analytically the field inside the elliptical chamber in a core gap of some distance.

As illustrated in Fig.1, the following are assumed: 1) the shape of the coating is elliptical; 2) the magnetic pole face is wide so that the effect of edge part is negligible; 3) the eddy current can be divided into symmetrical current loops Ii (i=1,2···).

The interaction between the current loop Ii and Ij is not only direct one but also includes ones through the influence of core. These interactions expressed in terms of mutual inductance Mji are calculated by using image currents which account for the effect of core. Then, using Faraday's law the following equations are given,

$$\frac{dIi}{dt}=\frac{1}{Li}\left(-\frac{d\Phi(t)ext,i}{dt}-IiRi-\sum_{j\neq i}Mji\frac{dIj}{dt}\right)(i=1,2,\cdots)$$

where $\Phi$(t)ext,i represents the flux given by the magnet, Ri is the resistance of the circumference of the loop i, and Li is its self inductance. These differential equations can be solved numerically by integrating dIi/dt for every very short time using a computer. The whole size of this computer program including graphics is 150 lines in BASIC, and the solver part is only 15 lines. This easy method is general and can be used for the calculation of eddy current and the dynamic magnetic field in the dipole magnet. If the coating thickness is much larger than the skin depth, the eddy current must be divided into multi loops on a few layers.

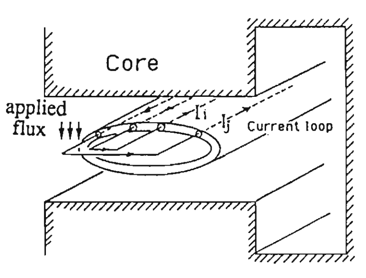


Fig. 1. Eddy current loops on an elliptical coating caused by an external magnetic field between the cores.

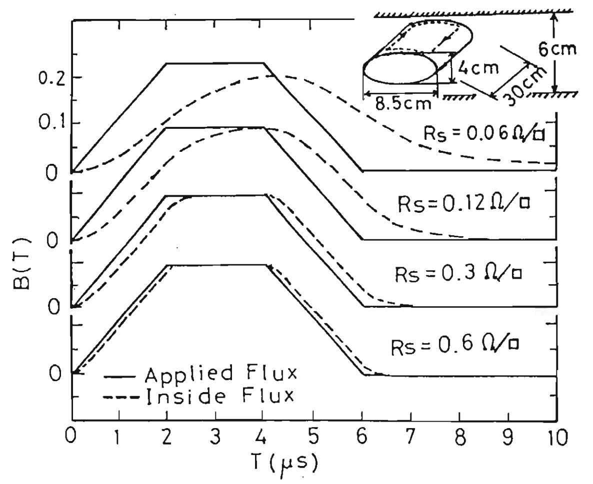


Fig. 2. The behaviour of B when Rs is changed.

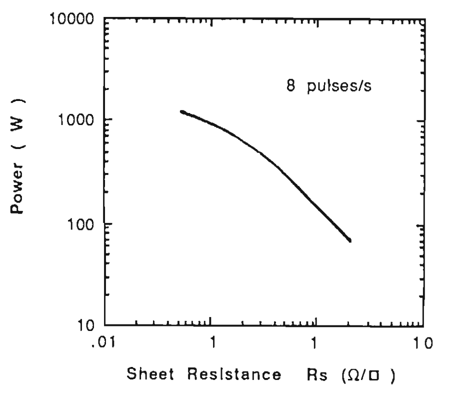


Fig. 3. Variation of heat power vs sheet resistance.

Figure 2 shows the behaviour of the magnetic flux density B at the center (x=0) and a shift point (x=1.6cm) on the median plane, when the coating thickness (the sheet resistance Rs) is changed. The B at x=0 was almost the same as that at x=1.6cm. If Rs=0.1Ω/□, a flat top of 1$\mu$s is impossible.

The averaged heat power including eight pulses during one second is plotted versus Rs in Fig.3. Since the shape of the magnetic flux must be trapezoidal and also in view of heat, it is desirable that the sheet resistance is larger than 1Ω/□.

(2) Core material for pulsed magnet

In order to obtain a magnetic field during a short time, ferrite has been used as a core material, because its high frequency characteristics is good. However the saturation B of ferrite is about 0.3 T (Tesla). Therefore we can not obtain a strong magnetic field with ferrite. On the other hand, the saturation B of steel or amorphous alloy is higher than 1 T. Though the high frequency characteristics of steel and amorphous alloy is worse than that of ferrite because of the eddy current etc., a gap in the magnet improves these characteristics. In order to determine the core material for bump magnets, the permeability and phase shift of several materials (thin steel, ferrite, amorphous, and dust core) were measured at high frequencies.

Figure 4 shows the effective permeabilities vs frequency at B = 0.001 T. The core shape made of a thin steel (25$\mu$m, 50$\mu$m) and amorphous 1,2 is cut core with an about 4cm × 6cm frame and that of others is toroidal with a radius from 2 cm to 3 cm. Phase shift shown in Fig.5 was obtained by measuring the time difference between two sinusoidal waves, that is, the current of the primary coil and dB/dt of the secondary coil.

Figure 6 shows the B obtained by integrating dB/dt, when the shape of the exciting current is trapezoidal. The ratio of the gap length lg to the magnet length lm is 2/15 (left), and 0 (right). This core material is "Steel (50$\mu$m)". These waveforms of B were similar to the calculated ones using the data in Figs.4 and 5.

Since actually used B is the order of 0.3 T, the raised B for a short time was examined. After the residual magnetization was disappeared by exciting the core by fading ac current, a linearly increasing current was applied for 2$\mu$s. Then the maximum B was obtained by integrating dB/dt. Figure 7 shows the maximum B which can be achieved in 2$\mu$s vs H. The B of a ferrite sample saturates at around 0.2 T, while that of steel, amorphous or dust core does not seem to saturate.

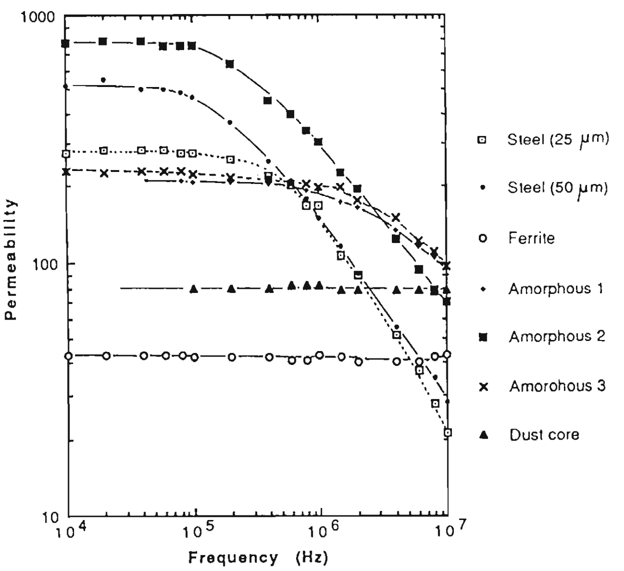


Fig. 4. Effective permeability vs frequency.

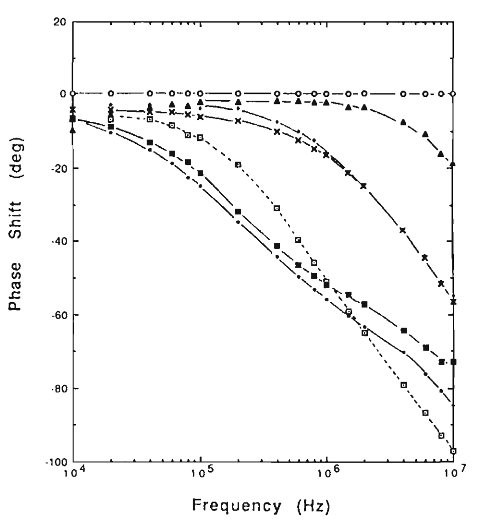


Fig. 5. Phase shift vs frequency.

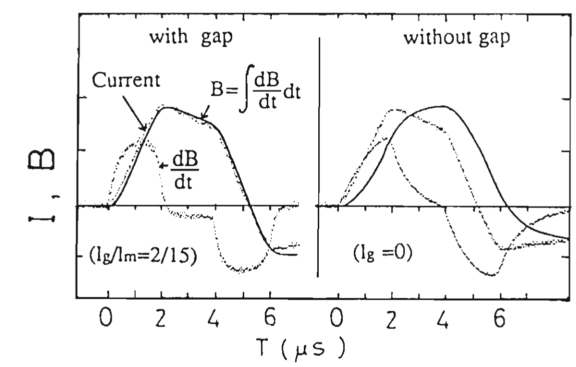


Fig. 6. Measured current and dB/dt and integrated B.

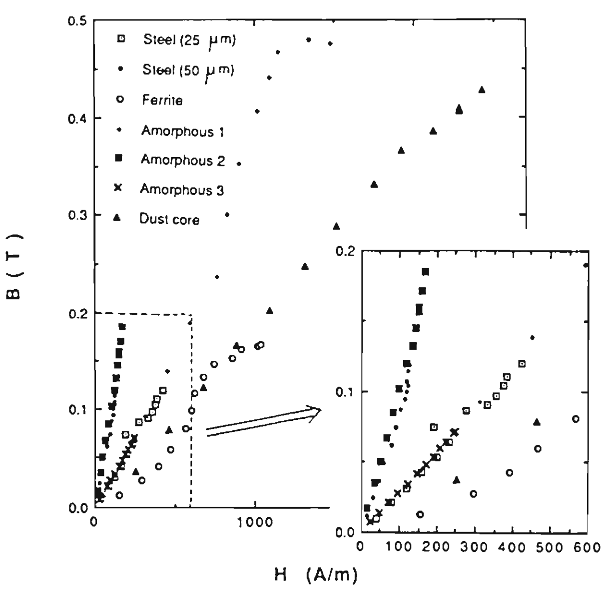


Fig. 7. B achieved in 2$\mu$s against H.

RIKEN Accel. Prog. Rep. 25 (1991)

# V-2-18. Measurement of Ripple Field in the B, Q, Sx Magnets with an Aluminium Vacuum Chamber for the SPring-8 Storage Ring

H. Takebe, S. Matsui, J. Ohnishi, K. Kumagai, S. Motonaga, and N. Kumagai

Detailed design for the SPring-8 storage ring magnet power supply system has been made. A high stability and low ripple current are required for the bending (B), quadrupole (Q), and sextupole (Sx) magnets. Magnetic field ripples, induced by current ripples, are modified by an aluminum vacuum chamber. This ripple fields were measured inside the vacuum chamber of the B, Q, and Sx magnets, in order to decide a current ripple tolerance of the power supply.[1)]

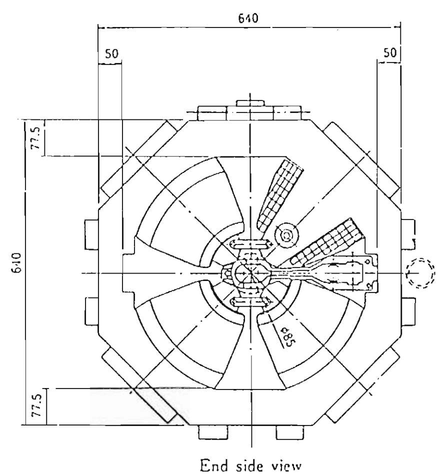


Fig. 1. Cross sectional view of the Q magnet with the vacuum chamber. The azimuthal-length of the model chamber is 40 cm, and the model magnet is 45 cm (Sx) and 50 cm (Q) in length, respectively.

The magnetic field ripple was measured inside and outside of the vacuum chamber. Figure 1 shows the cross sectional view of the model Q magnet and the model vacuum chamber. The length of the chamber is 40 cm, and the model magnet is 45 cm (Sx) and 50 cm (Q) in length, respectively. The schematic diagram of the measurement is shown in Fig. 2. The measurement was done for a ripple current of $\pm 0.85 \sim \pm 3.4$ A (0 to peak) and frequency of 30∼480 Hz. This current was supplied to the magnet exciting coil using a bipolar amplifier and a frequency generator. The magnetic field ripple was taken by a pick up coil ( 200 turn, 5 mm dia. for the Sx magnet and 2500 turn, 10 mm dia. for the B, Q magnets ), which was moved in X and Y directions. The output signal of this coil was connected to an FFT ( Frequency Fourier Transfer) analyzer.

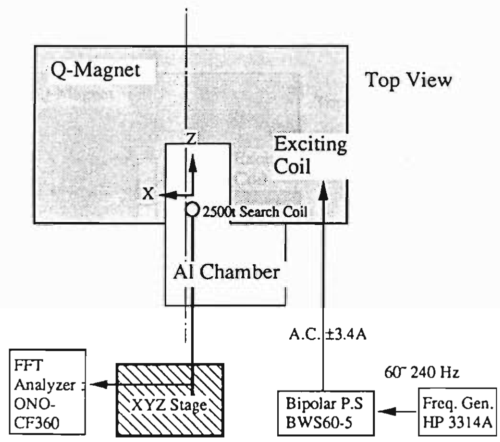


Fig. 2. The schematic diagram of the measurement for magnetic ripple field induced by the vacuum chamber.

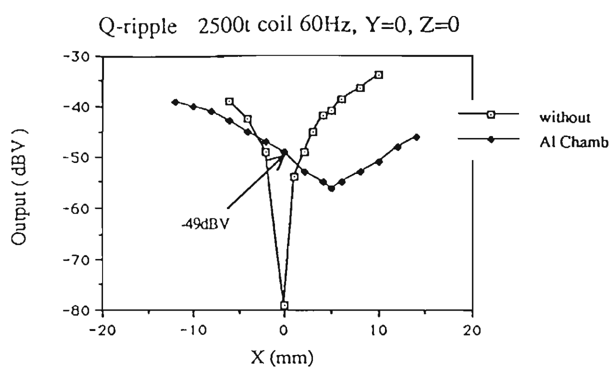


Fig. 3. Magnetic ripple field distribution of the Q magnet ($\pm 3.4$A, 60Hz) with / without the vacuum chamber.

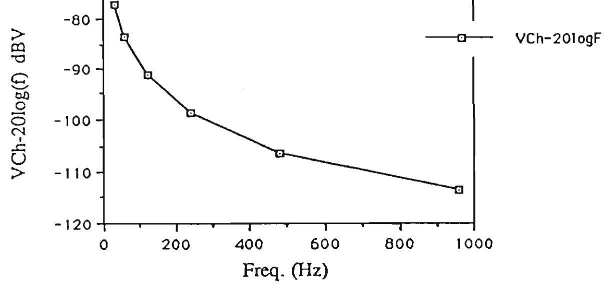


Fig. 4. Frequency dependance of the magnetic ripple field of the Q magnet (x=0 mm, I= $\pm 0.85$A) with the vacuum chamber.

Figure 3 shows ripple field distributions measured for the Q magnet with and without the vacuum chamber. The vertical scale is shown in a dBV unit which is 20 log(V). This field distribution without the chamber is the same as the sextupole DC field distribution. A different field distribution is induced by an eddy current in the aluminium vacuum chamber. The field strength is decreased with the frequency. Figure 4 shows the frequency dependance of the magnetic ripple field of the Q magnet (at $x = 0$ mm, $I = \pm 0.85$ A) with the vacuum chamber. The vertical scale is compensated for the search coil's output frequency characteristic.

Figure 5 shows the obtained ripple field distributions of the Sx magnet. The ripple field strength in the Sx magnet vacuum chamber at $I = \pm 3.4$ A ( 0 to peak, 60 Hz) is 4.2 gauss, which perturbs an electron beam position in 0.19 mm ($y = \beta \Delta Bl/(B\rho)$, where $\Delta B = 4.2 \times 10^{-4}$T, $\beta = 30$, $B\rho = 26.7$, $l = 0.40$m). In order to reduce this beam displacement to within 0.002 mm, the ripple current (Sx) must be less than $10^{-4}$. Similar measurements were done with the B magnet. The ripple field strength in the bending magnet is reduced to be less than 1/100 of the field without the chamber.[2] So, the ripple current allowance for the B magnet can be larger than that of Q and Sx magnets. The shapes of the vacuum chamber and magnets for the actual machine are slightly changed. The measurements for the real machine will be done next year.

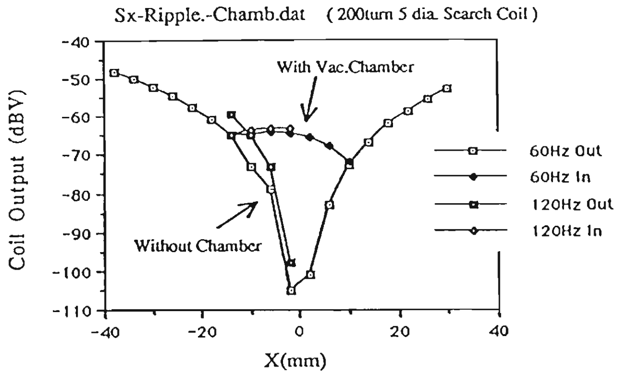


Fig. 5. Magnetic ripple field distribution of the Sx magnet ($\pm 3.4$A, 60 Hz) with / without the vacuum chamber.

References

1) H. Takebe *et al.*: Proc. 8th Symp. on Accel. Sci. & Tech.,Wako, Japan., p. 214 (1991).
2) H. Takebe *et al.*: Measurement of B, Q, and Sx Magnets Field Ripple Effected by Vacuum Chamber; Engineering Note. SPring-8 (1991).

RIKEN Accel. Prog. Rep. **25** (1991)

# V-2-19. Design of Magnet Power Supply Control System for the SPring-8 Storage Ring

H. Takebe, T. Wada, T. Masuda, and N. Kumagai

The total number of the 8 GeV storage ring (SR) magnet power supplies (PS) is more than 600, and 40 or 480 PSs are floated from the ground level with a few hundreds volts. A current control system for this huge number of PSs was investigated from a viewpoint of isolation, noise rejection, reliability and also economics. For these purposes, an optical fiber linked remote I/O (RIO) system was designed for the VME expansion system.

Table 1 shows the required current stability, ripple, and power consumption of the magnet and PS. The total number of the large PSs for B, Q, and Sx is 17. Magnets in the same group are connected in series and excited by one power supply.[1] The current stability and ripple are both within $1\times10^{-4}$.

Table 1. Required current stability, ripple, total power consumption, connection type and the number of the PSs in the PS rooms A,B,C and D.

| Magnet | PS-Name | Curr(A) | Volt(V) | Ripple | Stabi. | No. | kW |
|---|---|---|---|---|---|---|---|
| B | BP | 1270 | 1176 | 1E-4 | 1E-4 | 1 | 1540 |
| Q1~10 | QP1-10 | 392-568 | 431~1165 | 1E-4 | 1E-4 | 10 | 3749 |
| Sx1~7 | SP1-7 | 300 | 704~858 | 1E-4 | 1E-4 | 7 | 1611 |
| Q1~10 | QA1~10 | 4~23 | 19~44 | 3E-3 | 3E-3 | 480 | 52 |
| St1~12 | StP1~12 | 5 | 38~103 | 1E-2 | 1E-2 | 576 | 27 |

Some Q-magnets, which are connected in series, are adjusted by auxiliary PS circuits (in the long straight sections) to correct the modulation of the beta function and phase advance. These current corrections are needed up to a few % of the maximum current. These PSs (QA) are floated from the ground level with a few hundreds volts.

The steering magnets have independent power supplies. The total number of St-PSs is so large (576) that the maximum current must be small (5 A) to reduce manufacturing cost.

Each reference voltage for the large PS is given by a 16 bit DAC controlled by the digital output of the RIO type-B as seen in Fig.1-i). These DACs for the B, Q, and Sx PSs are installed in the PS cubicle's temperature controlled housing.

The St and Q-aux PSs are controlled by an analog signal ($-10\sim+10$V), using the RIO type-A. The installations of the RIO to the QA-PS and the St-PS are shown in Fig.1-ii), iii). The RIO card is installed in the PS chassis with the same guard level. The RIO operation power ( 5V, $\pm15$ V ) is supplied by them. The RIO type-A also has an ADC and monitors the actual current by a shunt resistance output.

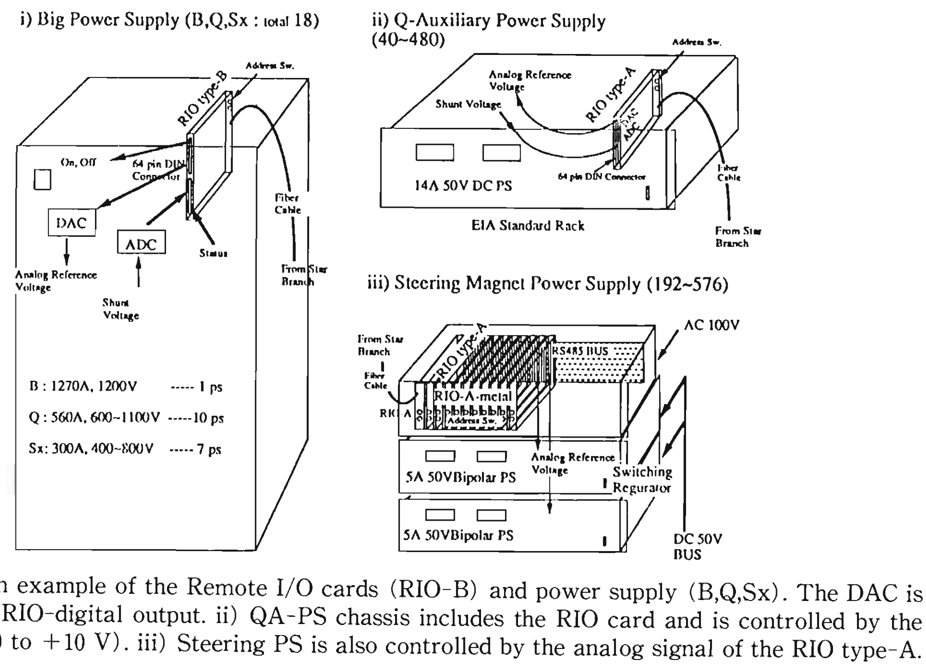


Fig. 1. i) Installation example of the Remote I/O cards (RIO-B) and power supply (B,Q,Sx). The DAC is isolated from the RIO-digital output. ii) QA-PS chassis includes the RIO card and is controlled by the analog signal (-10 to +10 V). iii) Steering PS is also controlled by the analog signal of the RIO type-A.

12 or 36 steering magnets power supplies (10 or 20 QA-PS) are enclosed in one power supply cubicle. A 16 bit status (power on/off, fuse, transistor break down, temperatures, oven, polarity, ext-interlocks, door, water flows, etc.) is read by the same RIO type-B.

This system consists of the following devices (see Fig. 2),

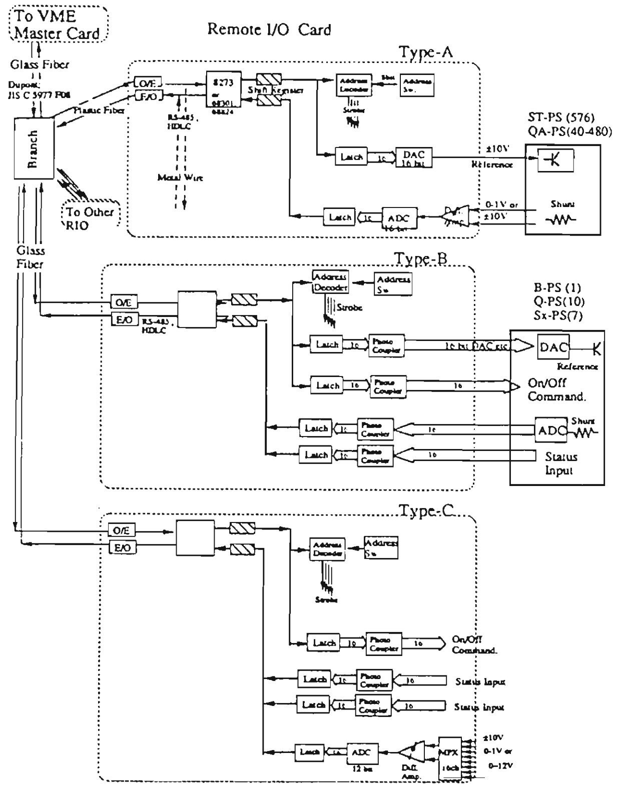


Fig. 2. Remote I/O cards (type-A, B and C). VME master controller sends data and address to register (Latch) for the ADC, DAC, DIO through a glass fiber and a star coupler. An integration type ADC has an accuracy of $1\times10^{-5}$.

1) Master card; VME module,
2) Star branch; glass fiber cable from the master to slave cards (1 : 62 ),
3) RIO (slave card) which has the following three types,
   - Type-A ; 16 bit DAC, 16 bit ADC (input ; 0-1V, 0-10V, ±1V, ±10V),
   - Type-B ; 32 bit digital output, 32 bit digital input ( photo isolated ),
   - Type-C ; 16 bit digital output, 32 bit digital input , 16 bit ADC + 16 ch MPX,
4) Optical fiber cable (Dupont Co.Ltd) with a connector: JIS-C 5977 F08.

The size of the RIO type-A is 128(H) ×172(D) mm (same as the VME module single height), and the size of type B and C is 262(H) ×172(D) mm. The RIO master controller, which has a dual port RAM, is a VME module. The interface between the master and slave (RIO card) is an RS485 and HDLC protocol with a transfer speed of 1 Mbps. Industrial products can be employed for this system. The data format is shown in Fig. 3. The transfer speed of six byte read write between 31 RIOs and VME master controller is estimated to be 6 mS. The optical fiber of glass and plastic can be used, because the connector pin specification is the same.

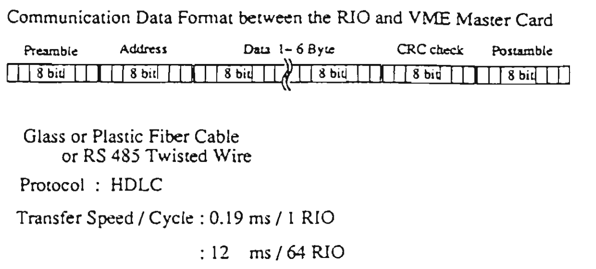


Fig. 3. Data format of the RIO and master module. The address data is 8 bit. The transfer speed of six byte read write between 31 RIOs and VME master controller is estimated to be 6 mS.

A VME system with a 68030 or 68020 CPU and MAP I/F (or TCP/IP) can be employed for a device controller. A UNIX work station will be used as a host computer for the program development and as a local control terminal.

The currents of the multiple PSs must be changed simultaneously for an orbit correction. Therefore, one VME CPU controls any combination of four St-PSs in any PS room (digital feedback system), if one VME CPU manages 576 RIO cards. Also, if a fast feedback for this correction is necessary, an analog signal can be added to the DAC's reference voltage.

References

1) H. Takebe, S. Motonaga, J. Ohnishi, and N. Kumagai: *RIKEN Accel. Prog. Rep.*, **24**, 1561 (1990).

RIKEN Accel. Prog. Rep. **25** (1991)

# V-2-20. Operation of a 1 MW Klystron for the SPring-8

Y. Kawashima, H. Ego, K. Inoue, T. Nakamura, Y. Ohashi, and M. Hara

An operation of a 1 MW high power klystron for the SPring-8 began from January 1991 and important data were obtained. Since the specification of the klystron itself was already mentioned in Ref. 1, only interesting results are briefly described.

Before high power operation, interlock system which cuts off ac-6.6 kV power line with the vacuum circuit breaker (VCB) within 20 ms was excessively checked for the sake of safety of operators and machines. The interlock system consists of many sensors, typically directional couplers to detect reflected power, arc sensors attached on waveguides, thermometers to measure temperatures of water fed to a 1 MW dummy load, 250 kW dummy loads and a collector of a klystron.

To test the capacity of a klystron, RF power from the klystron was guided through a WR1500 waveguide to a 1 MW dummy load. At first, the cathode and anode were set at 60 kV and 37 kV, respectively. Then 508.58 MHz input RF power was fed to the klystron. Under this condition the input RF power was gradually increased up to 300 kW. To raise the output RF power furthermore, the cathode was switched to 73.7 kV. Then output RF power was increased almost to 600 kW. However, big reflected power from a 1MW dummy load was suddenly detected, and in a moment the klystron power was automatically stopped because of the interlock system. We tried to overcome this trouble by changing the water flow rate from 500 l/min to 720 l/min, but failed. A few weeks later, at last we were able to know the cause of a big RF power reflection. The water used for the klystron system was purified water of the electric conductivity of around 1 $\mu$S/cm. Unfortunately such pure water absorbs little power near 500 MHz, tap water of the conductivity more than 100 $\mu$S/cm contrarily absorbs much power. Thus we switched pure water to tap water ( 120 $\mu$S/cm ). We began the klystron high power test again. The cathode was set to the maximum level of 90 kV, and the output RF power from the klystron attained to 1 MW smoothly. In Fig.1, we show the VSWR versus the output RF power in cases of pure water and tap water. There are no data at 1 MW RF power in the figure, since the reflected power in directional coupler disappeared due to the temperature rise in all waveguides by the high RF power.

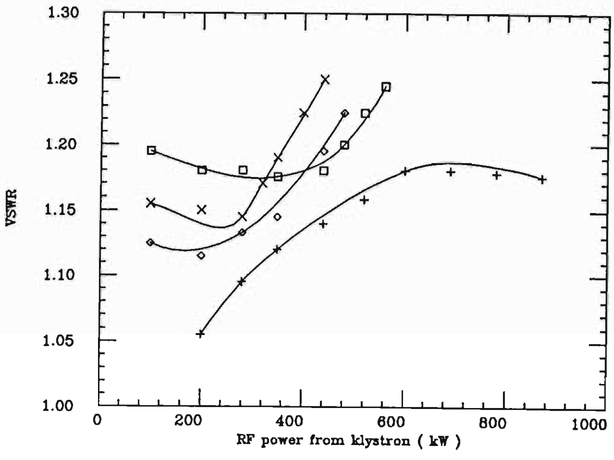


Fig. 1. Relation between VSWR and RF power in a 1MW dummy load. ×: water flow rate of 500 l/min, purity 0.2 $\mu$S/cm. ◇: water flow rate of 600 l/min, purity 0.2$\mu$S/cm. □: water flow rate of 720 l/min, purity 0.2$\mu$S/cm. +: water flow rate of 720 l/min, purity 120$\mu$S/cm. The full curves are eye fits to the data.

On the other hand, the RF radiation problem became serious; particularly the RF power leaked from a part of the joint of water. We therefore removed the rust around flanges and covered them with a glue including silver. Copper tapes, moreover, were wound round them. After all, RF radiation was suppressed to an allowable level. Now the klystron works stably and is used for the test of cavities.

References

1) K. Inoue, Y. Kawashima, T. Nakamura, and M. Hara: *RIKEN Accel. Prog. Rep.*, **24**, 166 (1990).

RIKEN Accel. Prog. Rep. 25 (1991)

# V-2-21. Development of a High Power RF Input Coupler for the SPring-8 Storage Ring

K. Inoue, T. Kusaka,* H. Suzuki,** T. Kojo,** H. Ego,
Y. Ohashi, Y. Kawashima, and M. Hara

In the SPring-8 storage ring, 32 couplers are needed in total. Each coupler feeds the RF (508 MHz, CW) power up to 100 kW to a single-cell cavity at 100 mA. It is necessary to use a coupler durable for the high power RF operation.

A high power RF input coupler of a loop coupling type has been developed. It consists of an adaptor with a door-knob type device from a WR1500 waveguide to a coaxial line, an RF window for vacuum seal, and a loop antenna. A cross section of this coupler is shown in Fig.1. The WR1500 waveguide is made of an A6061 aluminum alloy. The coaxial line is made of an OFHC copper and is terminated by the loop. Power loss at the coaxial line is estimated about 110 W for the input power of 100 kW. Both inner and outer conductors are cooled by water flow of 5 l/min. The coupling to the cavity is adjusted by rotating the direction of the loop, and consequently the effective coupling area to the magnetic field is varied. The RF window, 170 mm in diameter and 10 mm thick, made of a 95 % alumina disk is mounted on a choke structure of the coaxial line. It is estimated for the RF window to have a 30 W power loss at the input power of 100 kW. The RF window is directly cooled by forced air of 210 l/min by a blower. The choke structure is designed to be in impedance matching (50Ω) between the ceramics and the coaxial line.

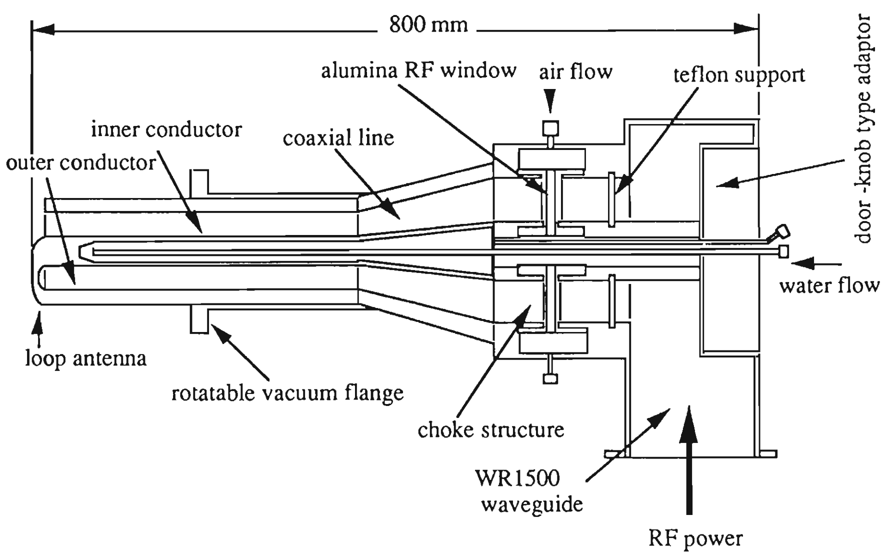


Fig. 1. Cross section of a prototype coupler.

The prototype coupler was tested by using a test stand of 1 MW klystron.[1] It was mounted on a coupler port of a five-cell prototype cavity which was developed for the booster synchrotron by JAERI SPring-8 design team. The five-cell cavity was evacuated by a turbomolecular pump (500 l/sec) and a sputter ion pump (400 l/sec). The RF power was slowly increased by keeping the pressure below $3 \times 10^{-7}$ Torr. The surface temperature of the RF window was monitored by

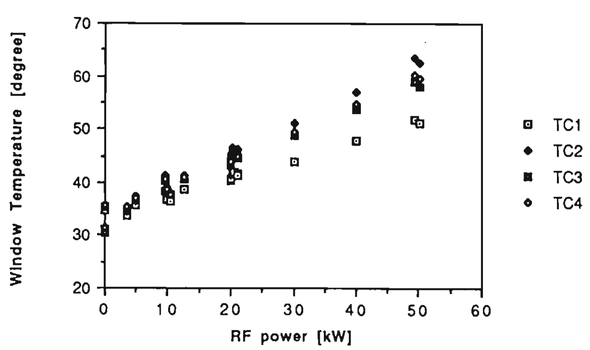


Fig. 2. Temperature of the RF window versus input power.

* Kobe Steel, Ltd.
** JAERI SPring-8 Design Team.

four thermocouples which were placed at the atmospheric pressure sides. At input power of 50 kW, no glow discharge was observed from a view port of the cavity just located on the opposite side of the coupler. But the RF window was heated up to about 60°C (see Fig.2). If the input power was further increased, breakdown of the RF window by the thermal stress might happen.[2) For that reason, the coupler power test was stopped. If only the cooling system would be improved, the RF power over 50 kW might be fed to the coupler. We will try again another high power test up to 100 kW after reinforcement of the cooling system.

References

1) K. Inoue, Y. Kawashima, T. Nakamura, and M. Hara: *RIKEN Accel. Prog. Rep.*, **24**, 166 (1990).
2) M. Akemoto and T. Yamazaki: Proc. 7th Symp. Accel. Sci. Technol., Osaka, Japan, p. 106 (1989).

RIKEN Accel. Prog. Rep. 25 (1991)

# V-2-22. High Power Test of a Five-Cell Cavity for the SPring-8

H. Suzuki,* T. Kojyo,* H. Yonehara,* K. Inoue, H. Ego, Y. Ohashi,
Y. Kawashima, and M. Hara

A five-cell cavity for the SPring-8 booster synchrotron was designed by Japan Atomic Energy Research Institute, as shown in Fig.1. The relevant parameters are listed in Table 1. Since this cavity has been tested from various points of view, the results experimentally obtained are briefly summarized.

Firstly, as to vacuum issues, after a bakeout at 120 °C for 24 hours, the pressure attained to $6.6\times 10^{-8}$Torr. And also, when a 250 kW RF power was fed to the five-cell cavity, the obtained pressure was $2\times 10^{-7}$ Torr. This is good enough for the booster synchrotron ring in a continuous RF high power operation. Secondly, for the RF characteristics, the dependence of resonant frequency on the temperature of the cavity was measured by heating up the cavity using a mantle heater which covered the whole cavity. It was observed that the resonant frequency ($TM_{010}$ $\pi$ mode) varied proportional to the temperature almost linearly as shown in Fig.2, and its changing rate was reduced to be 8.095 kHz/°C. Furthermore, it was obtained that the movement of a tuner position from −20 mm to +50 mm corresponds to 1.9 MHz on the band width of the resonant frequency, as shown in Fig.3. The obtained data were consistent with the expected values.

We fed RF power from the klystron to the cavity and could obtain important data. This was the first trial for the klystron to be operated for a high power test using a cavity. One day was spent for the aging of the cavity and input coupler at the level of around 50 kW RF power and then RF power was gradually increased to 250 kW in 5 days. During a high power test, serious

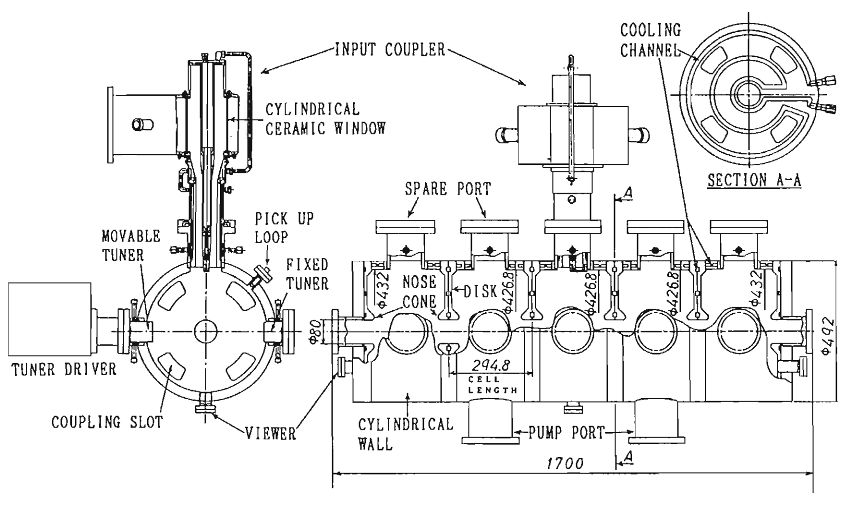


Fig. 1. Layout of the five-cell cavity.

Table 1. Relevant parameters of the five-cell cavity.

| | |
|---|---|
| $f_r$ | 508.58 MHz |
| $Q_a$ | 29300 |
| $R_{sh}$ | 42.265 MΩ/m |
| $R_{eff}$ | 22.987 MΩ/m |
| T | 0.736 |

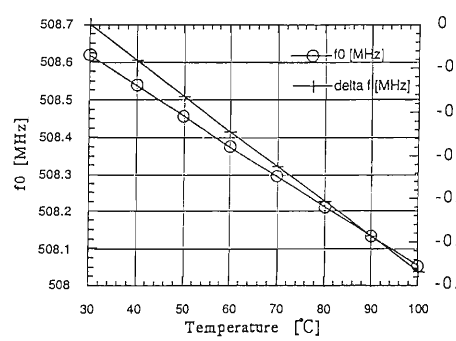


Fig. 2. Temperature dependence of the resonant frequency in the cavity.

* Japan Atomic Energy Research Institute.

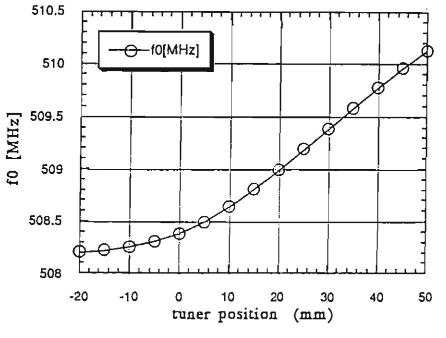


Fig. 3. Relation between the tuner position and resonant frequency.

troubles happened, for example unusual temperature rising at the ceramic window of an input coupler, pressure increasing in the cavity due to out gas from a wall induced by arc discharge (maybe, multipactaring). The former was solved by using cooled dry air. The latter was suppressed as time elapsed by the aging effect. The 250 kW high power operation was kept for 24 hours without any trouble. Thus the initial high power test was successfully completed.

RIKEN Accel. Prog. Rep. 25 (1991)

# V-2-23. RF Vacuum System for the SPring-8 Storage Ring

Y. Ohashi, H. Ego, K. Inoue, Y. Kawashima, and M. Hara

There are four RF acceleration stations in the SPring-8 storage ring, and each station consists of eight RF cavities(Cn) and a light absorber (AB) as in Fig. 1. Four pumping ports are distributed in each RF station. One is on the absorber and the other three are on the evacuation chambers (EC). Each pumping port will consist of a 2000 l/sec lumped non-evaporable getter pump (LNP), a 400 l/sec sputter ion pump (SIP). Expected pressure in the early stage of machine operation will be in mid $10^{-10}$ Torr without beam and mid $10^{-9}$ Torr with beam. Lower pressure will be expected after aging process through a prolonged period of stable machine operation. To keep oil free environment non-oil type pumps will be installed along with turbomolecular pumps (TMP) for rough evacuation. These mechanical pumps are to be shut off after startup, thus unnecessary vibration can be eliminated.

Two types of cavities have been investigated in the test setup shown in Fig. 2. One is constructed by diffusion bonding and the other by electron beam welding.[1] There are no significant differences between the two types from the view point of assembling methods, that is, both cavities reached 4 to 5 $\times$ $10^{-10}$ Torr by the extracter gauge(EXTR) after two days bakeout at 150 to 200°C. Above results are in good agreement with 1 to 5 $\times$ $10^{-10}$ Torr estimated with the cavity inner surface area of about 8000 cm$^2$, the pumping port conductance of 440 l/sec, and 140 l/sec SIP* assuming 1 to 5 $\times$ $10^{-12}$ Torr·l/sec/cm$^2$ of out gassing from oxygen free high conductivity copper. It implies that our primary goal is attainable in the configuration in Fig. 1 when beam is off.

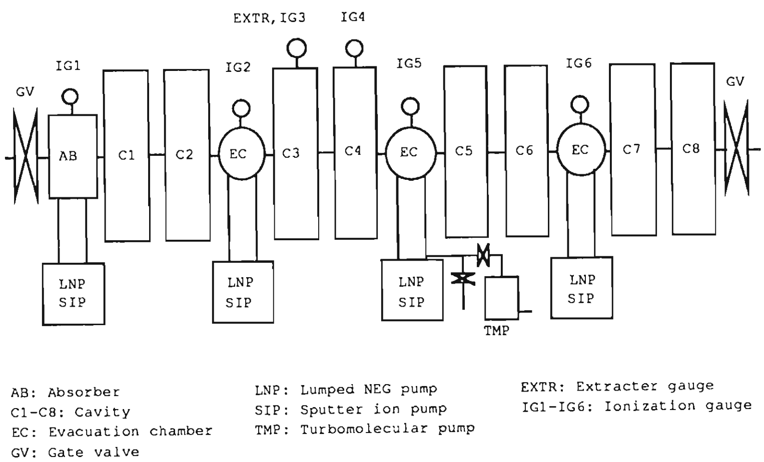


Fig. 1. Schematic layout of RF station.

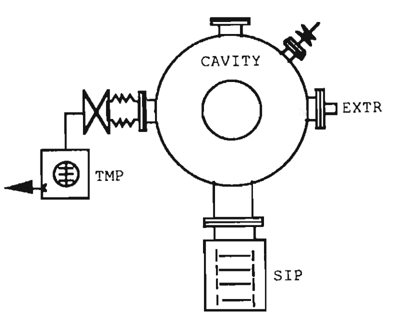


Fig. 2. Vacuum test setup.

There have been pointed out several problems on the present SIP, TMP, pressure gauges, control sequence, and layout of the components. We have been solving these problems and implementing the improvements towards the final design. In addition to the above problems some leakage appeared in the flange port joints after a few heat cycles, therefore, care must be taken especially in bonding or welding ports onto the cavity body. Taking advantages of higher bakable temperature and easy handling we have replaced

* Effective pumping power decreases from the specification value with the decreasing pressure below $10^{-6}$Torr.

** There were originally aluminum flanges and evacuation chamber with a light slit and RF shield.

aluminum components** by stainless steel ones.

We are currently concentrating on the following tasks as a final step: bakeout cycles, desorbed gas analysis, and vacuum control and interlock system design.

References

1) K. Inoue, Y. Kawashima, T. Nakamura, and M. Hara: *RIKEN Accel. Prog. Rep.*, **24**, 164 (1990).

RIKEN Accel. Prog. Rep. **25** (1991)

# V-2-24. Study on Impedances of the SPring-8 Storage Ring

T. Nakamura

Electron beams in storage rings interact electro-magnetically with their environment such as vacuum chambers, rf cavities, kickers, and so on, and sometimes become unstable. This phenomenon is called instabilities and limits the quality and/or quantity of electron beams.

Impedance is a figure of merit of an environment. It defines strength of interactions of the environment with electron beams, and should be carefully estimated in the design of the environment. In this study, the author focuses on above-cutoff high frequency broad band impedances of the vacuum chambers.

The broad band impedance has a low Q value, which means that the interaction is of short range and is responsible for single bunch instabilities. The longitudinal broad band impedance causes the instabilities which increase the energy spread in a bunch; hence it sets the required rf voltage for usual operation of the ring with the small number of bunches and it must be kept low enough in free electron laser experiments which are highly sensitive to the energy spread.

The transverse broad band impedance causes the instabilities which excite the transverse motion of electrons in a bunch and lead to the loss of beams.

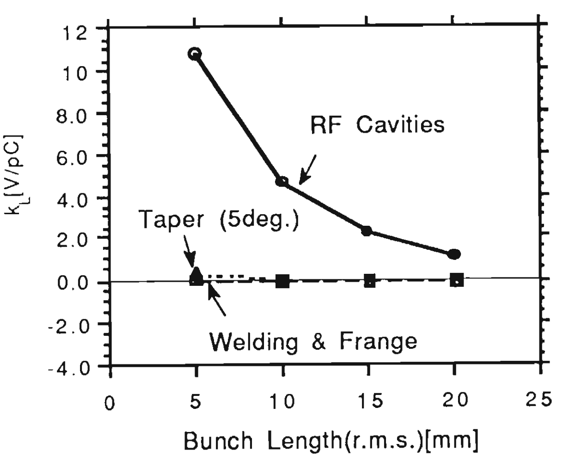


Fig. 1. Longitudinal loss parameters.

Loss parameters of several components of the storage ring, such as rf cavities, tapered transitions at insertion devices, weldings and franges are calculated with the 2-D code TBCI.[1] The loss parameter is the energy-gain of a bunch through the interaction with environments and is the measure of the relative strength of the impedances of individual components of an environment.

The results are shown in Figs. 1 and 2 for the longitudinal and transverse loss parameters respectively. The longitudinal impedance is dominated by the rf cavities. Here, the author subtract the contribution of the trapped high Q modes of rf cavities because the contribution of these modes to the impedace is easily estimated with the code URMEL-T.[2] The transverse impedance is dominated by the tapered transitions at the insertion devices.

Further studies on the impedance are necessary to get quantitative estimation of stabilities of the beam.

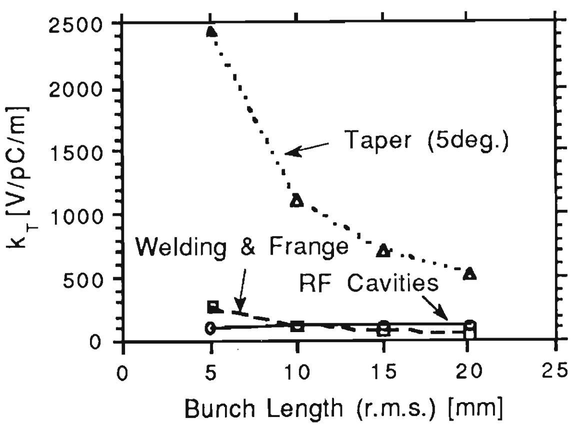


Fig. 2. Transverse loss parameters.


References

1) T. Weiland: *Nucl. Instrum. Methods in Phys. Res.*, **212**, 13 (1983).
2) P. Lauströer, U. van Rienen, and T. Weiland: "Urmel and Urmel-T user guide", DESY M-87-03(1987).

RIKEN Accel. Prog. Rep. **25** (1991)

# V-2-25. Straight Section Chamber

K. Watanabe, T. Nishidono,* C.Y. Xu, and S.H. Be

We designed a straight section chamber (SSC) for the SPring-8 storage ring, and improved the shape of the vacuum chamber as follows:

(1) We changed the inside shape of the beam chamber from the initial race track shape to an elliptical one, and the outside shape to the polygonal one, in order to avoid interference with the newly designed magnetpoles and make sealing space for the flange of the beam position monitor (BPM) electrode. The cross-sectional view and the interference diagram of the SSC with a quadrupole and a sextupole magnet are shown in Figs. 1 and 2, respectively.

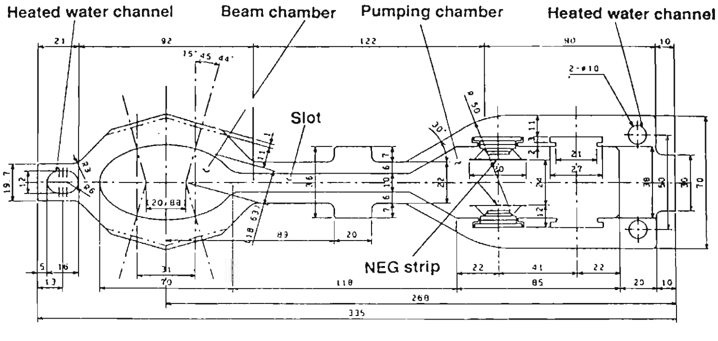


Fig. 1. Cross-sectional view of the SSC.

(2) Figure 3 shows the cross sectional view of the SSC assembled BPM electrode. The BPM electrode flanges are connected directly to the flanges machined on the vacuum chamber. A knife edge seal of a conflat flange could not be used because of the softness of an aluminum alloy A6063T5 vacuum chamber, which is 65-80 in the VICKERS hardness. We used a HELICOFLEX DELTA seal which has a characteristic of low sealing force of 100 daN/cm.

The HELICOFLEX DELTA seal consists of an INCONEL helical spring and a pure aluminum lining. Its flange thickness and bolt size are nearly the same as standard conflats. To obtain the tightening force required for the vacuum sealing, we are considering to use high-strength bolts such as chromium molybdenum steel ones, which have an allowable tensile stress of over 13 kg/mm$^2$.

We are planing to test and evaluate the HELICOFLEX DELTA seal.

(3) Due to the pressure difference between the atmospheric pressure and vacuum, the calculated deformation of the present chamber at the locations of BPM's was about 0.145 mm, while the deformation required for the BPM's chamber must be within the accuracy of 0.5 mm or less. Therefore, to suppress the chamber deformation, ribs are to be mounted on the chamber. We

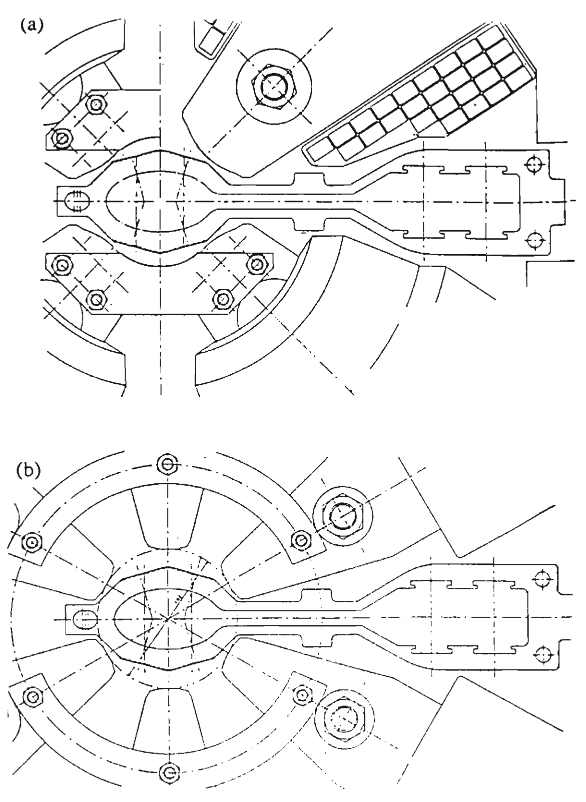


Fig. 2. Interference diagram of the SSC: (a) at a quadrupole magnet; (b) at a sextupole magnet.

* Ishikawajima-Harima Heavy Industries Co., Ltd.

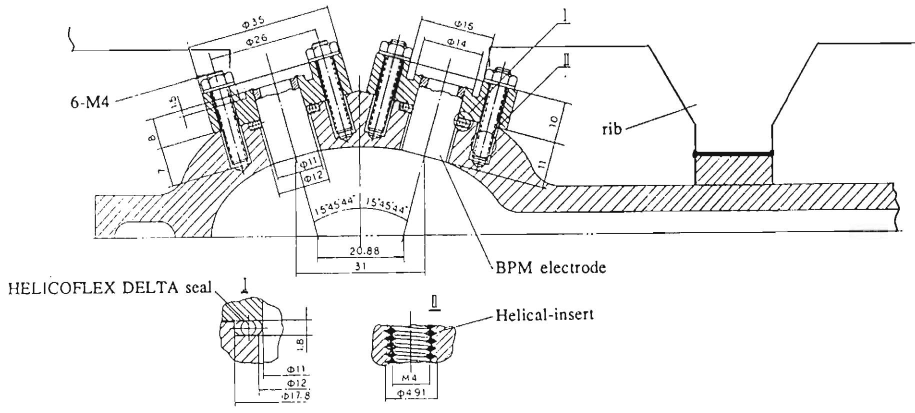


Fig. 3. Cross-sectional view of the SSC assembled BPM.

installed the boss on the slot of the SSC to joint the ribs, because the calculated deformation of the slot is largest.[1)]

(4) To bake out aluminum alloy SSC by means of a heated water bakeout system, we located two heated water channels of 10 mm in diameter at the pumping chamber side, and one racetrack-shaped channel (12 mm × 16 mm) at the opposite side.[2)]

Fundamental design for vacuum chambers has been fixed, but the detailed design remains to be done.

References

1) T. Nishidono *et al.*: Proc. Particle Accel. Conf., San Francisco, May (1991). (to be published)
2) S. Takahashi, S. Yokouchi, T. Nishidono, K. Watanabe, and S.H. Be: *RIKEN Accel. Prog. Rep.*, **24**, 185 (1990).

RIKEN Accel. Prog. Rep. 25 (1991)

# V-2-26. Pumping System of the SPring-8

H. A. Sakaue, Y. Hirano, S. Yokouchi, and S. H. Be

The vacuum system consists of two differently shaped aluminum alloy chamber extrusions, four types of absorbers, and various chamber components such as bellows, flanges and valves.

To achieve a beam lifetime of approximately 24 hours, the vacuum chamber with its pumping system should be designed so as to maintain the beam-on pressure of 1n Torr or less. The main pumping system is based on non-evaporable getter (NEG) strips, which are used in the straight and bending chamber. In addition to the NEG strips, a distributed ion pump is installed in the bending magnet chamber. Lumped NEG pumps, sputter ion pumps (SIP) and titanium sublimation pumps (TSP) are used at the crotch, absorber and beam line absorber locations.

It is one of our philosophy in the design of the vacuum system that the synchrotron radiation is almost intercepted by the crotches and absorbers placed just downstream and upstream of bending magnets, and not intercepted by the vacuum chamber all around the storage ring. Therefore, consentrative pumping system is needed in the crotches and absorbers.

Our main pumping system per unit cell of the ring, which is shown in Fig.1, is based on NEG strips. Lumped NEG pumps and SIP's are used at the crotch and absorber locations. Thus, the main pumping system is a mixed one, which consists of NEG strip, DIP, SIP and lumped NEG pump. The rough pumping system employs the mobile type pumping system (MPS), which consists of a turb molecular pump and a rotary pump.

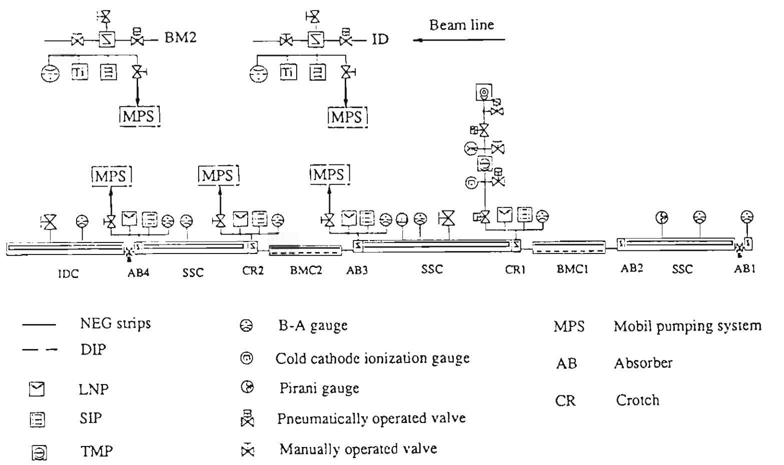


Fig. 1. Pumping system per one cell of the storage ring.

A pressure gradient profile is calculated based on the pumping system and the synchrotron radiation power distribution. In this calculation, we assumed that the distribution of SR-induced outgassing rate is in proportion to the rate of SR power deposited at crotches and absorbers, and that the compositions of residual gases is 80% $H_2$+20%CO. The pressure gradient profile over one cell is shown in Fig. 2. In this figure, three curves show the respective pressure profiles after the integrated stored current of 1,10, and 100 Ah. We can also find that the average pres-

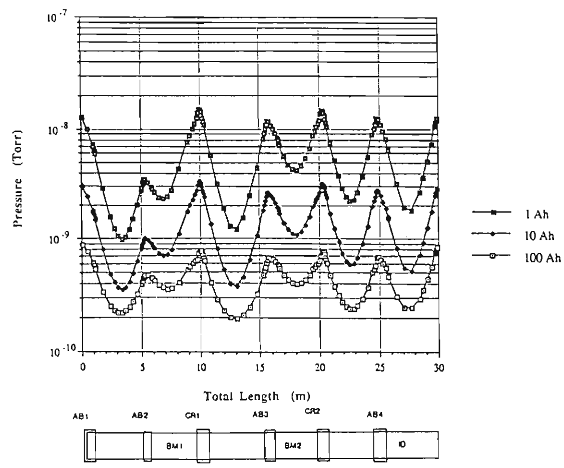


Fig. 2. Pressure gradient profiles after the integrated stored current of 1, 10, and 100 Ah.

sure over the ring decreases with an increase in the integrated stored current. The area where absorbers 1 and 2 are placed, shows the highest pressure in the ring. After 100 Ah, the average pressure is approximately 0.4 nTorr, and a beam lifetime of about 24 hours is expected to be achieved easily. The pressure at the bending magnet and straight sections, expect the area where the crotches and absorbers are placed, is not affected appreciably by the integrated stored current. Thus, we conclude that the pressure at the bending magnet sections and the straight sections is mainly governed by the thermal outgassing rate.

RIKEN Accel. Prog. Rep. **25** (1991)

# V-2-27. The Design of Absorber for SPring-8 Storage Ring

S. Takahashi, H. A. Sakaue, S. Yokouchi, and S.H. Be

Four absorbers (AB1∼AB4) per a cell will be installed at the SPring-8 storage ring to protect vacuum chambers and chamber components from being irradiated directly by photon beams from bending magnets. We are designing a new type absorber of a simple structure for AB1 and 2 using a finite element program ANSYS developed by Swanson Analysis Systems,Inc,.

The horizontal and vertical cross sections of AB1 are shown in Fig. 1. The body of AB1 is made of alluminum alloy(A6061), but the irradiated section is made of copper (OFHC-class1). We utilize the tight fit method to bond these two materials instead of an expensive transition joint such as explosion bonding or diffusion bonding methods, in order to reduce the cost. To evaluate this structure, we started to make the two-dimensional finite element analysis for a model shown in Fig. 2. We assume that the heat loading is deposited just on the node marked O in Fig. 2 for simplification. As the maximum power density perpendicular to the photon beam for AB1 is 12.9W/mm$^2$, we set the heat loading on the node (O) to be 6.45W/mm$^2$ because of symmetry. Heat transfer is set so as to occur only at the surface along which cooling water flows, while other surfaces are insulated. In calculation of the thermal stress, the fixed point and analytical symmetric surface are also considered as shown in Fig. 2.

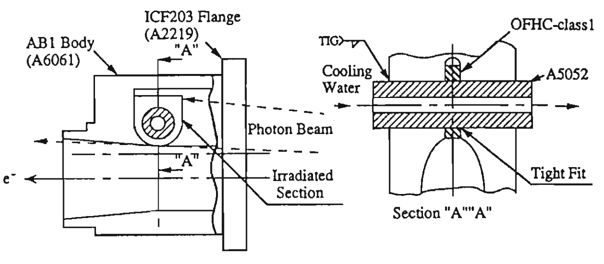


Fig. 1. Horizontal and vertical cross sections of the Absorber1.

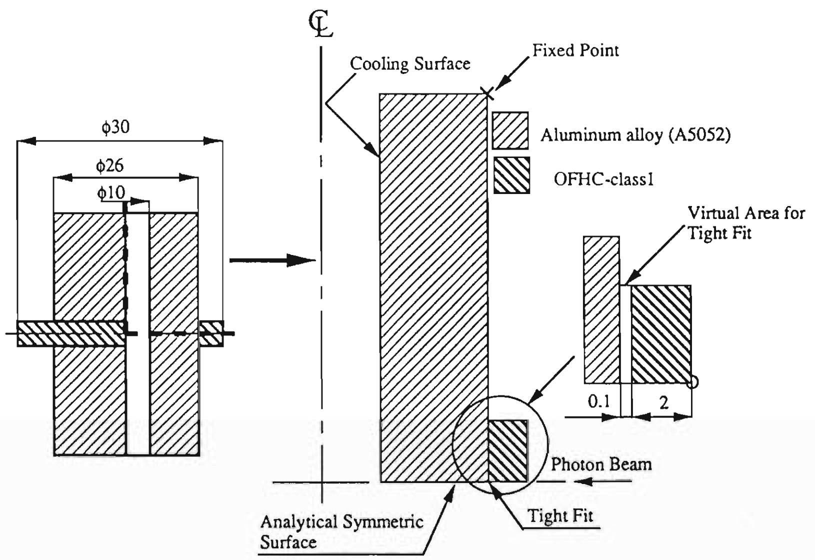


Fig. 2. Simplified model to calculate the temperature and thermal stress.

We investigated the effect of thermal contact resistance caused by the tight fit. When two bars are brought into contact, a temperature drop ($\Delta\theta$) at the contact plane arises as a result of the thermal contact resistance as shown in Fig. 3. Tachibana[1] derived the following equation to estimate $\Delta\theta$ considering a model which simplified a contact plane.

$$q=1/R_H\times\Delta\theta=\{(\lambda s/\delta+\delta_0)(p/H_B)+(\lambda g/\delta)(1-p/H_B)\}\times\Delta\theta \qquad (1)$$

q : Heat flux passing through the contact plane per unit area and time (W/mm$^2$)

$R_H$ : Contact resistance (mm$^2$ · °C/W)

$\lambda s$ : Thermal conductivity of a solid material =0.138 (W/mm · °C) for A5052

$\lambda g$ : Thermal conductivity of a gas material

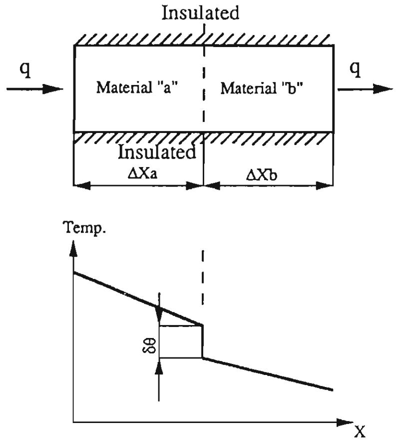


Fig. 3. Illustrations of the thermal contact resistance effect.

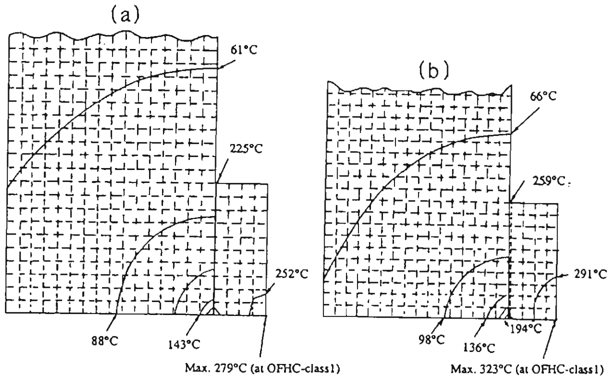


Fig. 4. Temperature distributions computed for the two cases.
(a) Without considering the contact resistance
(b) With considering the contact resistance

$=3.86 \times 10^{-5}$ (W/mm·°C) for air at 200°C

$H_B$ : Brinell hardness
$=70$ (kgf/mm$^2$) for A5052

p : Apparent contact pressure
$>10$ (kgf/mm$^2$)

$\delta$ : Length from the average line of roughness curve to the maximum value
$=0.4\times10^{-3}$ (mm) for $\nabla\nabla\nabla\nabla$ machining

$\delta_0$ : Equivalent length to the thermal resistance in a real contact area
$=(1\sim10)\times\delta$

Getting the temperature drop for the tight fit of about 3°C from Eq.(1), we estimate it 15°C taking account of a safety factor of 5. Carrying out the thermal analysis, we assumed a virtual area between A5052 and OFHC-class1 in order to consider the effect of the thermal contact resistance caused by the tight fit as shown in Fig. 2. The length of the area was set at 0.1mm only for convenience. The value of thermal conductivity of the area was decided so that the temperature drop of 15°C, as calculated above, may arise in the area.

Figure 4 shows the results of calculation of the temperature distributions for the two cases with and without considering the contact resistance. The maximum temperatures in OFHC and A5052 for the case of Fig. 4(b) are about 220°C and 320°C, respectively. As the maximum temperature on the cooling wall is less than 143°C (B.P. for 4kg/cm$^2$ water), we can say that this structure can withstand the power from the point of view of the temperature increase. Analysis for the thermal stress is in progress.

References

1) F. Tachibana: *J. JSME,* **55**, No.102 (1952).

RIKEN Accel. Prog. Rep. **25** (1991)

# V-2-28. PBL Absorber for the SPring-8 Storage Ring

C.Y. Xu, H.A. Sakaue, S. Yokouchi, K. Watanabe, and S.H. Be

The PBL (photon beam line) absorber is located at an 11–20 m distance from SR (synchrotron radiation) source points and intercepts the SR from the bending magnet and ID. Thus, we can protect the gate valve placed just downstream of the absorber. Main parameters for the SR and the absorber assembly are shown in Table 1. The absorber target irradiated by the SR is made of copper, which is cooled by flowing water through internal channels. The angle between the photontrajectory and the normal to the front surface of the target is 30°, and thereby the power density at the irradiated surface is reduced. An air cylinder drives the absorber up and down. A welded bellows is used to connect the flange with the movable absorber block for isolating the vacuum from the atmosphere. As shown in Fig. 1, the welding seams between the vacuum and water were considered to be avoided.

Table 1. Main parameters for the SR and the absorber assembly.

| | |
|---|---|
| absorber block material | OFHC-1 |
| distance between the absorber | |
| and the SR source point | 11000 mm (BM1) |
| | 14500 mm (BM2) |
| | 21276 mm (ID) |
| irradiated area | 0.58 $cm^2$ (BM1) |
| | 1.01 $cm^2$ (BM2) |
| | 1.7 $cm^2$ (ID: BM1+BM2) |
| beam power | 0.71 kW (ID: BM1+BM2) |
| power density0.536 $kW/cm^2$ (BM1) | |
| | 0.3 $kW/cm^2$ (BM2) |
| | 0.42 $kW/cm^2$ (ID: BM1+BM2) |
| stroke | 30 mm |
| closing time | <2 second |
| lifetime | 3.8 x $10^4$ cycles |
| working pressure of air cylinder | 5 $kg/cm^2$ |
| cooling water flux | 12 l/min |

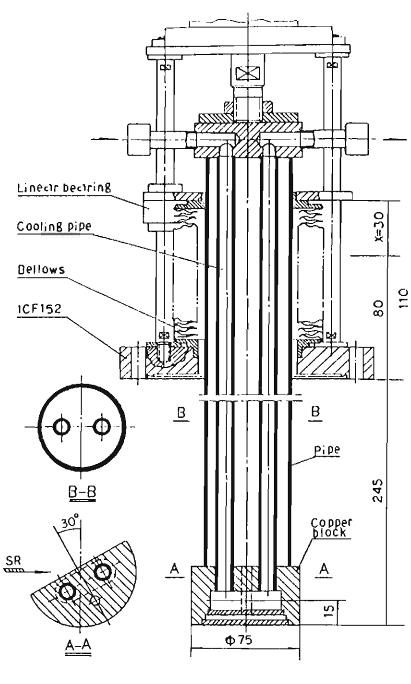


Fig. 1. Schematic diagram of PBL absorber assembly.

In the chamber design, gases released by photodesorption at the target are considered to be efficiently evacuated. In this absorber assembly, a mixed pumping system, which composed of a sputter ion (60 l/s) pump and a titanium sublimation one, will be employed. Further, the pressures with and without photon beam are required to be of the order of less $10^{-10}$ torr and $10^{-11}$ torr, respectively.

RIKEN Accel. Prog. Rep. **25** (1991)

# V-2-29. Synchrotron Radiation Shield of the Crotch for the SPring-8 Storage Ring

K. Watanabe and S.H. Be

In the SPring-8 storage ring, the majority of SR ( Synchrotron Radiation ) photons are consumed by interactions with a crotch placed just downstream of bending magnets. In the design of the crotch, thermal stress caused by high power deposited on the crotch absorber and gas desorption originated from the SR irradiation are two main problems to be considered. In addition, to avoid the excessive production of ozone and corrosives in the air surrounding the vacuum chambers, the SR shielding is also to be considered in the crotch design.

The crotch absorber is made of copper of approximately 30 mm in thickness, and the photons of energies less than 80 keV are almost stopped at the absorber (Fig. 1). To reduce further the radiation level outside the vacuum chamber, additional shielding is necessitated. The shielding is provided with a 2 mm thick tungsten plate. An effect of the additional shielding is also shown in Fig. 1. The additional shielding with a 2 mm thick lead plate is provided at the absorber just upstream of the bending magnet ( not shown here ).

The tracks of one hundred photons obtained by the Monte Carlo method are shown in Fig. 2. The photon with 200 keV is shot to a copper target of 20 mm in thickness. The tracks of photons passing through the copper target are drawn in the right area of copper target. The tracks of photons backscattered are shown in the left area of the copper target. In the copper target, the dispersed area of photons is about 20 mm in diameter.

Figure 3 shows the spectrum of bremsstrahlung passing through a copper target of 40 mm in thickness. This bremsstrahlung occurs by interaction of electrons and residnal gases in a vacuum chember. The following assumptions for the residnal gases were made. 1) The gaseous pressure is $1.33 \times 10^{-7}$ Pa ( $10^{-9}$ Torr ) . 2) The gaseous components are 80 %-$H_2$ and 20 %-CO in volume. The direct spectrum of bremsstrahlung is nearly independent of the electron energy and the intensity is about 5-6 photons/sec • 0.1% b.w. However, the intensity of passing spectrum increases to about 200 photons/sec • 0.1%b.w. in peak because of the shower effect. A pointed peak at 511 keV shows $\gamma$-rays due to annihilation of electron-pair. The intensity of bremsstrahlung is sufficiently less than the intensity of the SR from a bending magnet.

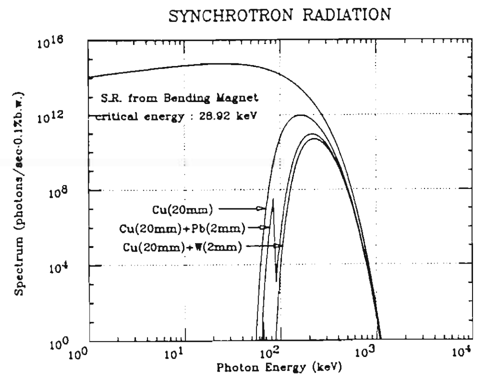


Fig. 1. The direct SR spectrum and the spectrum passing through different shields.

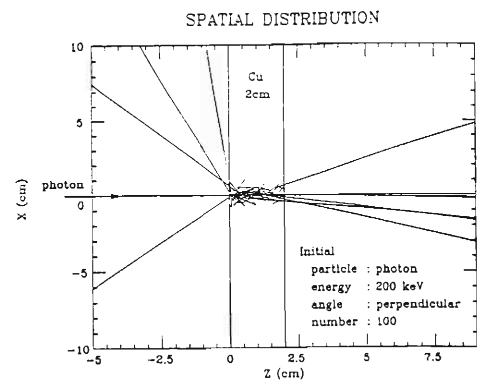


Fig. 2. The tracks of one hundred photons obtained by the Monte Carlo method.

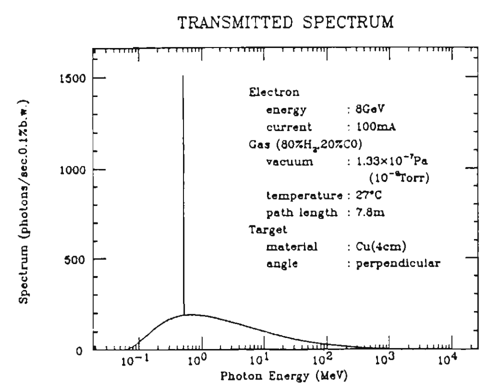


Fig. 3. The spectrum of bremsstrahlung passing through a copper target of 40 mm in thickness.

RIKEN Accel. Prog. Rep. **25** (1991)

# V-2-30. Comparison of Copper and Aluminum as the Chamber Wall Material of the Photon Absorber

S. R. In and S. H. Be

The photon absorbers to be installed in the SPring-8 storage ring are commonly composed of two parts ; a trapping chamber and a transition part with a cutting edge.[1] It is safely assumed that the latter part belongs to the beam chamber. Each part can be simplified as a model structure which has two components; an absorber interacting directly with the synchrotron radiation (SR), and a chamber confining back-scattered and reflected photons, photoelectrons, secondary electrons, and desorbed gas molecules as shown in Fig. 1. Glidcop is the most probable candidate material of the absorber. Copper (OFHC) and aluminum alloy (A6061) are reasonable chamber materials. Up to now copper has been considered as the best chamber material because mainly of its low photodesorption yield. However it is not surprising that aluminum alloy is newly under consideration as the chamber material from an economical point of view taking into account various conveniences in the whole fabrication processes. The effects of the two chamber materials to the total gas desorption is compared with each other.

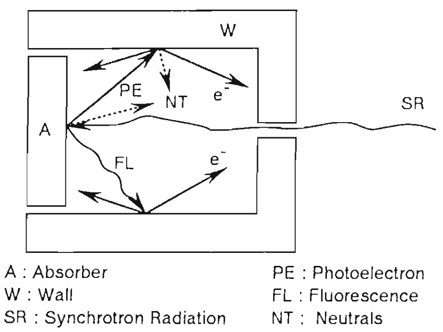


Fig. 1. Model structure of the photon absorber composed of separate absorber and chamber.

Let's consider three configurations ; (1) all copper system, (2) all aluminum system and (3) copper absorber + aluminum chamber system. In the first and third cases Glidcop is assumed to show nearly the same characteristics of the SR interaction as copper. The gas desorption from the copper chamber wall was estimated to be slightly larger than that of the copper absorber by about 15%. If the experimental photodesorption data of a certain material are available, the contribution of each component to the total photodesorption is independently evaluated.

The gas desorption from the copper absorber holds about 46.5% of the total photodesorption. By the same way it is recognized that the aluminum chamber charges about 52% of the photodesorption in the second case. Some experimental results show that the photodesorption rate of aluminum is much higher than that of copper by more than one order.[2] Therefore it seems very reasonable that the gas desorption is increased greatly by one order or several times in the composite system of the 3rd case compared with the first case.

However the gas desorption from the aluminum chamber installed with a copper absorber was calculated to be only 1/10 of the expected one in the second case. This is originated from the fact that the photoelectron yield of copper is about one-fifth of that of aluminum, and the photodesorption rate is approximately proportional to the emission rate of the photoelectrons. The contributions of secondary effects to the gas desorption from the chamber are merely 15%, 10% and 30% in the cases of (1), (2) and (3), respectively. The gas desorption rate of the aluminum chamber is only 2 times larger than that of the copper chamber as long as the absor-

Table 1. Comparison of the three configurations.

| Material \ Relative Photodesorption | Absorber | Chamber | Total |
|---|---|---|---|
| (1) All copper | 1 | 1.15 | 2.15 |
| (2) All aluminum | 10 | 11 | 21 |
| (3) Copper absorber + Aluminum chamber | 1 | 2 | 3 |

ber material is not changed from copper. Table 1 summarizes the results of the rough estimation of relative contributions of the absorber and the chamber to the total photodesorption for the three configurations.

From Table 1 the photodesorption rate in the third case is about 1.4 times larger than that of the first case.

References

1) S. Takahashi *et al.*: This Report, p. 223.
2) S. Ueda *et al.*: *Vacuum,* **41**, 1928 (1990).

RIKEN Accel. Prog. Rep. 25 (1991)

# V-2-31. Synchrotron Radiation Interactions in the Photon Absorber

S.R. In and S.H. Be

Only a few % of the total synchrotron radiation (SR) produced in the storage ring are utilized for experiments. The majority of the SR photons are consumed by interactions with photon absorbers. There are three main problems to be considered on the SR interaction in the photon absorber ; radiation shielding, thermal stress, pressure rise due to transmitted photons, absorbed photons energy, and photodesorption. The former two topics are discussed separately in this volume.[1,2] Here we report only on the last issue.

Photodesorption is a complicated process including all the phenomena concerning gas desroption originated from the SR irradiation on the absorber material. It is widely admitted that gas desorption is caused mainly by electron interactions, but rarely by direct photon interactions. Photoelectrons, reflected photons and fluorescences are generated by the SR photons. Further secondary electrons are produced from surrounding walls by the photoelectrons and the scattered photons. Gas molecules are desorbed from the material surface by both the emitted and incident electrons.

Photoelectrons produced by SR cannot easily escape from the absorber material because the mean free path of an electron is much less than that of a photon above ultraviolet. The photoelectron yield is increased with a decrease in the incident photon energy, but there is a threshold energy of a few eV corresponding to a work function depending on the material and the surface conditions. SR from a bending magnet has a broad spectrum from microwave to hard X-ray. The average photoelectron yield of a copper absorber for the SR spectrum in the SPring-8 storage ring was calculated to be about 0.01 using experimental quantum efficiencies (number of electrons produced by one photon of a certain energy).

The secondary electron yield of the incident photoelectrons on the chamber walls is safely assumed to be about 0.5 regardless of the material. The average energy of the secondary electrons is known to be a few eV, which is not sufficiently efficient to excite gas desorption from chemisorbed bondings.

The fluorescence yield was evaluated by the EGS4 (Electron Gamma Shower Version 4) code modified and supplemented with a low photon energy option and a fluorescence subroutine. The calculation results showed that the number of the photons back scattered by fluorescence is about 5 % of the incident photons, and the power fraction is about 3 %. The energy spectrum of the

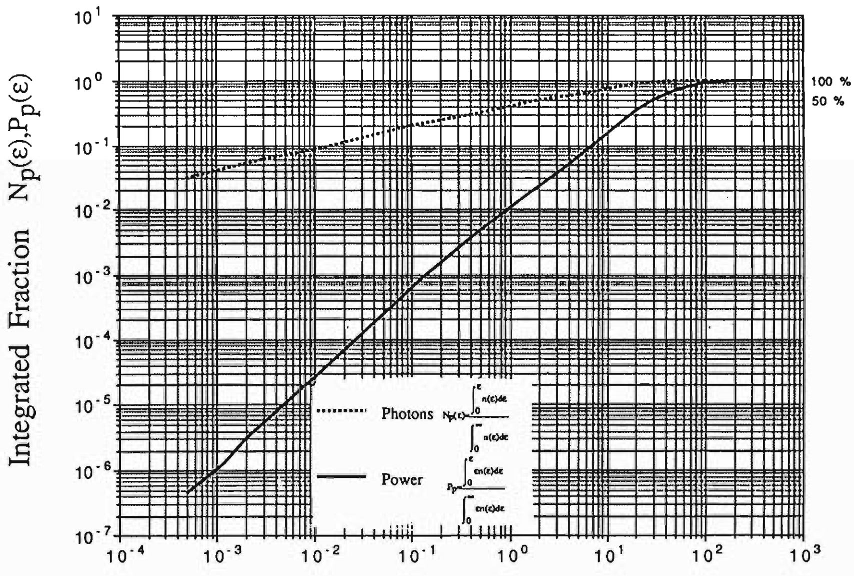


Fig. 1. Integrated fraction up to a given photon energy of photons and SR power from bending magnet.

fluorescences does not have a low energy part, and consequently the electron yield is much smaller than that of the SR photons.

Electromagnetic waves are reflected by atomic electrons of metals. Reflectivity is very high even at the normal incidence when the photon energy is less than a cut-off energy determined by the plasma oscillation frequency. At low photon energies only the valence electrons can contribute to the plasma oscillation but at sufficiently high energies all the inner shell electrons can be considered as free electrons. For example, the cut-off energy varies from 11 eV to 58 eV in copper. If the photon energy becomes larger than the cut-off energy, the reflectivity drops very rapidly for large incidence angles. There is a critical incidence angle below which the photons of a certain energy are totally reflected. The fraction of the photons which have the energies below 15 eV is about 10 % of the total photon spectrum (Fig.1), and the average reflectivity is approximately 50 % regardless of detailed shape of the material surface. The photoelectron yield of the reflected photons is higher by a few times than that of the parent SR photons. However the gas desorption power of these electrons is expected to be very low because of the low emission energy. The photons incident on the cutting edge with a small curvature can be easily reflected even in the X-ray range, but the viewing angle of the critical reflecting point is negligibly small in the practical geometry and the number of photons reflected actually is also very small.

As a conclusion the contribution of the secondary electrons produced by the photoelectrons, fluorescences and reflected photons to the gas desorption is not important compared with that of the photoelectrons generated by the SR photons.

References

1) K. Watababe *et al.* : This Report, p. 226.
2) S. Takahashi *et al.* : *ibid.*, p. 223.

# V-2-32. Simultaneous Calibration for Two UHV Gauge Heads

T. Hanasaka, Y. Hirano, S. Yokouchi,
H. Daibo, and S.H. Be

So far a calibration of ionization gauge heads has been done for one gauge head at the same time to avoid the mutual interference between gauge heads.[1,2] We investigated whether simultaneous calibration for two heads without the mutual interference is possible or not.

The calibration chamber (Manifold) is shown in Fig. 1. The diameter of the chamber is $\phi$197, and a gas inlet pipe ($\phi$10.5) is at the center of the chamber as shown in Fig. 1(a). Two nude B-A gauge heads of 75mm in length are attached to the port ① and ④ in Fig. 1(b). The inner diameter of the connecting tube to the chamber is $\phi$38. The lengths of the tube are 96.5 and 81.5mm, respectively. A spinning roter gauge (SRG) is used as the standard gauge.

The chamber was evacuated by means of a turbo-molecular pump continuously. The residual pressure was of the order of $10^{-8}$Pa. Argon was used as the calibration gas. The adjust knob position of a variable leak valve was kept constant so as to obtain the pressure of about $6\times10^{-4}$Pa in the chamber.

The filaments of the nude gauges were switched off for about 30 seconds and switched on for about 5 minutes periodically. During measurements of about 50 minutes, the switching-on/off was repeated about 10 times per the gauge in turn. The pressure during the switching-off of one B-A gauge was measured with the SRG and the other B-A gauge.

The changes in pressure (1) before, (2) during, and (3) after the switting-off were compared. If two gauges interfere each other,change in the pressure would be shown. However, there was no apparent change in the pressure by this switching operation of the filaments as shown below.

The changes in the pressure of the two nude gauges during the measurements were about ±0.7% and ±1.4%, respectively. The fluctuation in pressure of the SRG was within ±0.7% during the measurements. These three values (fluctuations in the SRG and two nude gauges) around ±1% were considered to be small enough, and, therefore, we can conclude that there is no apparent interference between the two gauges at the simultaneous calibration.

The changes in the emission current of one gauge at the switching-on/off of the other gauge were also monitored, but the digital indications of 3.99 and 3.98 mA did not change by the switching-on/off of the other gauge filament. This means that there is no electrical interference between the two nude gauges.

The simultaneous measurement under the residual pressure of the order of $10^{-8}$Pa was also carried out. In this pressure region, the outgas from the nude gauges could not be neglected. The

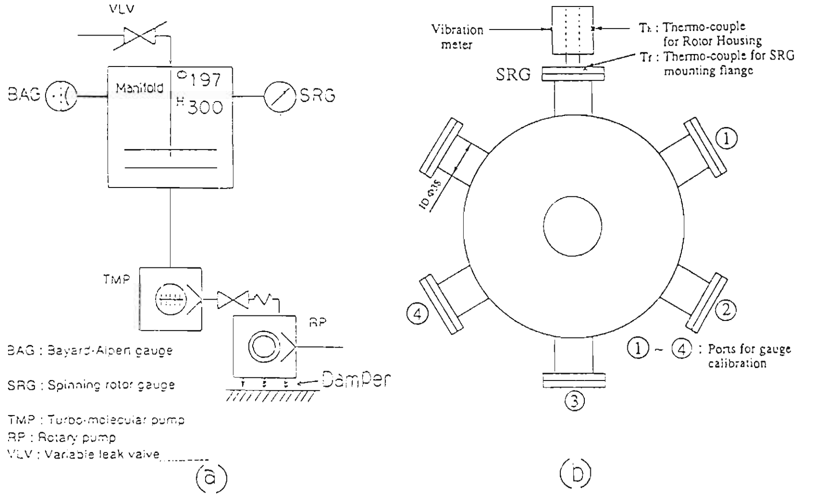


Fig. 1. Experimental setup for the calibration of vacuum gauges.
(a) Schematic diagram of the vacuum system.
(b) Upside view of the calibration chamber.

pressure of one gauge decreased at the turning-off of the other gauge filament by about 20% or so. However, there was also no special interference between the two gauges.

From these experiments, it is concluded that the simultaneous calibration of two gauge heads is possible. The calibration is to be carried out for the pressure range larger than $10^{-4}$Pa from a point of view of the SRG accuracy.

References

1) S.R. In, S. Takahashi *et al.*: *J. Vac. Soc. Jpn.*, **34**, 601 (1991).
2) H. Daibo, S.R. In *et al.*: *RIKEN Accel. Prog. Rep.*, **24**, 187(1990).

# V-2-33. Spectroscopy of Electron Produced by Synchrotron Radiation

H.A. Sakaue, K. Watanabe, K. Yano, T. Hanasaka, and S.H. Be

In the SPring-8 storage ring, synchrotron radiation (SR) is almost absorbed by crotches and absorbers placed just downstream and upstream of bending magnets and not intercepted by the vacuum chamber all around the storage ring. As the gas load due to photodesorption is several order higher than thermal gas load, the pressure rise due to the photodesorption influences critically the vacuum performance of the storage ring. Photoelectrons, reflected photons and fluorescences are generated by the SR photons. Further secondary electrons are produced from surrounding walls by the photoelectrons and the scattered photons. The gas desorption is caused mainly by electron interactions with absorber material, but rarely by direct photon interactions.

So far photodesorption yield (h) for SR of the critical energy of several keV has been measured, but data of h for SR of approximately 30 keV as in the SPring-8 storage ring are not available. We are planning experiments for acquisition of data concerning h for SR of high critical energies including elucidation of the photodesorption mechanism.[1] Measurements of photoelectron generated by the SR irradiation on the material are very important for elucidation of the photodesorption mechanism.

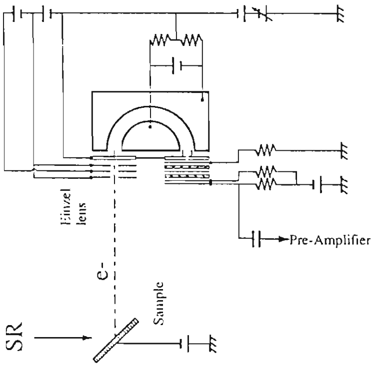


Fig. 1. Experimental apparatus of electron spectroscopy.

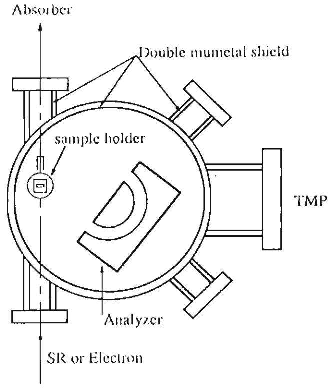


Fig. 2. Schematic drawing of the electron analyzer.

Figure 1 shows the experimental apparatus of electron spectroscopy, and Fig. 2 shows the electrostatic analyzer. This apparatus consists of the sample holder, energy analyzer and detector.

A hemispherical type analyzer with a mean radius of about 36 mm is employed for the electron energy analysis. The energy resolution is typically about 100meV in the full width at half maximum under a typical operating condition.

The electron energy is analyzed by the deceleration scan method and the energy of electrons passing the analyzer was constant. The deceleration lens is composed of a three element einzel lens. The energy-analyzed electrons were counted by a channel plate. The electron gun is installed in the chamber, and the voltage of lens is adjusted by the gun. The OFHC plate (10mm×10 mm) is installed in the sample holder which can be moved up and down.

For analyzing low energy electrons of a few eV, the magnetic field inside the chamber must be reduced to a few mG by double mumetal shieldings.

References

1) K. Watanabe, S. R. In, S. Yokouchi, K. Yano, and S. H. Be: *RIKEN Accel. Prog. Rep.*, **24**, 171 (1990).

RIKEN Accel. Prog. Rep. **25** (1991)

# V-2-34. Magnetic Field Measurements on JSR Undulator

T. Takada and S. Sasaki*

Magnetic field of the JSR[1](JAERI Storage Ring) undulator was measured. Parameters of this device are shown in Table 1 and the coordinate system used in this report is shown in Fig. 1.

The vertical component of the magnetic field, By, as a function of the electron path length, z, was measured with 2 mm step on z axis using a Hall probe and a measurement system (PC9801, gpib, motor driving system and laser distance measurement system, etc.) for electromagnetic magnets in SPring-8[2] at 10 different magnetic gap widths from 30 mm to 90 mm. The measured field, By(z), at 70 mm gap width is shown in Fig. 2 as a function of the path length, z, setting the origin of z axis at the center of the undulator. The average and the variance of peaks of the periodic sinusoidal field except the two peaks at both edges are shown in Fig. 3 as a function of the gap width. The peak field as a function of the magnetic gap width, g, for a pure permanent magnet type undulator is expressed by the following analytical expression:[3]

$$By_p(g)[T]=2Br[T]\frac{\sin(\pi/4)}{(\pi/4)}\left[1-\exp\left(-2\pi\frac{h[m]}{\lambda u[m]}\right)\right]\cdot\exp\left(-\pi\frac{g[m]}{\lambda u[m]}\right). \qquad (1)$$

Table 1. Parameters of a JSR undulator.

| | | | |
|---|---|---|---|
| Configuration | | Pure permanent magnet : Halbach design | |
| | | Planar type | |
| Magnet block material | | Nd-Fe-B alloy | |
| Nominal remnant field | | Br [T] | 1.223 |
| Magnetic period length | | λu [m] | 0.08 |
| Magnet block width | (x axis) | w [m] | 0.10 |
| Magnet block height | (y axis) | h [m] | 0.02 |
| Magnet block length | (z axis) | ℓ [m] = λu / 4 [m] | 0.02 |
| Number of periods | | Nu | 13 |
| Total length | | Lu [m] = λu [m] • Nu | 1.04 |
| Magnetic gap width range | | g [mm] | 45 – 90 |
| Average peak field range | | $By_p$ [T] | 0.276 – 0.045 |
| Deflection parameter range | | Ky = 93.4 $By_p$ [T] • λu [m] | 2.06 – 0.34 |

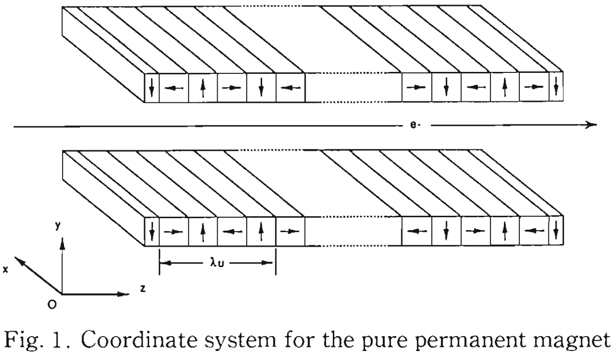


Fig. 1. Coordinate system for the pure permanent magnet type undulator.

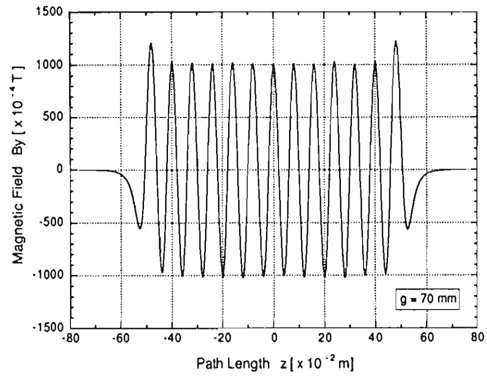


Fig. 2. Measured vertical magnetic field at 70 mm gap width as a function of path length.

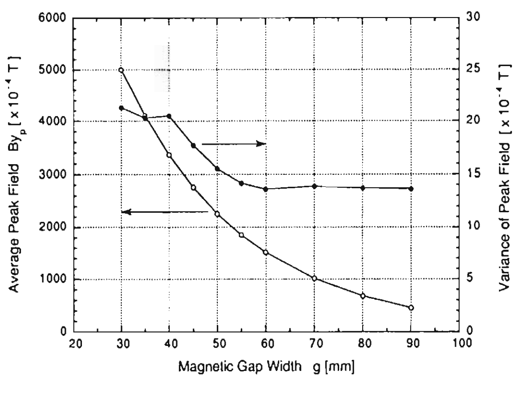


Fig. 3. Average and variance of peaks of the periodic sinusoidal field as a function of gap width.

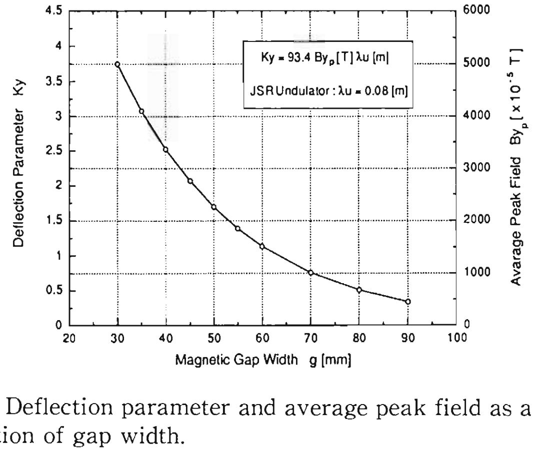


Fig. 4. Deflection parameter and average peak field as a function of gap width.

* JAERI (Japan Atomic Energy Research Institute), SPring-8 Project Team.

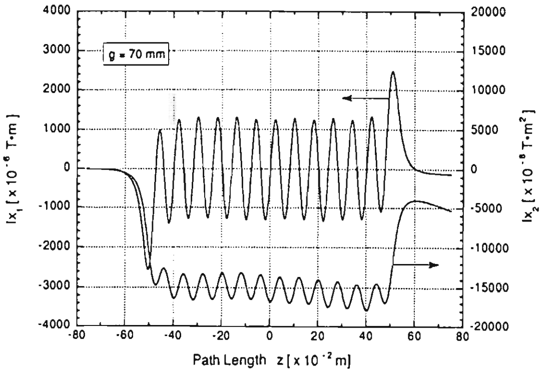


Fig. 5. 1st and 2nd integration of vertical magnetic field at 70 mm gap width as a function of path length. The definitions of $Ix_1(z)$ and $Ix_2(z)$ are given in the text.

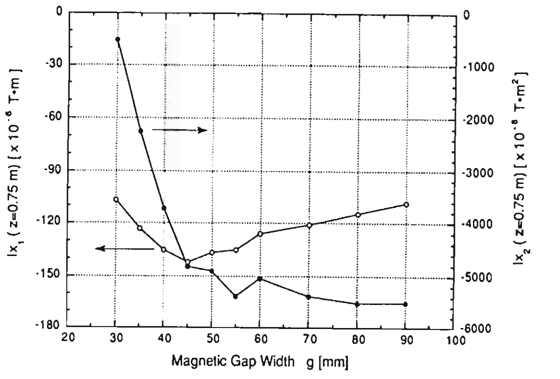


Fig. 6. 1st, $Ix_1$ (z=0.75 m), and 2nd integration, $Ix_2$ (z=0.75 m), of vertical magnetic field, which are integrated in the measured interval from −0.75 m to 0.75 m, as a function of gap width. The definitions of $Ix_1(z)$ and $Ix_2(z)$ are given in the text.

A least squares fit was made to the measured 10 data points with eq. (1), and Br was found to be 1.147 T, whereas the nominal value of Br of the magnetic material, Nd-Fe-B, is 1.223 T. In Fig.4, deflection parameter, Ky, is shown, which is calculated with the average peak field.

In order not to disturb the closed orbit of the electron in the storage ring, it is necessary to have the horizontal and vertical angles and displacements to be zero at the exit of undulator when installed in a straight section. The horizontal and vertical angles ($\Delta\theta_x$,$\Delta\theta_y$) and displacements ($\Delta x$,$\Delta y$) as a function of path length, z, can be expressed as follows:

$$\Delta\theta_x(z)[\mathrm{rad}]=\frac{e}{m_e c\gamma}Ix_1(z)=\frac{0.299}{Ee[\mathrm{GeV}]}Ix_1(z)[\mathrm{T\cdot m}], \quad (2)$$

$$\Delta\theta_y(z)[\mathrm{rad}]=\frac{e}{m_e c\gamma}Iy_1(z)=\frac{0.299}{Ee[\mathrm{GeV}]}Iy_1(z)[\mathrm{T\cdot m}], \quad (3)$$

$$\Delta x(z)[\mathrm{m}]=\frac{e}{m_e c\gamma}Ix_2(z)=\frac{0.299}{Ee[\mathrm{GeV}]}Ix_2(z)[\mathrm{T\cdot m^2}], \quad (4)$$

$$\Delta y(z)[\mathrm{m}]=\frac{e}{m_e c\gamma}Iy_2(z)=\frac{0.299}{Ee[\mathrm{GeV}]}Iy_2(z)[\mathrm{T\cdot m^2}], \quad (5)$$

where e is the elementary charge, $m_e$ is the electron mass, c is the velocity of light, $\gamma$ is called the 'relativistic energy factor' that is the ratio of the total electron energy to the rest mass, 511 keV, Ee is the electron energy, and $Ix_1$, $Iy_1$, $Ix_2$ and $Iy_2$ are defined as :

$$Ix_1(z)[\mathrm{T\cdot m}]=\int_{-\infty}^{z}By(z_1)[\mathrm{T}]dz_1[\mathrm{m}], \quad (6)$$

$$Iy_1(z)[\mathrm{T\cdot m}]=\int_{-\infty}^{z}Bx(z_1)[\mathrm{T}]dz_1[\mathrm{m}], \quad (7)$$

$$Ix_2(z)[\mathrm{T\cdot m^2}]=\int_{-\infty}^{z}\int_{-\infty}^{z_1}By(z_2)[\mathrm{T}]dz_2[\mathrm{m}]dz_1[\mathrm{m}], \quad (8)$$

$$Iy_2(z)[\mathrm{T\cdot m^2}]=\int_{-\infty}^{z}\int_{-\infty}^{z_1}Bx(z_2)[\mathrm{T}]dz_2[\mathrm{m}]dz_1[\mathrm{m}], \quad (9)$$

Figure 5 shows $Ix_1(z)$ and $Ix_2(z)$ at 70 mm gap width calculated by using measured field, By(z), as a function of the path length, z. Figure 6 shows $Ix_1$ (z=0.75 m) and $Ix_2$ (z=0.75 m) as a function of the gap width, which are integrated in the measured interval from -0.75 m to 0.75 m. These remained field integrations, $Ix_1$ and $Ix_2$, have to be compensated in some way, such as by using the steering magnets.

The JSR undulator is installed in a straight section of JSR without steering magnets, and undulator radiation in the visible light region is observed.[4]

References

1) H. Yokomizo, K. Yanagida, S. Harada, K. Mashiko, M. Yokoyama, H. Hashimoto, K. Nakayama, M. Kabasawa, T. Harami, and Y. Suzuki : *Nucl. Instrum. Methods,* **A291**, 472 (1990).
2) J. Ohnishi, H. Takebe, K. Kumagai, and S. Motonaga : to be published to Proc. 12th Int. Conf. on Magnet Technology.
3) K. Halbach : *Nucl. Instrum. Methods,* **A187**, 109 (1981).
4) K. Yanagida, S. Sasaki, T. Nagai, N. Matsuki, T. Takada, and H. Yokomizo : Proc. 8th Symp. on Accel. Sci. and Tech., p.338 (1991).

RIKEN Accel. Prog. Rep. **25** (1991)

# V-2-35. Magnetic Field Measurements on SPring-8 Prototype Undulator

T. Takada, N. Matsuki,* and S. Sasaki*

Magnetic field of the SPring-8 prototype undulator was measured. The parameters of this device are shown in Table 1 and its photograph is shown Fig. 1.

The SPring-8 prototype undulator was designed as planar type with a wedged-pole hybrid configuration. One of the advantages of the wedged-pole hybrid design[1] is its higher magnetic field strength on-axis than that of a pure permanent magnet type (Halbach design) and a conventional hybrid type undulators for the same magnetic gap width range available, that is, a wider tunability of photon energy for experiments is expected. The measurement of the vertical component of the magnetic field, By, on-axis was done for 21 different gap widths. The peak values of the periodic sinusoidal field on-axis were averaged, and the average peak fields are shown in Fig. 2 with open circle as a function of the magnetic gap width.

Table 1. Parameters of a SPring-8 prototype undulator

| | | |
|---|---|---|
| Configuration | Wedged-pole hybrid type [1] | |
| | Planar type | |
| Magnet block material | Nd-Fe-B alloy | |
| Nominal remnant field | Br [T] | 1.1 |
| Pole material | Vanadium permendur | |
| Magnetic period length | λu [m] | 0.033 |
| Number of poles | Np | 123 |
| Number of periods | Nu = Np / 2 | 61.5 |
| Total length | Lu [m] = λu [m] • Nu | 2.0295 |
| Minimum magnetic gap width | g [mm] | 13.5 |
| Maximum average peak field on-axis | $By_p$ [T] | 0.587 |
| Maximum deflection parameter | Ky = 93.4 $By_p$ [T] • λu [m] | 1.806 |

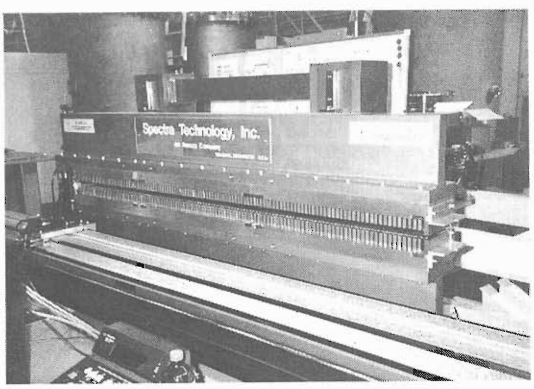

Fig. 1. Photograph of the SPring-8 prototype undulator with the magnetic measurement system.

* JAERI (Japan Atomic Energy Research Institute), SPring-8 Project Team.

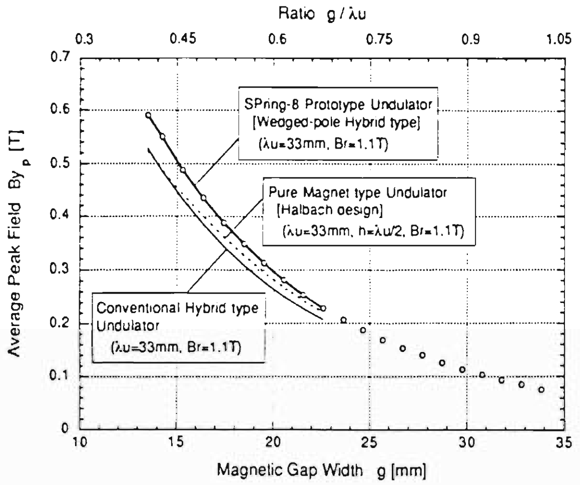


Fig. 2. Peak magnetic field on-axis as a function of magnetic gap width for the SPring-8 prototype (wedged-pole hybrid type), the pure permanent magnet type and the conventional hybrid type undulators.

The peak field on-axis as a function of the magnetic gap width for the pure permanent magnet type undulator is expressed by the following analytical formula[2]:

$$By_p(g)[T] = 2Br[T]\frac{\sin(\pi/4)}{(\pi/4)}\exp\left(-\pi\frac{g[m]}{\lambda u[m]}\right) \times \left[1-\exp\left(-2\pi\frac{h[m]}{\lambda u[m]}\right)\right], \quad (1)$$

where $By_p$ is the peak field on-axis, g is the magnetic gap width, Br is the remnant field of permanent magnet, λu is the magnetic period length and h is the height of magnet block. The peak field on-axis for the hybrid type undulator is expressed as following semi-emprical formula[3]:

$$By_p(g)[T] = 0.95a[T] \exp\left[-b\frac{g[m]}{\lambda u[m]}+c\left(\frac{g[m]}{\lambda u[m]}\right)^2\right], \quad (2)$$

where the factor 0.95 represents the "filling factor" of the high permeability blocks in the undulator assembly. For a conventional hybrid type undulator based on Nd-Fe-B permanent magnet blocks and vanadium permendur configuration, three coefficients a, b and c are given by[4)]

$$a[T] = 0.55Br[T] + 2.835, \quad (3)$$
$$b[\text{non-dimension}] = -1.95Br[T] + 7.225, \quad (4)$$
$$c[\text{non-dimension}] = -1.3Br[T] + 2.97, \quad (5)$$

where Br is the remnant field of Nd-Fe-B permanent magnet, and these expressions are valid for

$0.9 \leq$ Br $\leq 1.1$ and only in the interval $0.07 \leq g/\lambda u \leq 0.7$. When Br is 1.1 T, the peak field on-axis for the conventional hybrid type undulator is given by

$$By_p(g)[T] = 0.95 \times 3.44[T] \exp\left[-5.08\frac{g[m]}{\lambda u[m]} + 1.54\left(\frac{g[m]}{\lambda u[m]}\right)^2\right]. \quad (6)$$

On the other hand, a least squares fit was made[5] using 10 data points in the interval of $0.07 \leq g/\lambda u \leq 0.7$, during the measured 21 data points with eq. (2). The fitted function was found to be represented by

$$By_p(g)[T] = 0.95 \times 3.02[T] \exp\left[-4.12\frac{g[m]}{\lambda u[m]} + 0.63\left(\frac{g[m]}{\lambda u[m]}\right)^2\right]. \quad (7)$$

The fitted line to 10 data points is shown in Fig. 2 with bold line. In the interval $0.41 \leq g/\lambda u \leq 0.7$, that corresponds to 13.5 mm (minimum gap width) $\leq g \leq 23.1$ mm, the SPring-8 prototype undulator has always a higher magnetic field on-axis and gives an about 10 % wider field range than those of the pure permanent magnet type (dotted line) with the height of magnet block, h, of half period length and the conventional hybrid type (solid line) undulators whose remnant field and period length are the same as those of the SPring-8 prototype undulator.

The spectral angular flux density at zero electron beam emittance was calculated with the measured magnetic field distribution, and it was compared with the spectrum calculated with an ideal sinusoidal magnetic field in order to estimate the reduction due to the magnetic field error. As a result[6], the reduction of peak intensities and shift of photon energy at the peak intensity are remarkable for higher odd harmonics. The reduction of peak intensities for the fundamental, third and fifth harmonics are about 1 %, 13 % and 30 %, respectively.

References

1) D. C. Quimby and A. L. Pindroh : *Rev. Sci. Instrum.*, **58**, 339 (1987).
2) K. Halbach : *Nucl. Instrum. Methods.*, **A187**, 109 (1981).
3) K. Halbach, *et al.*: *ibid.*, **A208**, 117 (1983).
4) 6 GeV Synchrotron X-ray Source, Conceptual Design Report Supplement A, LS-52, Argonne National Laboratory (1986).
5) S. Sasaki, T. Takada, N. Matsuki, S. Sasaki, and H. Ohno : Contributed to IEEE 1991 Particle Accelerator Conf., San Francisco, U.S.A., May 6-9 (1991).
6) S. Sasaki, N. Matsuki, and T. Takada: to be published to *Rev. Sci. Instrum.*, **63**, No.1 (1992). (Contributed to be 4th SRI Conf., Chester, U.K., July 15-19, 1990.)

RIKEN Accel. Prog. Rep. **25** (1991)

# V-2-36. Effect of Electrode Displacement on the Measurement Accuracy of Beam Position Monitors for the SPring-8 Storage Ring

S. Sasaki

The beam position monitors (BPMs) used for the SPring-8 storage ring will be a type of capacitive pickup with four electrodes. Their measurement accuracy on electron beam transverse positions has large significance in performance of the storage ring. The overall accuracy is required to be within 100 $\mu$m for each BPM from the beam dynamics analysis; better than 50 $\mu$m is desirable.

The measurement accuracy depends on various factors such as electronic noise of the signal processing electronics, mechanical accuracy of the machining of electrodes and chambers, mechanical accuracy of the installation of BPMs, and so forth. This report presents the first results of the experimental measurement of the effect of the electrode displacements on the measurement accuracy of the BPM.

For the experiment a test chamber was used, which is schematically described in Fig.1. The electrodes can be moved along its axes guided by the screws embedded on the chamber, whose pitch is 0.5 mm / rotation. A diagram of the experimental set up is depicted in Fig. 2. The antenna was moved in transverse direction to scan the $\pm$7-mm region in the x-y plane. The position data were deduced from the signals on each electrode according to the following equations:

$$\Sigma = V_1+V_2+V_3+V_4,$$
$$\Delta_x = (V_1+V_4)-(V_2+V_3),$$
$$\Delta_y = (V_1+V_2)-(V_3+V_4),$$
$$u = \Delta_x/\Sigma,$$
$$v = \Delta_y/\Sigma,$$

where u and v are non-dimensional quantities proportional to x and y in a good linearity region, respectively, and $V_1$ through $V_4$ are the voltage induced on electrodes 1 to 4; the correspondence of the electrodes and their numbers are described in Fig. 1. The 508.58-MHz sinusoidal wave signals were input from a synthesized signal generator through a coaxial cable antenna, which was positioned by an x-y-z stage driven by stepping motors. The antenna covered the $\pm$7-mm region with a 1-mm step size in the x-y plane. At each point, the antenna position (x, y) and the voltage signal arisen on each electrode were recorded. The voltage signals were taken by a spectrum analyzer tuned to 508.58 MHz through a coaxial switch to select one of the four electrodes. All the experimental devices were controlled by a Macintosh personal computer through a GPIB.

The measurements were performed for the five settings, in which the electrode No.3 was inserted and drawn back with 1 mm and 2 mm from the reference position, and the reference setting. After the measurements in each setting, correction factors proposed by Lambertson were measured and multiplied.[1] These correction factors

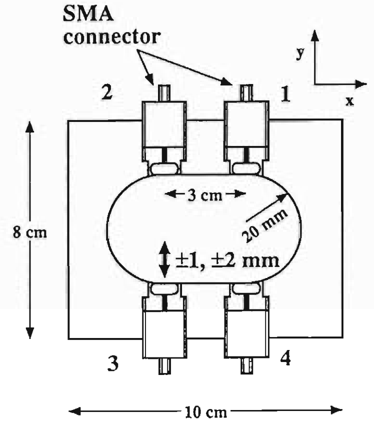


Fig. 1. Schematic cross sectional drawing of the BPM test chamber.

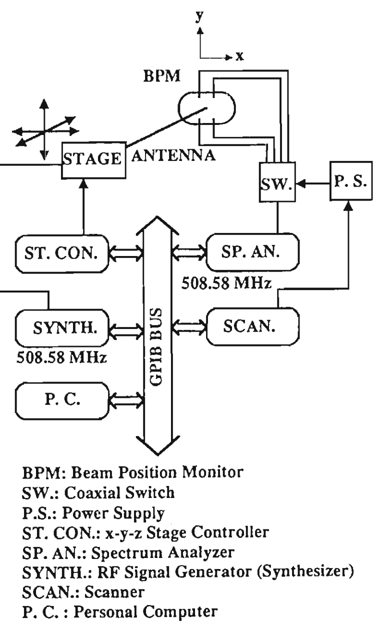


Fig. 2. A diagram of the experimental setup.

were at first proposed so that the factors can cancel out the channel to channel deviations of the electrical signals arisen from attenuation and amplification deviations of each channel electronic circuits and cables. Adopting this correction with some symmetry assumptions, mechanical and electrical centers of the BPM chamber agree with good precision. In the reference, Lambertson suggested the possibility to correct the small electrode displacements by this correction method.

An example of the measured data is shown in Fig. 3, each dot in the figure represents (u,v)-data at a certain position (x,y) with 1 mm step size. The origin, $x=y=0$, was defined as the point where u and v have the values close to zero as far as possible. The resolution of the measuring system is a few tens micro meters when converted to the position resolution, which is approximately consistent with the 8-bit vertical resolution of the spectrum analyzer. The sensitivity of the electric signal to the position was deduced from the measurement and found to be $\partial x/\partial u=16$ mm and $\partial y/\partial v=19$ mm near $x=y=0$. To see the effect of the electrode displacement, $\Delta x=\Delta u \partial x/\partial u$, and $\Delta y=\Delta v \partial y/\partial v$ are plotted against the displacement, where $\Delta u$ and $\Delta v$ are defined as follows;

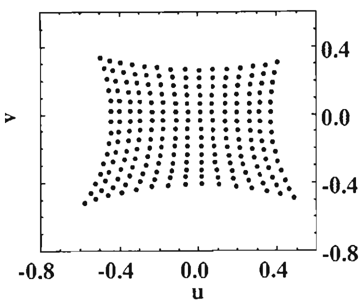


Fig. 3. An example of the measured mapping data.

$$\Delta u = u\,|_{x=y=0,\ \text{for displaced setting}} - u\,|_{x=y=0,\ \text{for reference setting}},$$
$$\Delta v = v\,|_{x=y=0,\ \text{for displaced setting}} - v\,|_{x=y=0,\ \text{for reference setting}}.$$

The sign of displacements is defined as follows; when the electrode is inserted into the inner area of the chamber, displacements has positive values.

Without the correction mentioned above, the values of $\Delta x$, $\Delta y$ are twice as big as the displacement values as shown in Fig. 4. However with the correction, they are reduced to one order of magnitude smaller values than those without the correction. This result shows that the displacement of electrodes has very little effects on the position measurement accuracy, provided that the correction is properly performed. Also the requirements to the machining accuracy of the chamber and the electrode positioning mechanism are not very strict; about 100-$\mu$m mechanical accuracy will be enough as far as the electrode displacements along their axes are concerned.

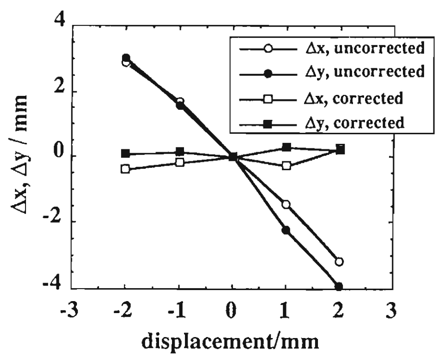


Fig. 4. Position measurement errors against the electrode displacement.

References

1) G. R. Lambertson: LASP Note-5, May 6 (1987); J. Hinkson: private communication.

# V-2-37. The Real Time Operating System of Front-End Processors for the SPring-8

T. Masuda, T. Nakamura, T. Wada, and Z. Wang

Accelerator complex of the SPring-8 is composed of a 1 GeV linac, an 8 GeV synchrotron and a main storage ring. The control system of the SPring-8 facility consists of a central control system and several sub-systems for each accelerator. Each sub-system consists of a host computer and several front-end processors (FEP) and an operator's console. These distributed computers are linked by a computer network. For upper hierarchy level computers such as a sub-system host computer, we use workstations (WS) which have the UNIX operating system. For lower hierarchy level FEPs such as VME (Versa Module European) systems, the real time operating system is adopted. For these operating systems, there are many commercially available real time operating systems, for examples, VRTX 32, pSOS +, VxWorks, PDOS and OS-9000.[1] We have introduced LynxOS for the R&D study of control of a klystron test bench, and OS-9 for that of a linac.

LynxOS is a product of Lynx Real Time Systems Inc., and one of the real time operating systems called "real time UNIX". It copes with multi-user and multi-tasking with a preemptive, priority-based task scheduler.

LynxOS is developed with emphasis on standardization and open systems. It has source level compatibility with a UNIX BSD 4.3 and binary level compatibility with a UNIX system V.3 (SVR3). And also LynxOS complies with POSIX 1003.1 (Application Program Interface) and POSIX 1003.4 (Real Time Extensions). POSIX (Portable Operating System Interface for Computer Environments) is a standard operating system proposed by the IEEE committee. Hence, LynxOS provides an almost complete UNIX developing environment, really we can use the "UNIX standard environment" such as X Window, TCP/IP (Transmission Control Protocol / Internet Protocal) and NFS (Network File System).

LynxOS is currently operated on many platforms which have a CISC chip such as i80386/486 and M680x0, and a RISC chip such as i860, M88000 and MIPS. In the future, LynxOS will support RS6000 and SPARC. The LynxOS for the SPARC will be binary compatible with a Unix System V.4 (SVR4). Hence, we will be able to use it on some kinds of workstations.

The kernel size of LynxOS is about 190KB, which is relatively small for these functions, and

Table 1. Examples of some real time operating systems.

| OS Name | | VRTX32 | pSOS+ | VxWorks | OS-9000 | LynxOS | PDOS |
|---|---|---|---|---|---|---|---|
| Company | | Ready Systems | Software Components | Wind River | Microware Systems | Lynx Real-Time S | Eyring Reseach I |
| Microprocessor | | 680X0, 80X86 SPARC | 680X0 80386 | 680X0 | 80386, i486 | 680X0, 80X86 i860, 88000 | 680X0 |
| Bus | | not fixed | not fixed | VME bus | not fixed | not fixed | |
| Network | | Ethernet | Ethernet | Ethernet | Ethernet | Ethernet | Ethernet |
| Protocol | | TCP/IP | TCP/IP | TCP/IP | TCP/IP | TCP/IP | TCP/IP |
| Kernel Size (KB) | | 8 | 11.5～13 | 60～465 | 53 | 190 | 25 |
| Task | Max. no. | 256 | 65535 | 65535 | No Limit | No Limit | |
| | Priority | 256 | 255 | 255 | 65536 | 32 | 225 |
| Multi-Processor | Bus | ○ | ○ | ○ | × | ○ | ○ |
| | Network | ○ | ○ | ○ | × | ○ | |
| File System | | MS-DOS | Dedicated, MS-DOS | RT-11, UNIX, MS-DOS | Dedicated, MS-DOS | i-node | |
| Exec. Time | Switching | 15μs | 19μs | 17μs | 220μs | 13μs | 26.2μs |
| | Interrupt Wait Time | 10μs | 7μs | 8μs | 40μs | 30μs | |
| | Measured Condition | 68020, 25MHz 1 Wait | 68020, 25MHz no Wait | 68020, 25MHz no Wait | 80386, 20MHz | 80386, 33MHz | 68020, 20MHz |
| AP Language | | C, ASM, Ada | C, ASM, Ada | C, ASM, Ada FORTRAN | C, ASM | FORTRAN, C ASM, Ada | FORTRAN, C |
| Environment for Devlopment | | UNIX, VMS | UNIX | UNIX | OS-9, UNIX OS-9000 | self UNIX | self UNIX |
| Remark | | V20/30/40/50, Gmicro | i860, 80960, 88000, 29000 | 68040, SPARC 80960 | VM86000, 68020/30 88000 | SPARC PS6000, HP | |

it is ROMable. Hence, it also enables us to use for the embeded systems.

We have purchased LynxOS 1.2.1 for Motorola MVME147 with TCP/IP software in September. It has been installed in a Motorola VME Delta system. Installation is relatively easy. However manuals and support for the installation were not adequate. We spent much time for installing LynxOS with unluckiness that it was installed in the VME system which had been used ever for OS-9.

As the default LynxOS shell is a dl shell (dlsh), it is not compatible with Bourne shell (bsh) nor Korn shell (ksh) nor with C shell (csh).

LynxOS is still young, hence what we are anxious about is errors (bugs) in it.

We need to consider the other real time operating systems. Table 1 shows some of the real time operating systems which we consider. OS-9, which is not in the table, has much reliability and it enables us to use many funds based on the relatively long and much use.

We intend to use expert systems mainly for the alarm message handling system, and partly for automatic operations. Introducing an AI tool "NEXPERT OBJECT", a feasibility study of an expert system for the operation of a test stand of a klystron is started.

References

1) K. Low, S. Acharya, M. Allen, E. Faught, D. Haenni, and C. Kalbfleiso: Proc. IEEE 1991 Particle Accel. Conf., San Francisco (1991).

RIKEN Accel. Prog. Rep. **25** (1991)

# VI. RADIATION MONITORING

## 1. Residual Radioactivity in the 160 cm Cyclotron and Its Surrounding Facilities

I. Kohno, M. Miyagawa, Y. Matsuzawa, S. Kagaya, H. Kato, and T. Katou

Residual $\gamma$-ray-emitting radio-nuclides in components of the RIKEN 160 cm cyclotron and its surrounding facilities were measured with a HPGe detector. These measurements were made before disassembling of the cyclotron and its surrounding facilities at about one year after the shutdown of the machine.

The cyclotron was shut down at the end of April 1990 after 23 years operation. During these 23 years the cyclotron was typically in use for 4000 to 5000 hours/year and produced beams of p, d, $^{3}He$, $^{4}He$ and light heavy ions ($^{12}C$, $^{14}N$, $^{16}O$, and $^{20}Ne$). Accelerated beam energies ranged from 5 to 16 MeV for p, 8 to 25MeV for d, 18 to 45 MeV for $^{3}He$, 16 to 50 MeV for $^{4}He$ and the internal currents of these beams were 10 to 50 $\mu$A. Heavy ions were accelerated at the energy from 60 to 150 MeV and the average internal

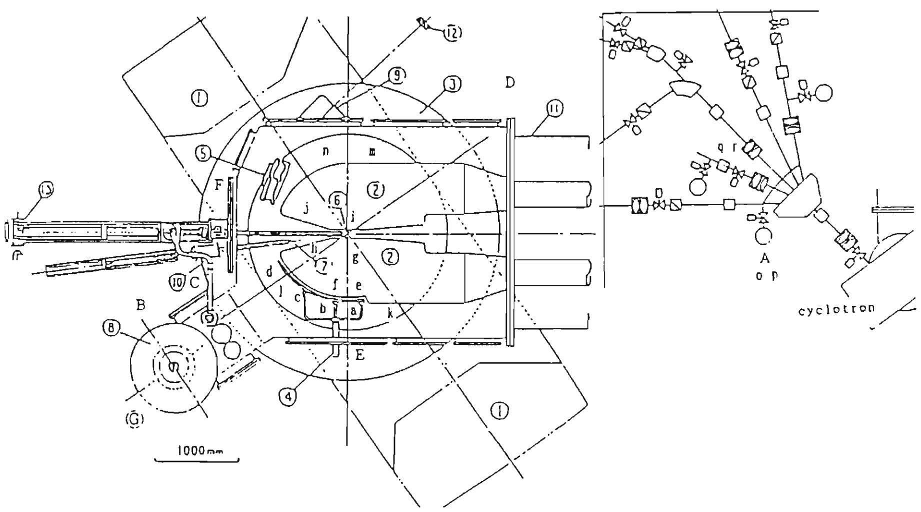

Fig. 1. Schematic view of the accelerating chamber arrangement and beam transport system.
1,Side yoke; 2,Dees; 3,Coiltank; 4,RF-deflector; 5,Beam focusing magnetic channel; 6,Ion source; 7,Beam probe; 8,32" oil diffusion pump; 9,Beam exit flange; 10,Exaust pipe for ion source; 11, Oscillator tank; 12, Gate drop probe; 13,Winch
A,B,C,D,E,F, and G indicate points where $\gamma$-ray was measured. point G is outside the bottom part of a diffusion pump.
Small alphabets indicate the points smeared. a,b,c,d, deflector electrode; e,f,septum electrode; g,h,i,j,Dees; k,l,m,n,earth plate; o,p,q,r,inside the slit box.

currents were about 1 e $\mu$A. At these energies and currents measurable levels of radioactivity were produced in the cyclotron and its surrounding facilities. For the purpose of discussing the possibility of disassembling of these facilities, it is necessary that is available the quantitative information on the degree of radioactivation.

$\gamma$-ray dose rates were measured at various points (A~G) outside the cyclotron at the same height as the beam line and the slit box as shown in Fig.1, with an ionization-chamber survey meter and a NaI scintillation survey meter. Table 1 summarizes the dose rates measured. $\gamma$-

Table 1. $\gamma$-ray dose measurd around the cyclotron. Alphabets indicate detection points.(see Fig.1)

| Detection point | NaI scintillation survey meter ($\mu$Sv/h) | Ionization chamber survey meter ($\mu$Sv/h) |
|---|---|---|
| A | | 1.4 |
| B | 2.9 | 1.5 |
| C | 8.0 | 8.0 |
| D | 1.0 | 0.8 |
| E | 9.5 | 7.0 |
| F | 5.5 | 4.0 |
| G | 4.0 | 2.4 |

ray spectra were measured with a HPGe detector at various points (A～G) to assign radionuclides. Radioactive nuclides assigned are $^{22}Na$, $^{54}Mn$, $^{56}Co$, $^{60}Co$, and $^{65}Zn$. $\gamma$-ray spectra of small samples smeared out from several materials (a～r in Fig.1) inside the vacuum chambers were measured. Radioactive nuclides assigned are $^{22}Na$, $^{54}Mn$, $^{60}Co$, $^{65}Zn$, $^{182}Ta$, $^{183}Re$, $^{184m}Re$, and $^{185}Os$. $^{182}Ta$, $^{183}Re$, $^{184m}Re$, and $^{185}Os$ were found in the samples smeared out from the deflector electrode and the septum (made of tungsten metal strip). As was expected, we found only long lived nuclides.

# VI-2. Routine Monitoring of the 160cm Cyclotron, RILAC, and TANDETRON

I. Sakamoto, K. Ogiwara, M. Yanokura, T. Kobayashi, M. Iwamoto, and I. Kohno

Routine radiation monitoring was carried out for the 160cm cyclotron, RILAC, and TANDETRON from January to September 1991.

(1) Residual activities of the cyclotron

In February 1991, the dose rates due to residual activities of the machine were measured at 9.5 months after the machine shutdown; the result is shown in Fig. 1.

(2) Contamination in the cyclotron building

Surface contamination was below $10^{-2}$ Bq/cm$^2$ on the floors of the cyclotron building.

Radioactive substances were handled in the hot laboratory and tow chemical laboratories. The radioactivity at the exit of the draft chambers was found to be small, of the order of $10^{-8}$ Bq/cm$^3$.

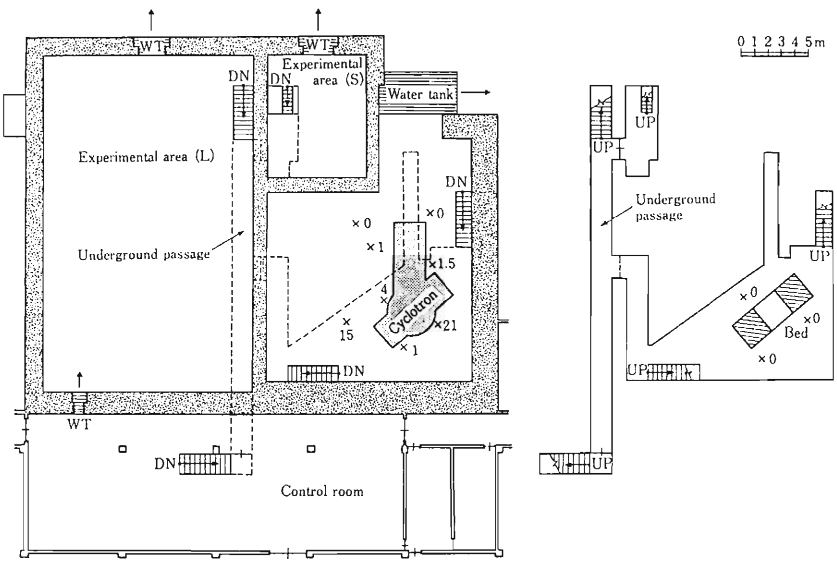


Fig. 1. Residual activities (1 cm dose-equivalent in $\mu$Sv/h) of the cyclotron.

(3) Contamination of drainages

Radioactivities in the drain water from the cyclotron and the RILAC buildings were found to be of the order of $10^{-4}$ Bq/cm$^3$. The total activity in aqueous effluents was 15 kBq.

(4) Radiation monitoring of RILAC and TANDETRON

The leakage radiation during operation of RILAC was measured outside the RILAC building every three months. No leakage of $\gamma$ rays and neutrons from the RILAC building was detected. No contamination due to residual activities was found on the floors of controled area and in conditioned air in the RILAC building.

X-ray monitoring was carried out for TANDETRON, when an aluminum target was bombarded with 1.5 MeV He$^+$ ions of 1 nA. The maximum irradiation dose rate measured around TANDETRON was 1 $\mu$Sv/h. No leakage of X-rays was detected around the target chamber and outside the TANDETRON room.

RIKEN Accel. Prog. Rep. **25** (1991)

# VI-3. Exposure Dose Monitoring of RIKEN Accelerator Workers

M. Miyagawa, I. Sakamoto, T. Katou, Y. Matsuzawa,
S. Kagaya, H. Kato, and I. Kohno

The external exposure doses received by RIKEN accelerator workers(374 persons) were measured by using $\gamma$ ray and neutron film badges. The external doses from January to March, 1991, are given in Table 1. One nuclear chemist gave the external dose of 0.1 mSv owing to $\gamma$ ray. The external doses owing to thermal and fast neutron exposures were below the detection limit.

Table 1. External exposure doses (effective dose-equivalent in mSv) received by RIKEN accelerator workers from January to March, 1991.

| Workers | Number of persons | | | | Collective dose (mSv) |
|---|---|---|---|---|---|
| | Dose undetectable | 0.1-1 (mSv) | > 1 (mSv) | Total | |
| Accelerator physicists and Operators# | 46 | 0 | 0 | 46 | 0 |
| Nuclear physicists | 105 | 0 | 0 | 105 | 0 |
| Reserchers in other fields | 198 | 1 | 0 | 199 | 0.1 |
| TANDETRON workers | 17 | 0 | 0 | 17 | 0 |
| Health physicists | 7 | 0 | 0 | 7 | 0 |
| Total | 373 | 1 | 0 | 374 | 0.1 |

# Operators: For RIKEN Ring Cyclotron and RILAC.
Average dose per person, 0.0002mSv; maximum individual dose, 0.1mSv.

RIKEN Accel. Prog. Rep. 25 (1991)

# VI-4. Residual Activities in the Ring Cyclotron Facility

S. Fujita, S. Okamoto, N. Nakanishi, I. Sakamoto, and T. Inamura

Residual activities have routinely been measured at various points in the RIKEN Ring Cyclotron facility every summer and those along the beam lines after every experiment. The results of measurements have been reported annually since 1986.

Figure 1 shows the variation of residual activities at the deflectors of the Ring Cyclotron and the injector AVF cyclotron. The residual activity at the deflector of the Ring Cyclotron from 1986

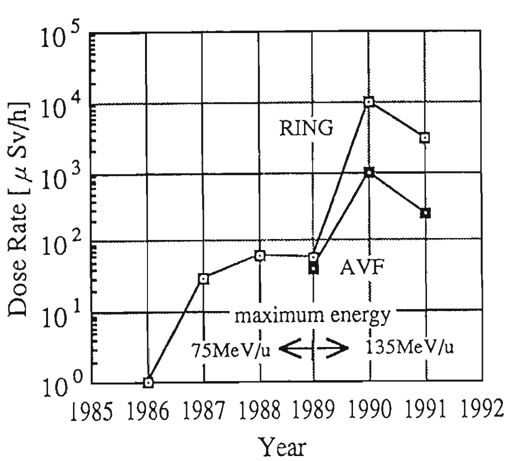


Fig. 1. Variation of the residual activities of the deflectors of the RIKEN Ring Cyclotron and the injector AVF cyclotron.

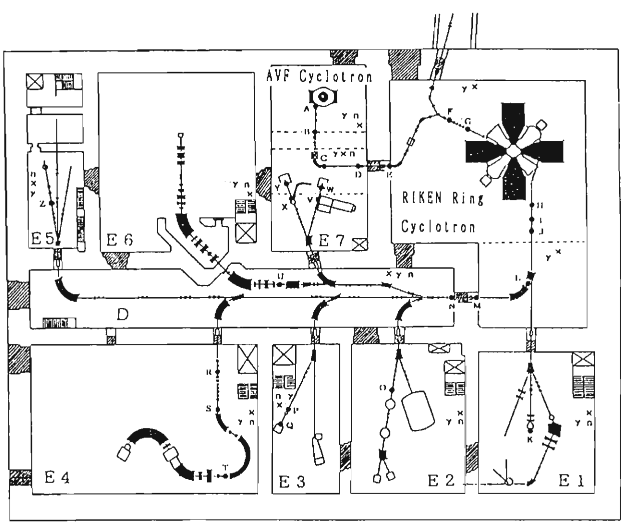


Fig. 2. Layout of the RIKEN Ring Cyclotron facility as of 1991. Monitoring positions are denoted by ×. Detection points of residual activities on the beam lines are denoted by alphabets.

Table 1. Summary of the residual activitics measured along the beam lines. Alphabets indicate the detection points in Fig. 3.

| Detection point | Ionization chamber survey meter ($\mu$Sv/h) | Date |
|---|---|---|
| A | 10 | Jun. 20, 1991 |
| B | 40 | Jun. 20, 1991 |
| C | 10 | Jun. 20, 1991 |
| D | 20 | Jun. 20, 1991 |
| E | 70 | Nov. 21, 1990 |
| F | 29 | Nov. 21, 1990 |
| G | 55 | Nov. 21, 1990 |
| H | 65 | Apr. 22, 1991 |
| I | 95 | Nov. 21, 1990 |
| J | 25 | Apr. 22, 1991 |
| K | 15 | Mar. 7, 1991 |
| L | 25 | Apr. 22, 1991 |
| M | 40 | Apr. 22, 1991 |
| N | 25 | Dec. 3, 1990 |
| O | 45 | Dec. 7, 1990 |
| P | 22 | Nov. 21, 1990 |
| Q | 120 | Nov. 21, 1990 |
| R | 40 | Jun. 18, 1991 |
| S | 40 | Feb. 16, 1991 |
| T | 11 | Feb. 16, 1991 |
| U | 1800 | Jun. 3, 1991 |
| V | 310 | Oct. 14, 1991 |
| W | 130 | Oct. 14, 1991 |
| X | 400 | Jun. 14, 1991 |
| Y | 1200 | Jun. 14, 1991 |
| Z | 13.5 | Jun. 14, 1991 |

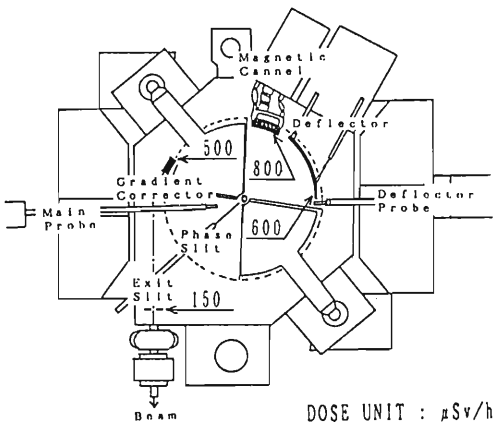


Fig. 3. Dose rates detected inside the injector AVF cyclotron. They are given in a unit of $\mu$Sv/h.

to 1988 was several tens $\mu$Sv/h, but it has become several thousands $\mu$Sv/h since 1990. This is due to the increase in maximum energy of the beam from the Ring Cyclotron from 75 MeV/nucleon to 135 MeV/nucleon.

The points where residual activities were measured along the beam lines and detected dose rates were above 10 $\mu$Sv/h are shown in Fig.2. Table 1 summarizes the detected dose rates and dates. In this period, the highest residual activity recorded along the beam line was 1800 $\mu$Sv/h at the point U ( the production target chamber of RIPS ) in the beam distribution corridor.

Besides the above routine measurement, residual activities inside the AVF cyclotron were measured when its acceleration chamber was opened on October 18 because of a trouble in vacuum. The measurement was made with a portable ionization chamber (AE-133/$\Lambda_1$ Applied Engineering Inc.). The results are shown in Fig. 3. The detected dose rates were of the highest level at the AVF cyclotron in this period.

RIKEN Accel. Prog. Rep. **25** (1991)

# VI-5. Leakage Radiation Measurement in the Ring Cyclotron Facility

S. Fujita, N. Nakanishi, T. Shikata, K. Ikegami, T. Takagi,
I. Sakamoto, and T. Inamura

The radiation safety control system has worked steadily this year, performing radiation monitoring continuously and automatically.

From September 28 to 29 and from October 3 to 4, experiments were carried out with 135 MeV/u $^{12}C^{6+}$ and $^{14}N^{7+}$ beams at intensities of about 5 pnA. The beams were stopped at the target point A in the experimental vault E1. Leakage radiation of neutrons from E1 was measured with three neutron dose rate meters, TPS-451S's (Aloka), with a signal out terminal. Each pulse was sent to a pulse counter, TC-532 (TENNELEC). The beam current was read at the target A and recorded with a personal computer, PC-9801RS (NEC), through a beam integrator 439 (ORTEC). Dose rates were normalized with respect to those at 0.1p$\mu$A. We also measured leakage radiation from the Ring Cyclotron at points 11, 12, and 13 when the beam was stopped in the Ring Cyclotron vault. Since we couldn't continuously measure beam currents immediately after the Ring Cyclotron, we measured several instantaneous current values and estimated the average beam current to be 50 enA. Figures 1-(a), (b), and (c) show the target point A and positions where leakage radiation was measured in this experiment. Results are summarized in Table 1. This year, the radiation level in the controlled area has been below the safety limit (1 mSv/week), and the level outside the controlled area has been much less than the safety limit (0.3 mSv/week). Leakage of neutrons has once been recorded with a monitor in a ground-floor computer room just above a bending magnet that guides beams from the Ring Cyclotron vault to the beam distribution corridor ( See Fig. 2). This radiation level, however, is far less than the safety limit (50 $\mu$Sv/year) required

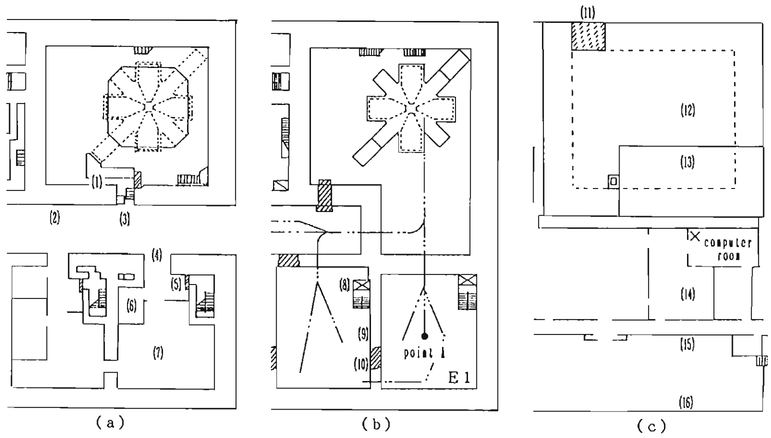


Fig. 1. Partial layout of the RIKEN Ring Cyclotron facility where the leakage radiation measurement was made.
(a) Part of basement 2nd floor;
(b) Part of basement 1st floor;
(c) Part of ground floor.
Leakage-radiation-dose measuring points are denoted by the numbers in parentheses. The monitoring position in the computer room is denoted by ×.

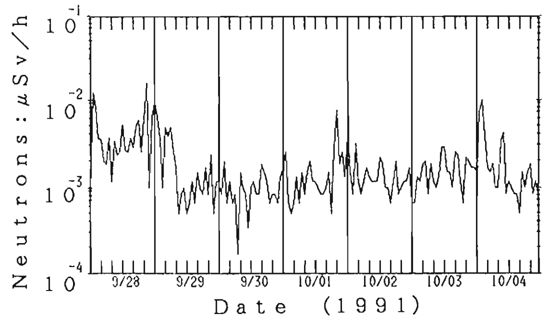


Fig. 2. Daily variation in the radiation level measured in the Ring Cyclotron facility. Detector is a BF3 counter in the computer room.

Table 1. Dose rates of neutron leakage radiation from the target point A in the experimental vault El. (See Figs. 1-(a), (b), (c).) Errors are statistical.

| measured position | $^{12}C^{6+}$(135 MeV/u)+ Fe dose rate μSv/h at 0.1pμA | | $^{14}N^{7+}$(135 MeV/u)+ Fe dose rate μSv/h at 0.1pμA | |
|---|---|---|---|---|
| (1) | 101.7 | ± 1.5 | --- | |
| (2) | 0.051 | ± 0.02 | --- | |
| (3) | 1.18 | ± 0.09 | --- | |
| (4) | 5.65 | ± 0.20 | --- | |
| (5) | 7.02 | ± 0.23 | 8.18 | ± 0.26 |
| (6) | 6.28 | ± 0.21 | 8.12 | ± 0.26 |
| (7) | 43.1 | ± 0.56 | 53.0 | ± 0.66 |
| (8) | 8.75 | ± 0.35 | 7.96 | ± 0.28 |
| (9) | 46.5 | ± 0.80 | 42.7 | ± 0.65 |
| (10) | 46.0 | ± 0.80 | 56.0 | ± 0.75 |
| (11) | 0.085 | ± 0.013 | --- | |
| (12) | 0.070 | ± 0.011 | --- | |
| (13) | 0.096 | ± 0.013 | --- | |
| (14) | 0.249 | ± 0.024 | 0.232 | ± 0.014 |
| (15) | 0.633 | ± 0.038 | 0.538 | ± 0.021 |
| (16) | 0.195 | ± 0.025 | 0.222 | ± 0.014 |

at the boundary of the facility. No leakage of $\gamma$ rays and neutrons was detected with environmental monitors set outside the building in this period.

# VI-6. Measurement of Neutrons Produced by 135MeV/nucleon Nitrogen Ions in an Iron Beam-Stopper with the Activation Method

T. Shikata, N. Nakanishi, K. Ikegami, S. Fujita, S. Nakajima, and T. Kosako

We have only a few data of energy- and angular- distributions of neutrons produced by heavy ion reactions in the energy region of 200 MeV/nucleon. Such data are needed for the shielding calculation for an accelerator facility like as the RIKEN Ring Cyclotron. We have carried out a spectrum measurement of neutrons produced by a 135 MeV/nucleon $^{14}N$ incident on an iron beam-stopper using the foil activation technique in order to reinvestigate the hypothetical spectrum ( 135 MeV/nucleon $^{12}C$ on $^{56}Fe$ ) which was used for the shielding calculation performed previously by some of the present authors. Though it is difficult to get the accurate spectra, mainly because of insufficient activation cross section data in the high energy region, we tried to obtain approximate spectra by extrapolating the cross section curves which were given by McLane et al.[1] and used by Broom et al.[2] and Shin et al,[3] to several 100 MeV.

Activation rate for a given reaction, A, is expressed as

$$A = \Sigma_j\ \sigma(E_j) \cdot \Phi(E_j),$$

where, $\sigma(E_j)$ and $\Phi(E_j)$ stand for the activation cross section and the neutron flux over the j-th energy bin, respectively. When the number of energy bins is larger than that of neutron-induced reactions which are a kind of detectors, the solution cannot be obtained uniquely. Therefore, we get solutions as follows: first, we selected spectra calculated by Fernandez[4] for a 100 MeV/nucleon $^{12}C$ incident on $^{56}Fe$ as an initial spectrum, and second, we attempted to modify these spectra so as to fit the calculated activation rates to measured ones.

In Fig. 1, the cross section curves used are shown. In Fig. 2, the angular dependence of measured activation rates is shown. Activities of $^{11}C$ and $^{194}Au$ decrease remarkably with increasing scattering angle, and the difference between the number of neutrons of energies above 20 MeV in each spectrum, however, is about two orders of magnitude for 0 and 135 degrees, even if the effect of proton-induced reactions in the beam-stopper is subtracted. Figure 3 shows the neutron spectra calculated by Fernandez, the

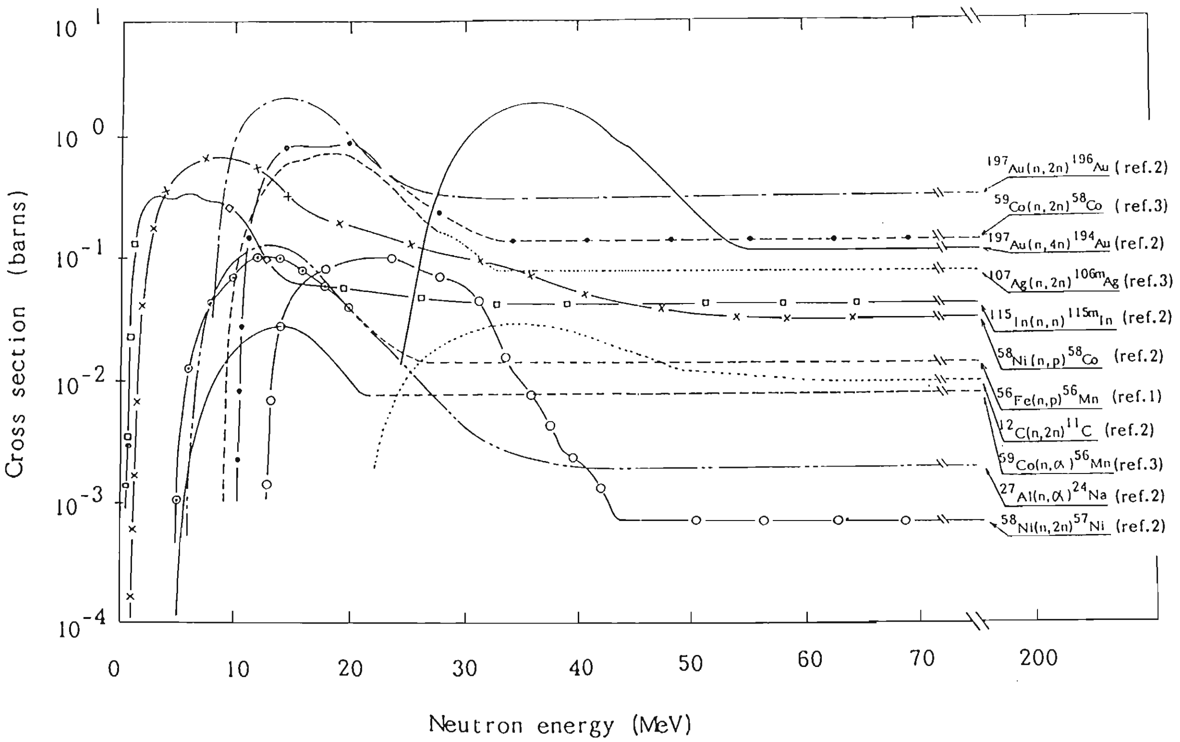


Fig. 1. Response functions.

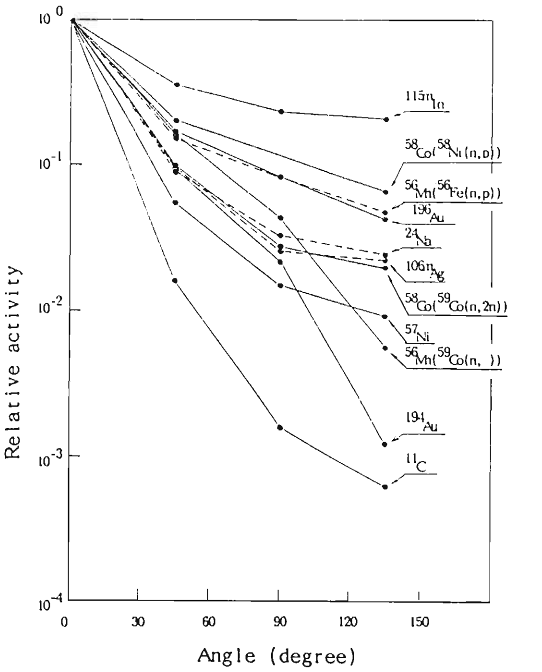


Fig. 2. Angular dependence of activities.

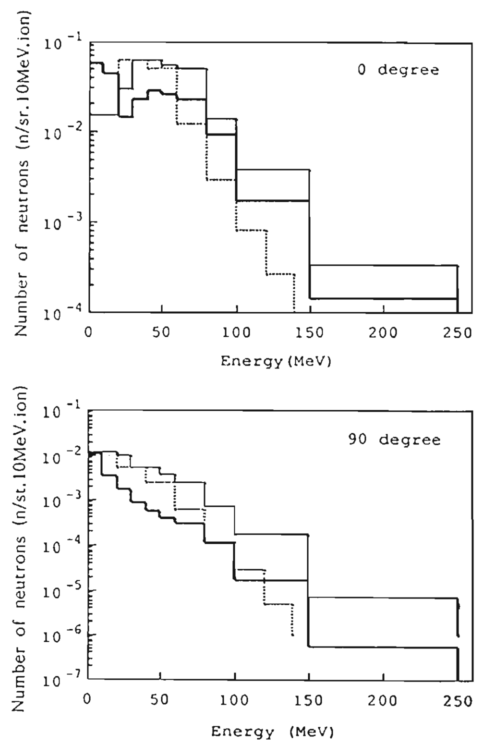


Fig. 3. Energy spectra.
——SC-SPECTRA, ——N-SPECTRA,
······FC-SPECTRA.

hypothetical spectra used for shielding calculations, and those obtained from this experiment (abbreviated as FC-SPECTRA, SC-SPECTRA, and N-SPECTRA, respectively). The distribution of neutrons of N-SPECTRA shows a remarkable forward peaking compared to that for FC-SPECTRA. Under the assumption that the N-SPECTRA and the spectra for a 135 MeV/nucleon $^{12}C$ on an iron beam-stopper have a similar shape, it became evident that the SC-SPECTRA were overestimated at large emission angles, even if the contribution of protons on activation reactions is considered.

References


1) V. McLane, C. L. Dunford, and P. F. Rose : *Neutron Cross Sections,* Vol. 2 (1988).
2) T. A. Broom, D. R. Perry, and G. B. Stapleton : *Health Phys.,* **44**, 487 (1983).
3) K. Shin, T. Saito, M. Fujii, and T. Nakamura : *Nucl. Instrum. Methods,* **187**, 587 (1981).
4) J. Drouet and A. Leleux: D. CEN-S/SPR/SRI/78-342, FRA-066JD/A1, mai (1978).

# VII. LIST OF PUBLICATIONS


1. Accelerator development and accelerator physics

1) M. Kase: "RIKEN Heavy Ion Accelerator Facility", *Indian J. Phys.*, **65**, Part A, No. 5, p. 357 (1991).
2) T. Harami, H. Yokomizo, H. Ohno, M. Hara, and T. Ueki: "Construction Plan of Large Synchrotron Radiation Facility (SPring-8) and Its Application", *J. Atomic Energy Soc. Jpn.*, **33**, 310 (1991).
3) T. Nakagawa: "Effect of Coating on the Plasma Chamber Wall in RIKEN ECR Ion Source", *Jpn. J. Appl. Phys.*, **30,** L930 (1991).
4) T. Nakagawa and T. Kageyama: "The Effect of an Electrode in the First Stage of RIKEN Electron Cyclotron Resonance Ion Source (ECRIS)", *ibid.*, L1588.
5) T. Wada, T. Kambara, I. Yokoyama, K. Shimizu, H. Takebe, M. Nagase, and H. Kamitsubo: "Control System of RIKEN Heavy Ion Accelerator Complex", *ibid.*, p. 2947.
6) R. Nagaoka, K. Yoshida, and M. Hara: "Nonlinear Dynamics with Sextupoles in Low-Emittance Light Source Storage Rings", *Nucl. Instrum. Methods in Phys. Res.*, **A302**, 9 (1991).
7) Y. Yano: "RIKEN Heavy Ion Accelerator Facility", Proc. 4th China-Japan Joint Symp. on Accel. for Nucl. Sci. and Their Applications, p. 18 (1990).
8) M. Hara, S.H. Be, H. Kamitsubo, N. Kumagai, S. Motonaga, R. Nagaoka, Y. Oikawa, S. Sasaki, H. Takebe, I. Takeshita, H. Tanaka, and T. Wada: "Storage Ring Design of SPring-8 8GeV Synchrotron Radiation Facility in Japan", Proc. 2nd European Particle Accelerator Conf. Nice, June 12-16, 1990, **1**, 466 (1991).
9) M. Hara: "Present Status of the SPring-8 (Storage Ring)", Proc. 8th Symp. on Accel. Sci. and Technol., 1991, Saitama, p. 40 (1991).
10) H. Suzuki, T. Kojyo, H. Yonehara, T. Harami, Y. Miyahara, Y. Kawashima, Y. Ohashi, K. Inoue, and M. Hara: "High Power Test of RF Cavity for SPring-8 Booster Synchrotron", *ibid.*, p. 113.
11) T. Nakamura, M. Hara, and H. Tanaka: "Study on a Free Electron Laser at a SPring-8 Long Straight Section", *ibid.*, p. 278.
12) R. Nagaoka, K. Yoshida, and M. Hara: "Nonlinear Dynamics with Sextupoles in Low-Emittance Light Source Storage Rings, Nonlinear Problems in Future Particle Accelerators", World Sci., Singapore, p. 336 (1991).

2. Nuclear physics and nuclear instrumentation

1) K. Nagamine: "X-Ray Spectroscopy of Exotic Atoms", AIP Conf. Proc. 215 on X-Ray and Inner-Shell Processes, Am. Inst. Phys., N.Y., p. 524 (1990).
2) K. Nagamine: "On the Cold Fusion Mediated by Special Particles", *Energy Rev.*, **11**, 48 (1990).
3) K. Nagamine: "Japanese Hadron Facility Plans and Future $\mu$SR", *Hyp. Int.*, **65**, 1149 (1990).
4) K. Ishida, T. Matsuzaki, K. Nagamine, H. Kitazawa, Y. Miyake, and E. Torikai: "Surface Muon Production in Medium Energy Heavy Ion Reaction at RIKEN", *ibid.*, p. 1159.
5) K. Nagamine: "1990 Muon Catalyzed Fusion Int. Conf.", *J. Atomic Energy Soc. Jpn.*, **32**, 1095 (1990).
6) K. Nagamine: "Muon Catalyzed Fusion", Kinou Zairyo, p. 11 (1990).
7) H. Toki: "Production of Pionic Atoms", Int. Workshop on Particle Production near Threshold, Bloomington, Sep. 30-Oct. 3, 1990, AIP, **221,** 223 (1991).
8) H. Ichinose, T. Doke, A. Hitachi, and T. Takahashi: "A Fluctuation of the Pulse Height for 5.3 MeV $\alpha$-Particles in Lig. Xe+TMA or TEA Ionization Chamber", *Bull. Sci. Eng. Res. Lab.,* Waseda Univ., **131**, 1 (1991).
9) T. Murakami, Y. Gono, M. Oshima, H. Kusakari, K. Morita, A. Yoshida, and H. Kumagai: "Isomer Decay of 136Ce Studied by Gas Filled Recoil Ion Separator", *J. Phys. Soc. Jpn.*, **60**, 1424 (1991).
10) H. Kumagai, S. Nakabayashi, S. Yamagata, S. Isomura, T. Ichihara, K. Yoshida, T. Suzuki, K. Takahashi, A. Kira, and I. Tanihata: "Attempts in Detection of Neutrons on So-Called Nuclear Fusion", *ibid.*, p. 2594.
11) T. Kohno, K. Munakata, T. Imai, A. Yoneda, C. Kato, M. Matsuoka, T.

Doke, J. Kikuchi, T. Kashiwagi, K. Nishijima, N. Hasebe, and H.J. Crawford: "Accelerator Experiments of a Prototype Cosmic Ray Heavy Ion Telescope", *ibid*., p. 3967.
12) R. Kadono: "$\mu$SR Study of Itinerant Magnet MnSi", *Solid State Phys.,* **26**, 705 (1991).
13) R. Kadono: "Quantum Diffusion of Muon/Muonium in Solids", *ibid*., p. 771.
14) I. Nomura *et al*.: "Pion Absorption in GeV Region", 46th Ann. Meet. Phys. Soc. Jpn., p. 9 (1991).
15) T. Matsuzaki, K. Nagamine, K. Ishida, Y. Watanabe, S. Sakamoto, E. Torikai, H. Kudo, M. Tanase, M. Kato, H. Sugai, K. Kurosawa, and H. Umezawa : "Doubly Sealed DT Target System for $\mu$CF Experiment at UT-MSL/KEK", *Muon Catalyzed Fusion*, **5-6** (1990-1991).
16) K. Yuasa-Nakagawa, S.M. Lee, T. Nakagawa, and I. Tanihata: "Property of the Timing Detector Using an Electron Multiplier", *Nucl. Instrum. Methods in Phys. Res*., **A300**, 538 (1991).
17) H. Ichinose, T. Doke, J. Kikuchi, A. Hitachi, K. Masuda, and E. Shibamura: "The Response of a Liquid Xe Ionization Chamber to 5.3 MeV $\alpha$-particles", *ibid*., **A305**, 111 (1991).
18) T. Mizota, K. Yuasa-Nakagawa, S.M. Lee, and T. Nakagawa: "Timing Properties of a Stop Detector for Time-of-flight (T.O.F.) System", *ibid*., p. 125.
19) T. Yamazaki, R. Hayano, and H. Toki: "d(HI, $^3$He) Reaction Spectroscopy for the Formation of Pionic Bound States", *ibid*., p. 406.
20) K. Masuda, E. Aprile, H. L. Ding, T. Doke, S. S. Gau, M. P. J. Gaudreau, A. Hitachi, H. Ichinose, N. Ishida, M. Kase, T. Kashiwagi, J. Kikuchi, T. Nakasugi, E. Shibamura, K. Sumorok, and T. Takahashi: "Measurement of Liquid Xenon Scintillation from Heavy Ions Using a Silicon Photodiode", *ibid*., **A309,** 489 (1991).
21) J. Péter, J. P. Sullivan, D. Cussol, G. Bizard, R. Brou, M. Louvel, J. P. Patry, R. Regimbart, J. C. Steckmeyer, B. Tamain, E. Crema, H. Double, K. Hagel, G. M. Jin, A. Péghaire, F. Saint-Laurent, Y. Cassagnou, R. Legrain, C. Lebrun, E. Rosato, R. MacGrath, S. G. Jeong, S. M. Lee, Y. Nagashima, T. Nakagawa, M. Ogihara, J. Kasagi, and T. Motobayashi: "Exclusive Study of Nucleus-Nucleus Reactions at Intermediate Energies: Impact Parameter Dependence of Pre-Equilibrium Emission, Collective Flow and Hot Nuclei Formation", *Nucl. Phys*., **A519**, 127c (1990).
22) J. Péter, D. Cussol, G. Bizard, R. Brou, M. Louvel, J.P. Patry, R. Regimbart, J.C. Steckmeyer, J.P. Sullivan, B. Tamain, E. Crema, H. Double, K. Hagel, G.M. Jin, A. Péghaire, F. Saint-Laurent, Y. Cassagnou, R. Legrain, R. Lebrun, E. Rosato, R. MacGrath, S.G. Jeong, S.M. Lee, Y. Nagashima, T. Nakagawa, M. Ogihara, J. Kasagi, and T. Motobayashi: "Global Variables and Impact Parameter Determination in Nucleus-Nucleus Collisions below 100 MeV/u", *ibid*., p. 611.
23) H. Toki, Y. Sugahara, D. Hirata, B.V. Carlson, and I. Tanihata: "Properties of Nuclei Far from the Stability Line in the Relativistic Hartree Theory", *ibid*., **A524**, 633 (1991).
24) H. Toki, S. Hirenzaki, T. Yamazaki, and R. Hayano: "Deeply Bound Pionic Atoms", (PANIC Int. Conf. MIT Cambridge, June, 25-29 (1990)), *ibid*., **A527**, 455c (1991).
25) K. Tanaka, W. Bentz, A. Arima, and F. Beck: "Landau Ghost and the Källén-Lehmann Representation in the Relativistic Many-Body Problem", *ibid*., **A528**, 676 (1991).
26) H. Toki, S. Hirenzaki, and T. Yamazaki: "Pion-transfer (n,d) and (d,$^3$He) Reactions Leading to Deeply Bound Pionic Atoms", *ibid*., **A530**, 679 (1991).
27) S. Ohta and S. Kim: "Finite Temperature Phase Structure of Lattice QCD for 8 and 17 Flavors in the 1990 Conference on Lattice Field Theory 'Lattice 90' ", (Tallahassee, 1989), Nucl. Phys., (Proc. Suppl.), eds. U.M. Heller et al., **20**, 268 (1991).
28) T. Suzuki, M. Fukuda, T. Ichihara, N. Inabe, T. Kubo, T. Nakagawa, K. Yoshida, I. Tanihata, T. Kobayashi, T. Suda, S. Shimoura, and M. Fujiwara: "Negative Pion Production in Subthreshold Heavy Ion Collisions", *Phys. Lett*., **B257**, 27 (1991).
29) T. Motobayashi, T. Takei, S. Kox, C. Perrin, F. Merchez, D. Rebreyend, K. Ieki, H. Murakami, Y. Ando, N. Iwasa, M. Kurokawa, S. Shirato, J. Ruan

(Gen), T. Ichihara, T. Kubo, N. Inabe, A. Goto, S. Kubono, S. Shimoura, and M. Ishihara: "Determination of the Astrophysical $^{13}N(p,\gamma)^{14}O$ Cross Section through the Coulomb Dissociation Method", *ibid.*, **B264**, 259 (1991).
30) S. Kox, C. Perrin, J. Arvieux, J.P. Bocquet, A. Boudard, J. Carbonell, G. Gaillard, M. Garçon, L. Ghedira, G. Guillaume, F. Merchez, T. Motobayashi, D. Rebreyend, C. Wilkin, and J. Yonnet: "The $^1H(d,2p)n$ Reaction as Basis for a Deuteron Tensor Polarimeter at Intermediate Energies", *ibid.*, **B266**, 264 (1991).
31) M. Fukuda, T. Ichihara, N. Inabe, T. Kubo, H. Kumagai, T. Nakagawa, Y. Yano, I. Tanihata, M. Adachi, K. Asahi, M. Kouguchi, M. Ishihara, H. Sagawa, and S. Shimoura: "Neutron Halo in $^{11}Be$ Studied via Reaction Cross Section", *ibid.*, **B268**, 339 (1991).
32) M. Tohyama and E. Suraud: "Weighted Particle Method for Solving the Boltzmann Equation", *Phys. Rev. C,* **43**, 1518 (1991).
33) A. Elmaani, N.N. Ajitanand, J.M. Alexander, R. Lacey, S. Kox, E. Liatard, F. Mercheaz, T. Motobayashi, B. Noren, C. Perrin, D. Rebreyend, T. U. Chan, G. Auger, and S. Groult: "Characterization of Very Highly Excited Composite Nuclei: Temparature, Spin Zone, Radial Extent and Lifetime Scale of $10^{-22}$s", *ibid.*, R2474.
34) D. Hirata, H. Toki, T. Watabe, I. Tanihata, and B.V. Carlson: "Relativistic Hartree Theory for Nuclei Far from Stability Line", *ibid.,* **44**, 1467 (1991).
35) S. Ohta and S. Kim: "Finite Temperature Phase Structure of Lattice QCD for 8 and 17 Flavors", *Phys. Rev. D,* **45**, 504 (1991).
36) R. Kadono and R.F. Kiefl: "Comment on 'Rapid Low-temperature Hopping of Hydrogen in a Pure Metal: the $ScH_x$ System'", *Phys. Rev. Lett.*, **66**, 2414 (1991).
37) K. Nagamine: "Slow $\mu^+$ and $\mu^-$ Beam Production and Next Generation of Muon Science", Proc. 18th INS Int. Symp. on Physics with High Intensity Hadron Acceleraters, World Scientific, Singapore, p. 79 (1990).
38) H. Takebe, T. Wada, T. Masuda, N. Kumagai, and S. Harada: "Design of Magnet Power Supply Control System for the SPring-8 Storage Ring", Proc. Int. Conf. CUM Workshop on Current Trends in Data Acquisition & Control Accel. VECC, Calcutta, India, p. 144 (1991).
39) I. Nomura: "Pion Absorption at 1GeV/c", 5th Int. Symp. on Mesons and Light Nuclei, p. 9 (1991).
40) H. Takebe, N. Kumagai, S. Motonaga, J. Ohnishi, K. Kumagai, and S. Matsui: "Design of Power Supply System for SPring-8 Storage Ring Magnets", Proc. 8th Symp. on Accel. Sci. Technol., Wako, p. 214 (1991).
41) M. Tohyama, P. Schuck, and S.J. Wang: "Approximate Ground State of the Lipkin Model Hamiltonian in Density-matrix Formalism", *Z. Phys. A,* **339**, 341 (1991).

3. Atomic and solid-state physics

1) N. Maeda, Y. Isozumi, R. Katano, S. Ito, and Y. Awaya: "Resolution of Read-out Patterns for Position-sensitive Proportional Counter", *Bull. Inst. Chem. Res.,* Kyoto Univ., **69**, 35 (1991).
2) S. Ito, M. Tosaki, R. Katano, Y. Isozumi, and Y. Awaya: "Position-Sensitive Proportional Counter for High-energy X-rays", *ibid.*, p. 43.
3) E. Yagi: "Behaviour of Krypton Atoms Implanted into Aluminium as Investigated by a Channelling Method", Fundamental Aspects of Inert Gases in Solids, ed. S.E. Donnelly and J.H. Evans, Plenum Press, New York and London, p. 257 (1991).
4) H. Tawara, T. Tonuma, H. Kumagai, T. Matsuo, and H. Shibata: "Cluster Ions and Multiply Charged Ions Formed in Frozen $CO_2$ Molecules under Heavy Impact", *J. Chem. Phys.*, **94**, 2730 (1991).
5) K. Shiraishi, K. Fukai, and E. Yagi: "Damage Profiles in a Stainless Steel Irradiated with Ar- and N-Ions", *J. Nucl. Mater.*, **179-181**, 550 (1991).
6) A. Hitachi, Y. Awaya, T. Kambara, Y. Kanai, M. Kase, H. Kumagai, J. Takahashi, T. Mizogawa, and A. Yagishita: "Angular Distribution of Ti K X-rays and Sn L X-rays Induced by 6 MeV/nucleon N-ion Impact", *J. Phys. B At. Mol. Opt. Phys.*, **24**, 3009 (1991).
7) H.A. Sakaue, Y. Awaya, A. Danjo, T. Kambara, Y. Kanai, T. Nabeshima, N.

Nakamura, S. Ohtani, H. Suzuki, T. Takayanagi, K. Wakiya, I. Yamada, and M. Yoshino: "Ejected Electron Spectra from Doubly-excited States (*2lnl'*) of He-like Ions Produced by the $B^{5+}$, $C^{6+}$ - He Collisions", *ibid.*, p. 3787.
8) T. Papp, Y. Awaya, A. Hitachi, T. Kambara, Y. Kanai, T. Mizogawa, and I. Török: "Angular Distribution Measurement of Various $L_3$ X-ray Transitions", *ibid.*, p. 3797.
9) Y. Awaya, T. Kambara, Y. Kanai, A. Hitachi, T. Mizogawa, and K. Kuroki: "Radiative Electron Capture Cross Section for 26 MeV/u $Ar^{18+}$ Ions on a Carbon Target", *Nucl. Instrum. Methods in Phys. Res.,* **B53**, 375 (1991).
10) S. Ohtani, Y. Kanai, I. Yamada, H.A. Sakaue, Y. Awaya, T. Kambara, T. Nabeshima, N. Nakamura, H. Suzuki, T. Takayanagi, K. Wakiya, A. Danjo, and M. Yoshino: "Electron Spectroscopy of Doubly-excited Helium-like Ions", *ibid.*, p. 383.
11) K. Shima, T. Mukoyama, T. Mizogawa, Y. Kanai, T. Kambara, and Y. Awaya: "On Shell Effects of Ionic Charge States in Solids", *ibid.*, p. 404.
12) H. Fukuda, T. Watanabe, I. Shimamura, and L. Végh: "Energy and Angular Distributions of Electrons Emitted and Ions Recoiled in Proton-impact Ionization of Helium Atoms", *ibid.*, p. 410.
13) K. Kawatsura, M. Sataka, H. Naramoto, M. Imai, K. Komaki, Y. Yamazaki, K. Kuroki, Y. Kanai, T. Kambara, Y. Awaya, J.E. Hansen, I. Kádár, and N. Stolterfoht: "High Rydberg and Auger Electrons from Fast Projectile Ions Studied by Zero-Degree Electron Spectroscopy", *ibid.*, p. 421.
14) T. Kambara, Y. Awaya, Y. Kanai, T. Mizogawa, M. Terasawa, H. Schmidt-Böchking, R. Dörner, and H. Vogt: "K-X-ray - scattered - particle Coincidence Measurement in Heavy-Ion Collisions", *ibid.*, p. 426.
15) H. Fukuda, I. Shimamura, L. Végh, and T. Watanabe: "Proton Angular Distributions and Highly Differential Cross Sections for Ionization of Helium Atoms by Proton Impact", *Phys. Rev. A,* **44**, 1565 (1991).
16) I. Kádár, H. Altevogt, R. Köhrbrück, V. Montemayor, A. Mattis, G. Schiwietz, B. Skogvall, K. Sommer, N. Stolterfoht, K. Kawatsura, M. Sataka, Y. Nakai, H. Naramoto, Y. Kanai, T. Kambara, Y. Awaya, K. Komaki, and Y. Yamazaki: "High-resolution Auger Spectroscopy of Na-like Argon and Sulfur Ions Singly Excited in High-energy Collisions with Light Target Atoms", *ibid.*, p. 2900.
17) P.H. Mokler, S. Reusch, A. Warczak, Z. Stachura, T. Kambara, A. Müller, R. Schuch, and M. Schulz: "Single Transfer-excitation Resonance Observed via the Two-photon Decay in He-like $Ge^{30+}$", *Phys. Rev. Lett.*, **65**, 3108 (1990).
18) N. Toshima and J. Eichler: "Identification of Thomas Peaks in Coupled-channel Calculations for Charge Transfer", *ibid.*, **66**, 1050 (1991).
19) E. Yagi: "Irradiation-Enhanced Solid Krypton Formation in Kr-Implanted Aluminum", *ibid.*, **67**, 3804 (1991).
20) T. Sekioka, M. Terasawa, and Y. Awaya: "Ion Storage in Kingdon Trap", *Radiat. Eff. Def. Solid*, **117**, 253 (1991).
21) K. Ishida: "$\mu^+$SR in Polyacetylenes", *Solid State Phys.,* **25**, 793 (1991).
22) N. Toshima and Chii-Dong Lin: "Coherence Parameters of Atomic Excited States: Comparision of Results from the CTMC and the Quantal Calculations", *Z. Phys. D*, **21**, 227 (1991).
23) G. Wintermeyer, V. Dangendorf, H. Schmidt-Böcking, T. Kambara, P. H. Mokler, R. Schuch, and I. Tserruya: "Search for Interference Structure in the Quasimolecular X-Ray and K-Vacancy Production in Close Collisions of 462 MeV Hydrogen-like Kr Ions on Mo Solid Targets", *Z. Phys. D-Atoms, Mol. Clusters*, **17**, 145 (1990).
24) Y. Kanai, H.A. Sakaue, S. Ohtani, K. Wakiya, H. Suzuki, T. Takayanagi, T. Kambara, A. Danjo, M. Yoshino, and Y. Awaya: "Electron Spectroscopy of Doubly-excited Helium Like Ions", *ibid.*, **24**, S225 (1991).
25) T. Kambara, Y. Awaya, Y. Kanai, H. Dörner, and H. Schmidt-Böcking: "Azimuthal Angular Dependence of the K-X-ray Emission", *ibid.*, S295.

4. Radiochemistry, radiation chemistry, and radiation biology

1) S. Ambe and F. Ambe: "Mössbauer Emission Study of Recoil $^{119}$Sb and $^{119m}$Te Atoms after Nuclear Decays and Reactions in SnS and SnSe", *Bull. Chem.*

*Soc. Jpn.*, **64**, 1289 (1991).

2) S. Ambe, S.Y. Chen, Y. Ohkubo, Y. Kobayashi, M. Iwamoto, M. Yanokura, and F. Ambe: "Preparation of a Radioactive Multitracer Solution from Gold Foil Irradiated by 135 MeV/nucleon $^{14}$N Ions", *Chem. Lett.*, **1991**, 149 (1991).

3) M. Watanabe, M. Suzuki, K. Watanabe, and K. Suzuki: "Comparison of the Frequency of Mutants and/or Transformants and Chromosome Damage Induced in SHE Cells by Various LET Radiations", *In vitro Toxicol.*, **4**, 93 (1991).

4) H. Nakai, K. Nakamura, S. Kuwahara, and M. Saito: "A New Gene, Developed through Mutagenesis, for Resistance of Rice to Bacterial Leaf Blight (*Xanthomonas campestris* pv. *oryzae*)", *J. Agric. Sci.*, **114**, 219 (1990).

5) H. Nakai, S. Kuwahara, and S. Sennga: "Genetic Analysis of an Induced Mutant for a Quantitative Resistance to Bacterial Leaf Blight", *Jpn. J. Breed.*, **40**, 397 (1990).

6) S. Ambe, Y. Ohkubo, M. Iwamoto, and Y. Kobayashi: "Preparation of Carrier-Free $^{111m}$Cd and $^{105,106m}$Ag and Their Chemical Behavior", *J. Rad. Nucl. Chem. Lett.*, **153**, 235 (1991).

7) H. Ohara, K. Kanai, H. Itsukaichi, K. Fukutsu, K. Eguchi-Kasai, H. Xu, K. Sato, F. Yatagai, T. Takahashi: "Fluctuation of RBE vs. LET with Carbon Ions", *J. Radit. Res.* (abstract), **32**, 105 (1990).

8) K. Kimura: "Track-depth Resolved Luminescence of 5 MeV/amu N-ions Injected into Near-liquid and Liquid Helium", KEK Proc., p. 66 (1991).

9) K. Kimura: "Track-depth Resolved Luminescence of 5 MeV/amu N-ions Injected into Nearliquid and Liquid Helium", *Nucl. Instrum. Methods in Phys. Res.*, **B53**, 301 (1991).

10) H. Kumagai, Y. Yatagai, N. Tajima, K. Nakano, F. Yatagai, and T. Takahashi: "Parallel-Plate Avalanche Counter for Dosimetry in the RIKEN Ring Cyclotron Biology Facility", *ibid.,* **A308**, 649 (1991).

11) H. Nakai: "Practical Value of Induced Mutants of Rice Resistant to Bacterial Leaf Blight", Plant Mutation Breeding for Crop Improvement, IAEA, Vienna, p. 113 (1991).

## 5. Material analysis

1) J. Kawai: "Chemical State Analysis by Soft X-ray Emission Spectra with Molecular-orbital Calculations", Adv. in X-Ray Analysis, Plenum Press, New York, **34**, 91 (1991).

2) K. Tanaka, M. Okada, T. Kohno, M. Yanokura, and M. Aratani: "Hydrogen Content and Bonding Structure of Diamond-Like Carbon Films Deposited by Ion Beam Deposition", *Nucl. Instrum. Mehtods in Phys. Res.*, **B58**, 34 (1991).

3) J. Kawai and K. Maeda: "Charge-transfer Multiplet in the L$\alpha$ X-ray Emission Spectra of Copper(II) Compounds", *Spectrochim. Acta,* **46B**, 1243 (1991).

# VIII. LIST OF PREPRINTS

1991

RIKEN-AF-NP

100 H. Kumagai, S. Nakabayashi, S. Yamagata, S. Isomura, T. Ichihara, K. Yoshida, T. Suzuki, K. Takahashi, A. Kira, and I. Tanihata; Feb. 1991, "Attempts in Detection of Neutrons on So-Called cold Nuclear Fusion"

101 K. Soutome, S. Yamaji, and M. Sano; Feb. 1991, "Target-Chatge Dependence of the Coulom Dissociation Cross Section of $^{11}$Li"

102 H. Hofmsnn, S. Yamagi, and A. S. Jensen; May 1991, "Distribution of Strength for Isoscalar Modes at Finite Temperature"

103 M. Fukuda, T. Ichihara, N. Inabe, T. Kubo, H. Kumagai, T. Nakagawa, I. Tanihata, Y. Yano, M. Adachi, K. Asahi, M. Kouguchi, M. Ishihara, H. Sagawa, and S. Simoura; May 1991, "Neutron Halo $^{11}$Be Studied via Reaction Cross Sections"

104 T. Kobayashi; July 1991, "Projectile Fragmentation of Exotic Nuclear Beams"

105 abstract of NN conf.;

106 T. Kobayashi; July 1991, "Spectroscopy of the Exotic Nucleus $^{11}$Li via Pion Double Charge Exchange Reaction $^{11}$B$(\pi^-, \pi^+)^{11}$Li"

107 I. Tanihata; July 1991, "On the Momentum Distribution of Fragments of $^{11}$Li and $^{11}$Be—Possible Indication of Di-neutron Fromation—"

108 T. Suzuki; July 1991, "Pion Production in Intermediate Energy Nucleus-nucleus Collisions"

109 M. Koizumi; Sep. 1991, "Velocity Distribution of Ion Beams from The RIKEN IGISOL"

110 I. Nomura; Sep. 1991, "Pion Absorption at 1 GeV/C"

111 K. Ikeda; Oct. 1991, "Structure of Neutron Rich Nuclei-A Typical Exemple of the Nucleus $^{11}$Li-"

112 R.N. Boyd, I. Tanihata, N. Inabe, T. Kubo, T. Nakagawa, T. Suzuki, and M. Yanokura; Oct. 1991, "Measurement of the $^{8}$Li(alpha,n) $^{11}$B Reaction Cross Section at Energies of Astrophysical Interest"

113 T. Wada, N. Carjan, and Y. Abe (c); Oct. 1991, "Multi-Dimensional Langevin Approach to Fission Dynamics"

114 T. Wada; Oct. 1991, "Multi-Dimensional Dissipative Dynamics of Nuclear Fission"

115 K. Morita, A. Yoshida, T. Inamura, M. Koizumi, T. Nomura, M. Fujioka, T. Shinozuka, H. Miyatake, K. Sueki, H. Kudo, Y. Nagai, T. Toriyama, K. Yoshimura, and Y. Hatsukawa; Nov. 1991, "RIKEN Isotope Separator ON-LINE GARIS/IGISOL"

116 K. Soutome, S. Yamaji, and M. Sano; Nov. 1991, "Target-Charge Dependence of the Coulomb Dissociation Cross Section of $^{11}$Li"

117 M. Koizumi, T. Inamura, K. Morita, M. Wakasugi, A. Yoshida, M. Azuma, H. Katsuragawa, T. Horiguchi, T. Ishizuka, I. Nakamura, M. Nakaoka, A. Iivonen, K. Valli, S. Matsuki, T.

Murayama, K.` Shimoura, T. Shinozuka, I. Sugai, and Y. Tagishi; Nov. 1991, "Collinear Fast Atomic-Beam Laser Spectroscopy at RIKEN GARIS/IGISOL"

118 K. Suzuki and H. Toki; Nov. 1991, "Pauli-Gursey Symmetry on Baryon and Meson Masses"

# IX. PAPERS PRESENTED AT MEETINGS

## 1. Accelerator development and accelerator physics

1) M. Hara and T. Furuya: "Overview of Storage Ring Design", Report Meet. of R & D for SPring-8 Project, Tokyo, Feb. (1991).
2) K. Inoue, T. Nakamura, Y. Kawashima, I. Takeshita, and M. Hara: "Current Status of RF System of the Storage Ring", *ibid*.
3) T. Takada and M. Hara: "Insertion Devices II-Calculation of Spectrum Distribution", *ibid*.
4) M. Nakano, K. Sato, K. Yoshiyuki, M. Hara, and I. Takeshita: "Fabrication of RF Cavities", Symp. of Vacuum for SR, Wako, Mar. (1991).
5) Y. Muroo, T. Kusaka, M. Hara, I. Takeshita, and K. Inoue: "Manufacturing Method of Accelerating Cavities", *ibid*.
6) Y. Kawashima, K. Inoue, T. Nakamura, and M. Hara: "Design of 508MHz Klystron Test Stand for SPring-8", Spring Meet. of the Phys. Soc. Jpn. Tokyo, Mar. (1991).
7) M. Hara: "Insertion Devices of SPring-8", 4th Meet. Jpn. Soc. for Synchrotron Rad. Res., Nagoya, Apr. (1991).
8) K. Inoue, T. Nakamura, Y. Kawashima, I. Takeshita, and M. Hara:"Status of Development of SPring-8 RF System", *ibid*.
9) T. Kusaka, Y. Muroo, O. Morioka, K. Inoue, I. Takeshita, and M. Hara: "Design and Manufacture of Hot Model Cavities for SPring-8 Storage Ring", *ibid*.
10) T. Takada and M. Hara: "Specrtum Distribution of Insertion Devices for SPring-8", *ibid*.
11) T. Wada: "Design of the Control System for the SPring-8", *ibid*.
12) M. Hara, H. Kamitsubo, N. Kumagai, and Accelerator Design Group: "Status of the SPring-8 Project (Storage Ring)", IEEE 1991 Particle Accel. Conf., San Francisco, May (1991).
13) K. Inoue, T. Nakamura, Y. Kawashima, and M. Hara: "Current Status of RF System for the SPring-8", *ibid*.
14) N. Kumagai, J. Ohnishi, H. Takebe, K. Kumagai, and S. Motonaga: "Design of the Magnet for the SPring-8 Storage Ring", *ibid*.
15) E. Ikezawa, Y. Miyazawa, M. Hemmi, M. Kase, Y. Chiba, T. Chiba, T. Aihara, T. Ohki, and H. Hasebe: "RIKEN Heavy Ion Linac with ECR Ion Source", 14th Symp. on Ion Sources and Ion-Assisted Technol., Tokyo, Jun. (1991).
16) M. Hara: "8th GeV Synchrotron Radiation Facility (SPring-8) Project",Japan-Korea Symp. on Radio-Isotope Utilization, Seoul, Korea, Jun. (1991).
17) J. Ohnishi: "Field Measurement of Magnets for the SPring-8 Storage Ring", 7th Int. Magnet Measurement Workshop, Darmstadt, F.R.G., Jun. (1991).
18) J. Ohnishi, H. Takebe, K. Kumagai, and S. Motonaga: "Field Measurements of Prototype Magnets for the SPring-8 Storage Ring", 12th Int. Conf. Magnet Technol., Leningrad, U.S.S.R., Jun. (1991).
19) M. Hara, T. Nakamura, T. Takada, and H. Tanaka: "Use of Long Straight Sections of SPring-8", 4th Int. Conf. on Syncrotron Radiation Instrumentation, Chester, U.K., Jul. (1991).
20) M. Hara, S.H. Be, I. Takeshita, and T. Namba: "Extraction of Infrared Radiation from SPring-8", *ibid*.
21) M. Hara: "Storage Ring of the SPring-8", 2nd Workshop on XAFS by using Large High-Brilliance Photon Source, Wako, Sep. (1991).
22) T. Kusaka, Y. Moro, O. Morioka, K. Inoue, Y. Kawashima, T. Nakamura, Y. Ohashi, and M. Hara:"Design of Hot Model Cavity for SPring-8 Storage Ring", 46th Ann. Meet. Phys. Soc. Jpn., Sapporo, Sep. (1991).
23) Y. Kawashima, K. Inoue, T. Nakamura, Y. Ohashi, and M. Hara: "Test of Cavity for SPring-8 Storage Ring", *ibid*.
24) T. Shikata, N. Nakanishi, K. Ikegami, S. Fujita, S. Nakajima, T. Takagi, S. Okamoto, and T. Kosako: "Measurement of Neutrons Produced by 135MeV/n Nitrogen Ions in an Iron Beam-stoper with Activation Detectors", *ibid*.
25) T. Nakagawa and Y. Kageyama: "Recent Developments of RIKEN ECRIS", *ibid*.
26) H. Takebe and S. Matsui: "Measurement of Ripple Field in Vacuum Cham-

bers in B, Q, and Sx Magnets for the SPring-8 Storage Ring", *ibid*.
27) M. Hara: "Current Status of SPring-8 Project and Extraction of Infrared Radiation", Workshop of Infrared Radiation Subgroup, Sapporo, Oct. (1991).
28) M. Hara: "Development of High-Brilliant X-ray Source", Symp. on New Beams, Tokyo, Oct. (1991).
29) M. Kase, I. Yokoyama, and M. Nagase: "Control System of RIKEN Ring Cyclotron", Int. Conf. of Accel. Control and Large Experimental Phys., Tsukuba, Nov. (1991).
30) M. Hara: "Overview of the SPring-8 Project", 2nd Japan-Korea Joint Synchrotron Radiat. Symp. Tsukuba, Nov. (1991).
31) I. Kohno, M. Miyagawa, Y. Matsuzawa, S. Kagaya, H. Kato, and T. Katou: "Residual Radioactivity in the 160 cm Cyclotron and Its Surrounding Facilities", 8th Symp. on Accel. Sci. and Technol., Wako, Nov. (1991).
32) K. Ikegami, Y. Chiba, M. Hemmi, Y. Taniguchi, T. Fujisawa, and Y. Kawamura: "Measurement of Surface Resistance of High-Tc Superconductor ($(Bi, Pb)_2Sr_2Ca_2Cu_3O_x$) At 10.5 GHz", *ibid*.
33) K. Ikegami, Y. Chiba, Y. Kawamura, M. Hemmi, Y. Taniguchi, and T. Fujisawa: "Measurement of Surface Resistance of High-Tc Superconductor ($(BiPb)_2Sr_2Ca_2Cu_3O_x$) at 10.5 GHz", *ibid*.
34) K. Kumagai, S. Matsui, and H. Miyade: "Field Measurement of a Pulsed Septum Magnet as an R & D for SPring-8", *ibid*.
35) M. Hara: "Present Status of the SPring-8 (Storage Ring)", *ibid*.
36) H. Suzuki, T. Kojyo, H. Yonehara, T. Harami, Y. Miyahara, Y. Kawashima, Y. Ohashi, K. Inoue, and M. Hara: "High Power Test of RF Cavity for SPring-8 Booster Synchrotron", *ibid*.
37) T. Nakamura, M. Hara, and H. Tanaka: "Study on a Free Electron Laser at a SPring-8 Long Straight Section", *ibid*.
38) S. Matsui, K. Kumagai, H. Miyade, N. Kumagai, and H. Takebe: "Calculation of Magnetic Field Attenuation by Metalized Coating and Core Material for Pulsed Magnet", *ibid*.
39) T. Shikata, N. Nakanishi, K. Ikegami, S. Fujita, S. Nakajima, T. Takagi, S. Okamoto, and T. Kosako: "Measurement of Neutrons Produced by 135MeV/n Nitrogen Ions in an Iron Beam-stopper with Activation Detectors", *ibid*.
40) M. Hara: "Overview of the SPring-8 Project", Workshop on Accel. • Radiat. Source, Japan Atomic Energy Forum Inc. Tokyo, Dec. (1991).

## 2. Nuclear physics and nuclear instrumentation

1) T. Inamura: "Present Status of the Experimental Project on Systematical Mesurement of Hyperfine Structure Anomaly with ISOLDE at CERN", 1st Specialist Res. Meet. on the Electromagnetic Isotope Separators and Their Appl., Kumatori, Jan. (1991).
2) M. Koizumi: "Velocity Distribution of RIKEN IGISOL Ion Beams", *ibid*.
3) T. Wada, N. Carjan, and Y. Abe: "Multi-Dimensional Langevin Approach to Induced Fission", RIKEN Symp. on Heavy-Ion Nucl. React., Wako, Jan. (1991).
4) H. Okuno: "Spin-Polarization Phenomenon in the Projectile Fragmentation", RIKEN Symp. on Heavy Ion React., Wako. Feb. (1991).
5) T. Matsuzaki and R. Kadono: "Generation of Low-Energy Short-Lived Ion Beams by SLOW", RIKEN Symp. on Non Nucl. Phys. Res. by RRC, Wako, Feb. (1991).
6) M. Koizumi, M. Azuma, T. Inamura, T. Ishizuka, H. Katsuragawa, H. Kosuga, K. Shimomura, I. Sugai, M. Takami, M. Nakaoka, I. Nakamura, S. Matsuki, T. Murayama, K. Morita, A. Yoshida, and K. Valli: "Dependence of the Velocity Distribution of IGISOL Ion Beams on He-Gas Pressure", 1991 Spring Meet. Phys. Soc. Jpn., Tokyo, Mar. (1991).
7) M. Tohyama, P. Schuck, and S.J. Wang: "Stationary Solution of the Time-Dependent Density-Matrix Theory", *ibid*.
8) H. Okuno, K. Asahi, M. Ishihara, T. Nakamura J. Kura, M. Adachi, T. Ichihara, N. Inabe, T. Kubo, A. Yoshida, T. Shimoda, N. Takahashi, H. Miyatake, D. Beaumel, D. Mikolas, D.J. Morrissey, Y. Ohkubo, Y. Kobayashi, J. Nakamura, and K. Asai: "Spin-Polarization Measurement of Projectile-like Fragments $^{12}B$ and $^{13}B$ in $^{15}N$ (69.5MeV/u) + $^{197}Au$, $^{159}Tb$,

$^{93}$Nb, $^{27}$Al", *ibid*.
9) Y. Futami, Y. Honjo, T. Mizota, Y.H. Pu, K. Yuasa-Nakagawa, H. Fujiwara, H. Toyokawa, T. Nakagawa, and S.M. Lee: "Development of $BaF_2$+Plastic Phoswich Detector", *ibid*.
10) S. Matsuki: "Laser Nuclear Spectroscopy of Unstable Nuclei in Solids", *ibid*.
11) S. Kim and S. Ohta: "Finite Temperature Phase Structure of QCD with 8 Flavors on $16^3 \times 6$ Lattice", *ibid*.
12) K. Shimomura, I. Ogawa, Suzuki, T. Kohmoto, M. Kitano, Y. Kido, T Shinozuka, H.T. Duong, T. Inamura, T. Nomura, M. Fujioka, and S. Matsuki: "Nuclear Polarization of Unstable Nuclei with Optical Pumping in GaAs", *ibid*.
13) T. Nakamura, T. Kubo, N. Inabe, A. Yoshida, H. Okuno, K. Asahi, K. Abe, and M. Ishihara: "Production Cross Section of Projectile Fragments in $^{40}$Ar (94MeV/u) + Be", *ibid*.
14) T. Motobayashi, T. Takei, K. Ieki, H. Murakami, Y. Ando, N. Iwasa, M. Kurokawa, C. Perrin, F. Merchez, S. Kox, D. Rebreyend, M. Ishihara, T. Ichihara, T. Kubo, N. Inabe, S. Shimoura, and S. Kubono: "Determination of Astrophysical Reaction Rates through the Coulomb Breakup Reaction", *ibid*.
15) T. Wada, Y. Abe, and N. Carjan: "Induced Fission Studied with Multi - Dimensional Langevin Equation II", *ibid*.
16) T. Wada: "Resonating-Group-Method Study of $^{16}$O-$^{16}$O Elastic Scattering", *ibid*.
17) C. Kato, T. Imai, H. Kato, T. Kohno, M. Matsuoka, K. Munakata, and A. Yoneda: "Characteristics of Position Sensitive detectors Obtained by Accelerator Experiments", *ibid*.
18) K. Ishida and K. Nagamine: "Accelerator Plans (KEK)", Workshop on Future of Muon Phys., Heidelberg, F.R.G., May (1991).
19) T. Motobayashi: "Coulomb Dissociation of $^{14}$O for Determination of Astrophysical $^{13}$N (p, $\gamma$) Gross-section", Workshop on Fragmentationof Light Nuclei, Brussels, Belgium, May (1991).
20) S. Hirenzaki: "Formation of Deeply Bound Pionic Atoms", Int. Workshop on Pions in Nuclei., Peniscola, Spain, Jun. (1991).
21) S. Kubono, M. Ohura, N. Ikeda, M.H. Tanaka T. Nomura, Y. Funatsu, T. Kubo, N. Inabe, A. Yoshida T. Ichihara, M. Ishihara, I. Tanihata, H. Orihara, S. Kato, H. Okuno, T. Nakamura, S. Shimoura, H. Toyokawa, K. Asahi, S. Yun, H. Ohnuma, and T. Kajino: "Study of the Decay Property of $^{20}$Na for the Rapid-Proton Process", Int. Workshop on Unstable Nuclei in Astrophysics, Tokyo, Jun. (1991).
22) T. Motobayashi: "Experimental Study on the Coulomb Breakup of $^{14}$O", *ibid*.
23) H. Toki, D. Hirata, Y. Sugahara, I. Tanihata, and R. Brockmann: "Relativistic Hartree Theory for Supernova and Neutron Stars Constrained by Nuclear Properties far from Stability Line", Int. Symp. on Nucl. Astrophys. Tokyo, Jun. (1991).
24) S. Shimoura: "Incident Energy and Target Dependence of Interaction Cross Sections and Density Distribution of Neutron Drip-Line Nuclei", Int. Symp. on Structure and Reactions of Unstable Nuclei, Niigata, Jun. (1991).
25) K. Soutome, S. Yamaji, and M. Sano: "Targer-Charge Dependence of the Coulomb Dissociation Cross Section of the Weakly-Bound Nucleus $^{11}$Li", *ibid*.
26) M. Ishihara: "Perspectives of Radioactive Beam Experiments", *ibid*.
27) S. Daté and H. Sumiyoshi: "Particle Production in Target Fragmentation Region in Ultrarelativistic Heavy Ion Collisions", Int. Symp. on High Energy Nuclear Collisions and Quark Gluon Plasma, Yukawa Inst. Kyoto Univ. Jun. (1991).
28) Shigemi Ohta: "Lattice QCD at finite temperature", *ibid*.
29) K. Yuasa-Nakagawa, T. Nakagawa, B. Heusch, Y.H. Pu, S.C. Jeong, H. Fujiwara, T. Mizota, K. Ieki, T. Sugimitsu, T. Matsuse, and S.M. Lee: "Complex Fragments Mass Distributions in $^{84}$Kr+$^{27}$Al at 10 MeV/u", Int. Symp. NIKKO '91 Towards a Unified Picture of Nucl. Dyn., Nikko, Jun. (1991).
30) R. Kadono: "Diffusion Processes and Defect Dynamics", HFI-IX Review Seminar, Toyonaka, Jun. (1991).
31) S. Hirenzaki, H. Toki, and T. Yamazaki: "Formation of Deeply Bound Pionic Atoms", Int. Workshop on Pions in Nuclei Held in Peninscola, Spain, Jun.

(1991).
32) T. Fukuda and A. Yoshida: "Study of the Sub-Barrier Fusion Reaction Cross Section with Neutron-Rich Unstable Nuclei", Post Conf. of 4th Int. Conf. on Nucleus-Nucleus Collis., Niigata, Jun. (1991).
33) M. Ishihara: "RIKEN Radioactive-beam Experiments", 4th Int. Conf. on Nucleus-Nucleus Collis., Kanazawa, Jun. (1991).
34) K. Soutome, S. Yamaji, and M. Sano: "Target-Charge Dependence of the Coulomb Dissociation Cross Section of $^{11}$Li", *ibid*.
35) N. Inabe, T. Kubo, T.Nakagawa, H. Kumagai, I. Tanihata, S. Shimoura, T. Nakamura, H. Okamura, H. Okuno, H. Sakai, and M. Ishihara: "Soft Giant Dipole Resonance of Neutron Drip Nuclei $^{11}$Li", *ibid*.
36) S. Datē: "Nucleon Level Monte Carlo Simulator MCMAA for Ultrarelativistic Heavy Ion Collisions", *ibid*.
37) S. Kubono, M. Ohura, N. Ikeda, M.H. Tanaka, T. Nomura, Y. Funatsu, T. Kubo, N. Inabe, A. Yoshida, T. Ichihara, M. Ishihara, I. Tanihata, H. Orihara, S. Kato, H. Okuno, T. Nakamura, S. Shimoura, H. Toyokawa, K. Asahi, S. Yun, H.Ohnuma, and T. Kajino: "Study of the Decay Property of $^{20}$Na for the Onset Mechanism of the Rapid-Proton Process", *ibid*.
38) T. Wada, N. Carjan, and Y. Abe: "Multi-Dimensional Langevin Approach to Fission Dynamics", *ibid*.
39) T. Motobayashi, T. Takei, C. Perrin, F. Merchez, S. Kox, D Rebreyend, K. Ieki, H. Murakami, Y. Ando, N. Iwasa, M. Kurokawa, T. Ichihara, T. Kubo, N. Inabe, S. Kubono, S. Shimoura, and M. Ishihara: "Coulomb Dissociation Measurement for Determination of the Astrophysical $^{13}$N (p, $\gamma$) Cross Section", *ibid*.
40) A. Yoshida, T. Fukuda, K. Asahi, N. Ikeda, M. Ishihara, K. Kimura, S. Kouda, T. Kubo, S. Kubono, J. Kura, T. Nakamura, I. Nomura, T. Nomura, H. Okuno, T. Shimoda, S. Shimoura, and T. Shinozuka: "Measurement of Sub-Barrier Fusion Cross Section with Unstable Neutron-Rich Al Isotopes", *ibid*.
41) H. Toki: "Chiral Bag Model with Vector Mesons", Int. Symp. on Cluster Models in the Occasion of the 70th Birthday of Prof. Wildermuth, Tuebingen, F.R.G., Jul. (1991).
42) R. Kadono and T. Yamazaki: "*eqQ* in MnSi Studied by $\mu$LCR", HFI-IX Workshop, Kumatori, Jul. (1991).
43) T. Kohno: "Solar Proton Intensity Magnitudes of Large Flares on Fall 1991 Observed at Synchronous Orbit", 22nd Int. Cosmic Ray Conf., Dublin, Ireland, Aug. (1991).
44) S. Ohta and S. Kim: "Finite Temperature Phase Structure of Lattice QCD for Many Flavors", Hot Summer Daze: QCD at Nonzero Temperature and Density, Brookhaven, U.S.A., Aug. (1991).
45) N. Inabe, T. Kubo, T. Nakagawa, H. Kumagai, I. Tanihata, S. Shimoura, T. Nakamura, H. Okamura, H. Okuno, H. Sakai, and M. Ishihara: "Soft Giant Dipole Resonance of Neutron Drip Nuclei $^{11}$Li", 2nd Int. Conf. on Radioactive Nucl. Beams, Louvain-la-Neuve, Belgium, Aug. (1991).
46) S. Shimoura: "Neutron Halo in 11 Be Studied by Reaction Cross Sections", *ibid*.
47) T. Motobayashi, T. Takei, C. Perrin, F. Merchez, S. Kox, D. Rebreyend, K. Ieki, H. Murakami, Y. Ando, N. Iwasa, M. Kurokawa, T. Ichihara, T. Kubo, N. Inabe, S. Kubono, S. Shimoura, and M. Ishihara: "Coulomb Dissociation of $^{14}$O, Simulation of the Astrophysical $^{13}$N (p, $\gamma$) Process", *ibid*.
48) S. Yamaji, H. Hofmann, and A.S. Jensen: "Temperature Dependent Isoscalar Vibrational Strength Functions", Tours Symp. on Nucl. Phys., Tours, France, Aug. (1991).
49) T. Motobayashi: "Coulomb Breakup Measurements for Astrophysical Reaction Rates", *ibid*.
50) T. Wada, N. Carjan, and Y. Abe: "Multi-Dimensional Langevin Approach to the Dissipative Dynamics of Nuclear Fission", *ibid*.
51) M. Ishihara: "Intermediate-Energy Heavy-Ion Reactions and Application to RI-beam Experiments", Symp. on Nucleus-Nucleus Collis. Mech., 4th Chem. Congr. of North America, New York, U.S.A., Aug. (1991).
52) H. Toki, D. Hirata, and I. Tanihata: "Nuclear Properties Far from the Stability Line with the Relativistic Mean Field Theory", Int. Symp. on Lasers for Nucl. Phys., Wako, Sep. (1991).

53) M. Koizumi, M. Azuma, T. Horiguchi, T. Inamura, T. Ishizuka, A. Iivonen, H. Katsuragawa, S. Matsuki, K. Morita, T. Murayama, M. Nakaoka, I. Nakamura, K. Shimomura, T. Shinozuka, I. Sugai, Y. Tagishi, M. Takami, K. Valli, M. Wakasugi, and A. Yoshida: "Collinear Fast Atomic-beam Laser Spectroscopy at RIKEN GARIS/IGISOL", *ibid*.
54) S. Matsuki: "RADOP in Solids", *ibid*.
55) T. Harada: "Production and Structure of the $^{4}_{\Sigma}$He-Hypernucleus", 5th Int. Symp. of Mesons and Light Nuclei, Prague, Czechoslovakia, Sep. (1991).
56) K. Ishida, T. Matsuzaki, R. Kadono, A. Matsushita, and K. Nagamine: "A Large Solid-Angle Secondary-Beam Collector Using Axially Symmetric Superconducting Magnetic Field", 12th Int. Conf. on Electromagnetic Isotope Seperators and Techn. Related to Their Appl. (EMIS-12), Sendai, Sep. (1991).
57) S. Matsuki: "OPERA: an On-Line System of Optical Pumping in Solids for Unstable Nuclei", *ibid*.
58) S. Kubono, M. Ohura, N. Ikeda, M.H. Tanaka, T. Nomura, Y. Funatsu, T. Kubo, N. Inabe, A. Yoshida, T.Ichihara, M. Ishihara, I. Tanihata, H. Orihara, S. Kato, H. Okuno, T. Nakamura, S. Shimoura, H. Toyokawa, K. Asahi, S. Yun, H. Ohnuma, and T. Kajino: "Proton Decay Measurement with RIPS for Astrophysical Interest", *ibid*.
59) T. Matsuzaki, R. Kadono, K. Ishida, A. Matsushita, and K. Nagamine: "On-line Mass Spectrometry of Thermal Energy Isotope Ions Emitted from Solid Surfaces in High Energy Heavy Ion Reactions", *ibid*.
60) T. Inamura, M. Koizumi, K. Morita, A. Yoshida, M. Takami, T. Ishizuka, I. Nakamura, M. Nakaoka, T. Murayama, I. Sugai, M. Azuma, H. Katsuragawa, K. Shimomura, S. Matsuki, A. Iivonen, and K.Valli: "Velocity Distribution of RIKEN IGISOL Ion Beams", *ibid*.
61) K. Yuasa-Nakagawa, T. Nakagawa, B. Heusch, Y.H. Pu, S.C. Jeong, H. Fujiwara, T. Mizota, K. Ieki, T. Sugimitsu, T. Matsuse, and S.M. Lee: "Complex Fragments Mass Distributions for $^{84}$Kr+$^{27}$Al at 10MeV/u", 46th Ann. Meet. Phys. *Soc. Jpn.,* Sapporo, Sep. (1991).
62) N. Inabe, T. Kobo, T. Nakagawa, H. Kumagai, I. Tanihata, S. Shimoura, T. Nakamura, H. Okamura, H. Okuno, H. Sakai, and M. Ishihara: "Measurement of Interaction Cross Section of $^{11}$Li+C, Al, Cu and Pb at 43MeV/u and 75MeV/u", *ibid*.
63) M. Koizumi, M. Azuma, T. Inamura, T. Ishizuka, H. Katsuragawa, T. Shinozuka, K. Shimomura, I. Sugai, M. Takami, Y. Tagishi, M. Nakaoka, I. Nakamura, T. Horiguchi, S. Matsuki, T. Murayama, K. Morita, A. Yoshida, and M. Wakasugi: "Development of a Device for Collinear Laser Spectroscopy at RIKEN", *ibid*.
64) R. Kadono, R.F. Kiefl, S.R. Kreitzman, Q. Li, T. Pfiz, T.M. Riseman, H. Zhou, R. Wäppling, S.W. Harris, O. Hartmann, E. Karlsson, R. Hempelmann, D. Richter, T.O. Niinikoski, L.P. Le, G.M. Luke, B.J. Sternlieb, and E.J. Ansaldo: "Diffusion of Charged Impurity ($\mu^+$; muon) in Disordered System", *ibid*.
65) Schin Daté: "Pion Absorption Effects in Ultrarelativistic Heavy Ion Collisions", *ibid*.
66) Shigemi Ohta: "Lattice QCD Simulation on Parallel Supercomputer AP1000", *ibid*.
67) T. Masuda: "The Stopping Power Dependence of the Decay Time of CsI (Tl) Scintillator", *ibid*.
68) A. Ferragut, Y. Gono, T. Murakami, M. Nakajima, H. Seki M. Ogawa, B.J. Min, M. Oshima, T. Morikawa, H. Kusakari, K. Morita, A. Yoshida, and H. Kumagai: "Coulomb Excitation of Unstable Nucleus $^{152}$Dy", *ibid*.
69) H. Orihara, M. Ohura, M. Hosaka, H. Ohnuma, M. Yosoi, T. Niizeki, H. Toyokawa, Y. Tajima, H.Y. Yoshida, C.C. Yoon, S. Kato, H. Shimizu, H. Sakai, H. Okamura, S. Ishida, N. Sakamoto, H. Ohtsu, S. Kubono, M.H. Tanaka, Y. Fuchi, T. Ichihara, and K. Hatanaka: "General Performance Test of RIKEN SMART", *ibid*.
70) K. Tanaka and W. Bentz: "Nuclear Matter Properties Including Higher Order Quantum Corrections", *ibid*.
71) M. Kato, W. Bentz, K. Tanaka, and K. Yazaki: "Neutral Pion Condensation in Quark Matter", *ibid*.
72) M. Kurokawa, T. Motobayashi, T. Nishio, T. Nomura, K. Morita, and A. Yoshida: "Properties of a Position-Sensitive Silicon Strip Detector", *ibid*.

73) M. Suzuki, T. Takahashi, and S. Kubota: "Application of a Scintillation Proportional Imaging Chamber to the Investigation of $\beta\beta$-Decay", *ibid*.
74) M. Tohyama and E. Suraud: "Weighted Particle Method for Solving the Boltzmann Equation", *ibid*.
75) N. Ishida, T. Doke, J. Kikuchi, T. Kashiwagi, K. Masuda, M. Suzuki, T. Takahashi, E. Aprile, and K. Sumorok: "Measurement of Liquid Xenon Scintillation Using Si Photodiodes", *ibid*.
76) N. Iwasa, T. Motobayashi, J. Uchiyama, M. Takano, and K. Ishihara: "A Detector System for Particle Correlation Measurements", *ibid*.
77) S. Mukai, T. Harada, and Y. Akaishi: "Light $\Sigma$-Hypernuclei", *ibid*.
78) S. Hirenzaki and H. Toki: "Formation of Deeply Bound Pionic Atoms", *ibid*.
79) T. Harada and Y. Akaishi: "$\Sigma$-Continuum Spectrum in $^{4}$He (stopped $K^-$, $\pi^+$) Reactions", *ibid*.
80) T. Harada: "$\Sigma$-Hypernuclear Productions by ($K^-$, $\pi$) Reactions on $^{3,4}$He Targets", *ibid*.
81) T. Murakami, Y. Gono, A. Ferragut, M. Nakajima, H. Seki, M. Ogawa, B.J. Min, M. Oshima, T. Morikawa, H. Kusakari, K. Morita, A. Yoshida, and H. Kumagai: "Isomer Search Using a Recoil Mass Separtor", *ibid*.
82) T. Wada, N. Carjan, and Y. Abe: "Induced Fission Studied with Multi - Dimensional Langevin Equation III", *ibid*.
83) Y. Hasegawa, H. Yuta, F. Suekane, T. Kondo, Y. Unno, H. Iwasaki, Y. Sakai, Y. Watanabe, T. Tanimori, K. Kaneyuki, L. Soso, T. Doke, A. Hitachi, T. Ito, E. Shibamura, and K. Masuda: "Liquid Argon Ionization Chamber Using Photoionization Effect", *ibid*.
84) A. Yoshida, T. Fukuda, *et al*.: "Transport Efficiency Measurement of the RIKEN Unstable Beam Line RIPS/GARIS", *ibid*.
85) T. Nakamura, S. Shimoura, T. Kobayashi, N. Inabe, T. Kubo, Y. Watanabe, K. Abe, R.H. Siemssen, I. Tanihata, and M. Ishihara: "Study of the Soft Giant Dipole Resonance of $^{11}$Li", *ibid*.
86) H. Okuno, K. Asahi, M. Ishihara, T. Nakamura, J. Kura, M. Adachi, H. Ueno, H. Sato, T. Ichihara, N. Inabe, T. Kubo, A. Yoshida, Y. Ohkubo, T. Shimoda, N. Takahashi, H. Miyatake, D. Beaumel, D. Mikolas, D.J. Morrissey, W.-D. Schmidt-Ott, and R. Neugart: "G-Factors of Ground States of $^{14}$B and $^{15}$B", *ibid*.
87) M. Ishihara: "Nuclear Physics Studies with RIPS Fragment Separator", APS Workshop on Physics with Radioactive Ion Beams, East Lansing, U.S.A., Oct. (1991).
88) M. Ishihara: "Studies on Exotic Nuclei Using RIPS Spectrometer", Int. Conf. on Exotic Nuclei, South Crimia, U.S.S.R., Oct. (1991).
89) S. Daté: "Particle Production in Nuclear Fragmentation Regions in Ultrarelativistic Heavy Ion Collisions", 9th Int. Conf. on Ultrarelativistic Heavy Ion Collisions, Gatlinburg, U.S.A., Nov. (1991).
90) S. Ohta: "QCD Thermodynamics with Eight Staggered Quark Flavors on $16^3\times$ 6 Lattice", Conf. Lattice Field Theory 'Lattice 91', Tsukuba, Nov. (1991).
91) S. Ohta: "Toward Lattice QCD Simulations on Parallel Supercomputer AP1000", *ibid*.
92) T. Matsuzaki and K. Ishida: "Present Status of RIKEN Muon Channel Construction at RAL", RIKEN Symp. on Muon Science 1991, Wako, Nov. (1991).
93) R. Kadono: "Defect Dynamics Probed by $\mu$SR", *ibid*.
94) T. Harada: "Production and Structure of Light $\Sigma$-Hypernuclei", 20th INS Int. Symp. on Hypernuclear and Strange Particle Phys., Shimoda, Dec. (1991).

### 3. Atomic and solid-state physics

1) I. Shimamura: "Muon-Catalyzed Fusion", Symp. on Theor. of the Dyn. of Chem. Reac. Appl., Atagawa, Jan. (1991).
2) Y. Kanai: "High Energy Ions-Atom Collisions (experiments)", Jt. Semi. on Atomic Phys., Solid State Phys. and Mater. Sci. in the Energy Reg. of Tandem Accel., Tokai, Jan. (1991).
3) E. Yagi: "Study on the State of Hydrogen in Metals by Means of the Channelling Method", RIKEN Symp. on Appl. of Nucl. Solid State Phys. Meth. to Chem., Wako, Feb. (1991).
4) I. Shimamura: "Position-Atom and Positron-Molecule Collisions", 2nd Workshop on the Use of Positrons, Tokyo, Feb. (1991).

5 ) K. Aono, M. Iwaki, and S. Namba: "Tb-ion Implantation Into $CaF_2$ II", 38th Spring Meet. Jpn. Soc. Appl. Phys. (and Related Societies), Hiratsuka, Mar. (1991).
6 ) I. Shimamura: "Mechanisms of the Formation of Exotic Helium, Atoms", Symp. Metastable Antiprotonic Helium Atoms, Tokyo, Mar. (1991).
7 ) I. Shimamura: "Calculations of the Cross Sections for Electron Collisions by the R-Matrix Method", Symp. Gaseous Electronics, Tokyo, Mar. (1991).
8 ) T. Okada, K. Asai, and T. Yamadaya: "Mössbauer Study of $BiPbSr_2FeO_6$",45th Ann. Meet. Jpn. Soc. Phys., Gifu, Mar. (1991).
9 ) Y. Matsuo, H. Maeda, and M. Takami: "Ion Trap and Laser Cooling", RIKEN Symp. on Laser Science (13th), Wako, Mar. (1991).
10) H. A. Sakaue, T. Nabeshima, N. Nakamura, Y. Kanai, I. Yamada, Y. Awaya, S. Ohtani, T. Kambara, H. Suzuki, T. Takayanagi, A. Danjo, M. Yoshino, and K. Wakiya: "Ejected Electron Spectra from Doubly Excited States *(2lnl')* Produced by $C^{6+}$, $B^{5+}$ -He Collisions", 1991 Spring Meet., Phys. Soc. Jpn., Tokyo, Mar. (1991).
11) I. Shimamura and E.A.G. Armour: "Rotational Excitation of Hydrogen Molecules by Positron Impact", *ibid*.
12) R. Katano, Y. Isozumi, S. Ito, and Y. Awaya: "Development of PSPC for Soft-X-Rays (<1keV)", *ibid*.
13) Y. Awaya: "Multiple Inner-Shell Ionization of Atom via the Heavy-Ion Impact", *ibid*.
14) Y. Kanai, T. Kambara, Y. Awaya, T. Niizeki, K. Shima, Y. Zou, and A. Hitachi: "Electron Capture Process of 80 MeV/u $Ar^{18+}$ Ions in a Carbon Foil", *ibid*.
15) Y. Kanai, T. Kambara, Y. Awaya, T. Niizeki, K. Shima, Y. Zou, and A. Hitachi: "Charge-state Distributions of 80 MeV/u Ar Ions after Passage Through a Carbon Foil", *ibid*.
16) Y. Kanai, T. Kambara, Y. Awaya, P. Hvelplund, M. Sataka, M. Imai, H. Tawara, H. Watanabe, K. Kuroki, K. Komaki, and Y. Yamazaki: "Binary Electron Production in $Si^{q+}$+He Collision", *ibid*.
17) Y. Matsuo, H. Maeda, and M. Takami: "RF Trap of Alkaline Earth Ions by Laser Ablation", *ibid*.
18) T. Okada, K. Asai, T. Matsumoto, and R.N. Shelton: "$^{57}$Fe Mössbauer Study of Single Crystal $YBaCu_{3-x}{}^{57}Fe_xO_{7-y}$", Int. Conf. on M²S-HTSC, Kanazawa, Jul. (1991).
19) T. Matsuo, T. Tonuma, H. Kumagai, H. Shibata, and H. Tawara: "Secondary Ions Produced from Frozen $CO_2$ and $H_2O$ Targets in Energetic Heavy Ion Impact", 1st Int. Conf. on Atomic and Molecular Dynamics, Taipei, Taiwan Jul. (1991).
20) T. Tonuma, H. Kumagai, T. Matsuo, and H. Tawara: "Production of Atomic and Molecular Recoil Ions Accompanied by Electron Loss and Capture of Energetic, Heavy Ions", *ibid*.
21) T. Kambara: "K Vacancy Production Probabilities in 31 and 58 MeV $Si^{11+}$ and Ar Collisions", 12th Int. Semi. on Ion-Atom Collis., Gold Coast, Australia, Jul. (1991).
22) Y. Awaya: "Electron Capture and Loss Cross Sections for 26 MeV/u and 77 MeV/u Ar Ions on a Carbon Target", *ibid*.
23) E.A.G. Armour, M. Plummer, and I. Shimamura: "The Calculation of Rotational and Differential Cross Sections for Low Energy $E^+$ -$H_2$ Scattering Using the Kohn Variational Method", 17th Int. Conf. Phys. Elec. Atom. Colls., Brisbane, Australia, Jul. (1991).
24) H. Fukuda, I. Shimamura, L. Végh, and T. Watanabe: "Ionization of Helium by Proton Impact at High Energies", *ibid*.
25) K. Fujima, Y. Naito, F. Koike, T. Watanabe, and Y. Awaya: "The Sublevel Dependence of Inner-Shell Excitation of Projectile Ne by Collisions of Ne Target", *ibid*.
26) N. Toshima and J. Eichler: "Identification of Thomas Peaks in Coupled-Channel Calculations for Charge Transfer", *ibid*.
27) N. Toshima and C.D. Lin: "Comparison of Coherence Parameters of Atomic Excited States Obtained from the CTMC and the Quantal Calculations", *ibid*.
28) T. Kambara, Y. Kanai, Y. Awaya, M. Terasawa, J. Euler, and H. Schmidt-Böcking: "Impact Parameter Dependence of K-X Ray Emission in Ne-Ne

and Si-Ar Collisions", *ibid*.
29) T. Matsuo, T. Tonuma, H. Kumagai, H. Shibata, and H. Tawara: "Multiply Charged Ions and Cluster Ions Produced from Frozen Gas Targets in Energetic Heavy Ion Impact", *ibid*.
30) T. Nabeshima, N. Nakamura, Y. Awaya, A. Danjo, T. Kambara, Y. Kanai, S. Ohtani, H.A. Sakaue, H. Suzuki, T. Takayanagi, K. Wakiya, I. Yamada, and M. Yoshino: "Ejected Electron Spectra from Doubly Excited States *(2lnl')* Produced by $^{11}B^{5+}+He$ Collision", *ibid*.
31) T. Sekioka, M. Terasawa, and Y. Awaya: "Ion Storage in an Electrostatic Ion Trap", *ibid*.
32) Y. Yamazaki, H. Watanabe, T. Azuma, K. Komaki, K. Kuroki, N. Kakutani, H. Tada, K. Kawatsura, Y. Kanai, T. Kambara, and Y. Awaya: "Multiple Ionization of Helium and Neon Atoms in Collision with Relativistic Heavy Ions", *ibid*.
33) T. Tonuma, H. Kumagai, T. Matsuo, H. Shibata, and H. Tawara: "Molecular and Cluster Ions Produced from Frozen $C_2H_2$ Molecules under Energetic, Heavy Ion Impact", 14th Int. Conf. on Atomic Collis. in Solids, Salford, U.K., Jul. (1991).
34) A. Koyama: "Convoy Electron Acceleration", *ibid.* Aug. (1991).
35) H. Ishikawa, A. Misu, A. Koyama, T. Iitaka, M. Uda, and Y. Ohtsuki: "$Z_2$-Dependence of Energy Spectra of Electrons Excited by Grazing Angle Incident Heavy Ions", *ibid*.
36) Y. Awaya: "Present Status of SPring-8", 16th Meet. Soc. for Atomic Colli. Res., Tokyo, Aug. (1991).
37) Y. Matsuo, H. Maeda, and M. Takami: "High Resolution Laser Spectroscopy of Metallic Atoms and Molecules in RF Ion Trap", Int. Symp. on Lasers in Nucl. Phys., Wako, Sep. (1991).
38) E. Yagi: "Behaviour of Kr Atoms in Kr-Implanted Aluminium", 46th Ann. Meet. Phys. Soc. Jpn., Sapporo, Sep. (1991).
39) H. Ishikawa, A. Misu, A. Koyama, T. Iitaka, M. Uda, and Y. Ohtsuki: "$Z_2$-Dependence of Energy Spectra of Electrons Excited by Grazing Angle Incident Heavy Ions", *ibid*.
40) I. Shimamura: "Introduction to the Symposium on 'Exotic Atoms and Related Topics' ", *ibid*.
41) M.R. Harston, I. Shimamura, and M. Kamimura: "Energy Level Shift of $(dt\mu)^+$ in the Molecule $[(dt\mu)^+\text{-}d^+]e^- e^-$", *ibid*.
42) M. Sataka, M. Imai, Y. Yamazaki, K. Komaki, K. Kawatsura, Y. Kanai, and H. Tawara: "Binary Electron Production in Collisions between Heavy-Ion and Helium-Atom (II)", *ibid*.
43) M. Sakurai, T. Sekioka, M. Kimura, H. Yamaoka, S. Ohtani, M. Terasawa, Y. Awaya, and J. Yoda: "Storage of Xe Multiply Charged Ions Created by Synchrotron Radiation", *ibid*.
44) T. Kambara, Y. Awaya, Y. Kanai, M. Ohura, M. Terasawa, T. Sekioka, and J. Euler: "Charge Exchange and K-X-ray Emission Probabilities in 31 MeV $Si^{11+}$ and Ar Collisions", *ibid*.
45) T. Okada, Y. Kobayashi, K. Asai, T. Matsumoto, and R.N. Shelton: "$^{57}$Fe Mössbauer Study of Single Crystal $YBaCu_{3-x}{}^{57}Fe_xO_{7-y}$", *ibid*.
46) T. Sekioka, M. Terasawa, and Y. Awaya: "Characteristics of Kingdon Type Ion Trap III", *ibid*.
47) T. Sekioka, M. Terasawa, and Y. Awaya: "Characteristics of Kingdon Type Ion Trap III", *ibid*.
48) T. Tonuma, H. Kumagai, T. Matsuo, H. Shibata, and H. Tawara: "Ionization Process of Frozen Gas Targets under Energetic Ion Impact", *ibid*.
49) Y. Matsuo, H. Maeda, and M. Takami: "RF Trap of Heavy Metallic Ions from Laser-Produced-Plasma", *ibid*.
50) Y. Yamazaki, K. Komaki, T. Azuma, K. Kuroki, K. Kawatsura, Y. Kanai, T. Kambara, and Y. Awaya: "X Ray Production in 95 MeV/u $Ar^{17+}+C$ Foil Collisions", *ibid*.
51) Y. Zou, T. Kambara, Y. Kanai, Y. Awaya, K. Ando, M. Ohura, and A. Hitachi: "Target Element Dependence of the Intensity Ratio of $K\alpha$ Hypersatellites to Satellites for 50-95 MeV Ar Projectile", *ibid*.
52) A. Koyama: "Convoy Electron Acceleration", RIKEN Symp. on Muon Science 1991, Wako, Nov. (1991).
53) E. Yagi: "Related Research for $\mu$SR of Magnetic Materials, Semiconductors and Metals", *ibid*.
54) I. Shimamura: "Muon-Catalyzed Fusion: Introduction and the Present

Status (Theory)", *ibid*.

55) K. Aono, M. Iwaki, Y. Aoyagi, and S. Namba: "Tb-ion Implantation Into $CaF_2$ III", 52nd Autumn Meet. Jpn. Soc. Appl. Phys. Okayama, Oct. (1991).

56) I. Shimamura: "Reaction Dynamics of Exotic Atoms", Symp. Theor. of Chem. React. — Computational Approaches, Okazaki, Oct. (1991).

57) I. Shimamura: "The Wigner-Eisenbud R-Matrix Theory: Developments in Atomic and Molecular. Physics", Symp. Theor. Methods for Dyn. in Atomic. Mol., and Nucl. Phys., Okazaki, Dec. (1991).

## 4. Radiochemistry, radiation chemistry and radiation biology

1) K. Kimura: "Track-Depth Resolved Luminescence of 5 Mev/amu N-Ions Injected into Near-Liquid and Liquid Helium", 6th Workshop on Radiation Detectors and Their Uses. KEK Tsukuba, Jan. (1991).

2) E. Taniguchi, A. Shinohara, M. Narita, R. Yoshida, M. Furukawa, S. Kojima, H. Kusawake, T. Saito, Y. Ohkubo, F. Ambe, and S. Shibata: "Heavy-Ion Induced Reactions on Cupper in the Intermediate Energy Region", 61st Spring Ann. Meet. of the Chem. Soc. of Jpn., Yokohama, Mar. (1991).

3) H. Kusawake, K. Takesako, T. Saito, A. Yokoyama, M. Kiriu, N. Takahashi, H. Baba, Y. Ohkubo, and A. Shinohara: "Angular Momentum Effect in the $^{40}Ar + ^{141}Pr$ Fusion Reaction System", *ibid*.

4) Y. Itoh and T. Takahashi: "Positron Annihilation Satudy on Defects in LEC-GaAs grown from Ga-rich Melt", 38th Spring Meet. Jpn. Soc. Appl. Phys., Hiratsuka, Mar. (1991).

5) T. Takahashi, F. Yatagai, K. Izumo, and N. Miyabe: "Analytical Formula for the Dose Around the Path of an Ion", *ibid*.

6) Y. Itoh and T. Takahashi: "The Study on Defects in LEC-GaAs by Positron Annihilation", 3rd RIKEN Symp. on Appl. of Hyperfine Tech. to Chem., Wako, Mar. (1991).

7) Y. Ohkubo, Y. Kobayashi, Y. Yanagida, K. Harasawa, T. Okada, M. Iwamoto, K. Asai, and F. Ambe: "TDPAC and Emission Mössbauer Studies on $^{99}Ru$ Arising from $^{99}Rh$ in $\alpha$-$Fe_2O_3$ and $Fe_3O_4$", *ibid*.

8) E. Taniguchi, A. Shinohara, M. Furukawa, S. Kojima, Y. Ohkubo, F. Ambe, T. Saito, K. Takesako, and S. Shibata: "Heavy-Ion Reactions of Copper with Intermediate Energy $^{14}N$ and $^{40}Ar$ Ions", 60th Nat. Meet. Chem. Soc. Jpn. (Spring), Yokohama, Apr. (1991).

9) S. Koike, K. Ando, M. Kimoto, T. Kanai, and H. Ohara: "Tumor Growth Delay Induced by Heavy-Ion Carbon Beams", 30th Meet. of Biol. Division, Jpn. Radiol. Soc., Tokyo, Apr. (1991).

10) S.Y. Chen, S. Ambe, Y. Ohkubo, M. Iwamoto, Y. Kobayashi, N. Takematsu, and F. Ambe: "Study of the Removal Mechanism of Metal Elements from Seawater Using Tracers", 1991 Spring Meet. of the Oceanographical Soc. Jpn., Tokyo, Apr. (1991).

11) T. Takahashi, M. Ueno, T. Kasuya, H. Onishi, and K. Ogura: "Solid State Nuclear Track Detector for the Biological Experiments in IML-1 Space Programme", 9th Track Detector Symp., Tokyo, Apr. (1991).

12) K. Kimura: "Depth-Resolved Luminescence Measurements on Ion-Tracks", Semi. of Atomic Collis. Theory. Tokyo, Jun. (1991).

13) K. Kimura: "Depth-Resolved Dynamics of Excited States of Ion-Track and 100 ps Dexay Measurement with Heavy-Ion Excitation", IAEA Advisory Group Meet., Maryland, U.S.A., Jul. (1991).

14) K. Kimura: "Track-Depth Resolved Luminescence of 5 Mev/amu N-Ions Injected into Near-Liquid and Liquid Helium", 9th Int. Congr. Radiat. Res., Toronto, Canada, Jul. (1991).

15) M. Suzuki, M. Watanabe, K. Suzuki, K. Nakano, and K. Matsui: "Heavy-Ion-Induced Chromosome Break in Syrian Hamster Embryo Cells", *ibid.*

16) S.Y. Chen, S. Ambe, Y. Ohkubo, M. Iwamoto, Y. Kobayashi, N. Takematsu, and F. Ambe: "Adsorption Metal Elements on the Sea Sediments, Hydrated Ferric Oxide and Clay Minerals", 28th Ann. Meet. on Radioisot. in the Phys. Sci. and Industries, Tokyo, Jul. (1991).

17) M. Watanabe M. Suzuki, K. Suzuki, K. Watanabe, and K. Nakano: "Biological Meaning of Chromosomal Abberations Induced by Radiations, In 'Workshop on Development of New Experimental Models in the Life Sciences' ", Progrum

of Sci. and Technol. Agency of Jpn., Tokyo, Jul. (1991).
18) H. Ohara, K. Kanai, K. Ando, K. Kasai, H. Itsukaichi, K. Fukutsu, K. Kawachi, and K. Sato: "Studies on Physics and Biology of Carbon Beams of RIKEN and NIRS", The NIRS Int. Workshop on Heavy Charged Particle Therapy and Related Subjects, Chiba, Jul. (1991).
19) Y. Ohkubo, Y. Kobayashi, K. Asai, T. Okada, K. Harasawa, S. Ambe, S. Shibata, and F. Ambe: "TDPAC and Emission Mössbauer Studies on $^{99}$Ru Arising from $^{99}$Rh in $\alpha$-$Fe_2O_3$, $Fe_3O_4$, and $YBa_2Cu_3O_{7-\delta}$", KUR Symp. on Hyperfine Interactions, Kumatori, Jul. (1991).
20) M. Iwamoto: "Separation of Multitracers by Heating under Reduced Pressure", RIKEN Symp. on New Appl. Tech. of RI Tracers, Wako, Jul. (1991).
21) S. Ambe: "Preparation of Multitracer by RIKEN Ring Cyclotron and Its Applications", *ibid.*
22) S.Y. Chen: "Study of Adsorption of Metal Elements on Clay Minerals and Sea Sediments by using Multitracer", *ibid.*
23) T. Okada, Y. Kobayashi, K. Asai, N. Yamada, and T. Yamadaya: "$^{57}$Fe Mössbauer Studies of $BiPbSr_2FeO_6$", Int. Conf. on M$^2$S-HTSC III, Kanazawa, Jul. (1991).
24) S. Ambe, S.Y. Chen, Y. Ohkubo, Y. Kobayashi, M. Iwamoto, M. Yanokura, and F. Ambe: "Preparation of Radioactive Multitracer Solutions from Au, Ag, and Cu Foils Irradiated with High Energy Heavy Ions", The IUPAC Int. Congr. on Anal. Sci. 1991 (IUPAC-ICAS '91), Makuhari, Aug. (1991).
25) S.Y. Chen, S. Ambe, Y. Ohkubo, M. Iwamoto, Y. Kobayashi, N. Takamatsu, and F. Ambe: "Study of Removal Mechanism of Metal Elements from Seawater Using Multitracers", *ibid.*
26) S.Y. Chen, S. Ambe, Y. Ohkubo, M. Iwamoto, Y. Kobayashi, N. Takematsu, and F. Ambe: "Study of Removal Mechanisms of Metal Elements from Seawater using Radioactive Multitracers", *ibid.*
27) M. Iwamoto, Y. Kobayashi, S.Y. Chen, Y. Ohkubo, S. Ambe, M. Yanokura, A.N. Garg, and F. Ambe: "Separation of Multitracers from Heavy-Ion-Irradiated Targets by Melting under Reduced Pressure", *ibid.*
28) Y. Itoh, H. Murakami, and T. Suzuki: "Defects in Electron or Proton Irradiated Undoped and Si-doped GaAs Studied by Positron Annihilation", 9th Int. Conf. on Positron Annihilation, Szombathely, Hungary, Aug. (1991).
29) Y. Kobayashi, T. Okada, M. Watanabe, M. Katada, H. Sano, and F. Ambe: "$^{99}$Ru Mössbauer Spectroscopy on Salts of Ruthenocene with Halogens", Int. Conf. on the Appl. of the Mössbauer Effect, Nanjing, China, Sep. (1991).
30) Y. Ohkubo, Y. Kobayashi, Y. Yanagida, K. Harasawa, S. Shibata, K. Asai, S. Ambe, M. Iwamoto, T. Okada, and F. Ambe: "Emission Mössbauer and TDPAC Studies on $^{99}$Ru Arising from $^{99}$Rh in $Fe_3O_4$, $\alpha$-$Fe_2O_3$, and $YBa_2Cu_3O_{7-\delta}$", *ibid.*
31) K. Kimura: "Regeneration and Annihilation Processes of Helium Excimers at High Density", Fall Meet. Chem. Soc. Jpn., Sapporo, Sep. (1991).
32) K. Kimura: "Effect of Heavy-Ion Irradiation on the Auger-Free Luminescence of Alkaline Earth Halides", *ibid.*
33) K. Ijiri, K. Tao, and T. Takahashi: "Heavy Ions on the Embryonic Development of *Oryzias letipes*", 5th Annu. Meet. Jpn. Soc. Biol. Sci. Space, Tokyo, Sep. (1991).
34) K. Kimura: "Depth- and Velocity-Resolved Dynamics of Excited States in the Ion-Track in Near Liquid Helium", Seminar on Liquid Radiat. Detectors. Tokyo, Sep. (1991).
35) Y. Itoh, T. Suzuki, and H. Murakami: "Positron Annihilation Study on Defects in Proton Irradiated LEC-GaAs Crystals", 52th Fall Meet. Jpn. Soc. Appl. Phys., Okayama, Oct. (1991).
36) K. Kimura: "Space and Time-Resolved Optical Studies on Ion-Tracks", 34th Conf. Radiat. Chem. Osaka, Oct. (1991).
37) K. Kimura: "Characteristics of Ion-Induced Auger-Free Luminescence", *ibid.*
38) E. Taniguchi, A. Shinohara, M. Furukawa, S. Kojima, Y. Ohkubo, F. Ambe, K. Takesako, T. Saito, and S. Shibata: "Nuclear Reaction Products in the Interaction of Intermediate Energy $^{14}$N, $^{15}$N and $^{40}$Ar Ions-I (Yield and Mean Recoil Ranges for various Reaction Systems)", 35th Symp. on Radio-Chem. Osaka,

Nov. (1991).
39) A. Shinohara, E. Taniguchi, M. Furukawa, S. Kojima, Y. Ohkubo, F. Ambe, K. Takesako, T. Saito, and S. Shibata: "Nuclear Reaction Products in The Interaction of Intermediate Energy $^{14}N$, $^{15}N$ and $^{40}Ar$ Ions-II (The Mechanism of Target Fragmentation)", *ibid*.
40) S. Ambe, S.Y. Chen, Y. Ohkubo, M. Iwamoto, Y. Kobayashi, M. Yanokura, and F. Ambe: "Study on the Selective Adsorption of Metal Elements on $\alpha$-$Fe_2O_3$ Using a Multitracer", *ibid*.
41) S. Ambe, S.Y. Chen, Y. Ohkubo, M. Iwamoto, Y. Kobayashi, F. Ambe, J. Kawarada, T. Yaita, Y. Saito, and K. Kimura: "Study on the Ion Exchange Adsorption of Various Elements on Superacid Resin NAFION Using a Multitracer", *ibid*.
42) S. Ambe, S.Y. Chen, Y. Ohkubo, M. Iwamoto, Y. Kobayashi, M. Yanokura, and F. Ambe: "Production of Multitracers by the RIKEN Ring Cyclotron", *ibid*.
43) M. Iwamoto, Y. Kobayashi, A.N. Garg, S.Y. Chen, S. Ambe, Y. Ohkubo, M. Yanokura, and F. Ambe: "Separation of Multitracers by Heating under Reduced Pressure", *ibid*.
44) H. Kusawake, K, Takesako, T. Saito, A. Yokoyama, M. Kiriu, S. Watanabe, N. Takahashi, H. Baba, Y. Ohkubo, and A. Shinohara: "Angular Momentum Effect in the $^{40}Ar+^{141}Pr$ Fusion Reaction System", *ibid*.
45) Y. Ohkubo, Y. Kobayashi, S. Ambe, T. Okada, F. Ambe, S. Shibata, K. Asai, K. Harasawa, and M. Takeda: "$\gamma$-ray PAC and Emission Mössbauer Spectroscopy of $^{99}Ru$ in YBCO Using $^{99}Rh$ as a Source Nuclide", *ibid*.
46) Y. Ohkubo, Y. Kobayashi, K. Asai, T. Okada, and F. Ambe: "TDPAC and Emission Mössbauer Studies on $^{99}Ru$ Arising from $^{99}Rh$ in $Fe_3O_4$", *ibid*.
47) H. Yoshinaga, Y. Itoh, T. Suzuki, H. Murakami, and R. Iwata: "Defects in Electron Irradiated GaAs Crystals Studied by Positron Annihilation", *ibid*.
48) T. Takatsuji, H. Okumura, T. Takahashi, K. Nakano, and F. Yatagai: "Effect of Spacial Distribution of Energy Absorption to the Chromosome Aberration", 34th Ann. Meet. Radiat. Res. Soc., Tokyo, Nov. (1991).
49) T. Takatsuji, Y. Okumura, T. Takahashi, K. Nakano and F. Yatagai: "Spatial Distribution of Energy Deposistion and Induction of Chromosome Aberrations", *ibid*.
50) S. Ambe, S.Y. Chen, Y. Ohkubo, M. Iwamoto, Y. Kobayashi, and F. Ambe: "Study on the Selective Adsorption of Metal Elements by Using a Multitracer", 40th Annu, Meet. Jpn. Soc. Anal. Chem., Yokohama, Nov. (1991).
51) O. Yatou, E. Amano, and T. Takahashi: "Genetical Effects of Heavy Ion Irradiation in Maize and Soybean", Int. Conf. Evolut. Beam Appl., Takasaki, Nov. (1991).
52) M. Suzuki and T. Takahashi: "A Scintillation Proportional Imaging Chamber and its Application to Heavy Ion Detection", *ibid*.
53) K. Kimura: "Depth-Resolved Dynamics of Excimers Along 4 MeV/amu N-Ion Tracks in Dense Helium", *ibid*.

**5. Material analysis**

1) E. Hayashi, K. Maeda, Y. Sasa, Y. Yokode, and M. Uda: "Multielemental Analysis of Salivary Stone by PIXE", 38th Spring Meet. Jpn. Soc. Appl. Phys., Hatano, Mar. (1991).
2) E. Hayashi, K. Maeda, Y. Sasa, Y. Yokode, and M. Uda: "Application of Particle Induced X-Ray Emission to Biological Materials: Salivary Stone", 2nd Meet. Jpn. Soc. Biomed. Res. on Trace Element, Suita, Jul. (1991).
3) J. Kawai and K. Maeda: "Charge-Transfer Effects in the Cu L$\alpha$ X-Ray Emission Spectra of Copper (II) Compounds", Int. Conf., Materials and Mechanisms of Superconductivity, High Temperature Superconductors, Kanazawa, Jul. (1991).
4) K. Nakajima, M. Sakai, Y. Gohshi, and J. Kawai: "Cu L X-Ray Fluorescence Spectra of High-Tc Superconductors", *ibid*.
5) T. Kanai, A. Fukumura, S. Minohara, M. Sudou, T. Kohno, E. Takada, F. Soga, and K. Kawachi: "Dosimetry of Heavy Ion Beam for Biological Experiments", World Congr. on Med. Phys. and Biol. Eng., Kyoto, Jul. (1991).
6) J. Kawai, K. Maeda, and Y. Gohshi, "L$\alpha$ X-Ray Line Shape of Copper (II) Compounds and Their Covalency", Pacific-Int. Congr. on X-Ray Anal. Methods, Honolulu, U.S.A. Aug. (1991).

7) J. Kawai, K. Maeda, Y. Sasa, M. Takami, T. Hanada, and M. Uda: "Nickel Lα X-Ray Spectra of Nickel Alloys Measured by a High Resolution Particle Induced X-Ray Emission (PIXE) Spectrometer", Int. Congr. on Analytical Sci., Makuhari-Messe, Aug, (1991).
8) K. Nakajima, J. Kawai, M. Skai, and Y. Gohshi: "Copper Lα and Lβ X-Ray Fluorescence Spectra: Intensity Modifications Due to Self-Absorption", *ibid.*
9) K. Maeda, Y. Sasa, and M. Uda: "High Resolution Soft X-Ray Spectrometer Designed for Chemical State Analysis by PIXE", *ibid.*
10) S. Adachi, K. Takemoto, K. Maeda, and Y. Sasa: "PIXE Analyses of Hilar Gland for Evaluation of Individual History of Exposure", 32th Ann. Meet. Jpn. Soc. Air Pollution, Kitakyushu, Oct. (1991).
11) R. Murai, K. Maeda, Y. Sasa, K. Sakurai, S. Yoshimura, and M. Uda: "Non-Destructive Analysis of Archaeological Samples by PIXE Method", 1991 Fall Meet. Jpn. Soc. Appl. Phys., Okayama, Oct. (1991).
12) H. Akiyama, J.S. Zheng, M. Yanokura, and M. Aratani: "Quantitative Analysis of Hydrogen in $EuVO_3$ by Heavy-Ion Beam", 35th Symp. Radiochem., Toyonaka, Nov. (1991).
13) H. Akiyama: "Light-Element Impurities in Standard Matters Studied by Heavy-Ion Rutherford Scattering", *ibid.*
14) T. Ozawa, K. Suzuki, K. Sakamoto, K. Maeda, Y. Sasa, and A. Okada: "Analysis of Chinese Desert Soil by PIXE Method", Ann. Meet. Soc. Environ. Sci., Jpn., Tokyo, Nov. (1991).
15) M. Aratani and M. Yanokura: "All-Direction Simultaneous Rutherford Scattering by Use of Heavy-Ion Beam from RILAC (RIKEN LINEAR ACCELERATOR)", Int. Conf. on Evol. Beam Appl., Takasaki, Nov. (1991).
16) J. Kawai, K. Maeda, M. Takami, and M. Uda: "Are the Transition-Metal L X-Ray Satellites Multiple Ionization Satellites?", RIKEN Symp. on PIXE, Sendai, Nov. (1991).
17) M Aratani: "Volcanic Ejecta from Daisen, Sakurajima, and Unzen", RIKEN Symp. on Heavy-Ion Rutherford Scattering Applied to the Environ. Charact., Wako, Nov. (1991).
18) H. Akiyama: "Impurities in Standard Matters of High-Purity", *ibid.*

# X. LIST OF SEMINARS

1991

**Radiation Lab., Cyclotron Lab., Linear Accelerator Lab.**

1) P. Moller, Los Alamos National Lab. (USA), 5 Jan.
"Spontaneous Fission Property at the End of the Periodic System"

2) Z. Yizhong, Institute of Atomic Energy (China), 9 Jan.
"From Nucleon-Nucleus Optical Potential to Heavy Ion Collisions Based on Walecka Model"

3) C. Glashausser, Rutgers Univ. (USA), 28 Jan.
"The Spin Response of Nuclei to Intermediate Energy Protons"

4) S. Ohta, RIKEN, 6 Feb.
"Finite Temperature Phase Structure of Lattice QCD with Many Flavors"

5) Y. Yamaguchi, Tokai Univ. (Kanagawa), 7 Mar.
"Unstable Particles, Resonances and CP Violation"

6) T. Hatsuda, Univ. of Washington (USA), 13 Mar.
"Strange Quark, Heavy Quarks and Gluon Contents of Light Hadrons"

7) D.L. Olson, LBL (USA), 18 Mar.
"The EOS TPC and the Experimental Program at LBL/Electromagnetic Dissociation of $^{16}O$"

8) T. Ueda, Osaka Univ. (Osaka), 26 Mar.
"Meson-Nucleon-Nucleon Systems"

9) Y. Hirabayashi, Osaka City Univ. (Osaka), 2 Apr.
"Effects of Break-up Channels on $^{11}Li$ Elastic Scattering"

10) T. Cheon, Hosei Univ. (Tokyo), 15 May
"Some Aspects of Quantum Chaology"

11) T. Harada, RIKEN, 29 May
"Production and Structure of Light $\Sigma$-Hypernuclei"

12) B. Tribble, Texas A & M Univ. (USA), 5 June
"MARS and Other New Developments at the TAMU K500"

13) A. Ogloblin, Kurchatov Inst. (USSR), 20 June
"Nuclear Reaction Studies at Kurchatov Institute, Moscow"

14) M. Zhukov, Kurchatov Inst. (USSR), 20 June
"Neutron Halo Structure and Particle Momentum Correlations in $^{6}He$ and $^{11}Li$ Nuclei in the Framework of Three-Body Model"

15) H.G. Bohlen, HMI, Berlin (Germany), 24 June
"Spectroscopy of Light Neutron-Rich Nuclei with Multi-Nucleon Transfer Reactions"

16) Li Zhuxia, Institute of Atomic Energy (China), 10 July
"Transition from Binary Process to Multi-Fragmentation Process in Intermediate Energy Heavy Ion Collisions with QMD"

17) K. Yabana, Niigata Univ. (Niigata), 17 July
"Reactions of $^{11}Li$ at Intermediate Energy Region"

18) H. Ejiri, Osaka Univ. (Osaka), 31 July
"Double $\beta$-Decay and Neutrino"

19) S. Hirenzaki, RIKEN 18 September
"Formation of Deeply Bound Pionic Atoms"

20) D.W. Miller, Indiana Univ. (USA), 16 Oct.
"IUCF Status and Planning for Spectrometer in the Cooler Ring"

21) Nguyen Van Giai, IPN, Orsay (France), 18 Oct.
"Response Functions in Infinite Systems of Fermions"

22) S. Hatori, Kyoto Univ. (Kyoto), 25 Oct.
"Optical research of the recoil mass spectrometer CARP and its application to the measurement of $\beta$-delayed protons from sd-shell proton rich nuclei with $T_z = -3/2$"

23) N. Takigawa, Tohoku Univ. (Miyagi), 26 Oct.
"Collisions of Halo Nuclei"

24) K. A. Gridnev, Sanct Petersburg Univ. (USSR), 6 Nov.
"Nonlinear Effects in Heavy-Ions Collisions"

25) Khin Swe Myint, Hokkaido Univ. (Hokkaido), 7 Nov.
"Double Strangeness Five-Body System"

26) N. Carjan, CEN Bordeaux (France), 12 Nov.
"Time-Dependent Schrödinger Approach to $\alpha$-decay and Related Phenomena"

27) I. Tanihata, RIKEN, 13 Nov.
"Present Status of GSI"

28) K. Tanaka, RIKEN 27 Nov.
"Double Strangeness Five-Body System"

29) G. Bizard, Caen Univ. (France), 4 Dec.
"Measurement of Collective Flow in Ar+Al Reaction between 25 and 85 MeV/nucleon"

30) J. Lukstins, JINR Dubna (USSR), 18 Dec.
"Nuclotron Accelerator and Hypernuclear Physics"

**Atomic Physics Lab.**

1) Y. Azuma, ANL (USA), 8 Jan.
"Atomic Physics with Hard X Rays: Activities in ANL for Next Generation SOR Project"

2) H. Schmidt-Böcking, Univ. of Frankfurt (Germany), 29 Jan.
"Frankfurt ECR-RFQ-Highly Charged Ion Beam Facility"

3) T.E. Åberg, Helsinki Univ. of Technology (Finland), 2 Aug,
"Stusy of Atomic Physics by Synchrotron Radiation"

4) J. F. McCann, Univ. of Durham (U.K.), 18 Sept.
"Ion-Atom Collisions at High Energies"

5) J. Pálinkás, Inst. of Nuclear Research (Hungary), 25 Oct.
"Evidence for Electron-Electron Scattering in Transfer Ionization of He by 1 MeV Proton Impact"

6) H. Knudsen, Univ. of Aarhus (Denmark), 22 Nov.
"Ionization in Antiparticle-Atom Collisions"

**Metal Physics Lab.**

1) V. M. Lobashev, Academy of Science (USSR), 7 Nov.
"Status of Proton Linear Accelerator at Moscow Meson Factory"

2) Y. Yamazaki, KEK (Tsukuba), 7 Nov.
"Proton Linear Accelerator at Japanese Hadron Project"

3) M. Mizumoto JAERI (Tokai), 7 Nov.
"Proton Linear Accelerator at Omega Project"

4) Y. Totsuka, Cosmic Ray Institute (Tokyo), 7 Nov.
"Cold Fusion Experiment at KAMIOKA"

5) K. Nagamine, Univ. of Tokyo (Tokyo) and RIKEN (Wako), 7 Nov.
"$\mu$ CF Related Experiments at KEK and TRIUMF"

6) Y. Akaishi, Hokkaido Univ. (Sapporo), 7 Nov.
"Recent Topics in $\mu$CF Theory"

**Nuclear Chemistry Lab.**

1) O.E. Morgensen, Roskilde Univ. (Denmark), 25 Nov.
"Nanometer Cavities Measured by Positron Annihilation"

**Synchrotron Radiation Facility Design Group**

1) Rarry Terner, Argonne National Laboratory (USA), 6 Feb.
"Design of the Magnet System of APS"

2) T.T. Luong, GANIL (France), 19 Nov.
"Status of GANL and Its Control System"

# XI. LIST OF PERSONNEL

**Steering Committee**

AMBE Fumitoshi 安部文敏
CHIBA Yoshiaki 千葉好明
HANAOKA Fumio 花岡文雄
ISHIHARA Masayasu 石原正泰
KATSUMATA Koichi 勝又紘一
MATSUOKA Masaru 松岡 勝
NAGAMINE Kanetada 永嶺謙忠
TANIHATA Isao 谷畑勇夫
AWAYA Yohko 粟屋容子
INAMURA Takashi 稲村 卓
KAMITSUBO Hiromichi 上坪宏道*
KIRA Akira 吉良 爽
KOHNO Isao 河野 功
MIYAZAWA Yoshitoshi 宮沢佳敏
TAKAMI Michio 高見道生
YANO Yasushige 矢野安重

*Chairman

**Cyclotron Operation and Maintenance Group**

FUJITA Shin 藤田 新
KAGEYAMA Tadashi 影山 正
OGIWARA Kiyoshi 荻原 清
IKEGAMI Kumio 池上九三男
KOHARA Shigeo 小原重夫

**Linac Operation and Maintenance Group**

CHIBA Yoshiaki 千葉好明
IKEZAWA Eiji 池沢英二
MIYAZAWA Yoshitoshi 宮沢佳敏
HEMMI Masatake 逸見政武
KASE Masayuki 加瀬昌之
YANOKURA Minoru 矢野倉 実

## Scientific and Engineering Personnel

**Cosmic Radiation Laboratory**

IMAI Takashi 今井 喬
KOHNO Tsuyoshi 河野 毅

(Visitors)
HASEBE Nobuyuki 長谷部信行 (Fac. Gen. Educ., Ehime Univ.)
KASHIWAGI Toshisuke 柏木利介 (Sci. Eng. Res. Lab., Waseda Univ.)
MUNAKATA Kazuoki 宗像一起 (Fac. Sci., Shinshu Univ.)
MURAKAMI Hiroyuki 村上浩之 (Fac. Sci., Rikkyo Univ.)
NAGATA Katsuaki 永田勝明 (Fac. Eng., Tamagawa Univ.)
NAKAMOTO Atsusi 中本 淳 (Fac. Sci., Rikkyo Univ.)
YANAGIMACHI Tomoki 柳町朋樹 (Fac. Sci., Rikkyo Univ.)

(Student)
KATO Chihiro 加藤千尋 (Fac. Sci. Eng., Saitama Univ.)

**Cyclotron Laboratory**

DATE Shin 伊達 伸
GOTO Akira 後藤 彰
IKEGAMI Kumio 池上九三男
INAMURA Takashi 稲村 卓
FUJITA Shin 藤田 新
HARADA Toru 原田 融
INABE Naoto 稲辺尚人
KAGEYAMA Tadashi 影山 正

KOHARA Shigeo 小原重夫
MORITA Kousuke 森田浩介
NAKAGAWA Takahide 中川孝秀
NAKANISHI Noriyoshi 中西紀喜
OOTA Sigemi 太田滋生
SHIKATA Takashi 四方隆史
YAMAJI Shuhei 山路修平
YOKOYAMA Ichiro 横山一郎
KUBO Toshiyuki 久保敏幸
NAGASE Makoto 長瀬　誠
NAKAJIMA Shunji 中島諄二
OGIWARA Kiyoshi 荻原　清
SAITOU Motozou 斎藤始三
SOUTOME Kouichi 早乙女光一
YANO Yasushige 矢野安重
WAKASUGI Masanori 若杉昌徳

(Visitors)
ABE Yasuhisa 阿部恭久 (Res. Inst. Fundam. Phys., Kyoto Univ.)
ARAI Eiichi 新井栄一 (Res. Lab. Nucl. Reactors, Tokyo Inst. Technol.)
EJIRI Hiroyasu 江尻宏泰 (Dep. Phys., Osaka Univ.)
FUJIOKA Manabu 藤岡　学 (Cyclotron Radioisot. Cent., Tohoku Univ.)
FUJISAWA Takashi 藤沢高志 (Denki Kogyo Co. Ltd.)
FUJITA Yoshitaka 藤田佳孝 (Dep. Phys., Osaka Univ.)
FUKUMOTO Sadayoshi 福本貞義 (KEK)
FURUNO Kohei 古野興平 (Inst. Phys. Tandem Accel. Cent., Univ. Tsukuba)
HASHIMOTO Osamu 橋本　治 (Inst. Nucl. Study, Univ Tokyo.)
HATANAKA Kichiji 畑中吉治 (RCNP, Osaka Univ.)
HATSUKAWA Yuichi 初川雄一 (JAERI, Tokai)
HAYANO Ryugo 早野龍五 (Dep. Phys., Univ Tokyo.)
HIRAO Yasuo 平尾泰男 (Nat. Inst. Radiol. Sci.)
HORIUCHI Hisashi 堀内　昶 (Dep. Phys., Kyoto Univ.)
HORIGUCHI Takayoshi 堀口隆良 (Dep. Phys., Hiroshima Univ.)
IKEDA Kiyomi 池田清美 (Dep. Phys., Niigata Univ.)
IKEDA Nobuo 池田信夫 (Inst. Nucl. Study, Univ. Tokyo)
IKEGAMI Hidetsugu 池上栄胤 (RCNP, Osaka Univ.)
INOUE Makoto 井上　信 (RCNP, Osaka Univ.)
ISHIZUKA Takeo 石塚武男 (Dep. Phys., Saitama Univ.)
IWAMOTO Akira 岩本　昭 (Japan Atomic Energy Res. Inst.)
IWASHITA Yoshihisa 岩下芳久 (Inst. Chem. Res., Kyoto Univ.)
KAMIMURA Masayasu 上村正康 (Dep. Phys., Kyushu Univ.)
KANMURI Tetsuo 冠　哲夫 (Dep. Phys., Osaka Univ.)
KATAYAMA Ichirou 片山一郎 (RCNP, Osaka Univ.)
KATORI Kenji 鹿取謙二 (Dep. Phys., Osaka Univ.)
KATSURAGAWA Hidetsugu 桂川秀嗣 (Dep. Phys., Toho Univ.)
KAWAI Mitsuji 河合光路 (Dep. Phys., Kyushu Univ.)
KOHMOTO Toshiro 河本敏郎 (Dep. Phys., Kyoto Univ.)
KIKUCHI Fumio 菊池文男 (Coll. Arts Sci., Univ. Tokyo)
KOBAYASHI Shinsaku 小林晨作 (Dep. Phys., Kyoto Univ.)
KOHMOTO Susumu 河本　進 (Univ. Electro-Commun.)
KOIZUMI Mitsuo 小泉光生 (Dep. Phys., Hiroshima Univ.)
KONDO Michiya 近藤道也 (RCNP, Osaka Univ.)
KOSAKO Toshiso 小佐古敏荘 (Atomic Energy Res. Cent., Univ. Tokyo)
KUDOU Hisaaki 工藤久昭 (Dep. Chem., Niigata Univ.)
KUROYANAGI Tokihiro 黒柳登喜大 (Dep. Phys., Kyushu Univ.)
LEE Sanmu 李　相茂 (Dep. Phys., Univ. Tsukuba)
MARUMORI Toshio 丸森寿夫 (Dep. Phys., Univ. Tsukuba)
MATSUKI Seishi 松木征史 (RCNP, Osaka Univ.)
MATSUYANAGI Keniti 松柳研一 (Dept. Phys., Kyoto Univ.)
MIURA Iwao 三浦　岩 (RCNP, Osaka Univ.)
MIYAMURA Osamu 宮村　修 (Fac. Sci., Osaka Univ.)
MIYATAKE Hiroari 宮武宇也 (Fac. Sci., Osaka Univ.)
MURAKAMI Tetsuya 村上哲也 (Dep. Phys., Kyoto Univ.)
MURAYAMA Toshiyuki 村山利幸 (Tokyo Univ. Mercantil Marine)

MUROTANI Shin 室谷　心 (Sch. Sci. & Eng., Waseda Univ.)
NAGAI Yasuki 永井泰樹 (Dep. Appl. Phys., Tokyo Inst. Technol.)
NAKAHARA Hiromichi 中原弘道 (Dep. Chem., Tokyo Metrop. Univ.)
NAKAI Koji 中井浩二 (KEK)
NAKAMURA Ichiro 中村市郎 (Dep. Phys., Saitama Univ.)
NAKAMURA Takashi 中村尚司 (Cyclotron Radioisot. Cent., Tohoku Univ.)
NIITA Koji 仁井田浩二 (JAERI, Tokai)
NOMURA Toru 野村　亨 (Inst. Nucl. Study, Univ. Tokyo)
OGATA Hiroshi 小方　寛 (RCNP, Osaka Univ.)
ONISHI Naoki 大西直毅 (Dep. Phys., Coll. Gen. Educ., Univ. Tokyo)
OOSUGA Toshiaki 大須賀敏明 (Coll. Art & Sci., Chiba Univ.)
SAKAI Hideyuki 酒井英行 (RCNP, Osaka Univ.)
SASAGAWA Tatsuya 笹川辰弥 (Dep. Phys., Tohoku Univ.)
SATO Kenichi 佐藤憲一 (Dep. Phys., Tohoku Coll. Pharm.)
SHIKAZONO Naoki 鹿園直基 (JAERI, Tokai)
SHINOZUKA Tsutomu 篠塚　勉 (Cyclotron Radioisot. Cent., Tohoku Univ.)
SUEKI Keisuke 末木啓介 (Inst. Nucl. Study, Univ. Tokyo)
SUGAI Isao 菅井　勲 (Inst. Nucl. Study, Univ. Tokyo)
SUMIYOSHI Hiroyuki 住吉広行 (Matsusho-Gakuen Junior Coll.)
TAGISHI Yoshihiro 田岸義宏 (Tandem Accel. Cent., Univ. Tsukuba)
TAKADA Kenjiro 高田健次郎 (Dep. Phys., Kyushu Univ.)
TAKEMASA Tadashi 武政尹士 (Dep. Phys., Saga Univ.)
TAKIGAWA Noboru 滝川　昇 (Dep. Phys., Tohoku Univ.)
TAMAGAKI Ryozo 玉垣良三 (Dep. Phys., Kyoto Univ.)
TANAKA Jinichi 田中仁市 (Inst. Nucl. Study, Univ. Tokyo)
TOHYAMA Mitsuru 遠山　満 (Dep. Phys., Kyorin Univ.)
TOMIMASU Takio 富増多喜夫 (Electro Tech. Lab.)
TORIYAMA Tamotsu 鳥山　保 (Dep. Appl. Phys., Tokyo Inst. Technol.)
TSUNEMOTO Hiroshi 恒元　博 (Natl. Inst. Radiol. Sci.)
VALLI K. (Dep. Phys., Jyvaskyla Univ., Finland)
WADA Michiharu 和田道治 (Dep. Phys., Tohoku Univ.)
WAKAI Masamichi 若井正道 (Dep. Phys., Osaka Univ.)
YAMANOUCHI Mikio 山内幹雄 (Tandem Accel. Cent., Univ. Tsukuba)
YAMAZAKI Takashi 山崎　魏 (RCNP, Osaka Univ.)
YOSHIDA Nobuaki 吉田宣章 (Dep. Phys., Univ. Tokyo)
YOSHIDA Shiro 吉田思郎 (Dep. Phys., Tohoku Univ.)
YOSHINAGA Naotaka 吉永尚孝 (Comput. Cent., Univ. Tokyo)

(Students)
FUKASHIRO Yasuyuki 深代康之 (Dep. Phys., Tohoku Univ.)
HAMADA Shingo 濱田真悟 (Dep. Nucl. Eng., Kyoto Univ.)
HIRASAWA Junichirou 平澤淳一郎 (Dep. Appl. Phys., Tokyo Inst. Technol.)
KOBAYASHI Takayuki 小林貴之 (Dep. Chem., Tokyo Metrop. Univ.)
KOSUGA Hiroyuki 小菅洋之 (Dep. Phys., Toho Univ.)
KURAMOTO Takeshi 蔵本武志 (Dep. Phys., Univ Tokyo.)
MARUYAMA Toshiki 丸山敏毅 (Dep. Phys., Kyoto Univ.)
NAKAOKA Masaya 中岡正哉 (Dep. Phys., Saitama Univ.)
NISHINAKA Ichiro 西中一郎 (Dep. Chem., Tokyo Metrop. Univ.)
OGAWA Izumi 小川　泉 (Dep. Phys., Kyoto Univ.)
SUNAOSHI Hitoshi 砂押　仁 (Dep. Phys., Tohoku Univ.)
SUZUKI Katsuhiro 鈴木勝博 (Dep. Phys., Kyoto Univ.)

**Linear Accelerator Laboratory**

CHIBA Toshiya 千葉利哉
CHIBA Yoshiaki 千葉好明

FUJIMAKI Masaki 藤巻正樹
HIRENZAKI Satoru 比連崎 悟
KOBAYASHI Toshio 小林俊雄
MIYAZAWA Yoshitoshi 宮沢佳敏
TANIHATA Isao 谷畑勇夫
WADA Takahiro 和田隆宏
YOSHIDA Koichi 吉田光一
HEMMI Masatake 逸見政武
KASE Masayuki 加瀬昌之
KUMAGAI Hidekazu 熊谷秀和
SUZUKI Takeshi 鈴木 健
TONUMA Tadao 戸沼正雄
YANOKURA Minoru 矢野倉 実

(Visitors)
FUJIWARA Ichiro 藤原一郎 (Inst. Atomic Energy, Kyoto Univ.)
FUJIWARA Mamoru 藤原 守 (RCNP, Osaka Univ.)
HIRATA Daisy (CTA, Inst. Estudos Avancados, Brasil)
ITO Noriaki 伊藤憲昭 (Dep. Cryst. Mater., Nagoya Univ.)
KATORI Kenji 鹿取謙二 (Fac. Sci., Osaka Univ.)
KIKUCHI Jun 菊地 順 (Sci. Eng. Res. Lab., Waseda Univ.)
KIMURA Kikuo 木村喜久雄 (Fac. Sci., Kyushu Univ.)
OBUTI Marcia M. (Sao Paulo Univ.; Saitama Univ.)
SAKAI Hideyuki 酒井英行 (Fac. Sci., Univ. Tokyo)
SUDA Toshimi 須田利美 (Fac. Sci., Tohoku Univ.)
SUGAWARA Masahiko 菅原昌彦 (Fundam. Sci., Chiba Inst. Technol.)
YAMAGUCHI Hiromi 山口裕美 (Sci. Eng. Res. Lab., Waseda Univ.)

(Students)
ABE Kenichi 阿部健一 (Fac. Sci., Osaka Univ.)
ITO Tatsuya 伊藤達也 (Sci. Eng. Res. Lab., Waseda Univ.)

**Radiation Laboratory**

FERRAGUT Alain
ICHIHARA Takashi 市原 卓
IZUMO Koichi 出雲光一
NOMURA Izumi 野村和泉
TAKAHASHI Tan 高橋 旦
TENDO Yoshihiko 天道芳彦
YOSHIDA Atsushi 吉田 敦
GONO Yasuyuki 郷農靖之
ISHIHARA Masayasu 石原正泰
KONNO Satoshi 金野 智
SUZUKI Masayo 鈴木昌世
TANAKA Kazuhiro 田中和宏
WATANABE Yasushi 渡邉 康

(Visitors)
ABE Yasuhisa 阿部恭久 (Res. Inst. Fundam. Phys., Kyoto Univ.)
ADACHI Minoru 足立 實 (Dep. Appl. Phys., Tokyo Inst. Technol.)
ANDO Yoshiaki 安藤嘉章 (Dep. Phys., Rikkyo Univ.)
APRILE Elena (Columbia Univ., U.S.A)
ASAHI Koichiro 旭 耕一郎 (Fac. Sci., Tokyo Inst. Technol.)
DOKE Tadayoshi 道家忠義 (Sci. Eng. Res. Lab., Waseda Univ.)
ENDO Saburo 遠藤三郎 (Fac. Eng., Sci. Univ. Tokyo)
FUCHI Yoshihide 渕 好秀 (Inst. Nucl. Study, Univ. Tokyo)
FUJIOKA Manabu 藤岡 学 (Dep. Phys., Tohoku Univ.)
FUKUDA Mitsunori 福田光順 (Fac. Sci., Osaka Univ.)
FUKUDA Tomokazu 福田共和 (Inst. Nucl. Study, Univ. Tokyo)
GUY Y. Bizard (CAEN Univ., France)
HASEGAWA Takeo 長谷川武夫 (Inst. Nucl. Study, Univ. Tokyo)
HASHIZUME Akira 橋爪 朗 (Japan Atomic Energy Relations Organization)
HITACHI Akira 月出 章 (Sci. Eng. Res. Lab., Waseda Univ.)
ICHIMURA Munetake 市村宗武 (Coll. Arts Sci., Univ. Tokyo)
IEKI Kazuo 家城和夫 (Fac. Sci., Rikkyo Univ.)
IJIRI Kenichi 井尻憲一 (Radioisot. Cent., Univ. Tokyo)

ISHIDA Nobumichi 石田伸道 (Seikei Univ.)
ISHIKAWA Masanobu 石川雅紀 (Tokyo Univ. Fisheries)
IWASAKI Hiroyuki 岩崎博行 (KEK)
KANEYUKI Kenji 金行健治 (Fac. Sci., Tokyo Inst. Technol.)
KASAGI Jirota 笠木治郎太 (Fac. Sci., Tokyo Inst. Technol.)
KASAI Kiyomi 笠井清美 (Natl. Inst. Radiol. Sci.)
KATO Seigo 加藤静吾 (Fac. Educ. Yamagata Univ.)
KATORI Kenji 鹿取謙二 (Fac. Sci., Osaka Univ.)
KAWAKAMI Hirokane 川上宏金 (Inst. Nucl. Study, Univ. Tokyo)
KAWASHIMA Hideo 川島英雄 (Inst. Nucl. Study, Univ. Tokyo)
KIKUCHI Jun 菊池 順 (Sci. Eng. Res. Lab., Waseda Univ.)
KIM Hee J. (Oak Ridge National Lab., U.S.A.)
KIM Jong-Chan 金 鐘賛 (Seoul Univ., Korea)
KITAHARA Yoshitaka 北原義孝 (Hoya Corp.)
KITAO Kensuke 喜多尾憲助 (Natl. Inst. Radiol. Sci.)
KOMAGATA Kazuyuki 駒形和行 (Asahi Glass Co., Ltd.)
KONDO Takahiko 近藤敬比古 (KEK)
KUBONO Sigeru 久保野 茂 (Inst. Nucl. Study, Univ. Tokyo)
KUBOTA Shinzou 窪田信三 (Fac. Sci., Rikkyo Univ.)
KUSAKARI Hideshige 草刈英榮 (Fac. Educ., Chiba Univ.)
LEE Sang Mu 李 相茂 (Inst. Phys., Univ. Tsukuba)
MAEDA Kazushige 前田和茂 (Coll. Gen. Educ., Tohoku Univ.)
MASUDA Kimiaki 増田公明 (Saitama Coll. Health)
MATSUDA Takeshi 松田 武 (KEK)
MIN Byung-Joo 閔 丙珠 (Korea Atomic Energy Res. Inst., Korea)
MIYATAKE Hiroari 宮武宇也 (Coll. Gen. Educ., Osaka Univ.)
MORINAGA Haruhiko 森永晴彦 (Sec. Phys. Tech. Univ. München)
MOTOBAYASHI Tohru 本林 透 (Fac. Sci., Rikkyo Univ.)
MURAKAMI Takeshi 村上 健 (Dep. Phys., Tokyo Inst. Technol.)
NAGAI Yasuki 永井泰樹 (Fac. Sci., Tokyo Inst. Technol.)
NAGASHIMA Yasuo 長島泰夫 (Dep. Phys., Univ. Tsukuba)
NAKAJIMA Mitsuo 中島充夫 (Graduate Sch. Nagatsuda, Tokyo Inst. Technol.)
NAKAYAMA Shintaro 中山信太郎 (Coll. Gen. Educ., Tokushima Univ.)
NGUYEN Van Giai (Paris Univ., France)
NIIZEKI Takashi 新関 隆 (Fac. Sci., Tokyo Inst. Technol.)
OGAWA Masao 小川雅生 (Graduate Sch. Nagatsuda, Tokyo Inst. Technol.)
OHNUMA Hajime 大沼 甫 (Fac. Sci., Tokyo Inst. Technol.)
OKAMURA Hiroyuki 岡村弘之 (Fac. Sci., Univ. Tokyo)
ORIHARA Hikonojo 織原彦之丞 (Cyclotron and Radioisot. Cent., Tohoku Univ.)
OSHIMA Masumi 大島眞澄 (Japan Atomic Energy Res. Inst.)
OSHIRO Takashi 尾城 隆 (Tokyo Univ. Fisheries)
OYAIZU Michihiro 小柳津充広 (Inst. Nucl. Study, Univ. Tokyo)
Qu Yun-he 屈 云河 (Inst. High Energy Phys., Chinese Academy of Sciences, China)
RUAN (GEN) Jian-zhi 阮 建治 (Dep. Phys., Rikkyo Univ.)
SAKAGUCHI Harutaka 坂口治隆 (Dep. Phys., Kyoto Univ.)
SAKAI Mitsuo 坂井光夫 (Inst. Nucl. Study, Univ. Tokyo)
SAKAI Yoshihide 堺井義秀 (KEK)
SATO Hiroshi 佐藤 竑 (Seikei Univ.)
SCHMIDT-OTT Wolf-Dieter (II Phys. Inst., Univ. Goettingen, Germany)
SHIBAMURA Eido 柴村英道 (Saitama Coll. Health)
SHIMIZU Hajime 清水 肇 (Fac. Educ., Yamagata Univ.)
SHIMODA Tadashi 下田 正 (Coll. Gen. Educ., Osaka Univ.)
SHIMOURA Susumu 下浦 享 (Fac. Sci., Univ. Tokyo)
SHIRATO Shoji 白土釥二 (Dep. Phys., Rikkyo Univ.)
SHIROYAMA Masaki 城山正樹 (Asahi Glass Co., Ltd.)
SUEKANE Fumihiko 末包文彦 (Fac. Sci., Tohoku Univ.)

SUGAWARA Masahiko 菅原昌彦 (Chiba Inst. Technol.)
TAKADA Eiichi 高田栄一 (Natl. Inst. Radiol. Sci.)
TAKAHASHI Noriaki 高橋憲明 (Coll. Gen. Educ., Osaka Univ.)
TAKIGAWA Noboru 滝川 昇 (Dep. Phys., Tohoku Univ.)
TANAKA Masahiko 田中雅彦 (Inst. Nucl. Study, Univ. Tokyo)
TANIMORI Tohru 谷森 達 (Fac. Sci., Tokyo Inst. Technol.)
TAO Kazuyuki 垰 和之 (Radioisot. Cent., Univ. Tokyo)
TOKI Hiroshi 土岐 博 (Dep. Phys., Tokyo Metrop. Univ.)
TOYOKAWA Hidenori 豊川秀訓 (Inst. Phys., Univ. Tsukuba)
UNNO Yoshinobu 海野義信 (KEK)
WATANABE Yasushi 渡辺靖志 (Fac. Sci., Tokyo Inst. Technol.)
YAMAYA Takashi 山屋 堯 (Dep. Phys., Tohoku Univ.)
YATO Osamu 矢頭 治 (Inst. Radiat. Breeding, NIAR)
YOSHIDA Kazuo 吉田和夫 (Hoya Corp.)
YOSHINAGA Naotaka 吉永尚孝 (Saitama Univ.)
YOSOI Masaru 與曽井 優 (Fac. Sci., Tokyo Inst. Technol.)
YUTA Haruo 湯田春雄 (Fac. Sci., Tohoku Univ.)
ZHANG Yu-hu 張 玉虎 (Inst. Mod. Phys., Acad. Sin., China)

(Students)
AKEBOSHI Yoshihiro 明星慶洋 (Fac. Sci., Tokyo Inst. Technol.)
BEN Sei 卞 正 (Sch. Sci. Eng., Waseda Univ.)
CHAE Soo-Joh (Seoul Univ., Korea)
DOI Masashi 土井雅史 (Fac. Sci., Tokyo Inst. Technol.)
FURUTAKA Kazuyoshi 古高和禎 (Fac. Sci., Tokyo Inst. Technol.)
FUTAMI Yasuyuki 二見康之 (Inst. Phys., Univ. Tsukuba)
HASEGAWA Yoji 長谷川庸司 (Fac. Sci., Tohoku Univ.)
HASUIKE Katsuhito 蓮池勝人 (Sch. Sci. Eng., Waseda Univ.)
HONJO Yoshio 本城義夫 (Inst. Phys., Univ. Tsukuba)
HOSAKA Masahito 保坂将人 (Cyclotron and Radioisot. Cent., Tohoku Univ.)
ICHIGE Masayuki 市毛正之 (Sch. Sci. Eng., Waseda Univ.)
ISHIDA Satoru 石田 悟 (Fac. Sci., Univ. Tokyo)
ITO Ken 伊藤 研 (Sch. Sci. Eng., Waseda Univ.)
ITO Tomoyuki 伊藤朋行 (Sci. Eng. Res. Lab., Waseda Univ.)
IWASA Naohito 岩佐直仁 (Dep. Phys., Rikkyo Univ.)
IZUMI Hideaki 出水秀明 (Fac. Sci., Tokyo Inst. Technol.)
KOGANEMARU Kenichi 小金丸健一 (Graduate Sch. Nagatsuda, Tokyo Inst. Technol.)
KURA Jumpei 蔵 純平 (Fac. Sci., Tokyo Inst. Technol.)
KUROKAWA Meiko 黒川明子 (Dep. Phys., Rikkyo Univ.)
KUWAHARA Kōta 桑原宏太 (Sch. Sci. Eng., Waseda Univ.)
LU Jun 呂 駿 (Inst. Phys., Univ. Tsukuba)
MIZOTA Takeshi 溝田武志 (Inst. Phys., Univ. Tsukuba)
MORIKAWA Tsuneyasu 森川恒安 (Fac. Sci., Hiroshima Univ.)
NAGANUMA Masayuki 永沼正行 (Graduate Sch. Nagatsuda, Tokyo Inst. Technol.)
NAKAI Yoichi 中井陽一 (Dep. Phys., Kyoto Univ.)
NAKAMURA Takashi 中村隆司 (Fac. Sci., Univ. Tokyo)
NUNOYA Yoshihiko 布谷嘉彦 (Dep. Phys., Rikkyo Univ.)
OHNISHI Hiroko 大西裕子 (Coll. Agric. Vet. Med., Nihon Univ.)
OHNO Mariko 大野真理子 (Radioisot. Cent., Univ. Tokyo)
OHSAKI Yoshinori 大嵜美紀 (Graduate Sch. Nagatsuda, Tokyo Inst. Technol.)
OHTSU Hideaki 大津秀暁 (Fac. Sci., Univ. Tokyo)
OKUNO Hiroki 奥野広樹 (Fac. Sci., Univ. Tokyo)
PU Y.H. 蒲 越虎 (Inst. Phys., Univ. Tsukuba)
SAKAMOTO Naruhiko 坂本成彦 (Fac. Sci., Univ. Tokyo)
SATO Hiromi 佐藤広海 (Fac. Sci., Tokyo Inst. Technol.)
SAWADA Shinya 澤田真也 (Dep. Phys., Kyoto Univ.)

SEKI Hiroyuki 関　宏之 (Graduate Sch. Nagatsuda, Tokyo Inst. Technol.)
SEKINE Takashi 関根　隆 (Fac. Sci., Tokyo Inst. Technol.)
SHIMADA Kenji 島田健児 (Fac. Sci., Tokyo Inst. Technol.)
SOSO Lucio (Fac. Sci., Tokyo Inst. Technol.)
TAJIMA Yasuhisa 田島靖久 (Fac. Sci., Tokyo Inst. Technol.)
TERANISHI Takashi 寺西　高 (Fac. Sci., Univ. Tokyo)
TOMITA Shigeo 富田成夫 (Inst. Phys., Univ. Tsukuba)
YAJIMA Akira 矢嶋　亨 (Fac. Sci., Tokyo Inst. Technol.)
YAMAZAKI Hiroshi 山崎弘詞 (Fac. Sci., Tokyo Inst. Technol.)
YASHIRO Yoshinori 矢代義徳 (Fac. Sci., Tokyo Inst. Technol.)
YOON Chong Cheor 尹　鐘哲 (Fac. Sci., Tokyo Inst. Technol.)
YOSHIDA Hiroshi 吉田浩司 (Fac. Sci., Tokyo Inst. Technol.)
YOSHIDA Kenichiro 吉田健一郎 (Dept. Phys. Kyoto Univ.)
YUASA-NAKAGAWA Keiko 中川恵子 (Inst. Phys., Univ. Tsukuba)

**Atomic Physics Laboratory**

ANDO Kozo 安藤剛三
AWAYA Yohko 粟屋容子
FUKUDA Hiroshi 福田　宏
HARSTON Michael R.
KAMBARA Tadashi 神原　正
KANAI Yasuyuki 金井保之
KRAVIS Scott
NISHIDA Masami 西田雅美
OHURA Masaki 大浦正樹
SHIMAMURA Isao 島村　勲

(Visitors)
AZUMA Toshiyuki 東　俊行 (Coll. Arts Sci., Univ. Tokyo)
DANJO Atsunori 壇上篤徳 (Dep. Phys., Niigata Univ.)
DePAOLA Brett D. (Kansas State Univ., U.S.A.)
EULER Joachim (Univ. Frankfurt, Germany)
FUJIMA Kazumi 藤間一美 (Fac. Eng., Yamanashi Univ.)
HARA Shunsuke 原　俊介 (Inst. Phys., Univ. Tsukuba)
HINO Ken-ichi 日野健一 (Univ. Electro-Commun.)
HITACHI Akira 月出　章 (Inst. Sci. Technol., Waseda Univ.)
ISHII Keishi 石井慶之 (Dep. Eng. Sci., Kyoto Univ.)
ISOZUMI Yasuhito 五十棲泰人 (Inst. Chem. Res., Kyoto Univ.)
ITO Shin 伊藤　真 (Radioisot. Res. Cent., Kyoto Univ.)
ITOH Yoh 伊藤　陽 (Fac. Sci., Josai Univ.)
IWATA Yasushi 岩田康嗣 (Coll. Arts Sci., Univ. Tokyo)
KARASHIMA Shosuke 唐島照介 (Dep. Electron. Eng., Tokyo Univ. Sci.)
KAWATSURA Kiyoshi 川面　澄 (Kyoto Inst. Technol.)
KNUDSEN Helge (Univ. Aarhus, Denmark)
KOBAYASHI Nobuo 小林信夫 (Dep. Phys., Tokyo Metrop. Univ.)
KOIKE Fumihiro 小池文博 (Sch. Med., Kitasato Univ.)
KOIZUMI Tetsuo 小泉哲夫 (Dep. Phys., Rikkyo Univ.)
KOMAKI Ken-ichiro 小牧研一郎 (Coll. Arts Sci., Univ. Tokyo)
KUROKI Kenro 黒木健郎 (Natl. Res. Inst. Police Sci.; Inst. Phys. Coll. Arts Sci., Univ. Tokyo)
MATSUO Takashi 松尾　崇 (Dep. Pathol., Tokyo Med. Dent. Univ.)
MATSUZAWA Michio 松澤通生 (Dep. Eng. Phys., Univ. Electro-Commun.)
McCANN Jim (Univ. Durham, U.K.)
MIZOGAWA Tatsumi 溝川辰巳 (Nagaoka Coll. Technol.)
MUKOYAMA Takeshi 向山　毅 (Inst. Chem. Res., Kyoto Univ.)
OHTANI Shunsuke 大谷俊介 (Inst. Laser Sci., Univ. Electro-Commun.)
OKUNO Kazuhiko 奥野和彦 (Dep. Phys., Tokyo Metrop. Univ.)
PÁLINKÁS József (Inst. Nucl. Phys. (ATOMKI), Hungarian Academy Sci., Hungary)
SATO Hiroshi 佐藤浩史 (Dep. Phys., Ochanomizu Univ.)

SCHMIDT-BÖCKING Horst (Univ. Frankfurt, Germany)
SEKIOKA Tsuguhisa 関岡嗣久 (Himeji Inst. Technol.)
SHIBATA Hiromi 柴田裕実 (Res. Cent. Nucl. Sci. Technol., Univ. Tokyo)
SHIMA Kunihiro 島 邦博 (Tandem Accel. Cent., Univ. Tsukuba)
SHIMAKURA Noriyuki 島倉紀之 (Gen. Educ. Dep., Niigata Univ.)
SUZUKI Hiroshi 鈴木 洋 (Dep. Phys., Sophia Univ.)
TAWARA Hiroyuki 俵 博之 (Natl. Inst. Fusion Sci.)
TERASAWA Mititaka 寺沢倫孝 (Himeji Inst. Technol.)
TSURUBUCHI Seiji 鶴淵誠二 (Fac. Technol., Tokyo Univ. Agric. Technol.)
WAKIYA Kazuyoshi 脇谷一義 (Dep. Phys., Sophia Univ.)
YAMAZAKI Yasunori 山崎泰規 (Coll. Arts Sci., Univ. Tokyo)
YOSHINO Masuhiro 吉野益弘 (Lab. Phys., Shibaura Inst. Technol.)
ZOU Yaming (Jiao Tong Univ., China)

(Students)
KAKUTANI Nobukazu 角谷暢一 (Coll. Arts Sci., Univ. Tokyo)
KASUGA Masahito 春日真人 (Coll. Arts Sci., Univ. Tokyo)
NABESHIMA Takayuki 鍋島貴之 (Dep. Phys., Sophia Univ.)
NAKAMURA Nobuyuki 中村信行 (Dep. Phys., Sophia Univ.)
SAKAUE Hiroyuki 坂上裕之 (Dep. Phys., Sophia Univ.)
TADA Hiroshi 多田 宏 (Coll. Arts Sci., Univ. Tokyo)
WATANABE Hiroshi 渡部比呂志 (Coll. Arts Sci., Univ. Tokyo)
YAMAGATA Masahiro 山形昌広 (Coll. Arts Sci., Univ. Tokyo)

**Metal Physics Laboratory**

ISHIDA Katsuhiko 石田勝彦
KOYAMA Akio 小山昭雄
MATSUSHITA Akira 松下 明
NAGAMINE Kanetada 永嶺謙忠
KADONO Ryosuke 門野良典
MATSUNO Shun-ichi 松野俊一
MATSUZAKI Teiichiro 松崎禎市郎
YAGI Eiichi 八木栄一

(Visitors)
AKAISHI Yoshinori 赤石義紀 (Fac. Sci., Hokkaido Univ.)
FUJIOKA Manabu 藤岡 学 (Cyclotron Radioisot. Cent., Tohoku Univ.)
JONES E. Steven (Dep. Phys. and Astronomy, Brigham Young Univ., U.S.A.)
KAMIMURA Masayasu 上村正康 (Fac. Sci., Kyushu Univ.)
KUMAGAI Kenichi 熊谷健一 (Fac. Sci., Hokkaido Univ.)
MINAMISONO Tadanori 南園忠則 (Fac. Sci., Osaka Univ.)
MIYAKE Yasuhiro 三宅康博 (Meson Sci. Lab., Univ. Tokyo)
MORITA Masato 森田正人 (Fac. Sci., Jyosai Univ.)
TANAKA Koki 田中幸基 (Nippon Steel Corp.)
TORIKAI Eiko 鳥養映子 (Fac. Eng., Yamanashi Univ.)
WATANABE Tsutomu 渡部 力 (ICU)

(Student)
STRASSER Patrick (Fac. Eng., Univ. Tokyo)

**Magnetic Materials Laboratory**

OKADA Takuya 岡田卓也

**Plasma Physics Laboratory**

OYAMA Hitoshi 大山 等
YANO Katsuki 矢野勝喜

(Visitor)
SAKAMOTO Yuichi 坂本雄一 (Electr. Eng. Dep., Toyo Univ.)

**Semiconductor Laboratory**

(Visitor)
AONO Keiko 青野桂子 (Coll. Lib. Arts, Kitasato Univ.)

**Inorganic Chemical Physics Laboratory**

AMBE Shizuko 安部静子
MAEDA Kuniko 前田邦子
KAWAI Jun 河合 潤
TAKAMI Michio 高見道生

(Visitors)
ISHII Keizo 石井慶造 (Cyclotron Radioisot. Cent., Tohoku Univ.)
KUSUYAMA Hiroyuki 楠山弘之 (Saitama Med. Sch.)
SASA Yoshihiko 佐々嘉彦 (Lab. Materials Sci. Technol., Waseda Univ.)
UDA Masayuki 宇田応之 (Dep. Mater. Sci. Eng., Waseda Univ.)

**Nuclear Chemistry Laboratory**

AMBE Fumitoshi 安部文敏
ITOH Yoshiko 伊東芳子
KOBAYASHI Yoshio 小林義男
ARATANI Michi 荒谷美智
IWAMOTO Masako 岩本正子
OHKUBO Yoshitaka 大久保嘉高

(Visitors)
ASAI Kichizo 浅井吉蔵 (Univ. Electro-Commun.)
BABA Hiroshi 馬場 宏 (Fac. Sci., Osaka Univ.)
CHEN Shaoyong 陳 紹勇 (South China Sea Inst. Oceanol., China)
FURUKAWA Michiaki 古川路明 (Fac. Sci., Nagoya Univ.)
IMAI Masato 今井正人 (Komatsu Electronic Metals Co., Ltd.)
KIMURA Kan 木村 幹 (Coll. Sci. Eng., Aoyamagakuin Univ.)
KOJIMA Sadao 小島貞男 (Nucl. Med. Cent., Aichi Medical Univ.)
MURAKAMI Hideoki 村上英興 (Tokyo Gakugei Univ.)
NOZAKI Tadashi 野崎 正 (Sch. Hygienic Sciences., Kitasato Univ.)
OKADA Shigenobu 岡田繁信 (R/D Eng., Shimazu Corp.)
OOHIRA Shigeo 大平重男 (Nikkei Techno Res. Co., Ltd.)
SAITO Kazuo 斉藤和男 (Toshiba Corp., R & D Cent.)
SAITO Tadashi 斎藤 直 (Fac. Sci., Osaka Univ.)
SHIBATA Seiichi 柴田誠一 (Inst. Nucl. Study, Univ. Tokyo)
SHINOHARA Atsushi 篠原 厚 (Fac. Sci., Nagoya Univ.)
SUGAI Isao 菅井 勲 (Inst. Nucl. Study, Univ. Tokyo)
TAZAKI Kazue 田崎和江 (Fac. Sci., Shimane Univ.)
YOKOYAMA Akihiko 横山明彦 (Fac. Sci., Osaka Univ.)
YUKAWA Masae 湯川雅枝 (Nat. Inst. Radiol. Sci.)
ZHANG Guilin 張 桂林 (Shanghai Inst. Nucl. Res., China)

(Students)
AKIYAMA Hiroshi 秋山 浩 (Dep. Metal Eng., Shibaura Inst. Technol.)
KAWARADA Jun 河原田 淳 (Coll. Sci. Eng., Aoyamagakuin Univ.)
KIRIU Masaru 桐生 大 (Fac. Sci., Osaka Univ.)
KURACHI Junji 倉知淳史 (Fac. Sci., Nagoya Univ.)
NAKAMURA Jin 中村 仁 (Univ. Electro-Commun.)
SHINTAI Junichirou 新帯淳一郎 (Fac. Sci., Nagoya Univ.)

TAKESAKO Kazuhiro 竹迫和浩 (Fac. Sci., Osaka Univ.)
TANIGUCHI Eugene 谷口勇仁 (Fac. Sci., Nagoya Univ.)
WATANABE Seiya 渡辺誠也 (Fac. Sci., Osaka Univ.)
YANO Daisaku 矢野大作 (Fac. Sci., Osaka Univ.)
YOSHINAGA Hiroshi 吉永 宏 (Dep. Metal Eng., Shibaura Inst. Technol.)

**Chemical Dynamics Laboratory**

KIMURA Kazuie 木村一宇

(Visitor)
ITO Yasuo 伊藤泰男 (Res. Cent. Nucl. Sci. Technol., Univ. Tokyo)

**Cellular Physiology Laboratory**

HANAOKA Fumio 花岡文雄
KITAYAMA Shigeru 北山 滋
YATAGAI Fumio 谷田貝文夫

(Visitors)
ANDO Kohichi 安藤興一 (Natl. Inst. Radiol. Sci.)
BAVERSTOCK Keith F. (Radiobiol. Unit, Med. Res. Counc., U.K.)
FUKUMURA Akifumi 福村明史 (Natl. Inst. Radiol. Sci.)
FURUSAWA Yoshiya 古沢佳也 (Natl. Inst. Radiol. Sci.)
HASHIMOTO Shozo 橋本省三 (Fac. Med., Keio Univ.)
HOSHINO Kazuo 星野一雄 (Natl. Inst. Radiol. Sci.)
ITOH Hisao 伊東久夫 (Fac. Med., Keio Univ.)
KANAI Tatsuaki 金井達明 (Natl. Inst. Radiol. Sci.)
KAWACHI Kiyomitsu 河内清光 (Natl. Inst. Radiol. Sci.)
KAWASHIMA Katsuhiro 川島勝弘 (Natl. Inst. Radiol. Sci.)
KIMOTO Masafumi 木元正史 (Natl. Inst. Radiol. Sci.)
KOBAYASHI Yasuhiko 小林泰彦 (Japan Atomic Energy Res. Inst.)
KOHNO Toshiyuki 河野俊之 (Natl. Inst. Radiol. Sci.)
KOIKE Sachiko 小池幸子 (Natl. Inst. Radiol. Sci.)
KOJIMA Eiichi 小島栄一 (Natl. Inst. Radiol. Sci.)
KOSAKA Toshifumi 小坂俊文 (Dep. Vet. Radiol., Nihon Univ.)
McINTYRE Cindy L. (Radiobiol. Unit, Med. Res. Counc., U.K.)
MINOHARA Shinichi 簑原伸一 (Natl. Inst. Radiol. Sci.)
NAKAI Hirokazu 中井弘和 (Dep. Agric., Shizuoka Univ.)
OHARA Hiroshi 大原 弘 (Dep. Gen. Cul., Okayama Univ.)
SOGA Fuminori 曽我文宣 (Inst. Nucl. Study, Univ. Tokyo)
SUDO Michio 須藤美智雄 (Natl. Inst. Radiol. Sci.)
TAKATUJI Toshihiro 高辻俊宏 (RI Cent., Nagasaki Univ.)
TANAKA Kaoru 田中 薫 (Natl. Inst. Radiol. Sci.)
TSUBOI Atsushi 坪井 篤 (Natl. Inst. Radiol. Sci.)
WATANABE Hiroshi 渡辺 宏 (Japan Atomic Energy Res. Inst.)
WATANABE Masami 渡辺正己 (RI Cent., Fac. Med., Yokohama City Univ.)
YAMASHITA Shoji 山下昌次 (Natl. Saitama Hospital)

(Student)
SUZUKI Masao 鈴木雅雄 (RI Cent., Fac. Med., Yokohama City Univ.)

**Safety Control Affairs Office**

KAGAYA Satoru 加賀屋 悟
KATOU Hiroko 加藤博子

KATOU Takeo 加藤武雄
MATSUZAWA Yasuhide 松沢安秀
SAKAMOTO Ichiro 坂本一郎
USUBA Isao 薄葉 勲
KOHNO Isao 河野 功
MIYAGAWA Makoto 宮川真言
SHINOHARA Shigemi 篠原茂己

**Surface Characterization Center**

IWAKI Masaya 岩木正哉
SAKAIRI Hideo 坂入英雄
KOBAYASHI Takane 小林 峰

**Laser Science Research Group**

NAMBA Susumu 難波 進 (Osaka Univ.)

**Synchrotron Radiation Facility Design Group**

BE Suck Hee 裵 碩喜
HARA Masahiro 原 雅弘
KAWASHIMA Yoshitaka 川島祥孝
MASUDA Takemasa 増田剛正
MOTONAGA Shoushichi 元永昭七
OHASI Yuuji 大橋裕二
OIKAWA Yoshifumi 老川嘉郁
SAKAUE Hiroyuki 坂上裕之
TAKEBE Hideki 武部英樹
TANAKA Hitoshi 田中 均
WATANABE Kowashi 渡邊 剛
EGO Hiroyasu 恵郷博文
KAMITSUBO Hiromichi 上坪宏道
KUMAGAI Noritaka 熊谷教孝
MATSUI Sakuo 松井佐久夫
NAKAMURA Takeshi 中村 剛
OHNISHI Junichi 大西純一
OUCHI Tetsuya 大内徹也
SASAKI Sigeki 佐々木茂樹
TAKESHITA Isao 竹下勇夫
WADA Takeshi 和田 雄
YANO Katsuki 矢野勝喜

(Visitors)
HANASAKA Takao 花坂孝雄 (Shimazu Co.)
HIRANO Yoshiki 平野芳樹 (Anelva Co.)
INOUE Koji 井上浩司 (Kobe Steel, Ltd.)
KUMAGAI Keiko 熊谷桂子 (Fuji Electric Co., Ltd.)
SHIMIZU Akira 清水 明 (Irie Koken Co., Ltd.)
TAKADA Takeo 高田武雄 (Shin-Etsu Chemical Co., Ltd.)
TAKAHASHI Sunao 高橋 直 (Kobe Steel, Ltd.)
XU Choyin 徐 朝銀 (Univ. Sci. Tech. China)
YAMAMOTO Yuuichi 山本雄一 (Mitsubishi Electric Co.)
YOKOUCHI Shigeru 横内 茂 (Osaka Vacuum Ltd.)

(Students)
HAYASHI Katuyuki 林 勝之 (Coll. Hum. Sci., Nihon Univ.)
ONODERA Masahiro 小野寺正博 (Coll. Hum. Sci., Nihon Univ.)
SAITOH Hiroaki 斉藤広明 (Coll. Hum. Sci., Nihon Univ.)
SONO Fumitake 園 文武 (Coll. Hum. Sci., Nihon Univ.)

# AUTHOR INDEX

**RIKEN Accelerator Progress Report**

**理化学研究所加速器年次報告　第25巻**（1991）

印　刷　平成4年（1992）3月20日
発　行　平成4年（1992）3月29日
発行者　理化学研究所
代表者　小田稔
〒351-01　埼玉県和光市広沢2番1号
電話（0484）62－1111
編集者　理化学研究所加速器研究施設運営委員会

印刷所　勝美印刷株式会社
〒112　東京都文京区小石川1丁目3番7号

定価 5,000円
（消費税別）

理化学研究所
埼玉県　和光市　広沢